Modeling of Downstream and Direct Plasma Systems for Highly Selective and Anisotropic Etching

by

Shuo Huang

A dissertation submitted in partial fulfillment
of the requirements for the degree of
Doctor of Philosophy
(Electrical Engineering)
in the University of Michigan
2019

Doctoral Committee:

Professor Mark J. Kushner, Chair
Professor John Foster
Professor Yogesh B. Gianchandani
Professor Brian Gilchrist
Professor Wei Lu

Shuo Huang

shuoh@umich.edu

ORCID iD: 0000-0002-3055-646X

Dedication

This dissertation is dedicated to my wife, Zhou Zhang, and my daughter, Vivian.

Acknowledgements

When I started my Ph.D. career at the University of Michigan in August 2014, I was told that pursing a Ph.D. degree is once-in-a-lifetime experience and I should treasure every moment whether it is enjoyable or painful. Up to now, almost five years has passed and I am approaching the fulfillment of my study. Looking back to this fantastic journey, I would like to greatly appreciate all the help I received from the people surrounding me. Without their generous and tremendous amount of help, my Ph.D. career and this thesis would not be possible.

First, I would like to thank my advisor, Prof. Mark J. Kushner. It is my huge honor to be one of his students. He not only instructed me on how to investigate the world of plasma, but also taught me how to interact with the world of people as an engineer. I have gained unforgettable five-year practice and experience, which have certainly set up a solid foundation for my future career. The encouragement and enlightenment I received from my advisor have definitely equipped me with the confidence and courage to confront the adventures and challenges in my future life.

Second, I would like to thank my thesis committee members, Prof. John Foster, Prof. Wei Lu, Prof. Brian Gilchrist and Prof. Yogesh B. Gianchandani, for their patient and detailed guidance on my research. I would like to thank my project collaborators and paper coauthors: Sang Ki Nam, Vladimir Volynets, Sangheon Lee, In-Cheol Song, Siqing Lu and Seungbo Shim (Samsung Electronics); Prof. Jonathan Tennyson and James Hamilton (University College London); Prof. Wei Lu, Prof. Zhengya Zhang, Mohammed Zidan, YeonJoo Jeong,

Thomas Chen, Teyuh Chou, John Seymour and Dongxiao Yan (University of Michigan). I have investigated the state-of-the-art topics, practiced research and communication skills and learned invaluable knowledge through collaborations with them. Participating in multiple projects with different degrees of involvement is also a great experience which will certainly benefit me in the long run.

Third, I would like to thank all the members in our research group that I have worked together with during the past five years: Yiting Zhang, Peng Tian, Seth Norberg, Wei Tian, Chad Huard, Michael Logue, Soheila Mohades, Guy Parsey, Aram Markosyan, Juliusz Kruszelnicki, Steven Lanham, Amanda Lietz, Chenhui Qu, Xifeng Wang and Jordyn Polito. I was so lucky to be in a group with talented colleagues sitting around me every day. Communications and discussions with them make puzzles clear and problems solved more efficiently. I have learned so much from them, both in knowledge and life wisdoms. Also, I would like to thank Julia Falkovitch-Khain, who is so professional in all kinds of administrative procedures and travel arrangements and enabled me to fully concentrate on the research.

Finally, I would like to thank my family. I would like to thank my parents for raising me up and supporting me on pursing my goals. They advised me to choose electrical engineering as my undergraduate major, which finally led me here. Most importantly, I would like to thank my wife, Zhou Zhang, for all the contributions she has made to me and our family. Without her dedication, my Ph.D. degree would not be possible. I was granted with incredible luckiness to meet her when we were both studying in Shanghai in spring 2012, incredible luckiness to get married with her in fall 2014, and incredible luckiness to have our lovely daughter Vivian in winter 2017. With my wife and daughter together, I will firmly march forward in the future.

Table of Contents

List of Figures

List of Tables

List of Appendices

List of Acronyms

0-d	0-dimensional
2-d	2-dimensional
3-d	3-dimensional
ALE	Atomic Layer Etching
AR	Aspect Ratio
ARDE	Aspect Ratio Dependent Etching
CCP	Capacitively Coupled Plasma
CD	Critical Dimension
CDU	Critical Dimension Uniformity
CER	Contact Edge Roughness
CW	Continuous Wave
DBD	Dielectric Barrier Discharge
dc	direct current
DC	Duty Ratio
DF-CCP	Dual-frequency Capacitively Coupled Plasma
eMCS	electron Monte Carlo Simulation
EED	Electron Energy Distribution
EETM	Electron Energy Transport Module
EMM	Electromagnetic Module
FKPM	Fluid Kinetics Poisson Module
HAR	High Aspect Ratio
HPC	High Performance Computing
HPEM	Hybrid Plasma Equipment Model
IAD	Ion Angular Distribution
ICP	Inductively Coupled Plasma
IEAD	Ion Energy and Angular Distribution
IED	Ion Energy Distribution
LER	Line Edge Roughness
LTP	Low Temperature Plasma
MCFPM	Monte Carlo Feature Profile Model
MD	Molecular Dynamic
MF-CCP	Multi-frequency Capacitively Coupled Plasma

MPS	Memristor-based PDE Solver
MPU	Memory Processing Unit
NEAD	Neutral Energy and Angular Distribution
ODE	Ordinary Differential Equation
OES	Optical Emission Spectroscopy
ONO	Oxide-Nitride-Oxide
OSiO	Oxide-Silicon-Oxide
PCMCM	Plasma Chemistry Monte Carlo Module
PDE	Partial Differential Equation
PPA	Pulsed-period-averaged
PR	Photoresist
PRF	Pulse Repetition Frequency
PSI	Plasma Surface Interaction
rf	radio frequency
RPS	Remote Plasma Source
SF-CCP	Single-frequency Capacitively Coupled Plasma
S-G	Scharfetter-Gummel
SKM	Surface Kinetics Module
SOR	Successive-over-Relaxation
SSBM	Surface Site Balance Model
SVR	Surface-to-Volume Ratio
TF-CCP	Tri-frequency Capacitively Coupled Plasma

Abstract

The pursuit of higher integration has brought the semiconductor industry into the realm of nanoelectronics (e.g., 5 nm gate-all-round FET) and 3-dimensional structures (e.g., vertical NAND), which has imposed increasing challenges on selectivity and anisotropy in plasma etching processes. Etch properties (e.g., etch rate, surface profile and selectivity) result from surface reactions between solid materials and gas phase species whose fluxes and energy distributions are ultimately determined by the controlling properties of plasma reactors. Optimizing etching performance is therefore achieved through innovative design of plasma reactors and expert control of plasma operating conditions.

In this thesis, integrated reactor and feature scale modeling was performed for investigating and optimizing plasma etching process as well as assisting in reactor design. This was accomplished by developing reaction mechanisms and implementing acceleration techniques in the Hybrid Plasma Equipment Model (HPEM) to analyze plasma properties and in the Monte Carlo Feature Profile Model (MCFPM) to predict etch profiles. Gas phase reaction mechanisms of $Ar/NF_3/O_2$ and $NF_3/H_2/O_2$ mixtures were developed and validated with optical emission spectroscopy (OES) measurements. Surface reaction mechanisms of SiO_2 etching by $Ar/C_4F_8/O_2$ mixtures were developed and validated with experimentally obtained etch results.

Highly selective etching of Si_3N_4 was achieved using a downstream etch system which isolates the remote plasma source for radical production from the downstream chamber for material processing by long flow distance and showerheads. Plasma is mainly confined to the

source region with a weak ion-ion plasma sustained downstream. Neutral radicals are produced in the source region and flow downstream for material processing. In addressing limitations of the original system, optimizations were proposed for improving etch performances, such as use of a plenum for improving uniformity of etch rates across the wafer, use of pulsed power for increasing radical densities while decreasing ion density downstream, and use of multiple sources or multiple gas inlets for favorable and high-efficiency production of etchants. The principle goal of this process was to customize the reaction pathways and preferentially deliver energy into desirable reactions. This goal was accomplished based on developing and implementing comprehensive reaction mechanisms.

Highly anisotropic etching of high aspect ratio (HAR) features in SiO_2 with aspect ratios (ARs) up to 80 was simulated using multi-frequency capacitively coupled plasmas sustained in $Ar/C_4F_8/O_2$ mixtures. Key features in HAR etching such as mask erosion, bowing, tapered etch front and edge roughening were addressed with updates made in the MCFPM. The fundamental limiting factor in HAR etching was found to be the decreasing delivery of energy and species to the etch front with increasing AR. This decrease was mainly due to the energy and angular distributions of incident species and their scattering at sidewalls resulting in conduction limits and energy loss. Feature-to-feature variation becomes prominent as the critical dimensions (CDs) and pitch decrease to a few to tens of nm. These variations mainly result from the randomness in the fluxes of particles into adjacent features rather than reactor scale non-uniformities. This variation is enhanced by the charging of the features resulting in electric potential skewing and profile tilting, which can be optimized by elevating the bias power and ion energy, at the tradeoff of CD loss.

Chapter 1 Introduction

1.1 Low Temperature Plasmas in Semiconductor Processing

Plasma is one of the four fundamental states of matter, with solid, liquid and gas being the other three. Plasma is defined as a quasi-neutral gas of charged and neutral particles which exhibits collective behavior.[1] More than 99% of the matter in the visible universe is in the plasma state. Plasmas appear in nature in various forms, such as lightning, ionosphere and solar wind. Plasmas can also be artificially produced by applying external power, such as plasma displays, fluorescent lamps and ion thrusters. There is an enormous range of densities and temperatures for both space and laboratory plasmas, which are identified in Fig. 1.1.[2] Among the wide operation range for plasmas, the subject of this dissertation is the low temperature plasmas and their use for material processing.

The low temperature plasmas (LTPs) are partially ionized gases in bounded systems under non-equilibrium conditions.[3] LTPs are characterized by electron temperature $T_e \approx 1 - 10$ eV and electron density $n_e \approx 10^8 - 10^{13}$ cm^{-3}, with gas pressure $p \approx 1$ mTorr – 1 Torr and gas temperature $T_{gas} \approx 300 - 1{,}000$ K. LTPs are used in material processing in which the feedstock gases are electrically decomposed into positive ions, chemically reactive etchants and deposition precursors, which then transport to the substrate for surface reactions. Due to the non-equilibrium conditions ($T_e >> T_{ion} > T_{gas}$, where T_{ion} is the ion temperature), the LTPs mainly deliver energetic ions and reactive neutral radicals to the surface with only negligible amount of heating to the surface.

Use of LTPs in semiconductor processing is indispensable for manufacturing the very large scale integrated circuits and pursuing the Moore's law.[4] Materials and surface structures can be fabricated that are not attainable by any other commercial methods and the surface properties of the materials can be modified in unique ways. Before LTPs became widely used in semiconductor industry, wet etching in solution provided high selectivity but isotropic profiles due to the same etch rate in all directions. As the feature sizes decreased and the aspect ratios (etch depth divided by feature size) increased due to increasing demand on circuit integration, LTPs began to be used since the 1970's which can achieve anisotropic profiles and high ARs by controlling the plasma operation conditions (e.g., gas mixtures, pressure and bias power) as shown in Fig. 1.2.[5,6]

The LTPs have been enabling the feature sizes to shrink to below 10 nm and the structures to vertically scale so as to increase the bit density while maintaining the cost efficiency, which in turn impose new challenges in plasma processing to meet the demand of ever-shrinking size and dramatically increasing aspect ratio (AR) of the features to above 100 as shown in Fig. 1.3.[7] Fabrication of vertically stacked gate structures requires etching of high aspect ratio (HAR) holes through hundreds of oxide-nitride-oxide (ONO) layers. Developments in 3D-NAND and DRAM technologies have continued to scale through 3D integration and advanced pitch multiplication schemes.[8,9] The ability to make perfectly anisotropic profiles and maintain critical dimension uniformity (CDU) through controlling the production and transport of ions and neutrals in LTPs is highly desired in high-volume 3D manufacturing.

Fundamental mechanisms of LTPs and materials processing using LTPs with the focus on selective and anisotropic etching are computationally investigated in this dissertation. A brief overview of the plasma sources and basic plasma physics is in Chapter 1.2. A description of

plasma etching is in Chapter 1.3. The reactor scale modeling of the plasma sources and the feature scale modeling of the plasma etching processes are described in Chapters 1.4 and 1.5, respectively.

1.2 Plasma Sources

In the semiconductor industry, the LTPs are usually produced in plasma sources by applying external power into the gases confined in vacuum chambers. In all LTP sources produced for semiconductor processing, the separation of the plasma into bulk and sheath regions is an important phenomenon. The plasmas are mainly sustained by electron impact ionization in the bulk region, where charge neutrality is maintained. The electrons are accelerated by the electric field to gain energy until colliding with the neutral species, shown in Fig. 1.4(a). When an electron collides with a molecule, a specific reaction (e.g., excitation, dissociation and ionization) may occur depending on the energy of the incident electron and the cross section which is a quantity expressing the likelihood of an interaction event between two particles. The cross section set for electron impact O_2 molecule is shown in Fig. 1.4(b).[10] The cross section of elastic scattering has no threshold while the cross section of each inelastic collision has a threshold. Usually excitation (rotational, vibrational and electronic) has lower threshold, ionization has higher threshold and dissociation has medium threshold.

Due to the larger mobility of electrons than ions, a self-restoring force is established within the plasma to main the charge neutrality, resulting in oscillation of the electrons around the heavy ions with the plasma frequency

$$\omega_p = \sqrt{\frac{q^2 n_e}{\varepsilon_0 m_e}}, \qquad (1.1)$$

where q is the electron charge, n_e is the electron density and m_e is the electron mass. The average distance that the electrons travel during this oscillation is

$$\lambda_D = \sqrt{\frac{\varepsilon_0 T_e}{q^2 n_e}}, \qquad (1.2)$$

where T_e is the electron temperature. This is called the Debye length which represents the longest distance over which the plasma can be non-neutral.

1.2.1 Basic Plasma Sources

In semiconductor industry, these are two widely used low temperature plasma sources, i.e., inductively coupled plasma (ICP) which is excited by spiral coils and capacitively coupled plasma (CCP) which is excited between two parallel electrodes. These two plasmas are direct plasma systems in which the wafer is placed on the substrate in the reactor and directly exposed to the ions and radicals generated in the plasma. Optimization of basic plasma sources (e.g., remote plasma source, pulsed power plasmas, magnetron enhanced plasmas and multi-frequency capacitively coupled plasmas) enables desirable features for certain applications.

In a typical ICP reactor shown in Fig. 1.5(a), the rf power applied to the spiral antenna on top of the dielectric window creates time-varying electromagnetic fields in the reactor. The electrons are accelerated back and forth by the oscillating electric field in the azimuthal direction. The electrons are accelerated until colliding with the neutrals or phase change of the electric field. The electron loss to the surface is small as the direction of the electron acceleration is parallel to the chamber walls. In addition, power delivered into the plasma is not partitioned into ion acceleration as in CCP reactors. These features enable ICP to produce higher plasma densities more efficiently than CCP. In certain applications where ion energies are crucial to surface processes, additional rf bias is applied to the substrate which accelerate ions to the surface.

In a typical CCP reactor shown in Fig. 1.5(b), plasma discharge is generated between two parallel electrodes. The electrons are accelerated back and forth by the oscillating electric field that is perpendicular to the electrode. This configuration benefits from the optimal uniformity over the large area of electrodes due to uniform distributions of electric field between the two electrodes. The applied power also establish a high sheath potential which accelerates the positive ions from the plasma to the wafer surface, enabling surface reactions such as physical sputtering and chemically enhanced reactive etching. Besides, the bombardment of ions to the electrodes creates secondary electron emissions from the surface, which can significantly contribute to the ionization in CCP.

1.2.2 Remote Plasma Source

Remote plasma sources (RPS) are being developed for isotropic etching and thin film deposition in microelectronics fabrication.[11,12] The RPS is a component in the downstream plasma systems in which the source of plasmas are separated with the wafer processing chamber. The RPS produces fluxes of radicals for etching and surface passivation while minimizing the damage that may occur by charging, energetic ion bombardment and UV/VUV radiation.[13] By using long flow distance, grids or other discriminating barriers between the basic plasma sources (e.g., ICP and CCP) and the substrate, the flux of charged particles reaching the downstream etching chamber is small and the substrate is exposed dominantly to neutrals. RPS was first used from the late 1980s for isotropic etching processes such as chamber cleaning, resist stripping and highly selective etching.[14-16] With the continuing miniaturization of features, the RPS was recently used in state-of-the-art processes such as atomic layer deposition [17,18] and selective etching for fabricating nanowires[19,20].

Due to absence of energetic ions that can produce physical sputtering, RPS provides a

mechanism for high etch selectivity based only on chemical mechanisms. For example, high etch selectivity of Si_3N_4 over SiO_2 can be achieved by increasing the flow rate of O_2 in a RPS sustained in NF_3/O_2 [21] or by increasing the flow rate of N_2 through a RPS sustained in $CF_4/O_2/N_2$ [22]. This selectivity results from enhanced utilization of O and NO radicals in the etching of Si_3N_4 compared to SiO_2. RPS has also been implemented for processing materials such as low-k (porous SiOCH) interlayer dielectrics [23] and high-k (Al_2O_3 and SiC) gate dielectrics [24]. These remote processes minimize surface roughness and mixing typically produced by energetic ion bombardment. Recently, 3-dimensional structures such as stacked planar NAND [25] and vertical NAND [26] have been proposed to increase device density for flash memories. In these structures, RPS can be used to selectively etch the oxide and nitride in the horizontal direction between layers in the stack.

1.2.3 Multi-frequency Capacitively Coupled Plasma Source

Multi-frequency capacitively coupled plasmas (MF-CCPs) are intended to provide independent control of the fluxes of ion and neutral radical, and the ion energy and angular distributions (IEADs) incident onto the wafer in microelectronics fabrication. Due to the close coupling of ion flux and ion energy to the wafer in single-frequency capacitively coupled plasmas (SF-CCP), MF-CCPs are motivated to overcome this weakness and achieve large dynamic range available for tuning IEADs for process optimization.[27,28]

In SF-CCPs, adjusting the bias power and frequency is the main method for controlling IEADs to match different process requirements. The typical dual-frequency capacitively coupled plasma (DF-CCP) uses a low frequency (a few MHz or lower) to control the IEADs and a high frequency (tens of MHz or higher) to control the magnitude of the ion and radical fluxes.[29] However, even these choices of frequencies often result in the low frequency effecting the

magnitude of ion fluxes and the high frequency affecting the IEADs.[30] Therefore, MF-CCPs were proposed for further optimization in industrial applications by decreasing the low frequency (hundreds to thousands of Hz) and increasing the high frequency (hundreds of MHz) while adding a medium frequency (several to tens of MHz).[31,32] With a large separation between the low and high frequency, the ion flux is dominantly controlled by the low frequency and the IEADs are dominantly controlled by the high frequency. The medium frequency power serves as an extra knob for tuning the IEADs with a large dynamic range.

1.3 Plasma Etching

The pursuit of higher integration has brought more stringent requirements on plasma etching by LTPs, which cannot be satisfied by the traditional reactive ion etching. Several state-of-the-art plasma etching techniques have been developed. Atomic layer etching has been proposed for accurate control of the etching process at atomic scale by alternating two cycles (surface modification and ion bombardment).[33] Multi-frequency plasmas have been proposed to decouple the electron heating and ion acceleration with large dynamic range available for tuning IEADs for process optimization.[27,28] Pulsed power plasmas and direct current (dc) augmented plasmas have been proposed to more efficiently generate radicals than continuous-wave excited plasmas and mitigate the effect of surface charging.[34,35] All of these novel techniques are basically achieved through accurately manipulating the LTPs and controlling the fluxes, energies, angles and synergy of different etching species reaching the wafer.

The LTPs produce a variety of species, which can be classified into two categories: energetic ions and neutral radicals. These species transport from the bulk plasma to the surface where plasma surface interactions occur. The kinetic energy of the incident ions and the

chemical reactivity of the radicals enable efficient plasma processing of the surface materials. In the etching of poly-Si and dielectrics (e.g., SiO_2 and Si_3N_4) by LTPs, the balance of ion energy and radical exposure allows for etch mechanisms to be tailored for specific materials, providing selective etching of one material over another. Besides, the anisotropic nature of the IEADs and the isotropic flux of neutral radicals provide a method to tune the directionality of the etch process.

When an energetic ion strikes the surface, its kinetic energy can be transferred to the atoms at the surface. With high energy (tens to hundreds of eV) after acceleration by the sheath potential, the ion bombardment can efficiently weaken or even break the chemical bonds between the atoms in the solid, resulting in surface activation or direct sputtering of the atoms from the surface. The ion bombardment can also promote the mixing of atoms at the surface, which improves the quality of the thin film deposition.

When a reactive radical (particularly halogen radicals such as F, Cl, HF and CF_x) reaches the surface, it can bind with the target surface atom and form strong covalent bond. In terms of different radicals and surface materials, the radicals can weaken (CF_x radicals at SiO_2 surface), break or replace (F radicals at Si surface) the binding between the target surface atom and the surrounding or underlying lattice, resulting in surface passivation by forming new bonds between the target atom and the incident radical or chemical removal of surface atoms.

Combining the energetic ions and reactive radicals significantly boost the etch yield and etch rate, which was experimentally demonstrated by Coburn and Winters in 1979.[36] They found that the etch rate of silicon with the simultaneous use of XeF_2 gas and Ar^+ ions was about ten times larger than the etch rates with the use of individual species alone, as shown in Fig. 1.6. This increase in etch rate can be directly attributed to the reduction of surface binding energy

when the silicon becomes fluorinated by thermal decomposition of the XeF_2 on the surface. This synergistic effect of increased etch yield when a passivating radical is combined with ion bombardment has become referred to as chemically enhanced reactive etching, or chemical sputtering.

Due to the significant role of ions and radicals in plasma processing, their controllable production and transport is highly desired for process optimization, especially for achieving HAR features while maintaining critical dimensions (CDs) through anisotropic etching and conformal deposition. In this regard, controlling the IEADs to the wafer surface is required.

Different gases and gas mixtures are used for etching specific materials. Si etching is usually achieved by using halogen-containing plasmas sustained in gases such as F_2, Cl_2, Br_2, SF_6 and NF_3.[37-39] Isotropic etching of Si occurs as a result of chemical reactions between Si surface sites and F, Cl and Br atoms to form volatile products. To achieve anisotropic etching of Si, it is necessary to add species (e.g., oxygen species) which can coat or passivate the sidewall and inhibit lateral etching.[40,41] SiO_2 etching is usually achieved by using fluorocarbon plasmas sustained in gas mixtures such as $Ar/C_4F_8/O_2$, CF_4/O_2 and CH_2F_2/O_2.[42-44] The C_xF_y species produced through electron impact reactions passivate the oxide surface and form a polymer film on top of the oxide. Unlike processes that rely on films on the sidewall to suppress etching, the polymer film in oxide etching supplies reactants which are activated by ion bombardment and improves etching selectivity of SiO_2 over Si. As to other materials such as low-k dielectrics (e.g., porous SiOCH) usually used for insulating layer, and high-k dielectrics (e.g., Al_2O_3 and SiC) usually used for transistor gate, fluorocarbon containing plasmas are used to etch these materials. The polymer films that form at the surface during the etching play the

similar role as in oxide etching, which is controlling the etch rate of the film as well as allowing the etching to be selective to other materials.[45,46]

1.3.1 Ion Energy and Angular Distributions

In typical LTPs reactors, the wafer is placed on a substrate which is connected with a rf bias, V_{RF}, as shown in Fig. 1.7. Due to the asymmetry of reactor design in which the surface area of the powered wafer chuck is smaller than the remaining surface area (usually grounded) in the reactor, a dc bias voltage, V_{dc}, appears through imbalance in charging the blocking capacitor. Therefore, the potential drop in the sheath fluctuates between the minimum, Φ_0 (sheath potential at grounded surface), and the maximum, $\Phi_0 + V_{rf} + V_{dc}$, resulting in ions accelerated to the surface with a range of energy and angular distributions.

For the ion energy distributions (IEDs), one critical parameter determining the shape of the IEDs is τ_{ion}/τ_{RF}, where τ_{ion} is the ion transit time through the sheath which primarily depends on ion mass and τ_{rf} is the period of the rf power.[47] As the sheath potential is the potential drop between the plasma and the biased electrode, it is time dependent on the instantaneous rf voltage applied on the electrode.

In the low frequency regime ($\tau_{ion}/\tau_{rf} << 1$), the ions respond to the instantaneous electric field and reach the substrate with an energy nearly equal to the instantaneous sheath potential when they entered the sheath. Averaging over the rf period, the IED is broad and bimodal exhibiting a low energy peak and a high energy peak as shown in Fig. 1.8.[48] The separation between the two peaks, ΔE, approaches the maximum sheath potential during the rf period. In the high frequency regime ($\tau_{ion}/\tau_{rf} >> 1$), it takes the ions several rf cycles to cross the sheath. The ions strike the wafer surface with the energy almost equal to the average sheath potential. The phase of the rf cycle at which the ions enter the sheath and the instantaneous sheath voltage

are not particularly important for determining the shape of the IEDs. As the τ_{ion}/τ_{rf} increases, ΔE shrinks until the two peaks cannot be resolved. [49,50]

For the ion angular distributions (IADs), one critical parameter determining the IADs is eV_{sh}/kT_i, where V_{sh} is the sheath potential and T_i is the temperature of the ions when entering the sheath.[51] Assuming the sheath to be collisionless and time-independent and the ions to have an isotropic velocity distribution at the sheath edge, the angular distribution of ion fluxes directionally incident on the surface is shown in Fig. 1.9. As the eV_{sh}/kT_i ratio increases by increasing the sheath potential, the IADs becomes narrower, which is favorable for anisotropic etching of HAR features.

1.3.2 Physical Sputtering and Chemically Enhanced Reactive Etching

Physical sputtering and chemically enhanced reactive etching (also called chemical sputtering) are two typical plasma etching processes which both have energy and angular dependence on the incident ions. The basic mechanism of physical sputtering is the transfer of kinetic energy from incident ions to target atoms in the solid.[52] If the energy transferred to the target atom is large enough to overcome the surface binding energy, the atom can be ejected from the solid into the gas phase. The chemical sputtering includes chemical reaction resulting in loosely bounded surface atoms which are subsequently removed by incident ions.[36,53]

The dependence of the etch yield on ion energy and incident angle for physical sputtering and chemical sputtering in the situation that Cl^+ ion incidence on silicon surfaces is shown in Fig. 1.10.[54] The etch yield for physical sputtering is determined on blank silicon surface. The etch yield for chemical sputtering is determined on fully chlorinated silicon surface. Threshold energy for the release of an atom from the surface exists, below which the atom cannot be removed. The chemical sputtering has lower threshold energy (~ 10 eV) than physical

sputtering, which is about 30 eV. As the ion energy increases, the etch yield for chemical sputtering increases more significantly than the physical sputtering, with both etch yields scaling with the square root of ion energy shown in Fig. 1.10(a). For higher energies, the etch yield approaches saturation, while in some conditions, the etch yield decreases at very high ion impact energies due to the increasing penetration depth and increasing energy loss below the surface.[55,56]

Unlike similar dependence on the ion energy, the dependence on the incident angle is quite different for physical and chemical sputtering as shown in Fig. 1.10(b). These two processes can be simultaneously active, with chemical sputtering dominating at low ion energy and physical sputtering becoming more important as ion energy increases.[57,58] For physical sputtering, the etch yield increases with increasing obliqueness of the incident ions and reaches maximum at incident angle $\theta \approx 60 - 70°$. As the incident angle further increases to 90° (grazing incidence), the etch yield decreases to zero.[59] For chemical sputtering, the etch yield remains unity for normal incidence and angles up to about 45°, with a monotonic roll-off to zero probability at grazing incidence.[54]

1.3.3 Etching of High Aspect Ratio Features

Fabrication of high capacity 3D memory device requires etching of high aspect ratio (HAR) features in dielectrics with aspect ratios exceeding 100.[60-52] Controlling and mitigating phenomena such as aspect ratio dependent etching (ARDE), bowing and contact edge roughness (CER) are necessary to obtain anisotropic features and better critical dimension uniformity (CDU). However, the IEADs to the etch front, together with the balance between the ion and neutral radical fluxes to the etch front, significantly vary at different aspect ratios, resulting in difficulties in controlling the etch profiles.

The cross sectional SEM images of HAR holes in poly-Si/SiO_2 stack are shown in Fig. 1.11(a) [62] and the schematics addressing the processes which would occur in plasma etching of HAR features is shown in Fig. 1.11(b) [7]. As the etching propagates into deeper feature, the aspect ratio of etch front increases, resulting in less energetic ions and less thermal radicals reaching the etch front, and thus decreased etch rate. The decrease in etch rate for features with larger ARs is referred as the ARDE effect. ARDE can occur for simultaneously etched features whose initial CDs (e.g., mask opening) have different sizes, or within a single feature as the AR increases during etching. ARDE is a result of transport phenomena which depends on ARs and can be minimized through controlling the mass transfer rate to the etch front by tuning the bias power, gas pressure or substrate temperature.[63,64]

Etching of HAR features faces challenges in both the delivery of etchants to the etch front and the evacuation of etch products out of the feature. The probability of neutral radicals entering into the feature reaching and reacting on the etch front at the bottom of the feature decreases with increasing AR due to diffusive reflection from sidewalls.[65] The same trends apply to thermal etch products produced at the bottom of the feature. The larger the AR, the larger the number of collisions etch products will have with the surface inside the feature prior to exiting the top of the feature. These large number of collision may result in redeposition of the etch products. Conductance limits result in decreased neutral etchant delivery from the top to the bottom of the feature, and redeposition of etch products in transport from the bottom to the top of the feature, both of which can produce lower etch rates.[66,67]

The etch profiles in Fig. 1.11(a) show bowing in the upper portion of the feature, where the sidewalls deviate from purely anisotropic (straight) profile to being outward curvature. Bowing primarily results from the change in the acceptance angle of incident ions into the

feature due to erosion of mask material and subsequent reflection from the facets of resist, diffusive particle scattering within the feature or scattering from rough surfaces.[61,68]

With the CDs of features now less than 10 nm and the mask opening having a commensurately smaller area, the number and variety of particles incident into adjacent features are subject to statistical noise.[7,69,70] The result is that adjacent features may receive different fluxes and sequencing of individual species, imposing difficulties in maintaining the CDU. Besides, the CER in each individual feature originates from non-uniformities in the mask due to stochastic processes during etching or from the lithography-development process. These non-uniformities are then are imprinted into the sidewalls of the feature by anisotropic delivery of activation energy.[70,71]

In the etching of HAR features in dielectrics (e.g., SiO_2 and Si_3N_4), net charging usually occurs in the feature due to imbalanced fluxes of electrons and ions.[72] Electron charging dominantly occurs on the top and upper portion of the features due to nearly isotropic trajectories of incident electrons. Positive ions with more anisotropic IEADs reach the bottom of the feature and deposit positive charges to the surface.[73] The electric potential and electric field produced by the positive charging in the feature deviate the trajectories of subsequent ions while reducing their energy, resulting in twisting and an etch stop. Pulsed power excitation can address many of the detriments of charging by elevating the ion energy [74], reducing the thickness of fluorocarbon films on sidewalls [75] and enabling injection of negative ions to neutralize positive charge inside the feature [76,77].

1.4 Modeling of Low Temperature Plasmas

Modeling of low temperature plasmas is widely used for both investigating the physics and designing the plasma reactors. Modeling provides insights into fundamental physics which is usually difficult to measure in experiments. Besides, modeling has advantages as computer-aided design tools for developing and optimizing plasma processes and equipment.

One of the major challenges of modeling LTPs is the disparity in space (μm – m) and time (μs – s) scales. Despite the unprecedented improvement in computer performance, incorporating all aspects of a plasma system into one model might is impractical. Although there are limitations existing in any modeling approach, an educated selection of the plasma model can lead to remarkable agreement between modeling results and experimental observations and capture enough insights into the physics.

There are three major models used for LTPs, which are fluid model, hybrid model and kinetic model.[78] These models are obtained by extending the kinetic theory of gases and the hydrodynamics of fluids to the plasma state of matter. The choice of the modeling technique (fluid, hybrid or kinetic) is intimately determined by the characteristic time and space scales encountered in the environment of study. Generally speaking, fluid models cost the least computation time and kinetic models give the highest accuracy or fidelity as illustrated in Fig. 1.12(a). It is worthwhile mentioning that the fidelity of modeling depends not only on the assumptions intrinsic to each model, but also on the uncertainties of the input parameters (e.g., cross sections and secondary electron emission coefficients), which set an upper limit to the fidelity of the modeling results. Nevertheless, numerical modeling still provides insights into the physics of the plasma discharges and general trends can be identified.

Fluid models describe the plasma based on the density, mean velocity and mean energy of the constituent species. The values of these macroscopic quantities are obtained by solving the continuity, the flux and the energy equations for each species in the plasma. The Maxwell equations, or Poisson's equation in electrostatic conditions, are coupled with fluid equations to obtain self-consistent electromagnetic fields. The main advantage of fluid models is a speedy calculation, which allows more complex chemistries to be included and parametric investigations to be conducted so as to ascertain the effect of reactor design and operating parameters on discharge characteristics and process outcomes (e.g., etch rate and uniformity). The main disadvantage is that only average values of the variables, instead of distribution functions, are obtained.

Kinetic models, or particle models, take advantage of the collective behavior of charged particles in plasmas to model the kinetics of various species by simulating a reduced number of computer particles (i.e., pseudoparticles). Electrons and ions are usually tracked as pseudoparticles and the background neutrals are assumed to be uniformly distributed in space. Despite the reduced number of particles that are simulated (typically one pseudoparticle per 10^5 − 10^7 real particles), it was shown that plasma physics are retained by this modeling technique.[79,80] The pseudoparticles are tracked by solving fundamental equations (Newton–Lorentz equation for the motion of charged particles coupled with Maxwell equations) without making assumptions on their velocity distribution, so kinetic models are considered as more accurate approach. However, kinetic models are computationally expensive. The computation time is mainly proportional to the number of pseudoparticles being tracked and it is therefore important to carefully choose the number of pseudoparticles which can balance between computation time and sufficient statistical representation of the particles.[81]

Hybrid models are a combination of the fluid and kinetic models. By combining the fast speed of fluid models with the accuracy of particle models, the hybrid models are able to run faster than particle models and describe non-local kinetics more precisely than fluid models.[82] Depending on the physics to be captured, different hybrid models can be derived. To study the electron energy distributions, electrons are treated as particles while ions are modelled as a fluid.[83] To study the ion energy distributions impacting on wafer surface in semiconductor processing, ions are treated as particles while electrons can be treated as a Maxwellian fluid.[84]

One of the major issues in hybrid models is the communication between the fluid and kinetic modules, which have quite different requirements on time step.[85] This is the same problem confronted when physics occurring at different time scales (multiphysics) are included in one model. By using the smallest time step required for either of the modules captures the transient behavior at the cost of huge computation time. In the cases only focused on steady state solutions, the hybrid models can be divided into different modules to separate the time scales of electron, ions and neutrals. Each module is solved in its natural time scale and the simulations keep iterating in a hierarchical manner among the modules until convergence.[82] Besides, the computation time can be drastically reduced by predicting the plasma properties at future time based on the recent evolution of the discharge using acceleration techniques, at the cost of losing the transient behaviors.

1.5 Feature Profile Modeling of Plasma Etching

Material processing by LTPs (e.g., etching, deposition and passivation) occurs through plasma surface interactions (PSI), which in turn, affect the LTPs by modifying the boundary conditions, releasing impurities and changing the gas compositions, etc. The modeling of PSI

can be coupled with the modeling of LTPs with plasma models providing the boundary conditions and incident fluxes of species while the PSI models generating the fluxes of the products back to the plasmas.

The major challenge of modeling PSI is the large range in both space and time scales as shown in Fig. 1. 12(b). Different modeling techniques are used in terms of different degrees of accuracy. In ab initio models, interactions among particles are treated on the basis of quantum mechanics without introducing empirical parameter, which gives the highest accuracy but requires the most computation time.[86] In molecular dynamic (MD) models, the role of electronic system responsible for particle interactions is emulated by the use of empirical functions of individual particle coordinates. MD models have been used to explore reaction mechanisms in atomic scale, but are challenged at resolving large simulation domains to predict feature scale profile evolution. A MD simulation was used to investigate the consequences of hot CF_2 and CF_3 radicals in SiO_2 etching.[73,87] At low energies (10 eV), CF_2 was the main etchant to break the Si-O bond due to its higher chemical reactivity. At high energies (150 eV), CF_3 became the main etchant due to production of more reactive F atoms resulting in forming more Si-F bonds.

Kinetic models are developed to address the transport of incident etching species and the consequent evolution of the feature profile, provided that the surface mechanisms have been established based on ab initio models, MD models or experiments. The feature scale models typically rely on the string methods, level set methods or cell based methods as surface advancement technique.[88] The string methods are accurate for isotropic etching as the surface is represented by a string of nodes connected by straight line segments which are moved along the angle that bisects the normal of two adjacent segments.[89] The level set methods are used

to track the propagation of etch front in the presence of a locally varying forcing function which represents the rate of material removal or addition.[90] The level set methods are usually robust to complex deformations and computationally efficient when modeling large structures. The local rate of etch front propagation typically depends on the ratio of neutral to ion fluxes. This technique has been used to model the etching of Si with a pulsed Bosch process using two simultaneously propagating level sets to track the passivation front separately from the underlying silicon.[91] Etching of SiO_2 in fluorocarbon plasma was modeled by Shimada et al. using a single level set to track the etch front propagation.[92]

The cell based methods discretize the computation domain into a set of cells that are associated with different materials. The profile is defined by the solid cells adjacent to the gas cells. Cell sizes vary from atomic scale up to tens of nm. Cells can be rectangular in 2-dimension and cubic or spherical with close-packed arrangement in 3-dimension. Each cell has a material identity which is stored and updated after each plasma surface interaction based on the defined reaction mechanism. One typical model usually used for plasma etching is the kinetic Monte Carlo model which combines the cell based method for surface profile evolution and the random generation of the incident ions and neutrals based on velocity distribution functions.[88]

The etching of Si by chlorine plasmas and the etching of SiO_2 by Ar/C_4F_8 plasmas were investigated by a cellular model in which the simulation domain is divided into a computational grid where each cell represents a specific material.[93,94] The implantation of Cl^+ and O^+ ions into Si during plasma etching was investigated using cell based Monte Carlo techniques and the distribution of implanted reactants was used to obtain chemical sputtering probabilities.[95] The etching of high aspect ratio contact holes in SiO_2 was investigated using a voxel-slab model, which indicates that the physical damage was reduced by maintaining a critical thickness of the

overlaying polymer.[96,97] The cell based methods were also used to investigate plasma etching with the focus on phenomena such as surface pattern transition [95], ARDE [98,99], microtrenching and photoresist mask faceting [100].

The cell based methods have the advantages in straightforward tracking topological changes for arbitrary geometries, allowing incorporation of complete reaction mechanism, and simultaneously handling composition-dependent etching and deposition as the feature profile evolves. The challenges mainly lie in determining surface curvature and normal direction, setting up criteria for selecting cells to remove or deposit, and large computation memory and long computation time especially for 3-dimensional modeling.

1.6 Summary

The pursuit of Moore's law has taken the semiconductor devices into the realm of nanoelectronics and 3-dimensional structures, resulting in increasing challenges on selectivity and anisotropy especially in the etching of high aspect ratio features. As the etch profile results from surface reactions between solid materials and gas phase species whose fluxes, energy and angular distributions are determined by the plasma sources, solutions for optimizing the etching process is ultimately dependent on expert control of the reactor scale operating conditions. In this dissertation, reactor scale modeling of plasma sources and feature scale modeling of plasma etching are integrated to investigate the reaction pathways in plasmas, control the IEADs to the wafer surface and optimize the etch profiles.

In Chapter 2, the algorithms used and developed in the reactor and feature scale models are described. A 0-dimensional global model, Global_Kin, was mainly used for developing chemistry and exploring parameter space. A 2-dimensional Hybrid Plasma Equipment Model

(HPEM) was mainly used for reactor scale modeling of plasma sources including the remote plasma source and the multi-frequency capacitively coupled plasmas. A 3-dimensional Monte Carlo Feature Profile Model (MCFPM) was mainly used for investigating feature profile evolution with surface mechanism addressing etching, passivation and deposition.

In Chapter 3, the gas phase reaction mechanisms and surface reaction mechanisms developed for use in the reactor and feature scale models are described. Gas phase and surface reaction mechanisms including measured and calculated cross sections and rate coefficients for reactions with specific reactants and products are significant to enable the models to address the kinetics and chemistry in plasmas and at surfaces. Gas phase reaction mechanism for $Ar/NF_3/O_2$ and $NF_3/O_2/H_2$ mixtures were developed and comparisons have been made between experimental measurements and modeling results for validation. A surface reaction mechanism for the etching of SiO_2 using $Ar/C_4F_8/O_2$ mixtures was developed for investigating the etching of HAR features in SiO_2.

In Chapter 4, results from a computational investigation of RPS sustained in $Ar/NF_3/O_2$ mixtures are discussed with the focus on the fundamental reaction mechanisms and specific characteristics of the RPS for downstream etching process. Dissociative attachment and dissociative excitation of NF_x are the major sources of F radicals. The gas temperature in the source region can reach a thousand Kelvins due to Franck-Condon heating, which in turn enables a larger variety of endothermic reactions to occur. In the downstream afterglow, the highly attaching gas mixture rapidly transitions to an ion-ion plasma and the gas cooling due to thermal conduction to the walls results in rebound of gas densities.

In Chapter 5, results from a computational investigation of a downstream etch system used for the etching of Si_3N_4 are discussed. The simulation includes the plasma kinetics and

flow dynamics in the RPS, the transport channel and the downstream chamber. A surface site balance model is used to represent etching at the surface of Si_3N_4 covered wafer. Plasmas in this system are largely confined in the source region due to isolating showerheads and the highly attaching nature of the gas mixture. The main etchants are produced through electron impact reactions and endothermic heavy particle reactions in the RPS, and flow downstream. Adding a plenum between the RPS and the downstream etch chamber increases the uniformity of radical fluxes to the wafer surface and thus increases the uniformity of the silicon nitride etch rate.

In Chapter 6, results are discussed from integrated reactor and feature scale models for investigating the etching of HAR features in SiO_2 using a multi-frequency capacitively coupled plasma sustained in $Ar/C_4F_8/O_2$ mixtures. At low ARs where neutral transport is not conductance limited, abundant fluxes of CF_x radicals to the etch front passivate the oxide to form a complex. This complex is then removed by ions and hot neutrals through chemically enhanced reactive etching (i.e., chemical sputtering). As the etching proceeds to higher ARs, the fractional contribution of physical sputtering increases, as the fluxes of ions and hot neutrals to the etch front surpass that of the conduction constrained CF_x radicals. The general trend of ARDE, decreased instantaneous etch rate with increasing AR, mainly occurs due to decreased power delivery to the etch front while the flux of conduction limited neutrals also decreases.

In Chapter 7, the dependence of the etch profiles of HAR features in SiO_2 on the pattern in the PR is computationally investigated. As the critical dimension of the high aspect ratio features (e.g., contacts, trenches and holes) decreases to tenths of nm, the stochastic nature of the particles into the features becomes prominent and feature-to-feature variations (non-circular profiles) occurs due to randomness of particles into individual features. Interference between the holes due to charging effect especially in the etching of dielectrics reinforces the feature

distortion during the etching. Differential charging in different holes produces electric fields that affect the trajectories of ions in adjacent holes and the profiles tend to repel each other with more pattern distortion.

In Chapter 8, an overview of the research discussed in previous chapters is given with general conclusions. The chapter also contains suggestions of possible future work that could be performed.

1.7 Figures

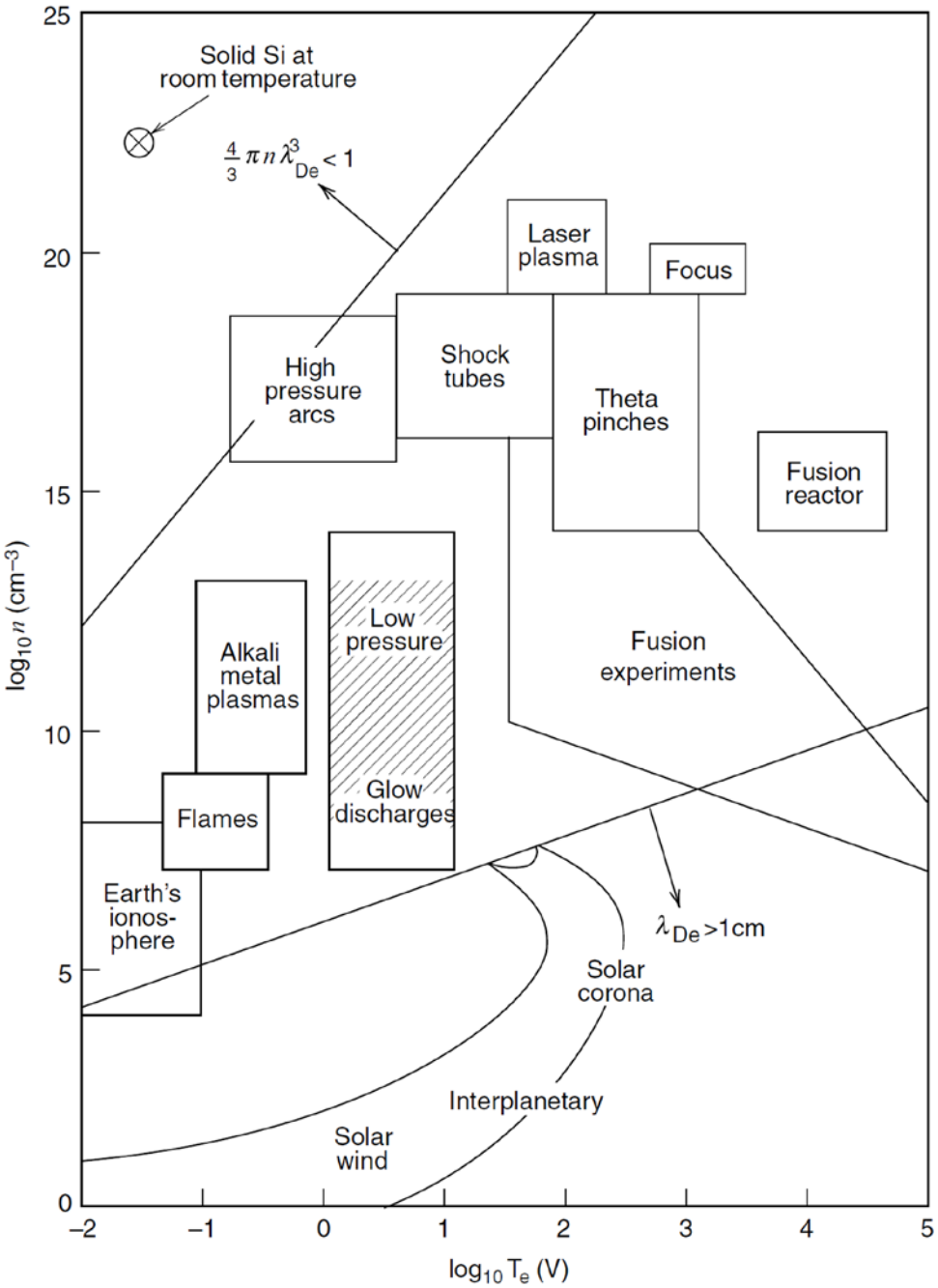

Fig. 1.1 Space and laboratory plasmas characterized by electron temperature (T_e) and electron density (n). The regime of low temperature plasmas is marked by the shadow area. Reproduced from Ref. [2].

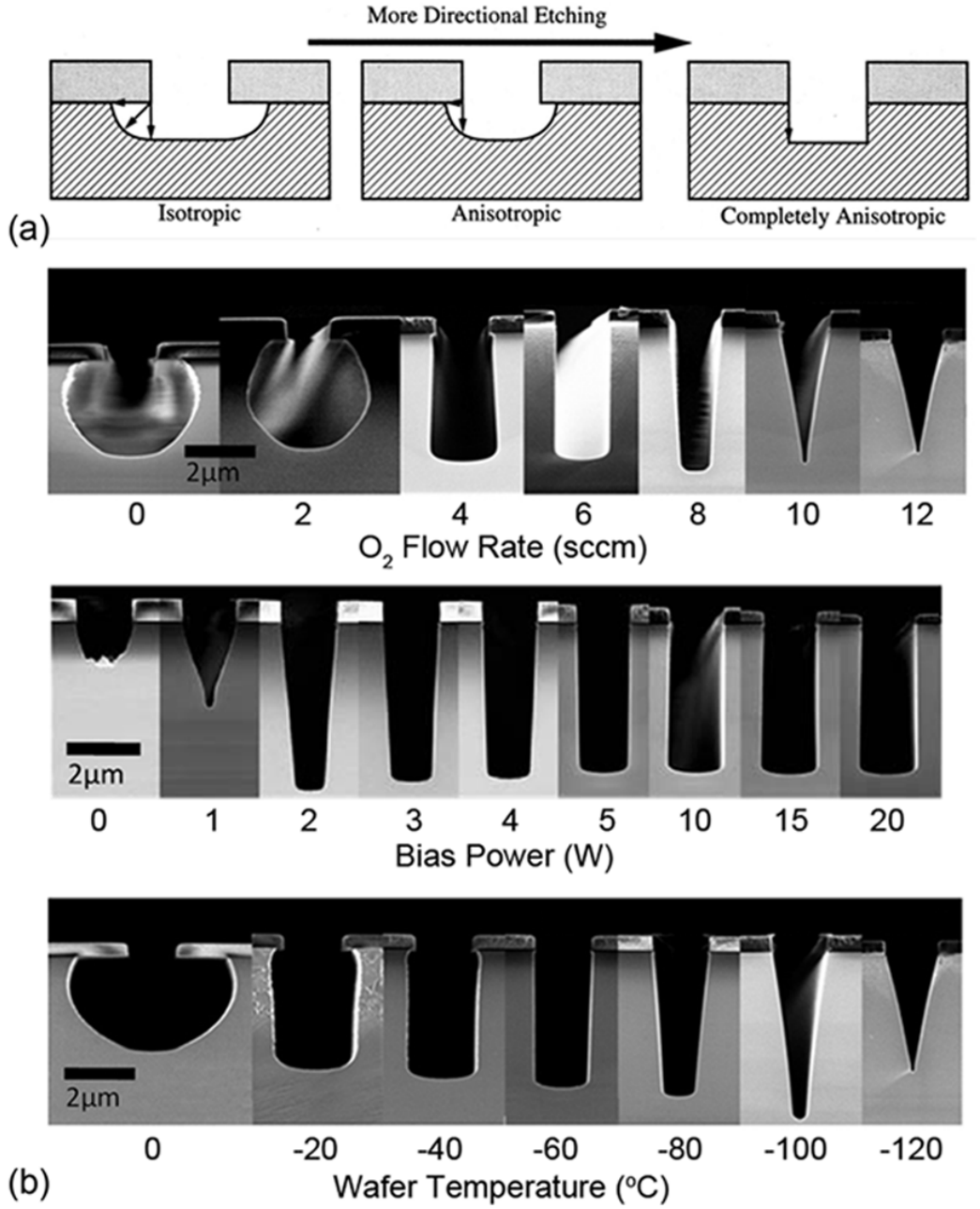

Fig. 1.2 (a) Schematics of etch profiles with different degrees of anisotropy. Reproduced from Ref. [5]. (b) SEM images of silicon trench etch profiles with different degrees of anisotropy controlled by plasma operating parameters (e.g., O_2 gas flow rate, bias power and wafer temperature). Reproduced from Ref. [6].

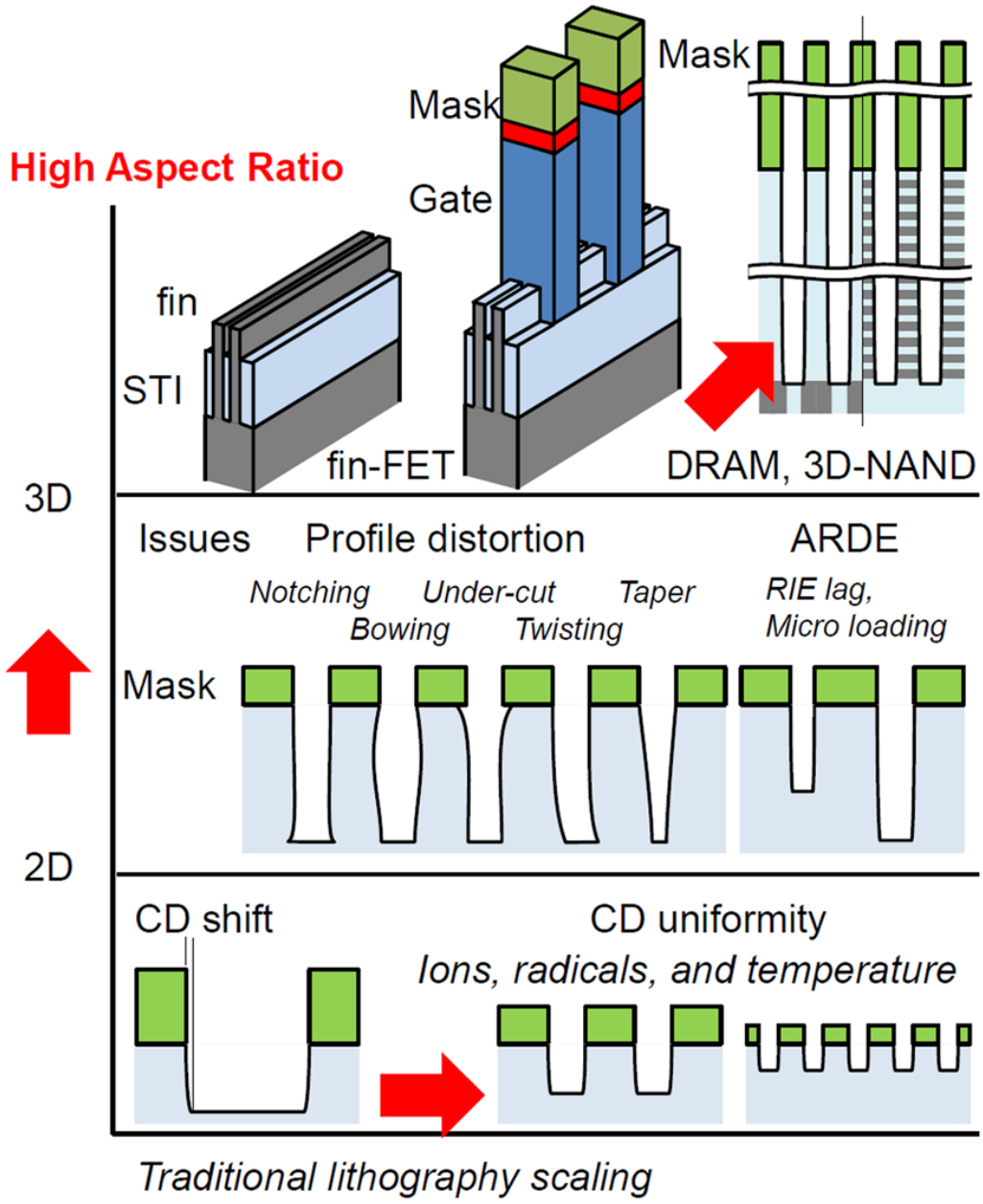

Fig. 1.3 The trends in the fabrication of electronics devices from feature size shrinking in 2d planar surface to vertical stacking in 3d structures, requiring highly selective etching recipes and highly anisotropic etching recipes for enabling extremely high aspect ratio features. ARDE: aspect ratio dependent etching; RIE: reactive ion etching; CD: critical dimension. Reproduced from Ref. [7].

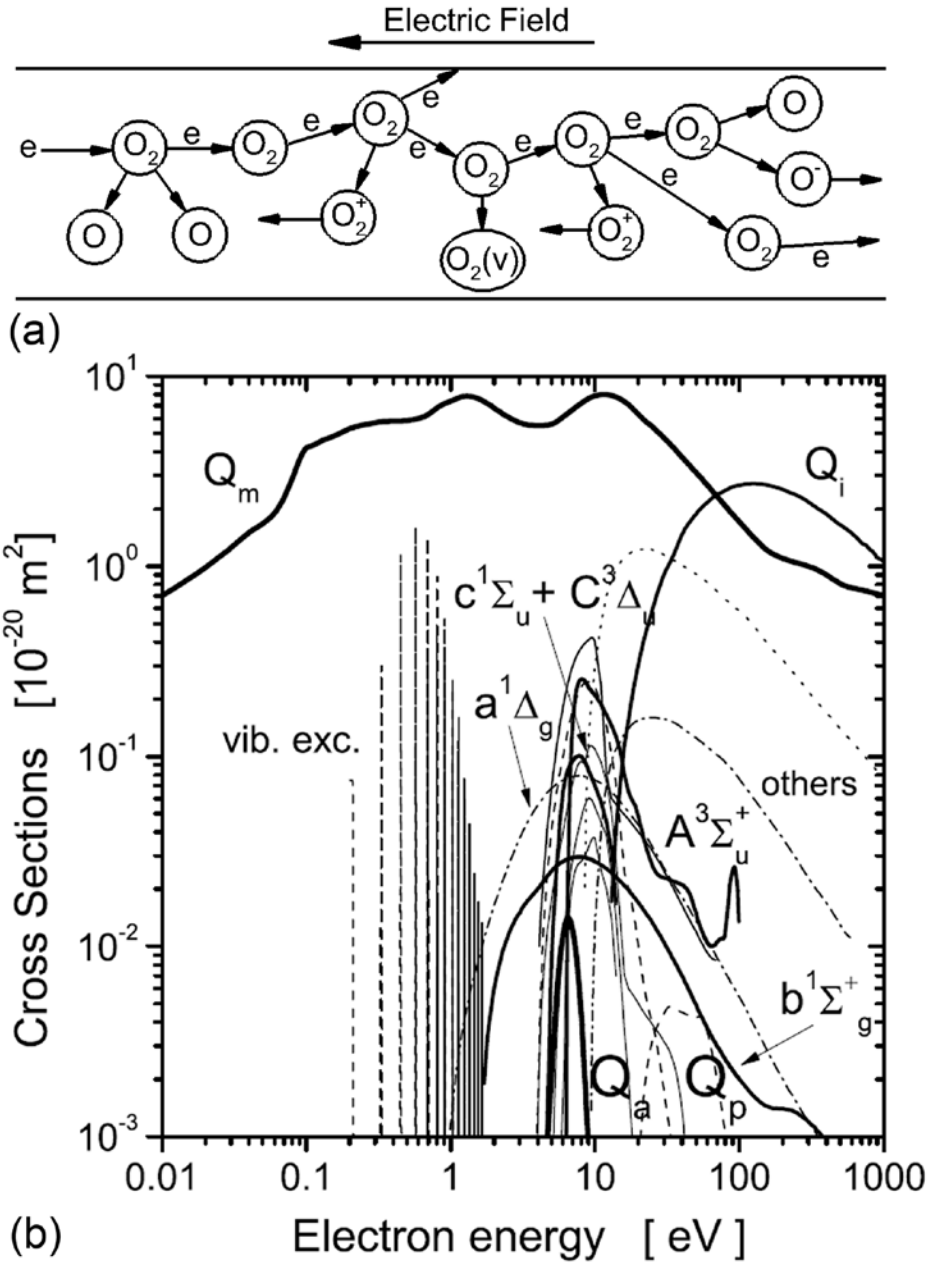

Fig. 1.4 (a) Electron impact reactions as the electron drifts in the electric field. Electrons and negative ions drift against the electric field and positive ions drift along the electric field. b) Electron impact O_2 cross section set. Q_m: momentum transfer, Q_a: attachment, Q_p: ion-pair formation and Q_i: ionization. Reproduced from Ref. [10].

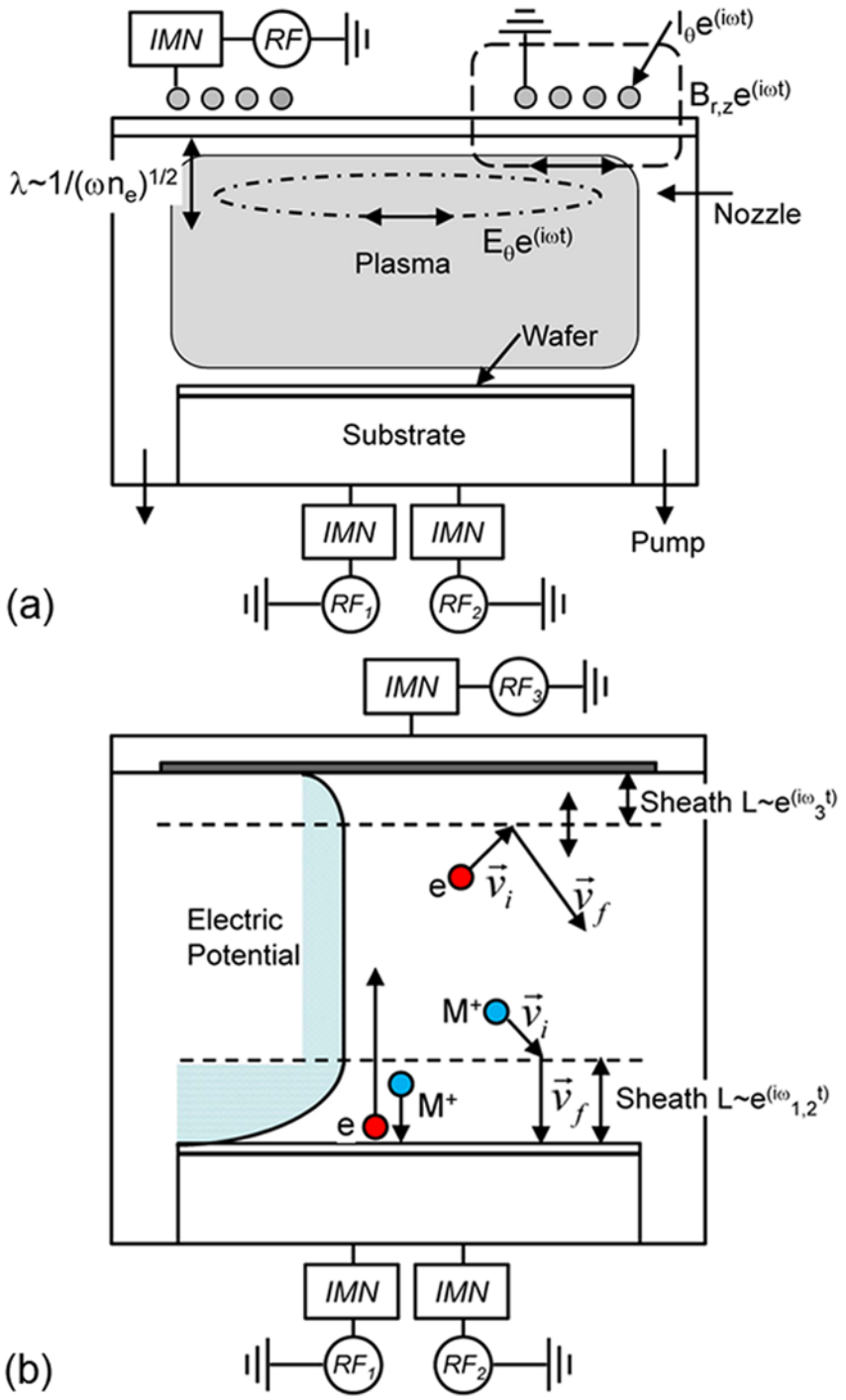

Fig. 1.5 Typical plasma sources for industrial applications: a) inductively coupled plasma excited by spiral rf coils with rf bias applied on the substrate and b) capacitively coupled plasma excited between two parallel plates by rf power applied on the substrate.

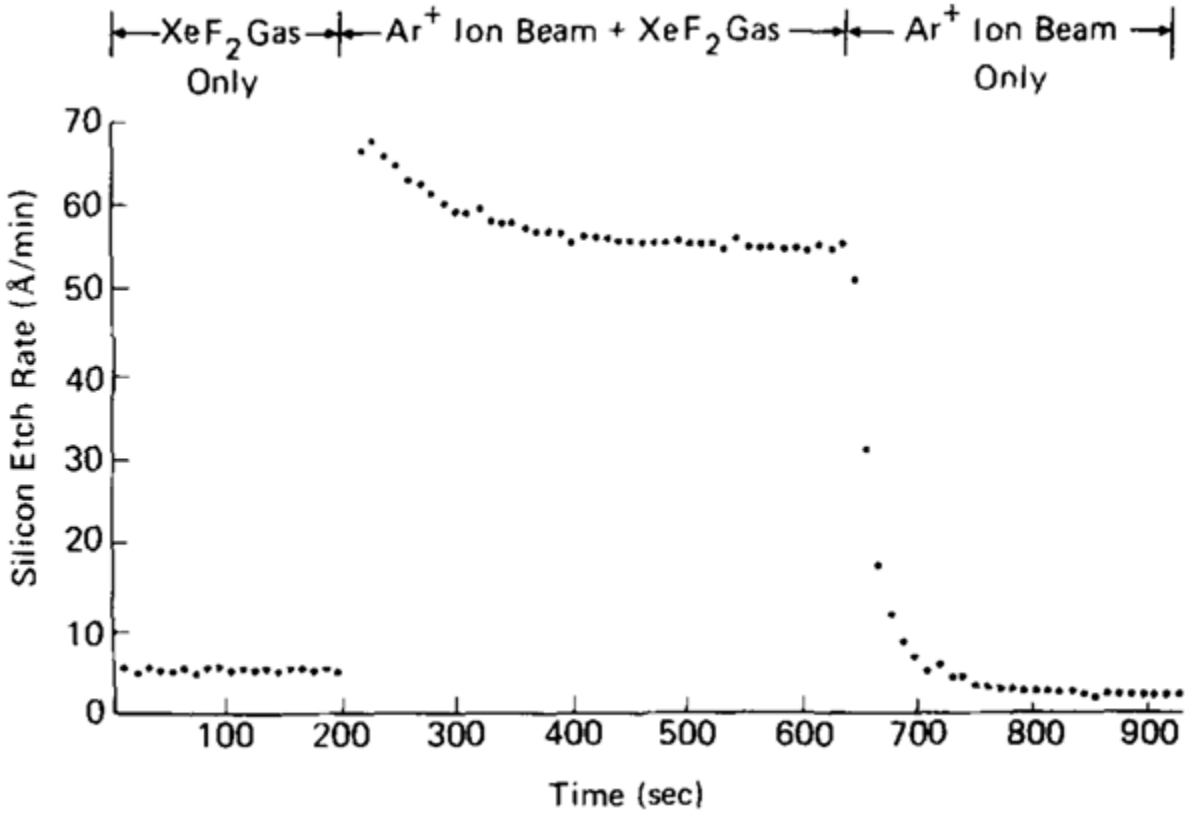

Fig. 1.6 Etch rate of silicon exposed to XeF_2 only, Ar^+/XeF_2 and Ar^+ ions only. The significant increase in etch rate when XeF_2 is combined with Ar^+ exposure is due to the reduced surface binding energy of fluorinated silicon. Reproduced from Ref. [36].

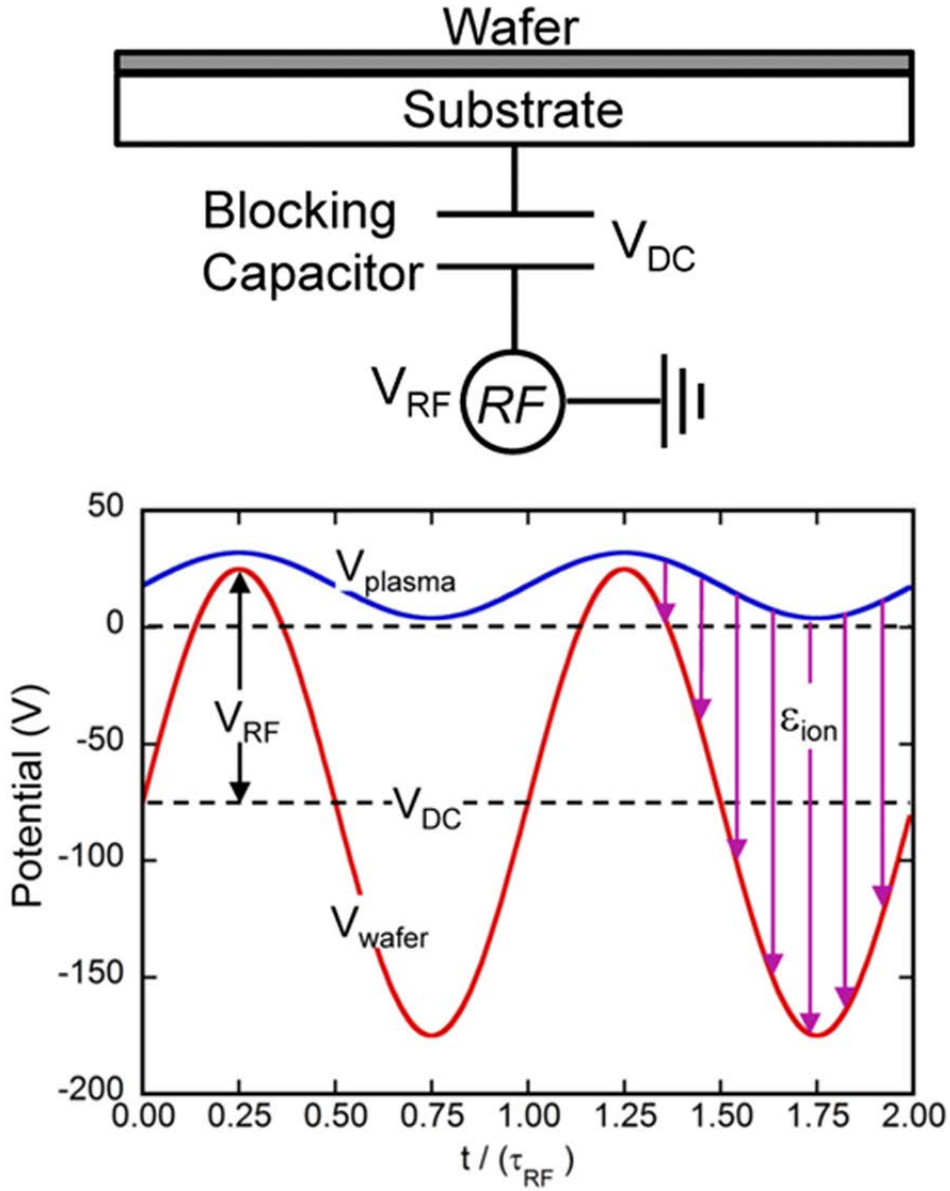

Fig. 1.7 Schematic example of the effect of applying a rf bias to a substrate in a plasma reactor for material processing on the wafer.

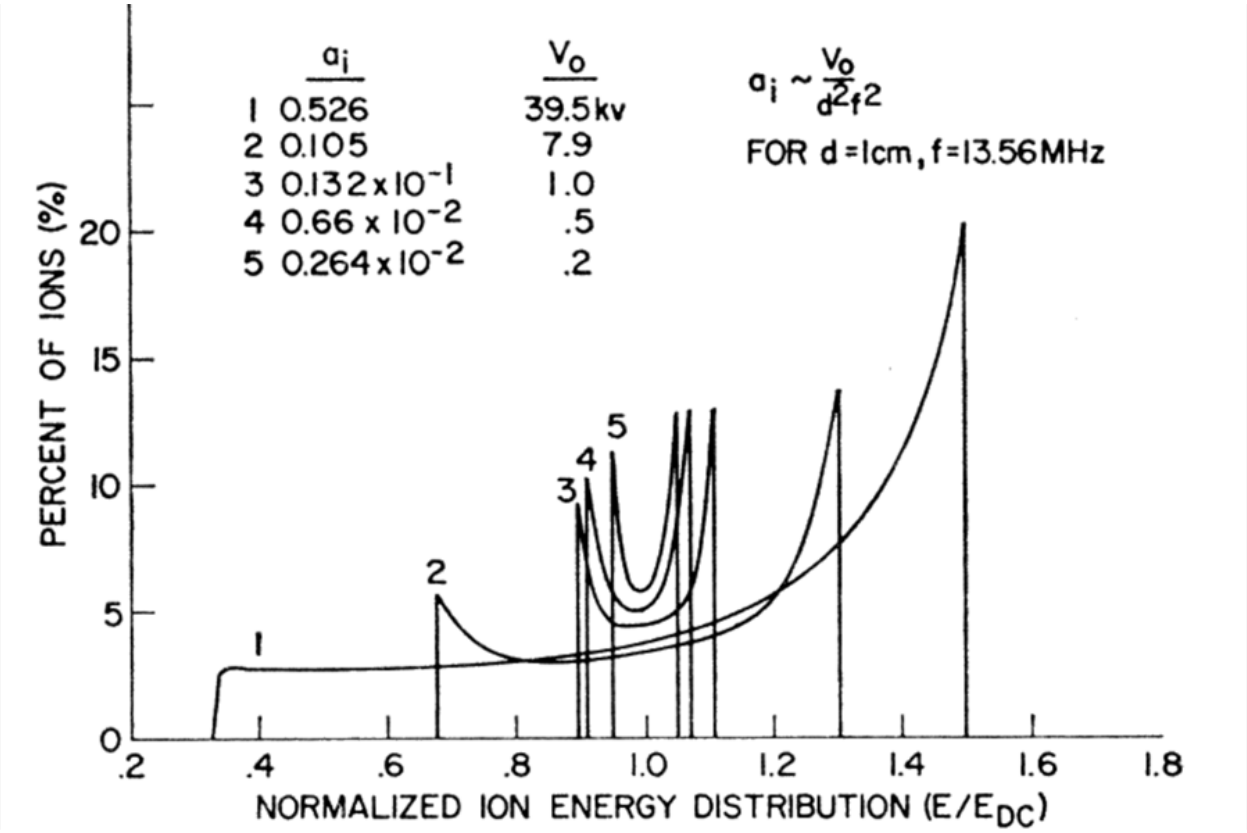

Fig. 1.8 Ion energy distributions to the surface of the substrate for different values of τ_{ion}/τ_{RF}. The curve marked 1 is the lowest τ_{ion}/τ_{rf} and 5 is the highest. Reproduced from Ref. [48].

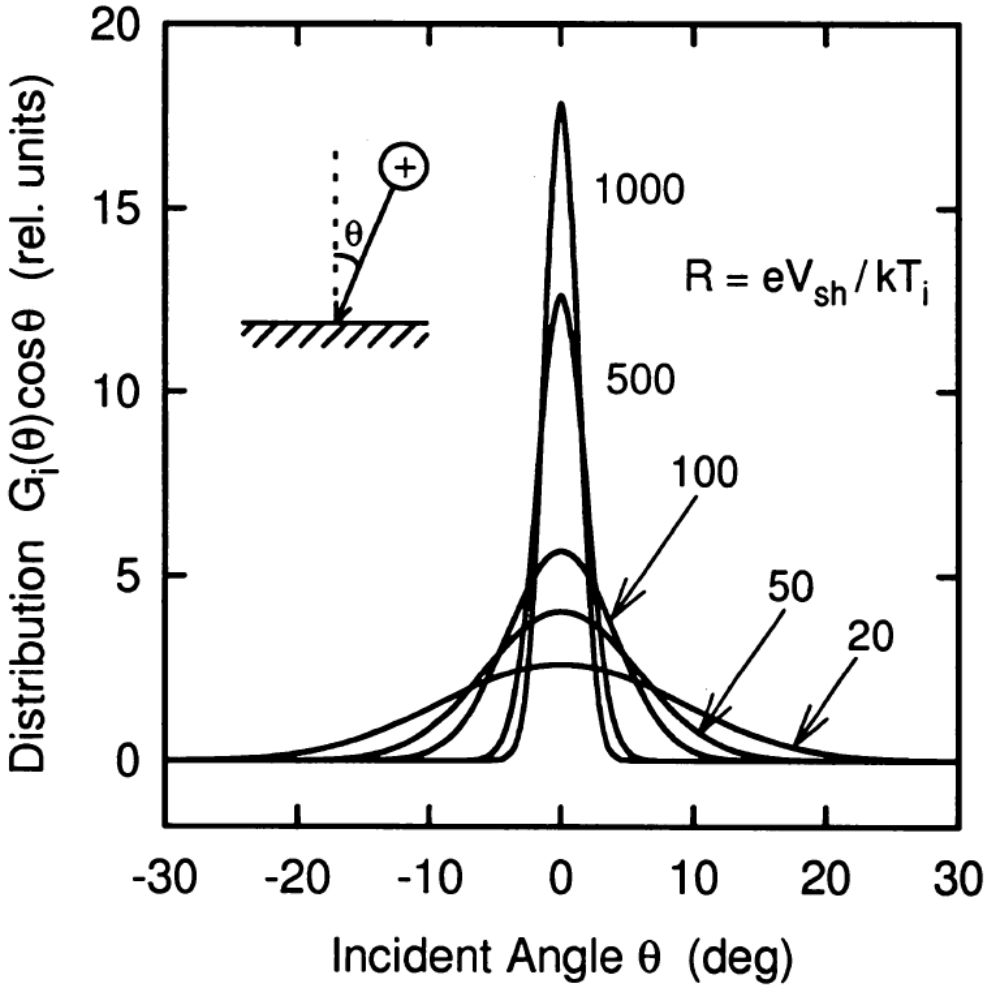

Fig. 1.9 Ion angular distribution to the surface of substrate for different ratios $R = eV_{sh}/kT_i$, where eV_{sh} is the ion energy gained in the sheath and kT_i is the ion temperature. Reproduced from Ref. [51].

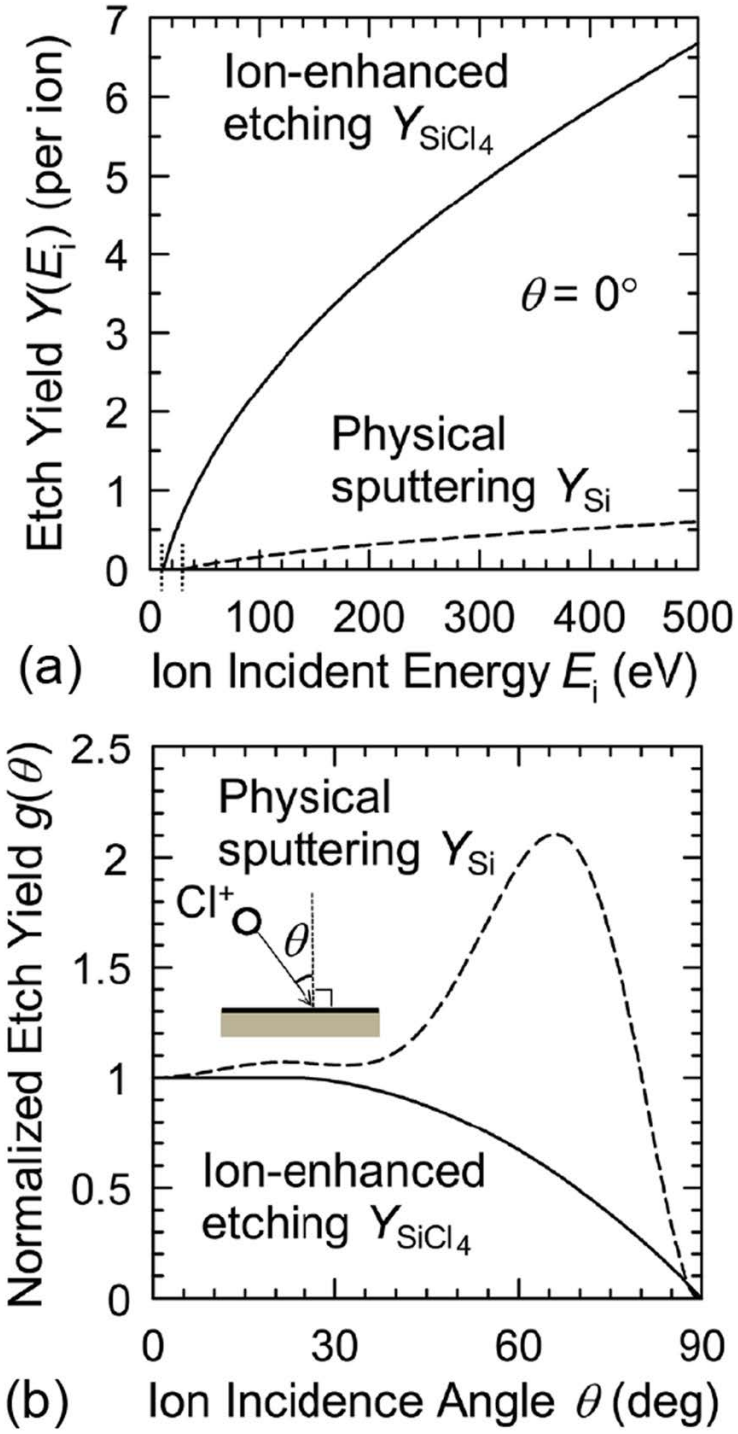

Fig. 1.10 Etch yields for physical sputtering and ion enhanced etching (chemical sputtering) for Cl^+ ion incidence on silicon surfaces as a function of ion incident (a) energy E_i and (b) angle θ. The etch yield for physical sputtering is determined on blank silicon surface. The etch yield for ion enhanced etching is determined on fully chlorinated silicon surface. Reproduced from Ref. [54].

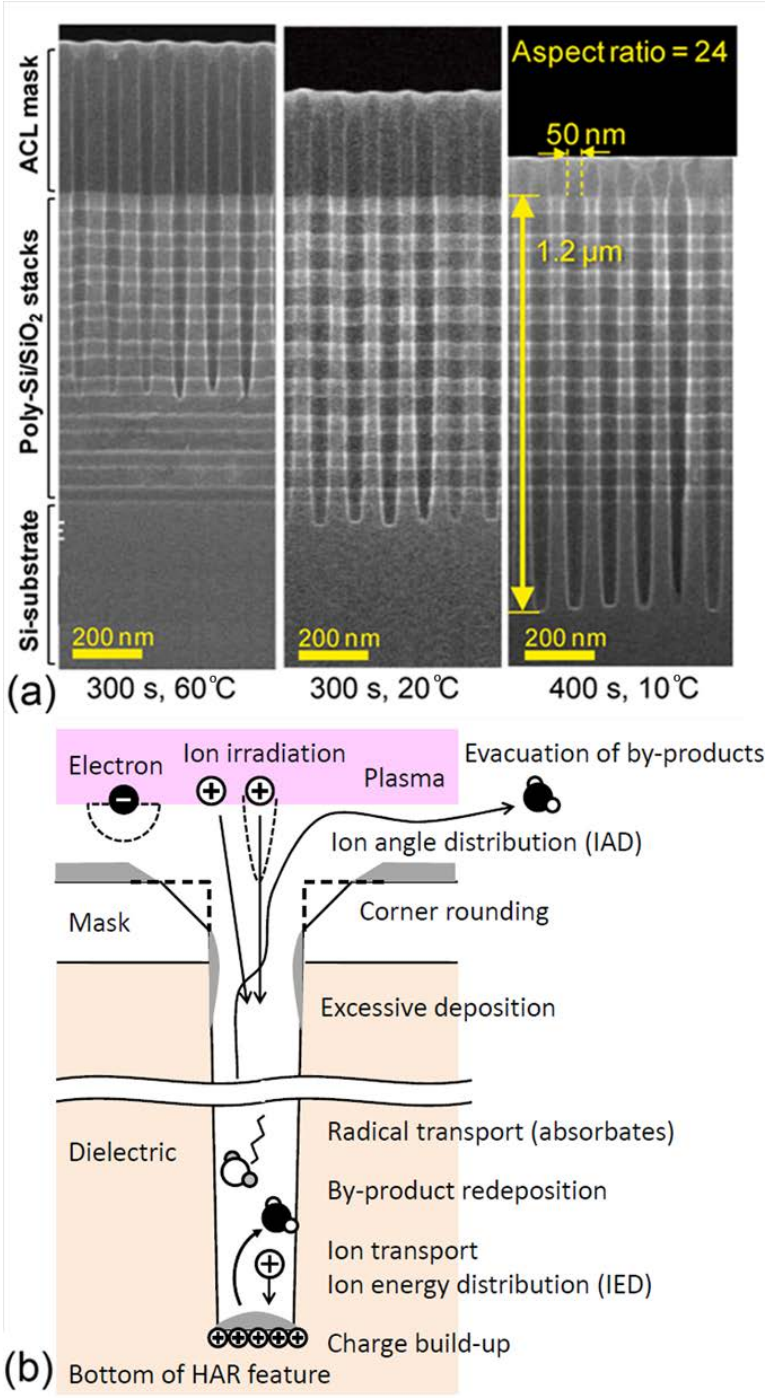

Fig. 1.11 (a) Cross-sectional SEM image of high aspect ratio poly-Si/SiO_2 stack etching profile at different etch time and wafer temperatures. Reproduced from Ref. [62]. (b) Schematic of plasma etching of high aspect ratio features in dielectric. Reproduced from Ref. [7].

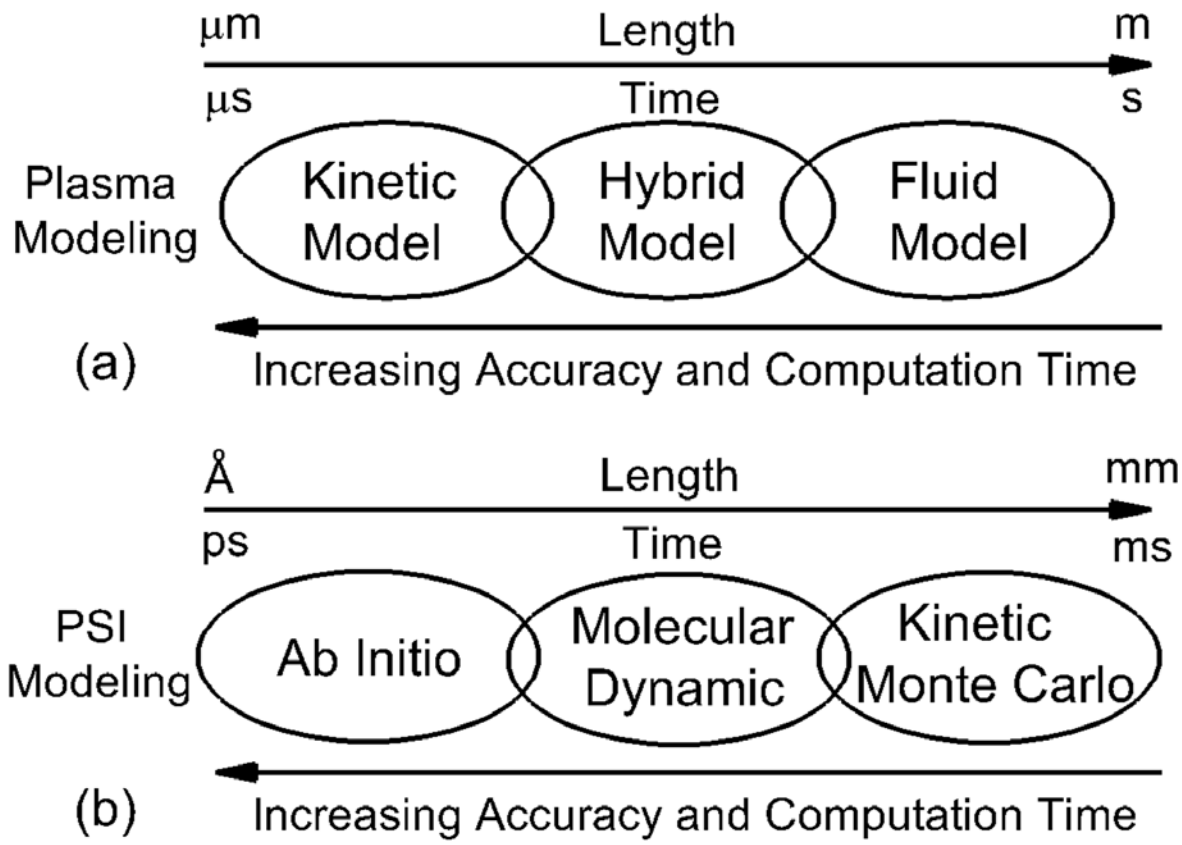

Fig. 1.12 Illustration of applicable time and space range for modeling a) low temperature plasmas and b) plasma surface interactions (PSI).

1.8 References

1. F. F. Chen, Introduction to Plasma Physics and Controlled Fusion Volume 1: Plasma Physics, Plenum Press, New York (1984), p. 3.
2. M. A. Lieberman and A. J. Lichtenberg, Principles of Plasma Discharges and Materials Processing 2nd Edition, John Wiley & Sons, New Jersey (2005), p. 9.
3. I. D. Kaganovich, V. Godyak and V. I. Kolobov, Phys. Plasmas **20**, 101501 (2013).
4. R. R. Schaller, IEEE Spectrum **34**, 52 (1997).
5. J. D. Plummer, M. D. Deal and P. B. Griffin, Silicon VLSI Technology: Fundamentals, Practice and Modeling, Prentice Hall, London (2000), Chp. 9.
6. Z. Liu, Y. Wu, B. Harteneck and D. Olynick, Nanotechnology **24**, 015305 (2013).
7. K. Ishikawa, K. Karahashi, T. Ishijima, S. I. Cho, S. Elliott, D. Hausmann, D. Mocuta, A. Wilson and K. Kinoshita, Jpn. J. Appl. Phys. **57**, 06JA01 (2018).
8. C. M. Compagnoni, A. Goda, A. S. Spinelli, P. Feeley, A. L. Lacaita and A. Visconti, Proc. IEEE **105**, 1609 (2017).
9. H. Yaegashi, K. Oyama, A. Hara, S. Natori and S. Yamauchi, Proc. SPIE **8325**, 83250B (2012).
10. S. Dujko, R. D. White, Z. L. Petrovic and R. E. Robson, Plasma Sources Sci. Technol. **20**, 024013 (2011).
11. N. Posseme, V. Ah-Leung, O. Pollet, C. Arvet and M. Garcia-Barros, J. Vac. Sci. Technol. A **34**, 061301 (2016).
12. Q. Qian, Z. Zhang, M. Hua, G. Tang, J. Lei, F. Lan, Y. Xu, R. Yan and K. J. Chen, Nanotechnology **28**, 175202 (2017).
13. V. M. Donnelly and A. Kornblit, J. Vac. Sci. Technol. A **31**, 050825 (2013).
14. L. M. Loewenstein, J. Vac. Sci. Technol. A **7**, 686 (1989).
15. R. E. Thomas, M. J. Mantini, R. A. Rudder, D. P. Malta, S. V. Hattangady and R. J. Markunas, J. Vac. Sci. Technol. A **10**, 817 (1992).
16. L. M. Loewenstein, J. A. Stefani and S. W. Butler, J. Vac. Sci. Technol. B **12**, 2810 (1994).
17. Y. Zhu, F. Li, R. Huang, T. Liu, Y. Zhao, Y. Shen, J. Zhang, A. Dingsun and Y. Guo, J. Vac. Sci. Technol. A **36**, 041501 (2018).
18. H. C. M. Knoops, T. Faraz, K. Arts and W. M. M. Kessels, J. Vac. Sci. Technol. A **37**, 030902 (2019).

19. E. Paragon, C. Petit-Etienne, L. Youssef, G. Thomachot and S. David, J. Vac. Sci. Technol. A **37**, 040601 (2019).
20. K. Wostyn, K. Kenis, H. Mertens, A. V. Chasin, A. Hikavyy, F. Holsteyns and N. Horiguchi, Solid State Phenom. **282**, 126 (2018).
21. B. E. E. Kastenmeier, P. J. Matsuo, G. S. Oehrlein and J. G. Langan, J. Vac. Sci. Technol. A **16**, 2047 (1998).
22. B. E. E. Kastenmeier, P. J. Matsuo, J. J. Beulens and G. S. Oehrlein, J. Vac. Sci. Technol. A **14**, 2802 (1996).
23. X. Liu, S. Gill, F. Tang, S. W. King and R. J. Nemanich, J. Vac. Sci. Technol. B **30**, 031212 (2012).
24. S. C. Heo, D. Lim, W. S. Jung, R. Choi, H.-Y. Yu and C. Choi, Microelectron. Eng. **147**, 239 (2015).
25. H. Tanaka, M. Kido, K. Yahashi, M. Oomura, R. Katsumata, M. Kito, Y. Fukuzumi, M. Sato, Y. Nagata, Y. Matsuoka, Y. Iwata, H. Aochi and A. Nitayama, IEEE Symposium on VLSI Technology 14, 2007.
26. J. Jang, H.-S. Kim, W. Cho, H. Cho, J. Kim, S. I. Shim, Y. Jang, J.-H. Jeong, B.-K. Son, D. W. Kim, K. Kim, J.-J. Shim, J. S. Lim, K.-H. Kim, S. Y. Yi, J.-Y. Lim, D. Chung, H.-C. Moon, S. Hwang, J.-W. Lee, Y.-H. Son, U.-I. Chung and W.-S. Lee, IEEE Symposium on VLSI Technology 192, 2009.
27. T. Kitajima, Y. Takeo, Z. L. Petrovic and T. Makabe, Appl. Phys. Lett. **77**, 489 (2000).
28. H. C. Kim and J. K. Lee, J. Vac. Sci. Technol. A **23**, 651 (2005).
29. E. Semmler, P. Awakowicz and A. Keudell, Plasma Sources Sci. Technol. **16**, 839 (2007).
30. M. M. Turner and P. Chabert, Plasma Sources Sci. Technol. **16**, 364 (2007).
31. S. H. Lee, P. K. Tiwari and J. K. Lee, Plasma Sources Sci. Technol. **18**, 025024 (2009).
32. S. Bienholz, N. Bibinov and P. Awakowicz, J. Phys. D: Appli. Phys. **46**, 084010 (2013).
33. K. J. Kanarik, T. Lill, E. A. Hudson, S. Sriraman, S. Tan, J. Marks, V. Vahedi and R. A. Gottscho, J. Vac. Sci. Technol. A **33**, 020802 (2015).
34. D. J. Economou, J. Phys. D: Appl. Phys. **47**, 303001 (2014).
35. M. Wang and M. J. Kushner, J. Appl. Phys. **107**, 023308 (2010).
36. J. W. Coburn and H. F. Winters, J. Appl. Phys. **50**, 3189 (1979).
37. D. L. Flamm, V. M. Donnelly and J. A. Mucha, J. Appl. Phys. **52**, 3633 (1981).

38. E. A. Ogryzlo, D. E. Ibbotson, D. L. Flamm and J. A. Mucha, J. Appl. Phys. **67**, 3115 (1990).
39. Z. H. Walker and E. A. Ogryzlo, J. Appl. Phys. **69**, 2635 (1991).
40. C. J. Mogab, A. C. Adams and D. L. Flamm, J. Appl. Phys. **49**, 3796 (1978).
41. R. Legtenberg, H. Jansen, M. de Boer and M. Elwenspoek, J. Electrochem. Soc. **142**, 2020 (1995).
42. T. E. F. M. Standaert, C. Hedlund, E. A. Joseph, G. S. Oehrlein and T. J. Dalton, J. Vac. Sci. Technol. A **22**, 53 (2004).
43. G. S. Oehrlein, Surf. Sci. **386**, 222 (1997).
44. M. Schaepkens and G. S. Oehrlein, J. Electrochem. Soc. **148**, C211 (2001).
45. N. Posseme, T. Chevolleau, O. Joubert, L. Vallier and P. Mangiagalli, J. Vac. Sci. Technol. B **21**, 2432 (2003).
46. D. Eon, V. Raballand, G. Cartry and C. Cardinaud, J. Phys. D: Appl. Phys. **40**, 3951 (2007).
47. M. S. Barnes, J. C. Forster and J. H. Keller, IEEE Trans. Plasma Sci. **19**, 2241 (1988).
48. R. T. C. Tsui, Phys. Rev. **168**, 107 (1968).
49. J. Liu, Q.-Z. Zhang, Y.-X. Liu, F. Gao and Y.-N. Wang, J. Phys. D: Appl. Phys. **46**, 235202 (2013).
50. J. W. Coburn and E. Kay, J. Appl. Phys. **43**, 4965 (1972).
51. K. Ono and M. Tuda, Thin Solid Films **374**, 208 (2000).
52. P. Sigmund, Phys. Rev. **184**, 383 (1969).
53. Y.-Y. Tu, T. J. Chuang and H. F. Winters, Phys. Rev. B **23**, 823 (1981).
54. K. Ono, N. Nakazaki, H. Tsuda, Y. Takao and K. Eriguchi, J. Phys. D: Appl. Phys. **50**, 414001 (2017).
55. C. Steinbruchel, Appl. Phys. A **36**, 37 (1985).
56. C. Steinbruchel, Appl. Phys. Lett. **55**, 1960 (1989).
57. J. M. Lane, K. H. A. Bogart, F. P. Klemens and J. T. C. Lee, J. Vac. Sci. Technol. A **18**, 2067 (2000).
58. M. E. Barone and D. B. Graves, Plasma Sources Sci. Technol. **5**, 187 (1996).
59. C. F. Abrams and D. B. Graves, J. Appl. Phys. **86**, 2263 (1999).
60. N. Negishi, M. Miyake, K. Yokogawa, M. Oyama, T. Kanekiyo and M. Izawa, J. Vac. Sci. Technol. B **35**, 051205 (2017).

61. T. Tandou, S. Kubo, K. Yokogawa, N. Negishi and M. Izawa, Precision Eng. **44**, 87 (2016).
62. T. Iwase, M. Matsui, K. Yokogawa, T. Arase and M. Mori, Jpn. J. Appl. Phys. **55**, 06HB02 (2016).
63. B. Wu, A. Kumar and S. Pamarthy, J. Appl. Phys. **108**, 051101 (2010).
64. H. W. Cheong, W. H. Lee, J. W. Kim, W. S. Kim and K. W. Whang, Plasma Sources Sci. Technol. **23**, 065051 (2014).
65. J. W. Coburn and H. F. Winters, Appl. Phys. Lett. **55**, 2730 (1989).
66. Y. Kim, S. Lee, T. Jung, B. Lee, N. Kwak and S. Park, Proc. SPIE **9428**, 942806 (2015).
67. S. Samukawa and T. Mukai, J. Vac. Sci. Technol. B **18**, 166 (2000).
68. M. Miyake, N. Negishi, M. Izawa, K. Yokogawa, M. Oyama and T. Kanekiyo, Jpn. J. Appl. Phys. **48**, 08HE01 (2009).
69. S.-M. Kim, S. Koo, J.-T. Park, C.-M. Lim, M. Kim, C.-N. Ahn, A. Fumar-Pici and A. C. Chen, Proc. SPIE **9048**, 90480A (2014).
70. J. K. Kim, S. H. Lee, S. I. Cho and G. Y. Yeom, J. Vac. Sci. Technol. A **33**, 021303 (2015).
71. V. Constantoudis, V.-K. M. Kuppuswamy and E. Gogolides, J. Micro/Nanolith. MEMS MOEMS **12**, 013005 (2013).
72. J. C. Arnold and H. H. Sawin, J. Appl. Phys. **70**, 5314 (1991).
73. H. Ito, T. Kuwahara, Y. Higuchi, N. Ozawa, S. Samukawa and M. Kubo, Jpn. J. Appl. Phys. **52**, 026502 (2013).
74. M. Wang and M. J. Kushner, J. Appl. Phys. **107**, 023309 (2010).
75. T. Shimmura, Y. Suzuki, S. Soda, S. Samukawa, M. Koyanagi and K. Hane, J. Vac. Sci. Technol. A **22**, 433 (2004).
76. H. Ohtake, B. Jinnai, Y. Suzuki, S. Soda, T. Shimmura and S. Samukawa, J. Vac. Sci. Technol. A **24**, 2172 (2006).
77. T. Ohmori and T. Makabe, Appl. Surf. Sci. **254**, 3696 (2008).
78. D. J. Economou, Plasma Process. Polym. **14**, 1600152 (2017).
79. V. Vahedi, G. Dipeso, C. K. Birdsall, M. A. Lieberman and T. D. Rognlien, Plasma Sources Sci. Technol. **2**, 261 (1993).
80. V. Vahedi, C. K. Birdsall, M. A. Lieberman, G. Dipeso and T. D. Rognlien, Plasma Sources Sci. Technol. **2**, 273 (1993).
81. C. K. Birdsall, IEEE Trans. Plasma Sci. **19**, 65 (1991).

82. M. J. Kushner, J. Phys. D. **43**, 185206 (2010).
83. T. J. Sommerer and M. J. Kushner, J. Appl. Phys. **71**, 1654 (1992).
84. R. K. Porteous and D. B. Graves, IEEE Trans. Plasma Sci. **19**, 204 (1991).
85. H. C. Kim, F. Iza, S. S. Yang, M. Radmilovic-Radjenovic and J. K. Lee, J. Phys. D: Appl. Phys. **38**, R283 (2005).
86. R. Schneider, Phys. Scr. **T124**, 76 (2006).
87. H. Ito, T. Kuwahara, K. Kawaguchi, Y. Higuchi, N. Ozawa, S. Samukawa and M. Kubo, J. Phys. Chem. C **118**, 21580 (2014).
88. W. Guo and H. H. Sawin, J. Phys. D: Appl. Phys. **42**, 194014 (2009).
89. R. E. Jewett, P. I. Hagouel, A. R. Neureuther and T. V. Duzer, Polym. Eng. Sci. **17**, 381 (1977).
90. S. Osher and J. A. Sethian, J. Comput. Phys. **79**, 12 (1988).
91. O. Ertl and S. Selberherr, Microelectron. Eng. **87**, 20 (2010).
92. T. Shimada, T. Yagisawa and T. Makabe, Jpn. J. Appl. Phys. **45**, 8876 (2006).
93. W. Guo, B. Bai and H. H. Sawin, J. Vac. Sci. Technol. A **27**, 388 (2009).
94. W. Guo and H. H. Sawin, J. Vac. Sci. Technol. A **28**, 250 (2010).
95. Y. Osano and K. Ono, Jpn. J. Appl. Phys. **44**, 8650 (2005).
96. N. Kuboi, T. Tatsumi, S. Kobayasgi, T. Kinoshita, J. Komachi, M. Fukasawa and H. Ansai, Appl. Phys. Express **5**, 126201 (2012).
97. N. Kuboi, M. Fukasawa and T. Tatsumi, Jpn. J. Appl. Phys. **55**, 07LA02 (2016).
98. Y. Osano and K. Ono, J. Vac. Sci. Technol. B, **26**, 1425 (2008).
99. C. M. Huard, Y. Zhang. S. Sriraman, A. Paterson, K. J. Kanarik and M. J. Kushner, J. Vac. Sci. Technol. A **35**, 031306 (2017).
100. A. P. Mahorowala and H. H. Sawin, J. Vac. Sci. Technol. B, **20**, 1064 (2002).

Chapter 2 Description of the Models

Modeling of plasmas and plasma surface interactions provides insights into the physics during material processing, from which optimized process control and reactor design can be achieved. In this thesis, the 2-dimensional Hybrid Plasma Equipment Model (HPEM) was used for reactor scale modeling mainly to investigate the plasma kinetics and chemistry and obtain the fluxes of ions and radicals and the ion energy and angular distributions (IEADs) to the wafer surface. The 3-dimensional Monte Carlo Feature Profile Model (MCFPM) was used for feature scale modeling mainly to investigate the etch properties (e.g., etch rate, critical dimensions, roughness and charging). Besides, a 0-dimensional global model, Global_Kin, was mainly used for developing gas phase reaction mechanisms and exploring the operational parameter space for reactor scale modeling.

2.1 Global Model

The global model, Global_Kin, is a 0-dimensional simulator for plasma chemistry, plasma kinetics and surface chemistry, described in details in Refs. [1,2]. The global model assists in more rapid development of the reaction mechanism and investigation of the operational parameter space for efficient production of desired species. The modular structure of Global_Kin is shown in Fig. 2.1. Given the gas phase and surface reaction mechanisms and the operating conditions, the densities and temperatures of electrons, ions and neutrals are predicted with the plasma chemistry module and surface chemistry module using the electron energy

distributions (EEDs) provided by the solution of the Boltzmann equation.

With electron impact cross sections and mole fractions of gas species, the Boltzmann equation is solved for the EEDs over a wide range of *E/N* (*E* and *N* are the electric field and the gas number density). These EEDs are computed while assuming a negligible ionization degree and so electron-electron collisions are not considered. The non-Maxwellian nature of the EEDs is then addressed.[3] This process produces a table having columns of *E/N*, average electron energy (or equivalent electron temperature, T_e) and electron impact rate coefficients. If T_e is a monotonic function of *E/N*, the column of *E/N* can be thrown away, leaving a lookup table of rate coefficients as a function of T_e. Rate coefficients are then obtained by interpolation of the table, $k_i(T_e)$. The table is periodically updated as mole fractions of species change.

In Global_Kin, the electron temperature, T_e, is calculated from the electron energy equation

$$\frac{\partial\left(\frac{3}{2}n_e k_b T_e\right)}{\partial t} = \vec{j}\cdot\vec{E} + \sum_i n_e \Delta\varepsilon_i k_i n_i + \sum_i \Delta\varepsilon_i k_i n_i m_i - \sum_i \frac{3}{2} n_e \nu_{mi}\left(\frac{2m_e}{M_i}\right) k_B (T_e - T_i), \qquad (2.1)$$

where n_e is the electron density and k_B is the Boltzmann's constant. The first term on the right-hand side is the power deposition into electrons. All the power is assumed to initially be deposited in electrons due to the low mobility of the ions. This assumption is reasonable for inductively coupled plasmas, but becomes less accurate for capacitively coupled plasmas where significant power is deposited in the sheath by ions. The power deposition is obtained from $\vec{j}\cdot\vec{E}$ which is calculated from the circuit module or directly specified as inductively coupled power. The second term represents changes in electron energy (positive or negative) due to inelastic collisions where $\Delta\varepsilon$ is the change in electron kinetic energy during the collision with the species of density n_i for the process having reaction rate coefficient k_i. The third term represents

sources of electron energy density due to collisions between gas phase species n_i and m_i such as Penning ionizations. The last term represents the electrons transferring momentum to the neutral atoms and molecules through elastic collisions where ν_{mi} is the momentum transfer collision frequency, m_e and M_i are the mass of the electrons and neutral species, and T_i is the temperature of the neutral gas.

Based on the user-defined reaction mechanism, the densities of gas phase species are calculated through constructing differential equations using

$$\frac{dn_i}{dt} = \sum_j \left\{ \left(a_{ij}^{(R)} - a_{ij}^{(L)} \right) k_j \prod_l n_l^{a_{ij}^{(L)}} \right\} + \frac{1}{\tau_{flow}} \left(n_{io} - n_i \left(1 + \frac{(p - p_0)}{p_0} \right) \right), \\ + \sum_m \left\{ -\frac{D_i n_i}{\Lambda^2} f_m S_{im} + \sum_k \frac{D_k n_k}{\Lambda^2} f_m S_{km} g_{ikm} \right\} \tag{2.2}$$

where the first term on the right-hand side represents the gas phase reactions which are sources or losses of species *i*. The two coefficients $a_{ij}^{(R)}$ and $a_{ij}^{(L)}$ are the number of molecules of species *i* which are on the right-hand side (products) and the left-hand side (reactants) of reaction *j*. The second term represents the sources and losses from the gas flow, where τ_{flow} is the average residence time of the gas in the volume, n_{io} is the number density of the species flowing into the reactor, p is the instantaneous pressure and p_0 is the desired operating pressure. The pressure dependent term accounts for change in flow speed that may occur due to increase in pressure resulting from dissociation or gas heating. Diffusion losses including recombination or reactions at the wall are addressed by the third term. The third term includes diffusion losses of species *i* at the surface of material *m* and the source due to the return flux after surface reactions occur with other species based on a user-defined surface mechanism. The coefficient f_m is the fractional area of wall material *m* and D_i is the diffusion coefficient of species *i*. For charged species this value is their ambipolar diffusion coefficient based on the instantaneous ion and

electron mobilities, and for other species this value is determined by mixture rules using Leonard-Jones potentials. The ambipolar diffusion coefficients are modified for positive ions (enhanced) and negative ions (decreased) so that the negative ions are more confined in the bulk plasma while the positive ions are accelerated through the sheath to the surface by the ambipolar field. Λ is the diffusion length of the plasma, defined by the geometry of the reactor. The sticking coefficient, S_{km}, is the fraction of the diffusion flux which disappears at the wall, and the give fraction, g_{ikm}, is the fraction of the consumed flux of species k which returns as species i.

The gas temperature is calculated by

$$\frac{d\left(\frac{3}{2}N_g c_p T_g\right)}{dt} = P_{ion} + \sum_i \frac{3}{2} n_e \nu_{mi} \left(\frac{2m_e}{M_i}\right) k_b (T_e - T_i) + \sum_i \Delta\varepsilon_i^{fc} R_i - \sum_i \Delta H_i R_i + \frac{1}{\tau_{flow}}\left(N_{g0} c_{p0} T_{g0} - N_g c_p T_g \left(\frac{p}{p_0}\right)\right) - \frac{\kappa}{\Lambda^2}(T_g - T_w) \quad , \quad (2.3)$$

where N_g is the total gas density, c_p is the specific heat of the gas, and T_g is the gas temperature. P_{ion} is the power deposited into the ions by the ambipolar electric field. The second term on the right-hand side is the gas heating due to elastic collisions between the electrons and all other species. Franck-Condon heating is captured by the third term, where $\Delta\varepsilon_i^{fc}$ is the energy released as gas heating in dissociation reactions and R_i is the rate of reaction i. The fourth term includes the change in enthalpy from all reactions, including charge exchange, where ΔH_i is the change in enthalpy of reaction i and R_i is the reaction rate. The fifth term is advective cooling due to gas flow, where N_{g0}, c_{p0} and T_{g0}, are the density, specific heat and temperature of the gas flowing into the reactor. The last term addresses thermal conduction to surfaces, where κ is the thermal conductivity and T_w is the surface temperature.

The power deposition in the plasma can be directly specified as a function of time for time-varying conditions (e.g., pulsed plasma) or as a function of position for space-varying

conditions (e.g., plug flow). For the modeling of the remote plasma source and downstream etch systems, the plug flow operation was implemented to address gas flow using plug flow or residence time approximations.

In the plug flow operation, the 0-dimensional time-dependent model is converted to a pseudo 1-dimensional position-dependent model where integration in time is mapped to integration in space by computing a time dependent flow speed.[4,5] By assuming a constant pressure, the flow speed, v_x, is determined by the thermal expansion (or contraction) of the gas due to changes in temperature and gas number density due to electron impact and heavy particle reactions, limited by requiring the flow to be subsonic accounting for gas expansion. According to the relationship between pressure, density and temperature given by the ideal gas equation $p = NK_BT_g$, for a given pressure the density is determined by the temperature at adiabatic conditions, which results in difference between the calculated density using Eq. 2.2 and using the ideal gas equation. This difference in density results in change in gas flow speed in or out of the volume, which is obtained by conversion of the mass flux

$$\frac{dv_x}{dt} = -\frac{v_x}{\rho}\frac{d\rho}{dt}, \tag{2.4}$$

where the mass density ρ is obtained from the instantaneous mixture averaged molecular weight and the number density. Integrating the flow velocity gives the location of the initial gas plug as a function of time. The ordinary differential equations (ODEs) for species densities, electron energy and flow velocity are normalized before being integrated to increase computational efficiency. The integration is performed by a double precision variable coefficient ODE solver developed at Lawrence Livermore National Laboratory as part of ODEPACK.[6,7]

2.2 Hybrid Plasma Equipment Model (HPEM)

The Hybrid Plasma Equipment Model (HPEM) is a 2-dimensional reactor scale model for investigating plasma physics and kinetics in low temperature and low pressure plasma processing reactors.[8] The HPEM is a kinetic-fluid hydrodynamics code which combines separate modules that address different physical phenomena in an iterative manner. The flow chart showing the iteration of physics parameters among different modules during the execution of the HPEM is shown in Fig. 2.2. In this thesis, the major modules used in the studies are the Electromagnetics Module (EMM), the Electron Energy Transport Module (EETM), the Fluid Kinetics Poisson Module (FKPM), the Surface Kinetics Module (SKM) and the Plasma Chemistry Monte Carlo Module (PCMCM).

2.2.1 Electromagnetics Module (EMM)

In the EMM, the inductively coupled electromagnetic fields originating from the azimuthal antenna currents are produced using a frequency domain solution of Maxwell's equations. By using finite difference method, the time-varying electromagnetic fields $\vec{E}$ are obtained by solving the frequency domain wave equation

$$-\nabla(\frac{1}{\mu}\nabla\cdot\vec{E})+\nabla\cdot(\frac{1}{\mu}\nabla\vec{E})=\omega^2\varepsilon^2\vec{E}+i\omega(\vec{j}_{coil}+\bar{\bar{\sigma}}\cdot\vec{E}), \tag{2.5}$$

where μ is the permeability, ε is the permittivity, and ω is the angular electromagnetic frequency. The current density has contributions from both the external antenna current $\vec{j}_{coil}$ and the conduction current generated in the plasma addressed through a conductivity tensor $\bar{\bar{\sigma}}$ with the form of

$$\bar{\bar{\sigma}}=\frac{\sigma_0}{(\alpha^2+|B|^2)}\times\begin{pmatrix}\alpha^2B^2{}_r & \alpha B_z+B_rB_\theta & -\alpha B_\theta+B_rB_z\\ -\alpha B_z+B_rB_\theta & \alpha^2+B^2{}_\theta & \alpha B_r+B_\theta B_z\\ \alpha B_\theta+B_rB_z & -\alpha B_r+B_\theta B_z & \alpha^2+B^2{}_z\end{pmatrix}, \tag{2.6}$$

where

$$\sigma_0 = \frac{e^2 n_e}{m_e} \frac{1}{\nu_m + i\omega}, \tag{2.7}$$

$$\alpha = \frac{m_e}{e}(\nu_m + i\omega), \tag{2.8}$$

B is the applied static magnetic file, e is the unit electron charge, n_e is the electron density, m_e is the electron mass and ν_m is the electron momentum transfer collision.[9]

For coil generated electromagnetic fields, the EMM is executed to compute inductively coupled electromagnetic fields as a function of position and phase. Due to the absence of static magnetic field in the cases studied in this thesis, the conductivity tensor is equal to its isotropic value, σ_0, and only the azimuthal electric field E_θ is produced. The electric field is normalized to provide total power deposition by calculating $\vec{j}_e \cdot \vec{E}$ if assuming collisional power deposition. In order to include non-collisional heating effects, the electron current, $\vec{j}_e$, needs to be calculated kinetically in the EETM and fed back to the electromagnetics calculation.

With the time-varying and position dependent electric field $\vec{E}(\vec{r},\varphi)$ calculated by Eq. 2.5, the magnetic field $\vec{B}(\vec{r},\varphi)$ is calculated by

$$\vec{B} = (i/\omega)\nabla \times \vec{E}, \tag{2.9}$$

with boundary conditions assuming no tangential electric field on all metal surfaces and $E_\theta = 0$.

2.2.2 Electron Energy Transport Module (EETM)

The EETM solves for electron impact rates $k(\vec{r},\varphi)$ and sources $S(\vec{r},\varphi)$ and electron transport properties by using the electromagnetic fields $\vec{E}(\vec{r},\varphi)$ and $\vec{B}(\vec{r},\varphi)$ from EMM and the electrostatic field $\vec{E}_s(\vec{r},\varphi)$ from FKPM. The electron properties can be computed using electron

Monte Carlo Simulation (eMCS) or time dependent electron energy equation. The eMCS is included in the EETM, while the time dependent electron energy equation is implicitly integrated in the FKPM to provide electron properties. In this thesis, the electron energy equation is used in the majority of the simulations for calculating the electron properties, while the eMCS is only used for calculating the secondary electron transport.

The eMCS is a fully kinetic approach for resolving electron transport in electromagnetic fields. The electrons are launched with velocities randomly chosen according to Maxwellian distribution and positions randomly selected in the reactor weighted by the electron density. Electron trajectories are then computed using the Lorentz equation

$$\frac{d\vec{v}}{dt} = \frac{e}{m_e}(\vec{E} + \vec{v}_e \times \vec{B}), \tag{2.10}$$

where $\vec{v}_e$ is the electron velocity. The electric fields consist of inductive fields $\vec{E}(\vec{r},\varphi)$ computed in the EMM and the electrostatic fields $\vec{E}_s(\vec{r},\varphi)$ computed from the FKPM, which are updated as the EMM, EETM and FKPM are sequentially and iteratively called during execution of the model.

The energy grid technique is used to collect collision frequencies and statistics. The energy grid is unequally separated into several energy ranges, e.g., 0 – 5, 5 – 10, 10 – 50, 50 – 300 and 300 – 1000 eV. The high energy ranges are mainly used to capture energy of the sheath accelerated secondary electrons and each range is divided into hundreds of bins. The total collision frequency of each energy bin, ν_i, is calculated by summing all possible collisions with every heavy particle species using

$$\nu_i = (\frac{2\varepsilon_i}{m_e})^{1/2} \sum_{j,k} \sigma_{ijk} N_j, \tag{2.11}$$

where ε_i is the average energy within bin *i*, σ_{ijk} is the cross section at energy *i* for species *j* and collision process *k*, and N_j is the number density of species *j*. Null collision cross sections are used to provide a constant collision frequency. In a particular energy range, the null collision frequency is equal to the difference between the actual collision frequency and its maximum value.[10]

The time step between collisions is determined by $\Delta t = -\ln(r)/\nu_{mj}$, where *r* is a random number distributed within (0, 1) and ν_{mj} is the maximum collision frequency in energy range *j*. The type of collision is determined by generating a series of random numbers and comparing their values with normalized collision frequencies. If a collision is null, the electron energy and its trajectory are not changed. Otherwise, the electron energy is modified according to the inelastic or elastic nature of the collision and the electron trajectory is scattered.[11]

The statistics for the electron energy distributions are collected into an array for each energy bin *i* and spatial bin *l*, using

$$F_{il} = \sum_j w_j \delta[(\varepsilon_i \pm \frac{1}{2}\Delta\varepsilon_i) - \varepsilon_i]\delta[(\vec{r}_l \pm \Delta\vec{r}) - \vec{r}_j], \qquad (2.12)$$

where w_j is the weighting of the particle by considering three factors: the relative number of electrons each pseudoparticle represents, the time step used to advance the particle trajectory, and a spatial weighting. At the end of an eMCS execution, F_{il} is normalized for computing the electron energy distributions, $f_e(\varepsilon, \vec{r})$, at each spatial location using

$$\sum_i F_{ij}\Delta\varepsilon_i = \sum_i f_e(\varepsilon, \vec{r})\varepsilon_i^{1/2}\Delta\varepsilon_i = 1. \qquad (2.13)$$

Similar as bulk electrons, the secondary electrons are addressed in the eMCS in a similar manner. Pseudoparticles of secondary electrons are perpendicularly launched from the surfaces

with a specified energy (usually set to be 4 eV in the cases studies in this thesis). Trajectories of secondary electron pseudoparticles are integrated over much longer time compared with the bulk electrons until the particles disappear by striking a surface or are eliminated from the secondary electrons when their energy decreases below the lowest electronic excitation threshold and treated as bulk electrons.

2.2.3 Fluid Kinetics Poisson Module (FKPM)

The electron energy equation is used as an alternative method to obtain electron properties in the FKPM as compared to the eMCS. The electron energy distribution $f_e(\varepsilon, \vec{r}, \varphi)$ is calculated by solving a two-term Boltzmann equation with collisional term over a range of values of *E/N* through

$$\frac{\partial f_e}{\partial t} = -\vec{v}\nabla_r f_e - \frac{e\left(\vec{E} + \vec{v} \times \vec{B}\right)}{m_e} \cdot \nabla_v f_e + \left(\frac{\partial f_e}{\partial t}\right)_{collisions}, \qquad (2.14)$$

where f_e is initially assumed in the form of a Maxwellian distribution and then solved by integrating the partial differential equation over time to convergence. ∇_r is spatial gradient, ∇_v is velocity gradient, and $\left(\frac{\partial f_e}{\partial t}\right)_{collisions}$ represents all the collision terms.

The calculated f_e using Eq. 2.14 is tabulated over the given range of *E/N* and the electron temperature is given by

$$\frac{\partial(\frac{3}{2} n_e k_B T_e)}{\partial t} = \nabla \kappa \nabla T_e + \nabla \cdot (\vec{\phi}_e T_e) = P_e, \qquad (2.15)$$

where κ is the thermal conductivity, $\vec{\phi}_e$ is the electron flux and T_e is the electron temperature equal to two thirds of the average electron energy, which is determined from f_e. P_e represents the total power delivered to the electrons

$$P_e = \vec{j}_e \cdot \vec{E} = e\vec{\phi}_e \cdot \vec{E}\,, \tag{2.16}$$

where the electron flux can be expressed in either a drift-diffusion formulation

$$\vec{\phi}_e = e\mu_e n_e \vec{E} - D_e \nabla n_e\,, \tag{2.17}$$

where μ_e is the electron mobilitt and D_e is the electron diffusion coefficient, or in the Scharfetter-Gummel (S-G) expression in which the flux between mesh points (i, i+1) is given by

$$\vec{\phi}_{i+\frac{1}{2}} = \frac{\alpha\overline{D}(n_{i+1} - n_i \exp(\alpha\Delta x))}{1-\exp(\alpha\Delta x)}, \tag{2.18}$$

where

$$\alpha = -e\overline{\mu}\left(\frac{\Phi_{i+1}-\Phi_i}{\Delta x}\right), \tag{2.19}$$

and Δx is the distance between vertex i and i+1, Φ_i is the potential at vertex i, $\overline{D}$ and $\overline{\mu}$ are the averaged diffusion coefficient and mobility in the interval.

The densities of all charged heavy particles and neutral species, $N(\vec{r})$, are obtained by solving the continuity, momentum and energy equations using

$$\frac{\partial N_i}{\partial t} = -\nabla \cdot \vec{\phi}_i + S_i \tag{2.20}$$

$$\frac{\partial \vec{\phi}_i}{\partial t} = \frac{\partial (N_i \vec{v}_i)}{\partial t} = -\frac{1}{m_i}\nabla(kN_iT_i) - \nabla\cdot(N_i\vec{v}_i\vec{v}_i) + \frac{q_i}{m_i}N_i(\vec{E}_s + \vec{v}_i \times \vec{B}) \tag{2.21}$$

$$-\nabla\cdot\overline{\overline{v}}_i - \sum_j \frac{m_j}{m_i+m_j} N_i N_j (\vec{v}_i - \vec{v}_j)\nu_{ij}$$

$$\frac{\partial N_i \varepsilon_i}{\partial t} = -\nabla \cdot \bar{\bar{\kappa}} \nabla T_i - p_i \nabla \cdot \vec{v}_i - \nabla \cdot (N_i \vec{v}_i \varepsilon_i) + q_i \vec{\varphi}_i \vec{E} - (\bar{\bar{\mu}}_i \nabla \cdot \nabla \vec{v}_i) \qquad (2.22)$$

$$-\sum_{m,j} k_{mij} N_i N_j \varepsilon_i + \sum_{m,j,l} k_{mjl} N_j N_l \Delta \varepsilon_{mjl}$$

where $\vec{\phi}_i$, N_i, $\vec{v}_i$, m_i, T_i, $\bar{\bar{\mu}}_i$, p_i and ε_i are the flux, density, velocity, mass, temperature, viscosity, pressure and average energy of species *i*, respectively.

Due to the tight coupling of electrostatic fields $\vec{E}_s(\vec{r},\varphi)$ and the densities of charged particles, the Poisson's equation is solved coincidentally with the continuity, momentum and energy equations using a semi-implicit method by linearly approximating the charge density as

$$\nabla \cdot (\varepsilon \nabla \Phi(t+\Delta t)) = -\rho(t+\Delta t) = -\rho(t) - \Delta t \frac{\partial \rho}{\partial t}|^{t+\Delta t}. \qquad (2.23)$$

The first term on the right hand side of Eq. 2.23 is expressed as

$$\rho(t) = \rho_m(t) + \sum_i q_i N_i(t), \qquad (2.24)$$

where ρ_m is the charge density in or on non-plasma materials, q_i is the charge of species *i*, and N_i is the density of species *i*. The charge density is evaluated at current time step *t*, and the potential is evaluated at future time $t+\Delta t$. For explicit method used for solving the Poisson's equation, the time step is limited by a specific fraction of rf period (normally less than one percent) and the dielectric relaxation time, which is the ratio of permittivity of free space to the plasma conductivity. With the semi-implicit method, the time step Δt for updating the charged particle densities can be larger than the dielectric relaxation time.[12]

By using the Scharfetter-Gummel form for the fluxes of electrons and ions which captures the upwind and downwind properties, $\frac{\partial \rho}{\partial t}|^{t+\Delta t}$ in the second term on the right hand side of Eq. 2.23 is evaluated as

$$\frac{\partial \rho}{\partial t}\Big|^{t+\Delta t} = \frac{\partial \rho_m(t')}{\partial t} - q_{e,j}\nabla\cdot\left(\vec{\phi}_e(t) + \frac{\partial \vec{\phi}_e}{\partial \Phi}[\Phi_s(t+\Delta t) - \Phi_s(t)]\right) \tag{2.25}$$

$$-\sum_i q_i \nabla\cdot\left(\vec{\phi}_i(t) + \frac{\Delta t}{2}\frac{\partial \vec{\phi}_i(t)}{\partial t}\right),$$

where $q_{e,j}$ is the charge of electrons (e) and ions (j), $N_{e,j}$ is the density of electrons (e) and ions (j), ε is the local permittivity, Φ_s is the electrostatic potential, and $\vec{\varphi}_{e,j}(t)$ is species flux with e and j representing electrons and ions. The *t'* donates that the charge density is evaluated at current time step *t*, and the potential is evaluated at future time $t+\Delta t$.

The Jacobian element $\frac{\partial \vec{\phi}_e}{\partial \Phi}$ in Eq. 2.25 is numerically evaluated by considering having a small fraction of potential change (typically $\Delta\Phi$ = 5%) within Δt by solving two first-order partial derivatives of the electron flux with respect to the potential $\Delta\Phi_{ij}$ using

$$\frac{\partial \vec{\phi}_{i,j}}{\partial \Phi_{i+1,j}} = \frac{\vec{\phi}_{i,j}(\Phi_{i+1,j} + \Delta\Phi_{i+1,j}) - \vec{\phi}_{i,j}(\Phi_{i+1,j})}{\Phi_{i+1,j}}, \tag{2.26}$$

where *i, j* are the radial and axial direction index, and $\Delta\Phi_{i+1,j}$ is a predefined perturbation with a typical value of $0.05\,\Phi_{i,j}$. The discretized equations are then solved using either a Successive-Over-Relaxation (SOR) method [13] or by direct sparse matrix solvers, which are DSLUCS and DSLUGM obtained from the SLAP library [14].

The boundary condition at surface of dielectrics are the charges that are computed from incident fluxes of electrons and ions from the bulk plasma, fluxes secondary electrons leaving the surfaces and coming from other locations collected by those surfaces, and conduction currents through the material. The boundary condition for solving the Poisson's equation on powered metals is the instantaneous applied potential with the addition of a dc bias,

$$\Phi(t+\Delta t) = \Phi(t) + \frac{\partial \Phi(t)}{\partial t}\Delta t + V_{dc}\,. \tag{2.27}$$

With a blocking capacitor connected in series to the bottom electrode in geometry asymmetric chambers, a dc self-bias is naturally generated on the electrodes, which ultimately determines the mean ion energy onto the substrate. The HPEM computes a dc self-bias to equalize rf currents to powered and grounded area as

$$V_{dc} = \frac{1}{C}\int \sum_i m_i \left(\sum_j \vec{\phi}_j \left(q_j + q\gamma_{ij}\right)\cdot \hat{n}_i + \frac{\partial\left(\varepsilon \vec{E}\cdot \hat{n}_i\right)}{\partial t}\right) dt\,, \tag{2.28}$$

where C is the blocking capacitance, $\vec{\phi}_j$ is the flux of charged particle *j* having charge q_j incident onto metal *i* have local normal $\hat{n}_i$, and γ_{ij} is the secondary electron emission coefficient for species *j* and metal *i*. The first summation is over metal surfaces where m_i is ±1 depending on whether the metal is on the grounded or powered side of the circuit. The second summation is over all the charged species.

The rf power applied on the electrode is implemented as a time-resolved boundary condition in the process of solving Poisson's equation in FKPM. For any form of voltage applied to the electrode, the time-averaged power on the electrode can be calculated using

$$\overline{P}_{rf} = \frac{1}{\tau}\iint V(t)\left[j\left(\vec{r},t\right) + \frac{d\left(\varepsilon \vec{E}\left(\vec{r},t\right)\right)}{dt}\right] dt dA\,, \tag{2.29}$$

where *A* is the electrode surface area, *V(t)* is the time-dependent voltage on the electrode, $j\left(\vec{r},t\right)$ is the conduction current density to the electrode, $\vec{E}\left(\vec{r},t\right)$ is the electric field over the electrode, and τ is the integration time which is a multiple of the rf period.

In multi-frequency CCPs, there are two or more rf sources with different frequencies applied to the system where the power associated with each frequency is maintained constant

over time. The power at each frequency must be separately computed so that the voltage at that frequency can be adjusted, which can be achieved by computing the discrete Fourier components of the bias current. The current is recorded as time series with a resolution from 10^3 to 10^4 points per rf period. These current time series are then used to calculate the discrete Fourier components of incident current at each frequency on the electrode. Up to six harmonics of current at each frequency are resolved. Integration is then performed for current-voltage pairs to calculate power deposition $\overline{P}_{rfi}$ at each applied frequency w_i averaged over a time which is a multiple of the period of the lowest frequency. The calculated $\overline{P}_{rfi}$ is compared with the desired power deposition from the corresponding frequency and the voltage of this frequency is then adjusted by a small fraction in the next iteration until the specified power is asymptotically reached for all the frequencies.

2.2.4 Surface Kinetics Module (SKM)

The etching process and the coupling between the bulk and surface processes are addressed by the SKM in the reactor scale modeling in which a Surface Site Balance Model (SSBM) is executed. The SSBM consists of rate equations for the fractional coverage of surface resident species based on reactions with fluxes from the gas phase or between surface sites. Based on these surface coverages, the reactive sticking coefficients for gas phase species on surfaces are updated.[15]

The fluxes of gas phase species incident onto the surface, $\vec{\phi}_{in}$, used in the SKM are provided by the results of the FKPM. The general form of a plasma-surface reaction is

$$A(\mathrm{g}) + B(\mathrm{s}) \rightarrow C(\mathrm{s}) + D(\mathrm{g}) + E(\mathrm{g}), \tag{2.30}$$

where g denotes a gas phase species and s denotes a surface site. The rate for the i^{th} reaction in the surface reaction mechanism between gas phase species A and surface site B on material m is

$$R_{im} = \alpha_i \phi_{Am} \theta_{Bm}\,, \tag{2.31}$$

where α_i is the reaction probability of the i^{th} reaction, ϕ_{Am} is the incident flux of gas phase species *A* on material *m*, and θ_{Bm} is the fractional occupancy of the surface sites by species *B* on material m. The evolution rates of the coverages of surface sites are obtained by summing up the rates of reactions generating or consuming the sites.

The steady state coverages of all surface sites, together with the fluxes of products leaving the surface back to the plasma, $\vec{\phi}_{out}$, are obtained by integrating the coupled rate equations for all surface sites using a third-order Runge–Kutta technique. The total time length to integrate the rate equations for the surface reactions is a few seconds, which is long enough for the results to converge. The reaction probability for an incident gas phase species is then the sum of fractional losses by all reactions removing the species.

2.2.5 Plasma Chemistry Monte Carlo Module (PCMCM)

When the calculated plasma properties reach steady state, the PCMCM is executed to compute ion and neutral trajectories from the bulk plasma through the time-varying sheath.[16] The ion energy and angular distributions (IEADs) and neutral energy and angular distributions (NEADs) of the tracked species are collected on specific surfaces. Time-resolved electric and magnetic fields, source functions and the densities of species are collected from the EMM, EETM and FKPM for PCMCM calculation.

Pseudoparticles which represent ions and neutrals are launched at locations weighted by their source functions throughout the plasma volume. Initial velocities are randomly chosen from a temperature-specified Maxwell-Boltzmann distribution with isotropic angular distribution. The trajectories of the pseudoparticles are integrated by interpolating the electric fields in time and space to compute accelerations. Collisions and energy are also addressed using a null-

collision technique on a separately defined energy grid. A set of collision probability arrays for heavy particle reactions are computed in advance to account for all possible collisions and provide actual collision frequency for the null-collision technique.

The time step for advancing the pseudoparticles in PCMCM is dynamically chosen such that it is not longer than a specific fraction of rf period or the time to traverse a specific fraction of a computational mesh cell. In the bulk plasma, this fraction is usually 0.2 – 0.5. When a pseudoparticle enters the sheath region and begins to be accelerated, the fraction is reduced such that a higher resolution can be achieved for collected ion energy on the surface. Hot neutrals can be created in the sheath region through heavy particle collisions between high energy ions and thermal neutrals, which results in neutrals incident on the surface with significant amount of energy for favorable material processing while minimizing the charging effect. Both the IEADs and the NEADs are computed by recording the pseudoparticles reaching the energy bins at a specific surface.

2.3 Mote Carlo Feature Profile Model (MCFPM)

The time evolution of etching profiles in poly-silicon, oxide and nitride using fluxes, energy and angular distributions of ions and neutrals provided by the HPEM are predicted by the MCFPM, described in detail in Refs. [17,18]. Briefly, in the MCPFM the feature is resolved using a 3-dimensional cubic mesh. A material identity is assigned to each cell in the mesh, often called a voxel. Gas phase species are represented by Monte Carlo pseudoparticles which are launched with energies and angles sampled from the distributions obtained from the HPEM. The trajectories of the pseudoparticles are tracked until they hit a solid mesh cell, where a surface reaction mechanism is used to determine the disposition of the gas particle and solid cell using

Monte Carlo techniques. Based on the selected reaction, the identity of the mesh cell at the site of collision will be changed (e.g., passivation), removed into the gas phase (e.g., etching) or covered by a new mesh cell (e.g., deposition).

The fluxes of species incident onto the etch front were measured by tallying the number of pseudoparticles that impact a user defined measurement window at the center of the feature at the depth of the lowest point of the feature. The number of impacts of each pseudoparticle representing a given species arriving at the etch front window was scaled by the weight of a single pseudoparticle (the number of atoms or molecules that each pseudoparticle represents), divided by the surface area of the cell collecting the particle and multiplied by the dot-product of the vector velocity of the particle and the surface normal at the site of incidence. To reduce the noise while capturing the general trend of the fluxes with increasing aspect ratio, a digital 3-point filter with coefficients of 0.25, 0.5 and 0.25 was used to smooth the fluxes. The etch depth is the vertical distance between the position of the etch front and the position of the interface between the material to be etched (e.g., Si and SiO_2) and the patterned mask (e.g., photoresist and amorphous carbon) at the top of the feature.

All of the initially released particles in the MCFPM are reactive species (e.g., ions, electrons and neutral radicals) and their trajectories are tracked through several collisions with the surface until the particle is either consumed or leaves the feature. The reactive etch or sputter products produced by surface reactions (e.g., SiF_x and CF_x) are also tracked in the MCFPM while the non-reactive products (e.g., CO and CO_2) are not tracked. The fluxes of reactive species out of the feature were measured by counting the number of pseudoparticles leaving the feature passing out of the top of the computational domain. For non-reactive species products of surface reactions, the fluxes out of the feature were accounted for by counting the non-reactive

species produced after surface reactions.

2.3.1 Energetic Particle Surface Reactions

In the MCFPM, the occurrence of each reaction is determined by the probabilities in the user defined reaction mechanisms. Probability arrays for the reaction of each gas phase species with each surface site are constructed while accounting for the energy and angular dependence of the process. When a pseudoparticle hits a surface cell, a random number is generated to select the reaction that would occur based on these probability arrays. For etching reactions having an energy dependence (e.g., physical sputtering and chemically enhanced reactive etching), the reaction yield for a particle incident onto a surface with an incident energy of E_i and an incident angle of θ with respect to the local surface normal is determined by [19,20]

$$p(E_i,\theta) = p_0\left(\frac{E_i - E_{th}}{E_r - E_{th}}\right)^n f(\theta), \tag{2.32}$$

where E_{th} is the threshold energy, E_r is a reference energy, p_0 is the yield at the reference energy, n is the energy dependent exponent (typically 0.5), and $f(\theta)$ is the relative probability at angle of incidence θ.

The angular dependence is often different between direct physical sputtering and chemically enhanced etching. These two processes can be simultaneously active, with chemically enhanced etching dominating at low ion energy and physical sputtering becoming more important as ion energy increases.[21,22] For physical sputtering, $f(\theta)$ is an empirical function with a maximum at 60^o, reduced probability at normal incidence and zero probability at grazing incidence.[20] For chemically enhanced etching, $f(\theta)$ is unity for normal incidence and angles up to 45°, with a monotonic roll-off to zero probability at grazing incidence.

Other than being etched by high energy ions with a reaction yield determined by Eq. 2.32, the surface complex and polymers can be activated when the energy of the bombarding ions is low.

These activated sites model the formation of dangling bonds on the surface due to low energy ion bombardment. The activated site, with its larger number of available dangling bonds, then has a higher sticking probability for polymerizing species (e.g., CF_x radicals) for polymer deposition. The probability for the activation of the complex and polymer sites by low energy ions is,

$$p(E_i,\theta) = p_0 \times \max\left(0, 1-\frac{E_i}{E_m}\right) f(\theta), \tag{2.33}$$

where E_m is the maximum energy of the process and p_0 is the yield at zero incident energy.

Since the probability of a particle striking the surface upon arrival is, by definition, unity, the following procedure is followed to normalize selection of reaction probabilities. The cumulative yield of all allowed processes for the energy and angle of incidence is computed. For all such interactions, there is an elastic collision – meaning a reflection from the surface without changing the state of the surface. If the cumulative yield of non-reflective processes is less than unity, then the elastic scattering yield is increased so that the cumulative yield is unity. If the cumulative yield is greater than unity, the elastic yield is reduced so that the cumulative yield is unity. If after scaling the elastic yield to zero, the cumulative yield is still greater than unity, then the yields of all processes are scaled to provide a unity cumulative yield. The scaled probability array is then used to randomly select the process that occurs.

In the etching of high aspect ratio features, energetic particles (originating as ions and proceeding as hot neutrals) can undergo several collisions with the sidewalls before reaching the etch front. In the MCFPM, an angle dependent energy loss is used to determine the retained energy of the reflected particle after colliding with the surface. For an energetic particle striking a surface with an incident energy of E_i and an incident angle of θ, the energy of the scattered particle is determined by

$$E_s(\theta) = E_i \left(\frac{E_i - E_c}{E_{ts} - E_c} \right) \left(\frac{\theta - \theta_c}{90^\circ - \theta_c} \right), \quad \theta > \theta_c \text{ and } E_c < E_i < E_{ts}, \qquad (2.34)$$

where E_{ts} is the threshold for complete specular scattering, E_c is the cutoff energy for diffusive scattering and θ_c is the lower cutoff angle for specular reflection. Incident particles with $E_i > E_{ts}$ are assumed to retain all of their energy. Incident particles with $\theta < \theta_c$ or $E_i < E_c$ are assumed to diffusively scatter. In the studies of etching of high aspect ratio features in oxide and ONO stacks in this thesis, E_{ts} = 100 eV, E_c = 10 eV and $\theta_c = 70^\circ$.

2.3.2 Surface Charging

Electrostatic charging of features results from the deposition of charge from ions which neutralize upon striking surfaces (top of feature or sidewalls within features) and electrons which deposit on surfaces. Charge is then retained on the voxel upon which it is deposited until neutralized by electrons (for positive charge) or ions (for negative charge). If a voxel with charge is removed through surface reactions (e.g., physical and chemical sputtering), the removed cell is does not carry away its charge into the gas phase. The charge is retained in the mesh by redistributing it to the adjacent mesh cells. The voxel harboring the charge can also be buried by polymer or redeposition of etch products. This surface-resident or buried charge produces electric fields which in turn accelerate or deviate the trajectories of incident charged particles. The changes in velocities of charged particles from these electric fields are included in the simulation by adding the resulting the Lorentz forces to the equations of motion of charged particles as their trajectories are integrated. These electric fields are computed in the following manner.

On a time averaged basis, the net conduction current to the wafer in a capacitively coupled plasma is zero. With this boundary condition, the net flux of positive and negative ions launched towards the feature is balanced by a flux of electrons to sum to zero net current. The

initial trajectories and fluxes of ions are given by the PCMCM. The current of ions launched towards the surface is determined from the randomly chosen fluxes.

A corresponding flux of electrons pseudoparticles is also launched to provide charge neutrality. In CCPs, the electron flux typically arrives at the surface only when the sheath collapses during the anodic portion of the cycle. The trajectories of the electrons therefore arrive at the surface with nearly isotropic trajectories having a temperature nearly the same as in the bulk plasma. Electron pseudoparticles are therefore launched towards the feature with velocity randomly chosen from an isotropic Maxwellian distribution having a specified temperature. Although experimentally electrons typically arrive at the surface in bursts during the anodic portion of the cycle, in the simulation an electron particle is launched after every positive ion particle is launched with adjustments made if negative ions are also launched.

The algorithms for computing electric fields in the feature are discussed in Ref. [23] and so will be only summarized here. The time rate of change of charge density in numerical cell k, ρ_k (C/cm^3) is

$$\frac{d\rho_k}{dt} = \sum_i \frac{q_i w_i}{\Delta V_k} - \nabla \cdot \rho_k \mu_k \vec{E}\,, \tag{2.35}$$

where $\vec{E} = -\nabla\Phi$ is the electric field, Φ is the electric potential, and the sum is over incident particles i having weighting w_i and carrying charge q_i. The numerical cell has volume ΔV_k and the charge has electrical mobility μ_k in that cell. The electric potential is obtained by implicitly solving Poisson's equation, $-\nabla \cdot \varepsilon \nabla \Phi = \rho$, using finite volume techniques. Computationally, this is performed using the Successive-Over-Relaxation algorithm employing a parallel red-black technique. Each material included in the simulation is assigned a dielectric constant and mobilities for positive and negative charge transport. The dielectric constants and mobilities in

the computational mesh then vary as the material identities change. Due to the computational expense of solving Poisson's equation, the potential is updated only after hundreds of charged particle strikes a surface. This is a large enough number to provide some computational efficiency, but a small enough number that there are not significant unaccounted for changes in electric potential as millions of charged particles are launched during the simulation.

Reflective boundary conditions for electric potential are used in the lateral (x-y) dimensions and a zero-gradient boundary condition is used on the top surface of the computational domain. The bottom of the computational domain is grounded. In reality, the bottom electrical boundary condition is as far away as the other side of the wafer, which is a distance far greater than what can be resolved in the simulation. However, what is important is that the capacitance of the system is accurately represented. To achieve that end, the dielectric constant of the bottom 2 – 3 layers of computational cells above the ground plane are adjusted so that the capacitance of the feature with respect to the ground plane is the same as for the actual thickness of the wafer.

All positive ions neutralize upon their first collision with a surface, with the former ion proceeding as a hot neutral with an angle and energy given by the previous expressions. Other than for the neutralizing collision with the surface, hot neutrals have the same reaction mechanism as ions. When the energy of a hot neutral falls below a specified low energy such as 5 eV, it is reclassifed as a thermal neutral.

2.4 Acceleration Techniques

One of the major advantages of hybrid plasma modeling is the trade-off between the accuracy of physics and the computational speed, which gives the opportunity to obtain more

details and insights of physics provided that acceleration techniques can be implemented into the codes. In this thesis, two acceleration techniques of the HPEM were performed from the perspective of the software and the hardware, respectively. The acceleration based on software is through optimizing the algorithms in the subroutines of the code to reduce redundancy and increase computational efficiency.[24] The acceleration based on hardware is through implementing a memristor based partial differential equation (PDE) solver, which is an analog solver as opposed to the default digital solver usually used in solving the Poisson's equation.[25,26]

2.4.1 Optimizing Algorithms

Several modifications were made to the HPEM to increase the numerical efficiency, especially to better represent cases with multiple plasma regions having significantly different mole fractions of reactants and large fraction of non-plasma materials in the mesh as shown in Fig. 2.3. The HPEM uses a rectilinear structured mesh with computational loops that are nested by, for example, radial and axial mesh points. OpenMP parallelization directives are employed on the outer loop for computational efficiency. An outer-mesh covers the entire computational domain, which consists of plasma points denoted by colored regions and non-plasma points such as dielectrics, surrounding air and electrical ground planes denoted by the uncolored regions in Fig. 2.3. Within the outer-mesh, a sub-mesh covers a region which only captures the plasma.

Due to the rectilinear structure, even within the sub-mesh computational domain, only a subset of the mesh points may represent plasma, with the remainder representing solid materials (e.g., flow tubes, substrates and electrodes) or surrounding air. In order to maximize numerical pipeline, pre-fetch and parallelization efficiencies, all plasma transport equations are solved at all points in the sub-mesh. The pipeline efficiency resulting from looping over the structured mesh

provides higher net computational speed even if some of the mesh points are non-plasma. A stencil used to identify plasma points and zero out calculations at non-plasma points. If the fraction of the sub-mesh points that are not plasma is sufficiently small, then the pipeline and pre-fetch efficiencies win out over the additional work to compute at non-plasma points, and the net computing speed is higher.

For those conditions where a large fraction of the sub-mesh is not plasma, the just described technique is not computationally efficient. For those cases, a node-and-neighbor technique is used to loop over only plasma points. A list of plasma mesh points and their nearest neighbors is constructed, and OpenMP loops are performed over the plasma node-list. Although this is not as efficient with respect to pre-fetch opportunities, the end result is faster overall computations if at least ≈ 1/3 of the sub-mesh is not plasma. To deploy this technique, several node-lists are required – for plasma points at which densities, temperatures and potentials are computed, for radial and for axial momenta which are computed at the half-points between plasma points, and for non-plasma points bounding plasma points.

When using the electron energy equation, rate coefficients for collisional processes (e.g., electron impact ionization) are required as a function of electron temperature, T_e, or average electron energy, $<\varepsilon_e>$. This is accomplished by solving Boltzmann's equation for the electron energy distribution over a wide range of *E/N* and constructing a look-up table for rate coefficients as a function of T_e. This table is periodically updated as the mole fractions of species change due to reactions. In the modeling of remote plasma sources, the mole fractions of gases may greatly vary as a function of position. For these conditions, the numerical mesh is divided into different regions or zones which individually cover volumes of the plasma having significantly different mole fractions as shown in Fig. 2.3. Separate lookup tables for rate

coefficients are generated for each region to address these spatially dependent differences in mole fractions. Although there is computational expense associated with generating and updating multiple look-up tables, the resulting rate coefficients are better representations than using volume averaged rate coefficients over all plasma regions.

2.4.2 Implementing Memristor-based PDE Solver

One of the major bottlenecks to achieve high performance computing (HPC) is the time spent on the data transfer in interconnect between the logic and the memory.[27] Although the processes and the memories are already fast enough, they have to wait for the data to come in and out due to the traditional architecture and functionality of the components on the chip. Under the circumstances that significant amount of time is spent on the interconnect, the memory processing unit (MPU) which directly performs multiplication on memory has been proposed as a candidate to overcome the data transfer bottleneck in traditional von Neumann architecture and gain efficient computation especially for solving large sparse matrix for deep neural machine learning.[28]

Memristors offer co-located memory and processing properties and have been extensively studied for data-intensive tasks such as artificial neural networks which can tolerate low computing precision without suffering from performance degradation.[29,30] Here a memristor-based PDE solver (MPS) was demonstrated as an alternative approach for solving the Poisson's equation in HPEM while maintaining the accuracy and providing the opportunity to speed up the simulation through in-memory computation. The Possion's equation solved in the HPEM in Eq. 2.23 is generally in the form of

$$u_{xx} + u_{yy} = f(x, y), \tag{2.36}$$

which can be numerically formulated as solving an $A \cdot X = B$ problem, where A is the coefficient matrix which is usually sparse and asymmetric when several coupled equations are simultaneously solved as shown in Fig. 2.4(a), X is the unknown vector to be solved for (e.g., electric potentials), and B is the constant vector containing the boundary conditions (e.g., surface charges and applied electric field). While such problem can be solved using several numerical techniques, here the Jacobi method was used as it can be directly mapped to the memristor crossbar systems using entirely iterative vector-matrix operations.

In the Jacobi method, a new estimate of the unknown vector X^{i+1} is computed based on the last obtained X^i as

$$X^{i+1} = C - R \cdot X^i, \tag{2.37}$$

where R is a modified coefficient matrix with the diagonal elements removed, and C is a constant vector that includes the boundary values. Eq. 2.37 can be implemented in a crossbar array by mapping R and C to the crossbar with numerical values represented by the memristor device conductance, as shown in Fig. 2.4(a). By applying X^i to the input rows of this crossbar as voltage pulses, the output currents collected at the columns represent the new estimated value of X^{i+1}. The process is then repeated iteratively by feeding X^{i+1} to the system as the next input until desired accuracy is achieved.

The above approach was tested by inserting the MPS into the workflow of HPEM for modeling an ICP reactor sustained in argon gas commonly used in the semiconductor industry for material processing as shown in Fig. 2.4(b). In this ICP system, a spiral coil on top of a dielectric window is connected to a rf power source which launches an electromagnetic wave into the reactor through the dielectric window. Argon gas flows into the reactor from the nozzle in the center of the dielectric window. Electrons are accelerated by the inductive electric fields,

colliding with the argon gas to produce excited species and ions. In an actual plasma etching system, the gas is reactive, producing radicals and ions which flow downstream towards a rf biased stage upon which a wafer is mounted. The radicals and ions perform etching of the wafer. The residues of the process (the etch products) are then pumped out of the system.

Numerical PDE solvers provide the core functions for both HPEM and other industry-standard numerical simulators. The simulation goes through a hierarchy of outer loops that provide densities, fluxes and temperatures of electrons, ions and neutrals, which are obtained by solving a set of fluid-dynamics equations. The inner-most loop of the simulator is the solution of Poisson's equation for the electric potential. The particular implementation of Poisson's equation is semi-implicit based on Eq. 2.23 in which charge densities at time t are augmented by predictions of charge densities at $t + \Delta t$. The solution for the electric potential (and electric field) is then used to update the fluid-dynamics equations to obtain new charged particle distributions. This process is repeated for each time step. In HPEM, the solver usually used for solving the Poisson's equation is the floating-point solver using the DSLUCS subroutine from the SLAP Library.[14] Here another option for solving the Poisson's equation using the MPS was implemented. The MPS was first modeled for demonstration before being fabricated for real hardware test.

The ICP system was simulated using a 94×52 grid mesh and a coefficient matrix having 2.4×10^7 elements. Within the inner loop, Poisson's equation for electric potential is formulated as an $A \cdot X = B$ problem. Note although the mesh in the HPEM is structured, the crossbar method is also applicable to unstructured meshes using finite element or finite volume methods. The structure of the mesh and method of discretization of the PDEs may change the format of the A matrix, but has no impact on the solver's solution.

To make certain that the crossbar approach is general enough to address all such possibilities, the matrix was divided into 32 × 32 sized slices assuming no common patterns in the coefficient matrix. Each slice was then treated independently to perform local vector-matrix operations. After solving the Poisson's equation at each time step within the memoristor-based solver, the solutions were transferred back to the subsequent modules in the HPEM for next iteration of updates. This process was performed in an automated manner, with the MPS fully integrated into the HPEM as a standard subroutine.

Due to the large matrix size required to address the plasma transport, the problem was solved through simulation using a device model for the MPS that represents actual device parameters. The MPS simulator incorporates matrix slicing and precision extension techniques, while accounting for device non-idealities and other circuit details.[25] The comparison of the time evolution of the plasma potential inside the ICP reactor obtained from the HPEM execution using DSLUCS and memristor solver MPS are shown in Fig. 2.4(c).

The MPS produces results that match well with those obtained using the double-precision (64-bit) floating-point DSLUCS solver. The two cases both clearly capture the initial quick rise of the plasma potential and the stabilization to a quasi-steady state after 1 μs. The oscillation in the plasma potential with a period of 0.1 μs results from the application of the 10 MHz rf bias on the substrate. The spatial distributions of the densities obtained from DSLUCS and MPS also agree quite well with each other with an average error of less than 0.3%. The ability of the MPS to produce accurate simulation results confirms the potential of the in-memory computing systems to achieve HPC while mitigating the device-level limitations.

2.5 Integrated Reactor and Feature Scale Design

The pursuit of Moore's law has taken microelectronics into the realm of nanoelectronics (e.g., FinFET and gate-all-around FET with gate length of less than 10 nm) [31,32] and 3-dimensional structure has been used for higher integration than the conventional 2-dimensioanl planar structure (e.g., vertical NAND) [33,34]. The etching of nanoscale features directly depends on microscopic parameters (e.g., energy and angular distributions of ions and neutrals), which are determined by the plasma properties (e.g., plasma density, electron temperature and electron energy distributions) modulated by macroscopic operating parameters (e.g., power, pressure and gas flow rate) through the knobs of the reactor. Confronted with increasing challenges on selectivity and anisotropy in the fabrication of nanoscale devices, integrated reactor and feature scale design is highly required for process optimization.

Reactor scale plasma models are mainly used to analyze and optimize plasma reactors used in the semiconductor processing industry. Feature scale models are mainly used to study profile evolution and charging resulting from plasma processing. Integrating reactor and feature scale models is important given their effect on each other. The non-uniformity of the plasma across the wafer causes differences in the evolution of the feature profiles across the wafer. Besides, the topography of the features on the wafer surface impact the sheath profile, charging, and etch products leaving the surfaces which effect the plasma on the reactor scale. As the etch profile results from surface reactions between solid materials and gas phase species whose fluxes, energy and angular distributions are determined by the plasma sources, solutions for optimizing the etching process is ultimately dependent on expert control of the reactor operating conditions.

The schematic of the integrated reactor and feature scale modeling is shown in Fig. 2.5. The reactor scale modeling (HPEM) gives the estimation of the plasma properties (e.g., densities and temperatures) based on the given operating conditions. The time evolution of profiles etched in the materials (e.g., Si, SiO_2 and Si_3N_4) are predicted by the feature scale modeling (MCFPM) using the fluxes of ions and neutrals, IEADs and NEADs provided by the surface kinetics and chemistry modeling (SKM) and sheath scale modeling (PCMCM), respectively. The gas phase and surface reaction mechanisms are developed based on cross sections, rate coefficients and surface reaction probabilities from experimental measurements or theoretical calculations, with validations for satisfying fidelity in capturing the physics.

In order to investigate the origins of undesirable phenomena (e.g., ARDE and bowing) and optimize the process such as etching of HAR features, parametric study should be performed in the feature scale modeling by varying the key parameters (e.g., fluxes of ions and neutrals, IEADs and NEADs). Variations of etch profile, etch rate and selectivity for different key parameters are analyzed to understand how to tune the parameters into the optimal window for optimized etch process with high anisotropy and selectivity. With the information and knowledge obtained from the feature scale modeling, control parameters in reactor scale modeling (e.g., power, pressure and gas flow rate) will be tuned to produce desirable fluxes and energy distributions of ions and neutrals in the above optimal window to optimize the etch process. A machine learning algorithms can be established between the etch properties and the reactor control parameters, which could be possibly trained for transferring the algorithms for prediction in different plasma processing recipes or reactors.

2.6 Figures

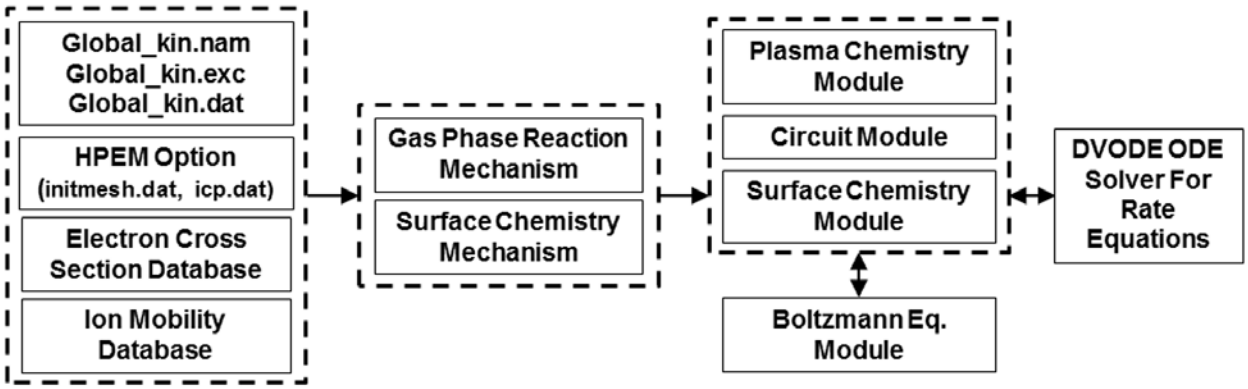

Fig. 2.1 Modular structure of the 0-dimensional global model (Global_Kin) used for investigating plasma chemistry, plasma kinetics and surface chemistry.

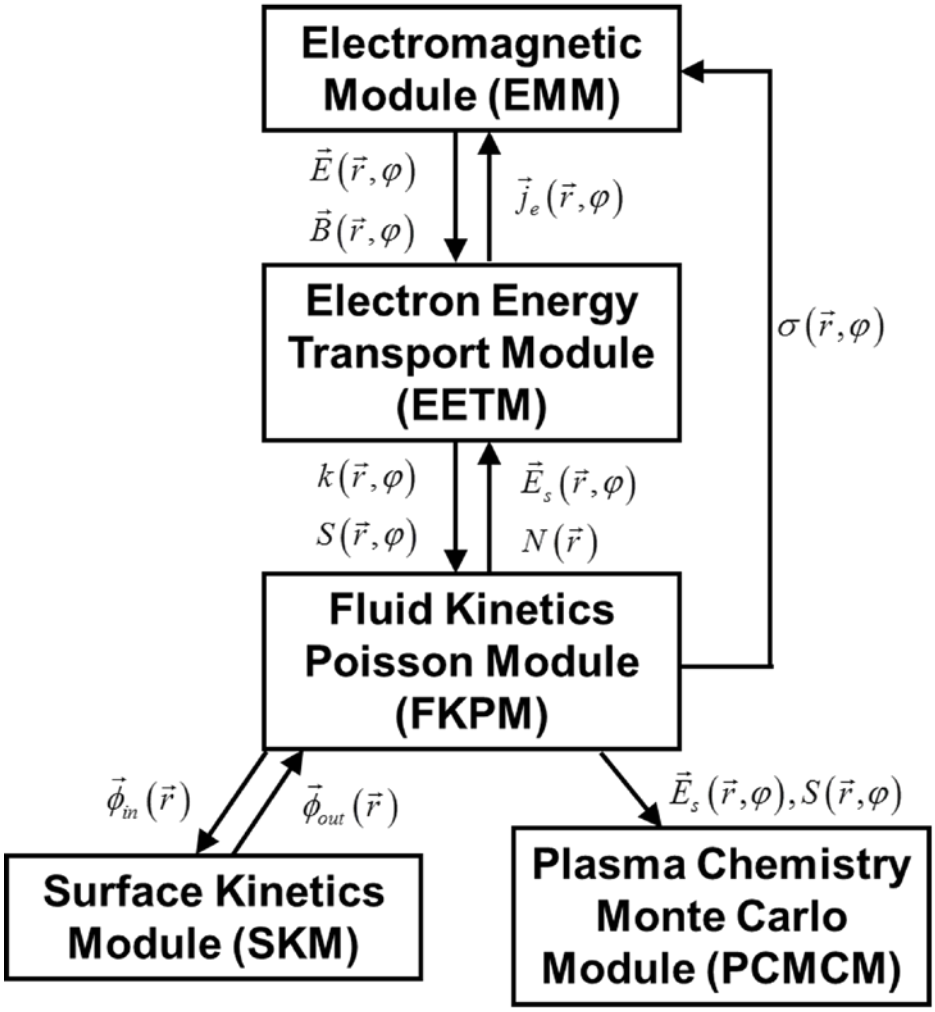

Fig. 2.2 Flow chart of the information exchange among the modules in the 2-dimensional Hybrid Plasma Equipment Model (HPEM).

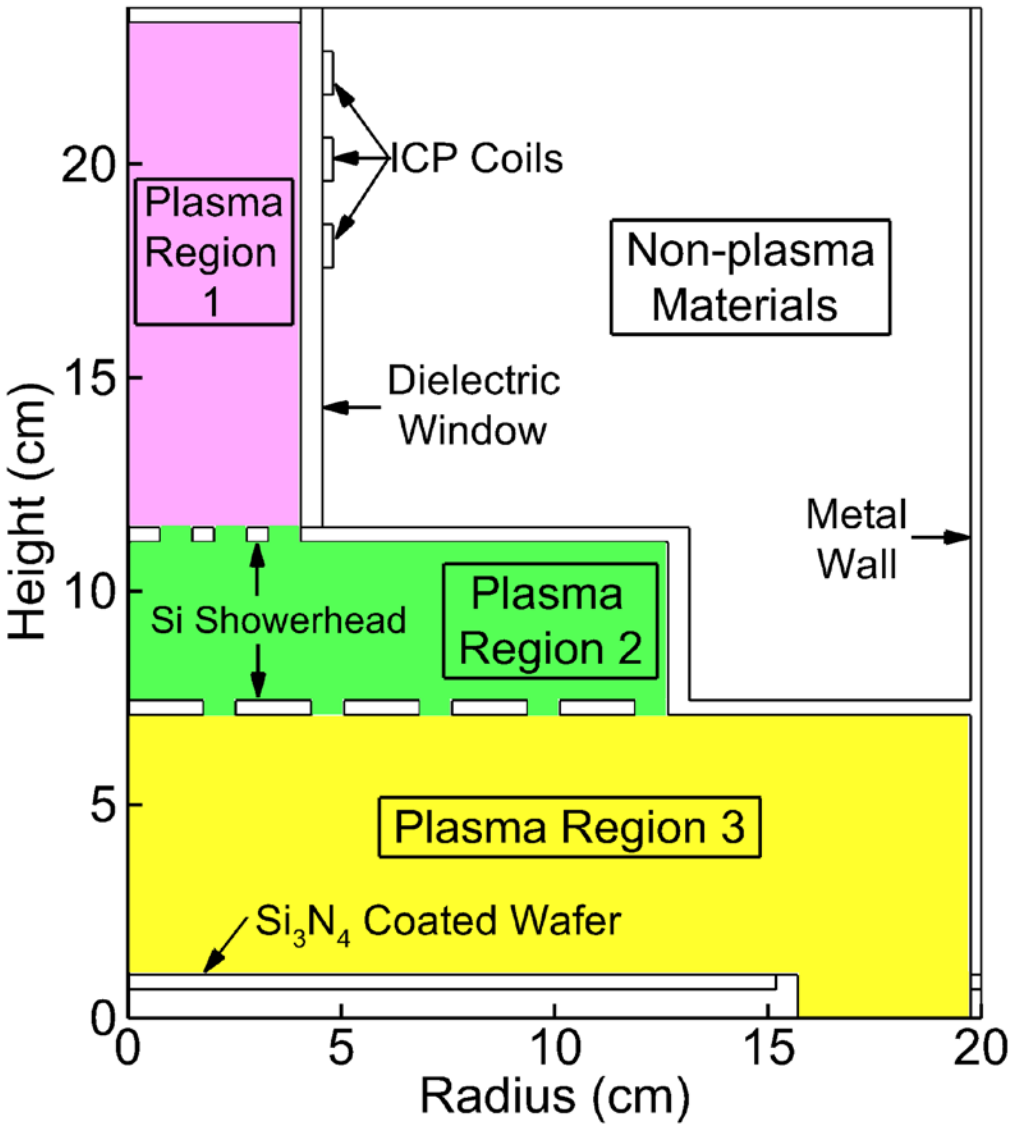

Fig. 2.3 Illustration of two algorithm optimizations (i.e., multiple plasma regions and separating plasma and non-plasma points in storage) implemented for increasing efficiency of modeling downstream etch systems consisting of remote plasma source, plenum and downstream chamber.

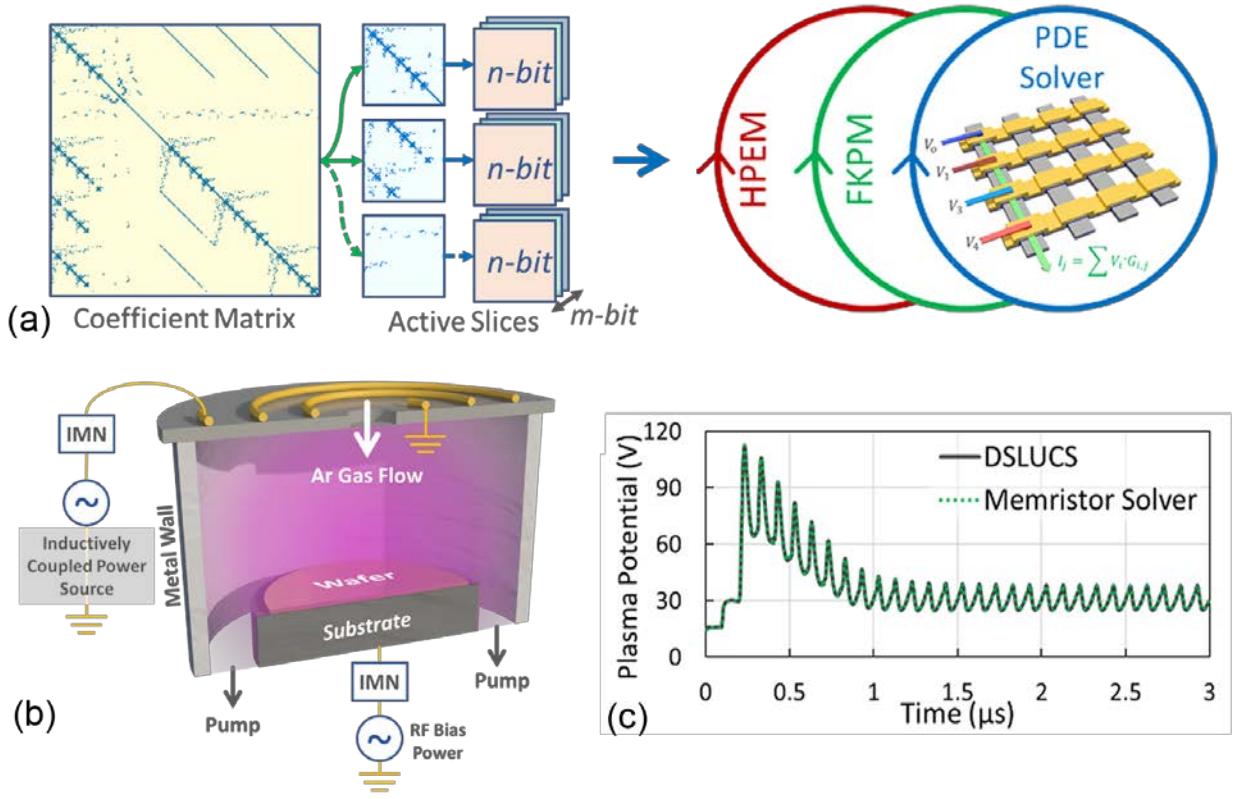

Fig. 2.4 Illustration of implementing memristor-based PDE solver for increasing efficiency of plasma modeling with an ICP reactor as an example.[25] (a) A sparse coefficient matrix generated from HPEM when solving for the plasma potential in the FKPM, which is sliced into patches and processed by memristor based crossbar arrays. (b) Schematic of the ICP reactor with rf bias on the substrate used as a test case. (c) Comparison of plasma potentials calculated using the numerical solver (DSLUCS) and memristor-based PDE solver (MPS).

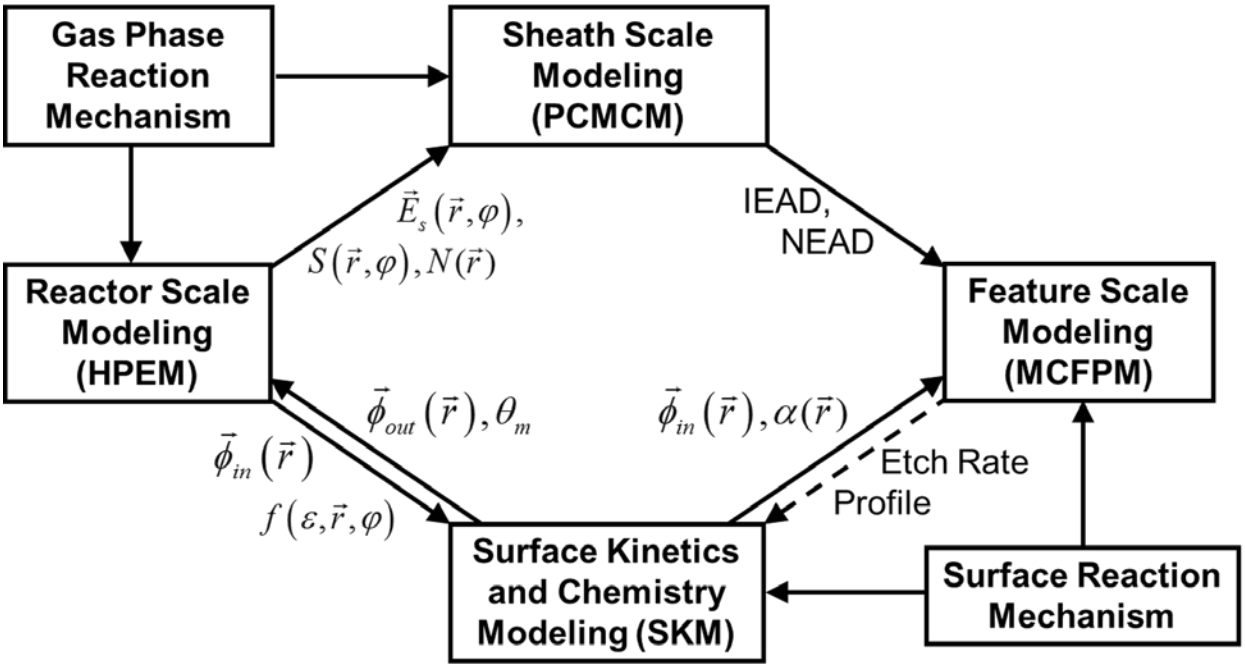

Fig. 2.5 Schematic of integrated reactor scale and feature scale modeling used for investigating physics and optimizing reactor design.

2.7 References

1. A. M. Lietz and m. J. Kushner, J. Phys. D: Appl. Phys. **49**, 425204 (2016).
2. R. Dorai and M. J. Kushner, J. Phys. D: Appl. Phys. **35**, 2954 (2002).
3. S. D. Rockwood, Phys. Rev. A **8**, 2348 (1973).
4. D. Stafford and M. J. Kushner, J. Appl. Phys. **96**, 2451 (2004).
5. D. Stafford and M. J. Kushner, J. Appl. Phys. **98**, 073303 (2005).
6. P. N. Brown, G. D. Byrne and A. C. Hindmarsh, SIAM J. Sci. Stat. Comput. **10**, 1038 (1989).
7. ODEPACK Library: https://computation.llnl.gov/casc/odepack/.
8. M. J. Kushner, J. Phys. D: Appl. Phys. **42**, 194013 (2009).
9. R. L. Kinder and M. J. Kushner, J. Vac. Sci. Technol. A **17**, 2421 (1999).
10. S. L. Lin and J. N. Bardsley, J. Chem. Phys. **66**, 435 (1977).
11. S.-H. Song and M. J. Kushner, Plasma Sources Sci. Technol. **21**, 055028 (2012).
12. P. L. G. Ventzek, T. J. Sommerer, R. J. Hoekstra and M. J. Kushner, Appl. Phys. Lett. **63**, 605 (1993).
13. W. H. Press, B. P. Flanney, S. A. Teukolsky and W. T. Vetterling, Numerical Recipes: The Art of Scientific Computing, Cambridge University Press, 1987.
14. SLAP Sparse Matrix Library: https://www.netlib.org/.
15. D. Zhang and M. J. Kushner, J. Vac. Sci. Technol. A **19**, 524 (2001).
16. Y. Zhang, M. J. Kushner, N. B. Moore, P. Pribyl and W. Gekelman, J. Vac. Sci. Technol. A **31**, 061311 (2013).
17. A. Sankaran and M. J. Kushner, J. Vac. Sci. Technol. A **22**, 1242 (2004).
18. C. Huard, Y. Zhang, S. Sriraman, A. Paterson, K. J. Kanarik and M. J. Kushner, J. Vac. Sci. Technol. A **35**, 031306 (2017).
19. C. C. Cheng, K. V. Guinn, V. M. Donnelly and I. P. Herman, J. Vac. Sci. Technol. A **12**, 2630 (1994).
20. C. F. Abrams and D. B. Graves, J. Appl. Phys. **86**, 2263 (1999).
21. J. M. Lane, K. H. A. Bogart, F. P. Klemens and J. T. C. Lee, J. Vac. Sci. Technol. A **18**, 2067 (2000).
22. M. E. Barone and D. B. Graves, Plasma Sources Sci. Technol. **5**, 187 (1996).
23. M. Wang and M. J. Kushner, J. Appl. Phys. **107**, 023309 (2010).

24. S. Huang, V. Volynets, J. R. Hamilton, S. K. Nam, I.-C. Song, S. Lu, J. Tennyson and M. J. Kushner, J. Vac. Sci. Technol. A, **36**, 021305 (2018).
25. M. A. Zidan, Y. Jeong, J. Lee, B. Chen, S. Huang, M. J. Kushner and W. D. Lu, Nat. Electron. **1**, 411 (2018).
26. M. A. Zidan, J. P. Strachan and W. D. Lu, Nat. Electron. **1**, 22 (2018).
27. R. Nair, Prof. IEEE **103**, 1331 (2015).
28. R. Nair, S. F. Antao, C. Bertolli, P. Bose, J. R. Brunheroto, T. Chen, C. Y. Cher, C. H. Costa, J. Doi, C. Evangelinos and B. M. Fleischer, IBM J. Res. Dev. **59**, 1 (2015).
29. D. B. Strukov, G. S. Snider, D. R. Stewart and R. S. Williams, Nature **453**, 80 (2008).
30. J. J. Yang, D. B. Strukov and D. r. Stewart, Nat. Nanotech. **8**, 13 (2013).
31. F.-J. Hou, P.-J. Sung, F.-K. Hsueh, C.-T. Wu, Y.-J. Lee, Y. Li, S. Samukawa and T.-H. Hou, IEEE Trans. Electron Devices **63**, 3837 (2016).
32. G. Larrieu, Y. Guerfi, X. L. Han and N. Clement, Solid State Electron. **130**, 9 (2017).
33. H. Tanaka, M. Kido, K. Yahashi, M. Oomura, R. Katsumata, M. Kito, Y. Fukuzumi, M. Sato, Y. Nagata, Y. Matsuoka, Y. Iwata, H. Aochi and A. Nitayama, IEEE Symposium on VLSI Technology 14, 2007.
34. J. Jang, H.-S. Kim, W. Cho, H. Cho, J. Kim, S. I. Shim, Y. Jang, J.-H. Jeong, B.-K. Son, D. W. Kim, K. Kim, J.-J. Shim, J. S. Lim, K.-H. Kim, S. Y. Yi, J.-Y. Lim, D. Chung, H.-C. Moon, S. Hwang, J.-W. Lee, Y.-H. Son, U.-I. Chung and W.-S. Lee, IEEE Symposium on VLSI Technology 192, 2009.

Chapter 3 Reaction Mechanisms

3.1 Introduction

When developing LTP sources used for material processing, modeling assists in exploring operational parameter space and optimizing reactor design for optimal performance (e.g., energy efficiency, uniformity and productivity). One of the most important parts in establishing plasma models is to develop the reaction mechanisms which describe how the particles react with each other. The fidelity of the plasma models highly depend on the accuracy of the developed reaction mechanisms, which require validation or verification before being used for predicting the physics and assisting in reactor design.

Gas phase reaction mechanisms usually consist of electrons, ions, neutrals, and the reactions which would occur among them (e.g., electron impact ionization, excitation and dissociation, charge exchange and neutralization). An electron impact reaction is usually characterized by its cross section, which has the unit of area (cm^2) and is a measure of the probability that a type of reaction would occur.[1] With the given cross sections, the Boltzmann equation is solved to obtain the electron energy distributions (EEDs) for a range of *E/N*, and the cross sections are averaged over the EEDs to determine the reaction rate coefficients. The cross sections can be numerically calculated using *ab initio* methods or experimentally measured using crossed beam methods.[2]

Surface reaction mechanisms are developed to predict the evolution of the profiles during plasma processing (e.g., etching, sputtering and deposition). The surface reaction mechanisms

for most material processing by LTPs are less investigated and characterized as compared with the gas phase reaction mechanisms, which results in more uncertainties in plasma surface interaction (PSI) models. Surface reaction mechanisms usually consist of gas phase species (e.g., electrons, ions and radicals) and surface sites (e.g., pristine site, passivated site and deposited site) and the reactions which would occur between the gas phase species and the surface sites, with the reaction probability, energy and angular dependences obtained from numerical and experimental investigations.[3]

In this thesis, three gas phase reaction mechanisms, $Ar/NF_3/O_2$, $NF_3/O_2/H_2$ and $NF_3/O_2/HBr$ were developed to model the downstream etch system with remote plasma sources sustained in NF_3 mixtures, which are presented in Sec. 3.2.2 – 3.2.4. Two surface reaction mechanisms were developed. One is for selective etching of Si_3N_4 using remote plasma sources in $Ar/NF_3/O_2$ mixtures, and the other is for anisotropic etching of SiO_2 using $Ar/C_4F_8/O_2$ mixtures, which are presented in Sec. 3.3.1 and 3.3.2.

3.2 Gas Phase Reaction Mechanisms

3.2.1 Electron Impact NF_x Cross Sections

The cross sections for electron impact on NF_3 used in the models are based on the compilation by Lisovskiy *et al.*[4] The cross section for dissociative attachment of NF_3 was extended to higher energies to agree with electron swarm data. In plasma sources for producing large amounts of F radicals, the NF_3 is heavily (if not totally) dissociated, producing large densities and mole fractions of NF_2 and NF, which in turn requires electron impact cross sections for NF_2 and NF. The electron impact cross sections for NF_2 and NF were calculated using the molecular R-matrix method.[5] The cross sections for electron impact on NF_3 compiled by

Lisovskiy *et al*. and for electron impact on NF_2 and NF calculated by the R-matrix method are shown in Fig. 3.1.

The R-matrix method divides the physical space for the problem of interaction between electron and molecule into two regions – an inner region containing the target molecule and an outer region containing the incident electron. The method solves Schrödinger's equation in the inner region independent of the energy of impact electron and then uses this solution to solve the Schrödinger equation in the outer region, which is energy dependent. The cross sections for electron impact processes including elastic scattering, dissociative attachment, dissociative excitation and ionization were calculated using the molecular geometries provided by the NIST database.[6,7] All cross sections were calculated using the R-matrix method from threshold to 20 eV. Above 20 eV, the cross section for dissociative attachment goes to 0, while the cross sections for other processes were extrapolated to higher energies using the scaled Born cross sections (for excitation and ionization) [8] or assuming dominant dipole transition (for other processes) and scaling with $\ln(\varepsilon)/\varepsilon$, where ε is the electron energy. The detailed R-matrix method used for calculation of the NF_x cross sections is described in Ref. [9].

3.2.2 $Ar/NF_3/O_2$ Mechanism

A reaction mechanism was developed for plasmas sustained in gas mixtures containing $Ar/NF_3/O_2$. The species included in the model are listed in Appendix A. The rate coefficients for heavy particle collisions are listed in Arrhenius form while the rate coefficients for electron impact reactions were calculated based on the EEDs produced by solutions of Boltzmann's equation. The reactions that would occur in a pure Ar plasma are the same as discussed in Ref. [10]. The electron impact reactions and radiative transitions that would occur in a pure O_2 plasma are the same as discussed in Ref. [11] and in a pure N_2 plasmas are the same as discussed

in Ref. [12]. The additional reactions required to complete the mechanism for $Ar/NF_3/O_2$ are electron impact with NF_x, F_2, F and N_xO_y and heavy particle reactions in $Ar/NF_3/O_2$ mixtures. These additional reactions are in Appendix A. The resulting reaction mechanism is intended to be as complete as practical for a discharge sustained in $Ar/NF_3/O_2$ mixtures. As such, there are rate coefficients whose values have never been experimentally or analytically determined, and so a subset of the reaction rate coefficients was estimated based on enthalpies of reactions and analogy with similar reactions. For example, the rate coefficient for Penning ionization between excited states of Ar was uniformly estimated to be $1.2 \times 10^{-9} T_n^{1/2}$ cm^3s^{-1} [13], the rate coefficient for charge exchange between ions and neutrals was assumed to be 1×10^{-11} cm^3s^{-1} (1×10^{-9} cm^3s^{-1} for resonant charge exchange) [14] and the rate coefficient for neutralization between positive and negative ions was assumed to be 2×10^{-7} cm^3s^{-1} [15]. As to the ion-ion neutralization involving diatomic or polyatomic anions, the rate coefficients can be calculated based on semi-analytic expressions [16].

Although vibrationally excited $NF_x(v)$ is not included as a separate species in the mechanism, electron energy losses for collisions with NF_x producing vibrational states are included. As the gas mixture is usually highly dissociated for producing radicals for material processing, the fractional dissociation and density of atomic species are sensitive to the sticking coefficient and recombination probability at the surface of the wall. In this mechanism, the wall recombination coefficients for atomic F, N and O were uniformly assumed to be 0.01.

NF_3 has a thermal dissociative electron attachment cross section enabled by the electron affinity of F (3.4 eV) being larger than the binding energy of NF_3 (D_0 = 2.4 eV).[17] The large rate coefficient of this process results in the dissociation of NF_3 being predominantly due to thermal attachment when the electron temperature is only a few eV. Electronic excitation of NF_3

also leads to dissociation of NF_3 producing NF_2, NF and F. NF_2 and NF are also thermally attaching species with a binding energy of 2.9 eV [17] and 2.8 eV [18] producing F^-. These radicals are also dissociated to NF, N and F through electronic excitation.

In a pure NF_3 discharge, thermodynamically the reaction pathway is terminated by forming N_2 and F_2 through wall recombination and gas phase reactions, although electron impact excitation, dissociation and ionization of these species also occur. With the addition of O_2 to NF_3, a variety of additional reactions are enabled, which diversifies the species produced in the discharge, as illustrated in the schematic of NF_3/O_2 reaction mechanism in Fig. 3.2. O_2 is dissociated into O atoms through electron impact dissociative excitation and attachment. In addition to dissociative processes, electron impact excitation to $O_2(a^1\Delta_g, b^1\Sigma_g^+)$ and $O(^1D, ^1S)$ produces species with large potential energy, which require lower activation energy in both electron impact reactions and heavy particle reactions. The high specific power deposition and contributions to gas heating from Franck-Condon processes produces high gas temperatures, which enable endothermic heavy particle reactions to occur. Endothermic reactions have a positive change in enthalpy ($\Delta H > 0$) whereas exothermic reactions have a negative change in enthalpy ($\Delta H < 0$).

With the addition of O_2 to NF_3, reactions between NF_x and O_x directly lead to the formation of FO through

$$NF_3 + O(^1D) \rightarrow NF_2 + FO, \qquad \Delta H = -1.6 \text{ eV}, \qquad (3.1a)$$

$$NF_2 + O \rightarrow NF + FO, \qquad \Delta H = 0.7 \text{ eV}, \qquad (3.1b)$$

$$F_2 + O \rightarrow F + FO, \qquad \Delta H = -0.7 \text{ eV}, \qquad (3.1c)$$

$$F + O_3 \rightarrow FO + O_2, \qquad \Delta H = -1.2 \text{ eV}. \qquad (3.1d)$$

The formation of NO occurs through endothermic reactions

$$N_2 + O \rightarrow N + NO, \qquad \Delta H = 3.2 \text{ eV}, \qquad (3.2a)$$

$$N_2 + O_2 \rightarrow NO + NO, \qquad \Delta H = 1.8 \text{ eV}, \qquad (3.2b)$$

and through exothermic reactions

$$N + O_2 \rightarrow NO + O, \qquad \Delta H = -1.4 \text{ eV}, \qquad (3.2c)$$

$$N + O_3 \rightarrow NO + O_2, \qquad \Delta H = -5.5 \text{ eV}. \qquad (3.2d)$$

The formation of N_2O dominantly occurs through the endothermic reaction

$$N_2 + O_2 \rightarrow O + N_2O, \qquad \Delta H = 3.5 \text{ eV}. \qquad (3.3)$$

FNO is largely produced by the exothermic reaction

$$NF_2 + O \rightarrow F + FNO, \qquad \Delta H = -2.9 \text{ eV}. \qquad (3.4)$$

These species produced in primary reactions lead to secondary reactions which form, for example, NO_2, through exothermic reactions

$$FNO + O \rightarrow F + NO_2, \qquad \Delta H = -0.8 \text{ eV}, \qquad (3.5a)$$

$$FO + NO \rightarrow F + NO_2, \qquad \Delta H = -0.9 \text{ eV}, \qquad (3.5b)$$

$$N_2O + NO \rightarrow N_2 + NO_2, \qquad \Delta H = -1.5 \text{ eV}, \qquad (3.5c)$$

$$NO + O_3 \rightarrow O_2 + NO_2, \qquad \Delta H = -2.1 \text{ eV}. \qquad (3.5d)$$

and the endothermic reaction

$$NO + O_2(a\ ^1\Delta_g) \rightarrow O + NO_2, \qquad \Delta H = 1.0 \text{ eV}. \qquad (3.5e)$$

The full reaction pathway is fulfilled by reactions among NF_x species, O_x species and newly formed species (e.g., FO, NO, N_2O, NO_2 and FNO), which are either endothermic or exothermic.

In systems where the gas temperature approaches and exceeds 1,000 K (0.1 eV), many of these endothermic reactions have appreciable rate coefficients, and so radical generation also occurs by heavy particle reactions in addition to electron impact. This is particularly important downstream of the plasma zone. For example, in addition to the primary reactions between NF_x

and O_x, the formation of N_2O also occurs through the endothermic reaction

$$NO + NO \rightarrow O + N_2O, \qquad \Delta H = 1.7 \text{ eV}, \qquad (3.6a)$$

and the exothermic reaction

$$N + NO_2 \rightarrow O + N_2O, \qquad \Delta H = -1.7 \text{ eV}. \qquad (3.6b)$$

The formation of NO also occurs through exothermic reactions

$$N + NO_2 \rightarrow NO + NO, \qquad \Delta H = -3.4 \text{ eV}, \qquad (3.7a)$$

$$NO_2 + O \rightarrow O_2 + NO, \qquad \Delta H = -2.0 \text{ eV}, \qquad (3.7b)$$

$$N_2O + O \rightarrow NO + NO, \qquad \Delta H = -1.7 \text{ eV}. \qquad (3.7c)$$

These reactions are not inhibited by the decrease in gas temperature as the gas flows downstream and results in NO being the dominant radicals in the downstream region. In addition to reaction in Eq. 3.4, the formation of FNO also occurs through exothermic reactions

$$NF_2 + NO_2 \rightarrow FNO + FNO, \qquad \Delta H = -2.1 \text{ eV}, \qquad (3.8a)$$

$$NF_2 + FO \rightarrow FNO + F + F, \qquad \Delta H = -0.6 \text{ eV}, \qquad (3.8b)$$

$$F_2 + NO \rightarrow FNO + F, \qquad \Delta H = -0.8 \text{ eV}. \qquad (3.8c)$$

Even through these reactions are not inhibited by the decrease in gas temperature in downstream, the FNO density does not increase since the consumption of FNO by O atoms through reaction in Eq. 3.5(a) offsets their contributions.

There is certainly need and desire for reduced reaction mechanisms which would not only be computationally more expedient in multi-dimensional models, but also might lead to more intuitive interpretation of the results. In this regard, we performed sensitivity studies beginning with the complete reaction mechanism while excluding certain species and reactions. For example, we found that removing N_2O, FO and O_3 (and their reactions) in the operating conditions usually used for remote plasma sources produced a change in the densities of major

species of less than 3%. Although this reduction in scope of the reaction mechanism provides reasonably consistent results with the complete mechanism, the reduced reaction mechanism would give considerably less good results if the pressure was increased to the degree that 3-body reactions became important. A similar conclusion would hold for temperature. A reduced reaction mechanism for low power operation in which the increase in gas temperature is nominal could be constructed by removing nearly all of the N_xO_y species. This reduced mechanism would be insufficient for high power operation where endothermic reactions are important.

3.2.3 $NF_3/O_2/H_2$ Mechanism

A reaction mechanism was developed for plasmas sustained in gas mixtures containing $NF_3/O_2/H_2$. The schematic of the mechanism is shown in Fig. 3.3. The species included in the models are listed in Appendix B. The rate coefficients for heavy particle collisions are listed in the Arrhenius form while the rate coefficients for electron impact reactions were calculated based on the EEDs produced by solutions of Boltzmann's equation. The reactions that would occur in NF_3/O_2 mixtures are the same as discussed in Section 3.2.2. The additional reactions required to complete the mechanism for $NF_3/O_2/H_2$ mixtures are electron impact collisions with H_2, H, NH_x, HF, H_xO_y and heavy particle reactions involving H atoms. These additional reactions are listed in Appendix B.

For plasmas sustained in NF_3/O_2 mixtures, the molecular gases are dissociated to form NF_2, NF, F and O by electron impact dissociative attachment and dissociative excitation

$$e + NF_x \rightarrow NF_{x-1} + F^-,\ x = 1 - 3, \tag{3.9a}$$

$$e + NF_x \rightarrow NF_{x-1} + F + e, \tag{3.9b}$$

$$e + O_2 \rightarrow O + O^-, \tag{3.9c}$$

$$e + O_2 \rightarrow O + O + e. \tag{3.9d}$$

These reactions, proceeding through electron dissociative states, have translationally hot fragments which contribute through Franck-Condon heating to gas heating. The resulting high gas temperatures then enable endothermic heavy particle reactions to occur. The reactions among the products of reactions in Eq. 3.9 and the background gases result in formation of reactive N_xO_y species which can be used as etchants for surface reactions or precursors for downstream reactions. In remote plasma systems, the gas temperature drops significantly from the plasma zone to the downstream chamber, enabling opportunities to customize endothermic and exothermic reactions and so radical production.

With the addition of H_2 downstream of the $NF_3/N_2/O_2$ plasma, reactions between H_2/H and the dominant downstream species (e.g., O, F, NF_x and N_xO_y) lead to a variety of products mainly through exothermic reactions. For instance, HF molecules are formed through reactions which usually have an exothermicity larger than the vibrational quanta of HF (0.5 eV), resulting in formation of vibrational states of HF, HF(v), through

$$H + NF_2 \rightarrow NF + HF(v=0,1,2,\ldots), \quad 0.71/0.22/0.07\ [19] \quad (3.10a)$$

$$H + F_2 \rightarrow F + HF(v=0,1,2,\ldots), \quad 0.01/0.03/0.96\ [20] \quad (3.10b)$$

$$F + H_2 \rightarrow H + HF(v=0,1,2,\ldots), \quad 0/0.15/0.85\ [21] \quad (3.10c)$$

$$F + OH \rightarrow O + HF(v=0,1,2,\ldots), \quad 0.36/0.46/0.18\ [22] \quad (3.10d)$$

$$F + H_2O \rightarrow OH + HF(v=0,1,2,\ldots), \quad 0.21/0.75/0.04\ [23] \quad (3.10e)$$

$$F + NH_3 \rightarrow NH_2 + HF(v=0,1,2,\ldots), \quad 0.10/0.29/0.61\ [24] \quad (3.10f)$$

where x/y/z following the reaction indicates the branching ratios for producing HF(v=0), HF(v=1) and HF(v≥2). These reactions occur through the atomic H extracting an F atom from the F-containing species or atomic F extracting H atom from the H-containing species to form

HF, which has a high binding energy of 5.9 eV [25] and so is more stable than the reactant molecules.

There are additional exothermic reactions which form HF,

$$H + NF_3 \rightarrow NF_2 + HF, \qquad \Delta H = -3.5 \text{ eV}, \qquad (3.11a)$$

$$H + NF \rightarrow N + HF, \qquad \Delta H = -3.1 \text{ eV}, \qquad (3.11b)$$

$$H + FO \rightarrow O + HF, \qquad \Delta H = -3.6 \text{ eV}. \qquad (3.11c)$$

No branching ratios for forming HF(v) have been measured or calculated according to available references. This may be due to the excess potential energy not being converted to vibrational energy but to other forms of kinetic energy (e.g., rotational energy and translational energy).

In addition to HF(v) being able to deliver energy to surfaces and contribute to surface reactions, HF(v) plays multiple roles in gas phase reactions including reducing activation energy as the vibrational level increases. For example, the endothermic reactions

$$HF + F \rightarrow F_2 + H, \qquad E_a = 50{,}640 \text{ K}, \qquad \Delta H = 4.3 \text{ eV}, \qquad (3.12a)$$

$$HF(v=1) + F \rightarrow F_2 + H, \qquad E_a = 44{,}843 \text{ K}, \qquad \Delta H = 3.8 \text{ eV}, \qquad (3.12b)$$

$$HF(v\geq 2) + F \rightarrow F_2 + H, \qquad E_a = 39{,}046 \text{ K}, \qquad \Delta H = 3.3 \text{ eV}, \qquad (3.12c)$$

have reduced change in enthalpy and lower activation energy with the reactant HF increasing in vibrational state. In exothermic reactions, the reactant HF(v) increases the exothermicity (thereby increasing gas heating), examples being,

$$HF + O^* \rightarrow OH + F, \qquad \Delta H = -0.5 \text{ eV}, \qquad (3.13a)$$

$$HF(v=1) + O^* \rightarrow OH + F, \qquad \Delta H = -1.0 \text{ eV}, \qquad (3.13b)$$

$$HF(v\geq 2) + O^* \rightarrow OH + F, \qquad \Delta H = -1.5 \text{ eV}. \qquad (3.13c)$$

In cases where reactions are marginally endothermic, HF(v) can convert endothermic reactions to exothermic reactions such as

$$HF + OH \rightarrow H_2O + F, \qquad \Delta H = 0.7 \text{ eV}, \qquad (3.14a)$$

$$HF(v=1) + OH \rightarrow H_2O + F, \qquad \Delta H = 0.2 \text{ eV}, \qquad (3.14b)$$

$$HF(v\geq 2) + OH \rightarrow H_2O + F, \qquad \Delta H = -0.3 \text{ eV}. \qquad (3.14c)$$

HF(v) molecules can also transfer their vibrational quanta to other molecular species in the system (e.g., H_2, N_2, O_2 and NH_3) through V-V processes

$$HF(v=1) + H_2 \rightarrow HF + H_2(v=1), \qquad \Delta H = 0, \qquad (3.15a)$$

$$HF(v=1) + N_2 \rightarrow HF + N_2(v), \qquad \Delta H = -0.2 \text{ eV}, \qquad (3.15b)$$

$$HF(v=1) + O_2 \rightarrow HF + O_2(v), \qquad \Delta H = -0.3 \text{ eV}, \qquad (3.15c)$$

$$HF(v=1) + NH_3 \rightarrow HF + NH_3(v), \qquad \Delta H = -0.1 \text{ eV}. \qquad (3.15d)$$

Similar to HF(v), these vibrational excited molecules can lower activation energies in reactions compared to their ground state molecules, favoring their reacting with other species in the downstream chamber.

In addition to being formed through reactions in Eqs. 3.10(e) and 3.13, OH is also formed through exothermic reactions

$$H + N_2O \rightarrow OH + N_2, \qquad \Delta H = -2.8 \text{ eV}, \qquad (3.16a)$$

$$H + NO_2 \rightarrow OH + NO, \qquad \Delta H = -1.3 \text{ eV}, \qquad (3.16b)$$

$$H + FO \rightarrow OH + F, \qquad \Delta H = -2,2 \text{ eV}, \qquad (3.16c)$$

and endothermic reactions

$$H_2 + O \rightarrow OH + H, \qquad \Delta H = 0.1 \text{ eV}, \qquad (3.16d)$$

$$H + O_2 \rightarrow OH + O, \qquad \Delta H = 0.7 \text{ eV}. \qquad (3.16e)$$

H_2O molecules are mainly formed with OH as the precursors through reactions in Eq. 3.14 and exothermic reactions

$$H_2 + OH \rightarrow H_2O + H, \qquad \Delta H = -0.6 \text{ eV}, \qquad (3.17a)$$

$$OH + OH \rightarrow O + H_2O, \qquad \Delta H = -0.7 \text{ eV}. \qquad (3.17b)$$

A small density of ammonia species are formed in the downstream chamber due to the low gas temperature which inhibit the endothermic reactions that form NH through

$$H_2 + N \rightarrow NH + H, \qquad \Delta H = 1.3 \text{ eV}, \qquad (3.18a)$$

$$H + N_2 \rightarrow NH + N, \qquad \Delta H = 6.5 \text{ eV}. \qquad (3.18b)$$

The resulting low densities of NH then limit the production of NH_2 and NH_3 through

$$NH + NH \rightarrow NH_2 + N, \qquad \Delta H = -0.9 \text{ eV}, \qquad (3.18c)$$

$$H_2 + NH_2 \rightarrow H + NH_3, \qquad \Delta H = -0.2 \text{ eV}. \qquad (3.18d)$$

3.2.4 $NF_3/O_2/HBr$ Mechanism

A reaction mechanism was developed for plasmas sustained in gas mixtures containing $NF_3/O_2/HBr$ or $NF_3/O_2/H_2/Br_2$. The schematic of the mechanism is shown in Fig. 3.4. The species included in the models are listed in Appendix C. The rate coefficients for heavy particle collisions are listed in the Arrhenius form while the rate coefficients for electron impact reactions were calculated based on the EEDs produced by solutions of Boltzmann's equation. The reactions that would occur in $NF_3/O_2/H_2$ mixtures are the same as discussed in Section 3.2.3. The additional reactions required to complete the mechanism for $NF_3/O_2/HBr$ or $NF_3/O_2/H_2/Br_2$ mixtures are electron impact collisions with Br_2, Br, HBr and heavy particle reactions involving Br-containing species. These additional reactions are listed in Appendix C.

HBr is frequently used as source of Br atoms, the main etchants of silicon-containing materials. Br atoms are mainly produced through electron impact dissociative attachment and dissociative excitation of HBr by

$$e + HBr\ (v=0,1,2,\ldots) \rightarrow H + Br^-, \qquad (3.19a)$$

$$e + HBr\ (v=0,1,2,\ldots) \rightarrow H + Br + e. \qquad (3.19b)$$

Due to the polar nature of HBr and low threshold for vibrational excitation, large amounts of vibrational states of HBr, HBr(v), exist in the HBr plasmas or HBr containing mixtures, which reduce the activation energy of gas phase reactions and deliver usable energy to the wafer for surface reactions. Besides, HBr can exothermically react with other neutral species to produce H, Br and OH radicals, which diversifies the species in the system and enables customizing the reaction pathway by flowing gases downstream of the RPS. In Br-containing mixtures, due to high electron affinity of Br atoms (3.4 eV), the electrons quickly attach to Br atoms in the afterglow or downstream of the plasma when the power is off, resulting in ion-ion plasma with Br^- as the major negative ions.

An example of customizing the reaction pathway by properly choosing the gas inlet locations in a downstream etch system consisting of a RPS, a plenum and a downstream chamber is shown in Fig. 3.5. $NF_3/N_2/O_2$ mixtures flow through the RPS from an upstream inlet and are excited by the power delivered from the ICP antenna of 300 W. The dominant radicals produced and flow downstream are F and O atoms through dissociative excitation and attachment of NF_3 and O_2 in Eq. 3.9. NO molecules are also formed through endothermic reactions among N_2, N, O_2 and O species in Eqs. 3.2 and 3.7.

With HBr/O_2 injected downstream of the plasma source, mixing with the plasma produced radicals enables another level of selectivity. Due to lack of electrons and low gas temperature (~ 350 K) in the plenum, HBr reacts with F and O through exothermic reactions

$$HBr + F \rightarrow HF + Br, \qquad \Delta H = -2.3 \text{ eV}, \qquad (3.20a)$$

$$HBr + O \rightarrow OH + Br, \qquad \Delta H = -0.3 \text{ eV}, \qquad (3.20b)$$

$$HBr + OH \rightarrow H_2O + Br, \qquad \Delta H = -1.6 \text{ eV}. \qquad (3.20c)$$

The densities of F and O atoms both decrease after passing the downstream inlet while the density of Br reaches maximum of 1.2×10^{13} cm^{-3} in the plenum as shown in Figs. 3.5(a-c). The dominant downstream radicals transition from F and O atoms to Br atoms. The ratio of Br to F fluxes reaching the wafer surface can be controlled by tuning the flow rate of HBr in the downstream inlet for optimized etching performance. In the downstream chamber, the density of Br slightly decreases without rebounding with the decreased gas temperature, which is mainly due to the consumption of Br atoms by wall recombination and exothermic reactions

$$Br + N_2O \rightarrow BrO + N_2, \qquad \Delta H = -0.6 \text{ eV}, \qquad (3.21a)$$

$$Br + FO \rightarrow BrO + F, \qquad \Delta H = -0.1 \text{ eV}, \qquad (3.21b)$$

$$Br + O_3 \rightarrow BrO + O_2, \qquad \Delta H = -1.3 \text{ eV}. \qquad (3.21c)$$

The gas temperature decreases from the RPS (~ 1,000 K), plenum (~ 350 K) to the downstream chamber (~ 330 K) as shown in Fig. 3.5(d). In the RPS, the high gas temperature is mainly due to Franck-Condon heating in electron impact dissociative processes which convert the potential energy of the excited species into the kinetic energy of the dissociated products. In the plenum and downstream chamber the gas temperature decreases to room temperature due to thermal conduction to the walls. This gradient in the gas temperature in the whole system can be used to customize endothermic and exothermic reactions and radical production by using multiple gas inlets at proper locations.

3.2.5 Mechanism Validation

To validate the $Ar/NF_3/O_2$ reaction mechanism, results obtained by global and 2-d models were compared with optical emission spectroscopy (OES) measurements. The experimental setup was a remote CCP source with a volume of 1,110 cm^3 sustained in an $Ar/NF_3/O_2$ = 5/10/100 gas mixture at 400 mTorr with a flow rate of 1,150 sccm. The total input

power was varied from 90 to 3,000 W. The relative density of neutrals was measured through OES using actinometry.[26] In actinometry, the density of a reactive species, such as F, relative to a nonreactive gas of known density, such as Ar, is obtained from the ratio of optical emission originating from excited states that have similar thresholds and rate coefficients for electron impact excitation. In this regard, optical emission intensities were recorded from F atoms at 704 nm ($3p^2P^o \rightarrow 3s^2P$) and from the reference actinometry species, Ar, at 750 nm ($4p'[1/2] \rightarrow 4s'[1/2]^o$). $F(3p^2P^o)$ is 14.8 eV above the ground state while the Ar(4p'[1/2]) is 13.5 eV above the ground state. The relative density of F atoms is given by

$$[F] = C_{Ar}^{F} \frac{I(F^*)}{I(Ar^*)}[Ar], \tag{3.22}$$

where $I(Ar^*)$ is the intensity of the Ar 750 nm emission line, $I(F^*)$ is the intensity of the F 704 nm emission line and C_{Ar}^{F} is the actinometric coefficient which is in principle a function of discharge parameters (e.g., EED, pressure and gas temperature).[27, 28] In order for Eq. 3.22 to be valid, the emitting states must be dominantly populated by electron-impact excitation from the ground state and should decay dominantly photon emission. The excitation to the emitting states of F and the actinometric species, Ar, should have similar thresholds and similar cross sections over the energy range of interest (a few to several tens of eV). That is, their rate coefficient for excitation should be similar. These requirements cannot always be strictly satisfied, however, it may be possible for $I(F^*)/I(Ar^*)$ to be proportional to $[F]/[Ar]$ over some range of plasma conditions which are chosen to make the actinometric coefficient a constant. It is possible to compute the dependence of the actinometric coefficient on the electron temperature with different types of EEDs (e.g., Maxwellian, bi-Maxwellian and Druyvesteyn) as discuss in Ref. [29]. Assuming emission from both states result from electron impact excitation of the ground state and the corresponding excitation cross sections for F and Ar have similar energy

dependence over the energy range of interest, the actinometric coefficient in Eq. 3.22 is assumed to be 1.

To model the RPS for validation, both the global model, Global_Kin, and the 2-d model, HPEM, were utilized. In the modeling of the CCP, as in the experiment, the power deposition is apportioned between ion acceleration in the sheath and electron heating in the bulk plasma (including secondary electrons). From a practical perspective, only the power deposition into electrons produces excited states and ionization. The power into electrons specified in the global model was determined by performing simulations using the 2-d model which explicitly calculates all forms of power deposition for the experimental conditions. The power dissipated into electrons from the 2-d model was then used as the input power in the global model so that side-by-side comparisons can be made to the experiments. In the 2-d model, total power deposition for any given case was obtained by adjusting the amplitude of the 10 MHz applied voltage. As the power increases from 90 to 3,000 W, the power dissipated by electrons indicated by the 2-d model increases from 58 to 388 W while the fractional power dissipated by electrons decreases from 64% to 13%. This scaling results from the increased applied voltage and sheath potentials favoring power deposition by ions relative to electrons.

The densities of F atoms measured by OES-actinometry and predicted by the global and the 2-d models are shown in Fig. 3.6. In both the experiments and simulations, the relative density of F atoms increases with power until saturating at high power. The density of F atoms predicted by the model reaches its maximum at about 1,200 W. As the power increases above 1,200 W, the density of F atoms slightly decreases as the increase of the F density produced by additional dissociation of NF_3 is counterbalanced by the rarefaction of the gas by increased gas temperature. The density of F atoms predicted by the 2-d model saturates at higher power

compared with experiments and results from the global model, however the differences are not large.

Other validation was made between results from the global model and OES measurements performed in a microwave plasma by Kastenmeier *et al*.[30] A plasma was sustained in an O_2/NF_3 mixture at 1 Torr with 1,400 W power at 2.45 GHz in a quartz cylinder of 190 cm^3, which was also the input power in the global model in plug flow mode. The NF_3 flow rate was 300 sccm for all cases. The densities of O, N_2 and NO predicted by the global model and measured by OES are shown in Fig. 3.7 as a function of the ratio of O_2 to NF_3 flow rate. The density of O atoms increases linearly with increasing flow rate of O_2 at low values, and beginning to saturate at high values due to the finite power deposition. The density of N_2 decreases in favor of the generation of NO. In the experiments, the density of NO remains almost constant for flow ratios of O_2/NF_3 (< 0.6) and sharply increases when the ratio is above 0.6. In the global simulations, the density of NO also remains nearly constant for a ratio of O_2/NF_3 smaller than 0.6 but increases less abruptly than that in the experiments for larger ratios.

The formation of NO is mainly through the endothermic reactions in Eqs. 3.2(a,b) with an activation energy of several eV which favors high gas temperature. The depletion of NO is mainly through exothermic reactions in Eq. 3.8(c) and

$$NO + NO \rightarrow N_2 + O_2, \qquad \Delta H = -1.8 \text{ eV}, \qquad (3.23a)$$

$$NO + N \rightarrow N_2 + O, \qquad \Delta H = -3.2 \text{ eV}. \qquad (3.23b)$$

NF_3 is almost fully dissociated for the given power. Adding O_2 contributes to more Franck-Condon heating, and so the gas temperature increases from 1,840 to 2,810 K as the flow rate of O_2 increases from 30 to 450 sccm, which benefits the formation of NO. The smaller slope obtained from the simulation when the ratio of O_2/NF_3 is larger than 0.6 may be due to

underestimates of the gas temperature or the sensitivity of the density of N_2 molecules to the wall recombination coefficients.

3.3 Surface Reaction Mechanisms

3.3.1 Etching of Si_3N_4 Using Remote $Ar/NF_3/O_2$ Plasma

The goal of many RPS is to confine ions, energetic particles and UV/VUV radiation to the remote source, resulting in the wafer being dominantly exposed to neutral radical fluxes. This investigation addresses the etching of Si_3N_4 by the neutral fluxes produced downstream of a RPS sustained in $Ar/NF_3/O_2$ mixtures. The surface reaction mechanism for the surface site balance model in the Surface Kinetics Module (SKM) of HPEM is listed in Appendix D. The notation of SiN is used for silicon nitride to simplify the reaction mechanism and mapping of species to surface sites. Although SiN is not strictly the same stoichiometry as Si_3N_4, this simpler model does provide insight to scaling relationships.

The initial surface composition of the wafer consists of pristine SiN sites containing Si and N subsites. The pristine SiN sites are consecutively passivated by F atoms through

$$SiNF_{m-1}(s) + F(g) \rightarrow SiNF_m(s, m = 1 - 3), \quad (3.24a)$$

where s denotes surface site and g denote gas phase species, and the Si subsites are etched by the formation of volatile SiF_4 through

$$SiNF_3(s) + F(g) \rightarrow SiF_4(g) + N(s). \quad (3.24b)$$

The notation N(s) represents the exposed N subsites in SiN(s) but still bonded to the substrate, whose removal is less straightforward. There have been several proposals for removing N(s) in similar gas mixtures. One proposal is based on the results from X-ray photoelectron spectroscopy measurements in the etching of silicon nitride by a RPS sustained in

NF_3/O_2 mixture.[31] The proposed removal process consists of two channels. The first is initiated by reaction with NO(g) which removes N surface sites by the formation of N_2 with the adsorption of O onto the surface (i.e., surface oxidation) through

$$N(s) + NO(g) \rightarrow N_2(g) + O(s). \quad (3.25a)$$

The O surface sites subsequently desorb through the formation of NO_2 and O_2 and the underlying SiN sites are exposed,

$$O(s) + NO(g) \rightarrow NO_2(g) + SiN(s), \quad (3.25b)$$

$$O(s) + O(g) \rightarrow O_2(g) + SiN(s), \quad (3.25c)$$

$$O(s) + O(s) \rightarrow O_2(g) + SiN(s). \quad (3.25d)$$

In the second channel, the N sites are etched with the formation of N_2O through

$$N(s) + NO(g) \rightarrow N_2O(g) + SiN(s). \quad (3.26)$$

Alternately gas phase N atoms can remove N sites which then expose the underlying SiN through

$$N(s) + N(g) \rightarrow N_2(g) + SiN(s). \quad (3.27)$$

The etching of SiN sites proceeds by iteratively etching the Si and N subsites. As these surface reactions are all thermally driven and occur in the absence of directional ion bombardment, the etching mechanism described in Appendix D is isotropic.

3.3.2 Etching of SiO_2 Using $Ar/C_4F_8/O_2$ Plasma

The surface reaction mechanism for the etching of SiO_2 using $Ar/C_4F_8/O_2$ mixtures in MCFPM is an updated version based on previous studies [32,33] to better address the HAR feature etching process. The gas phase species, surface sites and the reactions between gas phase species and surface sites are listed in Appendix E. The schematic of the mechanism is shown in Fig. 3.8.

The gas phase reactants are classified into the following categories. a) Ions, which are typically incident onto the feature with high energies). b) Hot neutral particles, which are produced by ions having neutralizing collisions with surfaces. Other than their charge, hot neutrals have the same reactive energy dependencies as their corresponding ions. c) Thermal neutral particles, whose sources are either radicals incident into the feature from the gas phase or hot neutrals which have slowed to thermal energies. d) Electrons, which in this mechanism are unreactive other than charging surfaces. e) Unreactive etch products, which are not tracked as pseudoparticles and removed from the simulation while accounting for their fluxes leaving the feature.

The fluorocarbon radicals come in the form of CF, CF_2 and CF_3, collectively referred to as CF_x; and in the form of C_mF_n, ($m > 1$, $n < 2m+1$). In the absence of fully dissociating the C_4F_8 feedstock gas, a significant fraction of the C_mF_n fluorocarbon radicals incident onto the substrate have only a single dangling bond. In many cases, if there was any finite surface reactivity of these single dangling bond species, there would be overwhelming polymer deposition that would prevent etching for conditions that robust etching is observed. Following extensive parameterization and sensitivity studies, we concluded that reactive C_mF_n radicals on surfaces must have at least 2 dangling bonds. Those having single dangling bonds have restricted reactivity due to steric factors. These multi-carbon fluorocarbon radicals having at least 2 dangling bonds (i.e., C_2F_3, C_3F_5 and C_3F_6) are collectively referred to as C_xF_y. For the purpose of describing specific reactions, C_2F_3 will be used as an example. In recognition of the higher reactivity of CF_x radicals having more dangling bonds, the following scaling was used. The default probability for a given reaction, p , is given by that for CF_3. The reaction probability for CF_2 is $1.5p$ and that for CF is $2p$, where the maximum allowed probability is 0.9. Although this

scaling is approximate, it does capture the trends shown in molecular dynamics simulations.

The SiO_2 can be directly sputtered by energetic ions through

$$SiO_2(s) + I^+ \rightarrow SiO_2 + I(h), \tag{3.28}$$

where s denotes a surface site, I^+ denotes any ion and I(h) denotes the hot neutral partner of I^+. The SiO_2 can be chemically removed through two steps. The first step is passivation of a pristine SiO_2 surface by CF_x and C_xF_y to form a passivated layer (complex) through

$$SiO_2(s) + CF_x \rightarrow SiO_2CF_x(s), \tag{3.29a}$$

$$SiO_2(s) + C_2F_3 \rightarrow SiO_2C_2F_3(s). \tag{3.29b}$$

The complex is chemically removed by energetic ions through

$$SiO_2CF_x(s) + I^+ \rightarrow SiF_x + CO_2 + I(h),\ x = 1 - 3, \tag{3.30a}$$

$$SiO_2C_2F_3(s) + I^+ \rightarrow SiOCF_3(s) + CO + I(h), \tag{3.30b}$$

$$SiOCF_3(s) + I^+ \rightarrow SiF_3 + CO + I(h). \tag{3.30c}$$

In addition to physical and chemical sputtering, the ions can also activate surface sites through

$$SiO_2(s) + I^+ \rightarrow SiO_2^*(s) + I(h), \tag{3.31a}$$

$$SiO_2C_mF_n(s) + I^+ \rightarrow SiO_2C_mF_n^*(s) + I(h), \tag{3.31b}$$

where $SiO_2^*(s)$ denotes the activated oxide surface site, $SiO_2C_mF_n(s)$ denotes the complex, and $SiO_2C_mF_n^*(s)$ denotes the activated complex. The CF_x and C_xF_y radicals have higher sticking probabilities on the activated complex sites than on the unactivated complex sites. Deposition of CF_x on activated sites produce the base layer of polymer P(s) through

$$SiO_2C_mF_n^*(s) + CF_x \rightarrow SiO_2C_mF_n(s) + P(s), \tag{3.32a}$$

$$SiO_2C_mF_n^*(s) + C_xF_y \rightarrow SiO_2C_mF_n(s) + P(s). \tag{3.32b}$$

Subsequent polymer growth occurs on top of the polymer layer through

$$P(s) + CF_x \rightarrow P(s) + P(s), \quad (3.33a)$$

$$P(s) + C_xF_y \rightarrow P(s) + P(s). \quad (3.33b)$$

The P(s) site can also be ion activated in the same manner as $SiO_2C_mF_n^*(s)$. The activated polymer site, $P^*(s)$, has a higher reaction probability than pristine polymer site, P(s). In the following context, P(s) refers to both pristine and activated polymer sites. The polymer can be thermally etched by F and O radicals through

$$P(s) + F \rightarrow CF_2, \quad (3.34a)$$

$$P(s) + O \rightarrow COF. \quad (3.34b)$$

and physically sputtered by energetic ions through

$$P(s) + I^+ \rightarrow I(h) + CF_2, \quad (3.35a)$$

$$P(s) + O^+ \rightarrow COF, \quad (3.35b)$$

$$P(s) + O_2^+ \rightarrow O(h) + COF. \quad (3.35c)$$

In the etching of SiO_2 in fluorocarbon gas mixtures, the polymer layer plays an important role. Thicker polymer layers result in limited availability of activation energy and reactants to the underlying complex, while thinner polymer layers result in limited amount of fuel for the removal of oxygen surface sites. Thus, controllable polymer deposition and polymer thickness is necessary to optimize the SiO_2 etching process.

In model geometry for SiO_2 etching in this dissertation, a hydrocarbon photoresist (PR) is the photolithographic mask and Si is the stopping layer underneath the SiO_2. Si can be sputtered by ions or thermally etched by F atoms through

$$Si(s) + I^+ \rightarrow Si + I(h), \quad (3.36a)$$

$$SiF_x(s) + I^+ \rightarrow SiF_x(g) + I(h),\ x = 1 - 3, \quad (3.36b)$$

$$SiF_{x-1}(s) + F \rightarrow SiF_x(s),\ x = 1 - 3, \quad (3.36c)$$

$$SiF_3(s) + F \rightarrow SiF_4. \quad (3.36d)$$

Similarly, PR can also be directly sputtered by energetic ions and thermally etched by O atoms,

$$R(s) + I^+ \rightarrow R + I(h), \quad (3.37a)$$

$$R(s) + O \rightarrow COH. \quad (3.37b)$$

The sputtered gas phase photoresist fragment, R, can then redeposit on any surface.

3.4 Figures

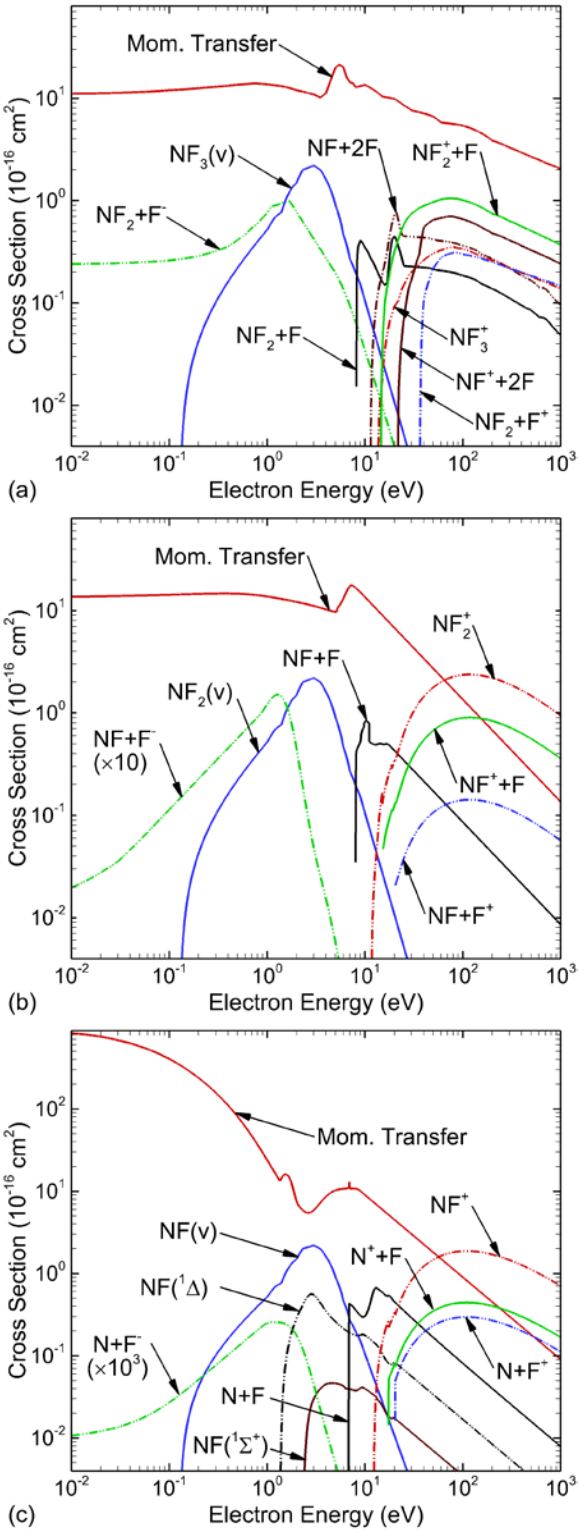

Fig. 3.1 Cross sections for electron impact reactions of a) NF_3 compiled by Lisovskiy *et al.*[4]; and b) NF_2 and c) NF calculated using the *ab initio* molecular R-matrix method [5].

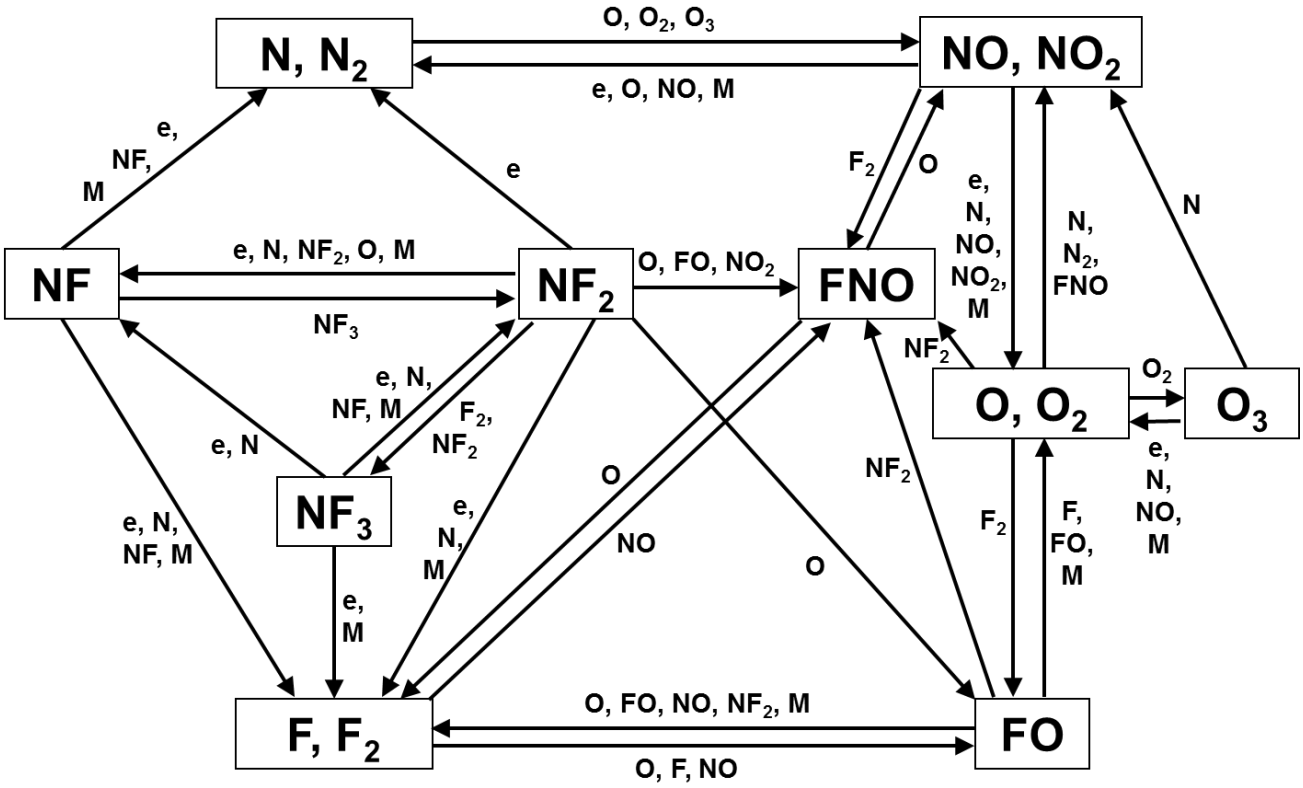

Fig. 3.2 Schematic of NF_3/O_2 gas phase reaction mechanism. M denotes any heavy particle species.

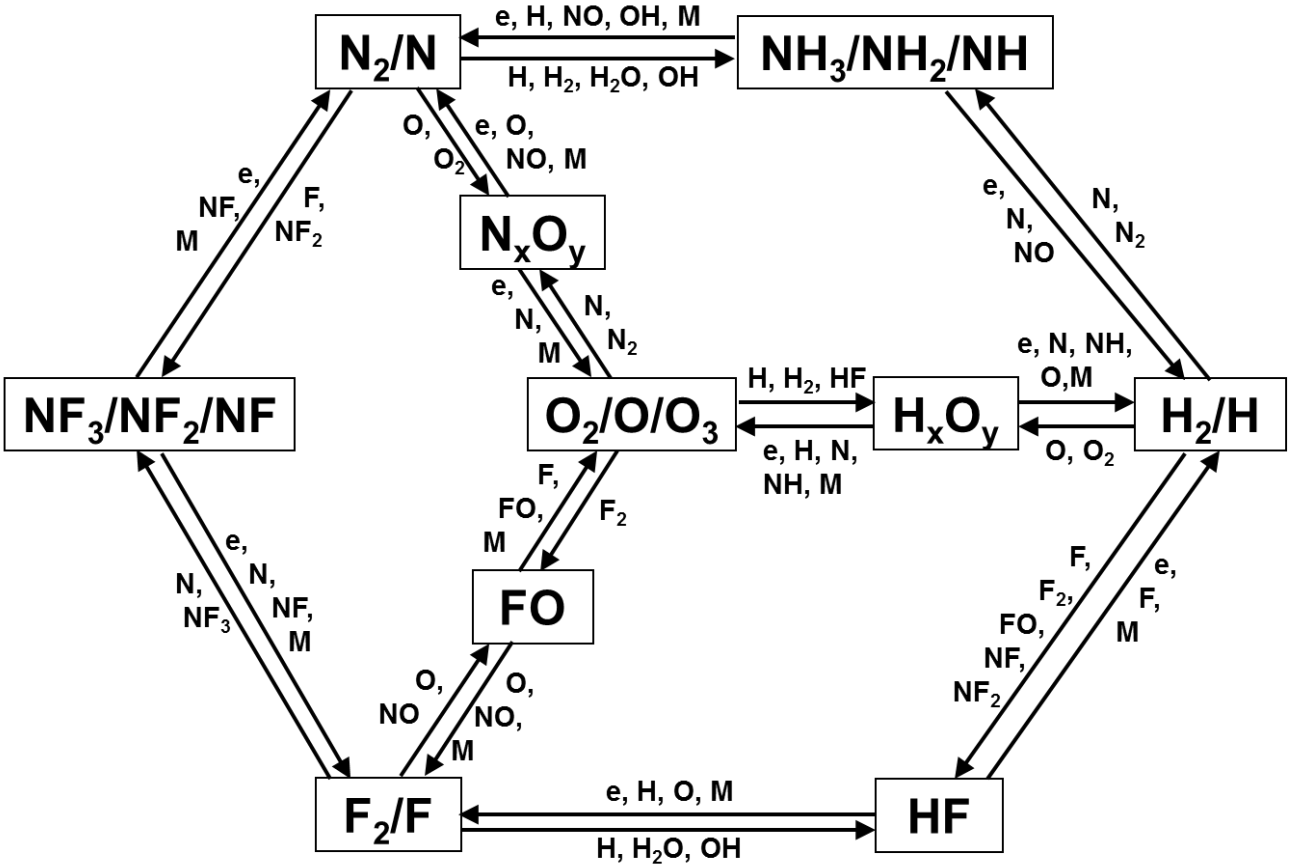

Fig. 3.3 Schematic of $NF_3/O_2/H_2$ gas phase reaction mechanism. M denotes any heavy particle species.

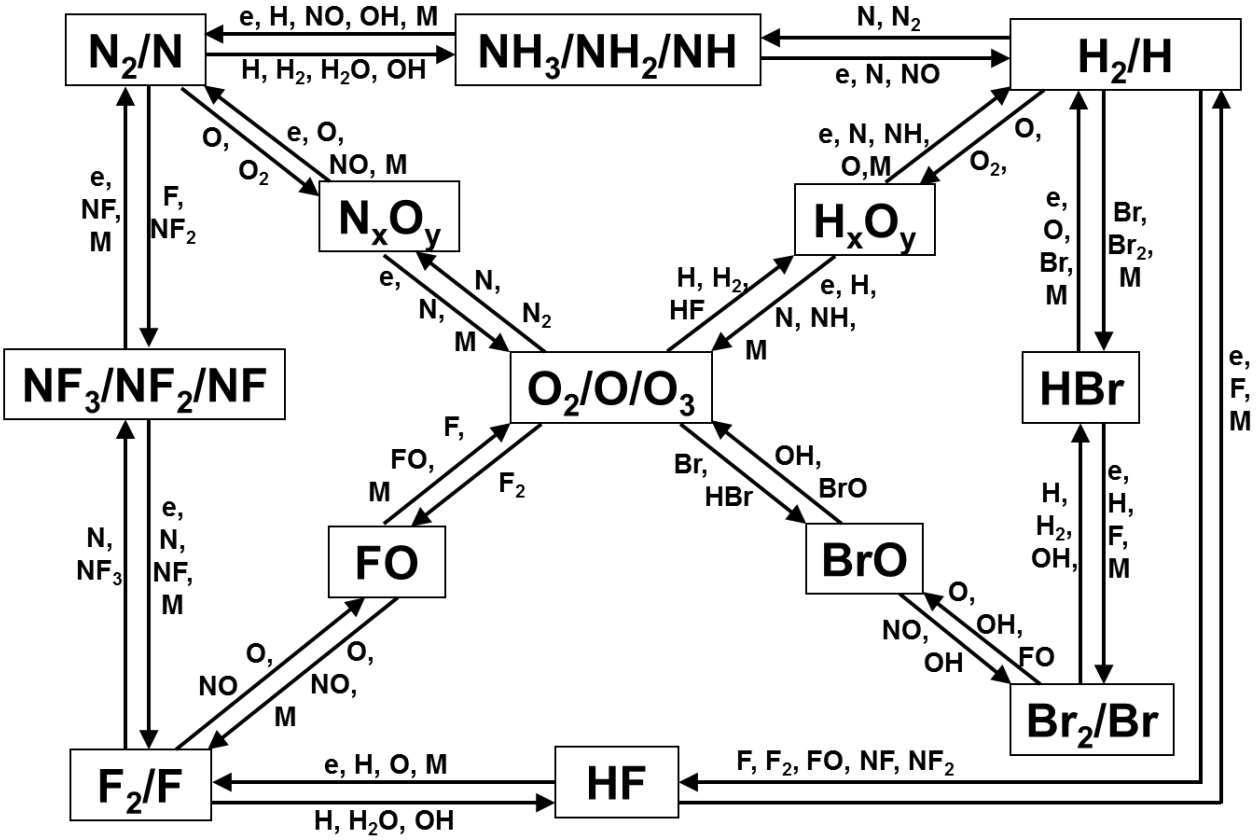

Fig. 3.4 Schematic of $NF_3/O_2/H_2/Br_2$ or NF_3/O_2/HBr gas phase reaction mechanism. M denotes any heavy particle species.

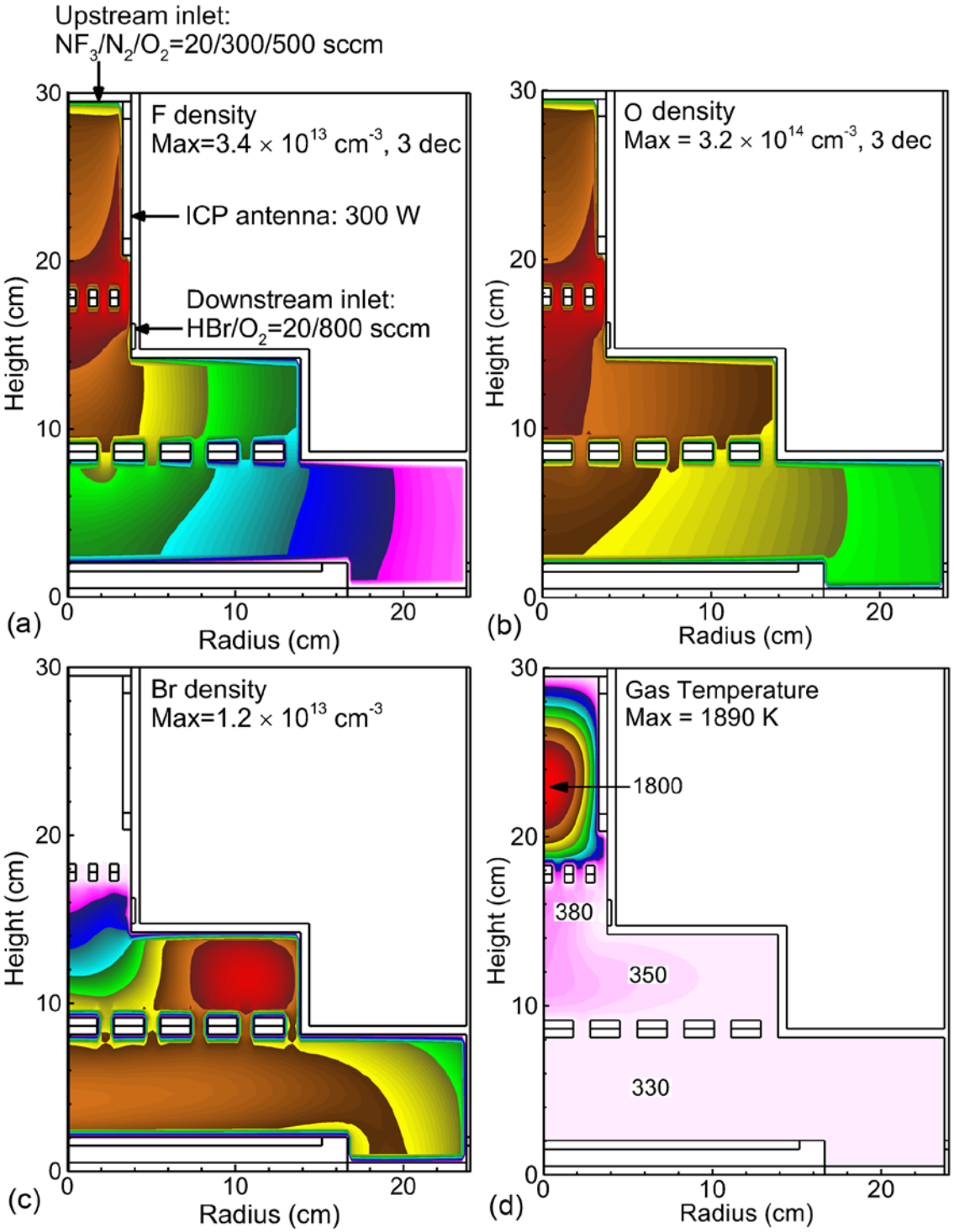

Fig. 3.5 Cases showing customizing the reaction pathways by choosing the gas injection location in a downstream etch system consisting of remote plasma source, plenum and downstream chamber. Densities of a) F, b) O and c) Br atoms and d) gas temperature are shown. Upstream inlet: $NF_3/N_2/O_2$ = 20/300/500 sccm, downstream inlet: HBr/O_2 = 20/800 sccm, gas pressure: 50 mTorr, ICP antenna power: 300 W.

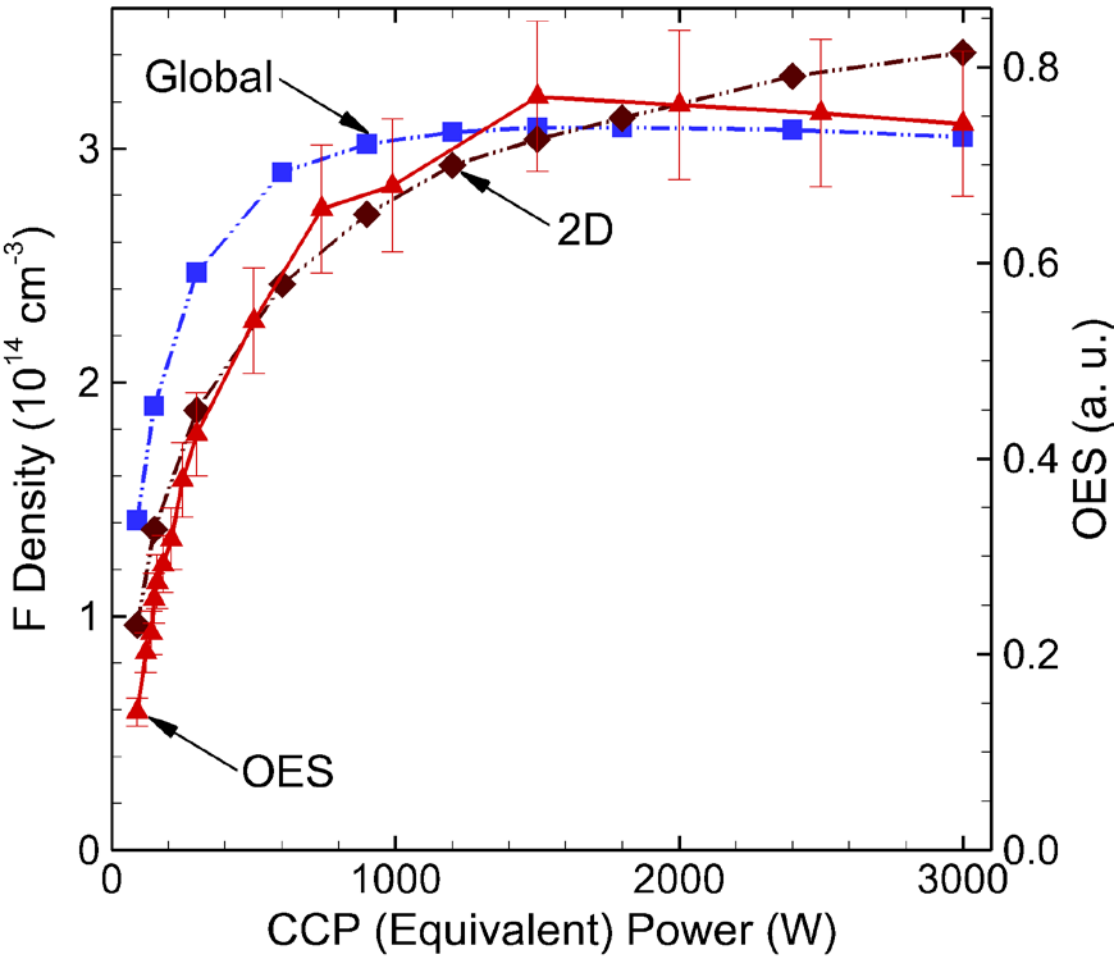

Fig. 3.6 Comparison of the global simulation results (blue dotted lines), the 2-d simulation results (brown dotted lines) and the OES measurements (red solid lines) for the densities of F atoms at the end of the plasma zone. Discharge conditions: $Ar/NF_3/O_2$ = 5/10/100, 400 mTorr, 1,150 sccm, CCP equivalent power: 90 – 3,000 W (power into electrons: 58 – 388 W).

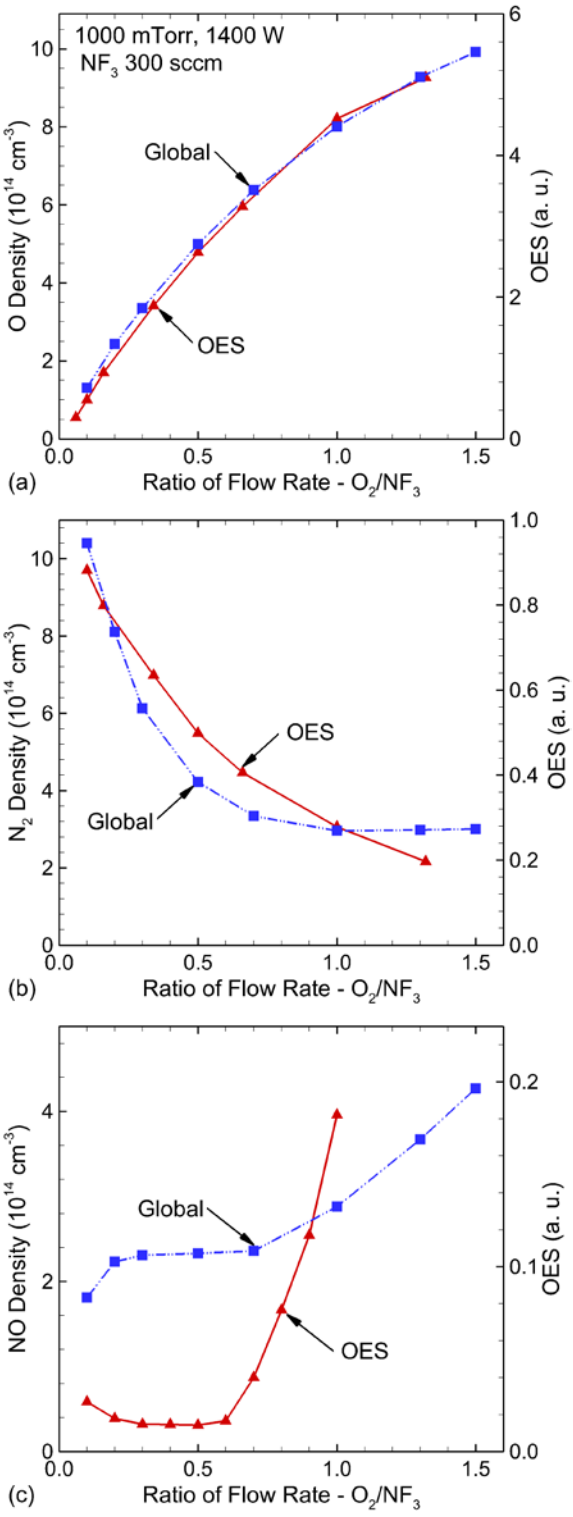

Fig. 3.7 Comparison of the global simulation results (blue dotted lines) and the OES measurements (red solid lines) for the densities of a) O atoms, b) N_2 molecules and c) NO molecules at the end of the plasma zone. The OES measurements are for a microwave discharge conducted by Kastenmeier *et al.*[30] Discharge conditions: ratio of flow rate for O_2/NF_3 = X, 1 Torr, (300+300X) sccm, X = 0 – 1.5, microwave power (into electrons): 1,400 W.

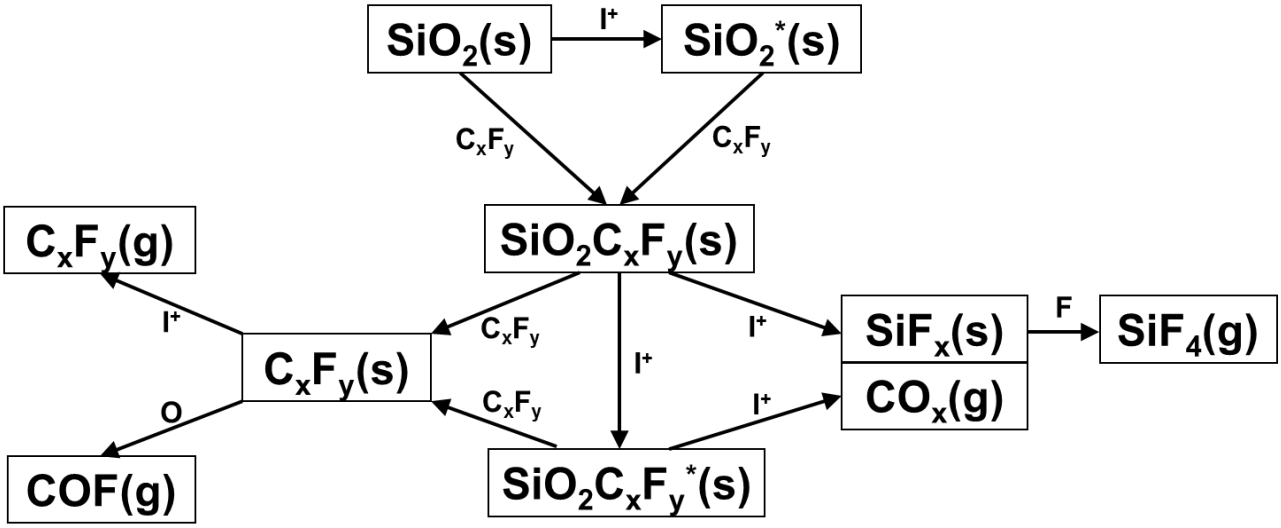

Fig. 3.8 Schematic of surface reaction mechanism for the etching of SiO_2 using plasmas sustained in fluorocarbon/oxygen mixtures. I^+ denotes ions, C_xF_y denotes polymerizing species, s denote solid surface sites and g denotes gas phase etch products.

3.5 References

1. M. A. Lieberman and A. J. Lichtenberg, Principles of Plasma Discharges and Materials Processing 2nd Edition, John Wiley & Sons, New Jersey (2005), p. 44.
2. M.-Y. Song, J.-S. Yoon, H. Cho, G. P. Karwasz, V. Kokoouline, Y. Nakamura, J. R. Hamilton and J. Tennyson, J. Phys. Chem. Ref. Data **46**, 043104 (2017).
3. V. M. Donnelly and A. Kornblit, J. Vac. Sci. Technol. A **31**, 050825 (2013).
4. V. Lisovskiy, V. Yegorenkov, P. Ogloblina, J.-P. Booth, S. Martins, K. Landry, D. Douai and V. Cassagne, J. Phys. D: Appl. Phys. **47**, 115203 (2014).
5. J. Tennyson, Phys. Rep. **491**, 29 (2010).
6. NIST Computational Chemistry Comparison and Benchmark Database: https://cccbdb.nist.gov/alldata2x.asp.
7. NIST Chemistry WebBook: https://webbook.nist.gov/cgi/cbook.cgi?ID=C7783542&Mask=1EFF.
8. Y.-K. Kim, Phys. Rev. A **64**, 032713 (2001).
9. J. R. Hamilton, T. Tennyson, S. Huang and M. J. Kushner, Plasma Sources Sci. Technol. **26**, 065010 (2017).
10. P. Tian and M. J. Kushner, Plasma Sources Sci. Technol. **24**, 034017 (2015).
11. D. S. Stafford and M. J. Kushner, J. Appl. Phys. **96**, 2451 (2004).
12. W. Tian, K. Tachibana and M. J. Kushner, J. Phys. D: Appl. Phys. **47**, 055202 (2014).
13. N. A. Dyatko, Y. Z. Ionikh, I. V. Kochetov, D. L. Marinov, A. V. Meshchanov, A. P. Napartovich, F. B. Petrov and S. A. Starostin, J. Phys. D **41**, 055204 (2008).
14. Y. Ikezoe, S. Matsuoka, M. Takebe and Viggiano, Gas Phase Ion Molecule Reaction Rate Constants Through 1986, Ion Reaction Research Group of the Mass Spectroscopy Society of Japan, Tokyo, Japan (1987).
15. R. E. Olson, J. R. Peterson and J. Moseley, J. Chem. Phys. **53**, 3391 (1970).
16. T. M. Miller, N. S. Shuman and A. A. Viggiano, J. Chem. Phys. **136**, 204306 (2012).
17. N. Ruckhaberle, L. Lehmann, S. Matejcik, E. Illenberger, Y. Bouteiller, V. Periquet, L. Museur, C. Desfrançois and J.-P. Schermann, J. Phys. Chem. A **101**, 9942 (1997).
18. M. Bettendroff and S. D. Peyerimhoff, Chem. Phys. **99**, 55 (1985).
19. R. J. Malins and D. W. Setser, J. Phys. Chem. **85**, 1342 (1981).
20. N. Jonathan, S. Okuda and D. Timlin, Mol. Phys. **24**, 1143 (1972).

21. N. Cohen and J. F. Bott, Review of Rate Data for Reactions of Interest in HF and DF lasers, Report No. SD-TR-82-86 (1982).
22. S. Gómez-Carrasco, L. González-Sánchez, A. Aguado, M. Paniagua, O. Roncero, M. L. Hernández and J. M. Alvariño, Chem. Phys. Lett. **383**, 25 (2004).
23. A. M. Zolot and D. J. Nesbitt, J. Chem. Phys. **129**, 184305 (2008).
24. A. S. Manocha, D. W. Setser and M. A. Wickramaaratch, Chem. Phys. **76**, 129 (1983).
25. R. K. Chaudhuri, K. F. Freed, S. A. Abrash and D. M. Potts, J. Mol. Struct. **547**, 83 (2001).
26. R. A. Gottscho and V. M. Donnelly, J. Appl. Phys. **56**, 245 (1984).
27. J.-S. Jenq, J. Ding, J. W. Taylor and N. Hershkowitz, Plasma Sources Sci. Technol. **3**, 154 (1994).
28. D. R. Boris, T. B. Petrova, G. M. Petrov and S. G. Walton, J. Vac. Sci. Techno. A **35**, 01A104 (2017).
29. D. V. Lopaev, A. V. Volynets, S. M. Zyryanov, A. I. Zotovich and A. T. Rakhimov, J. Phys. D: Appl. Phys. **50**, 075202 (2017).
30. B. E. E. Kastenmeier, P. J. Matsuo, G. S. Oehrlein and J. G. Langan, J. Vac. Sci. Technol. A **16**, 2047 (1998).
31. B. E. E. Kastenmeier, P. J. Matsuo, G. S. Oehrlein, R. E. Ellefson and L. C. Frees, J. Vac. Sci. Technol. A **19**, 25 (2001).
32. A. Sankaran and M. J. Kushner, J. Vac. Sci. Technol. A **22**, 1242 (2004).
33. A. Sankaran and M. J. Kushner, J. Vac. Sci. Technol. A **22**, 1260 (2004).

Chapter 4 Remote Plasma Source Sustained in NF_3 Mixtures[*]

4.1 Introduction

Remote plasma sources (RPS) are used in microelectronics fabrication to produce fluxes of radicals for etching and surface passivation while minimizing the damage that may occur by charging, energetic ion bombardment and UV/VUV radiation.[1] Due to long flow distances enabling recombination or attachment, grids or other discriminating barriers between the source and the substrate, the flux of charged particles reaching the etching chamber is small and the substrate is exposed dominantly to neutrals. RPS reactors have been used for isotropic etching processes such as resist stripping by plasmas sustained in N_2/O_2 and N_2/H_2 mixtures [2,3] and chemical drying etching of SiO_2 and Si_3N_4 by plasmas sustained in F-containing gas mixtures such as $CF_4/O_2/N_2$ [4] and NF_3/O_2 [5].

Nitrogen trifluoride (NF_3) is frequently used in RPS for the ease with which F atoms are produced by dissociative attachment. F atoms are the main etchants of silicon-containing materials such as SiO_2, SiC and Si_3N_4. RPS sustained only in NF_3 typically limits the reactive fluxes reaching the processing chamber to F, N, and NF_x. RPS sustained in NF_3 gas mixtures increases the variety of reactive species that can be produced and so enables more leverage in optimizing the process. For example, the use of NF_3/O_2 mixtures can selectively increase the etch rate of Si_3N_4 by production of NO which aids in the removal of N atoms from the

[*] The results discussed and portion of the text appearing in this chapter were previously published in the paper by Shuo Huang *et al.*, "Insights to scaling remote plasma sources sustained in NF_3 mixtures", J. Vac. Sci. Technol. A **35**, 031302 (2017).

surface.[5] The production of NO may, however, increase roughening of the surface.[6,7] The use of NF_3/N_2 mixtures can selectively increase the etch rate of SiO_2 by aiding in the removal of the O atoms, which in turn enhances the removal of Si through formation of the SiF_x etch product.[8] For certain applications it may be desirable to separately control, for example, F and N_xO_y fluxes so as to optimize the etch rates of SiO_2, Si_3N_4 and other materials. This separate optimization could, in principle, be performed using pulsed power or pulsed gas sources.

Plasma chemistry models of NF_3 mixtures have been developed to gain insights into scaling of RPS systems. Systems based on RPS for the etching of polysilicon and SiO_2 using NF_3/O_2 mixtures were modeled by Meeks *et al.*[9] and Vossen *et al.*[10] by addressing each component of the system with different levels of detail. The remote plasma source, the transport tube and the downstream etch chamber were modeled in tandem by a 0-d well mixed reactor model, a 1-d plug flow model and a 2-d axisymmetric reacting-flow model, respectively, which enabled the investigation of the impact of varying plasma source operating parameters on downstream etch results. The etch rate of polysilicon was found to be transport limited whereas the etch rate of SiO_2 was found to be surface-kinetics limited and depend more on pressure and less on flow rate than the etching of polysilicon. The densities at the exit of a remote plasma source sustained in $Ar/NF_3/N_2$ mixtures were predicted using a 0-dimensional kinetic model and served as input for a 1-dimensional model to investigate the dependence of atomic fluorine recombination on operating conditions.[11] An increase in wall temperature accelerated the desorption of atomic fluorine from the walls and increased the mole fraction of atomic fluorine. Increasing the flow rate or decreasing the gas pressure increased the fraction of atomic fluorine by decreasing the residence time or mitigating the volume recombination.

A parallel-plate reactor packed with ferroelectric pellets used for removing NF_3 from

exhaust gases in semiconductor processing was computationally investigated by Chang *et al*. using a 1-dimensional simulation.[12] The addition of O_2 or H_2 to the exhaust gases significantly attenuated the decomposition of NF_3 due to additional electron energy loss to the dissociation of the additives. The enhancement of the electric field resulting from the high dielectric constant of the ferroelectric pellets favored the decomposition of NF_3.

A dielectric barrier discharge (DBD) used for disposing of perfluorinated compounds was modeled by treating the DBD reactor as a series of discharge regions and non-discharge regions alternately placed along the axis of the reactor.[13] Electron impact and exothermic reactions with N atoms (e.g., $NF_2 + N \rightarrow NF + NF$ and $NF + N \rightarrow N_2 + F$) were found to be the major species responsible for the abatement of NF_x in NF_3/N_2 mixtures. An inductively coupled plasma sustained in Ar/NF_3 and Ar/CF_4 mixtures used for etching Si-containing materials was investigated using a global model in which particle balance equations are solved using the electron energy distribution functions measured by Langmuir probe.[14] The density of F atoms in Ar/NF_3 was found to be about 5 times higher than in Ar/CF_4 with the same input power primarily due to the low binding energy and large rate coefficients for dissociative processes of NF_3 compared with CF_4.

In this chapter, results from a computational investigation of RPS sustained in NF_3 containing gas mixtures at pressures of less than a few Torr using continuous-wave (CW) power for downstream low-damage etching applications are discussed. A comprehensive reaction mechanism for $Ar/NF_3/O_2$ was developed, which is described in Sec. 3.2.2 and listed in Appendix A. Two modeling approaches were used – 0-dimensional (0-d) global modeling to investigate fundamental reaction mechanisms and reactor scale 2-dimensional (2-d) modeling to address the spatial dynamics of flow through the system. We found that F atoms are mainly

created through thermal electrons attaching to NF_3 molecules and electronic excitation leading to dissociation. For power depositions typical of RPS systems, gas temperature excursions can exceed 1500 K, which in turn enable a larger variety of endothermic reactions to occur. The addition of O_2 leads to the formation of FO, NO, NO_2 and FNO species through endothermic and exothermic reactions, which are modulated by the gas temperature. In the downstream afterglow, the highly attaching gas mixture rapidly transitions to an ion-ion plasma. The end products are typically determined by the positive ion having the lowest ionization potential and the negative ion having the largest electron affinity, both of which are the end product of charge exchange reactions. For the NF_3 and O_2 containing gas mixtures investigated here, the terminal ion-ion plasma is composed of $[F^-] \approx [NO^+]$, a result enabled by the high gas temperature and large fractional dissociation that enables formation of NO.

Descriptions of the models are in Sec. 4.2. The scaling of RPS based on results from the plug flow mode of the global model is discussed in Sec. 4.3. The plasma properties and radical generation in a RPS sustained in CW capacitively coupled plasma (CCP) based on results from the 2-d model are discussed in Sec. 4.4. Concluding remarks are presented in Sec. 4.5.

4.2 Description of the Models

Two techniques were used to model the RPS – a global model, Global_Kin, using a plug flow approximation to address plasma and radical generation and a 2-d model, HPEM, combining fluid and kinetic approaches to address flow and electron kinetics in a RPS produced by a CCP. The Global_Kin and HPEM are described in details in Sec. 2.1 and 2.2. The gas mixtures used here were $Ar/NF_3/O_2$ mixtures. The species included in the two models are Ar, $Ar(1s_1)$, $Ar(1s_2)$, $Ar(1s_3)$, $Ar(1s_4)$, Ar(4p), Ar(4d), $Ar_2(^3\sum_u^+)$, Ar^+, Ar_2^+, NF_3, NF_2, NF, NF_3^+,

NF_2^+, NF^+, N_2, N_2(v), N_2(A $^3\sum_u^+$), N_2(B $^3\Pi_g$, higher), N, N(^{2}D), N_2^+, N^+, F_2, F_2(1 $^1\sum_u^+$), F, F(^{3}S), F_2^+, F^+, F^-, O_2, O_2(v), O_2(a $^1\Delta_g$), O_2(b $^1\sum_g^+$), O, O(^{1}D), O(^{1}S), O_3, O_2^+, O^+, O_2^-, O^-, O_3^-, FO, FNO, NO, N_2O, NO_2, NO^+, N_2O^+ and electrons. The reaction mechanism for $Ar/NF_3/O_2$ mixtures is described in detail in Sec. 3.2.2 and listed in Appendix A. The global model assists in more rapid development of the reaction mechanism and investigation of the operational parameter space. The 2-d model addresses spatially dependent electron heating mechanism and the dynamics of the flow including back diffusion.

The global model is implemented in a plug flow mode whereby integration in time is mapped to integration in space by computing a time dependent flow speed. Assuming a constant pressure, the flow speed is determined by the thermal expansion (or contraction) of the gas due to changes in temperature, changes in gas number density due to electron impact and neutral reactions, limited by requiring the flow to be subsonic. The power deposition is specified as a function of position.

More system specific issues of the downstream etch system were investigated using 2-d modeling with the HPEM. Use of the HPEM explicitly calculates all modes of power (electron and ion) self-consistently. Electron transport is addressed using fluid equations for bulk electrons and a kinetic Monte Carlo simulation for sheath accelerated secondary electrons, which play an important role in the electron heating mechanism in capacitively coupled plasmas. Non-local electron energy transport is accounted for through the thermal conductivity and convection terms of the electron energy equation that provide an electron temperature as a function of position.

4.3 Scaling of Remote Plasma Source by Plug Flow Modeling

The experimental setup was a remote CCP source with a volume of 1,110 cm^3 sustained in an $Ar/NF_3/O_2$ = 5/10/100 gas mixture at 400 mTorr with a flow rate of 1,150 sccm. To model this system, both the global model and the 2-d model were utilized. Schematics of the RPS addressed by the plug flow mode of the global model and by the CCP operation of the 2-d model are shown in Fig. 4.1. In the global model, total power deposition by electrons is specified for a tube 8.4 cm in diameter and 20 cm long. The afterglow then extends for another 15 cm. In the 2-d model, the RPS was simulated in Cartesian coordinates and has length of 20 cm, a width of 8 cm and a depth of 6.9 cm, values to better represent the experiment. The top electrode was powered and the bottom electrode was grounded as are other boundaries. The bounding dielectrics to the electrodes are alumina. The gas enters from the left boundary and exits through the right boundary.

In the base case addressed by the plug flow global model, the total input power to electrons is 237 W which corresponds to a total CCP power of 900 W. Densities of charged particles and neutrals as a function of flow distance are shown in Figs. 4.2 and 4.3. In the plasma zone, the discharge is highly electronegative with a ratio of negative ions to electrons of 25 – 70. The electron density increases during the flow to a maximum of 7.2×10^9 cm^{-3} while the electron temperature decreases from 4.0 to 3.5 eV. These trends result in part from the manner of specifying power. The power is specified to be uniform over the first 20 cm of the flow tube. The increase in electron density is due to the decrease in the mole fraction of molecular species and increase in the mole fraction of atomic species, the latter of which have a lower rate of specific power deposition than the molecular species. The electron density increases so as to maintain the desired uniform power deposition. The electron temperature decreases to reflect the

less attaching nature of the more dissociated (and more atom dominated) gas mixture as the gas flows downstream. A lower electron temperature is enabled by there being less ionization required to balance the reduced rate of attachment. This decrease in T_e occurs in spite of the increase in gas temperature and slow decrease in gas density which then increases the rate of loss of charged species by ambipolar diffusion.

The dominant positive ions in the plasma zone are O_2^+ and NO^+. With the dissociation of O_2 and the formation of NO, the density of O_2^+ decreases from 1.8×10^{11} to 0.9×10^{11} cm^{-3} while the density of NO^+ increases up to 7.6×10^{10} cm^{-3}. Although the ionization potential of NO (9.3 eV) is lower than O_2 (12.1 eV), and charge exchange to NO from all positive ions is exothermic, the significant difference in the density of parent molecules results in higher density of O_2^+ than NO^+ by about 20%. The formation of negative ions is largely due to dissociative attachment of NF_x (x = 1 – 3) by thermal electrons,

$$e + NF_x \rightarrow NF_{x-1} + F^-, \tag{4.1}$$

and dissociative attachment of O_2 by non-thermal electrons,

$$e + O_2 \rightarrow O + O^-. \tag{4.2}$$

There is essentially no energy threshold for dissociative electron attachment to NF_x, and so attachment rapidly occurs with thermal electrons (that is, electrons having a low, near ambient temperature). On the other hand, electron dissociative attachment with O_2 has a threshold energy of 3.6 eV, which is the potential energy difference between $O + O^-$ and the ground state O_2. As a result, there is production of both O^- and F^- in the plasma zone, but only production of F^- downstream where T_e rapidly decays to thermal values. In the downstream region, the plasma rapidly transitions to an ion-ion plasma (within a cm of the end of the plasma zone) composed dominantly of F^- and NO^+. There is essentially no electron impact ionization downstream of the

plasma zone, however, there is production and mixing of positive ions, through Penning processes and charge exchange. As the ionization potential of NO (9.3 eV) is the lowest among the major positive ions, charge exchange and Penning ionization predominantly favor the formation of NO^+ ions. The end result is that charge neutrality downstream is maintained by $[F^-] \approx [NO^+]$. Since the mobilities of F^- and NO^+ are commensurate, there is little ambipolar enhancement of the rates of diffusion of the ions. The steady decay of the densities of F^- and NO^+ in the downstream region predominantly results from ion-ion neutralization. The loss of ions by simple thermal diffusion accounts for less than 1% of the total loss.

The densities of neutrals and gas temperature T_g for the base case are shown in Fig. 4.3. In the plasma zone, NF_3 is rapidly depleted through electron dissociative attachment, $e + NF_3 \rightarrow NF_2 + F^-$, and dissociative excitation, $e + NF_3 \rightarrow NF_2 + F + e$. The densities of F and NF_2 sharply increase to 6×10^{12} cm^{-3} with approximately the same rate within 1 cm of the gas inlet. Further downstream, the density of NF_2 decreases while the densities of NF and FNO increase as NF_2 is decomposed to NF through electron impact dissociative attachment, $e + NF_2 \rightarrow NF + F^-$ and dissociative excitation, $e + NF_2 \rightarrow NF + F + e$. At this point, there is a sufficient density of dissociation fragments that mutual reactions add to the dissociation rate. For example, in addition to the reaction of $NF_2 + O$ producing FO ($NF_2 + O \rightarrow NF + FO$) and FNO ($NF_2 + O \rightarrow F + FNO$), NF_2 is depleted by reactions with N atoms,

$$NF_2 + N \rightarrow NF + NF, \qquad \Delta H = -0.1 \text{ eV}. \qquad (4.3)$$

Although the dominant trend is dissociation and fragmentation, there are bimolecular reactions that convert NF_2 back to NF_3,

$$NF_2 + F_2 \rightarrow F + NF_3, \qquad \Delta H = -1.0 \text{ eV}, \qquad (4.4a)$$

$$NF_2 + NF_2 \rightarrow NF + NF_3, \qquad \Delta H = 0.4 \text{ eV}. \qquad (4.4b)$$

As bimolecular recombination to reform NF_3 requires NF_2 and F_2 (the pressure is too low for 3-body processes to be important) adding O_2 which rapidly consumes NF_2 maintains the fractional dissociation of NF_3 and increases the density of F. This trend is consistent with the results of experiments where adding O_2 to NF_3 during etching of Si and SiO_2 generally increases rates of surface reactions requiring F atoms.[15]

NF dissociates to form N and F through electron impact dissociative excitation and attachment. NF can assist in the decomposition of NF_3 and reform NF_2 by

$$NF_3 + NF \rightarrow NF_2 + NF_2, \qquad \Delta H = -0.4 \text{ eV}. \qquad (4.5)$$

Another channel for the consumption of NF is through mutual reactions to form N_2 and F_2,

$$NF + NF \rightarrow N_2 + F + F, \qquad \Delta H = -3.6 \text{ eV}, \qquad (4.6a)$$

$$NF + NF \rightarrow N_2 + F_2, \qquad \Delta H = -5.2 \text{ eV}, \qquad (4.6b)$$

Although these reactions are both exothermic, the reaction in Eq. 4.6(a) has an activation energy of 1,250 K and so contributes less to the formation of N_2 and F_2 and the depletion of NF at temperatures significantly below 1,000 K. The F_2 formed by the mutual reaction of NF is itself rapidly dissociated in the plasma by dissociative attachment. In comparison, relatively N_2 is stable.

NO is dominantly generated by reactions of N_2 with O and O_2 through

$$N_2 + O \rightarrow N + NO, \qquad \Delta H = 3.2 \text{ eV}, \qquad (4.7a)$$

$$N_2 + O_2 \rightarrow NO + NO, \qquad \Delta H = 1.8 \text{ eV}, \qquad (4.7b)$$

while the source of N_2 is mainly through the mutual reactions of NF in Eqs. 4.6(a,b) and surface recombination. The contribution of reactions of N atoms with O_2 and O_3 ($N + O_2 \rightarrow NO + O$ and $N + O_3 \rightarrow NO + O_2$) to the formation of NO is small as the density of N atoms ($\sim 10^{10}$ cm^{-3}) is smaller than N_2 ($\sim 10^{12}$ cm^{-3}) by two orders of magnitudes. The density of NO is highly

dependent on the fragmentation of NF_3 to form NF which is the dominant gas phase precursor to N_2. The recombination probability of N at surfaces (assumed to be 0.01), not extensively investigated here, also impacts the inventory of N_2.

At the end of the plasma zone, F and O are the dominant dissociation products with densities of 3×10^{14} cm^{-3} and 8×10^{14} cm^{-3}, respectively. NO is the dominant molecular reaction product, with a density of 6×10^{13} cm^{-3}, produced by endothermic reactions facilitated by an increase in T_g to about 700 K at the end of the plasma zone. This increase in T_g temperature is mainly sustained by dissociative excitation and attachment which produces high-energy neutrals through the Franck-Condon effect. Being an atomic species which is not chemically depleted, the density of Ar indicates the heating, rarefaction, expansion and cooling of the gas. The decrease of Ar density in the plasma zone is due to gas heating and also due to the dissociation of the molecular feedstock gases which, for constant pressure, expands the gas and increases flow rate. Downstream of the plasma zone, T_g rapidly decreases to 470 K due to thermal conduction to the walls, resulting in contraction of the gas and a rebound in densities of Ar, NF_3, F and NO. The decrease in T_g and rebound in densities is likely over-estimated in the global model which does not account for diffusive axial transport or axial thermal conduction. The walls of the flowtube are also held at 325 K, which likely speeds the rate of thermal condition. In spite of the gas-temperature initiated rebound in densities, the density of NF decreases from 7.4×10^{12} to 3.5×10^{12} cm^{-3} downstream due to its depletion through mutual, exothermic reactions in Eqs. 4.6(a,b). From the perspective of relative rates of reaction, the formation of NF is an endothermic process whereas the depletion of NF is an exothermic process. The decrease in gas temperature (and electron temperature, discussed below) downstream favors depletion of NF.

4.3.1 Power Deposition

The densities of neutrals at the end of plasma zone and at the exit of the flow tube are shown in Figs. 4.4 and 4.5 as a function of CCP equivalent power of 90 to 3,000 W. As the densities of charged species and excited states are negligible compared with the densities of neutrals, the fractional dissociation of NF_3 can be approximated by

$$f_{NF_3} = \left(1 - \frac{[Ar]_0}{[Ar]}\frac{[NF_3]}{[NF_3]_0}\right)\cdot 100\% \qquad (4.8)$$

where, for example, $[Ar]_0$ is the density at the inlet. The fractional dissociation of NF_3 at the end of the plasma zone increases from 7% to 43% as the power increases from 90 to 3,000 W and the density of F atoms increases from 1.4×10^{14} cm^{-3} to saturate at 3.1×10^{14} cm^{-3}. In the plasma zone, the F atoms are created through 3 channels – dissociative attachment of NF_x by thermal electrons followed by neutralization of F^-, dissociative excitation of NF_x, and heavy particle collisions with F atoms as products. These latter reactions include the exothermic processes in Eq. 4.6(a) and

$$NF_2 + N \rightarrow N_2 + F + F, \qquad \Delta H = -3.7 \text{ eV}, \qquad (4.9a)$$

$$NF + N \rightarrow N_2 + F, \qquad \Delta H = -6.7 \text{ eV}. \qquad (4.9b)$$

$$NF_2 + O \rightarrow FNO + F, \qquad \Delta H = -2.9 \text{ eV}. \qquad (4.9c)$$

$$FNO + O \rightarrow NO_2 + F, \qquad \Delta H = -0.8 \text{ eV}, \qquad (4.9d)$$

The F atoms are mainly consumed through wall recombination to form F_2 and endothermic reactions with FO,

$$F + FO \rightarrow O + F_2, \qquad \Delta H = 0.7 \text{ eV}. \qquad (4.10)$$

As the power increases from 90 to 3,000 W, the T_g increases almost linearly from 395 to 985 K with increasing fractional dissociation of NF_3 reflecting the dominant role in gas heating due to the Franck-Condon effect. The density of F atoms does not monotonically increase. Rather, the

density of F saturates at 3.1×10^{14} cm^{-3} despite the increasing fractional dissociation of NF_3. A portion of that saturation results from the rarefaction resulting from gas heating. A similar trend holds for the density of NO, whose rate of formation based on endothermic processes in Eqs. 4.7(a,b) increases with increasing gas temperature while being offset by the rarefaction of the gas with gas heating.

The trends for neutral densities at the exit of the tube as a function of power (shown in Fig. 4.5) are similar to those at the end of plasma zone. The densities of most neutrals (e.g., Ar, NF_3, F, O and NO) at the exit are larger than at the end of plasma zone simply because of cooling of the gas. However, the densities of NF and FNO are smaller than those at the end of the plasma zone due to consumption of these species through exothermic mutual reactions and reaction with O atoms [Eqs. 4.6(a,b) and 4.9(d)]. Since these reactions are exothermic, they are not inhibited by the decrease in T_g as for endothermic reactions. The fractional dissociation of NF_3 continues to increase to the exit as exothermic reactions with metastable $O(^1D)$ through $NF_3 + O(^1D) \rightarrow NF_2 + FO$ and NF through reaction in Eq. 4.5 continue consuming NF_3.

4.3.2 NF_3 Flow Rate

Plasma properties were investigated for NF_3 flow rates from 50 to 500 sccm while maintaining 300 W into electrons, or an equivalent CCP power of about 1,600 W. The other discharge parameters are the same as the base case (400 mTorr, 50 sccm Ar and 1000 sccm O_2). The resulting densities of neutrals at the end of the plasma zone and at the exit of the flow tube are shown in Figs. 4.6 and 4.7. With constant power and with increasing NF_3 flow rate, the fractional dissociation of NF_3 decreases from 41% (50 sccm) to 22% (500 sccm). With the average density of NF_3 increasing with flow rate, the density of F increases and saturates at 5×10^{14} cm^{-3} at high flow rate. The saturation of the F density while the density of NF_3 continues to

increase indicates that radical production is power-limited although a portion of this saturation is due to rarefaction. With increasing flowrate of NF_3, T_e in the plasma zone increases from 3.2 to 4.5 eV to provide the additional ionization required to compensate the higher rate of attachment to NF_3.

The density of O_2 moderately decreases from 2.0×10^{15} to 1.3×10^{15} cm^{-3}, a consequence of the decrease in O_2 mole fraction, as the NF_3 flow rate increases while keeping pressure constant. The density of O significantly decreases from 1.2×10^{15} to 1.6×10^{14} cm^{-3} due to the larger fraction of the discharge power that is dissipated by NF_3, and the higher rate of reaction of O with NF_x radicals. The density of NO decreases from 5.1×10^{13} to 2.4×10^{13} cm^{-3} due to the decrease in density of O and the more rapid consumption of NO through reaction with F_2 (F_2 + NO $\rightarrow$ FNO + F), which produces the increasing density of FNO, from 1.8×10^{13} to 1.3×10^{14} cm^{-3}.

The gas temperature monotonically increases from 760 to 1,050 K at the end of the plasma zone and from 460 to 800 K at the exit for the increase in NF_3 flow rate of 50 – 500 sccm. The higher rate of dissociative attachment and excitation of NF_x with increasing flow rate produces significant Franck-Condon heating.

4.4 Scaling of Remote Plasma Source by 2-dimensional Modeling

Although global modeling is quite valuable for system studies and developing reaction mechanisms, geometrical and transport dependent processes are difficult to accurately represent. With the goal of investigating the consequences on radical generation of system specific parameters, the RPS was simulated with the 2-d model using the geometry schematically shown in Fig. 4.1(b). The secondary electron emission coefficient for ions was 0.15 on the electrodes,

0.05 on the dielectric and 0.02 on the metal walls. The base case conditions are the same as for the global model – $Ar/NF_3/O_2$ = 5/10/100 at 400 mTorr and a flow rate of 1,150 sccm. The voltage on the powered electrode was adjusted to 1,050 V to sustain the CCP with a total power deposition of 900 W. The self dc bias on the powered electrode is -293 V.

In addition to investigating the scaling of radical production in RPS systems, the following results serve as a case study for the extreme sensitivity of CCPs sustained in moderate pressure, highly attaching gas mixtures to reactor design parameters. The origin of this sensitivity is the very rapid transition between net attachment and net ionization as a function of electron temperature. For example, EEDs were generated by solving Boltzmann's equation for the initial gas mixture ($Ar/NF_3/O_2$ = 5/10/100, 400 mTorr) for a range of *E/N*. The net ionization coefficient, $\alpha' = \alpha - \beta$ (cm^{-1}) was computed, where α is the first Townsend coefficient for ionization and β is the second Townsend coefficient for attachment. Both α and β are sensitive functions of *E/N*, with α steeply increasing with increasing *E/N* and β steeply decreasing with *E/N*. α' changes from -0 .05 cm^{-1} (net attachment) to +0.05 cm^{-1} (net ionization) over a range of T_e of only 0.4 eV, or a fractional change in *E/N* of only 15%. In CCPs where electric fields can vary by an order of magnitude over a small fraction of the inter-electrode distance, this sensitivity can result in significant changes in plasma properties.

Time averaged densities of electrons, T_e, ionization source by bulk electrons, S_b, and ionization by secondary electrons emitted from electrodes, S_s, are shown in Fig. 4.8 for the base case. The electric field is naturally enhanced at the edge of the electrodes at the intersection with the alumina insulators, a triple point – additional enhancement is produced in the sheath. This electric field enhancement locally heats electrons and increases electron power deposition, which increases the local rate of ionization. This local enhancement produces a local maximum of 1.8

$\times 10^{10}$ cm^{-3} in electron density, whereas the electron density in the bulk plasma is 4×10^{9} cm^{-3}. This sharp gradient in plasma properties is in part enabled by the extreme sensitivity of α' to small changes in T_e and E/N.

Secondary electrons play an important role in CCPs sustained in electronegative gas due to their contribution to net ionization. S_s is quite uniform and high (2×10^{16} cm^{-3}s^{-1}) near the surface of the powered electrode whereas the net ionization by bulk electrons S_b is negative (meaning net loss by attachment and recombination) in most of the RPS region except the region near the edge of the powered electrode. The RPS is then sustained by ionization by secondary electrons.

In our investigation of RPS using the global model, the power deposited into electrons obtained from the 2-d model was used as input power. The electron density in the middle of the reactor from the global model is also about 5×10^{9} cm^{-3}, similar to that for the 2-d model. However, T_e in the global model, 3.8 eV, is significantly higher than predicted by the 2-d model in the bulk plasma, 2.6 eV. The lower T_e in the 2-d model for similar electron densities is enabled by the more efficient contributions to ionization by the secondary electrons. With there being only bulk electrons in the global model, a higher T_e is required to sustain the plasma. With axial transport and no barriers placed downstream, such as grids, the CCP is not confined in the source region. The effective plasma volume exceeds that strictly defined by the electrodes. The plasma extends downstream beyond the electrodes to the pump-port with density of 1.6×10^{9} cm^{-3}, with an electron temperature of about 3 eV. The specific power deposition (W/cm^3) is therefore smaller.

The densities of F^-, O_2^+ and NO^+ are shown in Fig. 4.9 for the CCP source. Similar to the global model, the density of F^- in the plasma zone is about 2×10^{11} cm^{-3}, producing an

electronegativity of about 50. (Electronegativity is the ratio of the density of all negative ions to the density of electrons $[M^-]/[e]$.) As the plasma flows downstream, there is a transition into a nearly ion-ion plasma in which charge neutrality is maintained by $[F^-] \approx [NO^+] + [O_2^+]$. NO^+ is the dominant positive ion with a density of 7×10^{10} cm^{-3} at the exit followed by O_2^+ with a density of 2×10^{10} cm^{-3}. The significant amount of O_2^+ is due to ionization which occurs downstream due to axial transport of electrons and thermal conductivity, an effect that his not captured in the global model where the downstream positive ion density is essentially all NO^+. Since expansion of the plasma downstream is nearly unavoidable at the pressures of interest, RPS must employ distance or grids to confine the charged particle fluxes, and so enable purely neutral driven etching downstream.

The time averaged densities of neutrals shown in Figs. 4.10 and 4.11 have similar dependencies on flow distance as predicted by the global model. NF_3 and O_2 dissociate and undergo rarefaction as they flow between the electrodes and are heated. The dominant radicals at the end of the plasma zone are F, O and NO, with densities of 2.7×10^{14}, 4.3×10^{14} and 0.7×10^{14} cm^{-3}, respectively. The major gas heating mechanism in the plasma zone is Franck-Condon heating following electron impact dissociation of molecular species. The gas temperature, shown in Fig. 4.11(f), increases from room temperature at the inlet to 670 K at the end of the plasma zone, which is accompanied by the increasing density of the dissociation products, F and O. The density of NO increases to 7×10^{13} cm^{-3} at the end of the plasma zone as the gas temperature increases. Recall that NO is predominantly produced through the endothermic reactions in Eqs. 4.7(a,b).

As NF_3 flows into the reactor, it is rapidly dissociated to NF_2, which in turn is dissociated to NF. The densities of NF_3 monotonically decrease from 1.0×10^{15} to 0.3×10^{15} cm^{-3} flowing

through the plasma zone, whereas NF_2 has a momentary maximum of 4.4×10^{12} cm^{-3}, a result of its production by dissociation of NF_3 and its depletion by its own dissociation. The densities of NF_x are asymmetric across the height of the reactor. The densities of NF_3 and NF_2 are lower and the density of NF higher near the upper powered electrode, a consequence of the higher power deposition at the edge of the sheath of the powered electrode. The F density monotonically increases from 0 to 3.4×10^{14} cm^{-3} with axial flow distance – first due to the integral production by dissociation of NF_x. The increase in density far downstream is in part a consequence of the gas cooling.

The same general trends hold for O_2 and O – a monotonic decrease in the density of O_2 from 1.0×10^{16} to 0.3×10^{16} cm^{-3}, more highly dissociated near the powered electrode, and a monotonic increase in O atom density from 0 to 4.9×10^{14} cm^{-3} with flow distance. The increasing densities of O and N_2, coupled with the increase in gas temperature results in a monotonic increase in the density of NO with flow distance. The density of N atoms also monotonically increases with flow distance, but its contribution to the creation of NO is negligible as the N density ($\approx 10^{10}$ cm^{-3}) is two orders of magnitude smaller than N_2 density ($\approx 10^{12}$ cm^{-3}).

The densities of FNO and NO_2 are less sensitive to flow and gas temperature, with densities in the gap which reflect the source of their precursors by electron impact. For example, the density of FNO increases from 4.7×10^{13} cm^{-3} at the center of the gap to 5.9×10^{13} cm^{-3} at the surface of the powered electrode, similar to the increase in NO_2 density from 2.7×10^{12} to 3.4×10^{12} cm^{-3}. This increase is in part due to the lower gas temperature at the electrodes due to thermal conduction. However, the formation of FNO occurs through exothermic reactions in Eq. 4.9(c) and

$$NF_2 + NO_2 \rightarrow FNO + FNO, \qquad \Delta H = -2.1 \text{ eV}, \qquad (4.11a)$$

$$NF_2 + FO \rightarrow FNO + F + F, \qquad \Delta H = -0.6 \text{ eV}, \qquad (4.11b)$$

$$F_2 + NO \rightarrow FNO + F, \qquad \Delta H = -0.8 \text{ eV}, \qquad (4.11c)$$

while the formation of NO_2 also occurs through exothermic reactions in Eq. 4.9(d) and

$$FO + NO \rightarrow F + NO_2, \qquad \Delta H = -0.9 \text{ eV}, \qquad (4.12a)$$

$$N_2O + NO \rightarrow N_2 + NO_2, \qquad \Delta H = -1.5 \text{ eV}, \qquad (4.12b)$$

$$NO + O_3 \rightarrow O_2 + NO_2, \qquad \Delta H = -2.1 \text{ eV}. \qquad (4.12c)$$

These exothermic reactions are not inhibited by this decrease in gas temperature. Since the precursors for these reactions are produced near the sheath edge, the densities of FNO and NO_2 are enhanced near the electrodes.

Downstream of the electrodes, the densities of most neutral species rebound due to the cooling of the gas from 670 to 610 K by thermal conduction to the walls, a similar trend as predicted by the global model. T_g is maximum in the middle of the gap near the end of the plasma zone, about 5 cm beyond the edge of the electrodes, which can be partially ascribed to axial diffusion and electron dissociative attachment occurring downstream, a process not accounted for in the global model. With this dissociative attachment comes Franck-Condon heating.

When varying power deposition, the relative contributions to ionization by bulk and secondary electrons changes due to the apportionment of power between electrons and ions. For example, the S_b and S_s are shown in Fig. 4.12 for power deposition of 300 to 2,400 W. The corresponding densities of electrons, F^-, O_2^+ and NO^+ at mid-gap as a function of flow are shown in Fig. 4.13. The voltage amplitude increases from 630 V (dc bias = -118 V) to 1,690 V (dc bias = -498 V) over this range of power, resulting in large sheath potential and thicker sheath. A

larger proportion of the power is then dissipated by ion acceleration in the sheath, which would otherwise reduce ionization. For a factor of 8 increase in power (300 to 2,400 W), the power dissipated by electron collisions increases by only a factor of 2.8 (130 to 360 W) whereas that for ions increases by a factor of 12 (170 to 2,040 W). However, the energy of secondary electrons emitted from the electrodes increases, which facilitates an increase in S_s above that due to the increase in ion current. For example, S_s increases by an order of magnitude 1.1×10^{15} to 1.0×10^{16} $cm^{-3}s^{-1}$ in the bulk plasma and from 7.9×10^{15} to 2.3×10^{16} $cm^{-3}s^{-1}$ in the sheath with this increase in power.

As the ionization by secondary electrons increases, the plasma responds by allowing more electron loss, which is achieved by lowering T_e and S_b, similar to externally sustained plasmas such as electron beam sustained discharges.[16] As the energy relaxation distance of the high energy secondary electrons is longer than for low energy bulk electrons, S_s is far more uniform across the gap than S_b which responds to the extreme sensitivity of α'. The electron density in the bulk plasma increases from 1.4×10^9 to 8.0×10^9 cm^{-3}, a larger increase in density than power dissipated by electrons due to the increased efficiency of S_s, The densities of F^-, O_2^+ and NO^+ in the bulk plasma generally increase sub-linearly with CCP power, reflecting the smaller increase in ionization processes compared to ion acceleration.

The densities of NF_3, F and NO, and the gas temperature along the axial flow distance are shown in Fig. 4.14 for CCP powers of 300 – 2,400 W. The fractional dissociation of NF_3 increases from 9% to 37% and the density of F increases from 1.9×10^{14} to 3.3×10^{14} cm^{-3} at the end of the plasma zone with increasing power. These increases are significantly less than might be expected from power deposition due to the smaller fraction of power dissipated by electrons and some rarefaction by gas heating. The fractional dissociation of NF_3 predicted by the 2-d

model is perhaps systematically smaller than predicted by the global model for the same range of power (16% – 40%), due to the expansion of the plasma zone beyond the confines of the electrodes. The peak gas temperature increases from 470 K at 300 W to 830 K at 2,400 W, and this increase in T_g facilitates the increase NO density from 4×10^{13} to 8×10^{13} cm^{-3} at the end of the plasma zone due to enhanced endothermic reactions.

4.5 Concluding Remarks

Global and 2-d modeling have been applied to the investigation of remote plasma sources sustained in $Ar/NF_3/O_2$ mixtures. Electron impact cross sections for NF_2 and NF were calculated and a reaction mechanism was developed for plasmas sustained in mixtures containing $Ar/NF_3/O_2$. Overall good agreement was obtained between model predictions and relative densities provided by experimental OES actinometry measurements. In the simulations, NF_x rapidly dissociates in the RPS primarily by dissociative attachment by thermal electrons and secondarily by dissociation due to electronic excitation. The Franck-Condon exothermicity in these dissociative processes is the dominant gas heating mechanism. Addition of O_2 to NF_3 diversifies the variety of radicals (e.g., NO and FNO) and increases radical production. Gas heating aids in the formation of NO due to its endothermic formation mechanisms while its loss mechanisms are generally exothermic. The formation of NO is determined by the availability of N_2, which in turn depends on the dissociation of NF_3 to form NF and the recombination probability of N atoms at surface.

Downstream of the plasma zone, the densities of most radicals increase due to gas cooling. However, the density of NF decreases due to exothermic reactions consuming NF and producing N_2 and F_2. In the global model, an ion-ion plasma maintained by $[F^-] \approx [NO^+]$ is

formed in the afterglow due to NO having the lowest ionization potential of major species, F having the highest electron affinity, and charge exchange leading to these species. In the 2-d model, axial transport and thermal conductivity enable the electron density and sources to extend downstream, which in turn enables an ionization source sustaining O_2^+ downstream and decreased power density. As a result, the fractional dissociation of NF_3 predicted by the 2-d model is smaller than the global model and the plasma transitions into a nearly ion-ion plasma with charge neutrality maintained by $[F^-] \approx [NO^+] + [O_2^+]$.

The trends predicted by the global and 2-d models generally agree with some exceptions, such as the axial distribution of F atoms, which can be attributed to the spatial distribution of gas temperature and axial diffusion, neither of which are accounted for in the global model. By better confining the plasma in the RPS region through barriers and grids, the efficiency for radical generation can be increased while the plasma will transition into a purely ion-ion plasma, which will lead to increased processing efficiency and less damaging etching downstream. The dominant reactions in the remote source region and in the downstream region are quite different, with electron impact reaction dominant in the source while heavy particle exothermic reactions dominate in the downstream, which then presents an opportunity to customize reaction mechanisms for production of desirable etching species.

4.6 Figures

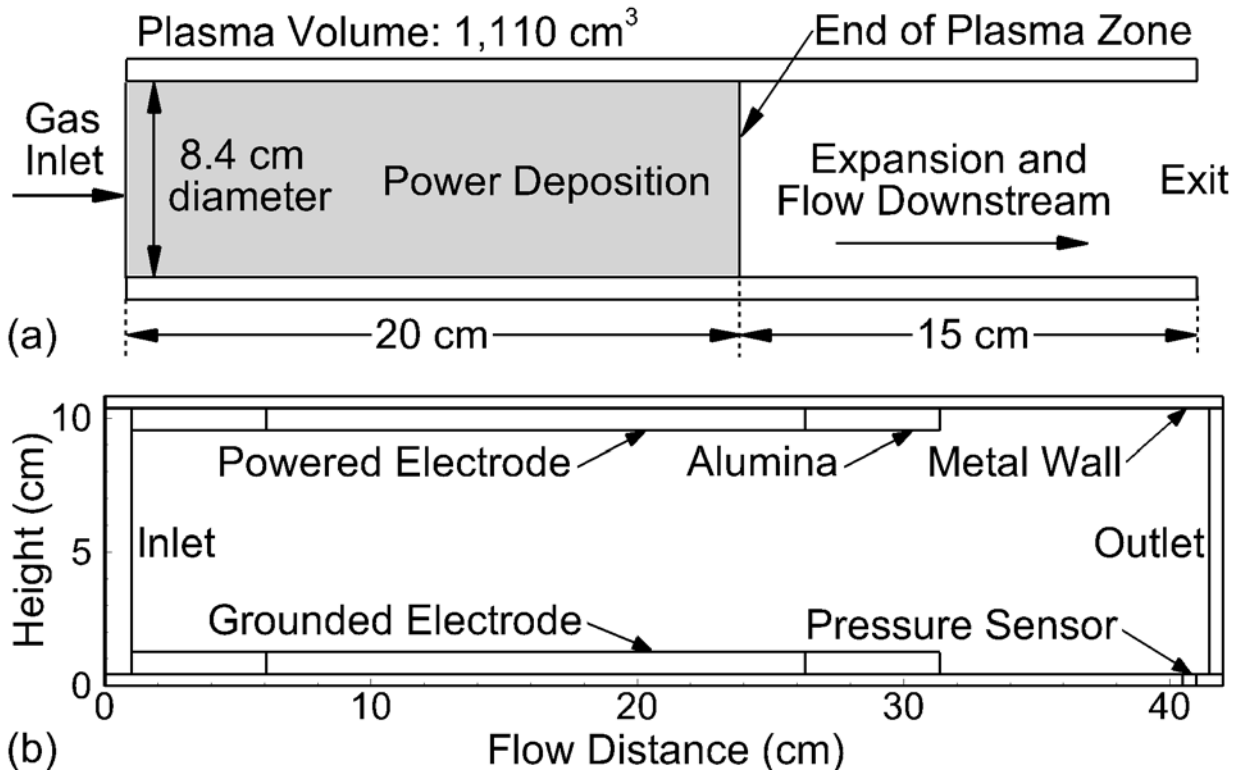

Fig. 4.1 Schematic of the remote plasma source addressed by a) the plug flow mode of the global model and b) the CCP operation of the 2-d model. The gas is pumped in from the left and exits at the right side.

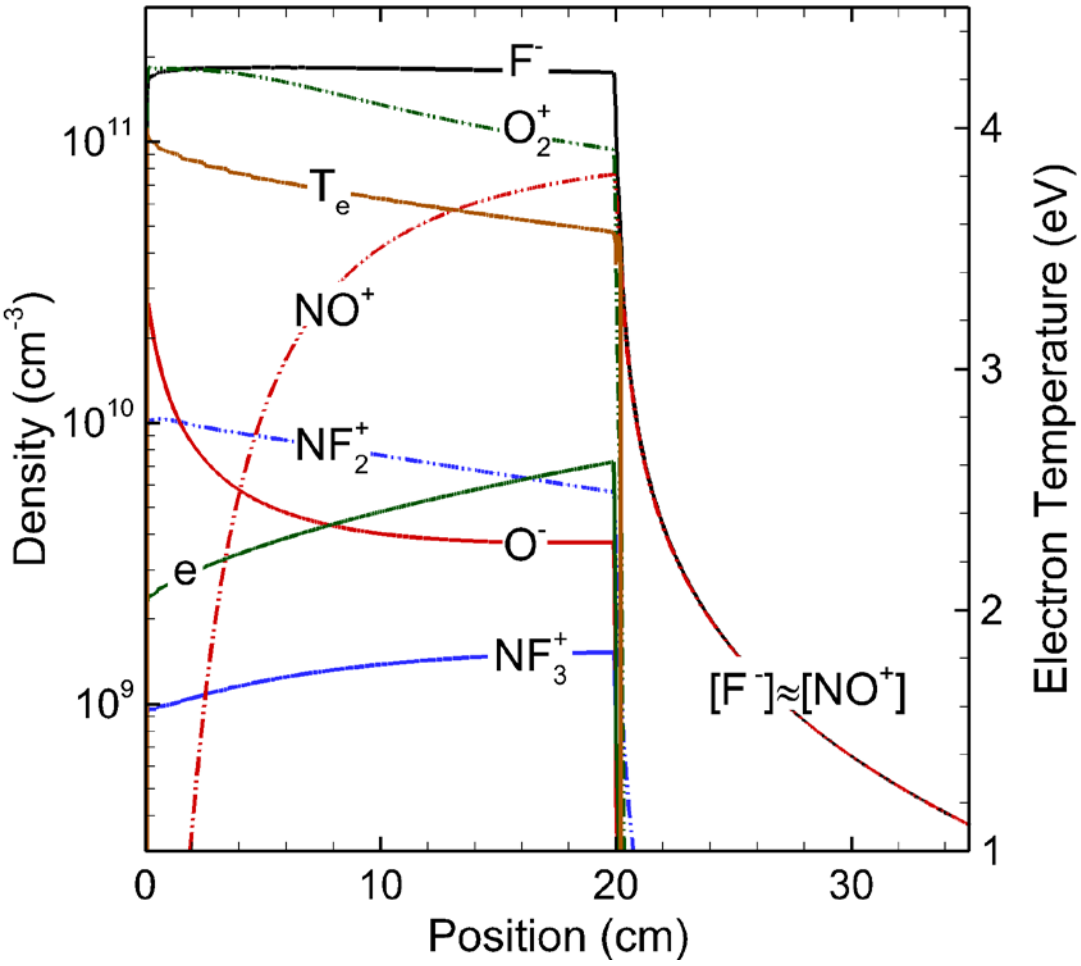

Fig. 4.2 Densities of charged particles and electron temperature in the plug flow mode of the global model. Discharge conditions: $Ar/NF_3/O_2$ = 5/10/100, 400 mTorr, 1,150 sccm, CCP equivalent power: 900 W (power into electrons: 237 W).

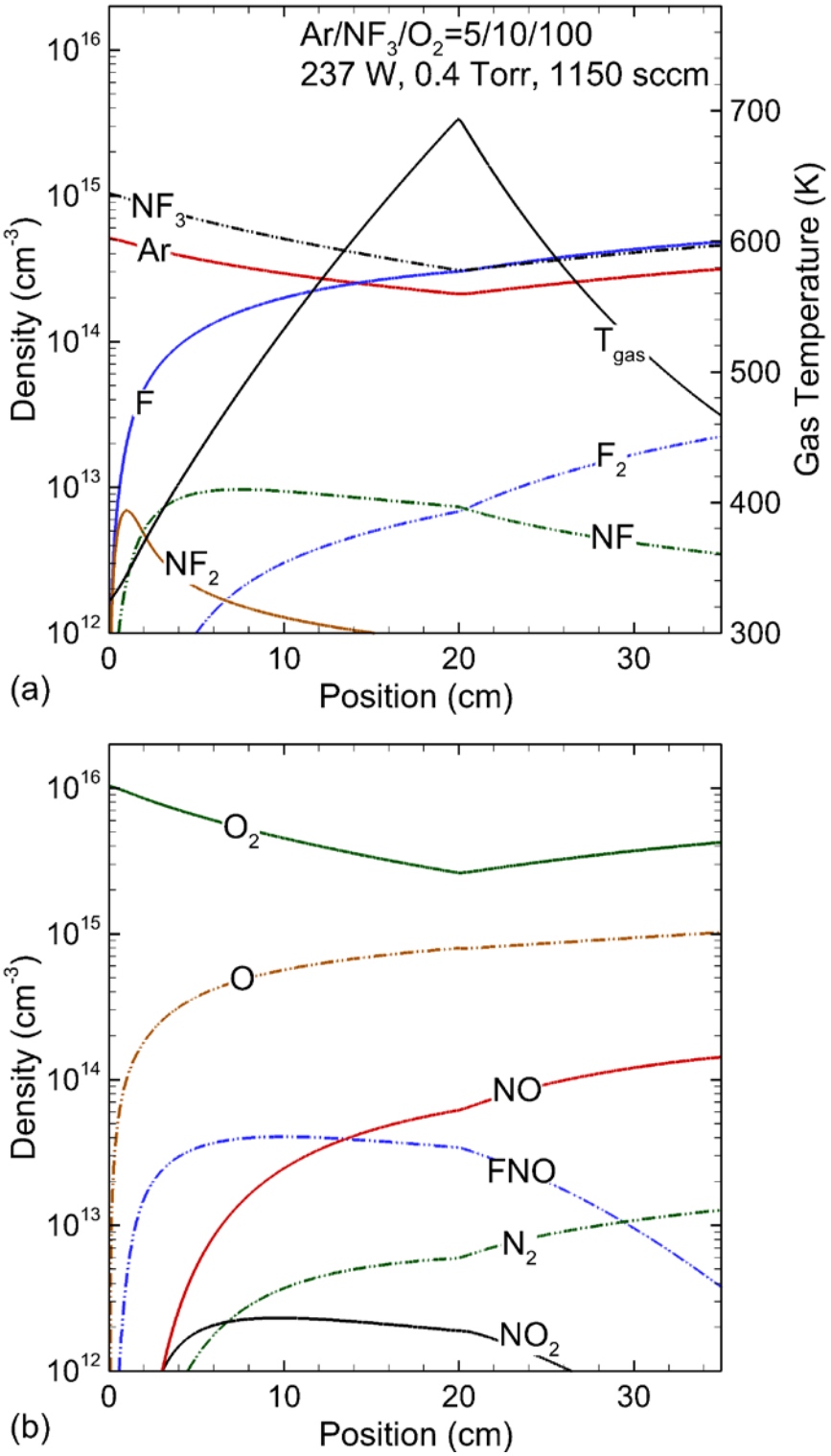

Fig. 4.3 Densities of neutrals and gas temperature in the plug flow mode of the global model. Discharge conditions: $Ar/NF_3/O_2$ = 5/10/100, 400 mTorr, 1,150 sccm, CCP equivalent power: 900 W (power into electrons: 237 W).

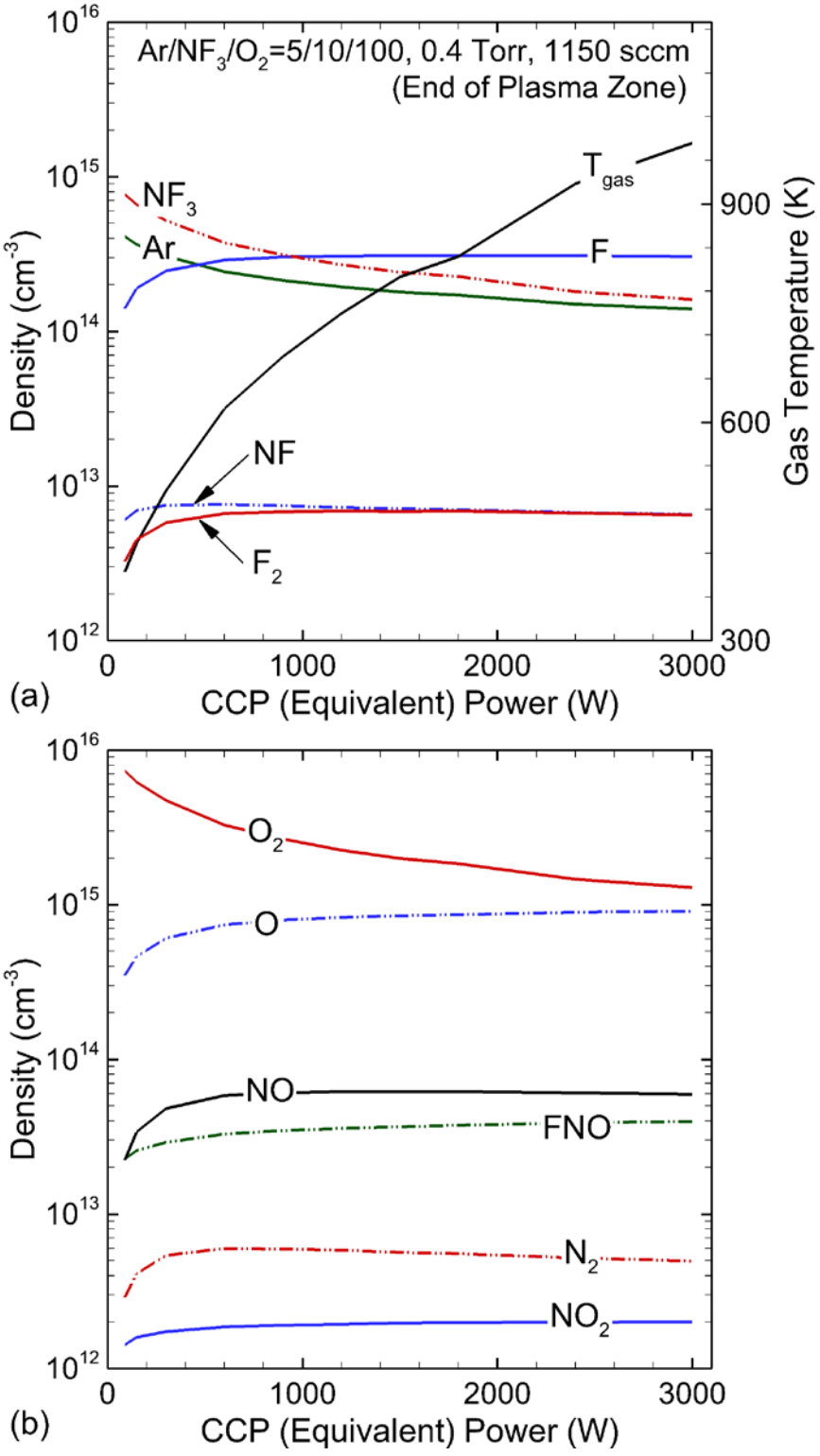

Fig. 4.4 Densities of neutrals and gas temperature at the end of the plasma zone in the plug flow mode of the global model. Discharge conditions: $Ar/NF_3/O_2$ = 5/10/100, 400 mTorr, 1,150 sccm, CCP equivalent power: 900 W (power into electrons: 237 W).

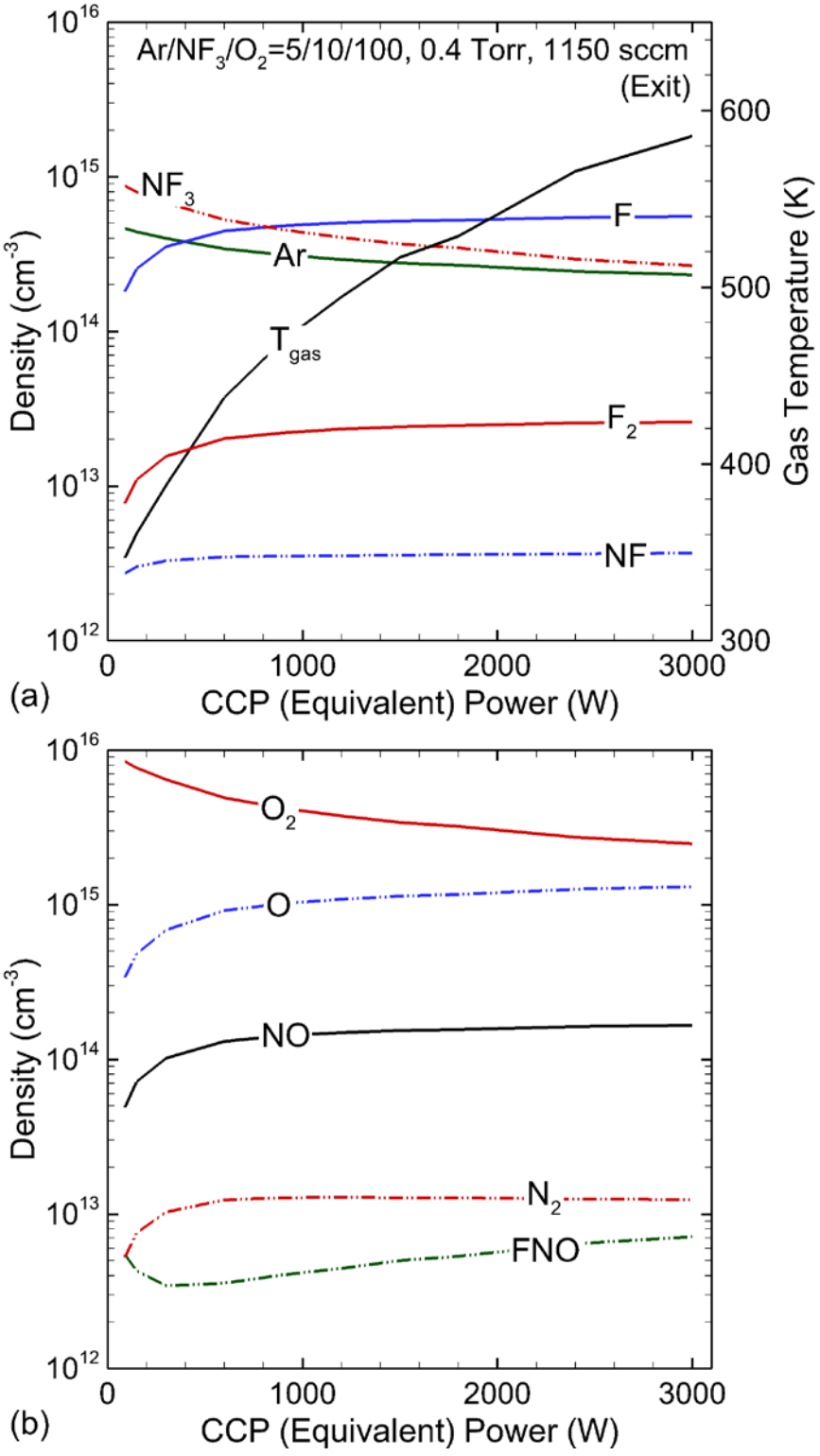

Fig. 4.5 Densities of neutrals and gas temperature at exit in the plug flow mode of the global model. Discharge conditions: $Ar/NF_3/O_2$ = 5/10/100, 400 mTorr, 1,150 sccm, CCP equivalent power: 900 W (power into electrons: 237 W).

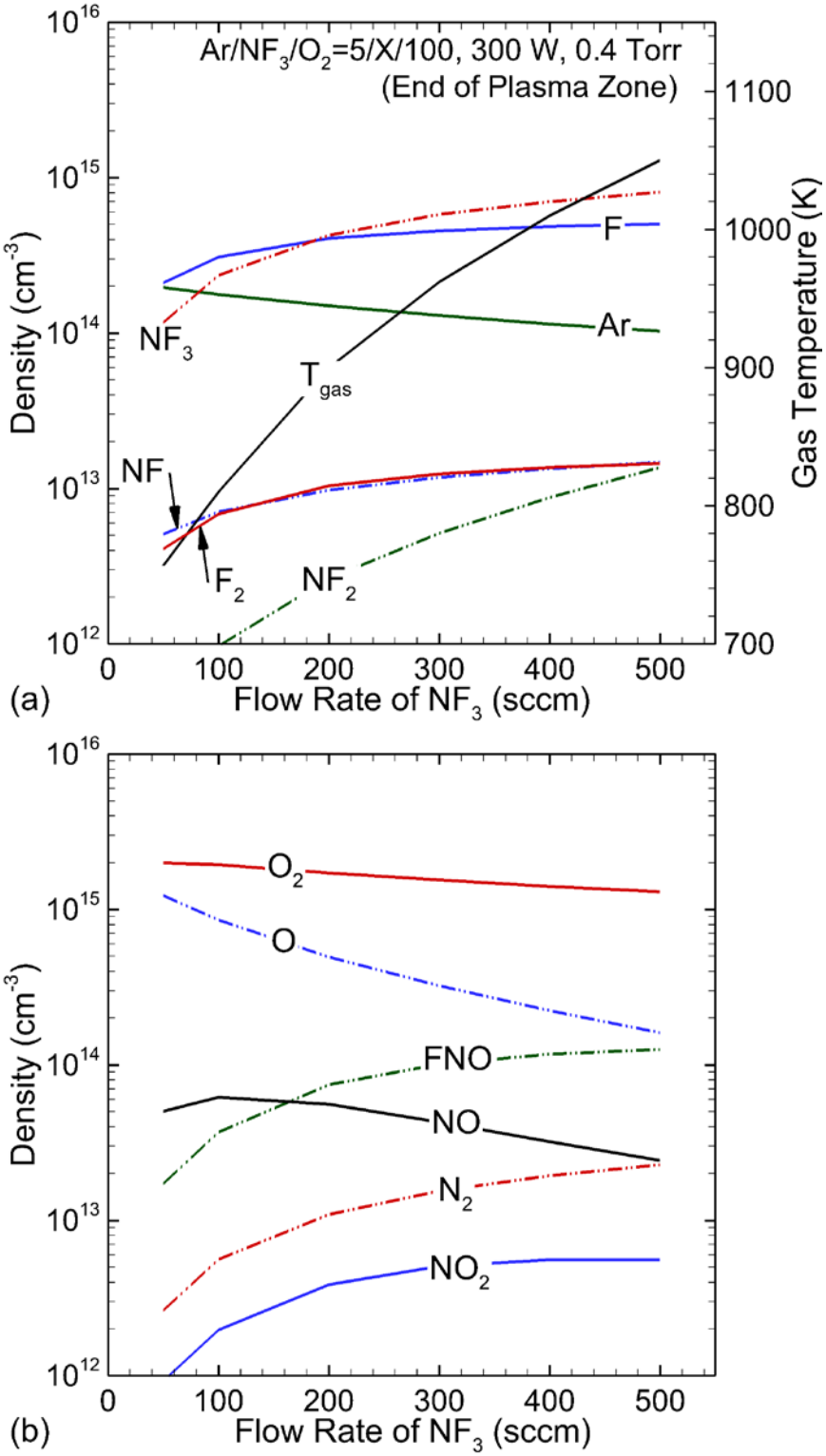

Fig. 4.6 Densities of neutrals and gas temperature at the end of the plasma in the plug flow mode of the global model. Discharge conditions: $Ar/NF_3/O_2$ = 5/X/100, 400 mTorr, (1,050+10X) sccm, X = 5 – 50, power into electrons: 300 W.

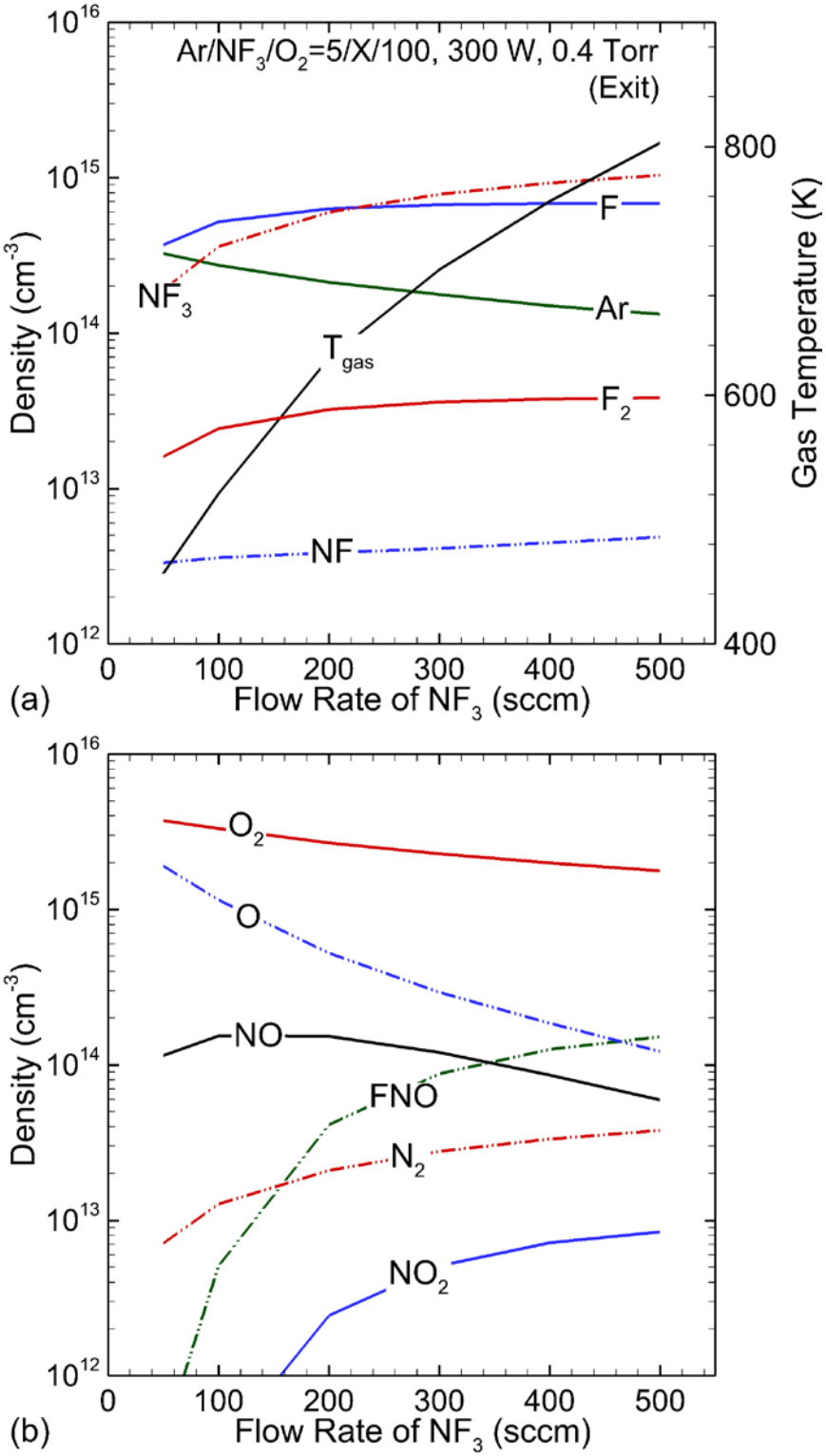

Fig. 4.7 Densities of neutrals and gas temperature at exit in the plug flow mode of the global model. Discharge conditions: $Ar/NF_3/O_2$ = 5/X/100, 400 mTorr, (1,050+10X) sccm, X = 5 – 50, power into electrons: 300 W.

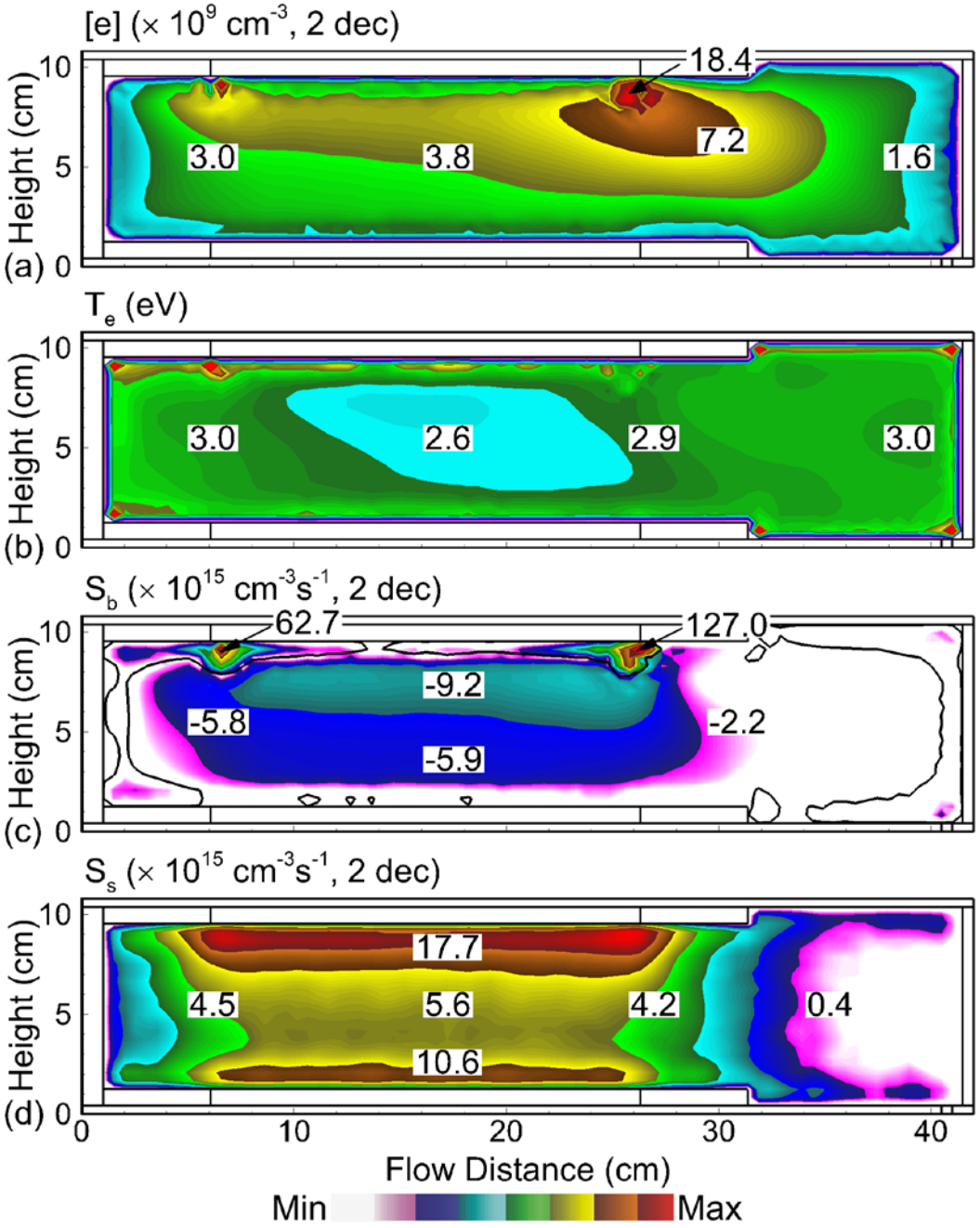

Fig. 4.8 Time averaged a) electron density, b) electron temperature, electron ionization source by c) bulk electrons and d) secondary electrons in a remote plasma source driven by capacitively coupled power. Discharge conditions: $Ar/NF_3/O_2$ = 5/10/100, 400 mTorr, 1,150 sccm, 900 W, 10 MHz.

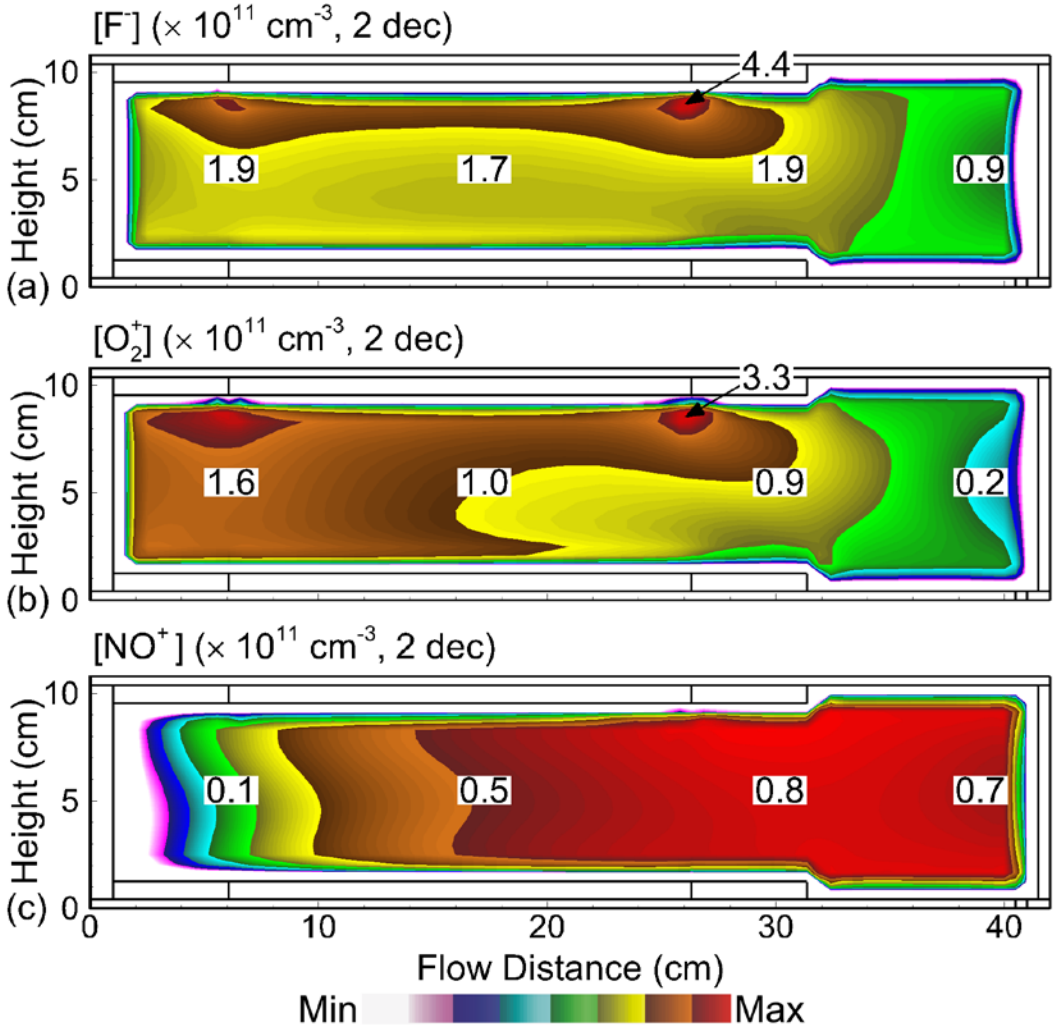

Fig. 4.9 Time averaged densities of a) F^-, b) O_2^+ and c) NO^+ ions in a remote plasma source driven by capacitively coupled power. Discharge conditions: $Ar/NF_3/O_2$ = 5/10/100, 400 mTorr, 1,150 sccm, 900 W, 10 MHz.

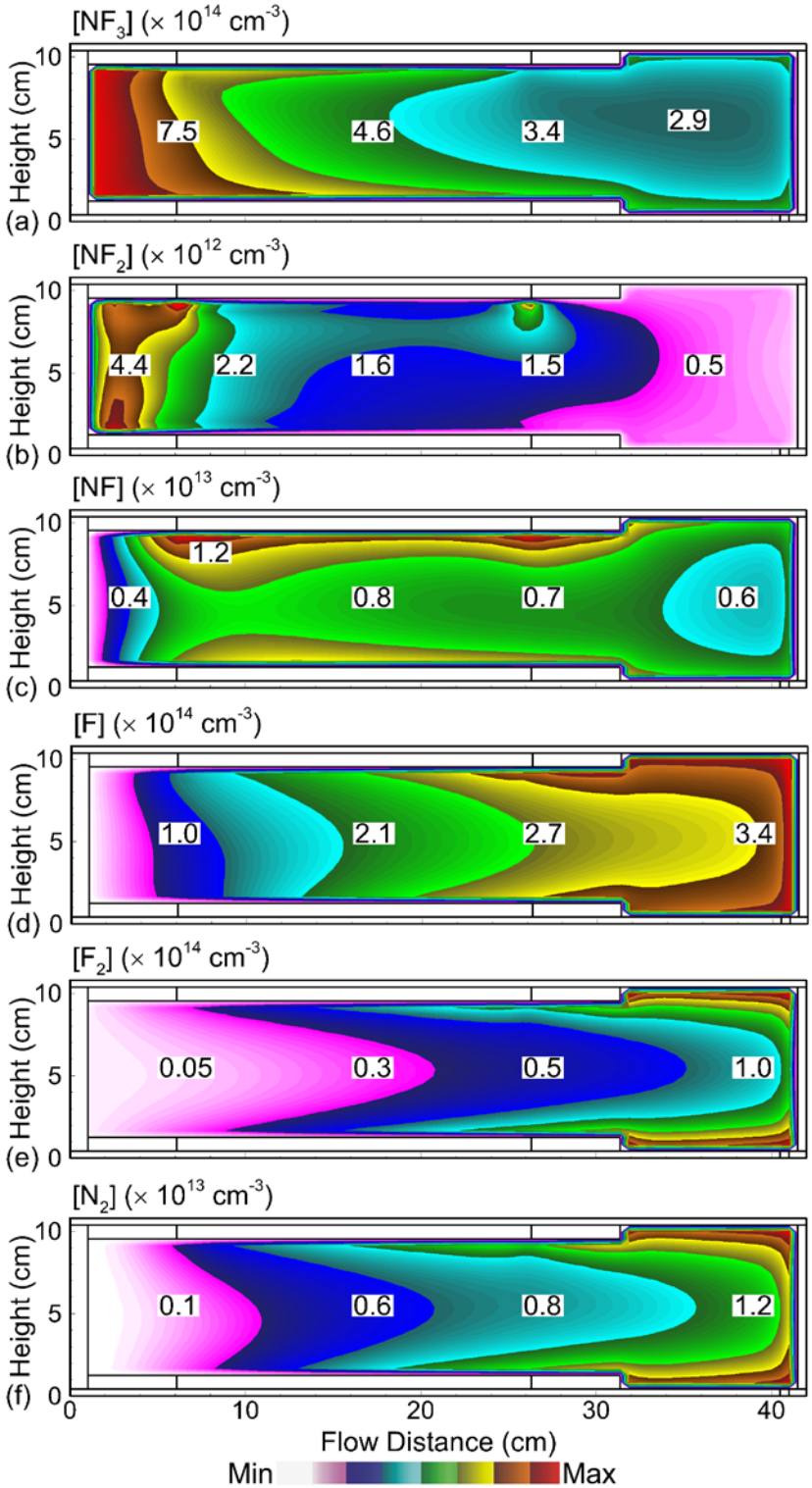

Fig. 4.10 Time averaged densities of a) NF_3, b) NF_2, c) NF, d) F, e) F_2 and f) N_2 in a remote plasma source driven by capacitively coupled power. Discharge conditions: $Ar/NF_3/O_2$ = 5/10/100, 400 mTorr, 1,150 sccm, 900 W, 10 MHz.

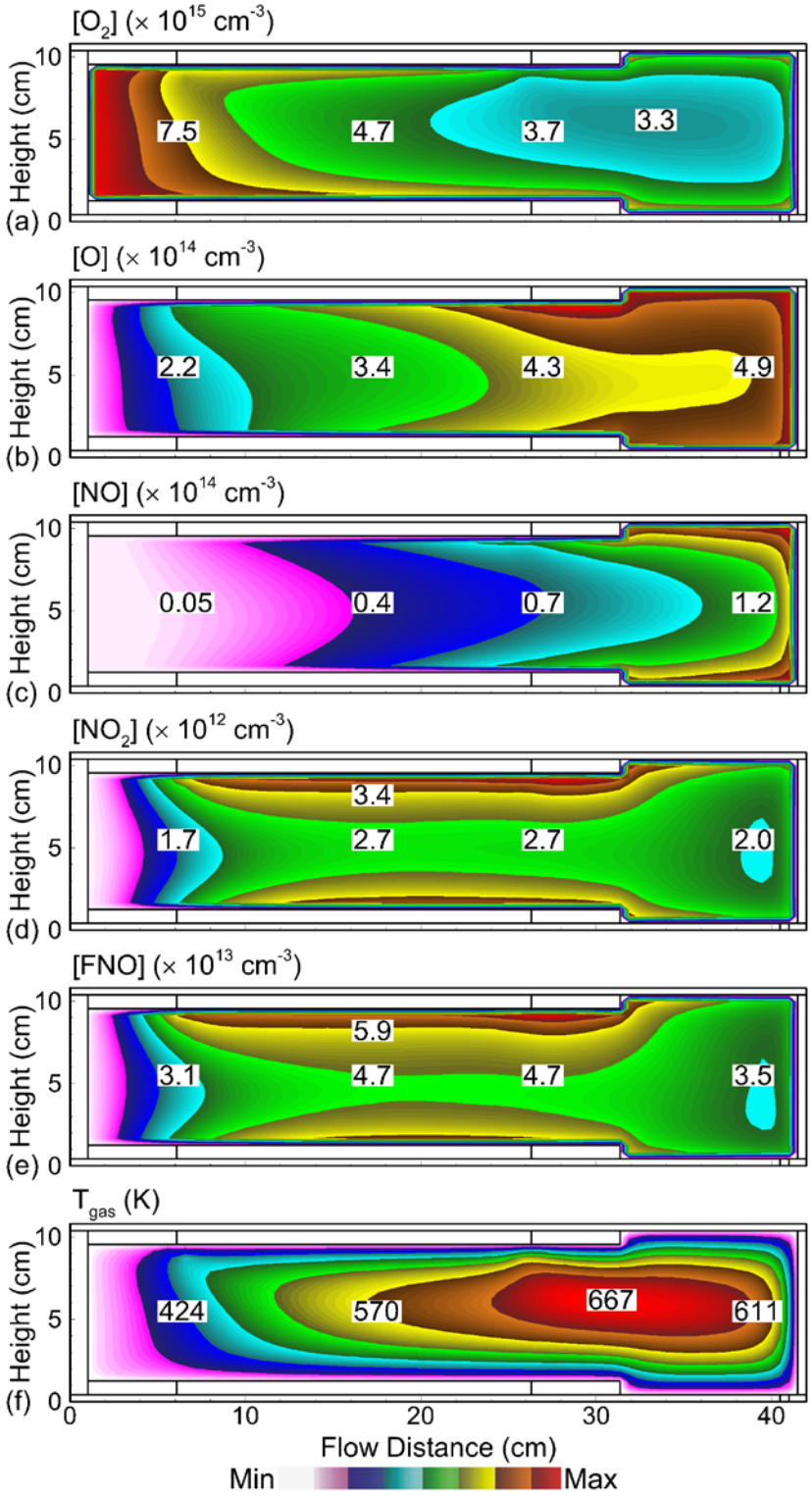

Fig. 4.11 Time averaged densities of a) O_2, b) O, c) NO, d) NO_2, e) FNO and f) the gas temperature in a remote plasma source driven by capacitively coupled power. Discharge conditions: $Ar/NF_3/O_2$ = 5/10/100, 400 mTorr, 1,150 sccm, 900 W, 10 MHz.

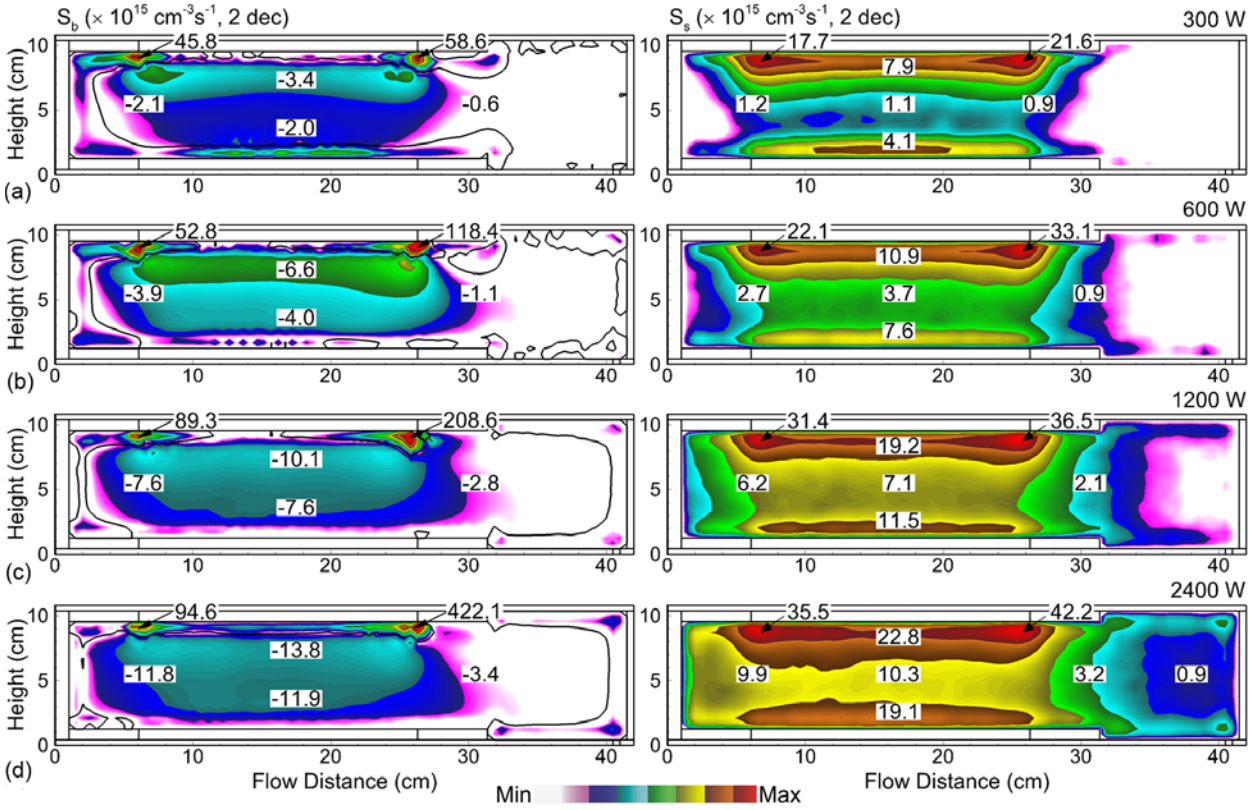

Fig. 4.12 Time averaged electron ionization source by bulk electrons and secondary electrons in a remote plasma source driven by capacitively coupled power of (a) 300 W, b) 600 W, c) 1200 W and d) 2400 W. Discharge conditions: $Ar/NF_3/O_2$ = 5/10/100, 400 mTorr, 1,150 sccm, 300 – 2400 W, 10 MHz.

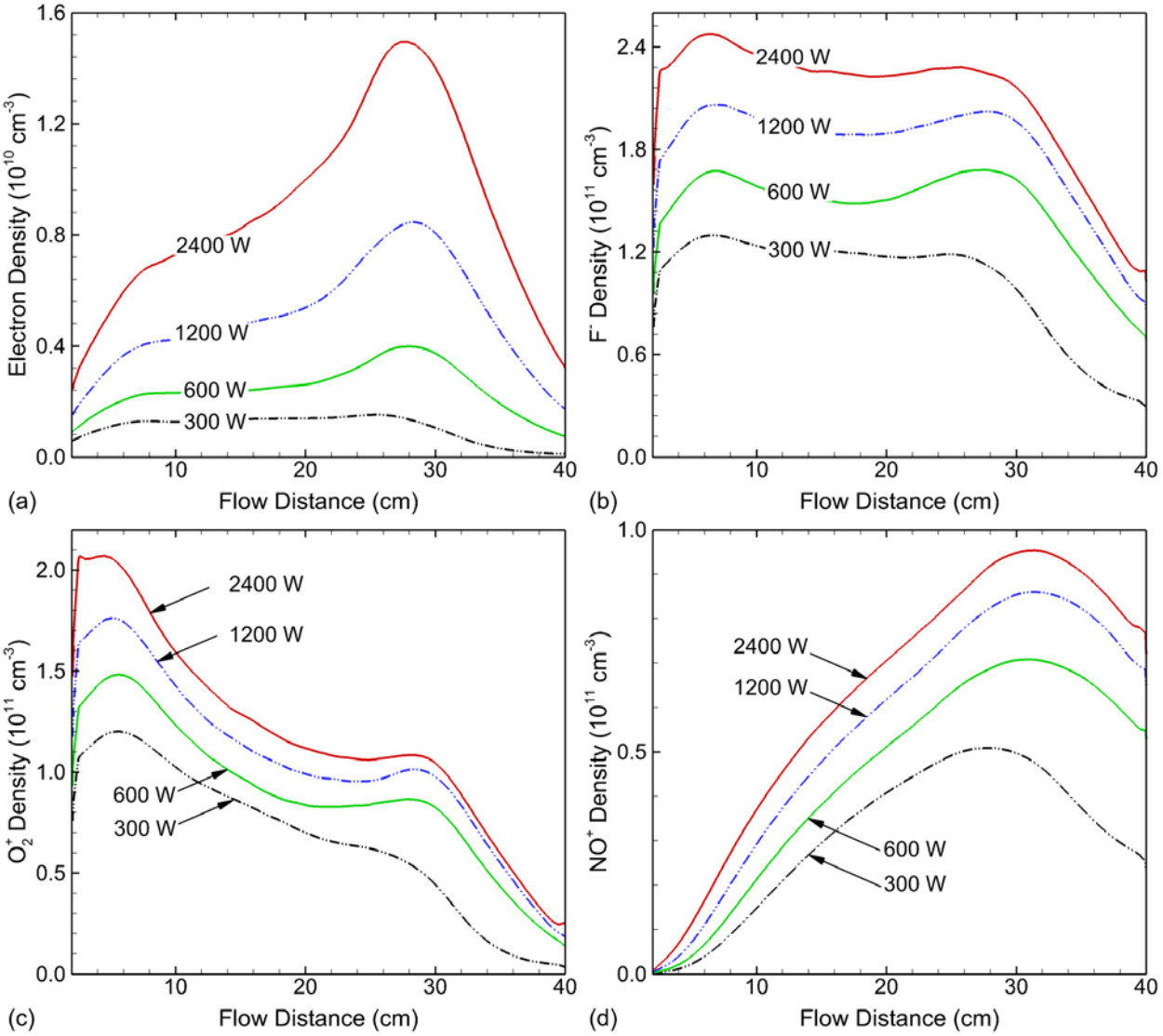

Fig. 4.13 Densities of a) electrons, b) F^-, c) O_2^+ and d) NO^+ ions along the central axial flow distance in a remote plasma source driven by capacitively coupled power of 300 W, 600 W, 1200 W and 2400 W. Discharge conditions: $Ar/NF_3/O_2$ = 5/10/100, 400 mTorr, 1,150 sccm, 300 – 2400 W, 10 MHz.

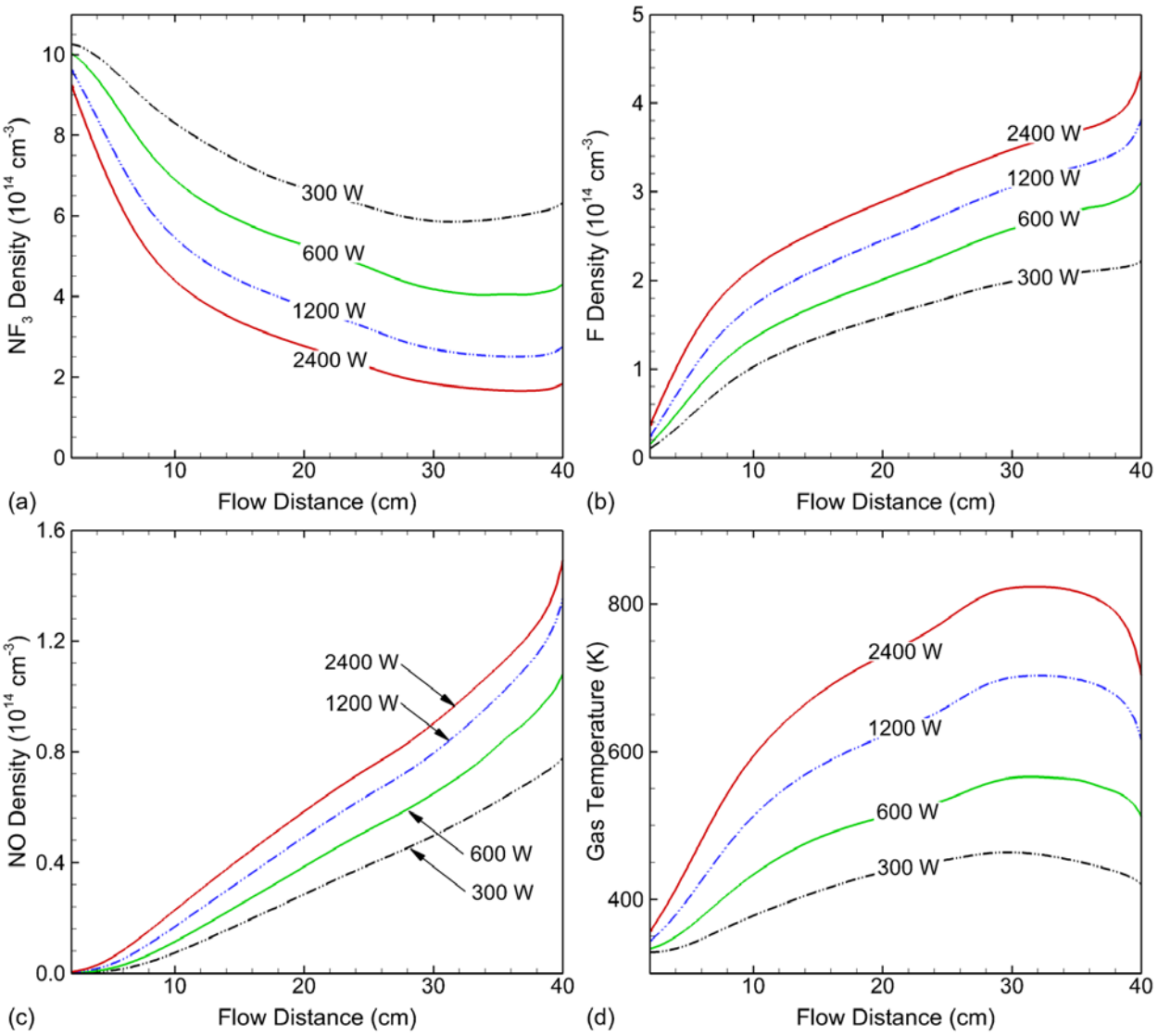

Fig. 4.14 Densities of a) NF_3, b) F, c) NO and d) gas temperature along the central axial flow distance in a remote plasma source driven by capacitively coupled power of 300 W, 600 W, 1200 W and 2400 W. Discharge conditions: $Ar/NF_3/O_2$ = 5/10/100, 400 mTorr, 1,150 sccm, 300 – 2400 W, 10 MHz.

4.7 References

1. V. M. Donnelly and A. Kornblit, J. Vac. Sci. Technol. A **31**, 050825 (2013).
2. S. Fujimura, K. Shinagawa, M. Nakamura and H. Yano, Jpn. J. Appl. Phys. **29**, 2165 (1990).
3. B. Thedjoisworo, D. Cheung and V. Crist, J. Vac. Sci. Technol. B **31**, 021206 (2013).
4. B. E. E. Kastenmeier, P. J. Matsuo, J. J. Beulens and G. S. Oehrlein, J. Vac. Sci. Technol. A **14**, 2802 (1996).
5. B. E. E. Kastenmeier, P. J. Matsuo, G. S. Oehrlein and J. G. Langan, J. Vac. Sci. Technol. A **16**, 2047 (1998).
6. Y. B. Yun, S. M. Park, D. J. Kim, N.-E. Lee, C. K. Choi, K. S. Kim and G. H. Bae, Thin Solid Films **516**, 3549 (2008).
7. W. Heo, J. H. Ahn and N.-E. Lee, J. Vac. Sci. Technol. A **28**, 1073 (2010).
8. D. J. Kim, Y. B. Yun, J. Y. Hwang, N.-E. Lee, K. S.Kim and G. H. Bae, Microelectron. Eng. **84**, 560 (2007).
9. E. Meeks, R. S. Larson, S. R. Vosen and J. W. Shon, J. Electrochem. Soc. **144**, 357 (1997).
10. S. R. Vosen, E. Meeks, R. S. Larson and J. W. Shon, J. Electrochem. Soc. **144**, 1514 (1997).
11. S. P. Gangoli, A. D. Johnson, A. A. Fridman, R. V. Pearce, A. F. Gutsol and A. Dolgopolsky, J. Phys. D: Appl. Phys. **40**, 5140 (2007).
12. J.-S. Chang, K. G. Kostov, K. Urashima, T. Yamamoto, Y. Okayasu, T. Kato, T. Iwaizumi and K. Yoshimura, IEEE Trans. Ind. Appl. **36**, 1251 (2000).
13. H. L. Chen, H. M. Lee and M. B. Chang, Plasma Process. Polym. **3**, 682 (2006).
14. T. Kimura and K. Hanaki, Jpn. J. Appl. Phys. **47**, 8546 (2008).
15. K. J. Nordheden and J. T. Verdeyen, J. Electrochem. Soc. **133**, 2168 (1986).
16. R. J. Commisso, R. F. Fernsler, V. E. Scherrer and I. M. Vitkovitsky, IEEE Trans. Plasma Sci. **PS-10**, 241 (1982).

Chapter 5 Downstream Selective Etching of Si_3N_4[*]

5.1 Introduction

Due to absence of energetic ions that can produce physical sputtering, remote plasma sources (RPS) provides a mechanism for high etch selectivity based only on chemical mechanisms, as discussed in Sec. 4.1. High etch selectivity of Si_3N_4 over SiO_2 can be achieved by increasing the flow rate of O_2 in a RPS sustained in NF_3/O_2 [1] or by increasing the flow rate of N_2 through a RPS sustained in $CF_4/O_2/N_2$ [2]. This selectivity results from enhanced utilization of O and NO radicals in the etching of Si_3N_4 compared to SiO_2. RPS has also been implemented for processing materials such as low-k (porous SiOCH) interlayer dielectrics [3] and high-k (Al_2O_3 and SiC) gate dielectrics [4]. These remote processes minimize surface roughness and mixing typically produced by energetic ion bombardment. Recently, 3-dimensional structures such as stacked planar NAND [5] and vertical NAND [6] have been proposed to increase device density for flash memories. In these structures, RPS can be used to selectively etch the oxide and nitride in the horizontal direction between layers in the stack.

Gas temperature is, in principle, a controllable process variable in RPS systems that can be used to produce desired reactants. The gas temperature, T_g, can be elevated in the RPS while near ambient in the downstream etch chamber. Endothermic reactions are then isolated to the RPS, uniquely producing reactants that are not generated downstream. For example, flowing an

[*] The results discussed and portion of the text appearing in this chapter were previously published in the paper by Shuo Huang *et al*., "Downstream etching of silicon nitride using continuous-wave and pulsed remote plasma sources sustained in $Ar/NF_3/O_2$ mixtures", J. Vac. Sci. Technol. A **36**, 021305 (2018).

NF_3/O_2 mixture through a RPS with high power deposition generating T_g exceeding 400 – 500 K will produce N_xO_y species in the source through endothermic reactions. The production of N_xO_y will cease downstream where T_g cools.[7] RPS also provides the possibility of selectively generating species by mixing of gases. For example, by flowing NF_3 gas into the downstream of a RPS sustained in H_2 [8] or H_2/H_2O [9], hot H atoms produced in the RPS react with NF_3 to form HF through exothermic reactions, an isotropic etchant of SiO_2. Due to the low gas temperature and absence of potentially damaging plasma in the downstream chamber, RPS serves as a mild and conformal method for fabricating atomic scale temperature-sensitive materials such as TiO_2 on Si substrates [10] and surface oxidation in the atomic layer etching of MoS_2 [11].

Chemical downstream systems for the etching of polysilicon and SiO_2 using NF_3/O_2 mixtures were modeled by Meeks *et al*.[12] and Vosen *et al*.[13]. In these efforts, the RPS, the transport tube and the downstream etch chamber in tandem were modeled using a 0-dimensional well mixed reactor model, a 1-dimensional plug flow model and a 2-dimensional axisymmetric reacting-flow model, respectively. The etch rate of polysilicon was found to be transport limited whereas the etch rate of SiO_2 was found to be surface-kinetics limited, depending more on pressure and less on flow rate than the etching of polysilicon.

Etch rates of Si_3N_4, SiO_2 and polysilicon, radical densities in the RPS measured by optical emission spectroscopy, and global modeling were recently reported Barsukov *et al*. for a NF_3/O_2 remote plasma.[14] They described an etching mechanism for Si_3N_4, including the role of NO in the etching of Si_3N_4 by atomic fluorine. Quantum chemistry modeling of the surface kinetics showed that NO reacts with the F–N bond to form N_2O, and the resulting fluorine migrates from the F–N bond to the neighboring silicon atom. By NO enhancing the rate of

fluorine migration on the Si_3N_4 surface from the nitrogen atom to the silicon atom, the etch rate of Si_3N_4 is increased.

In this chapter, the kinetics occurring in a RPS sustained in $Ar/NF_3/O_2$ and the downstream etching of Si_3N_4 are discussed using results from a 2-dimensional model. The simulation includes the plasma kinetics and flow dynamics in the RPS, the transport channel and the downstream chamber. A surface site balance model is used to represent etching at the surface of Si_3N_4 covered wafer. Both continuous-wave (CW) and pulsed systems are addressed. The electron impact cross sections for NF_2 and NF were produced using *ab initio* computational techniques based on the molecular R-matrix method.

We found that plasmas in this system are largely confined in the source region due to isolating showerheads and the highly attaching nature of the gas mixture. The main etchants of silicon nitride, F and N containing neutrals, are produced through electron impact reactions and endothermic heavy particle reactions in the RPS, and flow downstream with densities that rebound due to gas cooling from thermal conduction to the walls. Silicon nitride is etched by iteratively removing Si subsites by F atoms and removing N sites by NO and N. With fluorine rich fluxes to the wafer, the etch rate can be increased by using operating conditions that increase the gas temperature in the source (e.g., increasing the duty cycle during pulsed operation) to increase formation of NO and N. Adding a plenum between the RPS and the downstream etch chamber increases the uniformity of radical fluxes to the wafer surface and thus increases the uniformity of the silicon nitride etch rate.

A brief description of the computational model is in Sec. 5.2. The scaling of plasma and etch properties with operating conditions for RPS sustained by CW and pulsed power are discussed in Sec. 5.3 and Sec. 5.4, respectively. Concluding remarks are presented in Sec. 5.5.

5.2 Description of the Model

Reactor scale simulation of the downstream etch system was performed with the 2-dimensional Hybrid Plasma Equipment Model (HPEM). The HPEM is a kinetic-fluid hydrodynamics code which combines separate modules that address different physical phenomena in an iterative manner. Node-and-neighbor technique and multiple plasma region option, described in Sec. 2.4.1, were implemented into the HPEM to increase the numerical efficiency and better represent the regions of the RPS that have significantly different mole fractions of reactants.

The species included in the model and the reaction mechanism of $Ar/NF_3/O_2$ mixtures used here are the same as in Chapter 4 and described in details in Sec. 3.2.2. In this investigation, the major modules used are the Electromagnetics Module (EMM), the Electron Energy Transport Module (EETM), the Fluid Kinetics Poisson Module (FKPM) and the Surface Kinetics Module (SKM), which have been described in details in Sec. 2.2. In brief, the inductively coupled electromagnetic fields are produced by the EMM using a frequency domain solution of Maxwell's equations. The densities of all charged and neutral species and the electrostatic potentials are obtained from the FKPM. The electron energy equation is implicitly integrated in time to provide the electron temperature, impact rate coefficients and transport coefficients. These coefficients as a function of average electron energy are provided by solutions of Boltzmann's equation for the electron energy distribution. The etching process and the coupling between the bulk and surface processes are addressed by the SKM in which a Surface Site Balance Model (SSBM) is executed. The surface reaction mechanism implemented in the SKM for the etching of Si_3N_4 by remote plasmas sustained in $Ar/NF_3/O_2$ mixtures is described in Sec.

3.3.1 and listed in Appendix D. In this chapter, use of downstream etch system with a remote plasma source producing desirable radicals while eliminating ions from reaching the wafer surface by barriers and long flow distance creates conditions of purely neutral driven and thus selective etching of wafer materials in the downstream chamber.

5.3 Etching of Si_3N_4 by CW Remote Plasma Source

A schematic of the downstream etch system as implemented in the HPEM with one remote inductively coupled source sustained in $Ar/NF_3/O_2$ is shown in Fig. 5.1. The $Ar/NF_3/O_2$ mixture was pumped in through the inlet at the top of the RPS, dissociated in the RPS by the inductively coupled power to produce reactive species for downstream etching. The radius of the RPS is 4 cm. The wafer was placed 12 cm downstream from the RPS, with metal showerheads placed in between. The spacing of the showerheads is 0.75 cm, which even though is several times of the local Debye length (≈ 0.1 cm) still isolates the plasma from reaching the downstream chamber. The silicon nitride wafer was placed on the substrate with no applied bias. A pressure sensor was placed near the pump port, and the pumping rate was adjusted to maintain the gas pressure at 50 mTorr at the location of the sensor. For the base case, the inlet gas mixture is $Ar/NF_3/O_2$ = 90/5/5 with a flow rate of 1,000 sccm. The total power delivered from the ICP coils is 300 W. The intent of this work is to investigate reaction mechanisms and not necessarily to optimize the uniformity of processing.

Electrons are confined in the RPS region due to highly attaching nature of the gas mixture and the limiting nature of the showerhead. In the steady state, the electron density is 3.7 $\times 10^{11}$ cm^{-3} near the ICP coils, where the electron temperature peaks at up to 4.5 eV as shown in Fig. 5.2. NF_3 and its dissociation products, NF_2 and NF, are all thermal attaching molecules as

the electron affinity of F (3.4 eV) is larger than the binding energy of NF_3 (D_0 = 2.4 eV) [15], NF_2 (D_0 = 2.9 eV) [15] and NF (D_0 = 2.8 eV) [16] and so a high electron temperature is required to provide ionization to balance the high rate of attachment. The ICP power is deposited within the skin depth of the radio frequency field (≈ 1 – 2 cm) and only those electrons located in the skin depth are initially heated. Electrons outside the skin depth are heated by convection and thermal conduction. Combined with collisional losses, T_e decreases to 3.6 eV at the confining grid of the RPS. The net electron impact ionization source, S_e, peaks near the coils at 6.2×10^{16} $cm^{-3}s^{-1}$ as shown in Fig. 5.2(c). The dependence on T_e of both electron attachment (decreasing from low to high T_e) and ionization (increasing from low to high T_e) is quite steep, resulting in a clear demarcation between ionization dominated with net gain by electron impact (high T_e upstream) and attachment dominated with net loss by electron impact (low T_e, downstream). This transition occurs at about 4.0 eV, which produces a sharp boundary between the electron impact source function between positive and negative, as shown in Fig. 5.2(c). This line of demarcation occurs at higher T_e at the top of the RPS zone than at the bottom of the RPS zone, due to the dissociation of NF_3 flowing downstream which reduces the rate of attachment.

The electrons are largely confined to the upstream RPS zone. This occurs for at least two reasons – the first is the physical confinement by the grids and the second is the rapid transition of the plasma to an ion-ion system. The rate of attachment is sufficiently rapid as T_e decreases through the grids that the electrons are essentially totally depleted by attachment. Due to the large grid spacing, there is a small leakage of plasma through the grids; and this leakage is essentially an ion-ion plasma. The densities of the positive and negative ions are 10^{11} cm^{-3} in the RPS while leakage to the downstream chamber produces a density of 10^8 cm^{-3} as shown in Fig. 5.3. The dominant positive ions in the RPS region are Ar^+ (60%) and O_2^+ (25%) as shown in

Figs. 5.3(c,d) due to the large mole fraction of their parent gases. The dominant negative ions are F^- as shown in Fig. 5.3(f) due to thermal attaching NF_x (x = 1 – 3) and highest electron affinity of F among all the neutrals in the system. The fractions of NF_3^+, NF_2^+ and NF^+ are less than 3% due to high rates of dissociative attachment which decompose NF_x and moderate ionization potentials of their parent gases (12.9 eV for NF_3, 11.6 eV for NF_2 and 12.1 eV for NF).

5.3.1 Ion-ion Plasma

For electronegative, molecular gas mixtures, the electron loss is dominated by attachment and dissociative recombination, volumetric losses which contribute to confinement of the plasma in the remote source. For electropositive gases, weakly electronegative gas mixtures and mixtures dominated by atomic ions, the dominant mechanism for electron loss is diffusion and recombination on surfaces. As this transition occurs between rapid volumetric electron loss and slow diffusional wall losses, isolation of the plasma from the downstream chamber requires longer flow distances to enable time for the wall recombination to occur. Another strategy is to use openings in the showerhead that are smaller than the Debye length, to prevent the plasma from being conformal to the openings.

The weak ion-ion plasma downstream of approximately 10^8 cm^{-3} is maintained by $[NO^+] \approx [F^-]$ as shown in Figs. 5.3(e,f). There is essentially no electron impact ionization occurring downstream. However, there is production and mixing of positive ions through Penning ionization and charge exchange. As the ionization potential of NO (9.3 eV) is the lowest among all the important neutral species, charge exchange and Penning ionization predominantly favor the formation of NO^+ ions. The few electrons that may be produced by Penning ionization are quickly consumed by dissociative attachment to NF_x. Since the density of ions in the

downstream chamber is quite low and the mobilities of F^- and NO^+ are commensurate, there is little ambipolar enhancement of the diffusion rates for the ions and the majority of the positive and negative ions are lost through ion-ion neutralization. As a result, there is little accumulated charge on surfaces and the potential damage to the wafer by charging is small.

5.3.2 Neutral Production

The gas temperature reaches as high as 1,080 K in the RPS region, shown in Fig. 5.4(a), due largely to heating through dissociative attachment and dissociative excitation by the Franck-Condon effect. The contribution to gas heating by symmetric charge exchange (e.g., Ar^+ with Ar) in the ambipolar electric fields of the source reaction is small. In the downstream chamber, the electron density is small and there is essentially no electron impact dissociation that might additionally heat the gas through Franck-Condon processes. The exothermic and endothermic heavy particle reactions result in net heating in the downstream chamber as most of the endothermic reactions are significantly inhibited as gas temperature falls below 400 K. With the addition of thermal conduction and in spite of the allowance for slip and temperature jump at surfaces, the gas temperature decreases to nearly ambient near the wafer. Since the system is essentially isobaric, the densities of ambient neutrals (e.g., NF_3 and O_2) rebound with the decrease in gas temperature, as shown in Figs. 5.4(b) and 5.5(a).

The densities of NF_3 and its dissociation products, NF_2, NF, N and F, are shown in Fig. 5.4. In the RPS region, NF_3 is dissociated to form NF_2, NF and F through dissociative electron attachment

$$e + NF_3 \rightarrow NF_2 + F^-, \tag{5.1a}$$

and dissociative excitation

$$e + NF_3 \rightarrow NF_2 + F + e, \tag{5.1b}$$

$$e + NF_3 \rightarrow NF + F + F + e. \qquad (5.1c)$$

The density of NF_3 decreases from 8.3×10^{13} to 1.7×10^{13} cm^{-3} with the flow, reaching a fractional dissociation of 72% at the end of the RPS region. The density of F atoms increases from the gas inlet to a maximum of 9.4×10^{13} cm^{-3} at the end of the RPS region, becoming the dominant radical. In the downstream chamber where there is essentially no electron impact dissociation, the fractional dissociation of NF_3 slightly increases to 73% at the wafer surface as NF_3 is decomposed by radicals through exothermic reactions

$$NF_3 + O^* \rightarrow NF_2 + FO, \qquad \Delta H = -1.6 \text{ eV}, \qquad (5.2a)$$

$$NF_3 + N \rightarrow NF + NF_2, \qquad \Delta H = -0.5 \text{ eV}, \qquad (5.2b)$$

$$NF_3 + NF \rightarrow NF_2 + NF_2, \qquad \Delta H = -0.4 \text{ eV}, \qquad (5.2c)$$

where ΔH is the change in enthalpy of the reaction (negative ΔH indicates an exothermic reaction). However, the density of NF_3 slightly increases from 1.6×10^{13} cm^{-3} near the showerheads to 1.8×10^{13} cm^{-3} at the wafer surface. This rebound in density is caused by the gas temperature decreasing from nearly 1,080 K in the RPS source and 740 K at the grids, to 330 K at the wafer, as shown in Fig. 5.4(a). The decrease in gas temperature is due dominantly to thermal conduction to the walls in the downstream chamber.

The densities of NF_2, NF and N show similar trends, being formed in the RPS through electron impact reactions and reaching a density of 1.2×10^{13}, 6.3×10^{12} and 2.5×10^{12} cm^{-3} at the end of the RPS region, respectively. The densities of NF_2, NF and N peak at 1.9×10^{13}, 8.7×10^{12} and 3.2×10^{12} cm^{-3} near the coils where the electron impact ionization source and the electron temperature are the maximum and the electron impact dissociation reactions are favored. After entering the downstream chamber, the density of NF_2 decreases to 2.0×10^{12} cm^{-3} at the wafer surface due to consumption through exothermic reactions

$$NF_2 + O \rightarrow FNO + F, \qquad \Delta H = -2.9 \text{ eV}, \qquad (5.3a)$$

$$NF_2 + N \rightarrow N_2 + F + F, \qquad \Delta H = -3.7 \text{ eV}, \qquad (5.3b)$$

$$NF_2 + N \rightarrow NF + NF, \qquad \Delta H = -0.1 \text{ eV}, \qquad (5.3c)$$

$$NF_2 + FO \rightarrow FNO + F + F, \qquad \Delta H = -0.6 \text{ eV}. \qquad (5.3d)$$

The density of NF also decreases to 3.7×10^{12} cm^{-3} at the wafer surface due to the exothermic reactions in Eq. 5.2(c) and

$$NF + N \rightarrow N_2 + F, \qquad \Delta H = -6.7 \text{ eV}, \qquad (5.4a)$$

$$NF + NF \rightarrow N_2 + F_2, \qquad \Delta H = -5.2 \text{ eV}, \qquad (5.4b)$$

$$NF + NF \rightarrow N_2 + F + F, \qquad \Delta H = -3.6 \text{ eV}. \qquad (5.4c)$$

The density of N atoms decreases to 1.0×10^{11} cm^{-3} at the wafer surface in part due to the surface reaction

$$N(s) + N(g) \rightarrow N_2(g) + SiN(s), \qquad (5.5)$$

where s denotes surface site and g denote gas phase species, and in part due to gas phase exothermic reactions,

$$N + NO_2 \rightarrow NO + NO, \qquad \Delta H = -3.4 \text{ eV}, \qquad (5.6a)$$

$$N + NO_2 \rightarrow N_2 + O_2, \qquad \Delta H = -5.2 \text{ eV}, \qquad (5.6b)$$

$$N + NO_2 \rightarrow N_2O + O, \qquad \Delta H = -1.7 \text{ eV}. \qquad (5.6c)$$

$$N + NO \rightarrow N_2 + O. \qquad \Delta H = -3.2 \text{ eV}. \qquad (5.6d)$$

In the RPS region, N_2 molecules are mainly formed through surface recombination of N atoms with a probability of 0.01, so the density of N_2 increases from the center of the RPS to the surface of the tube where recombination occurs, as well as increasing with the flow from inlet to 4.0×10^{12} cm^{-3} at the end of the RPS. In the downstream chamber, the density of N_2 increases

from 0.4×10^{13} to 1.2×10^{13} cm^{-3} at the wafer surface as N_2 is formed in part through surface reactions in Eq. 5.5 and

$$N(s) + NO(g) \rightarrow N_2(g) + O(s). \quad (5.7)$$

The density of N_2 also increases through gas phase exothermic reactions of N with NF and NF_2, mutual reactions of NF, and reactions of NO and N [Eqs. 5.3(b), 5.4 and 5.6(b,d)]. Once generated outside the region of either high T_e or high T_g, N_2 is fairly stable, tends to accumulate and eventually flows out of the system.

Volatile SiF_4 is formed at the surface of the wafer through desorption of Si surface sites by successive passivation of F etchants through

$$SiNF_{m-1}(s) + F(g) \rightarrow SiNF_m(s, m = 1 - 3), \quad (5.8a)$$

$$SiNF_3(s) + F(g) \rightarrow SiF_4(g) + N(s). \quad (5.8b)$$

The density of SiF_4 increases from 3.0×10^{12} cm^{-3} at the center of the wafer to 6.0×10^{12} cm^{-3} at the edge of the wafer as shown in Fig. 5.4(h) as the reaction products accumulate in the gas flow.

The densities of O_2, O, FNO and N_xO_y species (NO, NO_2 and N_2O) are shown in Fig. 5.5. O_2 is dissociated in the RPS region through electron impact dissociative attachment and dissociative excitation

$$e + O_2 \rightarrow O + O^-, \quad (5.9a)$$

$$e + O_2 \rightarrow O + O + e. \quad (5.9b)$$

The density of O atoms peaks at 5.0×10^{13} cm^{-3} near the coils due to the locally high electron impact ionization source. In the downstream chamber, the density of O_2 increases from 2.0×10^{13} cm^{-3} near the showerheads to 3.0×10^{13} cm^{-3} at the wafer surface due to gas cooling. O_2 is also replenished through surface reactions abstracting O(s) sites,

$$O(s) + O(g) \rightarrow O_2(g) + SiN(s), \quad (5.10a)$$

$$O(s) + O(s) \rightarrow O_2(g) + SiN(s). \qquad (5.10b)$$

FNO is largely produced by the exothermic reaction of O and NF_2 [Eq. 5.3(a)]. The increased density of FNO from 1.5×10^{13} cm^{-3} at the showerheads to 2.1×10^{13} cm^{-3} at the wafer surface as shown in Fig. 5.5(c) is due to decreased gas temperature which both favors the exothermic reaction between O and NF_2 [Eq. 5.3(a)] over endothermic reactions and results in rebound in FNO density. The density of NO_2 has similar spatial variation with the flow as FNO, increasing from 3.0×10^{11} cm^{-3} at the showerheads to 1.0×10^{12} cm^{-3} at the wafer surface as NO_2 is predominantly formed through the exothermic reaction between FNO and O,

$$FNO + O \rightarrow F + NO_2, \qquad \Delta H = -0.8 \text{ eV}. \qquad (5.11)$$

The formation of NO and N_2O is heavily modulated by the gas temperature and surface reactions. NO is mainly produced in the RPS region through endothermic reactions

$$N_2 + O \rightarrow N + NO, \qquad \Delta H = 3.2 \text{ eV}, \qquad (5.12a)$$

$$N_2 + O_2 \rightarrow NO + NO, \qquad \Delta H = 1.8 \text{ eV}. \qquad (5.12b)$$

These reactions are aided by the high gas temperature (800 – 1,000 K) in the RPS and so the density of NO reaches its maximum of 4.4×10^{12} cm^{-3} at the showerheads prior to the gas cooling. In the downstream chamber, NO is the main etchant to remove N surface sites by forming N_2 and N_2O through reactions in Eq. 5.7 and

$$N(s) + NO(g) \rightarrow N_2O(g) + SiN(s), \qquad (5.13)$$

and to remove O surface sites by forming NO_2 through

$$O(s) + NO(g) \rightarrow NO_2(g) + SiN(s). \qquad (5.14)$$

The density of NO monotonically decreases to 1.2×10^{12} cm^{-3} approaching the wafer while the density of N_2O peaks at 2.5×10^{12} cm^{-3} at the wafer surface as it is an etch product. In addition to surface reactions, NO and N_2O are formed in the downstream chamber through gas phase

exothermic reactions of N with NO_2 in Eqs. 5.6(a,c), though the major source is by surface reactions.

The fluxes to the wafer of the etchants of silicon nitride, F, NO, O and N, are shown in Fig. 5.6. As the ICP power increases from 100 to 800 W, the fractional dissociation of NF_3 increases from 34% to 88%, and the flux of F atoms to the center of the wafer increases from 0.6 $\times 10^{18}$ to 1.7 $\times 10^{18}$ $cm^{-2}s^{-1}$. As the fractional dissociation of the NF_x species increases with power, the flux of F atoms to the wafer begins to saturate. There is only a nominal increase in the F flux when increasing the ICP power from 500 to 800 W. The flux of F atoms peaks at the center of the wafer due to the on-axis influx of reactants from the RPS.

As the power increases from 100 to 800 W, the gas temperature in the RPS increases from 630 to 1,600 K, resulting in enhanced formation of NO through endothermic reactions of N_2 with O and O_2 (Eq. 5.12) and the exothermic reaction having an activation energy of 3,270 K,

$$N + O_2 \rightarrow NO + O, \qquad \Delta H = -1.4 \text{ eV}. \qquad (5.15)$$

The density of NO near the center of the wafer surface increases by an order of magnitude (from 0.2 $\times 10^{12}$ to 2.0 $\times 10^{12}$ cm^{-3}), similar to the increase in the flux of NO to the wafer (0.3 $\times 10^{16}$ to 3.3 $\times 10^{16}$ $cm^{-2}s^{-1}$) while increasing ICP power from 100 to 800 W. The majority of this increase occurs between 100 W and 300 W, when the gas temperature increases from 630 to 1,080 K in the RPS. At these temperatures, endothermic reactions forming NO in the RPS begin to become effective. The flux of O atoms to the wafer surface almost linearly scales with the power, as only a single electron impact reaction with O_2 is required to produce O atoms by dissociative excitation and attachment [Eqs. 5.9(a,b)] while the initial O_2 is not significantly depleted.

The flux of N atoms to the wafer increases nonlinearly with increasing power, particularly above 300 W. N atoms are mainly formed through electron impact dissociative

reactions of NF and NO,

$$e + NF \rightarrow N + F^-, \quad (5.16a)$$

$$e + NF \rightarrow N + F + e, \quad (5.16b)$$

$$e + NO \rightarrow N + O^-, \quad (5.16c)$$

$$e + NO \rightarrow N + O + e. \quad (5.16d)$$

As the ICP power increases, the production of NF through electron impact dissociative excitation of NF_2 and NF_3 increases as NF_3 is more dissociated through reactions in Eq. 5.1(b,c), while the production of NO through endothermic reactions increases due to the increase in gas temperature. The end result is that the flux of N atoms to the center of the wafer non-linearly increases from 1.8×10^{14} $cm^{-2}s^{-1}$ at 100 W to 8.7×10^{16} $cm^{-2}s^{-1}$ at 800 W. At 800 W, the flux of N atoms to the wafer is almost 3 times that of NO, resulting in a transition of the dominant etchant for the removal of N subsites from NO (Eqs. 5.7 and 5.13) to N (Eq. 5.5).

5.3.3 Si_3N_4 Etching

The variations for the fractional coverage of Si(s) and N(s) subsites with ICP power are shown in Fig. 5.7 and the corresponding etch rates are shown in Fig. 5.8. Initially, the pristine silicon nitride surface consists of Si(s) subsites and N(s) subsites. The Si(s) subsites are rapidly removed by F atoms through the formation of volatile SiF_4 (Eq. 5.8), leaving the N(s) subsites, which are then removed by NO and N radicals through reactions in Eqs. 5.5, 5.7 and 5.13. For these conditions, the Si(s) subsites on the surface are almost completely etched due to the much larger flux of F atoms (etchant of Si(s) subsites) compared to fluxes of NO and N (etchants of N(s) subsites). The complete etch process is rate limited by the availability of NO and N neutrals to remove N(s), leaving the top surface N(s) rich.

As the ICP power increases from 100 to 800 W, the nonlinear increase of fluxes of NO

and N shown in Fig. 5.6 favors the more rapid removal of N(s) subsites compared to removal of Si(s) sites. These trends result in an increase in etch rate (from 20 to 320 nm/min at the wafer center and from 20 to 90 nm/min at the wafer edge) shown in Fig. 5.8. The exposure of Si(s) subsites increases while the fractional coverage of N(s) subsites at the center of the wafer decreases from 0.95 to 0.74, shown in Fig. 5.7(b). The fractional coverage of O(s) sites is less than 0.02 as the O flux which etches those sites is larger than the NO flux by an order of magnitude. Once O(s) surface sites are formed through surface oxidation by NO molecules in Eq. 5.7, they are quickly etched by gas phase O atoms through the formation of O_2 in Eq. 5.10(a).

The ratio of fluxes of F atoms to NO molecules and N atoms, $\phi_F/(\phi_{NO} + \phi_N)$, is a key parameter for determining etch rate and uniformity. For similar reaction probabilities, the ratio of the etchants of Si(s) subsites to the etchants of N(s) subsites should align with the stoichiometry of silicon nitride. The limiting factor for the etch rate in F rich condition is then the NO and N fluxes which remove N(s) surface sites. Thus, the etch rate nearly linearly increases with the fluxes of NO and N radicals to the wafer surface as shown in Fig. 5.8(b). The center peaked etch rates at the higher ICP powers can be attributed to the non-uniform fluxes of N and NO reaching the surface, which is due to radial diffusion of N and NO in the downstream chamber as shown in Figs. 5.4(f) and 5.5(e).

In the experiments of downstream etching of silicon nitride by a RPS sustained in NF_3/O_2 performed by Kastenmeier *et al*., the etch rate and degree of surface oxidation were proportional to the partial pressure of NO in the reactor chamber.[1,17] The small contribution of N atoms to the etch rate in their experiments was due to the small flux of N atoms to the wafer for their operating conditions.

5.3.4 Plenum

With the goal of this investigation being elucidating reaction mechanisms, an exhaustive study of methods to improve etch uniformity was not performed. The primary source of non-uniformities is the on-axis nozzle and relatively short downstream diffusion chamber. It is more typical in industrial reactors to use a plenum and wafer-diameter showerhead and taller downstream chamber to disperse the reactants more uniformly over the wafer. As a demonstration, limited studies were performed using a plenum connecting the RPS and the downstream reactor using the geometry shown in Fig. 5.9. The height of the plenum is 4 cm and the radius is 13 cm. The flow distance from the RPS to the wafer is 17 cm with two levels of showerheads placed in between – one at the end of the confined plasma zone and the other at the base of the plenum. The spacing of the showerheads (0.75 cm), the ICP power (300 W) and the other operating conditions are the same as the base case.

Gas temperature and reactant densities for the RPS with plenum are shown in Fig. 5.9. There is a significant gradient of the gas temperature from the source region (≈ 1,100 K) to the plenum (≈ 380 K) and the downstream chamber (≈ 330 K). This gradient provides opportunities to customize the gas reaction pathways and optimize radical production through combinations of endothermic and exothermic reactions by properly choosing the injection points for process gases. In the plenum, the neutrals diffuse more in the radial direction than in the vertical direction due to the higher pressure and resistance to the gas flow induced by the showerheads placed between the plenum and the downstream chamber. The densities of F and O radicals near the circumference of the plenum are about 60% of the values at the axis of the plenum. The density of N atoms decreases from 1.0×10^{12} cm^{-3} at the plenum axis to 0.1×10^{12} cm^{-3} near the fringe while the density of NO only slightly decreases from 5.8×10^{12} to 5.4×10^{12} cm^{-3}. These

trends are due to exothermic reactions of N with NO_2 and O_2 in Eqs. 5.6(a) and 5.15 which consume N atoms and produce NO molecules.

The neutral flow from the plenum into the downstream chamber through the array of showerheads produces more uniform densities in the downstream chamber, shown in Fig. 5.9, and more uniform fluxes to the wafer, shown in Fig. 5.10. With the gas temperature in the downstream chamber being nearly uniformly 330 K, there is no thermal radial gradient across the wafer, which could otherwise produce non-uniform neutral fluxes. The flux of F decreases from 6.2×10^{17} $cm^{-2}s^{-1}$ at the center of the wafer to 4.3×10^{17} $cm^{-2}s^{-1}$ at the edge of the wafer and the flux of NO decreases from 1.4×10^{16} to 1.0×10^{16} $cm^{-2}s^{-1}$, about a 30% difference compared to about 60% without the plenum.

As the flux of F to the wafer is one order of magnitude larger than that of NO and N, the Si(s) subsites are almost totally removed resulting in exposure of N(s) subsites, and so the uniformity of etching is mainly determined by the uniformity of the flux of NO and N to the surface. The etch rate shown in Fig. 5.10(c) decreases from 70 nm/min at the wafer center to 50 nm/min at the edge (30% difference), providing better uniformity than the base case without the plenum shown in Fig. 5.8(a). Although the addition of the plenum improves the uniformity of etching, the overall etch rate decreases due to the longer flow time (stagnation in the plenum) which affords more opportunity for recombination reactions of radicals and more opportunity for surface reactions with chamber walls. Uniformity can be further improved by increasing the volume of the plenum (at the cost of reducing the radical density), having a hole-pattern in the showerhead with larger diameter holes at larger radius and by increasing the distance between the showerhead and the wafer (again, at the cost of reducing radical density).

5.4 Etching of Si_3N_4 by Pulsed Power Remote Plasma Source

Pulsing enables both plasma and etch properties to be controlled beyond what may be possible with continuous wave (CW) excitation. For CW excitation, the electron source and loss need to be instantaneously balanced, producing a unique T_e for a given pressure and power. As a result, the balance between generating radicals and ions is fairly constrained. The use of pulsed power provides a means to customize the electron energy distribution by allowing the electron source and loss to be balanced over the pulse period as opposed to instantaneously.[18] The electron temperature can considerably vary during the pulse period. Although the gas temperature can also vary during a pulse period due to modulation of the gas heating sources by electron impact dissociative reactions, the degree of modulation is less due to the finite heat capacity of the system. The result is some ability to customize rate coefficients for both electron impact reactions and heavy particle endothermic and exothermic reactions. For systems with the wafer in direct contact with the plasma, the ion-ion plasma formed during the afterglow minimizes damage to the surface by reducing net charge accumulation on the wafer.[19]

The RPS was sustained with pulsed 10 MHz inductively coupled power with a 25 kHz pulse repetition frequency (PRF) and 25% duty cycle (DC). (DC refers to the fraction of the pulse period that power is applied, and PRF refers to the number of times per second the waveform is repeated.) The pulsed-period-averaged (PPA) power was 300 W. The other operating conditions were kept the same as those for the base CW case (50 mTorr, $Ar/NF_3/O_2$ = 90/5/5, 1000 sccm). The variations of volume averaged densities of charged particles and electron temperature with time are shown in Fig. 5.11. (These densities are volume averaged weighted by the electron density and so preferentially show densities in the RPS.) These values are shown after 26 pulsed periods so that a pulse-periodic steady state is achieved.

With a fast rising power pulse, increasing power from 0 to 1,200 W in 1.5 μs delivered into an initially small inventory of electrons having a density of ≈ 1.0×10^9 cm^{-3} produces a spike of electron temperature to 5.4 eV. This high T_e above the CW value (4.2 eV) and the higher power during the pulse enables more efficient excitation and ionization, which leads to an increased electron density of 5.0×10^{10} cm^{-3} compared to CW. During the pulse-on period, charge neutrality is mainly maintained by $[e] + [F^-] \approx [Ar^+] + [O_2^+]$. The dominant positive ions are Ar^+ and O_2^+ due to their large initial mole fractions. Due to low mole fractions (< 5%) and moderate ionization potentials (11 – 13 eV) of NF_x, the densities of NF_x^+ (~ 10^8 cm^{-3}) are two orders of magnitude lower than Ar^+. When the power is turned off, the electrons quickly attach to NF_x to form F^- or diffuse to the walls, resulting in transition of the dominant negative charge from electrons to F^- ions. The loss mechanism for the positive ions in the afterglow is recombination with electrons (20% of the total loss), neutralization with negative ions (80%) and diffusion to the walls (< 1%). As the ionization potentials of O_2 (12.1 eV) and NO (9.3 eV) are lower than Ar (16.0 eV) and O (16.2 eV), O_2^+ and NO^+ are replenished by charge exchange and Penning ionization in the afterglow and their densities have a slower decay rate compared to other positive charged species.

The spatial distributions of electron density, electron temperature and electron impact ionization source in the middle of the pulse-on period and the middle of the pulse-off period are shown in Fig. 5.12. During the pulse-on period the electron density and electron temperature peak at 2.6×10^{12} cm^{-3} and 4.5 eV in adjacent to the coils in the electromagnetic skin depth. The electron impact ionization source peaks at 3.6×10^{17} $cm^{-3}s^{-1}$ near the coils, which is about 6 times of the CW value shown in Fig. 5.2(c). During the pulse-off period, the electron density and electron temperature drop to 10^{10} cm^{-3} and below 0.3 eV. At these temperatures, thermal

attachment is favored over the ionization, resulting in S_e transitioning from positive in Fig. 5.12(a) (with regions of negative source away from the coil) to fully negative in Fig. 5.12(b). The maximum net loss of 6.2×10^{15} $cm^{-3}s^{-1}$ occurs at the center of the RPS reactor where the electron density is the largest in the afterglow.

The densities of F^- and NO^+ are shown in Fig. 5.13 during the power-on and power-off portions of the cycle. These ions are only moderately modulated by the pulsed power in the RPS region, being a factor of 2 larger during the pulse, whereas the electron density is modulated by an order of magnitude. The time for ion-ion recombination and for diffusion to the walls is longer than the interpulse period. With the low electron temperature and low electron density, there is little ambipolar enhancement to diffusion rates. The densities of F^- and NO^+ ions are also only slightly modulated in the downstream chamber, where charge neutrality is maintained by $[NO^+] \approx [F^-]$. The showerheads serve well to isolate the ions that have leaked into the downstream chamber from the dynamics occurring in the RPS. The ambipolar electric fields in the downstream chamber are small since the ion charge density is only marginally at the level of supporting ambipolar electric fields. As a result, the ions nearly freely diffuse. What modulation does occur is due to greater injection (or leakage) of ions from the RPS during the pulse-on period. The electron density in the downstream chamber is below 10^7 cm^{-3}, whereas the ion-ion plasma has a density of 10^8 cm^{-3}. As in the CW case, there is negligible flux of ions to the wafer surface and the etching of the silicon nitride wafer is almost purely neutral driven.

To investigate the effect of different strategies of pulsed power on the plasma and etch properties, the PRF was varied from 25 to 100 kHz and the DC was varied from 25% to 75%, while the PPA power was 300 W. The volume averaged densities of electrons and ions, and electron temperatures for different DCs and PRFs are shown in Figs. 5.11, 5.14 and 5.15. As the

DC decreases from 75% to 25% with the PRF maintained at 25 kHz, the peak power increases from 400 to 1,200 W. Over this range, the electron density in the pulse-on period increases from 1.8×10^{10} to 5.0×10^{10} cm^{-3} and the peak electron temperature increases from 5.2 to 5.4 eV, resulting in enhanced electron impact ionization source and increased densities of positive ions by 2 – 3 times as shown in Figs. 5.11 and 5.14. The electron loss through diffusion, attachment and recombination becomes larger with decreasing DC due to the longer pulse-off period, and so the electron density at the end of the pulse-off period decreases from 2×10^{9} cm^{-3} for DC = 75% to 1×10^{9} cm^{-3} for DC = 25%. With this reduced conductivity at the of the pulse-off period, there is proportionally more collisional heating at the beginning of the pulse-on period by there being a larger *E/N* in the bulk plasma.

As the PRF increases from 25 to 100 kHz with the DC maintained at 25%, the electron loss during the pulse-off period becomes smaller due to the shorter pulse-off period, leading to higher conductivity and lower *E/N* at the beginning of the next pulse-on period. As a result, the peak electron temperature decreases from 5.4 to 5.2 eV as shown in Figs. 5.11 and 5.15. As the PRF varies, the plasma properties during the pulse-on period are slightly modulated as the peak power is the same (1,200 W) due to the same DC (25%) and PPA power (300 W).

As radical lifetimes and the residence time of the flow (~ ms) are much longer than the pulse period (10 – 40 μs), varying the PRF (with constant DC) from 25 to 100 kHz results in little modulation in the densities and fluxes of neutrals to the wafer, and so the etch properties (e.g., etch rate and uniformity) are almost invariant when varying the PRF.

The pulse averaged fluxes of the etchants for silicon nitride (F, NO, O and N) to the wafer surface for different DCs for a constant PRF (25 kHz) are shown in Fig. 5.16. The pulse averaged fractional coverage of Si(s) and N(s) subsites and etch rates are shown in Fig. 5.17.

The pulse averaged flux of F atoms only slightly increases with decreasing DC from 100% (base CW case) to 25% as shown in Fig. 5.16(a). This small increase is due to the enhanced dissociation by the spike in electron temperature (5.2 – 5.4 eV) during pulsed cases above the CW value (4.2 eV). However, since the majority of F atoms are produced through dissociative attachment to NF_x by thermal electrons, this spiking of the electron temperature does not significantly affect the F atom production.

The pulse averaged flux of NO to the center of the wafer decreases from 2.5×10^{16} to 1.8×10^{16} $cm^{-2}s^{-1}$ with decreasing DC from 100% to 25% as shown in Fig. 5.16(b). NO is primarily formed through the endothermic reactions of N_2 with O and O_2 (Eq. 5.12) and exothermic reactions of N with O_2 (Eq. 5.15), the latter having an activation energy of 3,270 K. The density of NO is therefore highly dependent on excursions of the gas temperature that approach the activation energy. As the DC decreases from 100% to 25% and peak power increases, the volume averaged gas temperature in the RPS during the pulse-on period increases from 850 to 875 K while the peak temperature increases from 1,080 to 1,150 K. However, during the pulse-off period, T_g decreases from 850 to 635 K due to the longer period for thermal conduction to the walls. Overall, the enhancement of endothermic reactions for the formation of NO during the pulse-on period cannot compensate for losses due to exothermic reactions in the pulse-off period. As a result, the density of NO near the wafer surface decreases from 1.2×10^{12} to 0.9×10^{12} cm^{-3} with decreasing DC, and the flux of NO decreases as shown in Fig. 5.16(b).

The flux of F atoms to the surface monotonically decreases from the center to the edge of the wafer, while a minimum occurs for the flux of NO near the edge of the wafer at radius of 13 cm shown in Fig. 5.16(b). NO molecules are consumed by N(s) subsites to form N_2O. As the N_2O etch product diffuses from the wafer, the small increase in the flux of NO at the edge of the

wafer is then due to the exothermic reaction

$$N_2O + O \rightarrow NO + NO. \qquad \Delta H = -1.7 \text{ eV}. \qquad (5.17)$$

The electron density and electron temperature during the pulse-on period increase as DC decreases, which favors the formation of O atoms by electron impact dissociation of O_2 (Eq. 5.9) and the formation of N atoms through electron impact dissociation of NF and NO (Eq. 5.16). Nevertheless, the pulse averaged flux of O to the center of the wafer surface decreases from 5.4 $\times 10^{17}$ to 4.8 $\times 10^{17}$ $cm^{-2}s^{-1}$ and that of N decreases from 4.2 $\times 10^{15}$ to 1.6 $\times 10^{15}$ $cm^{-2}s^{-1}$. This trend is due to the increased production at lower DC not being able to compensate for the consumption of N and O during the longer afterglow.

The fractional coverages of Si(s) and N(s) subsites, and etch rate, as a function of DC are shown in Fig. 5.17. In fluorine rich conditions where the density of F atoms is two orders of magnitude larger than the densities of NO and N, the Si(s) subsites are almost completely removed by the F atoms through reaction in Eq. 5.8, resulting in a small (< 0.04) coverage of Si(s) subsites. As the fluxes of NO and N to the surface increase with increasing DC, the removal of N(s) subsites and re-exposure of underlying Si(s) subsites are favored. This leads to a small decrease in fractional coverage of N(s) subsites at the center of the surface from 0.88 to 0.84, and increased fractional coverage of Si(s) subsites from 0.025 to 0.035. The etch rate at the center of the surface increases from 96 to 138 nm/min with increasing DC. For fluorine rich conditions, the etch rate is limited by the availability of the etchants of N(s) subsites (i.e., NO and N). When increasing DC, the densities and fluxes of both NO and N increase, which being the rate limiting flux for completing the etch cycle, increases the etch rate.

5.5 Concluding Remarks

A downstream plasma etching system consisting of a RPS sustained in $Ar/NF_3/O_2$ mixtures with CW and pulsed ICP power, and a downstream chamber with silicon nitride coated wafer placed on the substrate has been modeled using a 2-dimensional simulation. In the RPS, the dominant positive ions are Ar^+ and O_2^+ due to large mole fraction of their parent gases and the dominant negative ions are F^- due to thermal attaching NF_x species. Most of the ions are confined in the source region, except that a weak ion-ion plasma maintained by $[NO^+] \approx [F^-]$ persists into the downstream chamber due to the lowest ionization potential being that of NO and the highest electron affinity being that of F among all the important neutral species in the system. As negligible fluxes of ions reach the surface of the wafer, etching is almost purely neutral driven, and so is nearly damage free and isotropic.

A surface reaction mechanism for the etching of silicon nitride by thermal neutrals was developed and implemented into the 2-dimensional model. The etching proceeds by iteratively removing Si and N surface subsites. Si subsites are removed through the formation of volatile SiF_4 by successive passivation by F atoms, while N subsites are etched through the formation of N_2O and N_2 by NO and N. As the ICP power increases for CW excitation, more F and N atoms are produced through electron impact dissociative reactions of NF_x and NO, leading to increased gas temperature due to Franck-Condon heating, which in turn favors the formation of NO through endothermic reactions in the source region. In fluorine rich conditions, the etch rate is limited by availability of the etchants of N subsites, NO and N, and so the etch rate nearly linearly increases with fluxes of NO and N to the wafer.

The downstream etching process has been investigated, and mildly optimized, using two approaches. From the perspective of geometry, a plenum added between the remote plasma

source and the downstream chamber favors transverse diffusion of neutrals and results in neutral fluxes to the wafer and etch rates of silicon nitride having higher uniformity. From the perspective of excitation power, use of pulsed power source provides a means to customize the electron impact reactions and heavy particle endothermic and exothermic reactions by enabling different electron temperatures and gas temperatures over the pulse period. As the powered portion of the cycle increases with increasing duty cycle, pulse averaged fluxes of NO and N to the wafer increase, resulting in more removal of N subsites and thus increased etch rates for these fluorine rich conditions.

In addition to using a plenum and pulsed power sources, other optimization strategies are suggested by these results. The etch rate can be better controlled and the efficiency for radical production can be improved by separately controlling the production of etchants of Si surface sites (F atoms) and etchants of N surface sites (N_xO_y species) using multiple remote sources. In this way, the ratio of the etchants of Si subsites (F atoms) to the etchants of N subsites (NO and N) reaching the wafer aligns with the stoichiometry of silicon nitride. In downstream etching systems, the gas temperature can exceed several thousand degrees K in the RPS while decreasing to near ambient in the downstream chamber. This natural gradient in gas temperature may enable customizing the reaction pathway using multiple gas inlets at different gas temperatures (for example, one inlet at the upstream of RPS and the other at the downstream of RPS as discussed in Sec. 3.2.4). The endothermic reactions mainly occur in the RPS, uniquely producing precursors which flow downstream and exothermically react with process gases injected from the downstream inlet to produce reactants for etching and surface modification at the wafer surface.

5.6 Figures

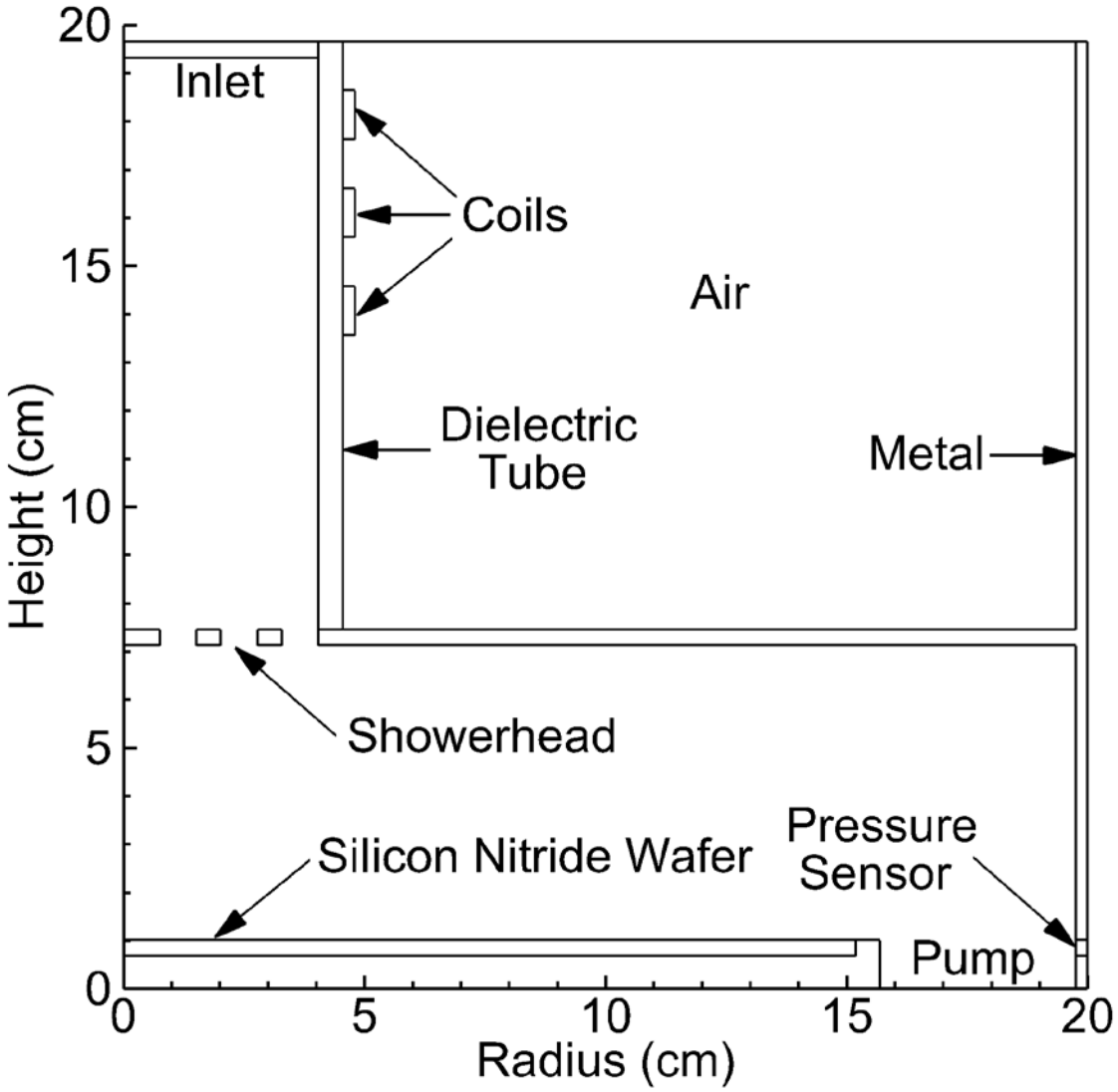

Fig. 5.1 Schematic of a downstream etch system consisting of a remote plasma source and a downstream reactor chamber with metal showerheads placed in between. The RPS is driven by inductively coupled power. Silicon nitride wafer is placed on the substrate in the downstream chamber with no bias imposed on it.

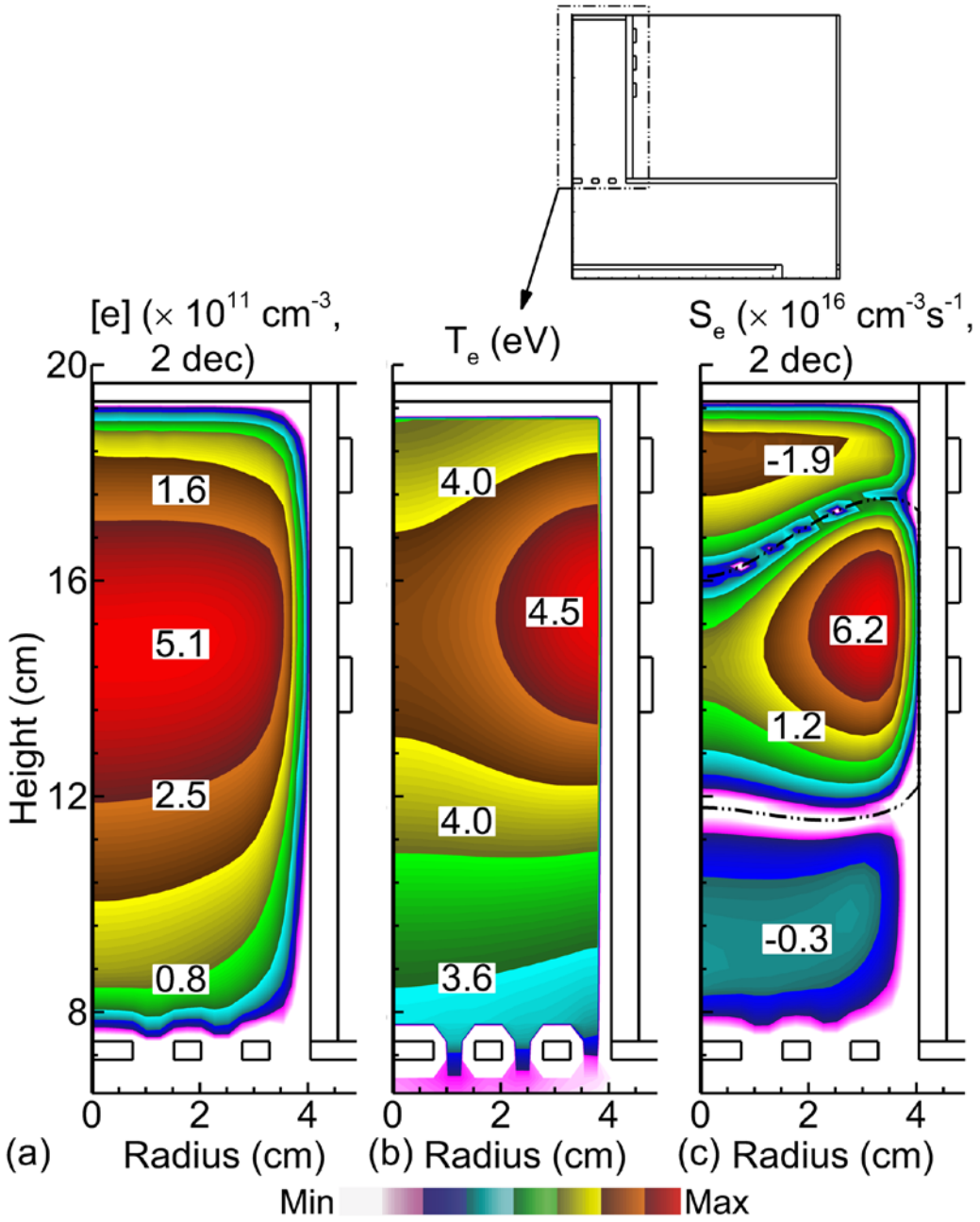

Fig. 5.2 Time averaged a) electron density, b) electron temperature and c) electron impact ionization source in a RPS driven by inductively coupled power. Operating conditions: $Ar/NF_3/O_2$ = 90/5/5, 50 mTorr, 1,000 sccm, 300 W, 10 MHz.

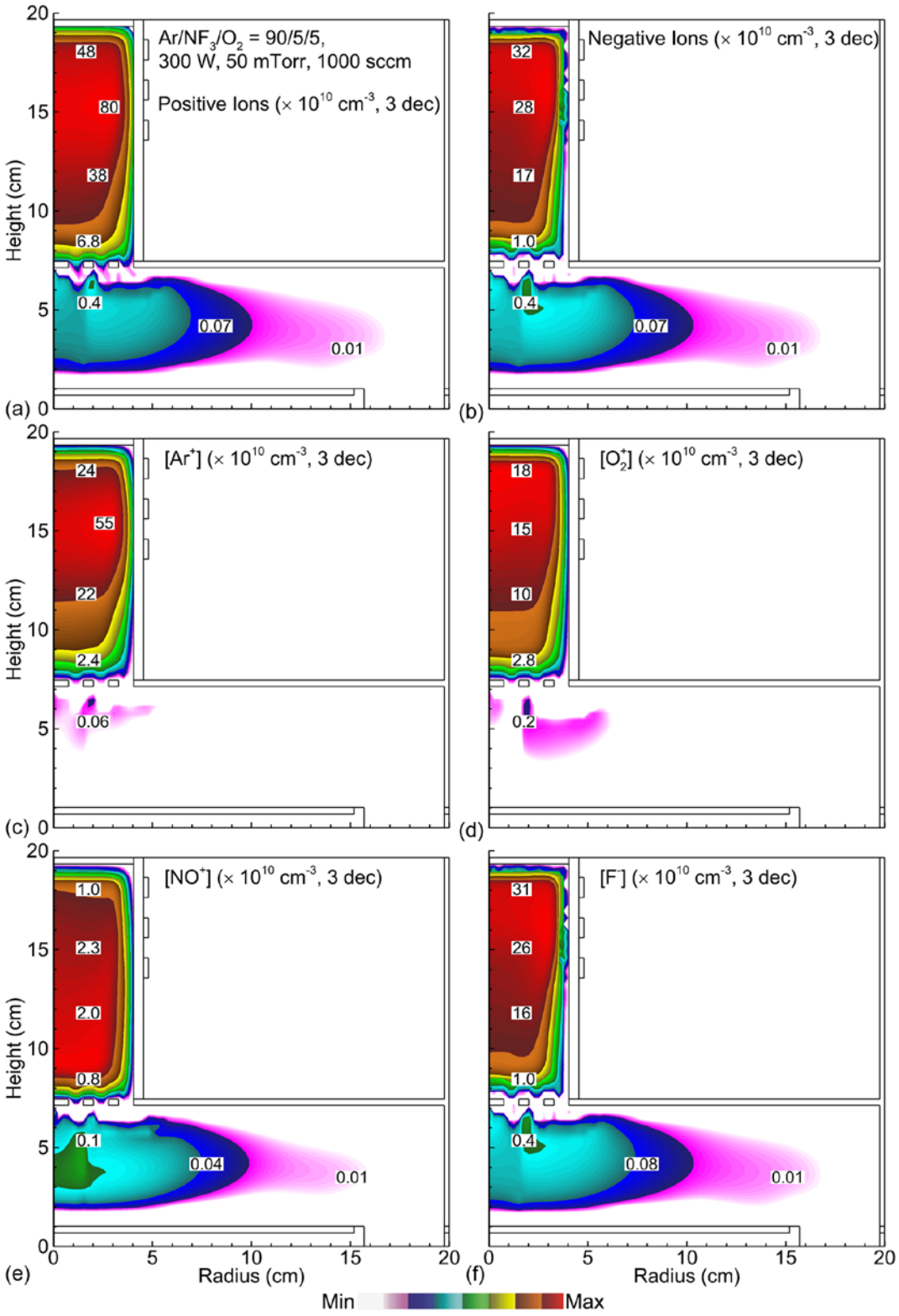

Fig. 5.3 Time averaged densities of a) all positive ions, b) all negative ions, c) Ar^+, d) O_2^+, e) NO^+ and f) F^- in a downstream etch system with a RPS driven by inductively coupled power. Operating conditions: $Ar/NF_3/O_2$ = 90/5/5, 50 mTorr, 1,000 sccm, 300 W, 10 MHz.

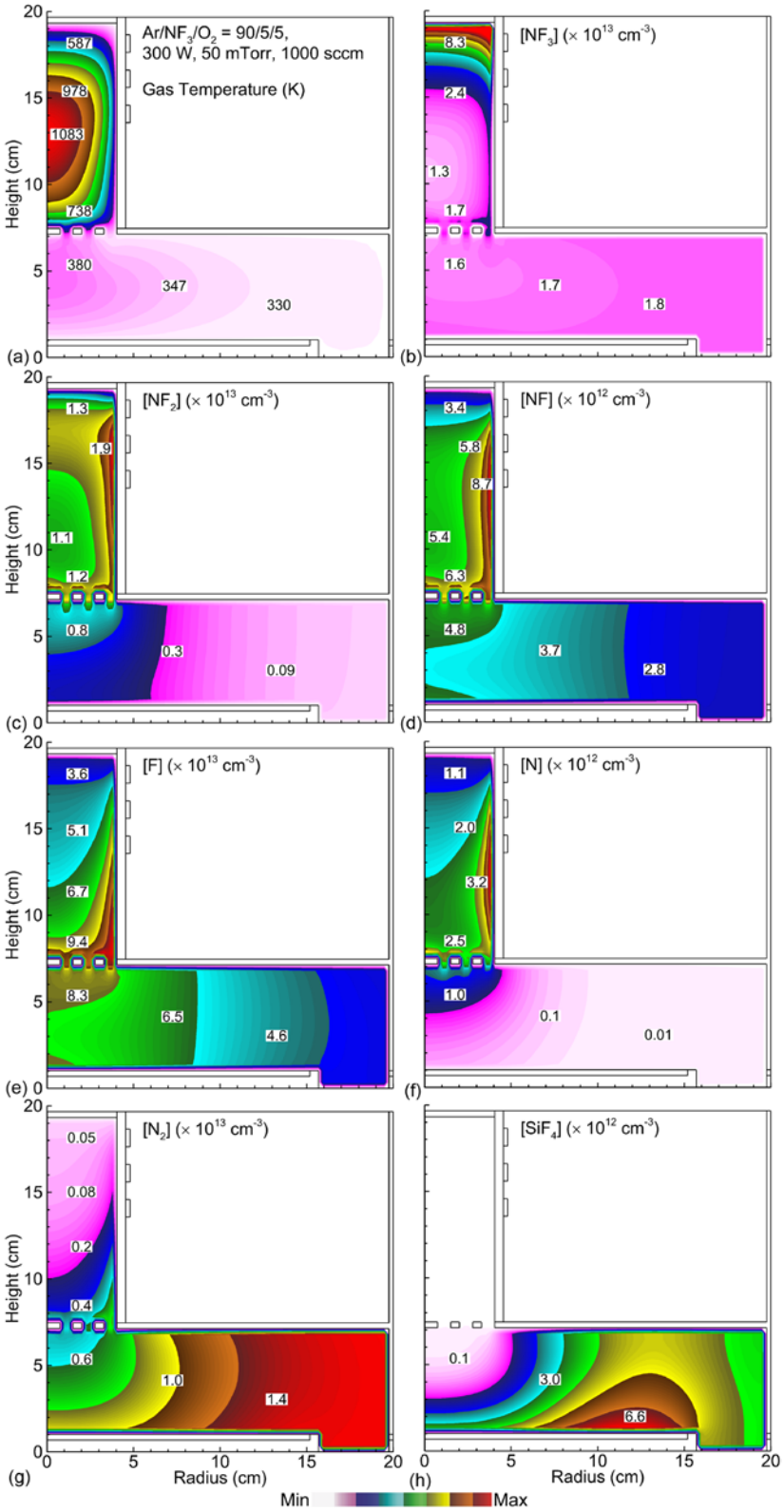

Fig. 5.4 Time averaged a) gas temperature and densities of b) NF_3, c) NF_2, d) NF, e) F, f) N, g) N_2 and h) SiF_4 in a downstream etch system with a RPS driven by inductively coupled power. Operating conditions: $Ar/NF_3/O_2$ = 90/5/5, 50 mTorr, 1,000 sccm, 300 W, 10 MHz.

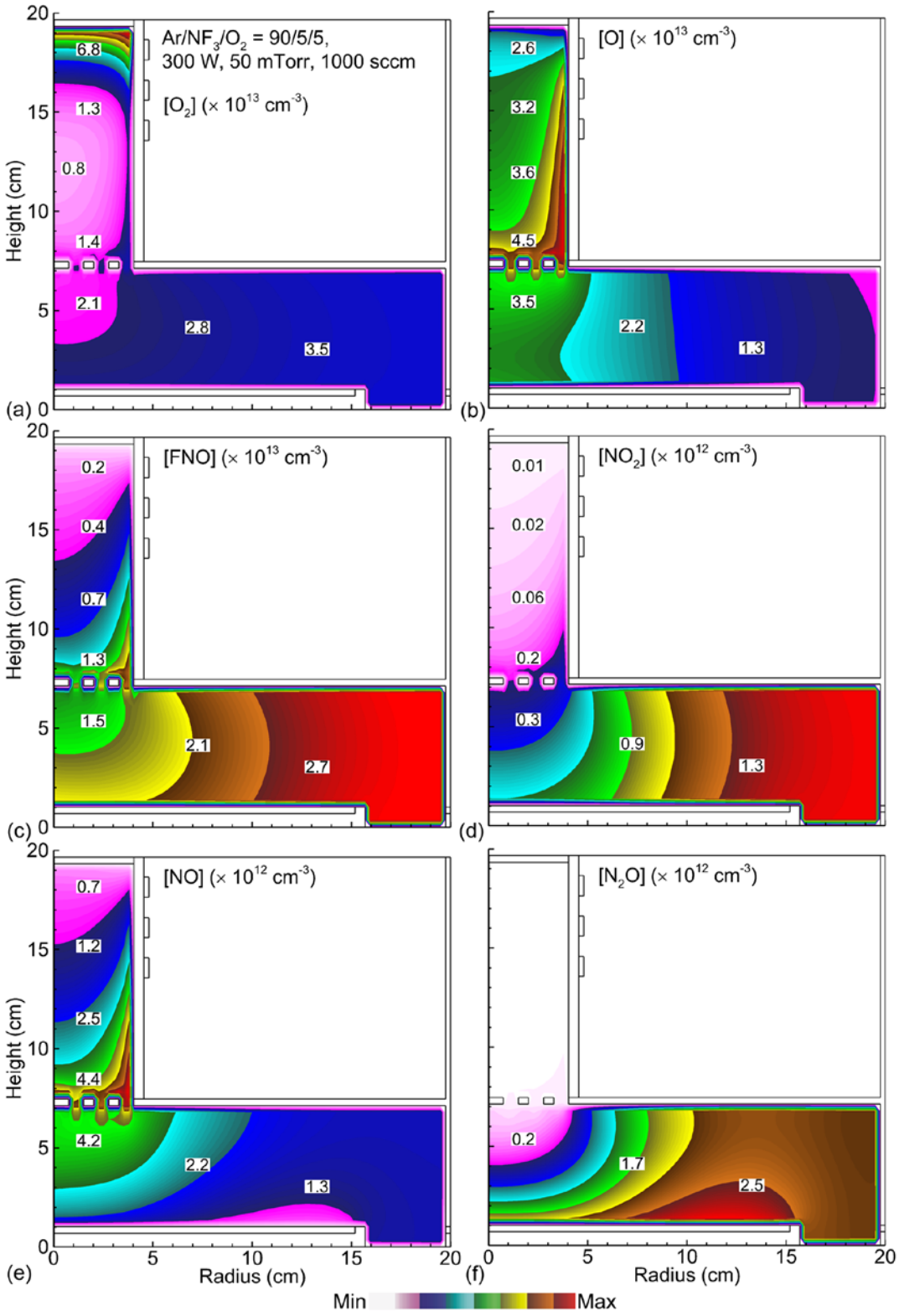

Fig. 5.5 Time averaged densities of a) O_2, b) O, c) FNO, d) NO_2, e) NO and f) N_2O in a downstream etch system with a RPS driven by inductively coupled power. Operating conditions: $Ar/NF_3/O_2$ = 90/5/5, 50 mTorr, 1,000 sccm, 300 W, 10 MHz.

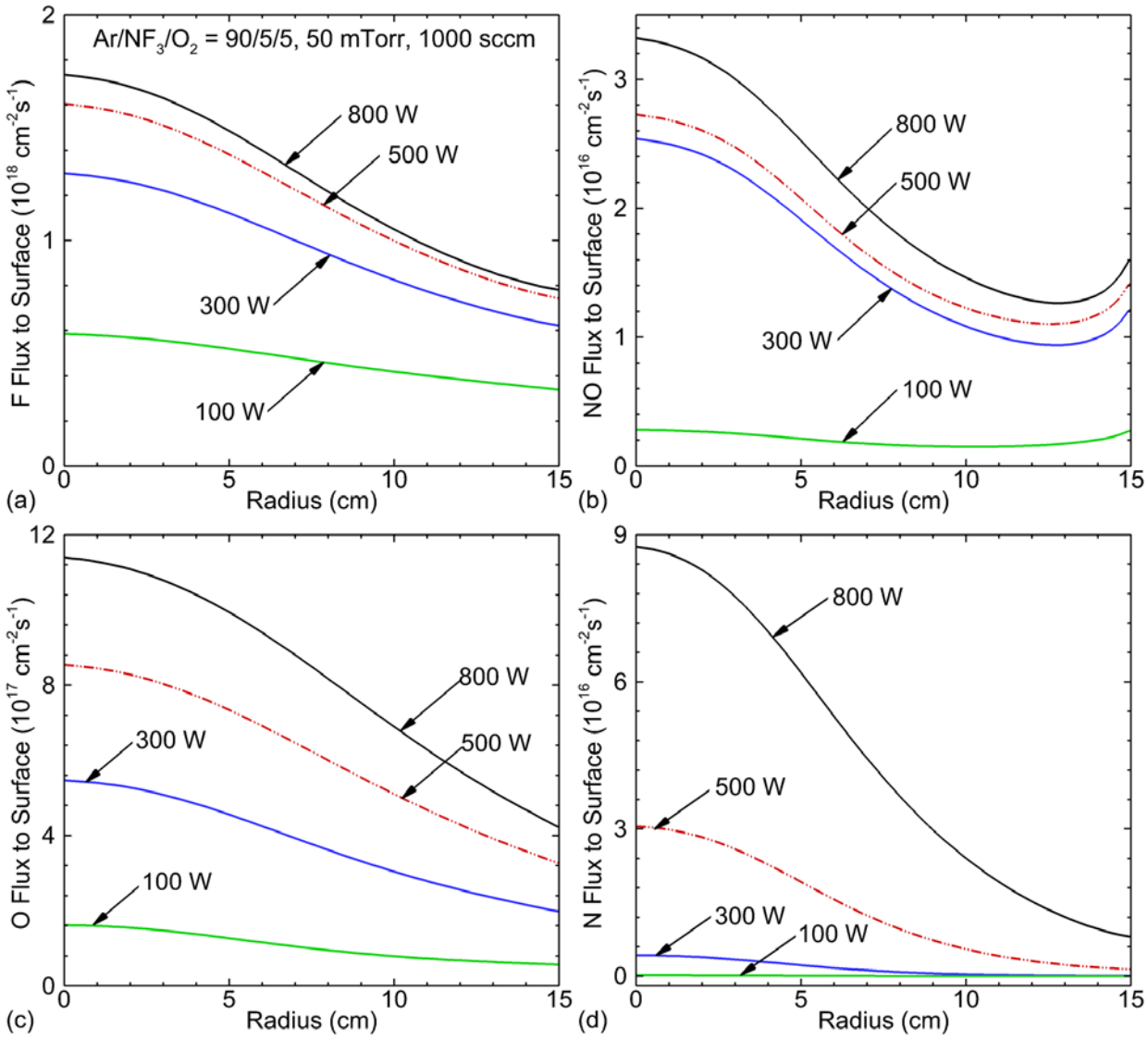

Fig. 5.6 Time averaged fluxes of a) F, b) NO, c) O and d) N to the surface of silicon nitride wafer in a downstream etch system with a RPS driven by inductively coupled power. Operating conditions: $Ar/NF_3/O_2$ = 90/5/5, 50 mTorr, 1,000 sccm, 10 MHz, 100 – 800 W.

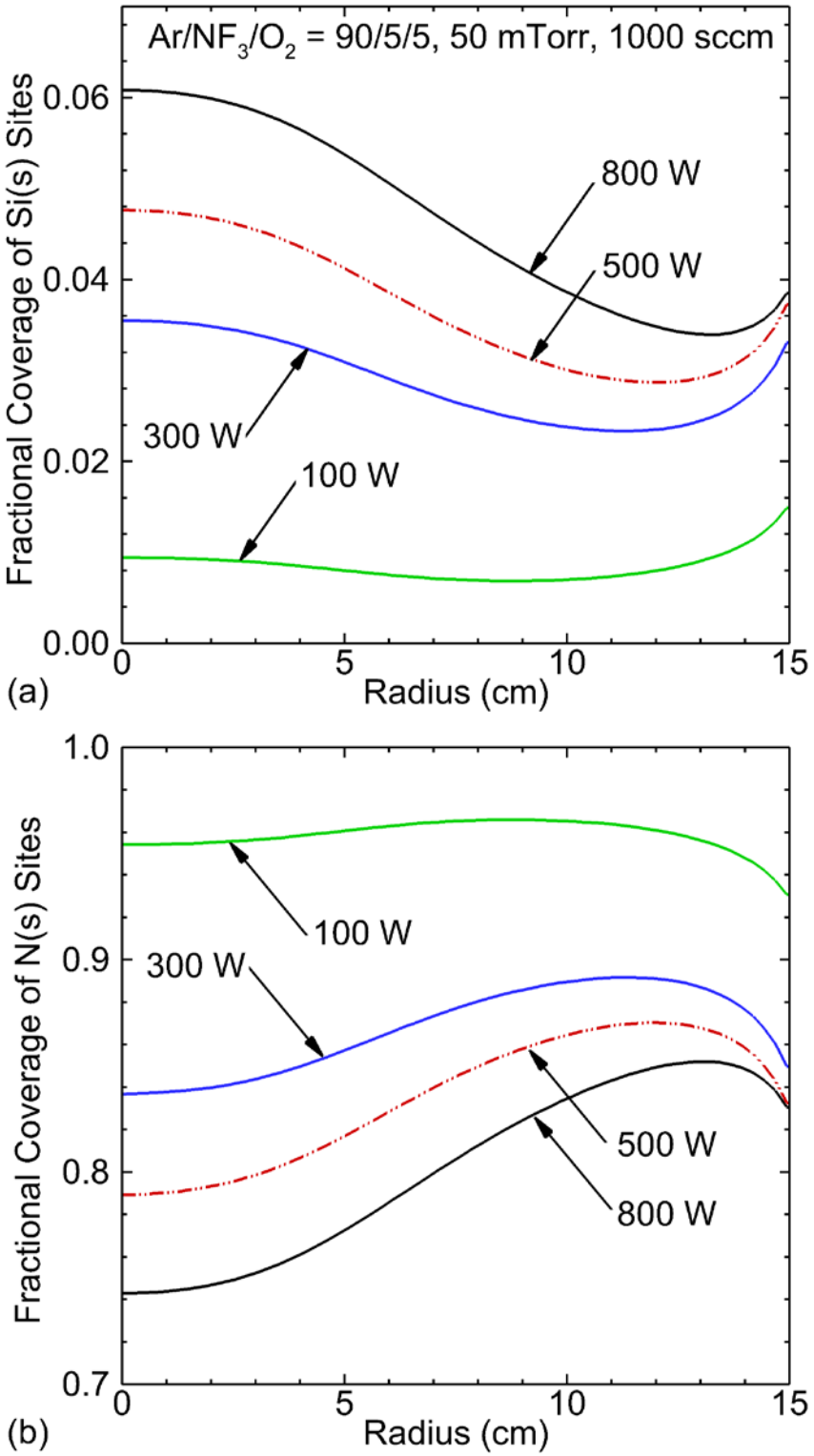

Fig. 5.7 Fractional coverage of a) Si and b) N subsites at the surface of silicon nitride wafer in a downstream etch system with a RPS driven by inductively coupled power. Operating conditions: $Ar/NF_3/O_2$ = 90/5/5, 50 mTorr, 1,000 sccm, 10 MHz, 100 – 800 W.

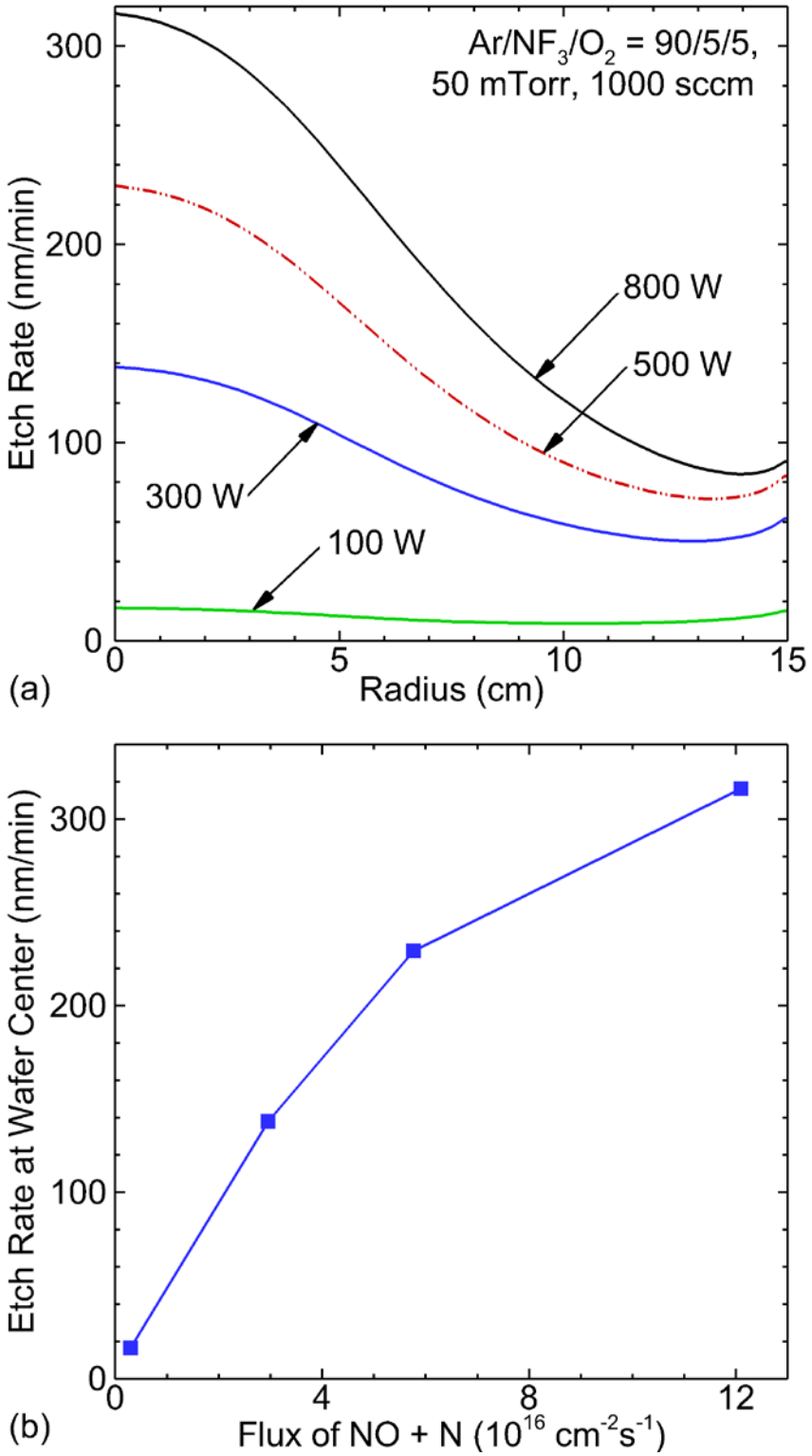

Fig. 5.8 Time averaged etch rates of silicon nitride (a) along the radius of the wafer at different ICP powers and (b) at the center of the wafer surface for different fluxes of NO and N radicals in a downstream etch system with a RPS driven by inductively coupled power. Operating conditions: $Ar/NF_3/O_2$ = 90/5/5, 50 mTorr, 1,000 sccm, 10 MHz, 100 – 800 W.

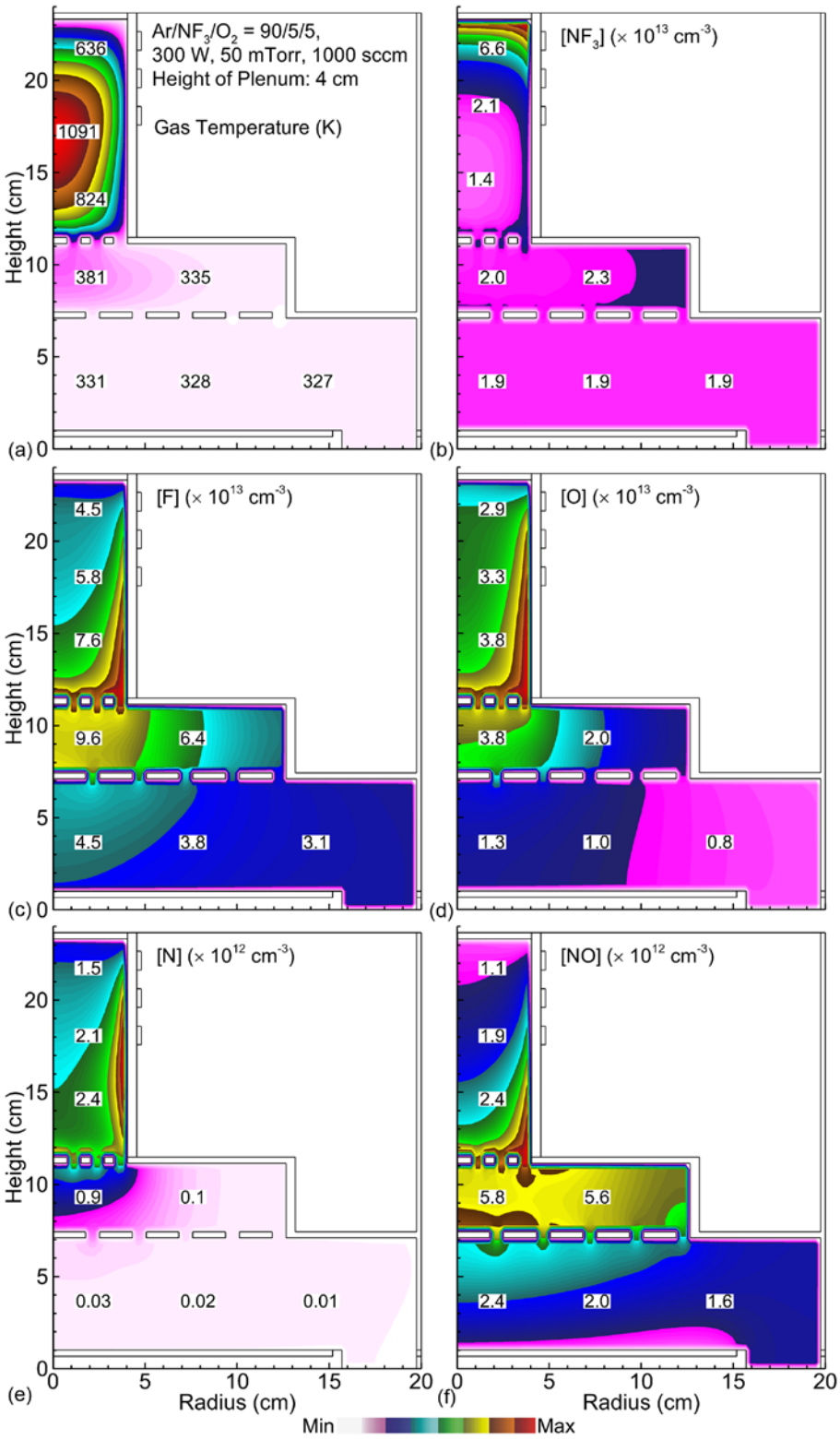

Fig. 5.9 Time averaged a) gas temperature and densities of b) NF_3, c) F, d) O, e) N and f) NO in a downstream etch system consisting of a RPS driven by inductively coupled power, a plenum with height of 4 cm and a downstream reactor. Operating conditions: $Ar/NF_3/O_2$ = 90/5/5, 50 mTorr, 1,000 sccm, 300 W, 10 MHz.

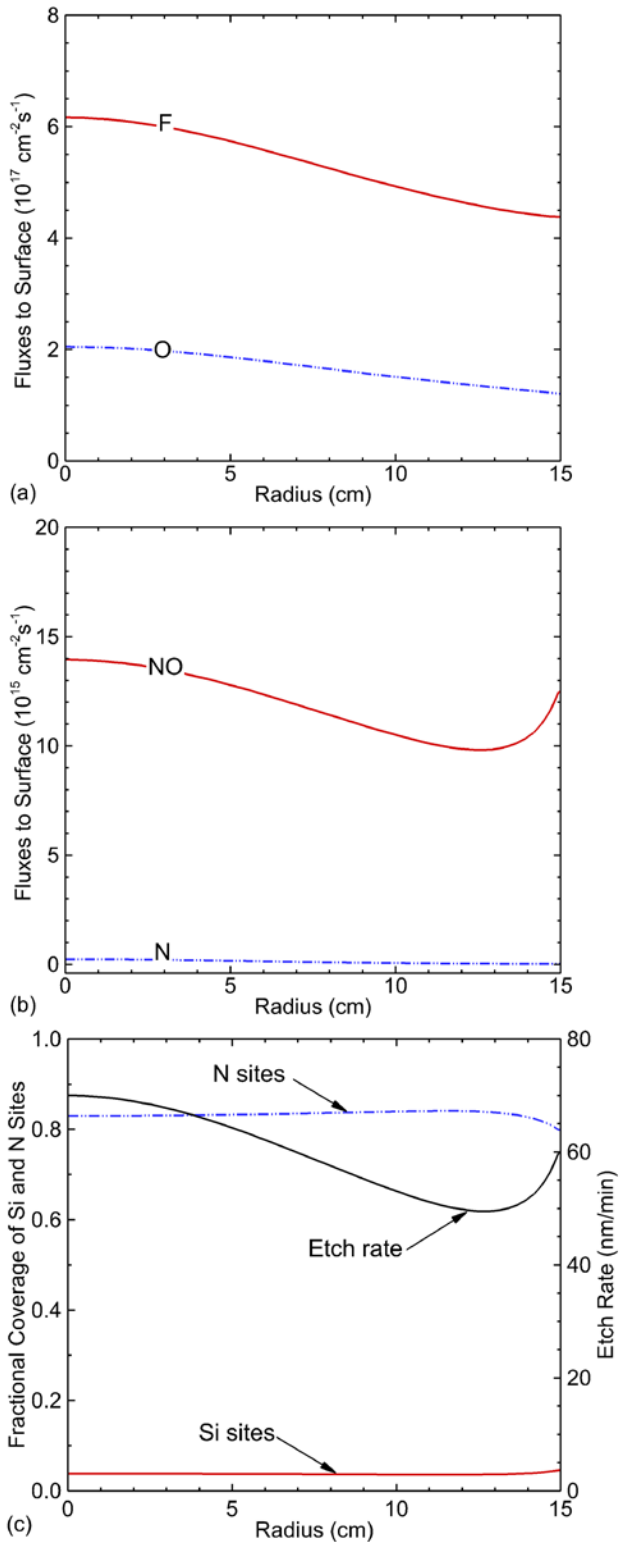

Fig. 5.10 Time averaged fluxes of a) F and O, b) NO and N, c) fractional coverage of Si and N subsites and etch rate of silicon nitride wafer in a downstream etch system consisting of a RPS driven by inductively coupled power, a plenum with height of 4 cm and a downstream reactor. Operating conditions: $Ar/NF_3/O_2$ = 90/5/5, 50 mTorr, 1,000 sccm, 300 W, 10 MHz.

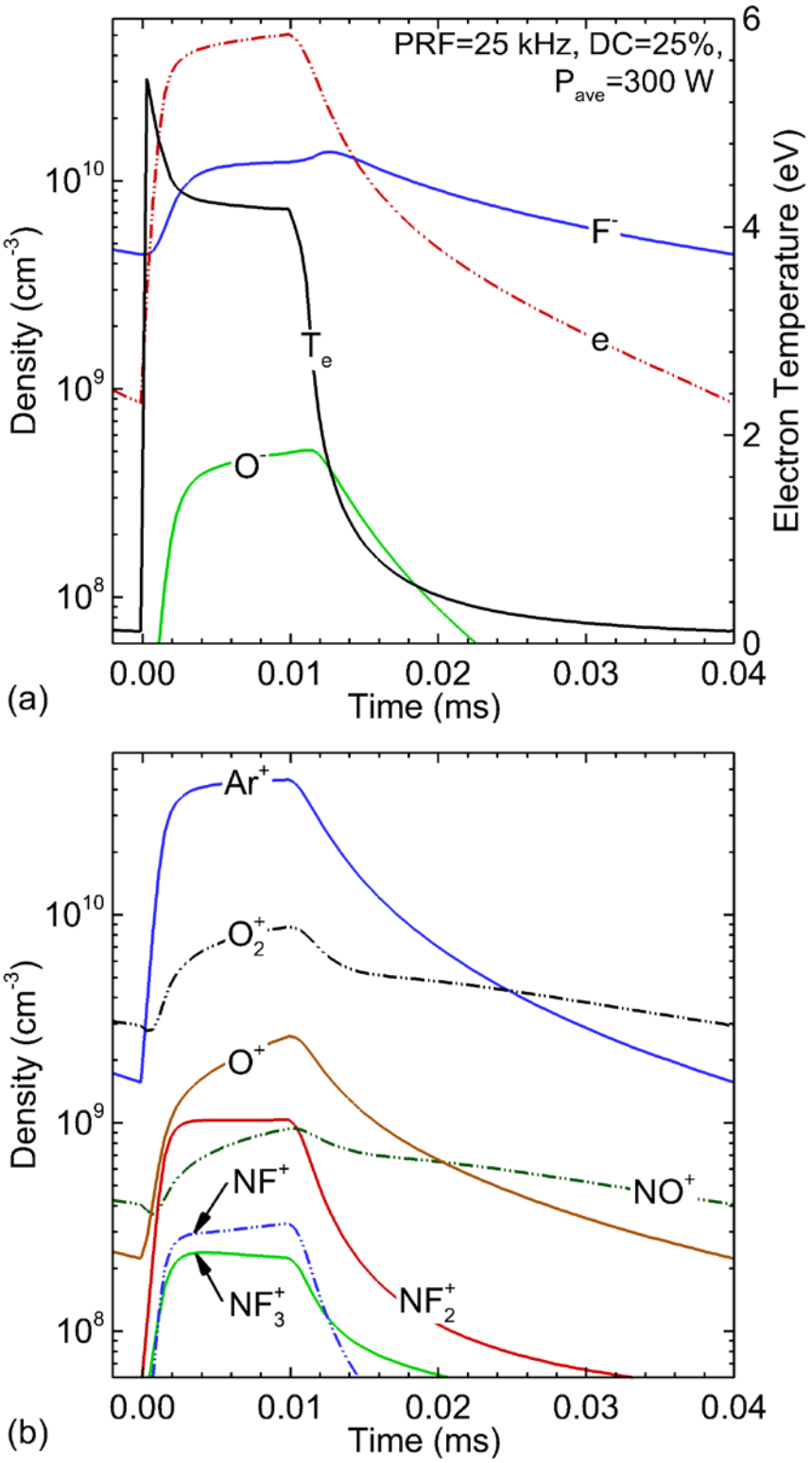

Fig. 5.11 Time variations for the volume averaged a) electron density, electron temperature and densities of negative ions, and b) densities of positive ions in a downstream etch system with a RPS driven by pulsed inductively coupled power. Operating conditions: $Ar/NF_3/O_2$ = 90/5/5, 50 mTorr, 1,000 sccm, PPA power: 300 W, PRF = 25 kHz, DC = 25%.

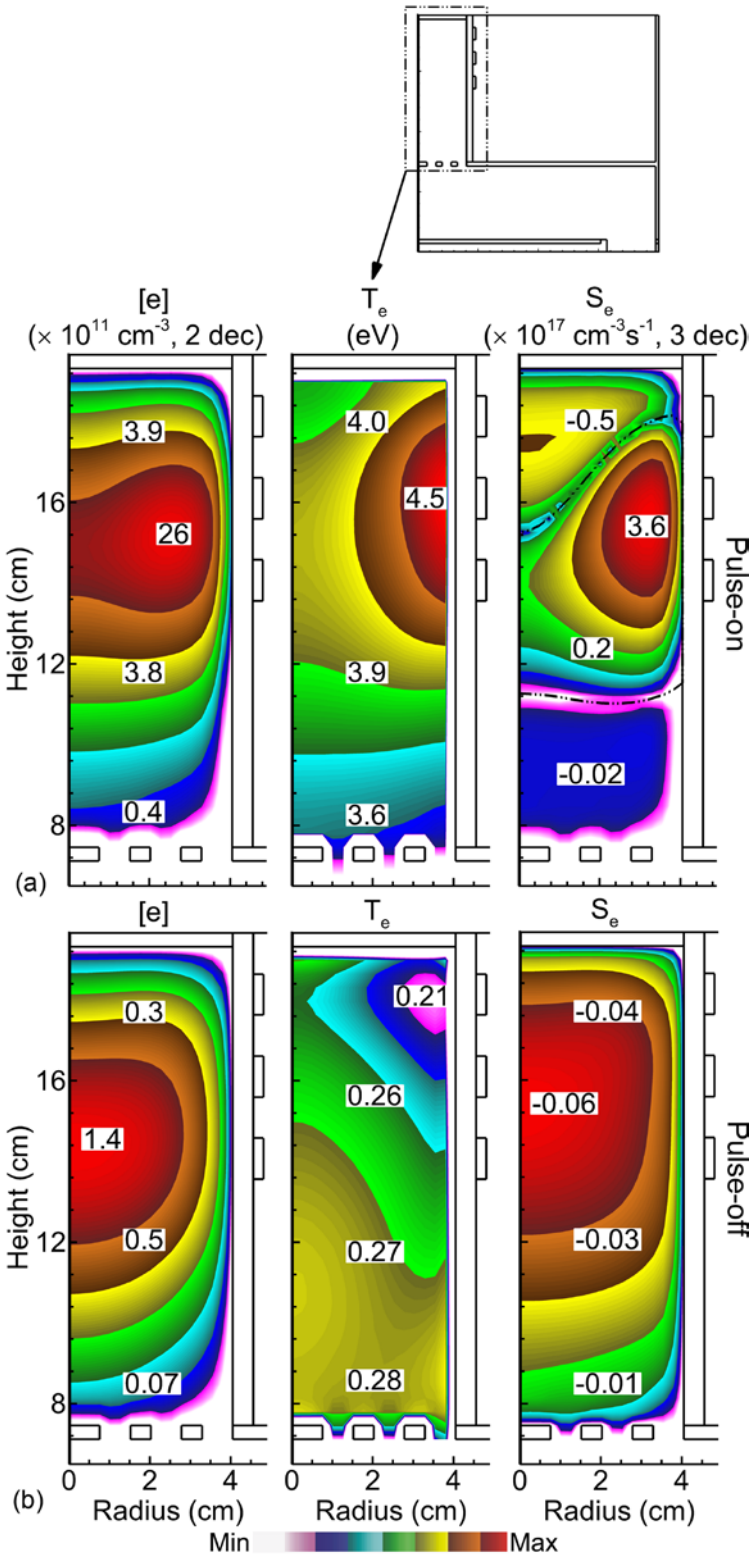

Fig. 5.12 Electron density, electron temperature and electron impact ionization source in the middle of a – c) pulse-on and d – f) pulse-off period in a RPS driven by pulsed inductively coupled power. Operating conditions: $Ar/NF_3/O_2$ = 90/5/5, 50 mTorr, 1,000 sccm, PPA power: 300 W, PRF = 25 kHz, DC = 25%.

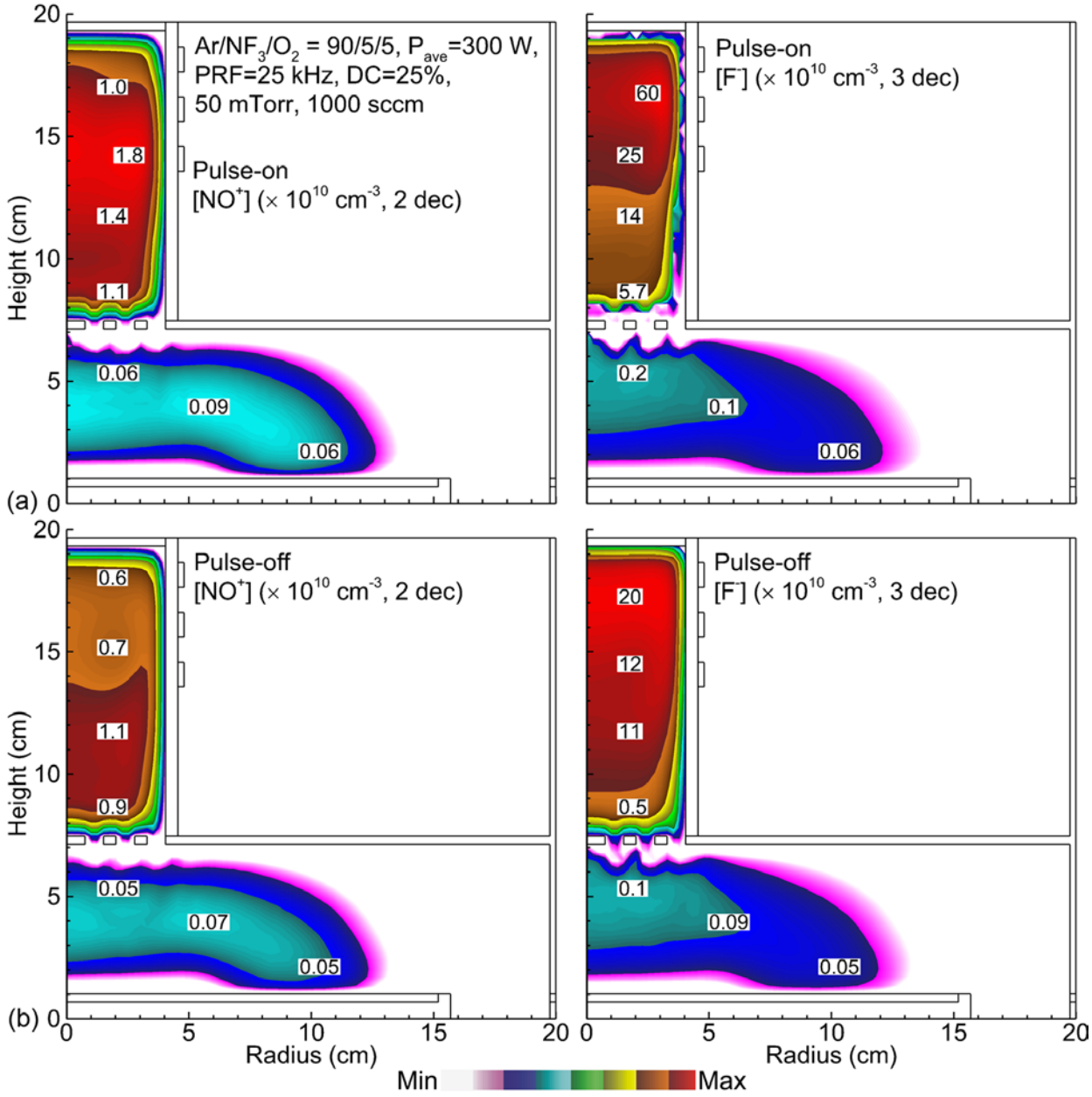

Fig. 5.13 Densities of NO^+ and F^- in the middle of a – b) pulse-on and c – d) pulse-off period in a downstream etch system with a RPS driven by pulsed inductively coupled power. Operating conditions: $Ar/NF_3/O_2$ = 90/5/5, 50 mTorr, 1,000 sccm, PPA power: 300 W, PRF = 25 kHz, DC = 25%.

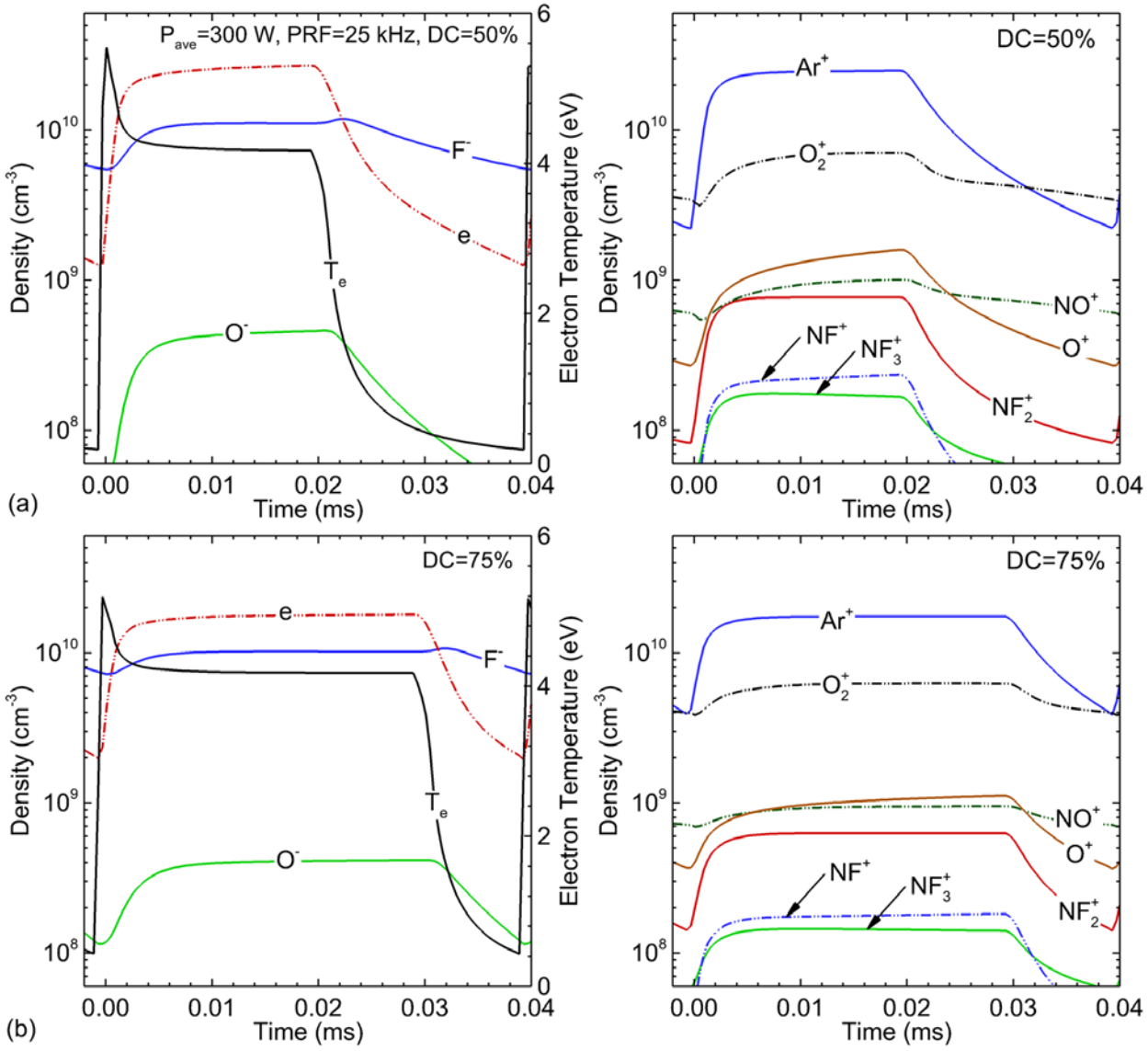

Fig. 5.14 Time variations for the volume averaged electron density, electron temperature and ion densities in a downstream etch system with a RPS driven by pulsed inductively coupled power with duty cycle of a – b) 50% and c – d) 75%. Operating conditions: $Ar/NF_3/O_2$ = 90/5/5, 50 mTorr, 1,000 sccm, PPA power: 300 W, PRF = 25 kHz, DC = 50%, 75%.

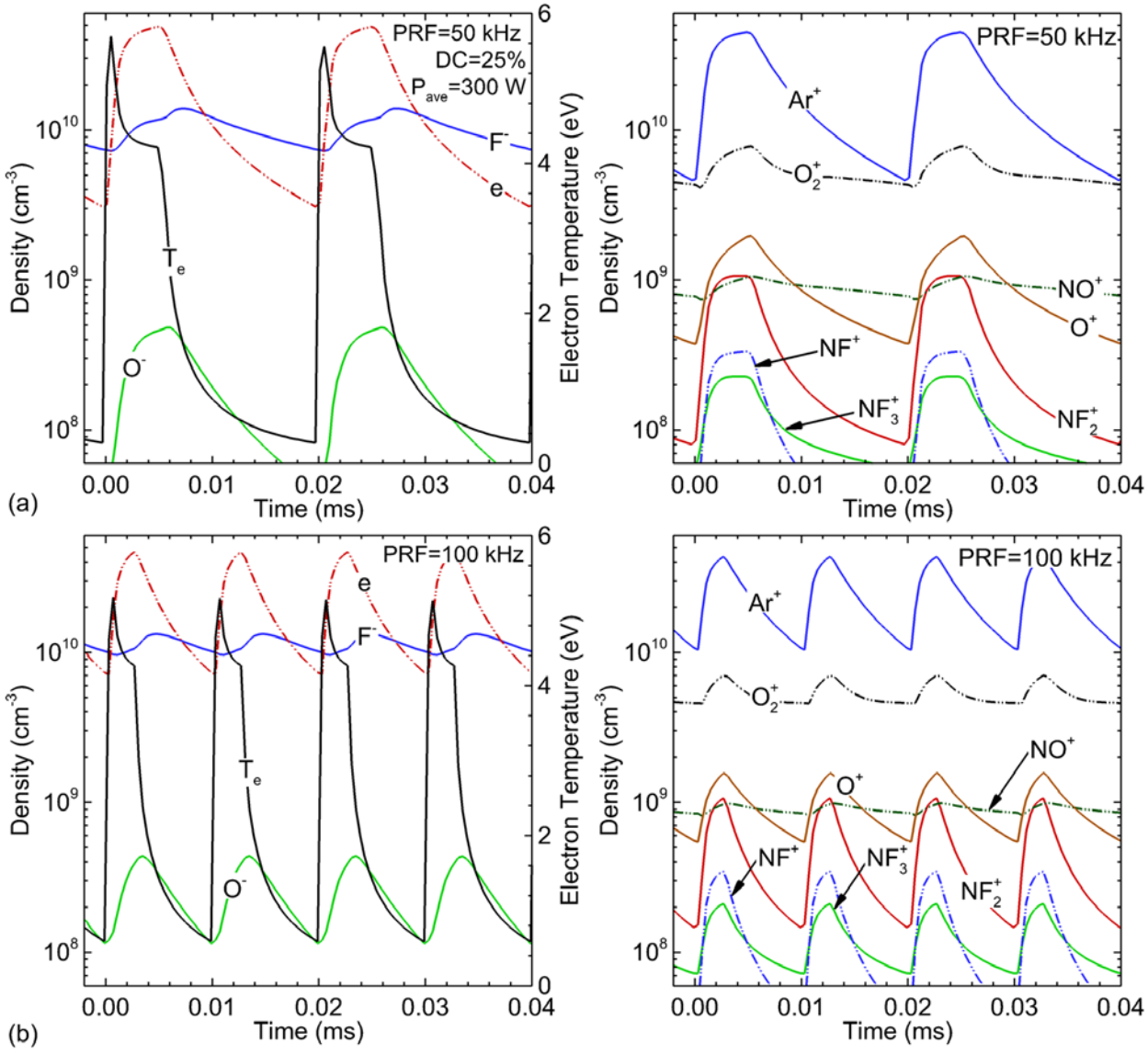

Fig. 5.15 Time variations for the volume averaged electron density, electron temperature and ion densities in a downstream etch system with a RPS driven by pulsed inductively coupled power with PRF of a – b) 50 kHz and c – d) 100 kHz. Operating conditions: $Ar/NF_3/O_2$ = 90/5/5, 50 mTorr, 1,000 sccm, PPA power: 300 W, PRF = 50, 100 kHz, DC = 25%.

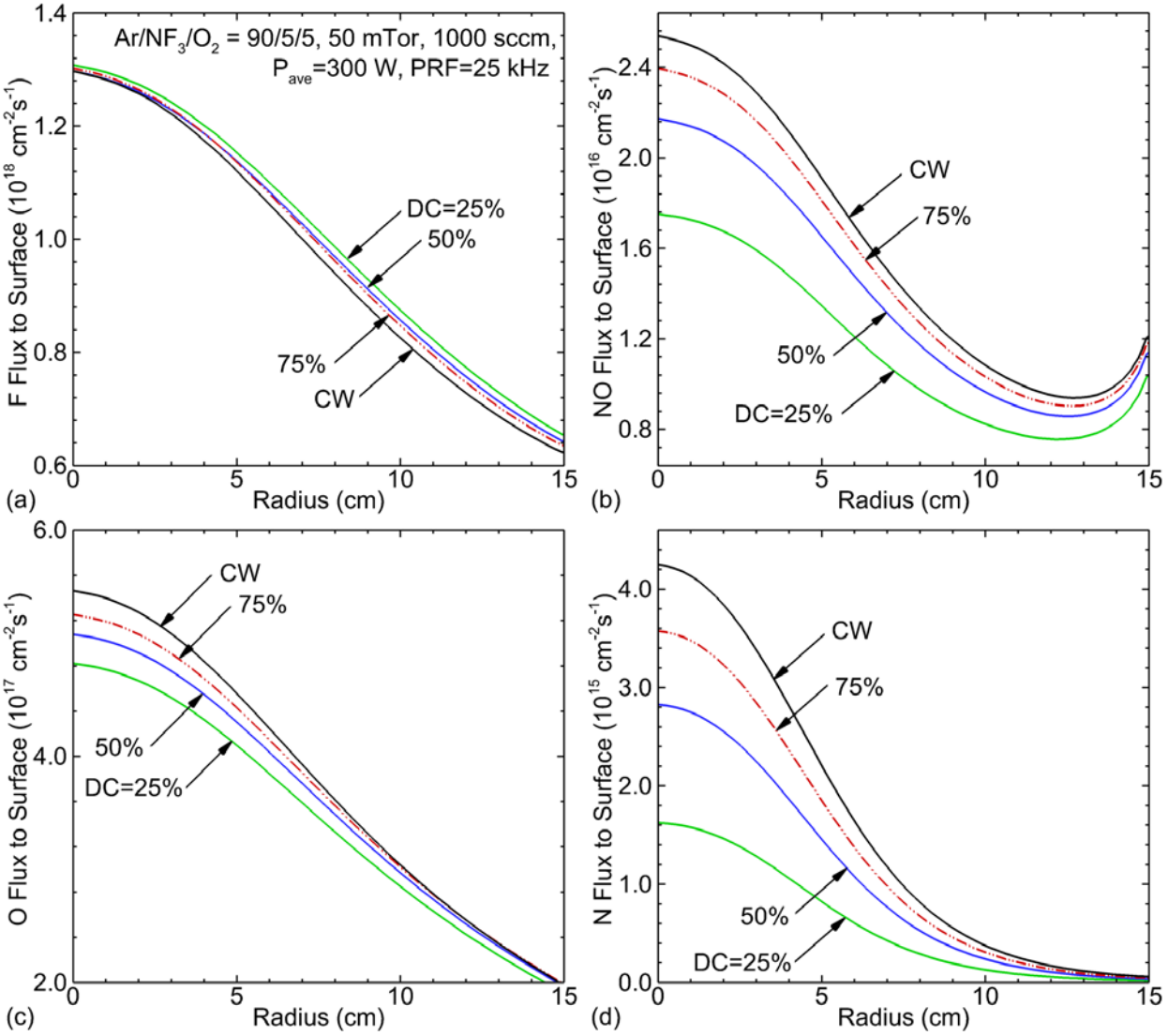

Fig. 5.16 Pulse averaged fluxes of a) F, b) NO, c) O and d) N to the surface of the silicon nitride wafer in a downstream etch system with a RPS driven by pulsed inductively coupled power. Operating conditions: $Ar/NF_3/O_2$ = 90/5/5, 50 mTorr, 1,000 sccm, PPA power: 300 W, PRF = 25 kHz, DC = 25% – 100%.

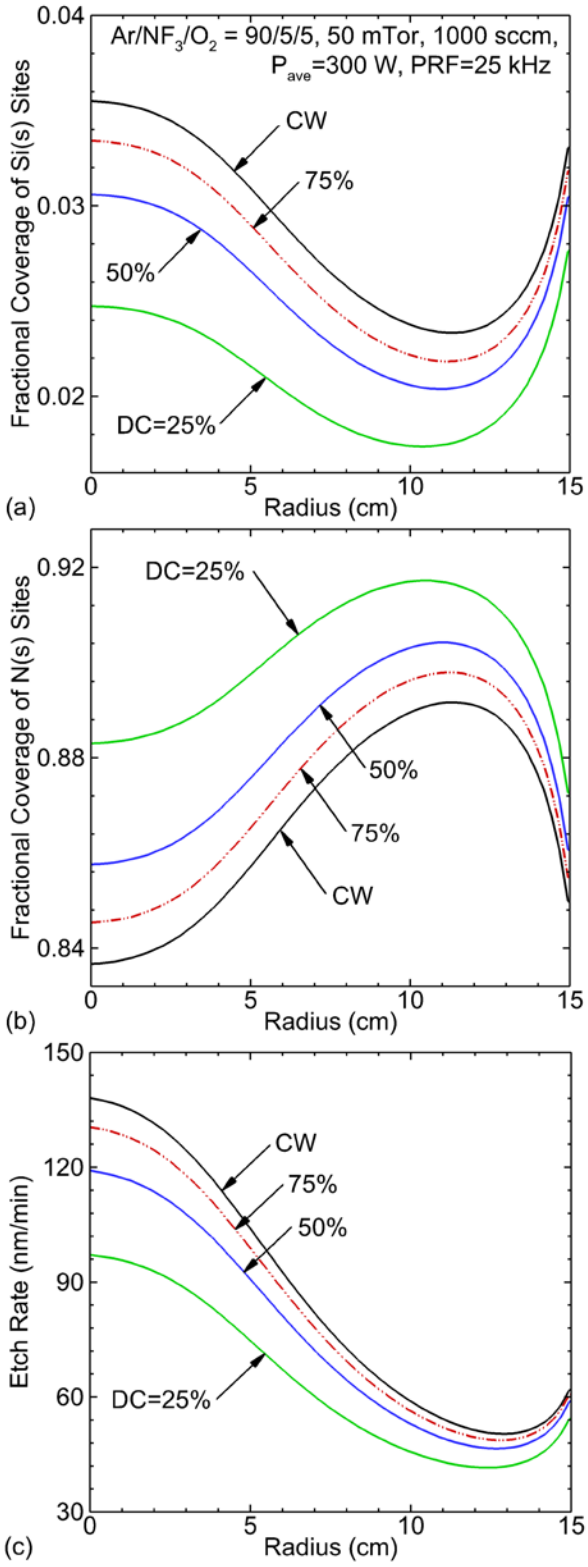

Fig. 5.17 Pulse averaged fractional coverage of a) Si and b) N subsites at the wafer surface and c) etch rates of silicon nitride in a downstream etch system with a RPS driven by pulsed inductively coupled power. Operating conditions: $Ar/NF_3/O_2$ = 90/5/5, 50 mTorr, 1,000 sccm, PPA power: 300 W, PRF = 25 kHz, DC = 25% – 100%.

5.7 References

1. B. E. E. Kastenmeier, P. J. Matsuo, G. S. Oehrlein and J. G. Langan, J. Vac. Sci. Technol. A **16**, 2047 (1998).
2. B. E. E. Kastenmeier, P. J. Matsuo, J. J. Beulens and G. S. Oehrlein, J. Vac. Sci. Technol. A **14**, 2802 (1996).
3. X. Liu, S. Gill, F. Tang, S. W. King and R. J. Nemanich, J. Vac. Sci. Technol. B **30**, 031212 (2012).
4. S. C. Heo, D. Lim, W. S. Jung, R. Choi, H.-Y. Yu and C. Choi, Microelectron. Eng. **147**, 239 (2015).
5. H. Tanaka, M. Kido, K. Yahashi, M. Oomura, R. Katsumata, M. Kito, Y. Fukuzumi, M. Sato, Y. Nagata, Y. Matsuoka, Y. Iwata, H. Aochi and A. Nitayama, IEEE Symposium on VLSI Technology 14, 2007.
6. J. Jang, H.-S. Kim, W. Cho, H. Cho, J. Kim, S. I. Shim, Y. Jang, J.-H. Jeong, B.-K. Son, D. W. Kim, K. Kim, J.-J. Shim, J. S. Lim, K.-H. Kim, S. Y. Yi, J.-Y. Lim, D. Chung, H.-C. Moon, S. Hwang, J.-W. Lee, Y.-H. Son, U.-I. Chung and W.-S. Lee, IEEE Symposium on VLSI Technology 192, 2009.
7. M. G. Blain, T. L. Meisenheimer and J. E. Stevens, J. Vac. Sci. Technol. A **14**, 2151 (1996).
8. T. Hayashi, K. Ishikawa, M. Sekine, M. Hori, A. Kono and K. Suu, Jpn. J. Appl. Phys. **51**, 016201 (2012).
9. J. Kikuchi, M. Iga, H. Ogawa, S. Fujimura and H. Yano, Jpn. J. Appl. Phys. **33**, 2207 (1994).
10. J. Lee, S. J. Lee, W. B. Han, H. Jeon, J. Park, W. Jang, C. S. Yoon and H. Jeon, Phys. Status Solidi A 210, 276 (2013).
11. H. Zhu, X. Qin, L. Cheng, A. Azcatl, J. Kim and R. M. Wallace, ACS Appl. Mater. Interfaces **8**, 19119 (2016).
12. E. Meeks, R. S. Larson, S. R. Vosen and J. W. Shon, J. Electrochem. Soc. **144**, 357 (1997).
13. S. R. Vosen, E. Meeks, R. S. Larson and J. W. Shon, J. Electrochem. Soc. **144**, 1514 (1997).
14. Y. Barsukov, V. Volynets, S. Lee, G. Kim, B. Lee, S. K. Nam and K. Han, J. Vac. Sci. Technol. A **35**, 061310 (2017).
15. N. Ruckhaberle, L. Lehmann, S. Matejcik, E. Illenberger, Y. Bouteiller, V. Periquet, L. Museur, C. Desfrançois and J.-P. Schermann, J. Phys. Chem. A **101**, 9942 (1997).
16. M. Bettendroff and S. D. Peyerimhoff, Chem. Phys. **99**, 55 (1985).

17. B. E. E. Kastenmeier, P. J. Matsuo, G. S. Oehrlein, R. E. Ellefson and L. C. Frees, J. Vac. Sci. Technol. A **19**, 25 (2001).
18. S.-H. Song and M. J. Kushner, Plasma Sources Sci. Technol. **21**, 055028 (2012).
19. S. Banna, A. Agarwal, K. Tokashiki, H. Cho, S. Rauf, V. Todorow, K. Ramaswamy, K. Collins, P. Stout, J.-Y. Lee, J. Yoon, K. Shin, S.-J. Choi, H.-S. Cho, H.-J. Kim, C. Lee and D. Lymberopoulos, IEEE Trans. Plasma Sci. **37**, 1730 (2009).

Chapter 6 Anisotropic Etching of High Aspect Ratio Features in SiO_2[*]

6.1 Introduction

Plasma etching of high aspect ratio (HAR) features in SiO_2 and Si_3N_4 with aspect ratios (ARs) exceeding 100 is being challenged to maintain critical dimensions (CDs) and achieve high selectivity while etching stacks of materials for high capacity 3-dimensional memory.[1-3] Controlling and mitigating phenomena such as aspect ratio dependent etching (ARDE), bowing and contact edge roughness (CER) are necessary to obtain anisotropic features and better critical dimension uniformity (CDU). ARDE refers to a decrease in etch rate for features having larger ARs for otherwise identical conditions. ARDE can occur for simultaneously etched features whose initial CDs (e.g., mask opening) have different sizes, or within a single feature as the AR increases during etching. ARDE is a result of transport phenomena that depend on AR and can be minimized through controlling the mass transfer rate to the etch front by tuning the bias power, gas pressure or substrate temperature.[4,5] Bowing refers to deviation of features from purely anisotropic profile with straight walls to having outward curvature. Bowing primarily results from the change in the acceptance angle of incident ions into the feature due to erosion of mask material and subsequent reflection from the facets of resist, diffusive particle scattering within the feature or scattering from rough surfaces.[2,6]

Maintaining CDU requires minimizing pattern distortion, in which an initially circular

[*] The results discussed and portion of the text appearing in this chapter were previously published in the paper by Shuo Huang *et al*., "Plasma etching of high aspect ratio features in SiO_2 using $Ar/C_4F_8/O_2$ mixtures: a computational investigation", J. Vac. Sci. Technol. A **37**, 031304 (2019).

mask opening is not preserved through the depth of the feature, evolving into ellipses or other non-circular shapes.[7-9] CER originates from non-uniformities in the mask due to stochastic processes during etching or from the lithography-development process. These non-uniformities are then are imprinted into the sidewalls of the feature by anisotropic delivery of activation energy.[9,10] Maintaining CDU also requires minimizing twisting, where the etch does not proceed strictly normal to the surface but deviates from the normal; and avoiding feature-to-feature variations in total etch depth.[6,11] Many of these CDU problems can be attributed to the stochastic nature of fluxes of radicals and ions incident into adjacent features. With the CDs of features now less than 10 nm and the mask opening having a commensurately smaller area, the number and variety of particles incident into adjacent features are subject to statistical noise. The result is that adjacent features may receive different fluxes and sequencing of individual species. These statistical sources of CDU are not the result of reactor scale non-uniformities and may be addressed by employing self-limiting processes, such as atomic layer etching (ALE) [12], or increasing the magnitude of fluxes in inverse proportion to the decrease in mask opening.

In addition to the challenges resulting from high aspect ratio and nanoscale feature size, the etching of HAR features in SiO_2 typically uses a complex reaction mechanism with multiple steps based on the use of fluorocarbon gas mixtures. For example, increasing bias power produces a higher SiO_2 etch rate in HAR vias due to higher ion energies delivered through sheath acceleration while deforming the vias by bowing and edge roughening.[13,14] Energy-controlled and mass-selected CF_2^+ and CF_3^+ ion beams were used with the goal of controlling the surface atomic composition and so control the removal rate of SiO_2.[15,16] Increasing the ion beam energy from 100 to 400 eV increased the F/O ratio of the surface layers due to enhanced surface fluorination and produced a higher etch yield of SiO_2. Extremely high ion energies

(several keV) damaged the SiO_2 and the underlying Si according to both experiments and numerical simulations. These effects can be mitigated by carefully controlling the overlying polymer thickness through the gas flow rate and the over-etch time.[17,18]

While being an etchant and providing activation energy, ions are also typically neutralized when striking surfaces on the top and inside of the feature. In doing so, positive charge is deposited on the surfaces.[19] Electrons also deposit charge, though due to their nearly isotropic trajectories incident onto the surface compared to ions, electron charging dominantly occurs on the top and upper portion of the features. Positive ions striking sidewalls at grazing angles neutralize and specularly reflect, and then proceed as hot neutrals retaining a large fraction of their initial energy. The electrical potential and electric fields produced by charge deposited on sidewalls and the etch front can deviate the trajectories of subsequent ions while reducing their energy, resulting in twisting and an etch stop. Pulsed power excitation can address many of the detriments of charging by elevating the ion energy [20], reducing the thickness of fluorocarbon films on sidewalls [21] and enabling injection of negative ions to neutralize positive charge inside the feature [22,23], with the tradeoff of increasing power matching challenges, ignition delay and long transients.

Optimizing plasma etching of HAR features requires precise control of both the fluxes of ions and neutrals. In fluorocarbon plasmas, fluxes of CF_x neutrals are produced by electron impact dissociation followed by diffusion to the wafer. In the absence of charge exchange collisions in the sheath that may produce anisotropic neutral fluxes, these fluxes typically arrive at the substrate with isotropic trajectories. Increasing C_4F_8 flow rate or decreasing O_2 flow rate in $Ar/C_4F_8/O_2$ mixtures increased SiO_2 etch rates due to deposition of thicker fluorocarbon films produced by larger CF_x fluxes to the surface.[24] Adding CH_4 or H_2 to C_2F_6 gas mixtures

resulted in decreased SiO_2 etch rates and increased SiO_2/Si selectivity by scavenging atomic fluorine in forming HF molecules, thereby decreasing the F/C flux ratio to the wafer.[25]

Etching of HAR features faces challenges in the delivery of thermal neutral radicals to the etch front whose incident velocities are isotropic and in the transport of etch products out of the feature. Due to the limits of vacuum conductance, the probability of neutral radicals entering into the feature reaching and reacting on the etch front at the bottom of the feature decreases with increasing AR.[26] This decreasing probability results from diffusive reflection from sidewalls during which some fraction of the incident flux is reflected back out of the feature to the plasma. The probability of reacting at the etch front further decreases if the radicals have a non-zero probability for reacting on sidewalls.[26] The same trends apply to thermal etch products produced at the bottom of the feature. The larger the AR, the larger the number of collisions etch products will have with the surface inside the feature prior to exiting the top of the feature. These large number of collision may result in redeposition of the etch products. Conductance limits result in decreased neutral etchant delivery from the top to the bottom of the feature, and redeposition of etch products in transport from the bottom to the top of the feature, both of which can produce lower etch rates. These effects can be partially mitigated by regulating the sticking coefficient of radicals to the sidewall through controlling the wafer temperature.[27-29]

Conductance limitations of neutral transport into HAR features largely result from the radicals having initially isotropic trajectories and diffusive isotropic scattering from sidewalls. Hot neutrals produced through neutralization of energetic ions at surfaces have higher conductance to the etch front than the thermal neutrals due to their initially more anisotropic angular distributions and more specular scattering. These hot neutrals deliver both energy to the etch front and upon slowing deeper in the feature, deliver neutral reactivity which enables

etching to proceed at high ARs. A molecular dynamics (MD) simulation was used to investigate the consequences of hot CF_2 and CF_3 radicals in SiO_2 etching.[19,30] At low energies (10 eV), CF_2 was the main etchant to break the Si-O bond due to its higher chemical reactivity. At high energies (150 eV), CF_3 became the main etchant due to production of more reactive F atoms resulting in forming more Si-F bonds. The etch yield was found to depend on the incident angle of hot radicals to the surface. An irradiation angle of 60^o resulted in the maximum yield of Si and O from the SiO_2 surface.[31]

Computational models for SiO_2 etching have been developed to investigate feature profiles in the etching of gate dielectrics (AR < 10) and conduction channel holes through insulating layers (AR > 50). An integrated reactor and feature scale model was used to investigate the etching of topographic layered and self-aligned Si_3N_4/SiO_2 structures using fluorocarbon plasmas.[32] The Si_3N_4/SiO_2 selectivity was optimized by controlling the thickness of the polymer at the top of the feature by tuning the time during etching and deposition phases in a cyclic plasma etch process. A semi-empirical profile simulator was employed to investigate the necking and bowing of etching of HAR features.[33] The necking resulted from a balance between polymer removal and deposition processes while the bowing was caused by surface scattering of ions from secondary facets. Non-uniform necking was found to cause an imbalance in the ion flux to the bottom of the feature, resulting in twisting irrespective of charging.[6]

Results from a voxel-slab model, developed to investigate contact hole etching in SiO_2, indicated that physical damage was reduced by maintaining a critical thickness of the overlaying polymer.[17,34] Bowing during the etching of HAR features was found to result from excessive fluxes of F and O radicals to the sidewalls according to the results of a line-of-sight profile simulator.[35] A model addressing pattern deformation and experimental measurements by

atomic force microscopy, indicated the ratio of line width roughness to line edge roughness decreases with increasing etch depth, and the depth at which twisting occurs is shallower for lower bias power.[1]

In this chapter, results are discussed from integrated reactor and feature scale models for investigating the etching of HAR features in SiO_2 using a tri-frequency capacitively coupled plasma (TF-CCP) sustained in $Ar/C_4F_8/O_2$ mixtures at several tens of mTorr. Reactor scale modeling was performed using the 2-dimensional Hybrid Plasma Equipment Model (HPEM), from which the fluxes, energy and angular distributions of ions and neutrals to the wafer surface were obtained. The feature scale modeling was performed using the 3-dimensional Monte Carlo Feature Profile Model (MCFPM). We found that at low ARs where neutral transport is not conductance limited, abundant fluxes of CF_x and C_xF_y radicals to the etch front passivate the oxide to form a complex. This complex is then removed by ions and hot neutrals through chemically enhanced reactive etching (i.e., chemical sputtering) with the formation of gas phase SiF_x, CO_x and COF etch products. As the etching proceeds to higher ARs, the fractional contribution of physical sputtering increases, as the fluxes of ions and hot neutrals to the etch front surpass that of the conduction constrained CF_x and C_xF_y radicals. The general trend of ARDE, decreased instantaneous etch rate with increasing AR, mainly occurs due to decreased power delivery to the etch front while the flux of conduction limited neutrals also decreases.

The models used in this chapter are briefly described in Sec. 6.2. Results from the reactor scale modeling of TF-CCP sustained in $Ar/C_4F_8/O_2$ mixtures are discussed in Sec. 6.3. Results from feature scale modeling of HAR etching of SiO_2 are discussed in Sec. 6.4. Concluding remarks are in Sec. 6.5.

6.2 Description of the Models

Reactor scale modeling of the TF-CCP sustained in $Ar/C_4F_8/O_2$ mixtures was performed with the 2-dimensional HPEM, described in detail in Sec 2.2. The HPEM combines fluid and kinetic methods, using a hierarchical approach where modules addressing different physical processes exchange information on different time scales. The major modules used in this study are the Fluid Kinetics Poisson Module (FKPM), the Electron Energy Transport Module (EETM) and the Plasma Chemistry Monte Carlo Module (PCMCM). The gas mixtures used here were $Ar/C_4F_8/O_2$ mixtures. A detailed description of the $Ar/C_4F_8/O_2$ gas phase reaction mechanism is in Refs. [36,37]. The species included are Ar, $Ar(1s_5)$, $Ar(1s_4)$, $Ar(1s_3)$, $Ar(1s_2)$, Ar(4p), Ar(4d), Ar^+, C_4F_8, C_4F_7, C_3F_7, C_3F_6, C_3F_5, C_2F_6, C_2F_5, C_2F_4, C_2F_3, CF_4, CF_3, CF_2, CF, C, $C_4F_8^+$, $C_4F_7^+$, $C_3F_7^+$, $C_3F_6^+$, $C_3F_5^+$, $C_2F_5^+$, $C_2F_4^+$, $C_2F_3^+$, CF_3^+, CF_2^+, CF^+, CF_3^-, F_2, F, $F(^3S)$, F_2^+, F^+, F^-, O_2, $O_2(a\ ^1\Delta_g)$, O, $O(^1D)$, O_2^+, O^+, O^-, CO_2, CO, FO, COF, SiF_4, SiF_3, SiF_2, SiF and electrons.

The time evolution of profiles etched in SiO_2 using fluxes, energy and angular distributions of ions and neutrals provided by the HPEM are predicted by the MCFPM, described in detail in Sec. 2.3. The dependence of the physical sputtering and chemical etching on energy and angle of incident ions and hot neutrals are determined by empirical functions and fitting curves from experimental measurements, described in Sec. 2.3.1. The algorithms and mechanisms updated to address the effect of charging are described in Sec. 2.3.2. The developed surface reaction mechanism for the etching of SiO_2 using $Ar/C_4F_8/O_2$ mixtures is described in Sec. 3.3.2 and listed in Appendix E.

6.3 Tri-frequency Capacitively Coupled Plasma

A tri-frequency capacitively coupled plasma (TF-CCP) reactor was used as model system

for simulations of etching of high aspect ratio (HAR) features in SiO_2. TF-CCPs are being developed for HAR etching due to the large dynamic range available for ion energy and angular distributions (IEADs) for process optimization. A schematic of the TF-CCP reactor used in this study is shown in Fig. 6.1, a design resembling TF-CCPs in use in industry. In this reactor, a 300 mm wafer is placed on the bottom electrode, confined by a Si focus ring. Power at 80 MHz is applied to the top electrode above the Si showerhead while 10 MHz and 5 MHz powers are applied to the bottom electrode through a blocking capacitor, with all the metal sidewalls being grounded. The gap between the top and bottom electrodes is 3 cm. The materials in contact with the plasma have fixed temperatures of 333 K except for the wafer and the focus ring which were cooled to 293 K. The secondary electron emission coefficient for ions was 0.15 on the wafer and focus ring, 0.05 on quartz and 0.005 on the alumina covering the sidewalls. In the base case, the powers of the 80 MHz, 10 MHz and 5 MHz sources were 400 W, 2,500 W and 5,000 W, respectively. During the execution of HPEM, the voltage of each frequency is dynamically adjusted to provide the specified power. In the base case, the voltages for to deliver the specified powers were 80/10/5 MHz = 125/1,030/2,450 V, with a dc bias of -1,690 V.

Fluorocarbon gas mixtures are usually used in SiO_2 etching to produce CF_x radicals which are the primary etchants. In this study, the gas mixture was $Ar/C_4F_8/O_2$ = 75/15/10, injected through the showerhead with a total flow rate of 500 sccm (standard cubic centimeters per minute). The gas pressure at the sensor near the foreline was kept at 25 mTorr by adjusting the flow rate leaving through the pump.

The time averaged electron density, ionization source by bulk electrons, S_b, ionization source by secondary electrons, S_s, and electron temperature, T_e, for the base case are shown in Fig. 6.2. The electron density has an edge-high profile and peaks at 3.8×10^{10} cm^{-3} at the outer

radius of the wafer due to electric field enhancement at the triple point composed of the wafer, focus ring and plasma. (No attempt was made to optimize the uniformity of the plasma or fluxes to the wafer in this system.) The ionization by bulk electrons is the dominant source of electrons, which also peaks at the edge of the wafer at 5.3×10^{15} $cm^{-3}s^{-1}$. The contribution of ionization by secondary electrons is about 1/5 of the bulk electrons. However, the ionization source by secondary electrons is quite uniform at the wafer surface with a rate of 1.2×10^{15} $cm^{-3}s^{-1}$ due to the ion bombardment of the surface, which improves the uniformity of the plasma density in the radial direction. The electron temperature in the bulk plasma is 4 eV, which is a typical value for electronegative plasmas to provide ionization sources to balance attachment. The time averaged thickness of the sheath at the wafer surface is about 0.8 cm due to the high bias voltage. This thick sheath is mildly collisional. (The thickness of the sheath is determined by the distance between the electrode surface and the position where the densities of electrons and ions begin to deviate.)

Fluxes of radicals and ions to the wafer surface for the base case are shown in Fig. 6.3. The feedstock C_4F_8 gas is dissociated dominantly by electron impact reactions to produce fluorocarbon radicals and ions resulting in a fractional dissociation of about 24%. The dominant electron impact dissociation product is C_2F_4, which is produced by,

$$e + C_4F_8 \rightarrow C_2F_4 + C_2F_4 + e, \quad (6.1a)$$

$$e + C_4F_8 \rightarrow C_2F_4^+ + C_2F_4 + e + e. \quad (6.1b)$$

Although C_2F_4 is not particularly reactive in oxide etching, further dissociation of C_2F_4 produces CF_x radicals and ions,

$$e + C_2F_4 \rightarrow CF_2 + CF_2 + e, \quad (6.2a)$$

$$e + C_2F_4 \rightarrow CF^+ + CF_3 + e + e. \quad (6.2b)$$

CF_2 and CF_3 are the dominant reactive fluorocarbon species incident onto the wafer with average fluxes of 1.4×10^{17} and 0.9×10^{17} $cm^{-2}s^{-1}$, respectively. O and F atoms are mainly produced through electron impact dissociation of O_2 and CF_x species, and diffuse to the wafer with average fluxes of 1.2×10^{17} and 0.8×10^{17} $cm^{-2}s^{-1}$, respectively.

Fluxes of ions to the wafer surface are lower than those for radicals by 1 – 2 orders of magnitudes due to the higher activation energy required for ionization than dissociation. Ar^+ has the highest flux to the wafer of 3.9×10^{15} $cm^{-2}s^{-1}$ due to the large mole fraction (75%) of the parent Ar. There is also a significant flux of $C_2F_4^+$ (2.0×10^{15} $cm^{-2}s^{-1}$) due to the large dissociation fraction of C_4F_8 producing a large volume averaged density of C_2F_4 (3.2×10^{13} cm^{-3}). The densities of $C_2F_4^+$ and $C_3F_5^+$ are larger than the densities of CF^+, CF_2^+ and CF_3^+ by one order of magnitude. In high plasma density sources, such as inductively coupled plasmas (ICPs), the majority of power is coupled into the electrons producing electron densities that are typically 10-100 times higher than in CCP while the gas pressures are lower. This results in higher fractional dissociation of feedstock gases and the dominant radicals and ions being CF_x and CF_x^+. In CCPs of the type discussed here, the majority of the power is dissipated in the sheath as ion acceleration with only about 20% of the power being coupled into the electrons. The end result is lower fractional dissociation of the feedstock gases, and larger densities of C_xF_y and $C_xF_y^+$ than CF_x^+ which would require multiple electron collisions to produce.

A parametric study of the TF-CCP was performed by varying the lowest 5 MHz power from 2.5 to 10 kW. The rationale for this choice is that 5 MHz power is dominantly dissipated by ion acceleration in the sheath (compared to 10 MHz and 80 MHz) and so has the most significant effect on IEADs to the wafer of the three frequencies. The time averaged IEADs of all the positive ions, the fluxes of ions and radicals and the average energy of ions to the wafer at

radius of 7.5 cm for different 5 MHz powers are shown in Fig. 6.4. The IEADs have multiple peaks, which are due to the sheath having components of all three frequencies and large range of ion masses (16 – 200 AMU). As the 5 MHz power increases from 2.5 to 10 kW, the 5 MHz voltage to deliver the power increases from 1,590 to 3,430 V while the dc bias increases from -1,450 to -2,250 V. These increases in voltage produce an extended IEAD having average ion energies from 1,630 eV (2.5 MHz) to 2,540 eV (10 MHz), and maximum energies of 2,300 eV to 4,000 eV. The IEAD becomes narrower in angle (incident angle of ions is less than 3^o with respect to surface normal) with increasing 5 MHz power due to the increasing acceleration of ions in the sheath perpendicular to the wafer, a desirable trend in HAR etching to reduce sidewall impacts in the feature and produce anisotropic etch profiles.

The thickness of the sheath at the surface of the wafer increases from 0.8 to 1.0 cm as the 5 MHz power increases from 2.5 to 10 kW as the overall waveform and amplitude of the sheath is dominantly modulated by the 5 MHz power. The narrowing of the angular spread of the IEAD is somewhat less than what one would expect by increasing the applied voltage by more than a factor of 2. Assuming collisionless acceleration of ions through the sheath, the angular spread of the IEADs striking the wafer should scale as $\Delta\theta \sim \left(T_{ion}/V_S\right)^{1/2}$, where V_S is the average sheath potential and T_{ion} is the ion temperature parallel to the sheath edge. If the plasma density remains constant, then the sheath thickness increases as $\lambda_S \sim V_S^{1/2}$. The thicker sheath enables more glancing angle elastic collisions, which increases the effective value of T_{ion}. The end result is that if the sheath (or presheath) are mildly collision, $\Delta\theta$ does not decrease with V_S as intended. To maintain that scaling, the λ_S should remain constant, which would then require that the electron density $n_e \sim V_S$. For low frequency biases whose power is dominantly dissipated by ion acceleration, there is little change in n_e with V_S. Maintaining a constant sheath thickness with

increasing V_S requires a corresponding increase in high frequency source power.

As the 5 MHz power increases from 2.5 to 10 kW, the total flux of all positive ions to the wafer at a radius of 7.5 cm increases by about 50%, from 0.8×10^{16} to 1.2×10^{16} $cm^{-2}s^{-1}$. This increase in ion fluxes results from an increase in the volume averaged ionization source by bulk electrons between the electrodes from 2.3×10^{15} to 5.0×10^{15} $cm^{-3}s^{-1}$, and a thickening of the sheath and presheath which captures more of the ion generation into wafer directed ion flux towards the wafer. The volume averaged electron density increases from 0.8×10^{10} to 1.0×10^{10} cm^{-3} with increasing 5 MHz power, resulting in a moderate increase in dissociation rates, which increase fluxes of CF_x and C_xF_y from 2.9×10^{17} to 3.2×10^{17} $cm^{-2}s^{-1}$.

6.4 Etching Profile of High Aspect Ratio Contacts in SiO_2

The features we are investigating are simple circular vias. The geometry of the 3-dimensional high HAR via in SiO_2 is shown in Fig. 6.5. The thickness of SiO_2 is 4,800 nm, with a 1,600 nm thick photoresist (PR) layer as the mask and Si as the stopping layer below the SiO_2. The diameter of the mask opening in the PR is 120 nm. The mask initially has beveled edges with an angle of 45 degrees and depth of 60 nm. The mask is otherwise azimuthally smooth. That is, in this study we are not considering the consequences of innate line-edge roughening of the mask. The mesh consisted of $60 \times 60 \times 1094$ cells, producing cubic voxels 6 nm on a side. The AR is defined by the PR mask opening divided by the etch depth in the oxide, so the AR of the feature in oxide is 40. The total aspect ratio including the mask at the start of etching is 53. Unless otherwise stated, the aspect ratio in the following context denotes the aspect ratio of the feature only in the oxide. Charging is not considered in etching the features discussed here and in Sec. 6.4.1 – 6.4.3. Charging of features is discussed in Sec. 6.4.4 and 6.4.5.

Although not a focus of this thesis, 2-dimensional simulations (e.g., infinite trenches) are often used to approximate vias. As part of this and related investigations, we have performed side-by-side comparisons of the simulations of trenches and vias. Although quantitative systematic trends are difficult to discern, there are clearly differences in the resulting profiles. These differences in large part result from the difference in the effective surface-to-volume ratio (SVR) of the features – the SVR is higher in the via than in the trench. The higher SVR of the vias results in side-wall scattering and deposition on the side-walls being more important in the via compared to the trench. We also found that simulating a trench in 2-d produces somewhat different results than simulating a trench in 3-d. The 3-d trench would be simulated, for example, by having a finite depth to the trench with periodic boundary conditions. This difference between 2-d trenches and 3-d trenches is particularly evident when including charging. This difference results from roughness (or charge) on the sidewall in 2-d appearing to have infinite depth, whereas roughness (or charge) on the sidewall in 3-d has a finite extent. Scattering from side-wall roughness in 2-d trenches will occur from the same height for all particles. Scattering from side-wall roughness in 3-d will be more statistical since the roughness is not uniform along the depth of the trench.

Using fluxes and IEADs obtained from the reactor scale base case, the time evolution of etching the via are shown in Fig. 6.5. These images are 3-d cut-out views and 2-d sectional slices taken through the middle of the feature. The bottoms of the 2-d sectional slices are not symmetric across the center line, an indication of pattern distortion which will be discussed below. As the etching proceeds, there is tendency towards bowing in the upper portion of the feature in SiO_2 for etch depths of 200 – 1,200 nm (AR of 2 – 10). The bowing is largely due to diffusive scattering of ions at the sidewalls of the PR and to a lesser degree from inside the

feature. This diffuse scattering produces hot neutrals at large angles. Also, the erosion of the PR results in increasing the area of facet at the top of PR and scattering of ions at the facet produces hot neutrals into the feature with broad angular distributions. For reflections from the facets to be a direct source of bowing in the SiO_2, there should be line-of-sight from the facet to the top of the SiO_2, which is not the case here. Reflections from the facets here broaden the angular distribution for subsequent sidewall collisions. The PR has been eroded by approximately 450 nm by the end of etch when the feature reaches the Si stopping layer, yielding a selectivity of SiO_2 over PR of 10.7.

The fluxes of ions, hot neutrals, CF_x and C_xF_y radicals incident onto the etch front as a function of the aspect ratio of the SiO_2 and of the total feature (PR + SiO_2) as the feature etches are shown in Fig. 6.6(a). The average energies and power flux striking the etch front by ions and hot neutrals are shown in Fig. 6.6(b). By definition, ions striking the etch front are those not having had collisions with the sidewalls as, in this mechanism, ions neutralize upon striking a surface and become hot neutrals. A given ion can only strike the etch front once, so the flux of ions to the etch front to some degree represents the decreasing view angle of the etch front subtending the ion angular distribution at that AR. For this reason alone, the ion flux to the etch front decreases with AR. On the other hand, thermal neutral species undergo diffusive scattering on the sidewalls are conductance limited in reaching the etch front as the AR increases. If a neutral has a non-unity reaction probability, once at the bottom of the feature that particle can strike the etch front multiple times. Each strike of the etch front by a neutral particle (either hot or thermal) increments the flux-count.

Even at low aspect ratio in the SiO_2, the flux of hot neutrals to the etch front is nearly the same as ions. This equivalence results from the PR itself having an AR of 13, so there is

considerable scattering of ions from the sidewalls of the PR with hot neutrals being the returning species at the start of etching. This scaling is demonstrated in Fig. 6.7 where the fluxes of ions and hot neutrals to the top of the SiO_2 the start of etching are shown as a function of the height of the PR. As the height of the PR increases from 0 to 2,400 nm, aspect ratios of the PR from 0 to 20, the flux of ions to the etch front monotonically decreases (4.2×10^{15} to 1.3×10^{15} $cm^{-2}s^{-1}$) while the flux of hot neutrals increases (0 to 2.9×10^{15} $cm^{-2}s^{-1}$). With increasing AR of the PR above the SiO_2, more ions are neutralized on the sidewalls of the PR producing hot neutrals before reaching the SiO_2 surface.

For the base case having PR with an AR of 13, as etching into the SiO_2 increasing the overall AR, sidewall scattering continually depletes ions converting them to hot neutrals, as shown in Fig. 6.6(a). (Recall that hot neutrals are those particles having energies as high as specularly reflected ions to as low as a few eV.) After converting ions to hot neutrals (including possible multiple collisions of hot neutrals with the etch front) there is a rapid increase in the hot neutral flux for an AR up to about 4 (or about 17 from the top of the PR). At larger AR, multiple scattering of the hot neutrals from the sidewalls reduces their energy. Reflections from the sidewalls can also include a stochastic diffusive component in the reflected velocity.[38] This results in a more isotropic velocity distribution as the average number of reflections increases and energy decreases. As the initially anisotropic hot neutrals become more isotropic, conduction limits begin to dominate and their fluxes to the etch front decrease with increasing AR.

As the etch depth increases up to 4,800 nm and AR = 40 (AR = 53 from top of PR), the maximum incident angle of an ion which can directly hit the etch front without first colliding with the sidewall decreases from about 4^o to 1^o (with PR included). This shadowing contributes

to a decrease in ion flux to the etch front from 2.0×10^{15} to 0.3×10^{15} $cm^{-2}s^{-1}$. The ions which do not directly reach the etch front are neutralized at the sidewall, charging the surface and are converted to their hot neutral partners with mostly specular reflection. The flux of hot neutrals to the etch front increases from 3.1×10^{15} to 8.0×10^{15} $cm^{-2}s^{-1}$ as the etch depth increases from 0 to 480 nm (AR = 4). As the feature further deepens to 960 nm (AR = 8), the flux of hot neutrals surpasses the fluxes of thermal CF_x and C_xF_y radicals whose fluxes are conductance limited. The hot neutral flux then becomes the dominant neutral species reaching the etch front. This initial increase in the flux of hot neutrals is mainly due to more ions striking sidewalls and being converted to hot neutrals, however there is also a component due to the etch front evolving from flat to a tapered profile. The tapered feature produces some focusing of specularly reflected hot particles towards the etch front. As the etch depth increases from 480 to 4,800 nm (AR = 40), the flux of hot neutrals to the etch front decreases to 1.1×10^{15} $cm^{-2}s^{-1}$, which is due to diffusive scattering from the sidewalls and thermalization of the hot particles following several collisions with the surfaces. The average energy of hot neutrals reaching the etch front first decreases with increasing AR and is then maintained at about 400 eV at ARs higher than 3. The flux of CF_x and C_xF_y to the top of the PR is 3.0×10^{17} $cm^{-2}s^{-1}$ resulting in polymer deposition on the top and sidewalls of the PR. This polymer deposition provides some protection of the PR from lateral etching.

In addition to energetic species (i.e., hot neutrals and ions), the chemical etching of SiO_2 depends on the availability of neutral radicals. The incident thermal neutrals have isotropic angular distributions and the delivery of neutrals deep into the feature is limited by gas conductance. As the etch depth increases from 0 to 1,200 nm (AR = 10), the flux of CF_x and C_xF_y radicals to the etch front decreases from 3.1×10^{16} to 0.4×10^{16} $cm^{-2}s^{-1}$. This decrease is

due to consumption by deposition as polymer on the sidewalls and diffusive scattering which reflects the neutrals out of the feature before reaching the etch front (neutral conduction limit). Recall that neutral particles that have non-unity reaction probabilities can strike the etch front several times, and are counted with every strike.

The oxide sidewalls of the feature are first passivated by fluorocarbon radical to form the $SiO_2C_mF_n$ surface complexes. The complex layer is then activated by hot neutrals and ions, which leads to the activated complex having a higher probability for CF_x and C_xF_y to deposit as polymer. The polymer deposition on sidewalls reduces the lateral etching by scattered hot neutrals and so reduces the bowing, enabling more directional etching and anisotropic profiles. As the etch depth further increases from 1,200 to 4,800 nm (AR from 10 to 40), the flux of CF_x and C_xF_y radicals to the etch front decreases from 4.4×10^{15} to 0.9×10^{15} $cm^{-2}s^{-1}$, resulting in a surface complex layer with little overlying polymer at the etch front. Due to the limited availability of CF_x and C_xF_y to thicken the polymer, the polymer is rapidly removed by ions and hot neutrals. Deep in the feature (AR > 10), the ions and hot neutrals have larger fluxes to the etch front than CF_x and C_xF_y by a factor of 2 – 3.

For AR greater than 3 (or AR about 16 from the top of the PR), the delivery of power to the etch front relies more on the hot neutral flux than the ion flux, as shown in Fig. 6.6(b). The power density is calculated as the sum of the fluxes of energetic particles multiplied by the average energy of that species at the etch front. The power density delivered by hot neutrals to the etch front is larger than the ions by about 20% for AR > 3. The ions initially incident into the feature have energies ranging between 1,300 and 3,000 eV with average energy of 1,950 eV and incident angles less than 4^o, as shown in Fig. 6.4. Since ions are counted as striking the etch front only if they have not had a collision with the sidewall, the average energy of the ions

reaching the etch front shown in Fig. 6.6(b) is nearly constant at 1,900 eV, approximately the average energy of incident ions. The small decrease in ion energy with AR results from the method of sampling and the tapering of the feature. If the bottom of the feature was absolutely flat with straight sidewalls, the average ion energy striking the etch front would increase with AR (subtending a smaller angle) since the higher energy ions have a narrow angular distribution as shown in Fig. 6.4(a). However, as the etch front tapers, more ions intersect the tapered sidewalls, which preferentially sample ions with a broader angular distribution having on average lower energies. With the average ion energy being nearly constant while the ion flux decreases, the power flux to the etch front monotonically decreases.

The average energy delivered to the etch front by hot neutrals only slightly decreases as the flux of neutrals to the etch front decreases with increasing AR, indicating that the energy delivery is dominated by hot neutrals having only 1 or 2 scatters from the sidewall. With the typical bowed geometry of a HAR feature, the first and second scattering events are usually small angle, occurring on the same side of the feature. With each reflection with a less grazing angle of incidence, the angle that the particle leaves the surface generally increases. Eventually, this angle will increase to the point that the particle traverses the width of the feature and interacts with the opposite side. Due to the bowing, once the particle traverses the feature, its next impact is often closer to being normal than the first grazing reflections. With the impact angle dependent energy loss described in Sec. 2.3.1, these interactions reduce the energy of the hot particle to point that the particle will no longer be tracked as a hot neutral species, but rather as its thermal neutral partner. The decrease in power delivery to the etch front with increasing AR is a major source of ARDE.

The neutral conductance in HAR features affects etching in at least two ways. The first is

to limit the delivery of neutral precursors to the etch front. The second is to impede the flow of etch products from deep inside of the feature out of the feature. The conductance limited transport of etch products out of the feature results in re-deposition deep inside the feature. The fluxes of gas phase etch products leaving the feature as a function of the aspect ratio as the etch proceeds are shown in Fig. 6.6(c). At low AR (< 10), the removal of oxide is mainly through passivation by CF_x and C_xF_y radicals,

$$SiO_2(s) + CF_x \rightarrow SiO_2CF_x(s), \quad (6.3a)$$

$$SiO_2(s) + C_2F_3 \rightarrow SiO_2C_2F_3(s), \quad (6.3b)$$

followed by chemical sputtering by energetic species,

$$SiO_2CF_x(s) + I^+ \rightarrow SiF_x + CO_2 + I(h),\ x = 1 - 3, \quad (6.4a)$$

$$SiO_2C_2F_3(s) + I^+ \rightarrow SiOCF_3(s) + CO + I(h), \quad (6.4b)$$

$$SiOCF_3(s) + I^+ \rightarrow SiF_3 + CO + I(h). \quad (6.4c)$$

At these depths, there are abundant polymerizing CF_x and C_xF_y fluxes. The etch rate is mainly limited by the availability of energetic species – that is, ion limited. The silicon surface sites are mainly removed by the formation of SiF_x (x = 1 – 3) as there is an ample F atom flux, and subsequent removal through chemical sputtering by energetic particles. The flux of SiF_x leaving the feature has a similar dependence on AR as the fluxes of hot neutrals and ions to the etch front shown in Fig. 6.6(a). This exiting flux of SiF_x peaks at a depth of 480 nm (AR = 4) at 3.6×10^{14} $cm^{-2}s^{-1}$.

At low ARs (< 10), the oxide surface sites are mainly removed by the forming CO_x(x = 1, 2) and COF species through chemical sputtering of the complex by energetic species. With increasing AR, both the fluxes of SiF_x (etch products of silicon sites) and CO_x (etch products of oxygen sites) decrease. The CO_x flux decreases less than the SiF_x flux as the CO_x species are

non-reactive (in this mechanism) and leave the feature without further reactions. On the other hand, the SiF_x species can redeposit on the sidewalls and the etch front, which contributes to tapering of the feature and slowing the etch rate (increasing ARDE). Thermal etching of SiF_x species is also possible by further fluorine exposure, generating a SiF_4 etch product. This product is volatile, and does not participate in re-deposition, but this pathway is not important for these conditions.

The flux of gas phase SiO_2 exiting the feature indicates the amount of oxide directly removed by physical sputtering through $SiO_2(s) + I^+ \rightarrow SiO_2 + I(h)$. For simplicity, the sputtered oxide is treated as a gas phase SiO_2 species as opposed to separately sputtering as Si and O atoms. This sputtered SiO_2 can redeposit on the surface or leave the feature into the plasma. The flux of O atoms entering the feature is many orders of magnitude larger than the flux of physical sputtering products exiting the feature; and so ignoring the O atoms as a physical sputtering product is likely not important. The flux of gas phase SiO_2 exiting the feature reaches a maximum at a depth of 960 nm (AR = 8) with a flux of 2.3×10^{14} $cm^{-2}s^{-1}$, decreasing to 0.5×10^{14} $cm^{-2}s^{-1}$ as the etch depth increases to 4,800 nm (AR = 40). At low ARs (< 10), the etching of oxide mainly occurs through chemical sputtering due the large supply of CF_x and C_xF_y radicals. As the AR increases above 8, the fractional decrease in the flux of gas phase SiO_2 out of the feature is smaller than for the chemical sputtering etch products. With increasing AR, the flux of SiO_2 out of the feature .approaches the fluxes of CO_x and SiF_x, indicating an increasing fractional contribution of physical sputtering and decreasing fractional contribution of chemical sputtering to the removal of oxide.

Overall the ratio of oxide removed by chemical sputtering compared to physical sputtering is 1.9 (measured by the ratio of passivated etch product SiF_x compared to the SiO_2

etch product). The flux of COF leaving the feature increases from 0.7×10^{16} to 1.5×10^{16} $cm^{-2}s^{-1}$ as the AR increases from 0 to 40. In addition to being formed through chemical sputtering of the $SiO_2C_mF_n$ complex, COF is also formed through etching of polymer by gas phase oxygen species (O, O^+ and O_2^+). Polymer etching by O containing species becomes the major source of COF at high ARs due to there being more polymer covered surface on the sidewalls with increasing AR.

The instantaneous etch rate of SiO_2 as a function of AR shown in Fig. 6.8 shows typical ARDE – decreasing etch rate with increasing etch depth or aspect ratio. The instantaneous etch rate is calculated by measuring the average height of the solid surface in a 18 × 18 nm window at the center of the feature for equally spaced time steps and taking the first order derivative of the height with respect to time. The instantaneous etch rates were normalized by setting the initial etch rate to 1. There is a small initial increase in etch rate which is due to tapering of the feature that funnels hot neutrals to the etch front. The etch rate then decreases by 80% by the time the AR reaches 40, following a similar trend as the fluxes and power densities of energetic species to the etch front shown in Figs. 6.6(a,b). This correlation results from the propagation of the etch front ultimately being driven by energetic species through physical and chemically enhanced sputtering. With the delivery of both energetic species and power to the etch front decreasing with increasing AR, the etch rate decreases resulting in ARDE. There is also a contribution to ARDE from redeposition of etch products, however the more dominant source of ARDE is the reduction in power to the etch front.

The instantaneous etch rate of the PR shown in Fig. 6.8 is nearly independent of AR, and is about 0.05 that of the initial oxide etch rate. Any changes in PR etch rate are due to the erosion of the PR which results in ions striking the surface at non-normal (top surface) or non-

grazing (side surface) angles, or redeposition of etch products. With the decrease in oxide etch rate due to ARDE, the selectivity (oxide etch rate/PR etch rate) decreases with increasing AR. The end result is that the relative rate of PR erosion increases as the AR increases, as shown in Fig. 6.5. This decreasing PR selectivity is a limiting factor in etching HAR features, motivating the use of hard non-eroding masks. For example, for the base case conditions, the PR mask is nearly fully eroded when reaching an AR of 60, as shown in Fig. 6.9. This loss of selectivity is not because the PR etches faster, but rather because the SiO_2 etches slower. There is a counter-intuitive positive contribution to the mask erosion. With thick masks having a finite AR before reaching the top surface of the SiO_2, there is already some conductance limit to transport of neutral radicals and sidewall scattering of ions, both of which contribute to ARDE. As the mask erodes, the conductance limit of neutrals into the SiO_2 portion of the feature relaxes and the unimpeded ion flux to the etch front increases. ARDE would be even more severe in the absence of PR erosion.

Having said that, there are several negative consequences of the mask erosion, including bowing of the via below the mask. The bowing results from ion reflection from the PR which produce energetic hot neutrals at non-grazing angles incident onto the sidewalls of the via below the mask. These trends have also been seen in previous studies in Refs. [2,6]. These non-grazing particles are produced either directly from reflection off the facets or sidewalls of the PR or following several reflections from the sidewalls of the PR. As the mask is eroded, the likelihood for direct line-of-sight reflection from the facet into the feature increases, thereby increasing the likelihood for bowing.

To examine the consequences of PR erosion, the probabilities of physical sputtering of PR by energetic ions, $R(s) + I^+ \rightarrow R + I(h)$, and thermal etching of PR by O atoms, $R(s) + O \rightarrow$

COH, a_0, were both decreased to 50%, 25% and 0% of their values in the base case, with the resulting etch profiles shown in Fig. 6.9. The selectivity (as indicated by the height of the PR) improves as the PR etch probability decreases while the bowing distortion decreases. Note that in the a_0 = 0.5 and 0.25 cases, there is significant bowing while there is no direct path for an ion reflecting from the PR facet to reach the location of bowing. The bowing for these conditions results from energetic particles having multiple reflections.

6.4.1 Bias Power

A parametric study was performed of HAR etching by varying the 5 MHz power from 2.5 to 10 kW. The powers of the other two frequencies were the same as the base case (80/10 MHz power = 0.4/2.5 kW). The central slice of the resulting etching profiles with 10% over-etch are shown in Fig. 6.10. (A 10% over-etch means that following the feature reaching the bottom Si, etching continued for an additional 10% of the time required to reach the bottom.) Over-etch is typically performed to remove the taper in the profile. The relative etch time is listed in Fig. 6.10. Only PR, SiO_2 and Si are shown. The surface complex and polymer have been blanked out of the figure, which is our prediction of the profiles after a cleaning process.

The fluxes of ions and hot neutrals to the etch front nearly double with increasing 5 MHz power from 2.5 to 10 kW as shown in Fig. 6.11(a). This doubling is due to the increase of the initial fluxes of ions into the feature by about 50% shown in Fig. 6.4(b) and the narrowing of the ion angular distributions shown in Fig. 6.4(a) resulting in less scattering from the sidewalls. The power delivered by ions and hot neutrals to the etch front increases by nearly a factor of 3 with increasing 5 MHz power, as shown in Figs. 6.11(b,c). This increase results from both the increase in fluxes of energetic species to the etch front and an increase of their average energies by about 55%. The fractional decrease in the power delivered to the etch front by ions and hot

neutrals with increasing AR is almost the same for all 5 MHz powers. These trends indicate that the transport of ions and hot neutrals into the feature is most sensitive to aspect ratio.

The average etch rate, selectivity and the critical dimensions (CDs) as a function of 5 MHz power are shown in Fig. 6.12. The average etch rate was obtained by dividing the thickness of the SiO_2 by the time for the etch front to reach the stopping layer and was normalized to 1 for the base case. The top CD was measured at the top of the oxide adjacent to the PR, the bottom CD was measured at the bottom of the oxide adjacent to the stopping layer and the bowing CD was measured at the height where the diameter of the via is largest.

The efficiency of etching (rate/power) decreases when increasing the 5 MHz power. For an increase in power of a factor of 4, the etch rate increases by only a factor of 2.7. The diminishing efficiency is partly due to the increase in power by a factor of 4 producing an increase in ion flux of only 50% and an increase in average ion energy of 55%, with a fraction of the power contributing to the production of other nonreactive species. With reaction probabilities scaling with $\varepsilon^{1/2}$, there is also a diminishing return on increasing reaction probability by increasing ion energy when the ion energy is already significantly above threshold, as is the case here.

With the flux of thermal neutrals being conduction limited to the bottom of the feature and not significantly increasing with 5 MHz power, the etching is neutral-starved at the higher powers. Polymerizing neutrals for chemical sputtering are largely delivered by slowing hot neutrals. Some etch rate is recouped by a moderate narrowing of the IEAD with increasing power which enables a larger fraction of incident ions to reach the etch front without scattering from the sidewalls.

The top, bowing and bottom CDs of the features all increase when varying 5 MHz power.

According to the final profiles having 10% over-etch shown in Fig. 6.10 and the measurements of CDs shown in Fig. 6.12(b), the top CDs are approximately 160 nm, which is about 40 nm larger than the original mask opening diameter of 120 nm. The bowing CD increases from 162 to 204 nm with increasing power, which is mainly due to the larger increase of ion flux compared to polymerizing radical flux which protects the sidewalls. More ions are diffusively scattered or reflected from sidewalls relative to the lower rate of sidewall passivation which results in enhanced lateral etching of sidewalls and bowing in the upper portion of the feature. The bottom CD is sensitive to the over-etch time which determines the degree of clearing of the corners. The bottom CDs are smaller than the original mask opening due to the relatively short 10% over-etch time. For tapered etch fronts, short over-etch time results in incomplete corner clearing and smaller bottom CDs (50 – 100 nm). For these conditions, longer etch times will begin to broaden the top of the feature.

6.4.2 $(CF_x + C_xF_y)$/Ion Flux Ratio

The transport of energetic species (hot neutrals and ions) and polymerizing radicals (CF_x and C_xF_y) into HAR features significantly varies with increasing AR, while these two groups of species play different roles in the etching of SiO_2. The CF_x and C_xF_y radicals contribute to passivation and polymer deposition while energetic hot neutrals and ions produce chemical and physical sputtering of the surface complex and oxide. The relative fluxes of the energetic species and fluorocarbon radicals are linked through the properties of the plasma which are in turn functions of power, pressure, flow rates, mole fractions, frequencies and pulse waveforms. However, artificially adjusting their relative fluxes does provide insight to the etching process. In this regard, the magnitude of the flux of all positive ions, I^+, was varied while keeping the shape of the IEADs and the incident neutral fluxes constant. In doing so, the $(CF_x + C_xF_y)/I^+$

flux ratio was varied from 5 to 40 where for the base case, the ratio is 30. The central slices of the resulting profiles with 10% over-etch are shown in Fig. 6.13. The average etch rate, selectivity and CDs are shown in Fig. 6.14.

As the $(CF_x + C_xF_y)/I^+$ flux ratio increases from 5 to 40, the average etch rate and selectivity both decrease – the flux of energetic species and power delivered to the etch front by those energetic species both decrease. The time required to etch through the oxide increases by 10 times as the $(CF_x + C_xF_y)/I^+$ flux ratio increases from 5 to 40, resulting in increased erosion of PR from 372 to 510 nm and decreased SiO_2/PR selectivity from 12.9 to 9.4. The strong dependence of etch rate on $(CF_x + C_xF_y)/I^+$ flux ratio is mainly due to the ion-driven etching process for oxide. Increasing the flux of ions results in a higher etch rate, but also leads to more pattern degradation by increasing the top and bowing CDs as shown in Fig. 6.14(b). As the $(CF_x + C_xF_y)/I^+$ flux ratio decreases by increasing the ion flux, the lateral etching by hot neutrals and ions increases, resulting in an increase of the top CD from 156 to 168 nm and an increase in bowing CD from 162 to 210 nm.

6.4.3 Fractional CF_x^+ and $C_xF_y^+$

The CF_x^+ and $C_xF_y^+$ ions play multiple roles in the etching of oxide. These energetic ions and their hot neutral partners can remove oxide directly through physical sputtering or remove the complex through chemically enhanced sputtering. After losing energy through several collisions with the sidewalls and etch front, these energetic species become thermal CF_x and C_xF_y radicals, which can passivate the oxide surface or deposit as polymer. In the base case, the majority of the CF_x and C_xF_y radicals at low AR (< 5), shown in Fig. 6.6(a), originate from the thermal neutrals incident into the feature from the plasma. As the AR increases to greater than 10, the neutralized and thermalized CF_x^+ and $C_xF_y^+$ ions become the main source (> 95%) of

radicals reaching the etch front. To investigate these processes, the fluxes of CF_x^+ and $C_xF_y^+$ were varied while the total ion flux was maintained constant by decreasing the flux of Ar^+ whose neutral partner is chemically non-reactive. In this manner, the fraction of CF_x^+ and $C_xF_y^+$ fluxes, (CF_x^+ and $C_xF_y^+$)/I^+, was varied from 15% to 60%. (For the base case, the fraction of CF_x^+ and $C_xF_y^+$ ions is 30%.) The final etch profiles with 10% over-etch are shown in Fig. 6.15. The average etch rate, selectivity and CDs are shown in Fig. 6.16.

As the majority of the CF_x and C_xF_y radicals reaching deep into the feature (AR > 10) originates from CF_x^+ and $C_xF_y^+$, the flux of CF_x and C_xF_y to the etch front at high AR increases by approximately 3 times when increasing fractional CF_x^+ and $C_xF_y^+$. This increase in fluorocarbon radicals to the etch front results in more surface passivation and polymer deposition which requires additional ions to remove the oxide. The neutral and thermalized partners of other ions are non-reactive species and diffuse out of the feature with no surface reactions (only scattering at the surface). There is little surface passivation or polymer deposition resulting from those thermalized species. Thus, the etch rate of oxide decreases by about 30% when increasing the fraction of CF_x^+ and $C_xF_y^+$, as shown in Fig. 6.16(a). The ratio of material removed by chemical sputtering versus physical sputtering increases with increasing fractions of CF_x^+ and $C_xF_y^+$, from 1.1 to 3.5. The etch rate of PR is almost invariant with the fraction of CF_x^+ and $C_xF_y^+$ as, in this model, all of the ions have the same energy and angular dependent probabilities for physical sputtering of the PR. Ions reflecting from the top of the PR as hot neutrals will, in most cases scatter back into the plasma, and not directly revisit the PR. Therefore, the SiO_2/PR selectivity also decreases by about 50% with the increasing fraction of CF_x^+ and $C_xF_y^+$. We expect that there will be a mass dependence on PR sputtering rates by different ions. However, since all ions are heavy compared to the components of the hydrocarbon polymer of the PR, that

mass dependence of sputtering will not be large.

An effect that has not been included in the reaction mechanism is dissociation of molecular ions and hot neutrals when striking the surface. There are large fluxes of fluorocarbon ions whose neutral counterparts are non-reactive, such as $C_2F_4^+$. However, $C_xF_y^+$ ions of many hundreds of eV to a few keV, as in this study, will likely fragment when striking the surface.[39] This fragmentation will then increase the flux of more reactive and smaller neutral species, CF_x, which are more likely to polymerize and form surface complexes.

The top, bowing and bottom CDs shown in Fig. 6.16(b) vary only slightly with increasing fractional CF_x^+ and $C_xF_y^+$, being maintained at about 156, 180 and 84 nm respectively. The increased fluxes of CF_x and C_xF_y radicals deep into the feature with increasing fractional CF_x^+ and $C_xF_y^+$ provides protection to the sidewalls from lateral etching, which is offset by the longer etch time resulting from the decrease in rate. The end result is only small variations in the CDs for different fractional CF_x^+ and $C_xF_y^+$. The small bottom CD of 42 nm with fractional CF_x^+ and $C_xF_y^+$ of 60% is mainly due to there being more polymerizing species from thermalized ion partners and longer over-etch time required for clearing the corner.

6.4.4 Charging of Features

Charging of the surfaces on the top and inside of the feature occurs in dielectric etching or in conductor etching using polymerizing gas mixtures. The same HAR geometry, IEADs and fluxes as in the base case were used simulations when including charging effects. The time evolution of the etch profiles and the electric potentials in and around the features are shown in Figs. 6.17 and 6.18(a). The profiles in Fig. 6.17 are shown at the same time intervals as those for the non-charging base case (Fig. 6.5) so that side-by-side comparisons can be made. The first frame in Fig. 6.18(a) is at the very beginning of etching where the maximum of the positive

potential is at the bottom of the feature, while the other 7 frames in Fig. 6.18(a) are sampled at the same time as the frames in Fig. 6.17.

The top surface of the PR is almost charge neutral or slightly negatively charged. Even though the electron flux has a Lambertian angular distribution while the positive ions have a narrow angular distribution about the normal, the net conduction current to a flat non-conducting surface should be zero averaged over the rf period. (The flux of negative ions is essentially zero compared to other charged particle fluxes.) However, this disparity in angular distributions of electrons and ions result in electrons dominantly initially charging the top surface and surfaces having small AR, while the ions can reach deep into the features.[40] The end result is that for small AR, the feature initially negatively charges on inside surfaces near the top, and positively charges near the bottom of the feature. This charging is reflected by the positive plasma potential which appears on the bottom of the feature at the beginning of etching, as shown in Fig. 6.18(a). The positive charging slows ions as they approach the bottom of the feature. If this situation persisted, the bottom of the feature would charge to a positive potential essentially equal to the energy of the incident ions which would deflect ions back out of the feature (or into walls) to prevent further charging. Etching would then cease. In the steady state, the positive potential attracts electrons into the feature to neutralize the continuous positive charge delivered by the anisotropic ions. The end result is a steady state positive charge and potential distribution in the feature.

We note that there are several other strategies to control charging of features that rely on pulsed plasmas.[22,23] In this approach, the source power is pulsed producing an active glow discharge, followed by an afterglow in which electrons rapidly attach to form a positive ion – negative ion plasma. Application of a bias during the afterglow then accelerates negative ions

into the feature to neutralize excess positive charge.

The net positive charge in the feature produce both vertical and lateral electric fields which can perturb the velocities and deviate the trajectories of the subsequent positive incident ions. The result is a decrease in etch rate and increased time to etch through the feature by about 30% compared with the non-charging case. This mild effect of charging is in part a consequence of the high aspect ratio. In high volume manufacturing, the etching of HAR vias in silicon oxide having an AR of 40-50 takes as long as 40 – 50 minutes. The predicted etch times here are 36 min for the base case without charging (Fig. 6.5) and 48 min for the base case with charging (Fig. 6.17), which are in reasonable agreement with experiments.

At the beginning of etching when the AR is small, the position of the maximum electric potential is near the etch front where most of the ions first hit the surface and deposit charge. As the etching proceeds and the AR increases, the position of the maximum potential initially moves downwards before becoming nearly static in the upper portion of the feature as shown in Fig. 6.18(b). By an AR of about 10, the majority of ions will have collided with the sidewalls where they deposit charge, then proceeding as hot neutrals which are not affected by the electric fields. When the etch front reaches the bottom stop layer, the maximum electric potential higher in the feature (AR ≈ 10) is 1,100 V, which is about 60% of the average energy of incident ions. Had this maximum been at the bottom of the feature, the ion energy incident onto the etch front would have decreased by about 60%. However with the maximum in potential being higher in the feature, ions are decelerated approaching the maximum in potential and accelerated when passing the maximum, with less net change in energy.

In previous experimental and numerical investigations of oxide plasma etching using fluorocarbon gas mixtures, the maximum electric potentials in the feature were 200 V at AR = 20

[1], 300 V at AR = 10 [41], and 150 V at AR = 15 [42]. In this study, the maximum potentials at ARs of 10 – 20 are 200 V – 400 V, which are commensurate with these prior results. Our higher in-feature potentials result in large part from the higher ion energies that are required for HAR etching. There is a secondary effect of transport of electron thermal flux from the plasma into the feature. There is some continual neutralization of positive charge on the sidewalls of features by electron flux that is pulled into the feature by the electric fields produced by the positive in-feature potential. As the AR increases, the available electron flux from the plasma to neutralize positive charge decreases.

Comparisons of the fluxes and average energies of ions and hot neutrals, and power delivered to the etch front as a function of AR with and without charging are in Fig. 6.19. The ion and hot neutral fluxes are nearly independent of charging. With the maximum of the electric potential appearing in the upper portion of the feature, the sequence of deceleration of ions at low ARs and then acceleration at high ARs results in only a nominal reduction of ion energy for low to moderate AR. As the AR increases to above 10, there is a gradual decrease in ion energy to the feature relative to the base case without charging. This decrease results in part from there being an increase in the positive potential that affects ions having progressively narrower angular distributions. For an AR of 40, charging produces a decrease of the average energy of ions to the etch front from 1,940 to 1,050 eV.

The hot neutrals originate from neutralized ions which undergo grazing incidence and specular reflection at sidewalls. The majority of the energy is maintained and the reflected angles are shallow enough to direct the hot neutrals to the etch front – with the hot neutrals being unaffected by the electric field in the feature. As a result, the fluxes of hot neutrals to the etch front are similar with and without charging, as shown in Fig. 6.19(a). The average energy of the

hot neutrals decreases by about 50 – 150 eV with charging, as shown in Fig. 6.19(b). This decrease results from the original ions being decelerated by the electric field at low ARs before being neutralized. If ions are converted to hot neutrals before being reaccelerated when passing below the maximum in potential, the hot neutrals proceed to the etch front with a lower energy. The power delivered to the etch front by hot neutrals with charging is smaller than without charging by about 15%, as shown in Fig. 6.19(c). This lower power flux is mainly due to the lower average energy of hot neutrals. The end result is a decrease in etch rate with charging.

The effect of charging is sensitive to the 5 MHz power due to the incident ions having different IEADs. When increasing 5 MHz power from 2.5 to 10 kW, the average energy of ions reaching the bottom of the feature (AR = 40) increases from 1,400 to 2,460 eV without charging while increasing from 475 to 1,760 eV with charging, as shown in Fig. 6.20(a). The fractional decrease in ion energy is more severe for lower power. The difference in ion energy with and without charging ($\Delta E = E_{chg} - E_0$) decreases from 925 eV at 2.5 kW to 700 eV at 10 kW, which corresponds to fraction decrease, $\Delta E/E_0$, from about 66% to 28%, as shown in Fig. 6.20(b). In fact, the decrease in ion energy produces an etch stop at 2.5 kW before reaching AR = 40. (The average ion energy in Fig. 6.20(a) for 2.5 kW is an extrapolation from smaller AR.) The charging of the sidewalls scale with the ion flux which is a weak function of 5 MHz power, whereas the energy of the ions scales as 5 MHz power. The end result is that the increase in plasma potential lags behind the increase in ion energy. There is also a secondary effect that the etch rate is higher at higher power. A higher etch rate translates to a shorter etch time and a smaller fluence of positive ions into the feature. This smaller fluence of positive ions results in less charge deposition and a smaller positive potential.

All of the materials in these features are non-conductors, and so the mobility of charge on

or through these materials is expected to be negligible. For example, the electron mobility through flourocarbon polymer (PTFE – polytetrafluoroethylene) is 10^{-11} $cm^2/V\text{-}s$ [43]. As a result, the charge on sidewalls in these simulations was static. That is, the charge did not move on or along the surface. The MCFPM has the ability to allow transport of charge through solid materials and include that change of charge in solution of Poisson's equation for the electric potential. This capability is needed in simulations with conducting material. To test our assumption that electron charge is static on surfaces, simulations were conducted where electrons on polymer were given a non-zero mobility, varied with values as large as 10^{-3} $cm^2/V\text{-}s$. The result was that charge did migrate through the polymer, which resulted in a net reduction of total charge in the feature due to recombination between positive and negative charge. However, the mobilities for which these effects were significant were many orders of magnitude larger than what might be expected for fluorine containing polymer. So our assumption of immobile electron change on surfaces is likely accurate.

6.4.5 Feature Distortion

Feature distortion refers to producing an etch profile that does not replicate the intended pattern defined by the photolithography. Feature distortion includes line (or contact) etch roughness, twisting and producing non-circular vias.[3,9,44] The latter feature distortion is shown in Fig. 6.21, where horizontal sections of the feature are shown (with and without charging) at different heights in the feature. A small amount of roughness occurs on the walls of the PR due to the randomness and statistical nature of the grazing angle sputtering of the mask. This roughness then results in more diffusive scattering of grazing angle ions, which then lead to bowing deeper in the feature. However, without charging, as deep as AR = 20, the cross section of the final feature is basically circular, with some statistical roughness. Deeper into the feature

(higher AR), the cross section of the feature deviates from a circular profile. This deviation occurs to some extent at all heights, resulting from the initially tapered etch front rarely being circular. However, an effective over-etch occurs at all heights above the bottom of the feature. (That is, heights above the etch front continue to experience sidewall scattering.) This effective over-etch is the time between achieving the desired CD at a given height to the end of etching. The over-etch tends to round previously non-circular features and removes the anomalies caused by the tapered etch front. The end result is that non-circular cross sections tend to occur in the lower portion of the feature that experience less effective over-etch. The rounding of the feature by over-etch is less effective with charging.

The thickness of polymer deposited on the sidewalls varies as a function of AR and is typically larger when including charging. Predicted polymer thickness ranges from 0 to about 20 nm with a maximum thickness occurring at AR = 8. Experimentally, the sidewall polymer thickness is a function of many operational parameters (e.g., bias power, pressure, gas mixture, wafer temperature); and has been measured to be 20 – 100 nm [1] and 5 – 20 nm [45] during HAR etching for ARs of 10 – 20 using fluorocarbon gas mixtures.

The origin of the non-circular cross sections is largely simply statistics. The area of the mask opening in HAR etching has decreased more rapidly than the reactant flux incident onto the mask has increased. The end result is that the number of particles/second entering the feature has decreased to the point that the type (e.g., radical vs ion), energy and angle of reactants is subject to statistic noise. This statistical noise produces statistically noisy reactions with the surface, from polymer deposition to chemical sputtering. As the etch depth and AR increases, the fluxes of reactants reaching the etch front decrease due to the conduction limits, resulting in more statistical sampling of these fluxes. The diameter of the hole also decreases with increasing

AR due to tapering. Holes with smaller diameters are more sensitive to small surface imperfections, which then producing shadowing deeper into the feature. The end result is a non-circular cross section of the feature. Over-etch improves upon those statistics by simply having more particles interact with the feature at that height.

Charging aggravates feature distortion by introducing more randomness and more persistence of randomness to the process. For example, horizontal slices at different heights of the final profile with 10% over-etch are shown with charging in Fig. 6.21 for the base case. With charging, feature distortion begins at ARs as low as 10. This additional distortion results from the randomness of charge deposition on sidewalls, and particularly charge that is trapped in polymer which is persistent. The polymer deposition on the sidewall with charging is thicker and less uniform than without charging, resulting in deeper trapped charge. The resulting electric fields then perturb the trajectories of ions, perturbations that are then imprinted into the specular hot neutrals. Since the charging of the feature is not azimuthally nor axial uniform, both of which have some randomness, feature distortion is worse with charging.

6.5 Concluding Remarks

The etching of HAR features in SiO_2 with aspect ratios up to 80 was investigated using integrated reactor and feature scale modeling. A triple-frequency CCP reactor sustained in $Ar/C_4F_8/O_2$ mixtures was used as a source of radicals and ions, and modeled in 2-dimensions. The IEADs and fluxes of ions and neutrals to the wafer obtained from the reactor scale modeling were used in the 3-dimensional MCFPM to predict feature evolution. In the TF-CCP reactor, the dominant fluxes of radicals to the wafer surface are CF_x, F and O, which are mainly produced through electron impact dissociation of feedstock C_4F_8 and O_2 gases. Fluxes of ions are lower

than those of radicals by 1 – 2 orders of magnitude. The incident ions have energies of up to several keV and incident angles of less than 4^{o}.

During HAR etching, bowing occurs in the upper portion of the feature due to diffusive scattering of ions at sidewalls of the PR and erosion of PR with increasing facet area for ion reflection which produce hot neutrals into the feature with broadened angular distributions. At low ARs (< 5), abundant fluxes of CF_x and C_xF_y radicals passivate the oxide surface to form complexes which are then removed by energetic species (hot neutrals and ions) through chemically enhanced sputtering with the formation of gas phase SiF_x, CO_x and COF. As the AR increases, conductance limits on the initially isotropic thermal radicals reduce their fluxes reaching deeply into the feature. For sufficiently large AR, the neutral radicals reaching the bottom of the feature originate from neutralized ions which can overcome conductance limits by virtue of their initially anisotropic trajectories. The dominant oxide removal process transitions from chemical to physical sputtering as the fluxes of energetic species to the etch front surpass that of radicals. As the AR further increases, even the energetic species with narrow angular distributions are scattered by the sidewalls, losing energy and resulting in an etch stop. The fundamental limiting factor in HAR etching is the decreasing power and fluxes of reactants delivered to the etch front with increasing AR.

ARDE, decreasing etch rate with increasing etch depth or AR, was observed in all cases. ARDE results from both lack of neutral radicals by conductance limits and by a decrease in the power delivered to the etch front as AR increases. Erosion of PR, being more akin to blanket etching, does not depend on either the height of the PR or the AR of the feature being etching. With ARDE decreasing the SiO_2 etch rate, the PR selectivity worsens with increasing AR. In this example, in etching to an AR of 80, the PR was almost fully eroded. This scaling would

suggest that increasing PR height with increasing AR to be etched would preserve CD. However there is a limit to this scaling as the PR itself has an AR adding to the effective AR that incident species experiences arriving at the SiO_2. This increase in AR affects ion and neutral transport in the same way that AR affects transport in the feature. Increasing the height of the PR increases ARDE by adding to conductance limits, and reducing ion and hot neutral energies reaching the SiO_2.

Parametric studies for the etch process were performed by varying the 5 MHz source power, $(CF_x + C_xF_y)$/ion flux ratio and fractional of the ion flux consisting of CF_x^+ and $C_xF_y^+$. The etch rate of oxide increases with increasing 5 MHz power while the SiO_2/PR selectivity remains almost invariant as the increase in fluxes of ions favors the removal of both SiO_2 and PR in the same ratios. Due to the coupling of the production of ions and radicals in plasmas, the fluxes were artificially adjusted to provide insights into the etching process. Decreasing the $(CF_x + C_xF_y)$/ion flux ratio by increasing the flux of incident ions results in higher etch rate and selectivity, at the cost of more bowing due to polymer deposition on the sidewalls being removed by energetic species. As the majority of the CF_x and C_xF_y radicals reaching deeply into the feature (AR > 10) originate from CF_x^+ and $C_xF_y^+$ ions, the flux of CF_x and C_xF_y to the etch front increases with increasing fraction of CF_x^+ and $C_xF_y^+$, resulting in more surface passivation and polymer deposition which requires additional ion flux to remove the oxide. Thus, the etch rate of oxide and SiO_2/PR selectivity both decrease with increasing fraction of CF_x^+ and $C_xF_y^+$. The parametric studies performed here provide general scaling laws and provide guidance for tuning plasma control parameters to optimize etching of HAR features in SiO_2. This guidance can be applied to other processes such as atomic layer etching and O-N-O stack etching.

When including charging, the top surface of the PR is almost charge neutral or slightly

negatively charged due to balancing of the Lambertian angular distributions of electrons and the anisotropic ions on flat surfaces. Energetic positive ions can reach deeply into features and deposit positive charge, producing electric fields which decelerate and deviate the subsequent ions. The deceleration results in a reduction in etch rate due to lower power delivered by the energetic species to the etch front. At low AR, the most positively charged surface is the bottom of the feature. With increasing AR, the most positive electric potential occurs on the sidewalls where ions have their first collisions. The effect of charging becomes less significant as the bias power increases mainly due to increased average energy of incident ions, which undergo smaller fractional energy loss when transporting to the bottom of the feature and shorter charging time producing a smaller potential buildup inside the feature.

The etching of extremely high aspect ratio features requires more stringent control of IEADs and neutral-to-ion flux ratios. This more stringent control has motivated development of multi-frequency sources having large dynamic ranges for tuning IEADs and flux ratios with the goal of having a large process window for optimization. At high AR, the reactive radicals CF_x and C_xF_y reaching the etch front mainly originate from the incident ion partners CF_x^+ and $C_xF_y^+$. To maintain process rates and CDs at high AR, it is necessary to control both the fractional fluxes of these ions while increasing ion fluxes to both provide activation energy and radicals to the etch front. Although at high AR, non-reactive ions such as Ar^+ provide activation energy to the etch front through their hot-neutral partner, these ions do not provide chemical reactivity. High AR processes thereby likely also require a larger fraction of CF_x^+ and $C_xF_y^+$ ions whose neutral partners are reactive.

This study has focused on HAR etching of a single via in a single material, SiO_2. However, many of the current etching challenges involve more complex conditions. For

example, pattern dependent effects have been observed where the CD of HAR features depends on the pattern with which those features are arranged on the die (e.g., rectilinear, honeycomb). The spacings of these features in 3D-NAND memory may be as small as 50 – 100 nm, dimensions so small that there is no systematic change in the incident reactant fluxes. These pattern dependent processes therefore likely result from interactions between features. 3D-NAND memory applications also bring the challenge of etching alternately deposited materials (e.g., oxide-nitride-oxide stacks). To minimize the sensitivity of processes etching different materials to small changes in reactive fluxes, these processes will be more stable when the etch mechanism is based more on physical than chemical reactions.

6.6 Figures

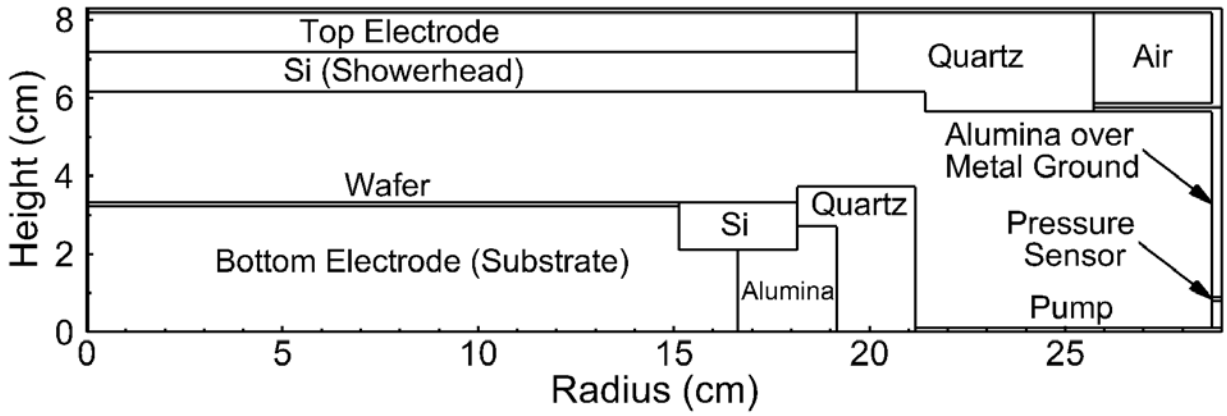

Fig. 6.1 Schematic of the tri-frequency capacitively coupled plasma (TF-CCP) reactor used in the simulation. 80 MHz power is applied to the top electrode. 10 MHz and 5 MHz powers are applied to the bottom electrode.

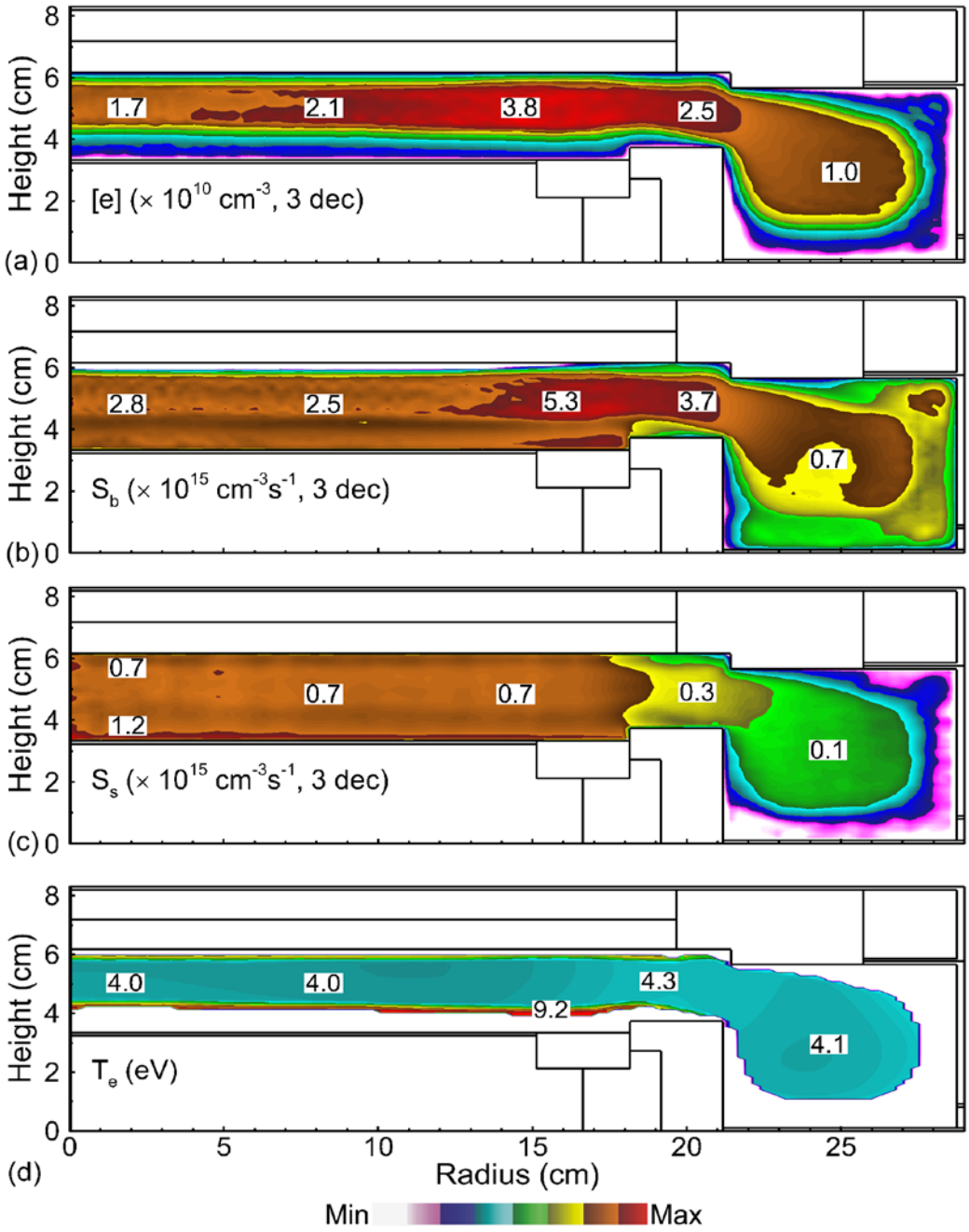

Fig. 6.2 Time averaged a) electron density, b) ionization source by bulk electrons, c) ionization source by secondary electrons, and d) electron temperature in a TF-CCP sustained in an $Ar/C_4F_8/O_2$ mixture. (Operating conditions: $Ar/C_4F_8/O_2$ = 75/15/10, 25 mTorr, 500 sccm, 80/10/5 MHz power = 0.4/2.5/5 kW.)

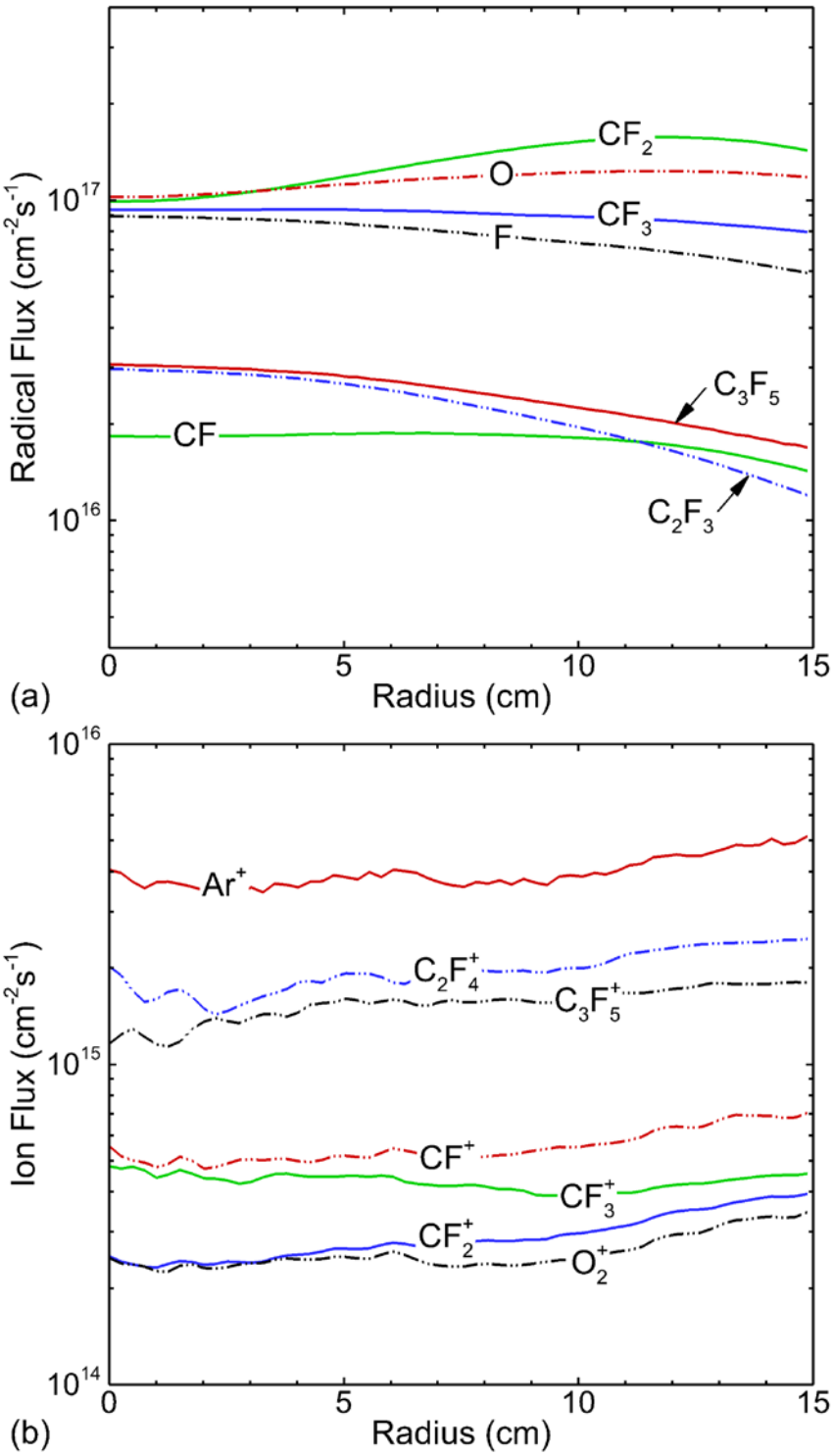

Fig. 6.3 Time averaged fluxes of a) radicals and b) ions to the wafer in a TF-CCP sustained in an $Ar/C_4F_8/O_2$ mixture. (Operating conditions: $Ar/C_4F_8/O_2$ = 75/15/10, 25 mTorr, 500 sccm, 80/10/5 MHz power = 0.4/2.5/5 kW.)

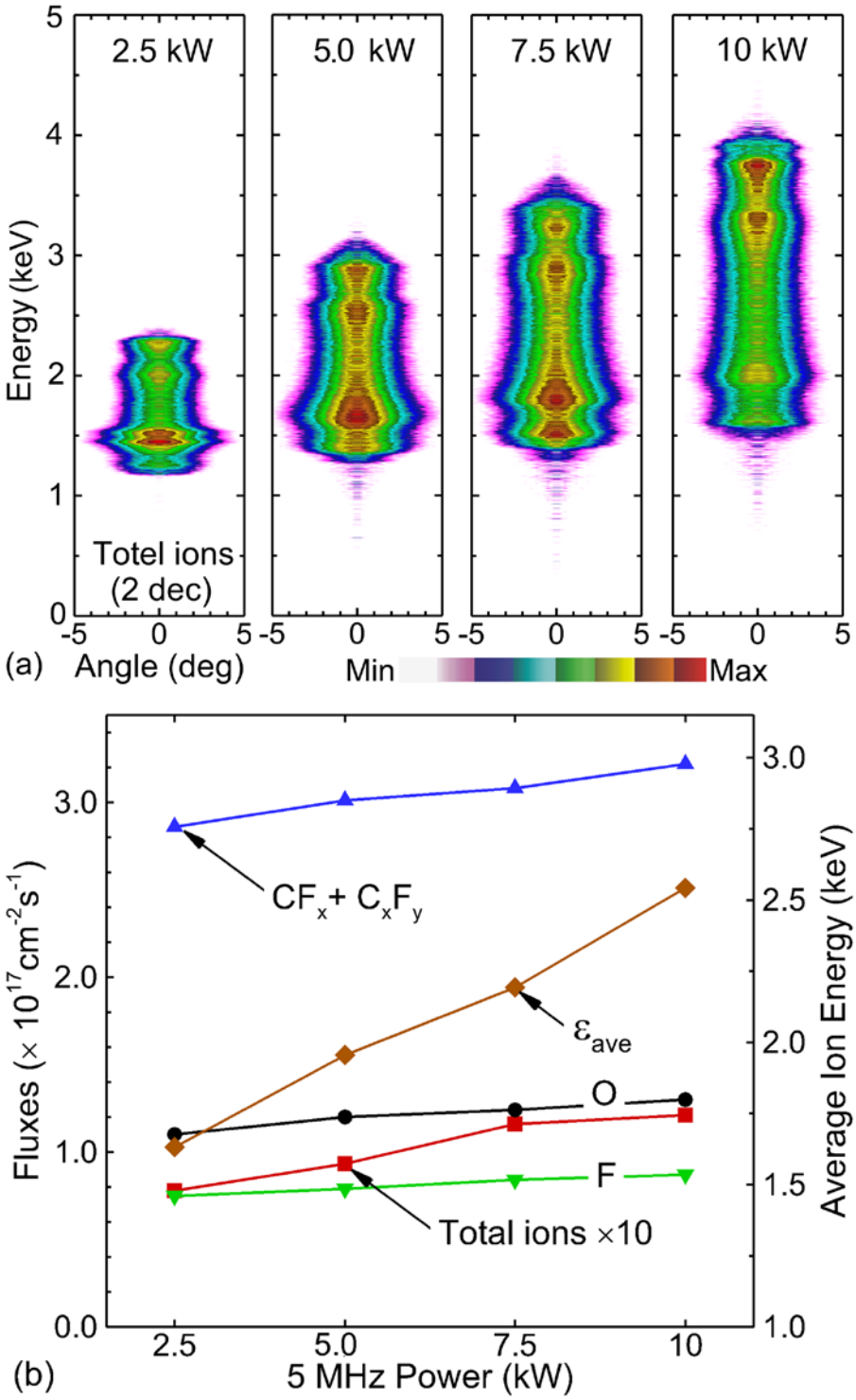

Fig. 6.4 Properties of fluxes to the wafer. a) Ion energy and angular distributions (IEADs) of all positive ions, and b) fluxes of ions and radicals and average energy of ions reaching the wafer at a radius of 7.5 cm for different 5 MHz powers. (Operating conditions: $Ar/C_4F_8/O_2$ = 75/15/10, 25 mTorr, 500 sccm, 80/10 MHz power = 0.4/2.5 kW, 5 MHz power: 2.5 – 10 kW.)

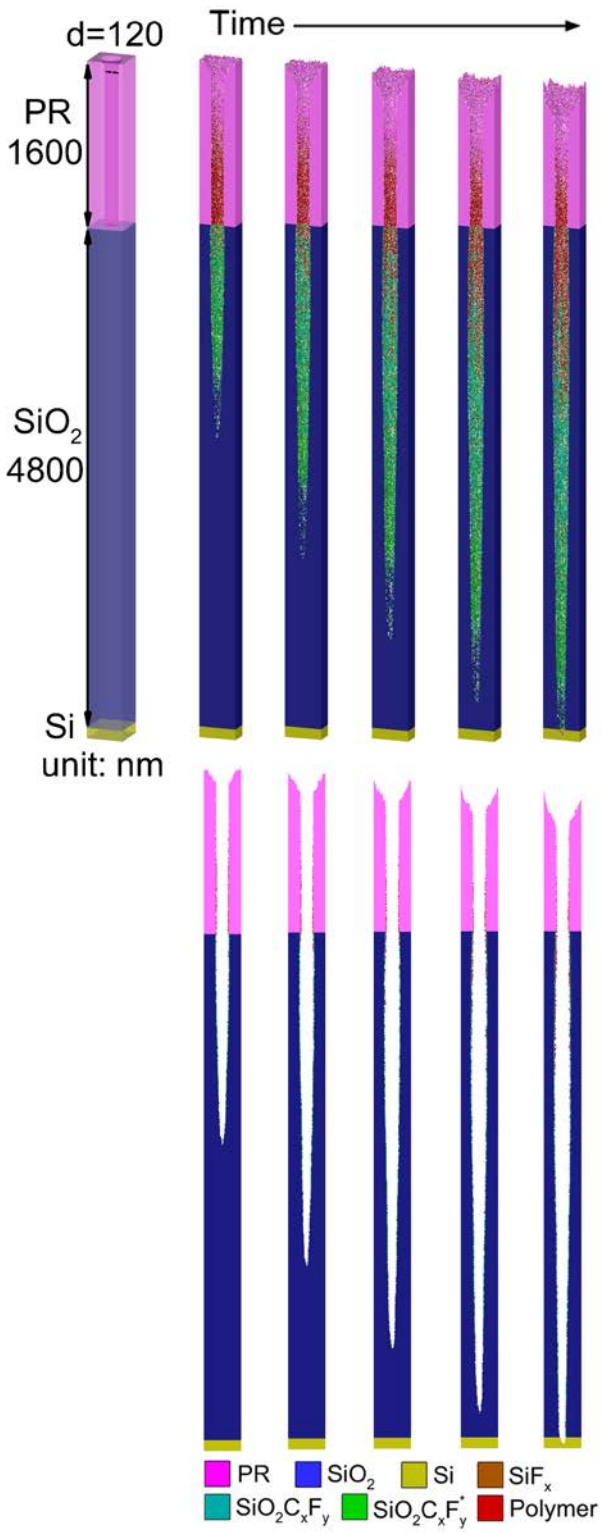

Fig. 6.5 HAR feature etching properties. Section view (top) and central slice (bottom) of the HAR feature showing the time evolution of the etch profile. The height of the SiO_2 is 4,800 nm with 1,600 nm thick photoresist as the mask and Si as the stopping layer. (Operating conditions: $Ar/C_4F_8/O_2$ = 75/15/10, 25 mTorr, 500 sccm, 80/10/5 MHz power = 0.4/2.5/5 kW.)

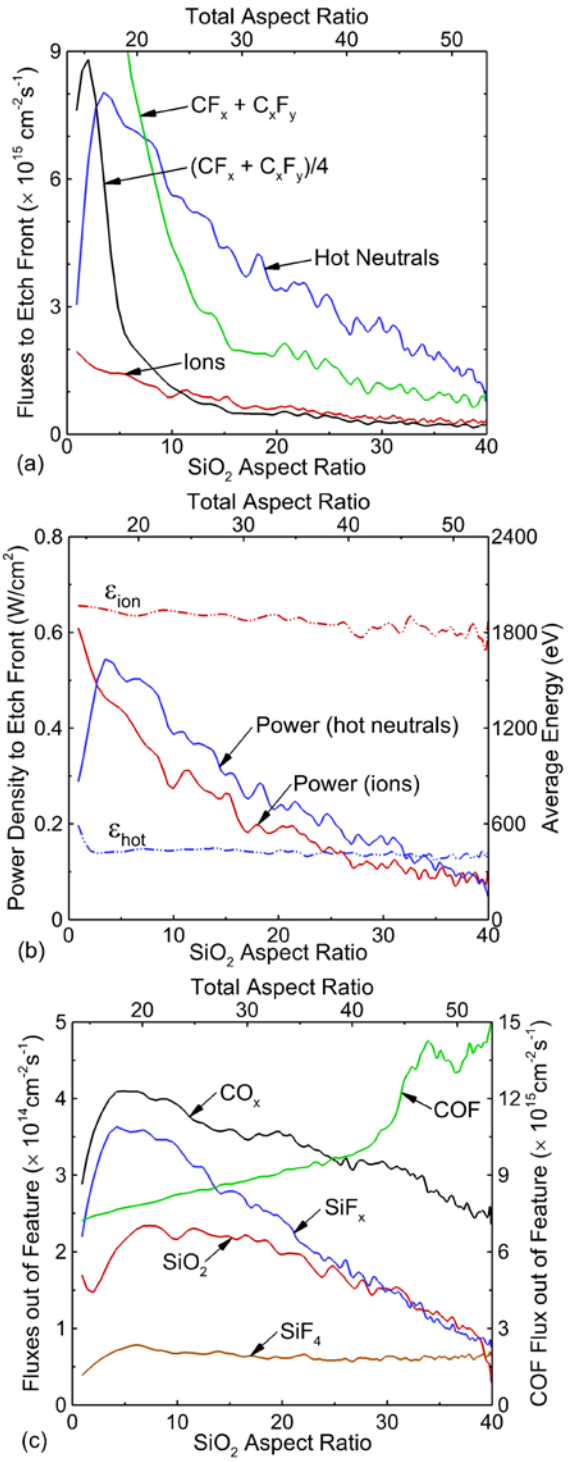

Fig. 6.6 Fluxes and powers to the etch front as a function of aspect ratio. a) Fluxes of ions, hot neutrals, CF_x and C_xF_y radicals to the etch front, b) power delivered to the etch front by ions and hot neutrals and the average energy of ions and hot neutrals to the etch frons, and c) fluxes of etch products leaving the feature as a function of the aspect ratio in HAR during etching. (Operating conditions: $Ar/C_4F_8/O_2$ = 75/15/10, 25 mTorr, 500 sccm, 80/10/5 MHz power = 0.4/2.5/5 kW.)

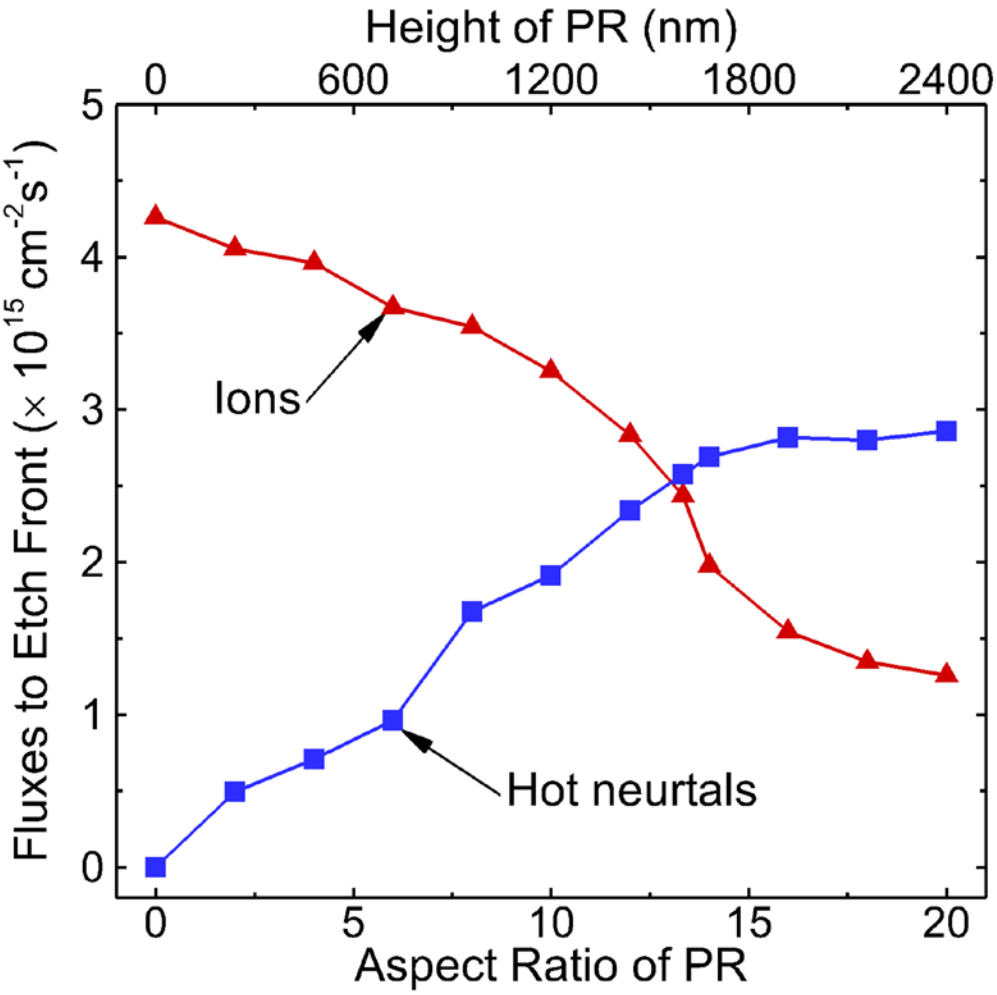

Fig. 6.7 Instantaneous etch rates of oxide and photoresist as a function of aspect ratio in HAR etching. (Operating conditions: $Ar/C_4F_8/O_2$ = 75/15/10, 25 mTorr, 500 sccm, 80/10/5 MHz power = 0.4/2.5/5 kW.)

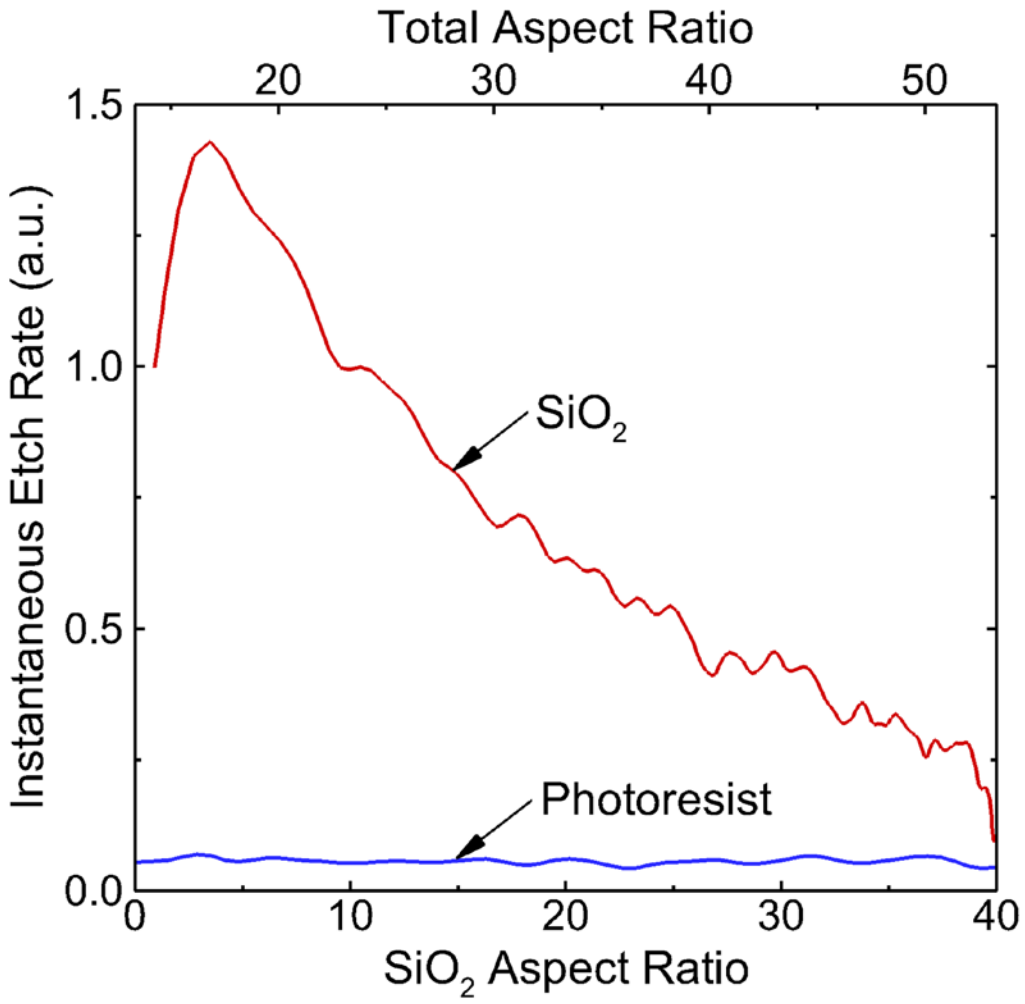

Fig. 6.8 Fluxes of ions and hot neutrals to the etch front at the beginning of the etching process for SiO_2 features while varying the height of the photoresist (PR) from 0 to 2,400 nm. The diameter of initial mask opening in the PR is 120 nm. (Operating conditions: $Ar/C_4F_8/O_2$ = 75/15/10, 25 mTorr, 500 sccm, 80/10/5 MHz power = 0.4/2.5/5 kW.)

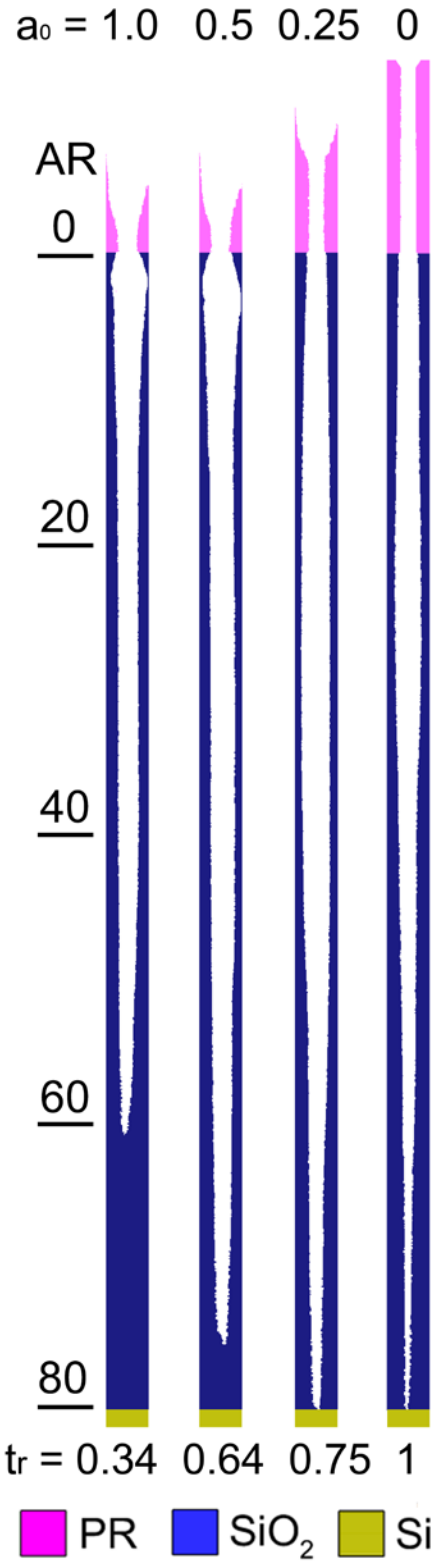

Fig. 6.9 Etch profiles (central slice) for features with aspect ratio of 80 while varying the relative photoresist (PR) etch probabilities, a_0, from 1.0 to 0.5, 0.25 and 0 of the values specified in Appendix E. The relative etch time, t_r, is listed below each profile.

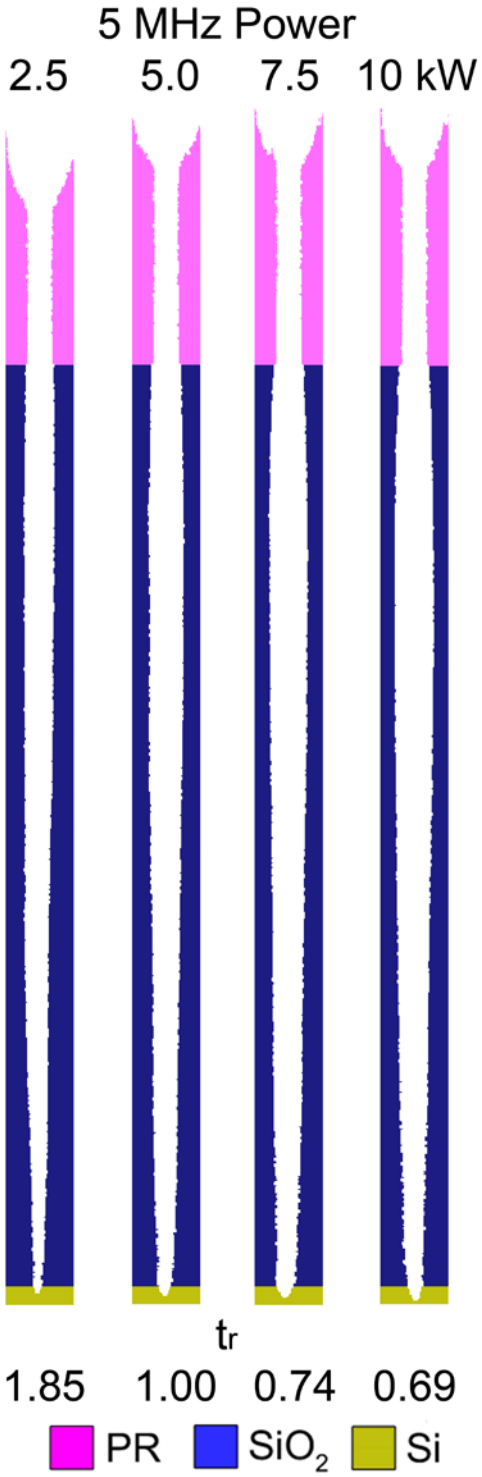

Fig. 6.10 Final etch profiles (central slice) with 10% over-etch of during HAR etching using fluxes and IEADs from the TF-CCP for different 5 MHz powers. Only the photoresist (PR), SiO_2 and Si are shown. The surface complex and polymers have been blanked out.) The relative etch time, t_r, is listed below each profile. (Operating conditions: $Ar/C_4F_8/O_2$ = 75/15/10, 25 mTorr, 500 sccm, 80/10 MHz power = 0.4/2.5 kW, 5 MHz power: 2.5 – 10 kW.)

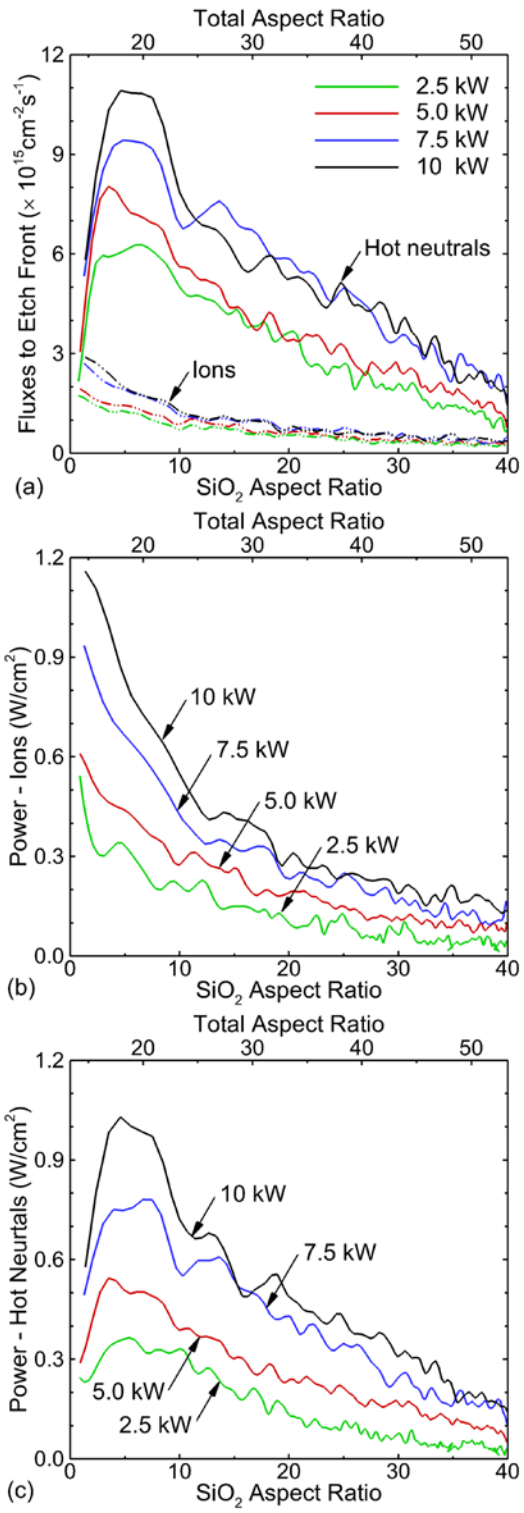

Fig. 6.11 Fluxes and powers to the etch front as a function of aspect ratio and power. a) Fluxes of ions and hot neutrals to the etch front, and power delivered to the etch front by b) ions and c) hot neutrals as a function of the aspect ratio for different 5 MHz powers. (Operating conditions: $Ar/C_4F_8/O_2$ = 75/15/10, 25 mTorr, 500 sccm, 80/10 MHz power = 0.4/2.5 kW, 5 MHz power: 2.5 – 10 kW.)

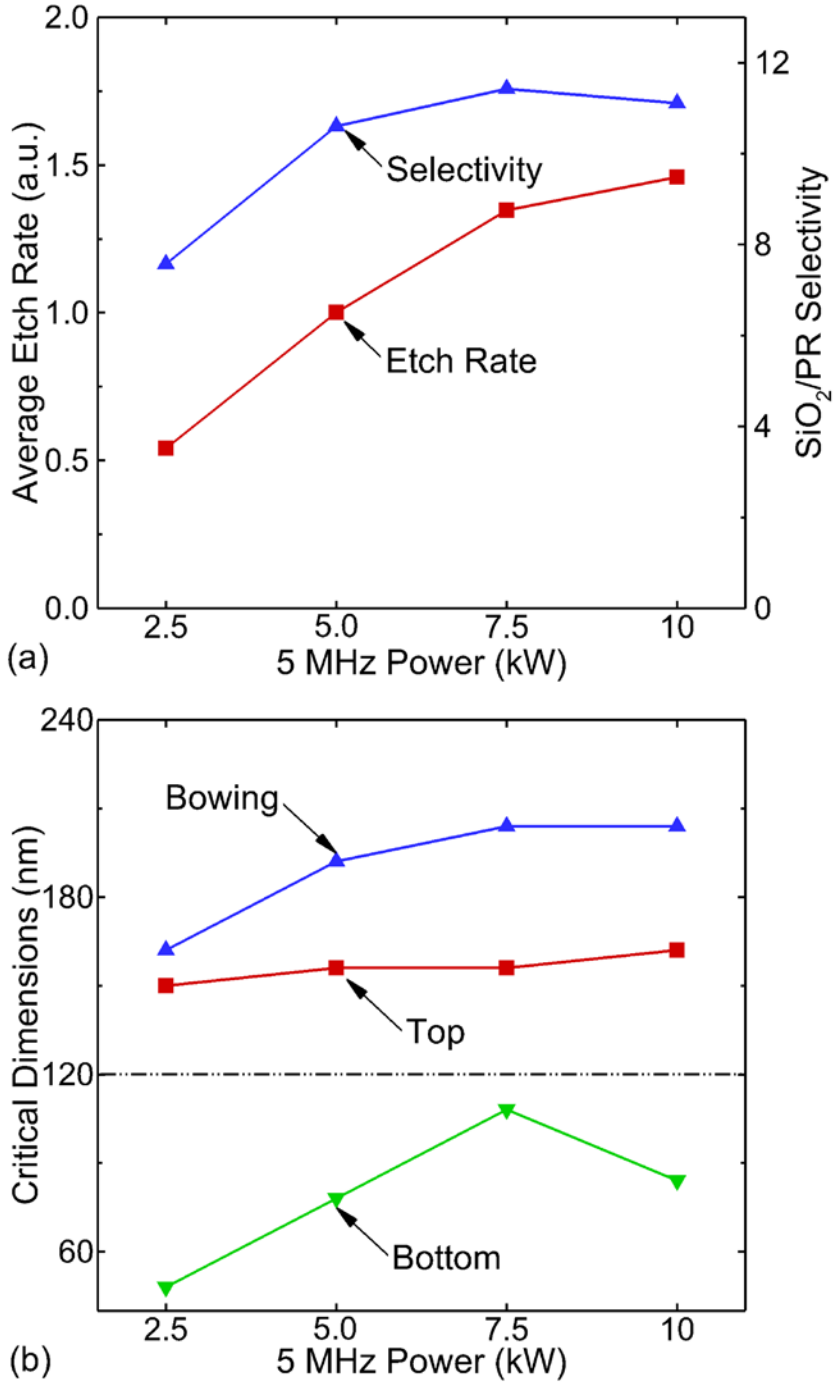

Fig. 6.12 Etch rates and critical dimensions for different 5 MHz power. a) Normalized average etch rate and SiO_2/PR selectivity, and b) top, bowing and bottom critical dimensions with 10% over-etch during HAR etching for different 5 MHz powers. The diameter of the initial mask opening is 120 nm.

Fig. 6.13 Final etch profiles (central slice) with 10% over-etch of during HAR etching for different ($CF_x + C_xF_y$)/ion flux ratios from 5 to 40. Only photoresist (PR), SiO_2 and Si are shown with the complex and polymers being blanked out. The ($CF_x + C_xF_y$)/ion flux ratio in the base case is 30. The fluxes of ions were varied while the fluxes of CF_x and C_xF_y remained constant. The same IEADs from the base case were used in all cases. The relative etch time, t_r, is listed below each feature.

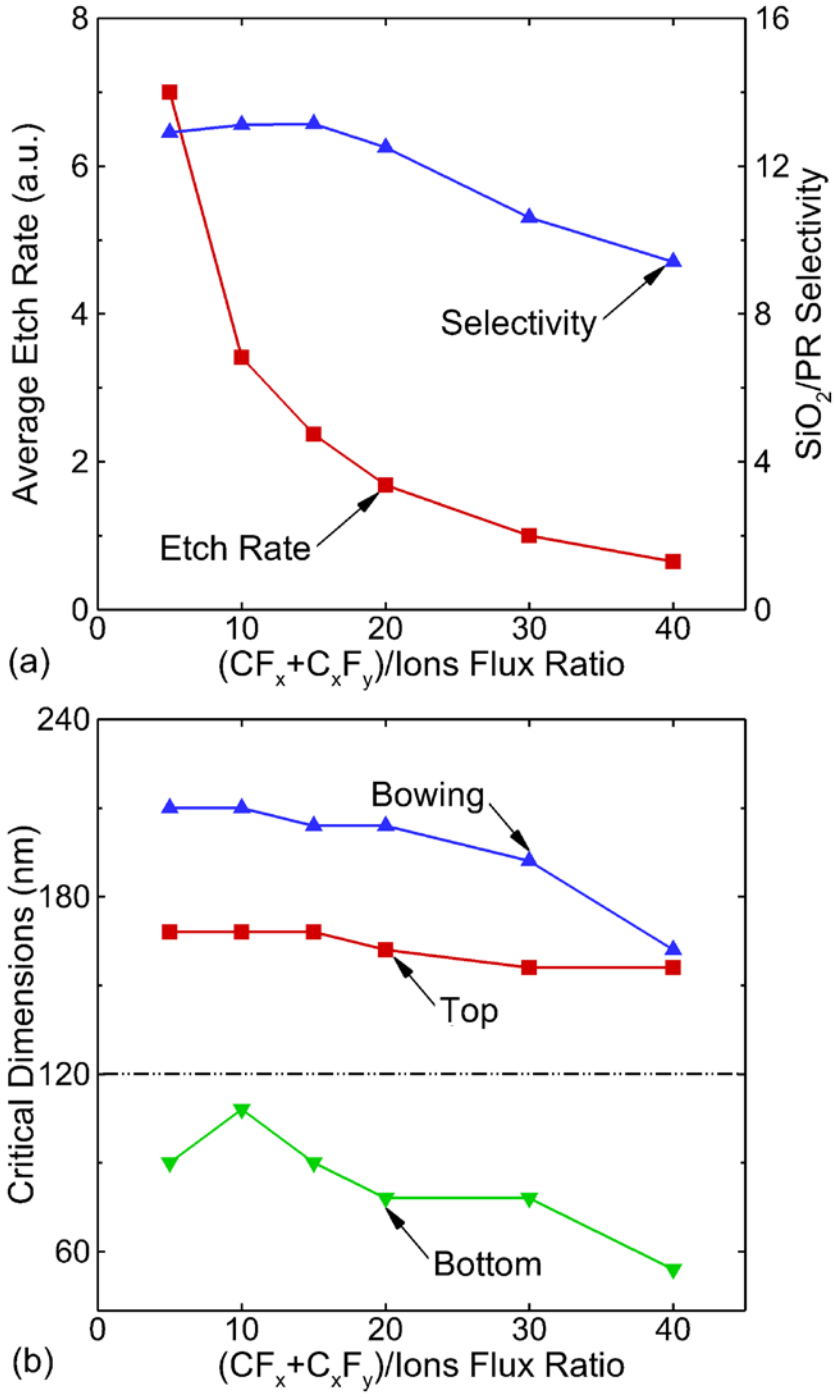

Fig. 6.14 Etch rates and critical dimensions for different radical to ion ratios. a) Normalized average etch rate and SiO_2/PR selectivity, and b) top, bowing and bottom critical dimensions with 10% over-etch for different (CF_x + C_xF_y)/ion flux ratios. The (CF_x + C_xF_y)/ion flux ratio in the base case is 30. The fluxes of ions were varied while the fluxes of CF_x and C_xF_y remained constant. The same IEADs from the base case were used for all cases. The diameter of the initial mask opening is 120 nm.

Fig. 6.15 Final etching profiles (central slice) with 10% over-etch for HAR etching for different fractional CF_x^+ and $C_xF_y^+$. Only the photoresist (PR), SiO_2 and Si are shown with the complex and polymers being blanked out. The fractional CF_x^+ and $C_xF_y^+$ in the base case is 15%. The fluxes of CF_x^+ and $C_xF_y^+$ ions were varied while the total ion flux was maintained constant by decreasing adjusting the flux of Ar^+. The same IEADs from the base case were used for all cases. The relative etch time, t_r, is listed below each feature.

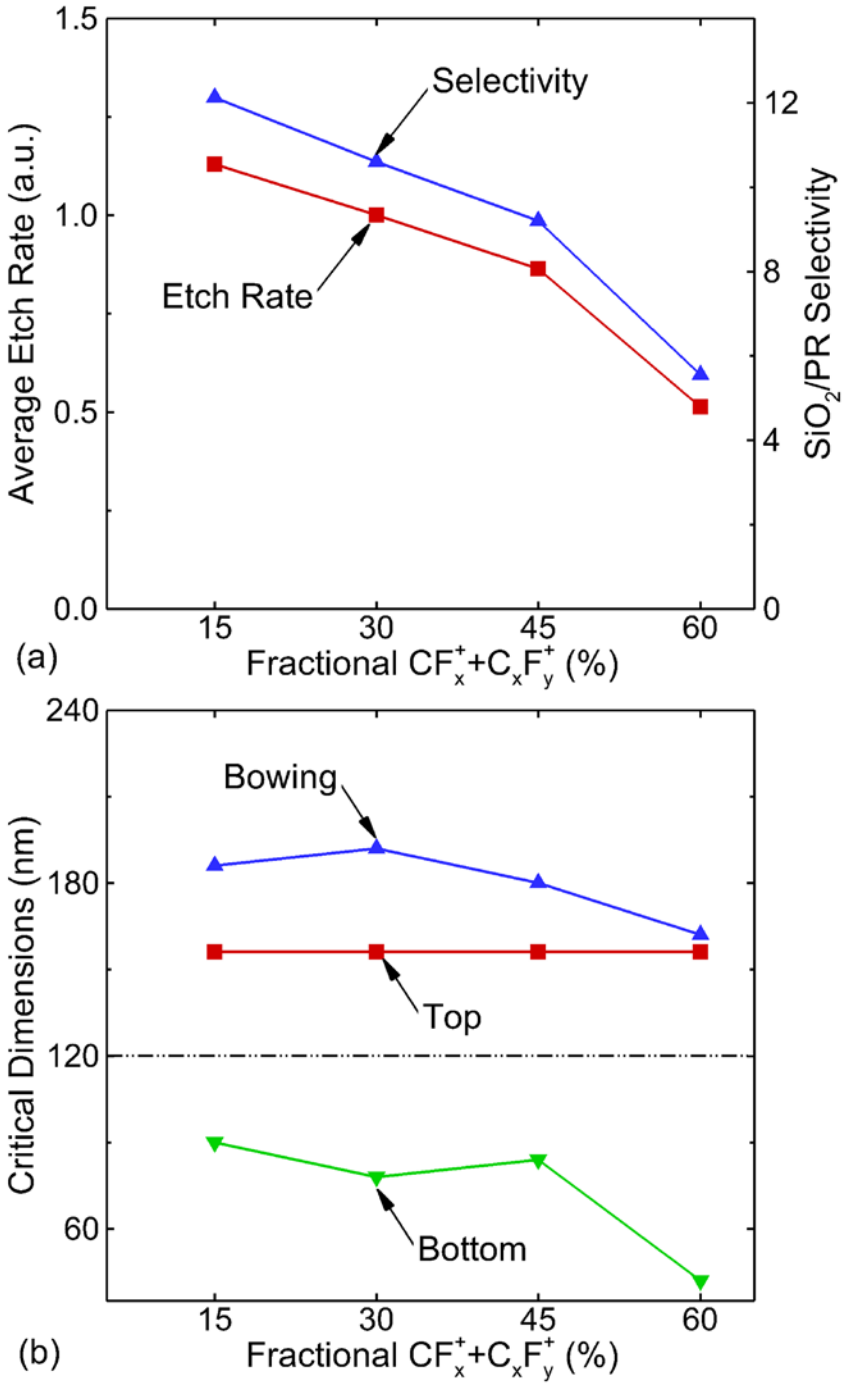

Fig. 6.16 Etch rates and critical dimensions as a function of fluorocarbon ion flux. a) Normalized average etch rate and SiO_2/PR selectivity, and b) top, bowing and bottom critical dimensions with 10% over-etch during HAR etching for different fractional CF_x^+ and $C_xF_y^+$. The fractional CF_x^+ and $C_xF_y^+$ in the base case is 15%. The fluxes of CF_x^+ and $C_xF_y^+$ ions were varied while the total ion flux was maintained constant by decreasing adjusting the flux of Ar^+. The same IEADs from the base case were used for all cases. The diameter of the initial mask opening is 120 nm.

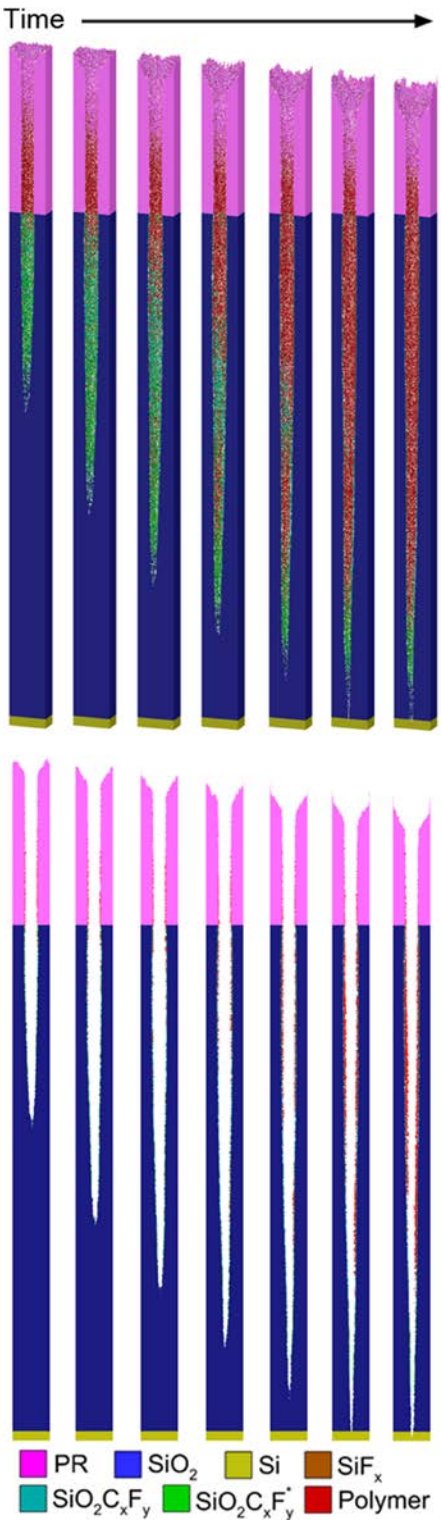

Fig. 6.17 Etch profiles during HAR etching with charging. Section view (top) and central slice (bottom). The same fluxes and IEADs from the TF-CCP were used as for the non-charging cases shown in Fig. 6.5. The time intervals between the adjacent profiles are the same as in Fig. 6.5. (Operating conditions: $Ar/C_4F_8/O_2$ = 75/15/10, 25 mTorr, 500 sccm, 80/10/5 MHz power = 0.4/2.5/5 kW.)

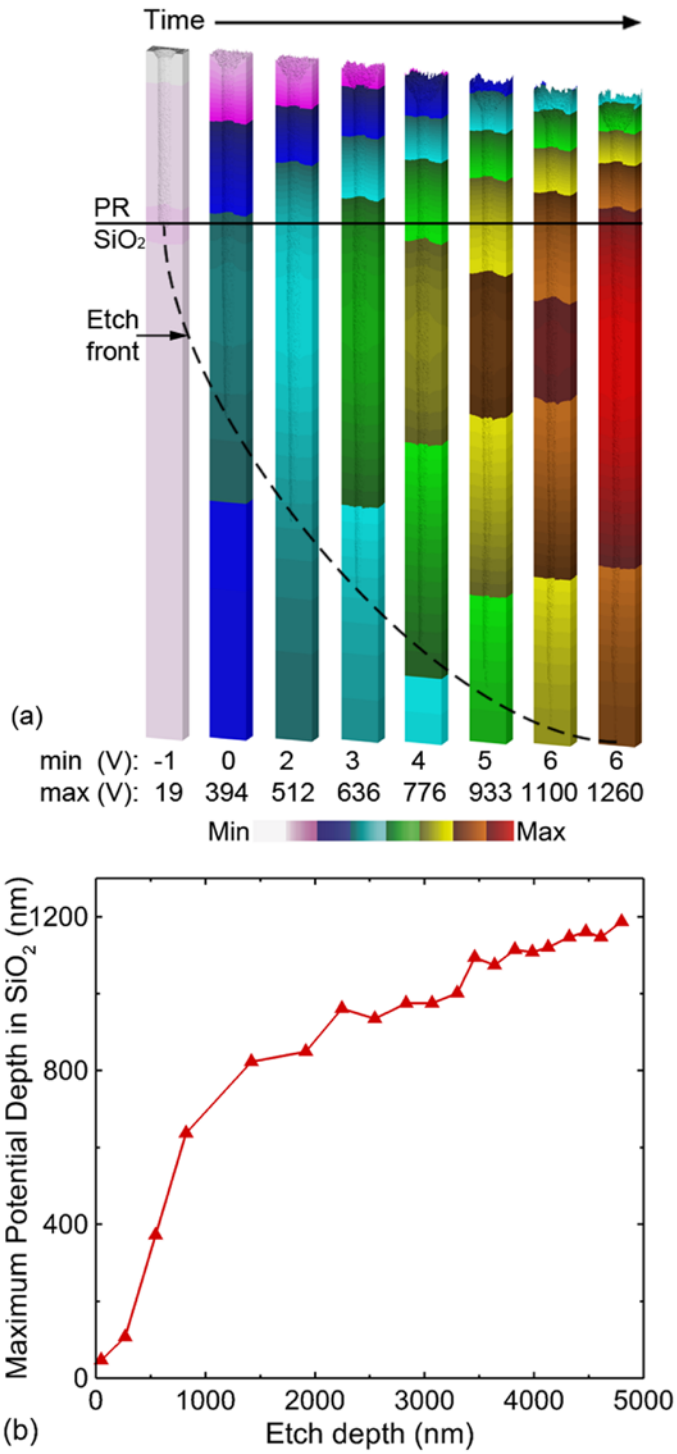

Fig. 6.18 Electrical potential due to charging. a) Time evolution of the electric potential (section view) in the feature and b) correlation between the depth of maximum potential in SiO_2 and the etch depth as the HAR etching proceeds. The first frame in a) is at the very beginning of the etching, while the other 7 frames in a) are sampled from at the same time as in Fig. 6.17. The location of the etch front is shown in a). The same fluxes and IEADs from were used as in the non-charging cases.

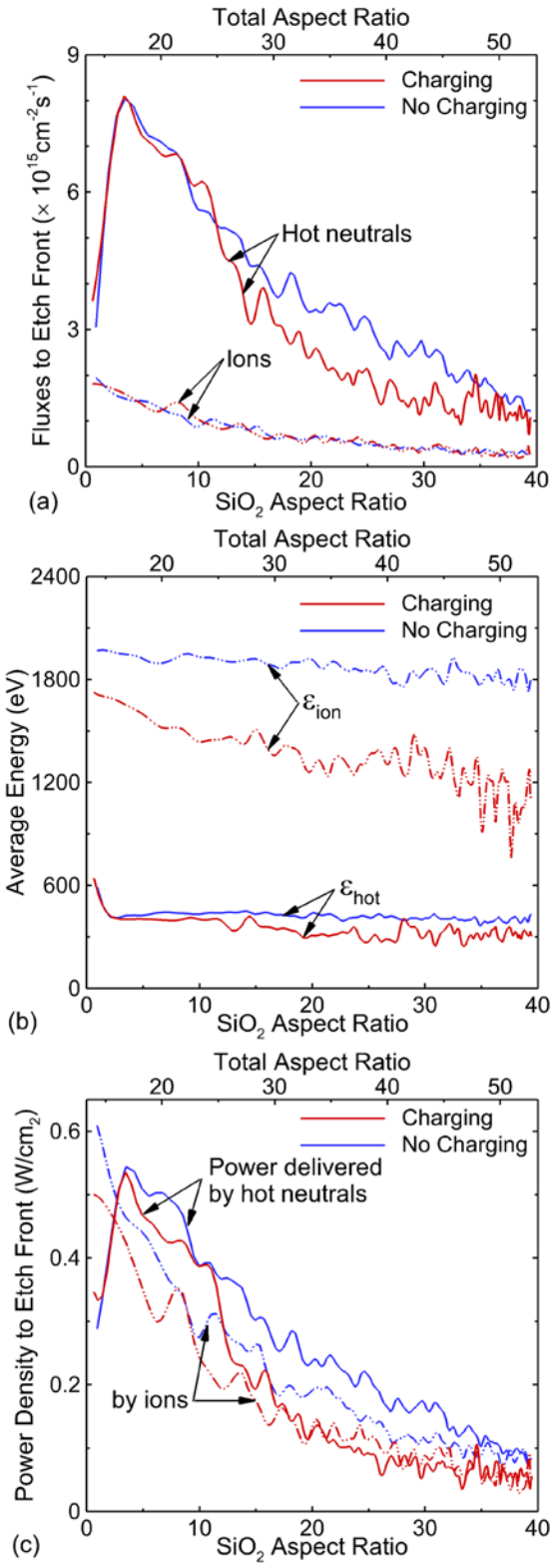

Fig. 6.19 Fluxes and powers to the etch front with and without charging. a) Fluxes and b) average energy of ions and hot neutrals to the etch front, and c) power delivered to the etch front by ions and hot neutrals as a function of the aspect ratio for the base case.

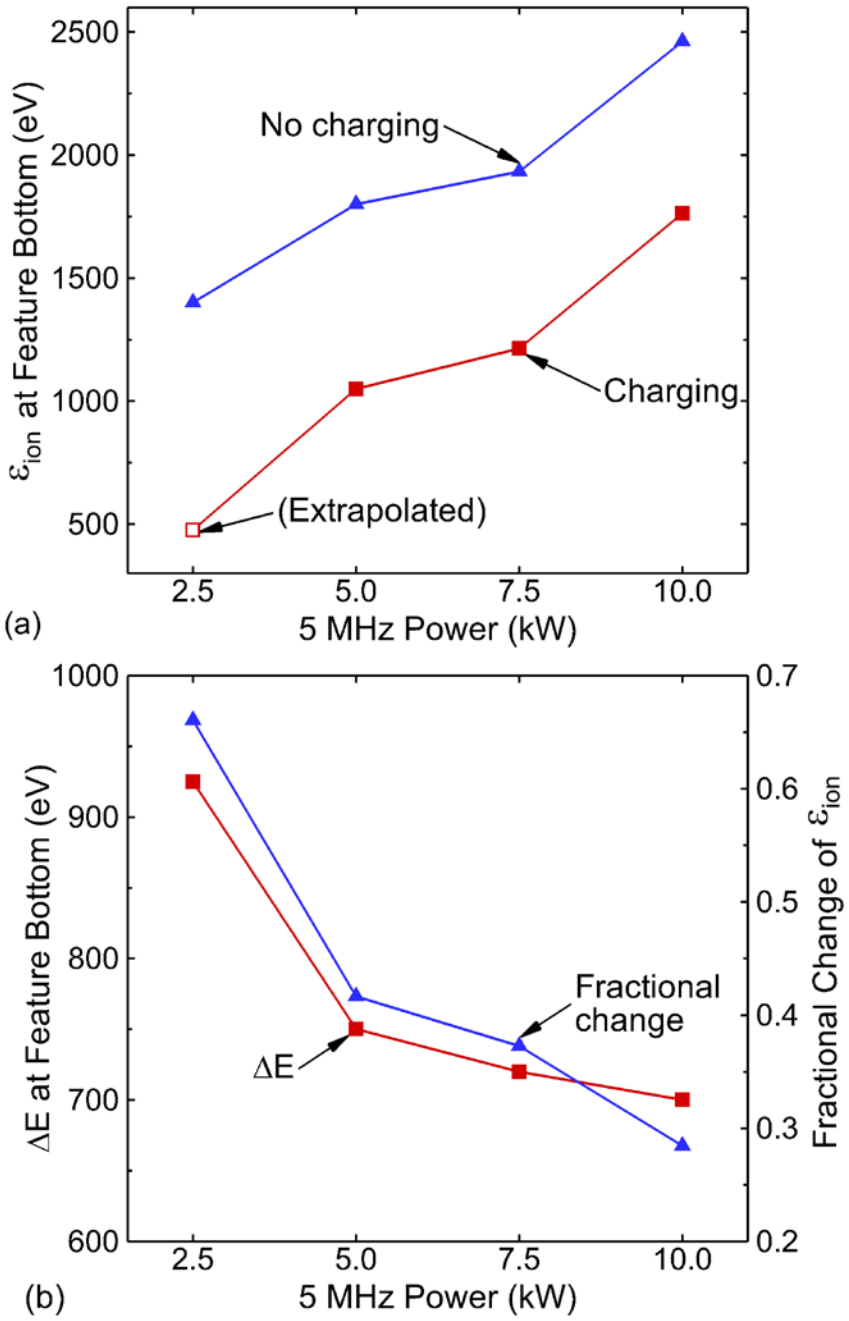

Fig. 6.20 Properties of ions striking the bottom of the feature with and without charging. a) The average energy of ions, and b) the absolute and fractional difference between the average energy of ions reaching the feature bottom for cases with and without charging.

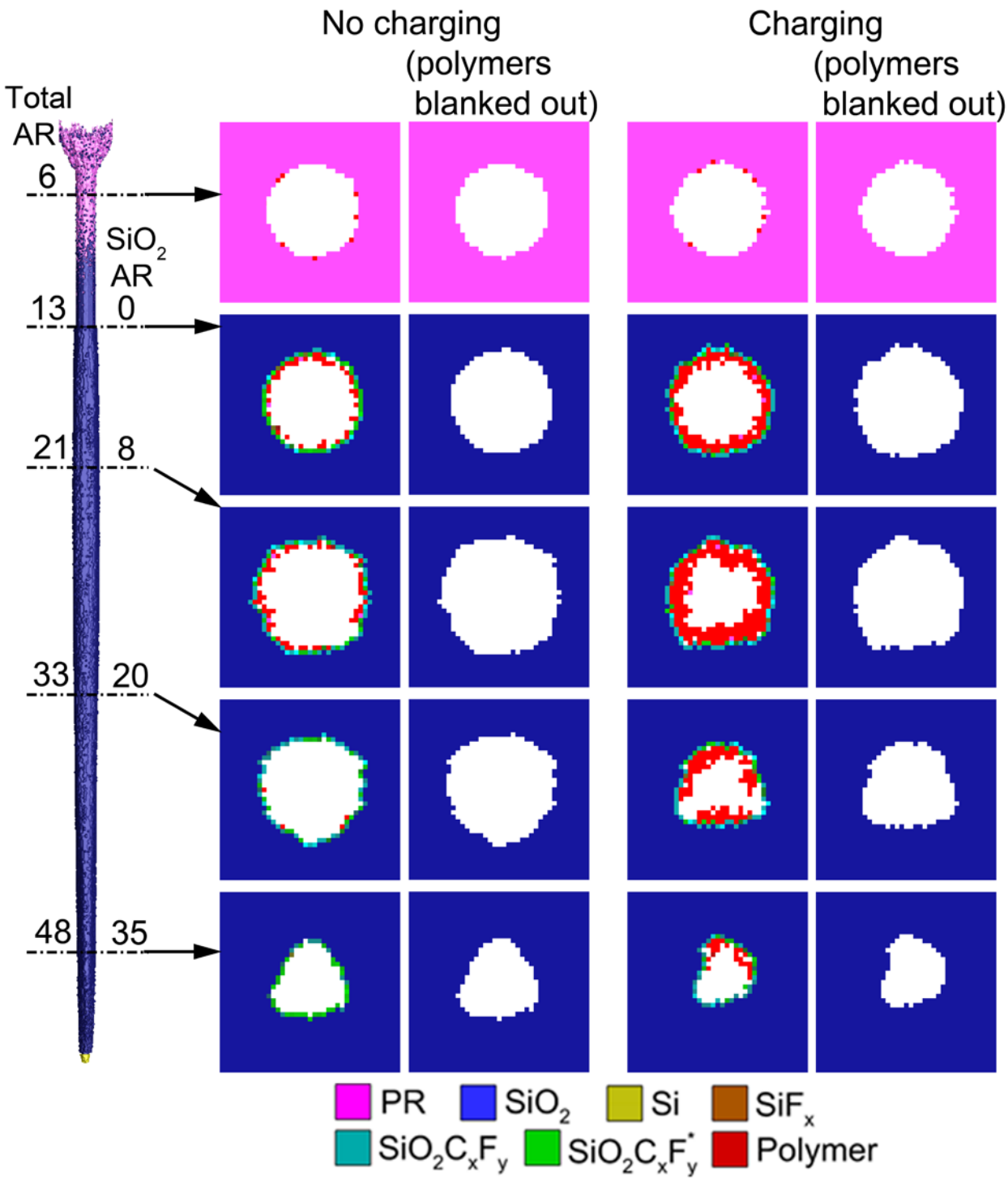

Fig. 6.21 Horizontal slices through the final etching profiles with 10% over-etch for the base case without and with charging. The left column shows profiles with the surface complex and polymers. The right column shows only the photoresist (PR), SiO_2 and Si with complex and polymers being blanked out. Stochastic processes produce non-circular profiles deep in the feature. (Operating conditions: $Ar/C_4F_8/O_2$ = 75/15/10, 25 mTorr, 500 sccm, 80/10/5 MHz power = 0.4/2.5/5 kW.)

6.7 References

1. N. Negishi, M. Miyake, K. Yokogawa, M. Oyama, T. Kanekiyo and M. Izawa, J. Vac. Sci. Technol. B **35**, 051205 (2017).
2. T. Tandou, S. Kubo, K. Yokogawa, N. Negishi and M. Izawa, Precision Eng. **44**, 87 (2016).
3. T. Iwase, M. Matsui, K. Yokogawa, T. Arase and M. Mori, Jpn. J. Appl. Phys. **55**, 06HB02 (2016).
4. B. Wu, A. Kumar and S. Pamarthy, J. Appl. Phys. **108**, 051101 (2010).
5. H. W. Cheong, W. H. Lee, J. W. Kim, W. S. Kim and K. W. Whang, Plasma Sources Sci. Technol. **23**, 065051 (2014).
6. M. Miyake, N. Negishi, M. Izawa, K. Yokogawa, M. Oyama and T. Kanekiyo, Jpn. J. Appl. Phys. **48**, 08HE01 (2009).
7. S.-M. Kim, S. Koo, J.-T. Park, C.-M. Lim, M. Kim, C.-N. Ahn, A. Fumar-Pici and A. C. Chen, Proc. SPIE **9048**, 90480A (2014).
8. K. Ishikawa, K. Karahashi, T. Ishijima, S. I. Cho, S. Elliott, D. Hausmann, D. Mocuta, A. Wilson and K. Kinoshita, Jpn. J. Appl. Phys. **57**, 06JA01 (2018).
9. J. K. Kim, S. H. Lee, S. I. Cho and G. Y. Yeom, J. Vac. Sci. Technol. A **33**, 021303 (2015).
10. V. Constantoudis, V.-K. M. Kuppuswamy and E. Gogolides, J. Micro/Nanolith. MEMS MOEMS **12**, 013005 (2013).
11. C. Petti, Proc. SPIE **10589**, 1058904 (2018).
12. K. J. Kanarik, T. Lill, E. A. Hudson, S. Sriraman, S. Tan, J. Marks, V. Vahedi and R. A. Gottscho, J. Vac. Sci. Technol. A **33**, 020802 (2015).
13. J.-K. Lee, I.-Y. Jang, S.-H. Lee, C.-K. Kim and S. H. Moon, J. Electrochem. Soc. **156**, D269 (2009).
14. J.-K. Lee, I.-Y. Jang, S.-H. Lee, C.-K. Kim and S. H. Moon, J. Electrochem. Soc. **157**, D142 (2010).
15. H. Toyoda, H. Morishima, R. Fukute, Y. Hori, I. Murakami and H. Sugai, J. Appl. Phys. **95**, 5172 (2004).
16. T. Shibano, N. Fujiwara, M. Hirayama, H. Nagata and K. Demizu, Appl. Phys. Lett. **63**, 2336 (1993).
17. N. Kuboi, T. Tatsumi, S. Kobayasgi, T. Kinoshita, J. Komachi, M. Fukasawa and H. Ansai, Appl. Phys. Express **5**, 126201 (2012).

18. N. Kuboi, T. Tatsumi, H. Minari, M. Fukasawa, Y. Zaizen, J. Komachi and T. Kawamura, J. Vac. Sci. Technol. A **35**, 061306 (2017).
19. H. Ito, T. Kuwahara, Y. Higuchi, N. Ozawa, S. Samukawa and M. Kubo, Jpn. J. Appl. Phys. **52**, 026502 (2013).
20. M. Wang and M. J. Kushner, J. Appl. Phys. **107**, 023309 (2010).
21. T. Shimmura, Y. Suzuki, S. Soda, S. Samukawa, M. Koyanagi and K. Hane, J. Vac. Sci. Technol. A **22**, 433 (2004).
22. H. Ohtake, B. Jinnai, Y. Suzuki, S. Soda, T. Shimmura and S. Samukawa, J. Vac. Sci. Technol. A **24**, 2172 (2006).
23. T. Ohmori and T. Makabe, Appl. Surf. Sci. **254**, 3696 (2008).
24. S. Rauf and A. Balakrishna, J. Vac. Sci. Technol. A **35**, 021308 (2017).
25. F. Gaboriau. G. Cartry, M.-C. Peignon and C. Chardinaud, J. Phys. D: Appl. Phys. **39**, 1830 (2006).
26. J. W. Coburn and H. F. Winters, Appl. Phys. Lett. **55**, 2730 (1989).
27. Y. Kim, S. Lee, T. Jung, B. Lee, N. Kwak and S. Park, Proc. SPIE **9428**, 942806 (2015).
28. S. Samukawa and T. Mukai, J. Vac. Sci. Technol. B **18**, 166 (2000).
29. A. C. Westerheim, A. H. Labun, J. H. Dubash, J. C. Arnold, H. H. Sawin, and V. Y. Wang, J. Vac. Sci. Technol. A **13**, 853 (1995).
30. H. Ito, T. Kuwahara, K. Kawaguchi, Y. Higuchi, N. Ozawa, S. Samukawa and M. Kubo, J. Phys. Chem. C **118**, 21580 (2014).
31. T. Kawase and S. Hamaguchi, Thin Solid Films **515**, 4883 (2007).
32. M. Wang, P. L. G. Ventzek and A. Ranjan, J. Vac. Sci. Technol. A **35**, 031301 (2017).
33. D. Kim, E. A. Hudson, D. Cooperberg, E. Edelberg and M. Srinivasan, Thin Solid Films **515**, 4847 (2007).
34. N. Kuboi, M. Fukasawa and T. Tatsumi, Jpn. J. Appl. Phys. **55**, 07LA02 (2016).
35. M. Izawa, N. Negishi, K. Yokogawa and Y. Momonoi, Jpn. J. Appl. Phys. **46**, 7870 (2007).
36. A. V. Vasenkov, X. Li, G. S. Oehrlein and M. J. Kushner, J. Vac. Sci. Technol. A **22**, 511 (2004).
37. A. V. Vasenkov and M. J. Kushner, J. Appl. Phys. **95**, 834 (2004).
38. B. A. Helmer and D. B. Graves, J. Vac. Sci. Technol. A **16**, 3502 (1998).
39. S. B. Wainhaus, E. A. Gislason and L. Hanley, J. Am. Chem. Soc. **119**, 4001 (1997).

40. J. C. Arnold and H. H. Sawin, J. Appl. Phys. **70**, 5314 (1991).
41. J. Matsui, K. Maeshige and T. Makabe, J. Phys. D: Appl. Phys. **34**, 2950 (2001).
42. B. M. Radjenovic, M. D. Radmilovic-Radjenovic and Z. L. Petrovic, IEEE Trans. Plasma Sci. **36**, 874 (2008).
43. G. M. Sessler and J. E. West, J. Appl. Phys. **47**, 3480 (1976).
44. N. Marchack, H. Miyazoe, R. L. Bruce, H. Tsai, M. Nakamura, T. Suzuki, A. Ito, H. Matsumoto, S. U. Engelmann and E. A. Joseph, J. Vac. Sci. Technol. A **36**, 031801 (2018).
45. M. Schaepkens and G. S. Oehrlein, J. Electrochem. Soc. **148**, C211 (2001).

Chapter 7 Pattern Dependent Profile Distortion

7.1 Introduction

In plasma etching for semiconductor fabrication, patterns are transferred from the overlying masks to underlying features, ideally replicating the mask pattern.[1,2] For achieving high selectivity in plasma etching, different mask materials are used such as photoresist (PR), amorphous carbon layer (ACL) and organic planarization layer (OPL).[3] As feature sizes shrink to sub-10 nm, the role of plasma etching becomes extremely important in transferring the complex and miniature patterns into silicon, oxide and metals owing to the anisotropic energy and angular distributions of ions incident to the surface. Despite the prevailing advantage in transferring anisotropic profiles, undesirable feature distortions occur during plasma processing such as twisting, tilting and surface roughening, which were ascribed to several reasons including charging, polymer deposition and pattern dependencies.[4-6] Besides, erosion of the mask by plasmas limits the selectivity and distorts the original pattern in the mask, which can be transferred into the underlying materials.[6,7] As the aspect ratio (AR) increases to higher than 50, slight distortion in mask patterns can lead to tilting and twisting, which decrease the space between adjacent holes and even lead to bridging of adjacent holes.[8,9]

As feature sizes shrink to sub-10 nm, there is no systematic change in the incident fluxes into adjacent features while the randomness becomes the dominant source for the disparity of these fluxes into the adjacent features. This randomness is especially enhanced at high aspect ratio (HAR) etch front due to conduction limit and diffusive reflection at sidewalls for the

etching species.[10,11] The time intervals between particles incident into the feature are much larger than the transit time of the particles in the feature, which makes the profiles sensitive to the sequence of the incident particles. Thus, small variations in energy, angle and sequence of incident etching species in different features may cause feature-to-feature variations in etch performances (e.g., etch rate and selectivity).

Charging on the walls of features by ions can produce interference between neighboring features through the resulting electrostatic fields.[12] In addition to the intrinsic randomness, the electrostatic interference is another source for profile distortion and feature-to-feature variation. With the developing lithography techniques, the critical dimensions (CDs) of the features and the pitch size continuously decrease, resulting in shortened distance between adjacent features and thus enhanced interference through electrostatic charging in the neighboring features.

Etching of multiple HAR holes in patterns by plasmas sustained in fluorocarbon/oxygen mixtures were experimentally investigated with hole diameters of 50 – 200 nm and ARs of 10 – 30 and statistical variations in profiles, etch rates and pattern distortions were observed from feature to feature. By properly adjusting the externally applied magnetic field, high SiO_2 etch rate and high SiO_2-to-ACL selectivity were achieved for inductively coupled plasmas due to increased plasma density.[13] By using a cyclic process of alternating etching and deposition phases, the bowing at low ARs (~ 5) and the variations in CDs at high ARs (> 20) were both reduced, with the anisotropy of the profiles being improved due to polymer deposition at the sidewall during the deposition phase.[14] The polymers deposited at the interface between the mask and the oxide were found to significantly affect the degree of pattern distortion, which could be alleviated by adding an in-situ polymer removal step during the over-etch.[7,15] When the mask is not thick enough, the degraded mask during plasma processing will be transferred to

the features. The degradation of the feature profiles at high ARs was found to be correlated with the roughness in the mask.[6] Suppressing mask degradation was found to decrease feature distortion and alleviate twisting at high ARs when transferring patterns in ACL into SiO_2 with different pitch size.

Feature-to-feature variations become more severe when etching hybrid materials such as alternately deposited oxide-silicon-oxide (O-Si-O) and oxide-nitride-oxide (O-N-O) stacks. In the etching of channel holes in O-Si-O stacks using HBr/fluorocarbon mixtures, the sidewall of the features changed from smooth to scalloped when the ratio of HBr was increased as surface adsorption of N-H and Br was enhanced resulting in reduced polymer thickness and enhanced Si etching.[16] The formation of NH_4Br was found to supply etchants of nitride and oxide to the bottom of the channel holes in the etching of O-N-O stacks using HBr/N_2/fluorocarbon mixtures, alleviating the dependence of the hole opening on the ARs and obtaining flattened etch front and features with high anisotropy.[17]

In the modeling and characterization of feature distortion during plasma etching of source/drain contacts, the effect of random variation in the patterned mask outweighed the effect of systematic variations as the CD decreases below 32 nm.[18,19] A voxel-slab model was used to investigate contact hole etching in SiO_2, showing that profile distortion due to physical damage in the SiO_2 was reduced by maintaining a critical thickness of the overlaying polymer.[20,21] A Monte Carlo model based on 3-d lattices indicates correlations between ion bombardment and surface roughness, which can be smoothed by reducing the effect of ions by introducing etch inhibitors.[22]

In this chapter, results are discussed from a computational investigation on feature distortion during pattern transfer from photoresist to underlying SiO_2 using tri-frequency

capacitively coupled plasmas (TF-CCPs) sustained in $Ar/C_4F_8/O_2$ mixtures. The reactor scale modeling was performed using the Hybrid Plasma Equipment Model (HPEM). The feature scale modeling was performed using the 3-dimensional Monte Carlo Feature Profile Model (MCFPM). The feature-to-feature variations mainly result from randomness in the fluxes of particles into the features rather than reactor scale non-uniformities when the critical dimensions decrease to several tens of nm or even smaller. The charging of the features in symmetric patterns results in feature tilting towards random directions, while in asymmetric patterns resulting in tilting towards preferential directions along the horizontal E-field induced by the electric potential skewing. The tilting can be alleviated or removed by increasing the bias power during plasma processing, which elevates the ion energy and decreases the etch time, resulting in decreased horizontal E-field and its effect on deviating the ion trajectories in adjacent features.

Descriptions of the models used in this chapter are in Sec. 7.2. Results and discussions on the etching of multiple vias in different patterns (array, off-axis and square) are presented in Sec. 7.3. Concluding remarks are in Sec. 7.4.

7.2 Description of the Models

The integrated reactor and feature scale modeling was used for investigating plasma etching of multiple HAR vias in SiO_2 using TF-CCPs. The fluxes of ions and radicals and the ion energy and angular distributions (IEADs) were obtained from the reactor scale modeling with the HPEM, which were used as the input parameters for the feature scale modeling with the MCFPM. The major modules used in the HPEM are the Fluid Kinetics Poisson Module (FKPM), the Electron Energy Transport Module (EETM) and the Plasma Chemistry Monte Carlo Module (PCMCM), which are described in Sec. 2.2. The $Ar/C_4F_8/O_2$ gas mixtures were

used for oxide etching. The species and gas phase reactions included in the reaction mechanism are the same as in Chapter 6 and described in Sec. 6.2.

The MCFPM is a 3-dimensional cell-based model utilizing rectilinear mesh with fine enough resolution (less than a few nm) to predict the profile evolution during plasma processing, described in detail in Sec. 2.3. Briefly, in MCFPM each cell within the mesh may represent a different solid material. Gas phase pseudoparticles are launched with their initial velocity sampled from the IEADs obtained from the HPEM. During the execution of MCFPM, the charging subroutine is called to solve the Poisson equation after hundreds of pseudoparticles are released so as to address the buildup of the electrostatic potential by the ions and electrons that deposit their positive and negative charges on the surface. The trajectories of ion and neutral pseudoparticles are tracked within the feature until they either react or leave the computational domain. The surface reaction mechanism used in MCFPM for modeling profile evolution in SiO_2 by $Ar/C_4F_8/O_2$ plasmas is described in Sec. 3.3.2.

7.3 Etching of Multiple Vias in Patterns

The geometries of the multiple HAR vias and the patterns in the PR after lithography process are shown in Fig. 7.1. Three patterns were studied here, which are 4 vias in a linear array, in off-axis arrangement and in 2 by 2 square pattern. Reflective boundary conditions were applied for determining the reflection of particles when reaching the boundaries of the simulation domain and the five-point stencils in solving the Poisson equation. By applying periodic boundary conditions, the unit pattern shown in Fig. 7.1 can represent full-pitch (for array and square unit) and half-pitch patterns (for off-axis unit).

The distance between the center of the adjacent vias are set to be the same (100 nm) for

the 3 patterns. The thickness of the SiO_2 is 2,000 nm, with 670 nm thick PR as the mask and Si as the stopping layer. The diameter of the holes in the PR mask is 50 nm. The meshes consist of $40 \times 160 \times 1084$ cells for linear pattern, $59 \times 146 \times 1084$ for off-axis pattern and $80 \times 80 \times 1084$ for square pattern, producing cubic voxels of 2.5 nm on a side. The total aspect ratio including the mask at the start of etching is 53. Unless otherwise stated, the aspect ratio in the following context denotes the aspect ratio of the feature only in the SiO_2, which varies from 0 at the beginning to 40 when the etch front reaches the stopping layer.

The fluxes of the ions and radicals, and the ion energy and angular distributions used for etching of multiple HAR vias were obtained from the reactor scale modeling of a TF-CCP sustained in $Ar/C_4F_8/O_2$ mixtures, which are shown in Figs. 6.3 and 6.4 and discussed in Sec. 6.3. Among the gas mixtures, Ar is mainly used to provide energetic Ar^+ ions incident on the surface for activation. C_4F_8 is dissociated by electron impact to produce polymerizing CF_x and C_xF_y species, which deposit at the surface of the oxide and serve as the fuel to remove silicon and oxygen sites while protecting the sidewalls. O_2 is mainly dissociated to O atoms which are used to leverage the amount of polymer deposition at the surface to avoid clogging while allowing etching species (e.g., ions and neutral radicals) to reach deeper features.

Three frequencies were used to provide large dynamic range for tuning the plasma properties and the IEADs. The 80 MHz power applied on the top electrode was mainly used as the source power for sustaining the plasmas. The 10 MHz and 5 MHz powers applied on the bottom substrate were mainly used to accelerate the ions to the surface with customized IEADs. For the base case, the powers of the three frequency sources (80/10/5 MHz) were set to be 400/ 2,500/5,000 W. The corresponding voltages to deliver the specified powers were 125/1,030/2,450 V, with a dc bias of -1,690 V. The ions have high energy (1,400 – 3,000 eV)

and narrow incident angles (less than 3^o), which are desirable for HAR etching in reducing sidewall impacts and producing anisotropic profiles. Charging of the features is not considered in Sec. 7.3.1 and 7.3.2. The effect of charging during the etching of multiple HAR vias is discussed in Sec. 7.3.3. The feature distortion for asymmetric patterns is discussed in Sec. 7.3.4.

7.3.1 Feature-to-feature Variation

The section view cleaved through the center of the 4 vias in an array and the central slices for the time evolution of the feature profile during plasma etching are shown in Fig. 7.2. The time spacing between each frame is equal. As to individual vias, the general trend of profile evolution is quite similar to the single HAR via shown in Fig. 6.5 and discussed in Sec. 6.4. Key features are captured including eroded PR mask, bowing in the upper portion of the features at AR of 5 and tapered etch front. Due to sputtering of energetic ions, the PR is eroded during plasma etching, resulting in a SiO_2-to-PR selectivity of 10. The erosion leads to roughness on the top and beveled surfaces of the PR.

As the etching proceeds, the etch front of each via all propagate strictly downwards (normal to the surface), without tilting or twisting. As the pitch of the pattern is 100 nm, there is no systematic change in the incident fluxes at this tiny distance according to the fluxes of radicals and ions to surface from the center to the edge of the wafer shown in Fig. 6.3. The randomness, or stochastic nature, becomes the dominant source for the disparity of these fluxes into adjacent features resulting in feature-to-feature variation.

With the diameter of the hole in PR being 50 nm and fluxes of ions and radicals incident into the hole being about 10^{15} $cm^{-2}s^{-1}$ and 10^{17} $cm^{-2}s^{-1}$, the ions and radicals incident into the feature with time interval of 10^{-5} s and 10^{-7} s, respectively. For the energy of the ions and hot neutrals (~ 1,000 eV) and the thermal neutrals (~ 0.03 eV), the transit time through the feature or

the traveling time within the feature before leaving is about 10^{-10} s (for ions and hot neutrals) and 10^{-8} s (for thermal neutrals), resulting in ions and radicals almost released into the feature one after another. Adjacent features will receive different number of species, different sequences of these species, and different energy and angles of each individual species. These differences cannot be rectified or averaged out during the whole processing time and so feature-to-feature variations in etch properties and consequent profiles occur. Due to the conduction limit, the fluxes of ions and radicals decrease by a factor of 10 and 50 as the AR in SiO_2 increases from 0 to 40 as indicated in Fig. 6.6(a), which enhances the randomness and stochastic variation in the etching species reaching the etch front. Furthermore, the MCFPM uses pseudoparticles with a weighting factor of several hundred (390 in the cases in this chapter) to represent gas phase particles, which exaggerates the effect of the stochasticity in sampling the pseudoparticles from the total fluxes as well as sampling energy and angle of the ions from the IEADs.

Due to the stochastic variations in the number, sequence, energy and angle of the incident particles into the features, the profiles in Fig. 7.2 show a maximum of 7% difference in the etch rates and 5% difference in the bowing CDs. One solution for removing or mitigating the feature-to-feature variation in the etch rate and CDs is to allow for some over-etch time to ensure that all the features are etched through and the bottom CDs are wide enough for the subsequently deposited contact metal to be enough conductive, with slight sacrifice in selectivity and bowing CDs. Fig. 7.3(a) shows the surfaces of the final etch profiles with 10% over-etch for different patterns. By allowing for 10% over-etch, the etch fronts all reach the stopping layer with at least 20 nm hole opening at the bottom. The bowing CDs slightly vary from feature to feature by less than 5%, with the maximum bowing CD being 72 nm. Overall, the disparities in feature profiles originating from small features and sparse species can be diminished by allowing for over-etch.

7.3.2 Contact Edge Roughness

Ideally the initially circular mask opening in the PR should be faithfully transferred to the feature during plasma processing. Due to non-uniformities and stochastic processes during plasma etching, feature distortions such as contact edge roughness (CER), line edge roughness (LER) or elliptical profiles can be developed.[7,23,24] The horizontal sections of the multiple vias in different patterns at ARs of 10 and 30 are shown are shown in Fig. 7.3(b). Profiles with polymers blanked out indicate the profiles obtained after cleaning process, which are prepared for subsequent steps such as metal or polysilicon deposition. Overall the profiles are close to circular with profiles at AR = 30 having smaller diameters (≈ 50 nm) and more anomalies due to tapering of etch front and profiles at AR = 10 having larger diameters (≈ 70 nm) and being more circular due to bowing.

As the etching proceeds, the PR is eroded by ion sputtering, resulting in PR having rough beveled and top surfaces as shown in Fig. 7.3(a). The PR isolation between adjacent vias becomes less stringent with the beveled surfaces of adjacent holes connecting each other. If the PR is not thick enough and becomes eroded to the extent that the beveled surface extends down to the SiO_2, scattering of the ions from the roughened beveled surfaces into the feature will be a significant source for CER. As the PR maintains thick during the whole etching process (only 30% loss of thickness), most of the ions incident onto the beveled surfaces are reflected back to the plasmas, the effect of the eroded PR and roughened beveled surfaces are negligible to the occurrence of CER in the SiO_2. A small amount of roughness occurs on the sidewalls of the PR due to the randomness in the grazing angle of ions sputtering the mask. This roughness then results in more diffusive scattering of grazing ions, which contribute to the edge roughness in SiO_2.

The horizontal section profiles in Fig. 7.3(b) indicate that even when we start from perfect circular mask obtained from lithography-development process, the roughness still occurs almost ubiquitously for most of the features after plasma processing. The CER in the SiO_2 mainly originate from the randomness in the energetic ions and polymerizing radicals into the features. Due to small amount of ions into the feature, the activation energy provided by the ions can hardly be uniformly distributed along the circumference of the feature at a specific AR during the whole processing time. Non-uniform polymer deposition along the sidewall surface adds on to the roughness caused by ions, especially at high AR (= 30) where only small portion of the surfaces are covered by polymers due to conduction limit as compared to low AR (= 10) where almost all surfaces are covered by polymers as shown in Fig. 7.3(b). These two non-uniformities result in differences in the etch rate in different radial directions at a specific AR, which is the CER shown from the horizontal slices of the features. At high ARs, partial polymer deposition preferentially protects the sidewall from being etched in specific directions and lead to serious feature distortion into anomalous profiles (e.g., triangle, spike and oval) for individual features and also feature-to-feature variations in CER.

7.3.3 Charging of Features

Charging of the surfaces on the top and inside of the feature occurs in dielectric etching or in conductor etching using polymerizing gas mixtures. The same patterns in PR, dimensions of the geometry, fluxes of radicals and ions and IEADs as the base cases were used with charging effects considered here. The time evolution of the etch profiles during the etching of 4 HAR vias in a linear array are shown in Fig. 7.4, with the same time intervals as those for the non-charging case shown in Fig. 7.2 so that side-by-side comparisons can be made.

The ion pseudoparticles are launched with velocities sampled from the IEADs obtained

from the HPEM. A corresponding flux of electron pseudoparticles is launched to provide charge neutrality, with velocity randomly chosen from an isotropic Maxwellian distribution having a specified temperature (4 eV in this case). Due to the computational expense of solving Poisson equation, the potential is updated only after 400 charged particles strike the surface. During the execution of the MCFPM, millions of charged particles are launched. Reflective boundary conditions for electric potential are used in the lateral (x-y) dimensions and a zero-gradient boundary condition is used on the top surface of the computational domain. The bottom of the computational domain is grounded. Three thin layers were added between the stopping layer and the ground plane with their dielectric constants adjusted so that the capacitance of the feature with respect to the ground plane is the same as for the actual thickness of the wafer.

After the charging is considered, the time for the etch front to reach the Si stopping layer is about 30% longer than the non-charging case in Fig. 7.2, with more polymer deposition at the sidewall and tapered etch front. For a single via, the differences in feature profiles and etch properties between the charging and non-charging conditions are discussed in Sec. 6.4.4. For multiple vias in a pattern, when the charging is considered, the features have slight tilting at high ARs (> 30) in Fig. 7.4 as opposed to the non-charging case in Fig. 7.2 in which all the profiles strictly etch downwards. As the AR increases during etching, the feature-to-feature variation becomes reinforced, rather than being attenuated, due to less ions and radicals reaching deeper features which are more subject to randomness. The tilting randomly occurs for some vias in arbitrary directions, as indicated in the surfaces of the final etch profiles for different patterns shown in Fig. 7.6(a). Once slight tilting is preferentially developed in one direction at low ARs, it will be enhanced and transferred into deeper features, rather than rectified or reversed, in continuous etching process without self-limiting or self-healing mechanism implemented. Take

the array pattern as an example, the second feature from the right slightly tilts rightwards while the first feature from the right slightly tilts leftwards at AR of 20 shown in Fig. 7.4. As the AR increases to 40, the tilting directions of these two features are still maintained with their etch front becoming closer with a distance of 90 nm, which is smaller than the PR pattern by 10 nm (10% loss in pitch).

The density of charges deposited at the top and inner surfaces of the features and the induced electrostatic potentials by these charges are shown in Fig. 7.5, with the same time intervals as in Fig. 7.4. The electrons predominantly deposit at the top surfaces, beveled surfaces and the shallow sidewalls of the PR, reaching a maximum of -46.4 C/cm^2 occurring at the beveled surface of the PR. The positive ions reach the deep features due to anisotropic IEADs with incident angle less than 3^o. The positive ions deposit their charges and return as hot neutrals after hitting the surfaces. With the accumulation of the positive charges in the SiO_2, the position of maximum electric potential occurs in the middle of the feature at AR = 15, which is the place where most ions first hit the sidewalls. An electric field is established pointing from the middle of the feature upwards to top surface, extracting the electrons into the inner surface for neutralization.

On a blanket (not patterned) surface, ions are accelerated to the surface by the time averaged sheath potential while the electrons reach the surface during the anode portion of the rf cycle. The equal fluxes of electrons and ions over the whole rf cycle results in charge neutrality at the surface. However, patterned surfaces customize the fluxes of electrons and ions into the features due to the difference in their energy and angular distributions, which results in spatial variation of the charge distribution and thus electric potential along the inner sidewalls of the features in SiO_2. Due to the reflective boundary conditions and the symmetric arrangement of

the vias, the potential in Fig. 7.5 is quite uniform, with a maximum of 1,040 eV at AR of 15 when the etch front reaches the stopping layer. Due to the uniform potential in the horizontal direction, there is little electrostatic interference between the adjacent vias due to almost no horizontal component of the electric field. The disparities in the etch profiles and the slight tilting at high ARs are mainly due to randomness of the incident species.

Horizontal slides at ARs of 10 and 30 of the final etch profiles with charging included are shown in Fig. 7.6(b). The polymer deposition at AR = 10 is very severe, with an average thickness of about 10 nm at the sidewalls. This is mainly due to decreased bombardment energy of ions after deceleration by the electric field and increased amount of polymerizing species which are converted from CF_x^+ and $C_xF_y^+$ ions through deceleration by the electric field and neutralizing at the sidewalls. The thick polymer layers at AR = 10 result in the profile of the polymer surface forming a pattern which filters and limits the incident species from reaching the deep features. Due to the thick polymer layers, the filtering pattern is small (diameter of about 40 nm or less), the effective aspect ratio at the bottom of the feature becomes 50, rather than 40 in the cases with thin polymer layers, resulting in even less particles (less by about 40% for hot neutrals and about 5% for thermal neutrals and ions) and enhanced randomness reaching the bottom of the feature compared with the non-charging base case. Due to the non-uniform and porous polymers, the filtering pattern is anomalous with rough surface, which may inhibit the energetic species with anisotropic velocities from transferring the circular pattern from the PR into the deep oxide. Therefore, the edge profiles at AR of 30 are very anomalous with small openings (~ 30 nm) even after 10% over-etch.

7.3.4 Asymmetric Patterns

Asymmetric patterns occur where the die reaches the edge or when features with different

sizes and shapes (e.g., circular, L-shape and U-shape) are adjacent and etched simultaneously.[13] Besides, failure or imperfection in the lithography process resulting in non-uniform patterning, which leads to local asymmetries within a large matrix of vias.[19,25]. When the pattern is asymmetric, the electric potential is not uniform due to lack of source of charges, which may deviate the etching from propagating strictly downwards and distort the etch profiles. Here the pattern is made asymmetric by removing one via from the pattern of linear array as shown in Fig. 7.7.

The final etch profiles with 10% over-etch are shown in Fig. 7.7 for the cases with 5 MHz power being 5 kW and 10 kW. Instead of random tilting to different directions, the features at 5 kW power are preferentially tilting to the direction towards the missing via. That is, the first feature from the left in Fig. 7.7(a) tilts to the right and the two features from the right tilt to the left, with a tilting angle of about $1^o - 2^o$. The tilting angle for the features next to the missing via is slightly larger than the more distant features. This systematic tilting is mainly due to the missing via which leads to lack of charges for producing the electric field. The electric potential is skewed in the vertical direction as shown in Fig. 7.7(b), which results in horizontal component of the electric field pointing towards the direction of the missing via. The trajectories of the incident ions are deviated by this horizontal E-field, resulting in tilting of the features to the same direction with the horizontal E-field. The direction of this systematic tilting is also from the dense pattern to the sparse pattern. An extreme case will be vias at the edge of the die or wafer near an open field, where features usually bend towards the direction of the open field. Due to smaller total amount of charges deposited in the features, the maximum electric potential is 810 V, less than the potentials in the features with symmetric patterns by 22%.

The asymmetric pattern with a missing via also causes non-uniform PR isolation between

the vias. The right two vias are isolated by the PR with 50 nm thickness while the left two vias are isolated by the PR with 150 nm thickness. This difference results in more height loss for the thinner PR than the thicker PR by about 80 nm. In this study, as the PR still maintains a considerable height of more than 400 nm after plasma etching, the difference in PR height loss affects little to the feature profiles in the oxide. However, for PR mask with small height or not highly selective etching recipes, the differential PR height loss may be a source for different etch properties and profiles for adjacent vias in a pattern.

As the power increases to 10 kW, the final etch profiles with 10% over-etch are shown in Fig. 7.7(c). The fluxes and IEADs for the 10 kW power are obtained from the HPEM and shown in Fig. 6.4. By doubling the 5 MHz bias power, the average energy of the ions increases from 1,900 to 2,500 eV and the fluxes of energetic ions increases from 0.9×10^{16} to 1.2×10^{16} $cm^{-2}s^{-1}$, resulting in an increase in the etch rate by about 55%. The etch time is decreased and the charges accumulated at the surfaces are decreased, resulting in smaller maximum potential in the features (750 eV). As the ion energy is elevated by 30% while the electric potential buildup in the features is decreased by 7%, the effect of skewed electric potential on the trajectories of the ions becomes much smaller when increasing the bias power from 5 kW to 10 kW. The tilting is almost removed and the feature profiles are normal to the surface.

7.4 Concluding Remarks

The etching of multiple HAR vias in different patterns (array, off-axis and square) by TF-CCPs sustained in $Ar/C_4F_8/O_2$ mixtures was investigated using the integrated reactor and feature scale modeling. The fluxes of ions and radicals and the IEADs were obtained from the reactor scale modeling with the HPEM, from which the pseudoparticles were sampled and launched in

the feature scale modeling with the 3-dimensional MCFPM. The evolution of the feature profiles was predicted through the reactions between the pseudoparticles and the surface sites based on the developed surface reaction mechanism of oxide etching using $Ar/C_4F_8/O_2$ plasmas.

The feature-to-feature variations in etch rates and profiles mainly result from the randomness of the fluxes into adjacent features when the CDs decrease to a few tens of nm or even smaller. The randomness is enhanced in deeper features due to the conduction limit of the incident ions and radicals, resulting in more anomalous profiles and CER at high ARs. By allowing for some over-etch, the effect of the randomness on the disparities in the feature profiles can be mitigated. The etch fronts of the features predominantly propagate downwards (normal to the surface) with no tilting or twisting when charging is not considered.

With the charging of the features considered, the features tend to tilt to random directions when the etch front propagate into high ARs in SiO_2 for symmetric patterns, while the features tilt to preferential directions for asymmetric patterns. For symmetric patterns, the electric potential is quite uniform due to quite similar profiles of charge deposition inside the adjacent features, resulting in electric potential gradient predominantly in the vertical direction. Ions are only decelerated or accelerated in the vertical direction with no horizontal deviation. The difference in the tilting directions of adjacent vias originates from the randomness of the velocities and sequence of the incident ions.

As the pattern is made asymmetric by removing a via, the electric potential is skewed due to lack of charges in the position of the missing via, resulting in horizontal component of the electric field pointing towards the direction of the missing via. The trajectories of the ions are deviated by being accelerated along the horizontal E-field. The features tend to tilt in the same direction as the horizontal E-field, which is the direction from the dense pattern to the sparse

pattern. By increasing the bias power, the ion energy is elevated while the etch time is decreased, resulting in decreased amount of charges deposited inside the features and thus smaller horizontal E-field for perturbing the ion trajectories.

In this chapter, the patterns in the PR affect the plasma processing and the consequent feature profiles from two aspects. One is the shrinking CDs which make the randomness dominant over the reactor scale non-uniformities in affecting the feature-to-feature variations. The other is the charging of the features which can induce horizontal E-fields for deviating ion trajectories when the patterns are asymmetric. The effect of randomness in the fluxes into the features can be mitigated by employing self-limiting processes, (e.g., atomic layer etching), or increasing the magnitude of fluxes in inverse proportion to the decrease in mask opening using high density plasma sources (e.g., ICP, ECR or magnetically enhanced ICP). The effect of charging, specially non-uniform charging producing horizontal E-field, can be possibly mitigated by increasing the bias power during plasma processing, or optimizing design of the masks to reduce or offset the asymmetries in the patterns.

7.5 Figures

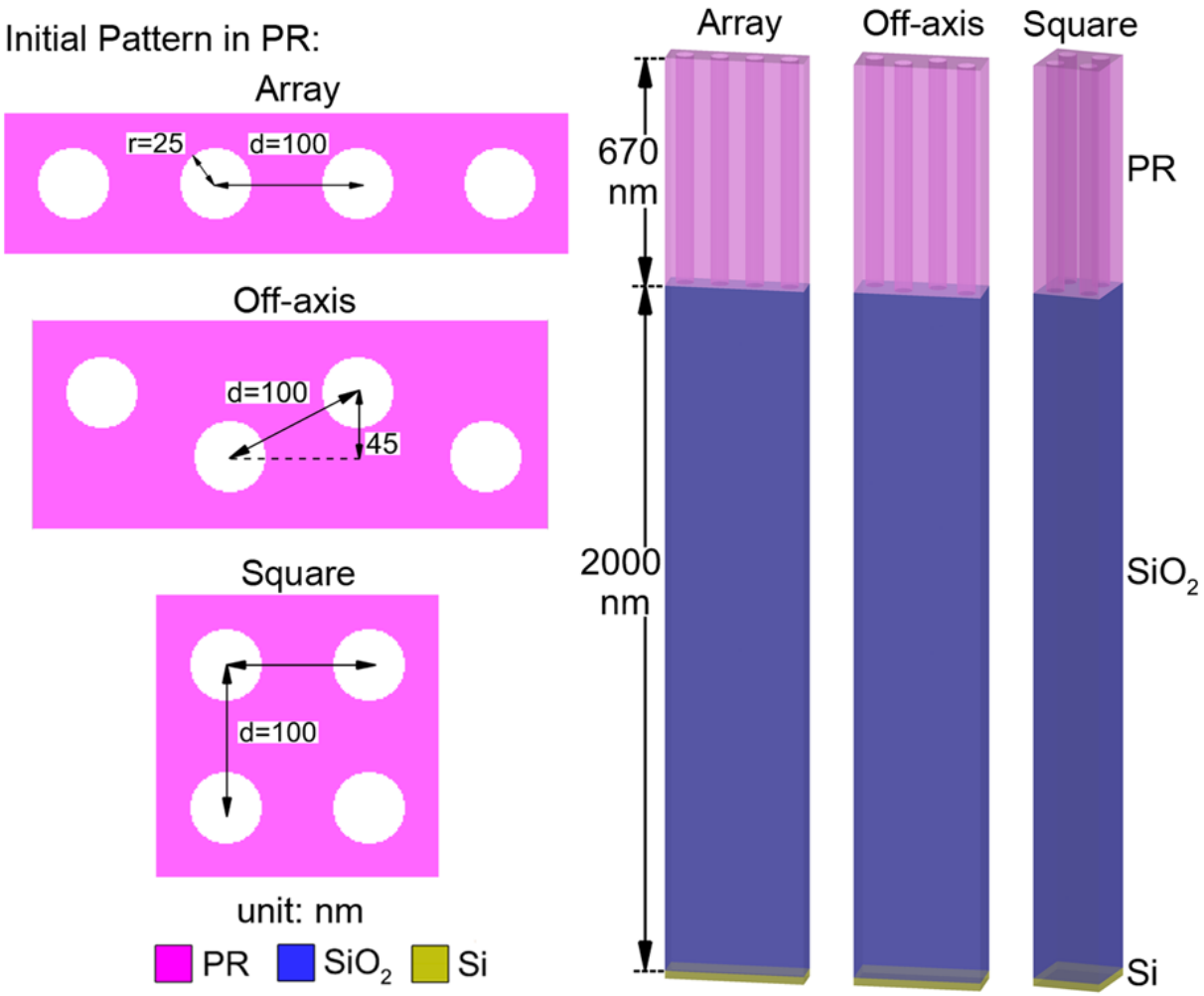

Fig. 7.1 Schematic of the patterns (array, off-axis and square) in the photoresist and the geometries of the initial profiles. The height of the SiO_2 is 2,000 nm with 670 nm thick photoresist as the mask and Si as the stopping layer.

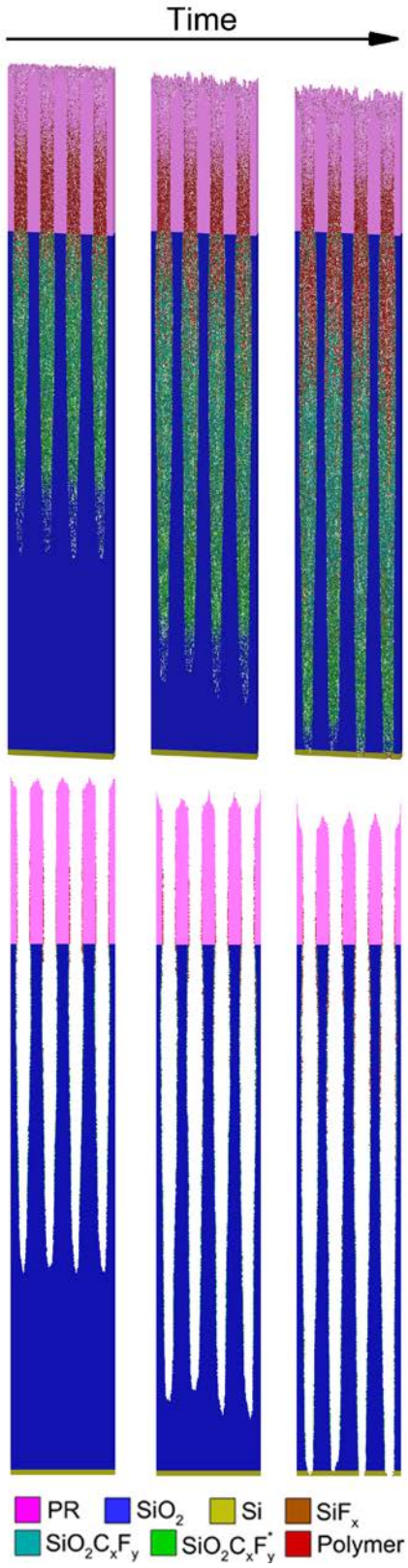

Fig. 7.2 Section view (top) and central slice (bottom) of profile evolution during etching of HAR features in a pattern of 4 linear vias.

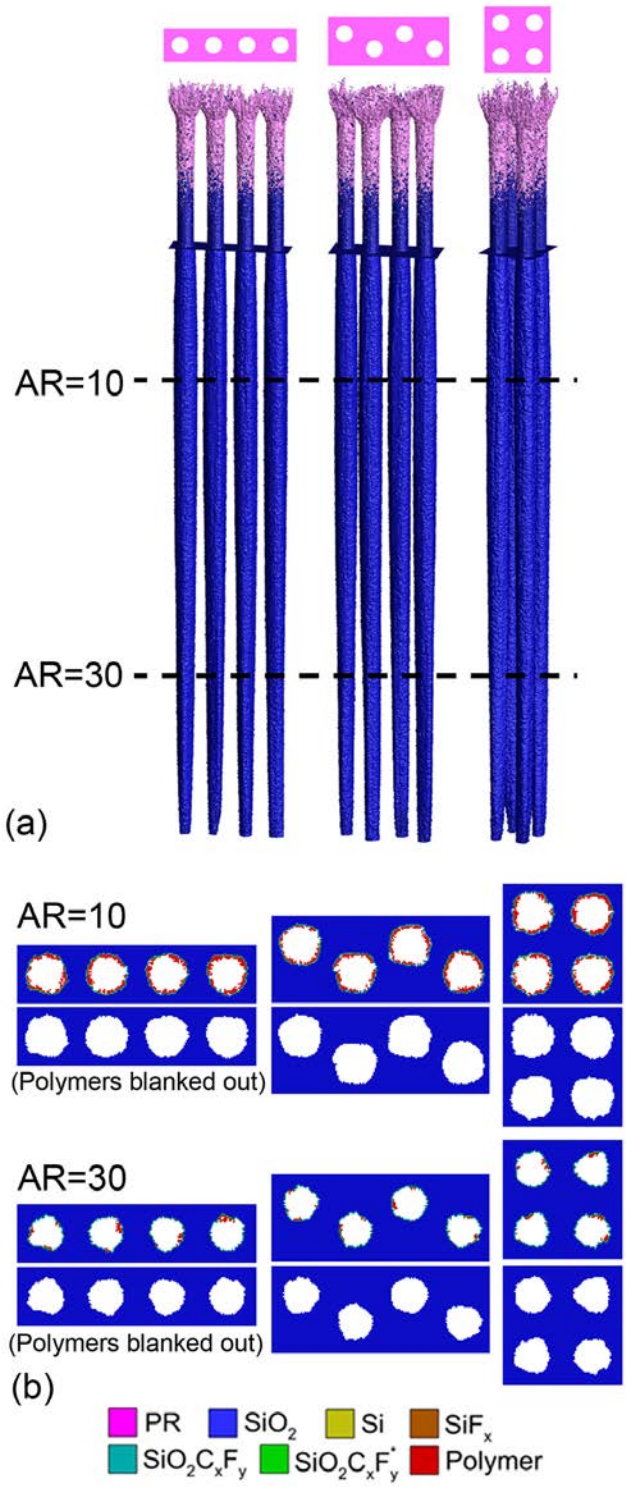

Fig. 7.3 (a) Surfaces of the final etch profiles with 10% over-etch for different patterns (array, off-axis and square). Only PR and SiO_2 surface sites are shown with complex and polymers being blanked out. (b) Horizontal slices at ARs of 10 and 30 in SiO_2. The top slices show profiles with the surface complex and polymers. The bottom slices show only the SiO_2 with complex and polymers being blanked out.

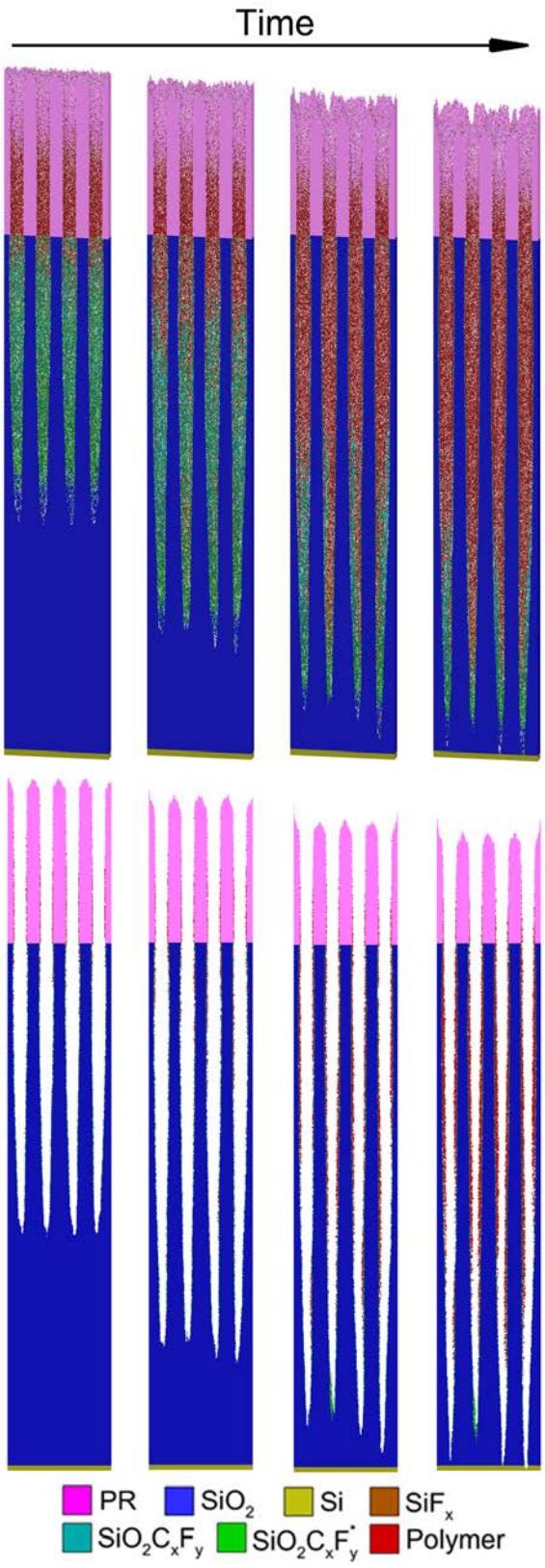

Fig. 7.4 Section view (top) and central slice (bottom) of profile evolution during etching of HAR features in a pattern of 4 linear vias with charging.

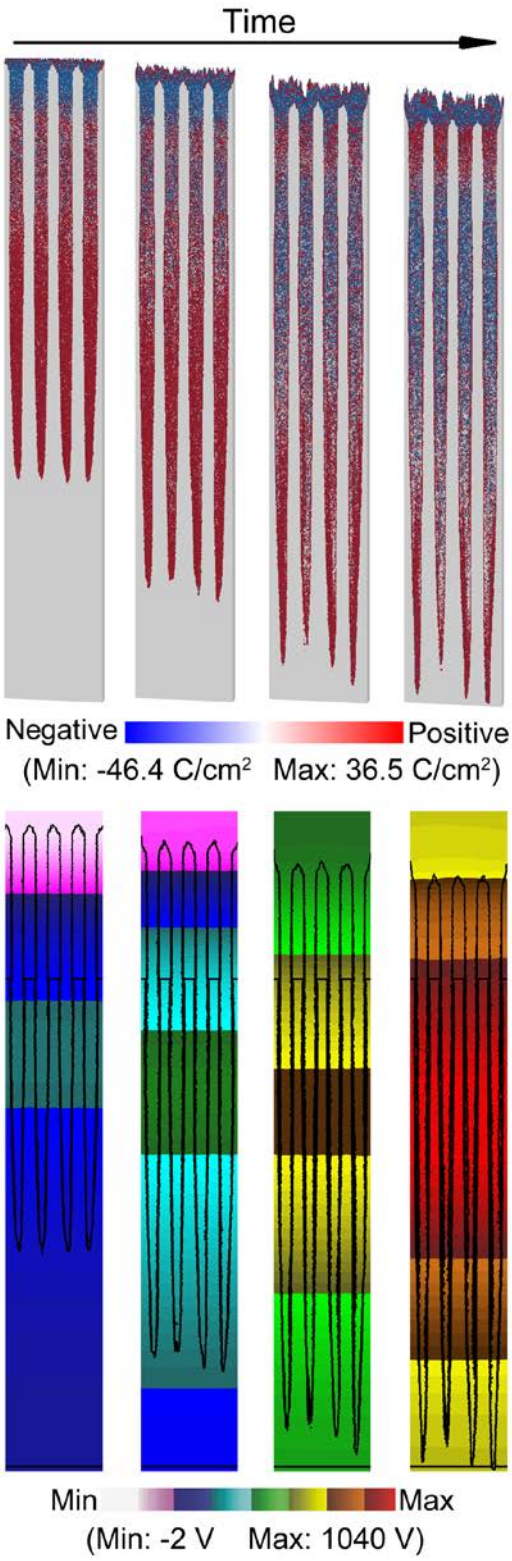

Fig. 7.5 Time evolution of surface charges (top, section view) and electric potentials (bottom, central slice) during etching of HAR features in a pattern of 4 linear vias with charging. The etch profiles are plotted together with electric potentials showing maximum potentials occurring in the middle of the features.

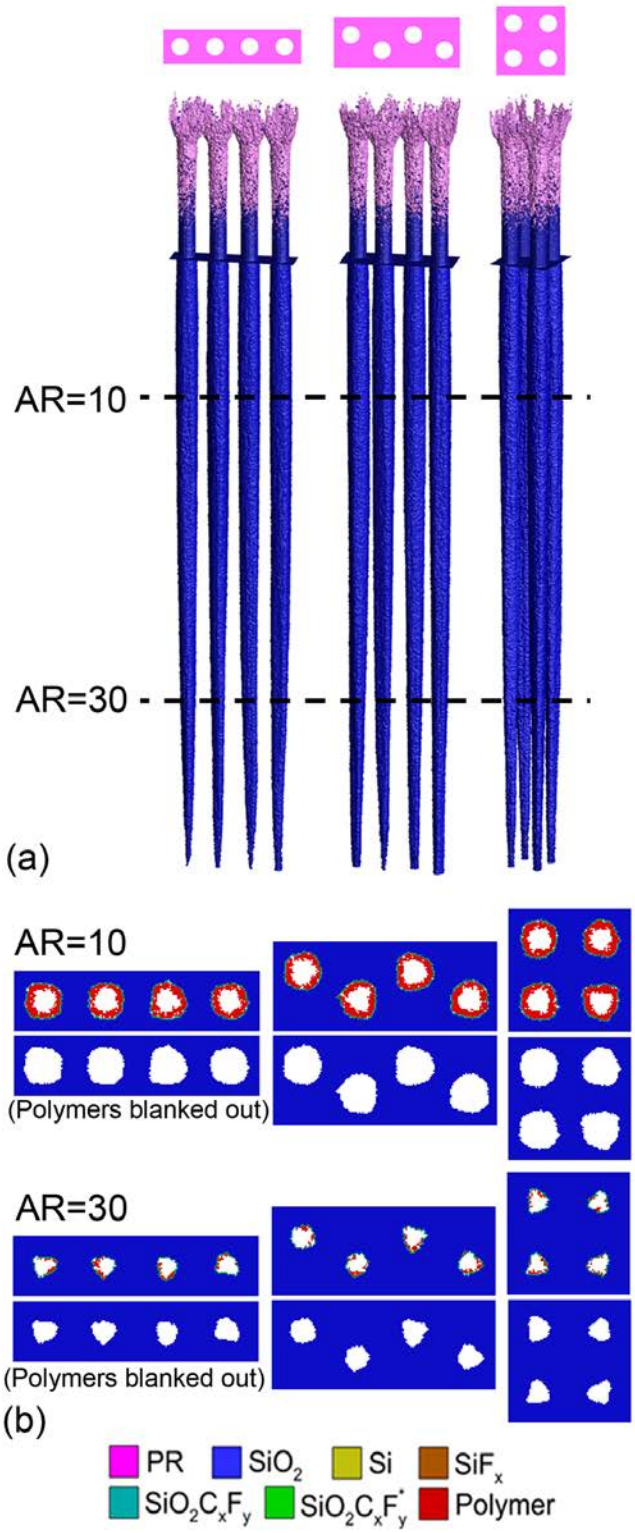

Fig. 7.6 (a) Surfaces of the final etch profiles with 10% over-etch for different patterns (array, off-axis and square) with charging. Only PR and SiO_2 surface sites are shown with complex and polymers being blanked out. (b) Horizontal slices at ARs of 10 and 30 in SiO_2. The top slices show profiles with the surface complex and polymers. The bottom slices show only the SiO_2 with complex and polymers being blanked out.

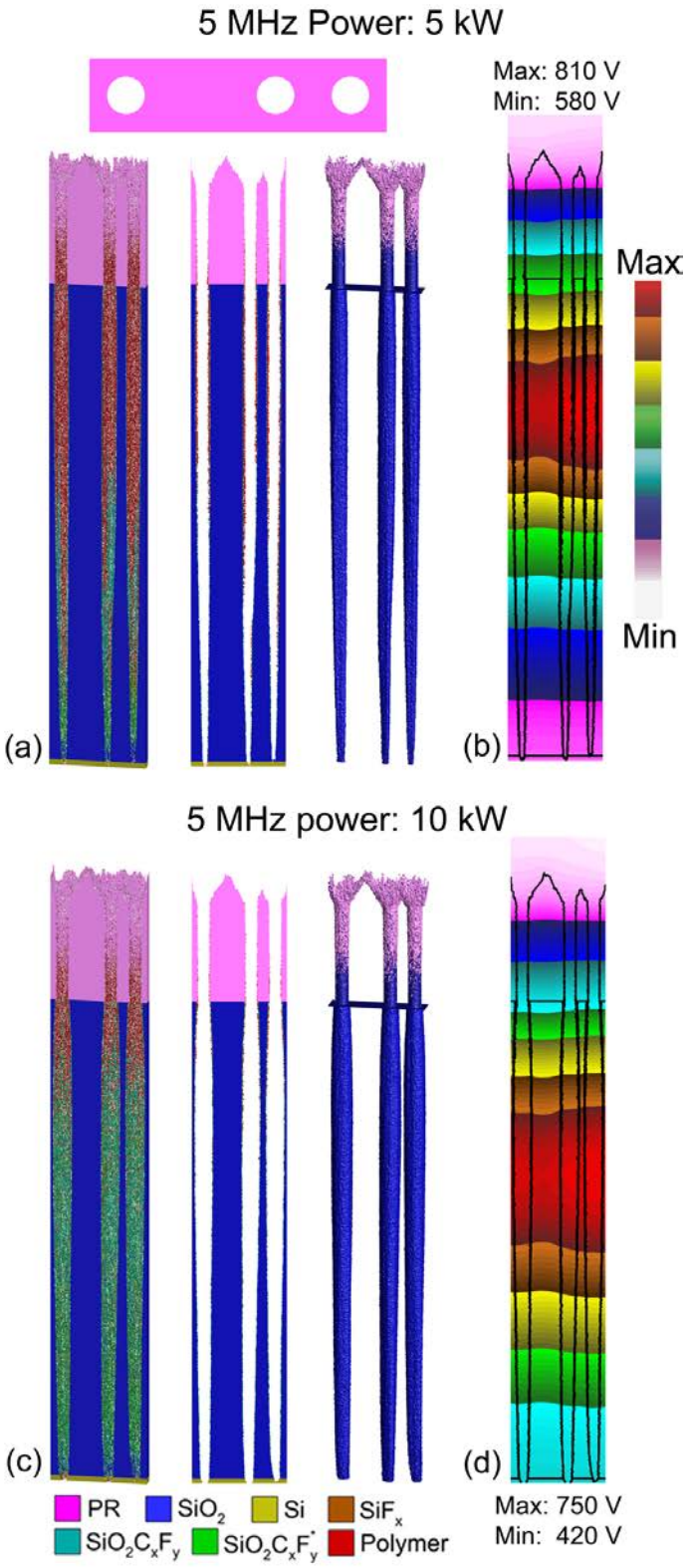

Fig. 7.7 Final etch profiles with 10% over-etch for asymmetric pattern with charging using 5 MHz power of (a, b) 5 kW and (c, d) 10 kW. The section view, central slice and surface of the etch profiles are shown in (a, c) and the electric potential profiles are shown in (b, d).

7.6 References

1. D. J. Economou, J. Phys. D: Appl. Phys. **47**, 303001 (2014).
2. C. G. N. Lee, K. J. Kanarik and R. A. Gottscho, J. Phys. D: Appl. Phys. **47**, 273001 (2014).
3. V. M. Donnelly and A. Kornblit, J. Vac. Sci. Technol. A **31**, 050825 (2013).
4. M. Wang and M. J. Kushner, J. Appl. Phys. **107**, 023309 (2010).
5. T. Shimmura, Y. Suzuki, S. Soda, S. Samukawa, M. Koyanagi and K. Hane, J. Vac. Sci. Technol. A **22**, 433 (2004).
6. N. Negishi, M. Miyake, K. Yokogawa, M. Oyama, T. Kanekiyo and M. Izawa, J. Vac. Sci. Technol. B **35**, 051205 (2017).
7. J. K. Kim, S. H. Lee, S. I. Cho and G. Y. Yeom, J. Vac. Sci. Technol. A **33**, 021303 (2015).
8. Y. Kim, S. Lee, T. Jung, B. Lee, N. Kwak and S. Park, Proc. SPIE **9428**, 942806 (2015).
9. Y. Feurprier, K. Lutker-Lee, V. Rastogi, H. Matsumoto, Y. Chiba, A. Metz, K. Kumar, G. Beique, A. Labonte, Y. Mignot, B. Hamieh and J. Arnold, Prof. SPIE **9428**, 94280F (2015).
10. J. W. Coburn and H. F. Winters, Appl. Phys. Lett. **55**, 2730 (1989).
11. C. Huard, Y. Zhang, S. Sriraman, A. Paterson and M. J. Kushner, J. Vac. Sci. Technol. A **35**, 05C301 (2017).
12. G. S. Hwang and K. P. Giapis, Phys. Rev. Lett. **79**, 845 (1997).
13. H. W. Cheong, W. H. Lee, J. W. Kim, W. S. Kim and K. W. Whang, Plasma Source Sci. Technol. **23**, 065051 (2014).
14. S.-W. Cho, J.-H. Kim, S. Kim, E. W. Shim and C.-K Kim, ECS J. Solid State Sci. Technol. **4**, P226 (2015).
15. T. Tandou, S. Kubo, K. Yokogawa, N. Negishi and M. Izawa, Precision Eng. **44**, 87 (2016).
16. T. Iwase, M. Matsui, K. Yokogawa, T. Arase and M. Mori, Jpn. J. Appl. Phys. **55**, 06HB02 (2016).
17. T. Iwase, K. Yokogawa and M. Mori, Jpn. J. Appl. Phys. **57**, 06JC03 (2018).
18. Y. Ban, Y. Ma, H. J. Levinson and D. Z. Pan, J. Micro/Nanolith. MEMS MOEMS **9**, 041211 (2010).
19. V. Constantoudis, V.-K. M. Kuppuswamy and E. Gogolides, J. Micro/Nanolith. MEMS MOEMS **12**, 013005 (2013).
20. N. Kuboi, T. Tatsumi, S. Kobayasgi, T. Kinoshita, J. Komachi, M. Fukasawa and H. Ansai, Appl. Phys. Express **5**, 126201 (2012).

21. N. Kuboi, M. Fukasawa and T. Tatsumi, Jpn. J. Appl. Phys. **55**, 07LA02 (2016).
22. G. Kokkoris, V. Constantoudis, P. Angelikopoulos, G. Boulousis and E. Gogolides, Phys. Rev. B **76**, 193405 (2007).
23. S.-M. Kim, S. Koo, J.-T. Park, C.-M. Lim, M. Kim, C.-N. Ahn, A. Fumar-Pici and A. C. Chen, Proc. SPIE **9048**, 90480A (2014).
24. K. Ishikawa, K. Karahashi, T. Ishijima, S. I. Cho, S. Elliott, D. Hausmann, D. Mocuta, A. Wilson and K. Kinoshita, Jpn. J. Appl. Phys. **57**, 06JA01 (2018).
25. V.-K. M. Kuppuswamy, V. Constantoudis, E. Gogolides, A. V. Pret and R. Gronheid, J. Micro/Nanolith. MEMS MOEMS **12**, 023003 (2013).

Chapter 8 Conclusion and Future Work

Selectivity and anisotropy are two of the most critical challenges in low temperature plasma processing for semiconductor fabrication, especially when 3-dimensional structures are used for higher integration and aspect ratios (ARs) of the features increase to 50 – 100. Downstream etch systems with remote plasma sources sustained in $Ar/NF_3/O_2$ mixtures for achieving highly selective etching of Si_3N_4 over SiO_2 were investigated using the 2-dimensional reactor scale model, HPEM, with the reaction mechanisms developed and validated using the 0-dimensional global model, Global_Kin. Tri-frequency capacitively coupled plasmas (TF-CCPs) for achieving highly anisotropic etching of high aspect ratio (HAR) features in SiO_2 were also investigated using the HPEM, while the feature profile evolution was predicted using the 3-dimensional feature scale model, MCFPM. By using integrated reactor and feature scale modeling, this dissertation contributes to improving fundamental understanding of the gas phase and surface reaction mechanisms and providing approaches to optimize reactor design and plasma etching process. Summaries of each chapter are presented in Sec. 8.1. Contributions of this work are described in Sec. 8.2. Future work is discussed in Sec. 8.3.

8.1 Summary

In Chapter 1, the basics of low temperature plasmas and their applications in semiconductor manufacturing were introduced. A brief review of plasma sources was presented with the focus on remote plasma sources and multi-frequency CCPs. A review and comparison

of plasma models and plasma etching models were presented. The basic physics and chemistries that enable plasma etching and the confronted challenges in selectivity and anisotropy when etching HAR features were presented.

In Chapter 2, details of the models used in this thesis were presented. The 0-dimensional global model, Global_Kin, was mainly used for developing reaction mechanisms and exploring operational parameter space. The 2-dimensional reactor scale model, HPEM, was updated to efficiently model the downstream etch systems with multiple regions where the plasma densities can be quite different. The 3-dimensional feature scale model, MCFPM, was updated to address charging of the features and etching of multiple features in patterns.

In Chapter 3, detailed description of the gas phase and surface reaction mechanisms developed in this work was presented, with validations made using the experimental measurements. Gas phase reaction mechanisms for $Ar/NF_3/O_2$ and $NF_3/H_2/O_2$ mixtures were developed and validated with optical emission spectroscopy (OES) measurements. A surface reaction mechanism for SiO_2 etching by $Ar/C_4F_8/O_2$ mixtures was developed and validated with experimentally obtained etch results (e.g., etch rates and profiles). $Ar/NF_3/O_2$ and $NF_3/H_2/O_2$ mixtures were used in remote plasma sources for producing F and NO radicals which flow downstream for selective etching of Si_3N_4. $Ar/C_4F_8/O_2$ mixtures were used in TF-CCP reactors for the etching of HAR features in SiO_2. Full lists of the species and reactions included in the reaction mechanisms were given in the Appendices.

In Chapter 4, remote plasma sources sustained in $Ar/NF_3/O_2$ mixtures were investigated. NF_3 is mainly used as a source of F radicals due to thermal attaching NF_3 and its dissociative products, NF_2 and NF. Addition of O_2 diversifies the variety of reactive species (e.g., NO, FNO and NO_2) through endothermic and exothermic reactions, which are modulated by the gas

temperature. In the downstream afterglow, the highly attaching gas mixture rapidly transitions to an ion-ion plasma. The dominant reactions in the remote source region and in downstream region are quite different, with electron impact reactions dominating in the source while heavy particle exothermic reactions dominant downstream. These differences provide an opportunity to customize the reaction mechanisms for favorable radical production.

In Chapter 5, downstream etch systems consisting of a remote plasma source, a transport tube, a plenum and a downstream chamber with Si_3N_4 coated wafer placed on the substrate were investigated. Plasmas in this system are largely confined in the source region due to isolating showerheads and the highly attaching nature of the gas mixture. The etching of Si_3N_4 proceeds through iteratively removing Si surface sites by F atoms and removing N sites by NO and N. High-efficiency etching requires separate control of the production of Si sites etchants and N sites etchants. Etching performance can be improved through better chamber design with the goal being customizing the reaction pathways. This is accomplished by channeling the power into desirable reactions, enabled by development and analysis of a comprehensive reaction mechanism. Use of pulsed power increases radical density while decreasing ion density in the downstream chamber by allowing for neutralization afterglow. Use of multiple gas inlets takes advantage of the large temperature gradient through the long system and customizes the reaction pathways without requiring another power source.

In Chapter 6, integrated reactor and feature scale modeling was used to investigate the etching of HAR features in SiO_2 with ARs up to 80 using TF-CCPs sustained in $Ar/C_4F_8/O_2$ mixtures. With updates made in the MCFPM, key features in the etching of HAR features were addressed such as mask erosion, bowing, tapered etch front and edge roughening. The fundamental limiting factor in HAR etching was found to be the decreasing delivery of energy

and species to the etch front with increasing AR. These trends are are mainly due to the energy and angular distributions of incident species and their scattering at sidewalls resulting in conduction limit and energy loss. Tuning the bias power, the polymer-to-ion flux ratio or the resistance of photoresist to plasma sputtering was found to enable etching higher ARs by balancing among the etch rate, selectivity and critical dimensions.

In Chapter 7, etching of multiple HAR vias in different patterns (arrays, off-axis and square) was investigated. The feature-to-feature variations in etch rates and profiles mainly result from the randomness in the fluxes of particles into adjacent features rather than reactor scale non-uniformities due to small critical dimensions and pitch sizes (50 – 100 nm). The randomness is enhanced in deeper features due to conduction limits, resulting in more anomalous profiles and contact edge roughness at high ARs. Some of these issues can be addressed using high density plasma sources. The charging of the features aggravates profile distortion for individual feature and feature-to-feature variation, especially for asymmetric patterns where non-uniform spatial charge distributions result in electric potential skewing and tilting of the features. These distortions can be made less severe by using higher bias power to elevate the ion energy and reduce the etching time, at the tradeoff of critical dimension loss.

8.2 Contributions

The work in this thesis contributes to improving fundamental understanding of the gas phase and surface reaction mechanisms and providing approaches to optimize plasma etching process in the following aspects.

1. Reaction mechanisms developed and validated for modeling of plasma sources and plasma etching processes.

Gas phase reaction mechanisms of $Ar/NF_3/O_2$ and $NF_3/H_2/O_2$ mixtures were developed for reactor scale modeling of remote plasma sources and validated through comparison with experimental measurements obtained using OES with actinometry. Surface reaction mechanisms for SiO_2 etching using $Ar/C_4F_8/O_2$ mixtures were developed for feature scale modeling. Implementation of these mechanisms into the models enabled insights into the kinetics and chemistry both in bulk plasmas and at surfaces. Parametric studies performed using these mechanisms produced scaling laws which assist in process optimization through expert control of operating conditions.

2. *Reactor and feature scale models updated for achieving high computational efficiency and addressing new geometries and phenomena.*

Two acceleration techniques were implemented into the HPEM to enable efficient modeling of downstream etch systems with multiple regions where plasma densities significantly vary. One is the optimization of the algorithms by using node-and-neighbor technique and division of multiple plasma regions. The other is the implementation of a memristor based PDE solver, which is an analog solver as opposed to the digital solver traditionally used in solving the Poisson's equation.

The charging subroutine in the MCFPM was updated with periodic and reflective boundary conditions to model the etching of single and multiple HAR features in SiO_2 with the effect of charge deposition at the surface considered. Surface reaction mechanisms were also updated to be compatible with the charging subroutine. 3D MCFPM mesh generator was updated to produce geometries of multiple HAR features in different patterns and oxide-nitride-oxide (O-N-O) stacks.

3. *Integrated investigation of downstream etch system consisting of remote plasma source, transport tube, plenum and downstream chamber with Si_3N_4 coated wafer.*

Rather than using separate models to address components of the downstream etch system in which timescales of different physics significantly vary, this work enabled the modeling of the downstream etch system as a whole using the HPEM, which directly correlates the remote source control parameters (e.g., input power and gas mixtures) to the etch performances at the wafer (e.g., etch rate and uniformity). This enabling partially depends on the advantages of the HPEM featuring hierarchical order and time slicing techniques and partially depends on the implemented acceleration techniques, so that the downstream etch system could be modeled within reasonable computation time. Systematic investigation of the whole downstream etch system can be conducted and optimizations in the design of reactors and plasma operating conditions can be proposed based on modeling results.

4. Integrated reactor and feature scale modeling of plasma etching of high aspect ratio features in SiO_2.

The etching of nanoscale features directly depends on microscopic parameters (e.g., fluxes and energy distributions of ions and neutrals), which are determined by the plasma properties (e.g., plasma density, electron temperature and electron energy distributions) modulated by macroscopic operating parameters (e.g., power, pressure and flow rate) through the control knobs on the reactors. By using integrated feature and reactor scale analysis, the dependence of the etch performances on the microscopic parameters were investigated using the MCPFM, which can be correlated to the macroscopic operating parameters through the HPEM. These correlations provide practical control parameters (e.g., power, pressure and flow rate) for process engineers to tune in fabrication or better design of the reactor for process optimization.

Parametric studies and sensitivity analysis were performed for exploring the optimal process window in HAR feature etching in SiO_2. Scaling laws were developed to guide HAR etching and can also be applied for other processes (e.g., atomic layer etching and O-N-O stack etching).

8.3 Future Work

In this thesis, reactor and feature scale models were updated and employed to simulate low temperature plasmas and plasma etching processes for achieving high selectivity and highly anisotropic profiles. Future work which could possibly improve the performance of plasma etching or the performance of plasma modeling is proposed as follows.

1. Etching of HAR features using high density plasmas or pulsed power plasmas.

Due to the relatively low plasma densities of the CCP source, the ions incident into the small features are subject to stochastic noise, which result in feature-to-feature variation and distortion such as edge roughness and tilting. The randomness is especially enhanced for HAR features due to conduction limit. Use of high density plasmas (e.g., inductively coupled plasmas, electron cyclotron resonance plasmas and magnetically enhanced plasmas) increases the plasma densities and ion fluxes by about one order of magnitude compared with the CCP sources, which could possibly reduce the effect of randomness on the etch profiles and transfer the pattern from the mask into higher aspect ratios (~ 100 or even higher) in SiO_2.

Confronted with charging of the features in plasma etching using continuous-wave power sustained plasmas, use of pulsed power scenarios (e.g., pulsed bias power, pulsed source power and synchronized pulsing) allows negative charged species to reach the surface for neutralization. Besides, pulsed power plasmas modulate the timing and sequence of the radicals and ions incident into the features, which could possibly improve the anisotropy of the feature profiles.

2. Reactor scale modeling using non-structured mesh for addressing fine structures.

In the current computational infrastructure of the reactor scale model for low temperature plasmas, uniform and rectilinear mesh is used. The spatial resolution is the same across the entire computation domain. However, fine structures (e.g., gap between wafer edge and focus ring, small showerheads and isolating barriers) which could significantly affect the plasma discharges cannot be properly addressed. Also, plasma densities may significantly vary in space in plasma tools such as downstream etch system. By using non-structured mesh which is formed by a tessellation of the computation domain into triangles or rectangles, varying spatial resolution in one simulation domain can be achieved so that fine structures can be addressed by locally refined mesh while bulk structures can be addressed by coarser mesh for high computational efficiency.

3. Implementation of machine learning algorithms for predicting plasma properties and etch performances based on control parameters.

In common machine learning algorithms for establishing relations between control parameters (e.g., input power and gas mixtures) and plasma properties (e.g., electron temperature and electron density) or etch performances (e.g., etch rate and critical dimensions), the neural networks are built up based on unitless non-physics parameters, which need to be rebuilt when the systems are change, for example, from inductively coupled plasma to capacitively coupled plasma. Use of physics parameters in establishing the neural networks may enable the neural networks to be transferred and reused when the plasma tools are changed, with some additional training data or modifications of the algorithms, rather than rebuilding the neural networks.

Appendix A Reaction Mechanism of $Ar/NF_3/O_2$ Plasma

Species[a]:

Ar	$Ar(1s_5)$	$Ar(1s_4)$	$Ar(1s_3)$	$Ar(1s_2)$	Ar(4p)	Ar(4d)
$Ar_2(^3\Sigma_u^+)$	Ar^+	Ar_2^+	NF_3	NF_2	NF	NF_3^+
NF_2^+	NF^+	N_2	$N_2(v)$	$N_2(A\ ^3\Sigma_u^+)$	$N_2(B\ ^3\Pi_g$, higher)	
N	$N(^2D)$	N_2^+	N^+	F_2	$F_2(1\ ^1\Sigma_u^+)$	F
$F(^3S)$	F_2^+	F^+	F^-	O_2	$O_2(v)$	
$O_2(a\ ^1\Delta_g)$	$O_2(b\ ^1\Sigma_g^+)$	O	$O(^1D)$	$O(^1S)$	O_3	O_2^+
O^+	O_2^-	O^-	O_3^-	FO	FNO	NO
N_2O	NO_2	NO^+	N_2O^+			

[a] For simplicity in the reaction list, following notation is used for excited states:

$Ar_2^* \leftrightarrow Ar_2(^3\Sigma_u^+)$,	$N_2^* \leftrightarrow N_2(A\ ^3\Sigma_u^+)$	$N_2^{**} \leftrightarrow N_2(B^3\Pi_g$, higher)
$N^* \leftrightarrow N(^2D)$	$F_2^* \leftrightarrow F_2(1\ ^1\Sigma_u^+)$	$F^* \leftrightarrow F(^3S)$
$O_2^* \leftrightarrow O_2(a\ ^1\Delta_g)$	$O_2^{**} \leftrightarrow O_2(b\ ^1\Sigma_g^+)$	$O^* \leftrightarrow O(^1D)$

Table A.1 List of reactions in the mechanism of $Ar/NF_3/O_2$ plasma.

Reactions[a]	Rate Coefficient[b]	Reference	ΔH (eV)[b]
<u>Electron Impact NF_x</u>			
$e + NF_3 \rightarrow NF_3 + e$	c)	[1]	d)
$e + NF_3 \rightarrow NF_2 + F^-$	c), e)	[1]	-1.0
$e + NF_3 \rightarrow NF_3(v) + e$	c), f)	[1]	
$e + NF_3 \rightarrow NF_2 + F + e$	c)	[1]	-5.8
$e + NF_3 \rightarrow NF + F + F + e$	c)	[1]	-6.1
$e + NF_3 \rightarrow NF_3^+ + e + e$	c)	[1]	
$e + NF_3 \rightarrow NF_2^+ + F + e + e$	c)	[1]	-0.5
$e + NF_3 \rightarrow NF^+ + F + F + e + e$	c)	[1]	-4.2
$e + NF_3 \rightarrow F^+ + NF_2 + e + e$	c)	[1]	-1.1[g]

$e + NF_2 \rightarrow NF_2 + e$	c)	[2]	
$e + NF_2 \rightarrow NF + F^-$	c)	[2]	-0.5
$e + NF_2 \rightarrow NF_2(v) + e$	c), f)	[2]	
$e + NF_2 \rightarrow NF + F + e$	c)	[2]	-5.1
$e + NF_2 \rightarrow NF_2^+ + e + e$	c)	[2]	
$e + NF_2 \rightarrow NF^+ + F + e + e$	c)	[2]	
$e + NF_2 \rightarrow F^+ + NF + e + e$	c)	[2]	
$e + NF \rightarrow NF + e$	c)	[2]	
$e + NF \rightarrow N + F^-$	c)	[2]	-0.6
$e + NF \rightarrow NF(v) + e$	c), f)	[2]	
$e + NF \rightarrow NF(^1\Delta) + e$	c), f)	[2]	
$e + NF \rightarrow NF(^1\sum^+) + e$	c), f)	[2]	
$e + NF \rightarrow N + F + e$	c)	[2]	-4.0
$e + NF \rightarrow NF^+ + e + e$	c)	[2]	
$e + NF \rightarrow N^+ + F + e + e$	c)	[2]	
$e + NF \rightarrow F^+ + N + e + e$	c)	[2]	
$e + NF_3^+ \rightarrow NF_2 + F$	$1 \times 10^{-7}\ T_e^{-1/2}$	est. [3], h)	-11.1
$e + NF_2^+ \rightarrow NF + F$	$1 \times 10^{-7}\ T_e^{-1/2}$	est. [3]	-6.3[g)]
$e + NF^+ \rightarrow N^* + F$	$1 \times 10^{-7}\ T_e^{-1/2}$	est. [3]	-7.1
Electron Impact F_2/F			
$e + F_2 \rightarrow F_2 + e$	c)	[4]	
$e + F_2 \rightarrow F^- + F$	c)	[4]	-1.8
$e + F_2 \rightarrow F + F + e$	c)	[4]	-1.6
$e + F_2 \rightarrow F_2^* + e$	c)	[4]	
$e + F_2 \rightarrow F_2^+ + e + e$	c)	[4]	
$e + F_2^+ \rightarrow F + F^*$	$1 \times 10^{-7}\ T_e^{-1/2}$	est. [3]	-0.6
$e + F \rightarrow F + e$	c)	[5]	
$e + F \rightarrow F^* + e$	c)	[5]	
$e + F \rightarrow F^+ + e + e$	c)	[5]	
$e + F^* \rightarrow F^+ + e + e$	c)	[5]	
$e + F^+ \rightarrow F^*$	$4.5 \times 10^{-13}\ T_e^{-0.5}$	est. [6]	
$e + e + F^+ \rightarrow F^* + e$	$5.12 \times 10^{-27}\ T_e^{-4.5}$	est. [6]	
Electron Impact N_xO_y			
$e + NO \rightarrow NO + e$	c)	[7]	
$e + NO \rightarrow N + O^-$	c)	[8]	-2.1
$e + NO \rightarrow N + O + e$	c)	[7]	-0.3
$e + NO \rightarrow NO^+ + e + e$	c)	[9]	
$e + NO \rightarrow N + O^+ + e + e$	c)	[9]	-0.1
$e + NO \rightarrow N^+ + O + e + e$	c)	[9]	-0.1
$e + NO^+ \rightarrow N + O$	$1 \times 10^{-7}\ T_e^{-1/2}$	est. [3]	-1.8
$e + NO_2 \rightarrow NO_2 + e$	c)	[10]	
$e + NO_2 \rightarrow NO^+ + O + e + e$	c)	[9]	-0.5

$e + N_2O \rightarrow N_2O + e$	c)	[11]	
$e + N_2O \rightarrow N_2 + O^-$	c)	[11]	-0.1
$e + N_2O \rightarrow N_2 + O + e$	c)	[11]	-0.2
$e + N_2O \rightarrow N_2O^+ + e + e$	c)	[11,12], i)	
$e + N_2O \rightarrow N_2 + O^+ + e$	c)	[11,12], i)	
$e + N_2O \rightarrow N_2^+ + O + e$	c)	[11,12], i)	
$e + N_2O^+ \rightarrow N_2 + O^*$	$1 \times 10^{-7}\ T_e^{-1/2}$	est. [3]	-7.0
Radiative Transitions			
$F_2^* \rightarrow F_2$	$2.44 \times 10^7\ s^{-1}$	[13]	
$F^* \rightarrow F$	$5 \times 10^7\ s^{-1}$	[14]	
Collisional Quenching			
$N_2(v) + M \rightarrow N_2 + M$	2×10^{-15}	[15]	-0.3
$N_2^* + M \rightarrow N_2 + M$	3×10^{-16}	[16]	-6.2
$N_2^{**} + M \rightarrow N_2^* + M$	3×10^{-16}	est. [16]	-2.2
$N^* + M \rightarrow N + M$	2×10^{-14}	[16]	-2.4
$O_2(v) + M \rightarrow O_2 + M$	$1 \times 10^{-14}\ T_n^{1/2}$	[17]	-0.2
$O_2^* + M \rightarrow O_2 + M$	$3 \times 10^{-18} \exp(-200/T_g)$	[18]	-1.0
$O_2^{**} + M \rightarrow O_2^* + M$	$3.6 \times 10^{-17}\ T_n^{1/2}$	[17]	-0.6
$O_2^{**} + M \rightarrow O_2 + M$	$4 \times 10^{-18}\ T_n^{1/2}$	[17]	-1.6
$O^* + M \rightarrow O + M$	5×10^{-12}	[19]	-1.9
$O(^1S) + M \rightarrow O^* + M$	$4.8 \times 10^{-12} \exp(-850/T_g)$	[18]	-2.3
$F_2^* + M \rightarrow F_2 + M$	3×10^{-18}	est. [18]	-2.0
$F^* + M \rightarrow F + M$	3×10^{-18}	est. [18]	-2.0
Penning Ionization			
$Ar^* + F_2^* \rightarrow F_2^+ + Ar + e$	$1.2 \times 10^{-9}\ T_n^{1/2}$	est. [20], j)	
$Ar^* + F^* \rightarrow F^+ + Ar + e$	$1.2 \times 10^{-9}\ T_n^{1/2}$	est. [20]	
$Ar^* + N_2^* \rightarrow N_2^+ + Ar + e$	$1.2 \times 10^{-9}\ T_n^{1/2}$	est. [20]	
$Ar^* + N_2^{**} \rightarrow N_2^+ + Ar + e$	$1.2 \times 10^{-9}\ T_n^{1/2}$	est. [20]	
$Ar^* + O_2^* \rightarrow O_2^+ + Ar + e$	$1.2 \times 10^{-9}\ T_n^{1/2}$	est. [20]	
$Ar^* + O_2^{**} \rightarrow O_2^+ + Ar + e$	$1.2 \times 10^{-9}\ T_n^{1/2}$	est. [20]	
$Ar^* + O(^1S) \rightarrow O^+ + Ar + e$	$1.2 \times 10^{-9}\ T_n^{1/2}$	est. [20]	
$Ar^* + NO \rightarrow NO^+ + Ar + e$	$1.2 \times 10^{-9}\ T_n^{1/2}$	est. [20]	
$Ar(4p) + N^* \rightarrow N^+ + Ar + e$	$1.2 \times 10^{-9}\ T_n^{1/2}$	est. [20]	
$Ar(4d) + N^* \rightarrow N^+ + Ar + e$	$1.2 \times 10^{-9}\ T_n^{1/2}$	est. [20]	
$Ar(4p) + O_2 \rightarrow O_2^+ + Ar + e$	$1.2 \times 10^{-9}\ T_n^{1/2}$	est. [20]	
$Ar(4d) + O_2 \rightarrow O_2^+ + Ar + e$	$1.2 \times 10^{-9}\ T_n^{1/2}$	est. [20]	
$Ar(4p) + O_2(v) \rightarrow O_2^+ + Ar + e$	$1.2 \times 10^{-9}\ T_n^{1/2}$	est. [20]	
$Ar(4d) + O_2(v) \rightarrow O_2^+ + Ar + e$	$1.2 \times 10^{-9}\ T_n^{1/2}$	est. [20]	
$Ar(4p) + O^* \rightarrow O^+ + Ar + e$	$1.2 \times 10^{-9}\ T_n^{1/2}$	est. [20]	
$Ar(4d) + O^* \rightarrow O^+ + Ar + e$	$1.2 \times 10^{-9}\ T_n^{1/2}$	est. [20]	
$Ar(4p) + NF_2 \rightarrow NF_2^+ + Ar + e$	$1.2 \times 10^{-9}\ T_n^{1/2}$	est. [20]	
$Ar(4d) + NF_2 \rightarrow NF_2^+ + Ar + e$	$1.2 \times 10^{-9}\ T_n^{1/2}$	est. [20]	

$Ar(4p) + NF \rightarrow NF^+ + Ar + e$	$1.2 \times 10^{-9}\ T_n^{1/2}$	est. [20]	
$Ar(4d) + NF \rightarrow NF^+ + Ar + e$	$1.2 \times 10^{-9}\ T_n^{1/2}$	est. [20]	
$Ar(4p) + N_2O \rightarrow N_2O^+ + Ar + e$	$1.2 \times 10^{-9}\ T_n^{1/2}$	est. [20]	
$Ar(4d) + N_2O \rightarrow N_2O^+ + Ar + e$	$1.2 \times 10^{-9}\ T_n^{1/2}$	est. [20]	
$Ar(4d) + N \rightarrow N^+ + Ar + e$	$1.2 \times 10^{-9}\ T_n^{1/2}$	est. [20]	
$Ar(4d) + NF_3 \rightarrow NF_3^+ + Ar + e$	$1.2 \times 10^{-9}\ T_n^{1/2}$	est. [20]	
$Ar(4d) + O \rightarrow O^+ + Ar + e$	$1.2 \times 10^{-9}\ T_n^{1/2}$	est. [20]	
$Ar_2^* + F_2^* \rightarrow F_2^+ + Ar + Ar + e$	$5.0 \times 10^{-10}\ T_n^{1/2}$	est. [21]	
$Ar_2^* + F^* \rightarrow F^+ + Ar + Ar + e$	$5.0 \times 10^{-10}\ T_n^{1/2}$	est. [21]	
$Ar_2^* + N_2^* \rightarrow N_2^+ + Ar + Ar + e$	$5.0 \times 10^{-10}\ T_n^{1/2}$	est. [21]	
$Ar_2^* + N_2^{**} \rightarrow N_2^+ + Ar + Ar + e$	$5.0 \times 10^{-10}\ T_n^{1/2}$	est. [21]	
$Ar_2^* + NO \rightarrow NO^+ + Ar + Ar + e$	$5.0 \times 10^{-10}\ T_n^{1/2}$	est. [21]	
$Ar_2^* + O_2^{**} \rightarrow O_2^+ + Ar + Ar + e$	$5.0 \times 10^{-10}\ T_n^{1/2}$	est. [21]	
$Ar_2^* + O(^1S) \rightarrow O^+ + Ar + Ar + e$	$5.0 \times 10^{-10}\ T_n^{1/2}$	est. [21]	
Positive Ion-Neutral Collisions			
$F^+ + F \rightarrow F + F^+$	1×10^{-9}	est. [22], k)	l)
$F^+ + Ar \rightarrow F + Ar^+$	1×10^{-11}	est.	-1.4
$F^+ + F_2 \rightarrow F + F_2^+$	1×10^{-11}	est.	-1.7
$F^+ + N_2 \rightarrow F + N_2^+$	9.7×10^{-10}	[23]	-1.8
$F^+ + N_2(v) \rightarrow F + N_2^+$	9.7×10^{-10}	est. [23]	-2.1
$F^+ + N \rightarrow F + N^+$	1×10^{-11}	est.	-2.9
$F^+ + O \rightarrow F + O^+$	1×10^{-10}	[24]	-3.8
$F^+ + NF_3 \rightarrow F + NF_3^+$	1×10^{-11}	est.	-3.9
$F^+ + N_2O \rightarrow F + N_2O^+$	1×10^{-11}	est.	-4.5
$F^+ + NF \rightarrow F + NF^+$	1×10^{-11}	est.	-5.1
$F^+ + O_2 \rightarrow F + O_2^+$	7.01×10^{-10}	[23]	-5.3
$F^+ + O_2(v) \rightarrow F + O_2^+$	7.01×10^{-10}	est. [23]	-5.5
$F^+ + NF_2 \rightarrow F + NF_2^+$	1×10^{-11}	est.	-5.8
$F^+ + NO \rightarrow F + NO^+$	8.64×10^{-10}	[23]	-8.1
$F^+ + Ar_2^* \rightarrow F + Ar_2^+$	1×10^{-11}	est.	-13.6
$F^+ + NO \rightarrow O + NF^+$	9.4×10^{-11}	[23]	-1.9
$F^+ + O_2 \rightarrow FO + O^+$	6.06×10^{-11}	[23]	-1.0
$F^+ + O_2(v) \rightarrow FO + O^+$	6.06×10^{-11}	est. [23]	-1.2
$Ar^+ + F_2 \rightarrow Ar + F_2^+$	1×10^{-11}	est.	-0.3
$Ar^+ + N_2 \rightarrow Ar + N_2^+$	1×10^{-11}	est.	-0.4
$Ar^+ + N_2(v) \rightarrow Ar + N_2^+$	1×10^{-11}	est.	-0.7
$Ar^+ + N \rightarrow Ar + N^+$	1×10^{-11}	est.	-1.5
$Ar^+ + O \rightarrow Ar + O^+$	1×10^{-11}	est.	-2.4
$Ar^+ + NF_3 \rightarrow Ar + NF_3^+$	1×10^{-11}	est.	-2.5
$Ar^+ + N_2O \rightarrow Ar + N_2O^+$	1×10^{-11}	est.	-3.1
$Ar^+ + NF \rightarrow Ar + NF^+$	1×10^{-11}	est.	-3.7
$Ar^+ + O_2 \rightarrow Ar + O_2^+$	5.1×10^{-11}	[22]	-3.9

$Ar^+ + O_2(v) \rightarrow Ar + O_2^+$	5.1×10^{-11}	est. [22]	-4.1
$Ar^+ + NF_2 \rightarrow Ar + NF_2^+$	1×10^{-11}	est.	-4.4
$Ar^+ + NO \rightarrow Ar + NO^+$	1×10^{-11}	est.	-6.7
$F_2^+ + F_2 \rightarrow F_2 + F_2^+$	1×10^{-9}	est.	
$F_2^+ + N_2 \rightarrow F_2 + N_2^+$	1×10^{-11}	est.	-0.1
$F_2^+ + N_2(v) \rightarrow F_2 + N_2^+$	1×10^{-11}	est.	-0.4
$F_2^+ + N \rightarrow F_2 + N^+$	1×10^{-11}	est.	-1.2
$F_2^+ + O \rightarrow F_2 + O^+$	1×10^{-11}	est.	-2.1
$F_2^+ + NF_3 \rightarrow F_2 + NF_3^+$	1×10^{-11}	est.	-2.2
$F_2^+ + N_2O \rightarrow F_2 + N_2O^+$	1×10^{-11}	est.	-2.8
$F_2^+ + NF \rightarrow F_2 + NF^+$	1×10^{-11}	est.	-3.4
$F_2^+ + O_2 \rightarrow F_2 + O_2^+$	1×10^{-11}	est.	-3.6
$F_2^+ + O_2(v) \rightarrow F_2 + O_2^+$	1×10^{-11}	est.	-3.8
$F_2^+ + NF_2 \rightarrow F_2 + NF_2^+$	1×10^{-11}	est.	-4.1
$F_2^+ + NO \rightarrow F_2 + NO^+$	1×10^{-11}	est.	-6.4
$F_2^+ + Ar_2^* \rightarrow F_2 + Ar_2^+$	1×10^{-11}	est.	-11.9
$N_2^+ + N_2 \rightarrow N_2 + N_2^+$	1×10^{-9}	est.	
$N_2^+ + N_2(v) \rightarrow N_2 + N_2^+$	1×10^{-9}	est.	-0.3
$N_2^+ + N \rightarrow N_2 + N^+$	8.0×10^{-12}	[25]	-1.1
$N_2^+ + O \rightarrow N_2 + O^+$	9.8×10^{-12}	[23]	-2.0
$N_2^+ + NF_3 \rightarrow N_2 + NF_3^+$	1×10^{-11}	est.	-2.1
$N_2^+ + N_2O \rightarrow N_2 + N_2O^+$	6×10^{-10}	[26]	-2.7
$N_2^+ + NF \rightarrow N_2 + NF^+$	1×10^{-11}	est.	-3.3
$N_2^+ + O_2 \rightarrow N_2 + O_2^+$	5×10^{-11}	[23]	-3.5
$N_2^+ + O_2(v) \rightarrow N_2 + O_2^+$	5×10^{-11}	est. [23]	-3.7
$N_2^+ + NF_2 \rightarrow N_2 + NF_2^+$	1×10^{-11}	est.	-4.0
$N_2^+ + NO \rightarrow N_2 + NO^+$	4.1×10^{-10}	[23]	-6.3
$N_2^+ + Ar_2^* \rightarrow N_2 + Ar_2^+$	1×10^{-11}	est.	-11.8
$N_2^+ + N_2O \rightarrow N_2 + N + NO^+$	4×10^{-10}	[26]	-1.4
$N_2^+ + NO_2 \rightarrow N_2O + NO^+$	5×10^{-11}	[26]	-4.8
$N_2^+ + O_2 \rightarrow NO + NO^+$	1×10^{-17}	[27]	-4.5
$N_2^+ + O_2(v) \rightarrow NO + NO^+$	1×10^{-17}	est. [27]	-4.7
$N_2^+ + O \rightarrow N + NO^+$	1.4×10^{-10}	[26]	-3.1
$N_2^+ + O \rightarrow N^* + NO^+$	$1.8 \times 10^{-10}\ T_n^{-1}$	[26]	-0.7
$Ar_2^+ + N \rightarrow Ar + Ar + N^+$	1×10^{-11}	est.	-0.2
$Ar_2^+ + O \rightarrow Ar + Ar + O^+$	1×10^{-11}	est.	-1.1
$Ar_2^+ + NF_3 \rightarrow Ar + Ar + NF_3^+$	1×10^{-11}	est.	-1.2
$Ar_2^+ + N_2O \rightarrow Ar + Ar + N_2O^+$	1×10^{-11}	est.	-1.8
$Ar_2^+ + NF \rightarrow Ar + Ar + NF^+$	1×10^{-11}	est.	-2.4
$Ar_2^+ + O_2 \rightarrow Ar + Ar + O_2^+$	1×10^{-11}	est.	-2.6
$Ar_2^+ + O_2(v) \rightarrow Ar + Ar + O_2^+$	1×10^{-11}	est.	-2.8
$Ar_2^+ + NF_2 \rightarrow Ar + Ar + NF_2^+$	1×10^{-11}	est.	-3.1

$Ar_2^+ + NO \rightarrow Ar + Ar + NO^+$	1×10^{-11}	est.	-5.4
$N^+ + N \rightarrow N + N^+$	1×10^{-9}	est.	
$N^+ + O \rightarrow N + O^+$	1×10^{-11}	est.	-0.9
$N^+ + NF_3 \rightarrow N + NF_3^+$	1×10^{-11}	est.	-1.0
$N^+ + N_2O \rightarrow N + N_2O^+$	1×10^{-11}	est.	-1.6
$N^+ + NF \rightarrow N + NF^+$	1×10^{-11}	est.	-2.2
$N^+ + O_2 \rightarrow N + O_2^+$	3.07×10^{-10}	[23]	-2.4
$N^+ + O_2(v) \rightarrow N + O_2^+$	3.07×10^{-10}	est. [23]	-2.6
$N^+ + NF_2 \rightarrow N + NF_2^+$	1×10^{-11}	est.	-2.9
$N^+ + NO \rightarrow N + NO^+$	4.72×10^{-10}	[23]	-5.2
$N^+ + Ar_2^* \rightarrow N + Ar_2^+$	1×10^{-11}	est.	-10.7
$N^+ + N_2O \rightarrow N_2 + NO^+$	5.5×10^{-10}	[26]	-10.1
$N^+ + NO \rightarrow O + N_2^+$	8.33×10^{-11}	[28]	-2.1
$N^+ + O_2 \rightarrow NO + O^+$	4.64×10^{-11}	[23]	-2.4
$N^+ + O_2(v) \rightarrow NO + O^+$	4.64×10^{-11}	est. [23]	-2.6
$N^+ + O_2 \rightarrow O + NO^+$	2.32×10^{-10}	[23]	-6.6
$N^+ + O_2(v) \rightarrow O + NO^+$	2.32×10^{-10}	est. [23]	-6.8
$O^+ + O \rightarrow O + O^+$	1×10^{-9}	est.	
$O^+ + NF_3 \rightarrow O + NF_3^+$	1×10^{-11}	est.	-0.1
$O^+ + N_2O \rightarrow O + N_2O^+$	6.3×10^{-10}	[26]	-0.7
$O^+ + NF \rightarrow O + NF^+$	1×10^{-11}	est.	-1.3
$O^+ + O_2 \rightarrow O + O_2^+$	2.1×10^{-11}	[23]	-1.5
$O^+ + O_2(v) \rightarrow O + O_2^+$	2.1×10^{-11}	est. [23]	-1.7
$O^+ + NF_2 \rightarrow O + NF_2^+$	1×10^{-11}	est.	-2.0
$O^+ + NO \rightarrow O + NO^+$	8×10^{-13}	[23]	-4.3
$O^+ + Ar_2^* \rightarrow O + Ar_2^+$	1×10^{-11}	est.	-9.8
$O^+ + N_2 \rightarrow N + NO^+$	1.2×10^{-12}	[23]	-1.0
$O^+ + N_2(v) \rightarrow N + NO^+$	1.2×10^{-12}	est. [23]	-1.3
$O^+ + N_2O \rightarrow NO + NO^+$	2.3×10^{-10}	[26]	-5.9
$O^+ + N_2O \rightarrow N_2 + O_2^+$	2×10^{-11}	[26]	-5.0
$O^+ + O_3 \rightarrow O_2 + O_2^+$	1×10^{-10}	[38]	-5.6
$NF_3^+ + NF_3 \rightarrow NF_3 + NF_3^+$	1×10^{-9}	est.	
$NF_3^+ + N_2O \rightarrow NF_3 + N_2O^+$	1×10^{-11}	est.	-0.6
$NF_3^+ + NF \rightarrow NF_3 + NF^+$	1×10^{-11}	est.	-1.2
$NF_3^+ + O_2 \rightarrow NF_3 + O_2^+$	1×10^{-11}	est.	-1.4
$NF_3^+ + O_2(v) \rightarrow NF_3 + O_2^+$	1×10^{-11}	est.	-1.6
$NF_3^+ + NF_2 \rightarrow NF_3 + NF_2^+$	1×10^{-11}	est.	-1.9
$NF_3^+ + NO \rightarrow NF_3 + NO^+$	1×10^{-11}	est.	-4.2
$NF_3^+ + Ar_2^* \rightarrow NF_3 + Ar_2^+$	1×10^{-11}	est.	-9.7
$N_2O^+ + N_2O \rightarrow N_2O + N_2O^+$	1×10^{-9}	est.	
$N_2O^+ + NF \rightarrow N_2O + NF^+$	1×10^{-11}	est.	-0.6
$N_2O^+ + O_2 \rightarrow N_2O + O_2^+$	2.24×10^{-10}	[26]	-0.8

$N_2O^+ + O_2(v) \rightarrow N_2O + O_2^+$	2.24×10^{-10}	est. [26]	-1.0
$N_2O^+ + NF_2 \rightarrow N_2O + NF_2^+$	1×10^{-11}	est.	-1.3
$N_2O^+ + NO \rightarrow N_2O + NO^+$	2.3×10^{-10}	est. [26]	-3.6
$N_2O^+ + Ar_2^* \rightarrow N_2O + Ar_2^+$	1×10^{-11}	est.	-9.1
$N_2O^+ + N_2O \rightarrow N_2 + NO + NO^+$	1.2×10^{-11}	[26]	-3.5
$N_2O^+ + NO_2 \rightarrow N_2 + O_2 + NO^+$	4.29×10^{-10}	[26]	-3.8
$N_2O^+ + O_2 \rightarrow NO_2 + NO^+$	4.59×10^{-11}	[26]	-3.2
$NF^+ + NF \rightarrow NF + NF^+$	1×10^{-9}	est.	
$NF^+ + O_2 \rightarrow NF + O_2^+$	1×10^{-11}	est.	-0.2
$NF^+ + O_2(v) \rightarrow NF + O_2^+$	1×10^{-11}	est.	-0.4
$NF^+ + NF_2 \rightarrow NF + NF_2^+$	1×10^{-11}	est.	-0.7
$NF^+ + NO \rightarrow NF + NO^+$	1×10^{-11}	est.	-3.0
$NF^+ + Ar_2^* \rightarrow NF + Ar_2^+$	1×10^{-11}	est.	-8.5
$NF^+ + NF_3 \rightarrow NF_2 + NF_2^+$	5.5×10^{-10}	[30]	-0.9
$O_2^+ + O_2 \rightarrow O_2 + O_2^+$	1×10^{-9}	est.	
$O_2^+ + O_2(v) \rightarrow O_2 + O_2^+$	1×10^{-9}	est.	-0.2
$O_2^+ + NF_2 \rightarrow O_2 + NF_2^+$	1×10^{-11}	est.	-0.5
$O_2^+ + NO \rightarrow O_2 + NO^+$	4.6×10^{-10}	[23]	-2.8
$O_2^+ + Ar_2^* \rightarrow O_2 + Ar_2^+$	1×10^{-11}	est.	-8.3
$O_2^+ + N \rightarrow O + NO^+$	1.5×10^{-10}	[23]	-4.1
$O_2^+ + N_2 \rightarrow NO + NO^+$	1×10^{-17}	[27]	-0.9
$O_2^+ + N_2(v) \rightarrow NO + NO^+$	1×10^{-17}	est. [27]	-1.2
$NF_2^+ + NF_2 \rightarrow NF_2 + NF_2^+$	1×10^{-9}	est.	
$NF_2^+ + NO \rightarrow NF_2 + NO^+$	1×10^{-11}	est.	-2.3
$NF_2^+ + Ar_2^* \rightarrow NF_2 + Ar_2^+$	1×10^{-11}	est.	-7.8
$NO^+ + NO \rightarrow NO + NO^+$	1×10^{-9}	est.	
$NO^+ + Ar_2^* \rightarrow NO + Ar_2^+$	1×10^{-11}	est.	-5.5
Negative Ion-Neutral Collisions			
$F^- + F \rightarrow F_2 + e$	1.4×10^{-10}	est. [31]	
$O_3^- + O \rightarrow O_2 + O_2 + e$	1.1×10^{-13}	[32]	
$O_3^- + F \rightarrow F^- + O_3$	5.5×10^{-10}	est. [32]	-1.3
$O_3^- + O \rightarrow O_2^- + O_2$	1×10^{-11}	[32]	-2.5
$O^- + N_2 \rightarrow N_2O + e$	1×10^{-12}	[26]	
$O^- + N_2(v) \rightarrow N_2O + e$	1×10^{-12}	est. [26]	
$O^- + N \rightarrow NO + e$	2.2×10^{-10}	[33]	
$O^- + NO \rightarrow NO_2 + e$	2.1×10^{-10}	[34]	
$O^- + O_2 \rightarrow O_3 + e$	5×10^{-15}	[32]	
$O^- + O_2(v) \rightarrow O_3 + e$	5×10^{-15}	est. [32]	
$O^- + O_2^{**} \rightarrow O + O_2 + e$	$6.9 \times 10^{-10}\ T_n^{1/2}$	[38]	
$O^- + O \rightarrow O_2 + e$	1.4×10^{-10}	[31]	
$O^- + O_3 \rightarrow O_2 + O_2 + e$	2×10^{-14}	[32]	
$O^- + F \rightarrow F^- + O$	5.5×10^{-10}	est. [32]	-1.9

$O^- + O_2 \rightarrow O_2^- + O$	2.5×10^{-14}	[35]	1.0
$O^- + O_2(v) \rightarrow O_2^- + O$	2.5×10^{-14}	est. [35]	0.8
$O^- + O_3 \rightarrow O_3^- + O$	5.5×10^{-10}	[32]	-0.6
$O^- + O_3 \rightarrow O_2^- + O_2$	1×10^{-11}	[32]	-3.0
$O_2^- + N \rightarrow NO_2 + e$	4×10^{-10}	[33]	
$O_2^- + O_2^* \rightarrow O_2 + O_2 + e$	2×10^{-10}	[36]	
$O_2^- + O \rightarrow O_3 + e$	$1.5 \times 10^{-10}\ T_n^{1/2}$	[22]	
$O_2^- + F \rightarrow F^- + O_2$	5.5×10^{-10}	est. [32]	-2.9
$O_2^- + N_2O \rightarrow O_3^- + N_2$	1×10^{-11}	[26]	-1.0
$O_2^- + O_2 \rightarrow O_3^- + O$	3×10^{-15}	[37]	2.5
$O_2^- + O_2(v) \rightarrow O_3^- + O$	3×10^{-15}	est. [37]	2.3
$O_2^- + O \rightarrow O^- + O_2$	$1.5 \times 10^{-10}\ T_n^{1/2}$	[22]	-1.0
$O_2^- + O_3 \rightarrow O_3^- + O_2$	3.2×10^{-10}	[32]	-1.6
<u>Ion-Ion Neutralization</u>			
$F^- + F_2^+ \rightarrow F + F_2^*$	2×10^{-7}	est. [38], m)	-4.4
$F^- + F^+ \rightarrow F + F^*$	2×10^{-7}	est.	-1.0
$F^- + NF_3^+ \rightarrow F + NF_2 + F$	2×10^{-7}	est.	-7.5
$F^- + NF_2^+ \rightarrow F + NF + F$	2×10^{-7}	est.	-2.6[g)]
$F^- + NF^+ \rightarrow F + N + F$	1×10^{-7}	est.	-5.8
$F^- + NF^+ \rightarrow F + N^* + F$	1×10^{-7}	est.	-3.4
$F^- + N_2^+ \rightarrow F + N_2^*$	2×10^{-7}	est.	-0.3
$F^- + N^+ \rightarrow F + N^*$	2×10^{-7}	est.	-0.2
$F^- + O_2^+ \rightarrow F + O_2^*$	2×10^{-7}	est.	
$F^- + O^+ \rightarrow F + O^*$	2×10^{-7}	est.	-0.7
$F^- + NO^+ \rightarrow F + NO$	2×10^{-7}	est.	-0.4[g)]
$F^- + N_2O^+ \rightarrow F + N_2O$	$2 \times 10^{-7}\ T_n^{-1/2}$	est. [26]	-9.5
$F^- + N_2O^+ \rightarrow F + N_2 + O$	1×10^{-7}	est. [26]	-7.7
$F^- + Ar^+ \rightarrow F + Ar(1s_5)$	1×10^{-7}	est.	-1.0
$F^- + Ar^+ \rightarrow F + Ar(1s_3)$	1×10^{-7}	est.	-0.9
$F^- + Ar_2^+ \rightarrow F + Ar + Ar$	2×10^{-7}	est.	-11.3
$O^- + F_2^+ \rightarrow O + F_2^*$	2×10^{-7}	est.	-1.3
$O^- + F^+ \rightarrow O + F^*$	2×10^{-7}	est.	
$O^- + NF_3^+ \rightarrow O + NF_2 + F$	2×10^{-7}	est.	-9.4
$O^- + NF_2^+ \rightarrow O + NF + F$	2×10^{-7}	est.	-4.5[g)]
$O^- + NF^+ \rightarrow O + N^* + F$	2×10^{-7}	est.	-5.3
$O^- + N_2^+ \rightarrow O + N_2^*$	2×10^{-7}	est.	-2.2
$O^- + N^+ \rightarrow O + N^*$	2×10^{-7}	est.	
$O^- + O_2^+ \rightarrow O + O_2^*$	2×10^{-7}	est.	-0.2
$O^- + O^+ \rightarrow O + O^*$	2×10^{-7}	est.	
$O^- + NO^+ \rightarrow O + NO$	2×10^{-7}	est.	g)
$O^- + N_2O^+ \rightarrow O + N_2O$	$2 \times 10^{-7}\ T_n^{-1/2}$	[26]	-11.4
$O^- + N_2O^+ \rightarrow O + N_2 + O$	1×10^{-7}	[26]	-9.6

$O^- + Ar^+ \rightarrow O + Ar(1s_5)$	1×10^{-7}	est.	-2.9
$O^- + Ar^+ \rightarrow O + Ar(1s_3)$	1×10^{-7}	est.	-2.8
$O^- + Ar_2^+ \rightarrow O + Ar + Ar$	2×10^{-7}	est.	-13.2
$O_3^- + F_2^+ \rightarrow O_3 + F_2^*$	2×10^{-7}	est.	-0.7
$O_3^- + F^+ \rightarrow O_3 + F^*$	2×10^{-7}	est.	-0.5
$O_3^- + NF_3^+ \rightarrow O_3 + NF_2 + F$	2×10^{-7}	est.	-8.8
$O_3^- + NF_2^+ \rightarrow O_3 + NF + F$	2×10^{-7}	est.	-3.9[g)]
$O_3^- + NF^+ \rightarrow O_3 + N^* + F$	2×10^{-7}	est.	-4.7
$O_3^- + N_2^+ \rightarrow O_3 + N_2^*$	2×10^{-7}	est.	-0.6
$O_3^- + N^+ \rightarrow O_3 + N^*$	2×10^{-7}	est.	
$O_3^- + O_2^+ \rightarrow O_3 + O_2^*$	$2 \times 10^{-7} T_n^{-1/2}$	[32]	-0.5
$O_3^- + O^+ \rightarrow O_3 + O^*$	$1 \times 10^{-7} T_n^{-1/2}$		-0.5
$O_3^- + NO^+ \rightarrow O_3 + NO$	2×10^{-7}	est.	-0.7[g)]
$O_3^- + N_2O^+ \rightarrow O_3 + N_2O$	$2 \times 10^{-7} T_n^{-1/2}$	[26]	-10.8
$O_3^- + N_2O^+ \rightarrow O_3 + N_2 + O$	1×10^{-7}	[26]	-9.0
$O_3^- + Ar^+ \rightarrow O_3 + Ar(1s_5)$	1×10^{-7}	est.	-2.3
$O_3^- + Ar^+ \rightarrow O_3 + Ar(1s_3)$	1×10^{-7}	est.	-2.2
$O_3^- + Ar_2^+ \rightarrow O_3 + Ar + Ar$	2×10^{-7}	est.	-12.6
$O_2^- + F_2^+ \rightarrow O_2 + F_2^*$	2×10^{-7}	est.	-0.2
$O_2^- + F^+ \rightarrow O_2 + F^*$	2×10^{-7}	est.	
$O_2^- + NF_3^+ \rightarrow O_2 + NF_2 + F$	2×10^{-7}	est.	-10.4
$O_2^- + NF_2^+ \rightarrow O_2 + NF + F$	2×10^{-7}	est.	-5.5[g)]
$O_2^- + NF^+ \rightarrow O_2 + N^* + F$	2×10^{-7}	est.	-6.3
$O_2^- + N_2^+ \rightarrow O_2 + N^* + N^*$	2×10^{-7}	est.	-0.5
$O_2^- + N^+ \rightarrow O_2 + N^*$	2×10^{-7}	est.	-0.5
$O_2^- + O_2^+ \rightarrow O_2 + O_2^*$	2×10^{-7}	est.	-0.4
$O_2^- + O^+ \rightarrow O_2 + O^*$	2×10^{-7}	est.	
$O_2^- + NO^+ \rightarrow O_2 + NO$	1×10^{-7}	est.	-0.5[g)]
$O_2^- + NO^+ \rightarrow O_2 + N + O$	1×10^{-7}	[26]	-2.2
$O_2^- + N_2O^+ \rightarrow O_2 + N_2O$	$2 \times 10^{-7} T_n^{-1/2}$	[26]	-12.4
$O_2^- + N_2O^+ \rightarrow O_2 + N_2 + O$	1×10^{-7}	[26]	-10.6
$O_2^- + Ar^+ \rightarrow O_2 + Ar(1s_5)$	1×10^{-7}	est.	-3.9
$O_2^- + Ar^+ \rightarrow O_2 + Ar(1s_3)$	1×10^{-7}	est.	-3.8
$O_2^- + Ar_2^+ \rightarrow O_2 + Ar + Ar$	2×10^{-7}	est.	-14.2
<u>Neutral-Neutral Collisions</u>			
$O_2 + O_2 \rightarrow O_3 + O$	$1.11 \times 10^{-11} \exp(-49{,}800/T_g)$	[39]	4.1
$O_2 + O_2(v) \rightarrow O_3 + O$	$1.11 \times 10^{-11} \exp(-47{,}481/T_g)$	[39]	3.9
$O_2(v) + O_2(v) \rightarrow O_3 + O$	$1.11 \times 10^{-11} \exp(-45{,}162/T_g)$	[39]	3.7
$O_2 + O_2^* \rightarrow O + O_3$	2.95×10^{-21}	est. [40]	3.1
$O_2(v) + O_2^* \rightarrow O + O_3$	2.95×10^{-21}	est. [40]	2.9
$O_2 + O^* \rightarrow O + O_2^{**}$	$2.56 \times 10^{-11} \exp(-67/T_g)$	[17]	-0.3
$O_2 + O^* \rightarrow O + O_2^*$	$1.6 \times 10^{-12} \exp(-67/T_g)$	[17]	-0.9

$O_2(v) + O^* \rightarrow O + O_2^{**}$	2.56×10^{-11}	est. [17]	-0.5
$O_2(v) + O^* \rightarrow O + O_2^{*}$	1.6×10^{-12}	est. [17]	-1.1
$O_2^* + O_2^* \rightarrow O_2 + O_2$	$9 \times 10^{-17} \exp(-560/T_g)$	[18]	-2.0
$O_2^* + O_2^* \rightarrow O_2^{**} + O_2$	$9 \times 10^{-17} \exp(-560/T_g)$	[18]	-0.4
$O_2^* + O(^1S) \rightarrow O^* + O_2^{**}$	2.9×10^{-11}	[38]	-1.7
$O_2^* + O(^1S) \rightarrow O + O_2$	1.1×10^{-10}	est. [38]	-5.2
$O_2^* + O(^1S) \rightarrow O + O + O$	3.2×10^{-11}	[38]	
$O_2^* + O_3 \rightarrow O_2 + O_2 + O$	$5.2 \times 10^{-11} \exp(-2{,}840/T_g)$	[31]	0.1
$O_2^{**} + O_2^{**} \rightarrow O_2^* + O_2$	$3.6 \times 10^{-17} T_n^{0.5}$	est. [41]	-2.2
$O_2^{**} + O_3 \rightarrow O + O_2 + O_2$	1.5×10^{-11}	[31]	-0.5
$O + O_3 \rightarrow O_2 + O_2$	$8.71 \times 10^{-12} \exp(-2{,}113/T_g)$	[42]	-4.1
$O + O_3 \rightarrow O_2^* + O_2$	$1 \times 10^{-11} \exp(-2{,}300/T_g)$	[31]	-3.1
$O^* + O_3 \rightarrow O_2 + O_2$	1.2×10^{-10}	[41]	-6.0
$O^* + O_3 \rightarrow O_2 + O + O$	1.2×10^{-10}	[41]	-0.8
$O(^1S) + O_3 \rightarrow O_2 + O_2$	5.8×10^{-10}	[43]	-8.3
$O_3 + O_3 \rightarrow O_2 + O_2 + O_2$	$7.42 \times 10^{-12} \exp(-9{,}460/T_g)$	[44]	-3.0
$N_2^* + N \rightarrow N_2 + N^*$	$4 \times 10^{-11} T_n^{-0.66}$	[16]	-3.8
$N_2^{**} + N \rightarrow N_2 + N^*$	$4 \times 10^{-11} T_n^{-0.66}$	est. [16]	-6.0
$N_2 + O_2 \rightarrow NO + NO$	$9.85 \times 10^{-6} \exp(-64{,}660/T_g)$	[45]	1.8
$N_2 + O_2(v) \rightarrow NO + NO$	$9.85 \times 10^{-6} \exp(-62{,}341/T_g)$	est. [45]	1.6
$N_2(v) + O_2 \rightarrow NO + NO$	$9.85 \times 10^{-6} \exp(-61{,}180/T_g)$	est. [45]	1.5
$N_2(v) + O_2(v) \rightarrow NO + NO$	$9.85 \times 10^{-6} \exp(-58{,}861/T_g)$	est. [45]	1.3
$N_2 + O \rightarrow N + NO$	$1.26 \times 10^{-10} \exp(-38{,}040/T_g)$	[42]	3.2
$N_2(v) + O \rightarrow N + NO$	$1.26 \times 10^{-10} \exp(-34{,}560/T_g)$	est. [42]	2.9
$N_2 + O_2 \rightarrow N_2O + O$	$1 \times 10^{-10} \exp(-55{,}200/T_g)$	[27]	3.5
$N_2 + O_2(v) \rightarrow N_2O + O$	$1 \times 10^{-10} \exp(-52{,}881/T_g)$	est. [27]	3.3
$N_2(v) + O_2 \rightarrow N_2O + O$	$1 \times 10^{-10} \exp(-51{,}722/T_g)$	est. [27]	3.2
$N_2(v) + O_2(v) \rightarrow N_2O + O$	$1 \times 10^{-10} \exp(-49{,}403/T_g)$	est. [27]	3.0
$N_2^* + O_2 \rightarrow N_2O + O$	7.8×10^{-14}	[27]	-2.7
$N_2^* + O_2 \rightarrow N_2O + O^*$	3×10^{-14}	[27]	-0.8
$N_2^* + O_2(v) \rightarrow N_2O + O$	7.8×10^{-14}	est. [27]	-2.9
$N_2^* + O_2(v) \rightarrow N_2O + O^*$	3×10^{-14}	est. [27]	-1.0
$N_2^* + O_2 \rightarrow N_2 + O_2^*$	$2 \times 10^{-13} T_n^{0.55}$	[38]	-5.0
$N_2^* + O_2 \rightarrow N_2 + O_2^{**}$	$2 \times 10^{-12} T_n^{0.55}$	[38]	-4.0
$N_2^* + O_2(v) \rightarrow N_2 + O_2^*$	$2 \times 10^{-13} T_n^{0.55}$	est. [38]	-5.2
$N_2^* + O_2(v) \rightarrow N_2 + O_2^{**}$	$2 \times 10^{-12} T_n^{0.55}$	est. [38]	-4.2
$N_2^* + O \rightarrow NO + N$	5×10^{-10}	[27]	-3.0
$N_2^* + O \rightarrow NO + N^*$	1×10^{-12}	[27]	-0.6
$N_2^* + O_3 \rightarrow NO + NO + O$	8.4×10^{-12}	[27]	-0.3
$N_2^{**} + O \rightarrow NO + N$	5×10^{-10}	[46]	-3.0
$N_2^{**} + O_3 \rightarrow NO + NO + O$	8.4×10^{-12}	[27]	-3.3
$N + O_2 \rightarrow NO + O$	$4.4 \times 10^{-12} T_n \exp(-3{,}270/T_g)$	[47]	-1.4

$N + O_2(v) \rightarrow NO + O$	$4.4 \times 10^{-12}\ T_n \exp(-951/T_g)$	est. [47]	-1.6
$N + O_2^* \rightarrow NO + O$	$2 \times 10^{-14} \exp(-600/T_g)$	[27]	-2.4
$N + O_2^{**} \rightarrow NO + O$	2.5×10^{-10}	[48]	-3.0
$N + O_3 \rightarrow NO + O_2$	5×10^{-16}	[49]	-5.5
$N^* + O_2 \rightarrow NO + O$	$1.22 \times 10^{-11} \exp(-317/T_g)$	[50]	-3.8
$N^* + O_2 \rightarrow NO + O^*$	$6 \times 10^{-12}\ T_n^{0.5}$	[26]	-1.9
$N^* + O_2(v) \rightarrow NO + O$	1.22×10^{-11}	est. [50]	-4.0
$N^* + O_2(v) \rightarrow NO + O^*$	$6 \times 10^{-12}\ T_n^{0.5}$	est. [26]	-2.1
$N^* + O_2^* \rightarrow NO + O$	2×10^{-14}	est. [27]	-4.8
$N^* + O_2^{**} \rightarrow NO + O$	2.5×10^{-10}	est. [48]	-5.4
$N^* + O_3 \rightarrow NO + O_2$	1×10^{-10}	[27]	-7.9
$N + NO_2 \rightarrow NO + NO$	1.33×10^{-12}	[27]	-3.4
$N + NO_2 \rightarrow N_2 + O + O$	1.12×10^{-12}	[45]	
$N + NO_2 \rightarrow N_2 + O_2$	1.41×10^{-12}	[42]	-5.2
$N + NO_2 \rightarrow N_2O + O$	$5.8 \times 10^{-12} \exp(220/T_g)$	[26]	-1.7
$N + NO \rightarrow N_2 + O$	3.14×10^{-11}	[51]	-3.2
$N^* + NO_2 \rightarrow NO + NO$	1.5×10^{-12}	[52]	-5.8
$N^* + NO_2 \rightarrow N_2 + O + O$	1.12×10^{-12}	est. [45]	-2.4
$N^* + NO_2 \rightarrow N_2 + O_2$	1.41×10^{-12}	est. [42]	-7.6
$N^* + NO_2 \rightarrow N_2O + O$	$1.5 \times 10^{-12} \exp(-570/T_g)$	[27]	-4.1
$N^* + NO \rightarrow N_2 + O$	6.3×10^{-11}	[52]	-5.6
$NO + O \rightarrow N + O_2$	$7.48 \times 10^{-13}\ T_n \exp(-19{,}500/T_g)$	[42]	1.4
$NO + O^* \rightarrow O_2 + N$	1.5×10^{-10}	[53]	-0.5
$NO + O_3 \rightarrow O_2 + NO_2$	$1.4 \times 10^{-12} \exp(-1{,}310/T_g)$	[54]	-2.1
$NO + NO \rightarrow N_2 + O_2$	$1.35 \times 10^{-11} \exp(-28{,}680/T_g)$	[44]	-1.8
$NO + NO \rightarrow N_2O + O$	$7.22 \times 10^{-12} \exp(-33{,}155/T_g)$	[27]	1.7
$NO_2 + O \rightarrow O_2 + NO$	$6.5 \times 10^{-12} \exp(120/T_g)$	[27]	-2.0
$NO_2 + O^* \rightarrow O_2 + NO$	3×10^{-10}	[27]	-3.9
$NO_2 + NO_2 \rightarrow NO + NO + O_2$	$2.63 \times 10^{-11} \exp(-13{,}790/T_g)$	[42]	1.2
$N_2O + N_2^* \rightarrow O + N_2 + N_2$	8×10^{-11}	[26]	-4.5
$N_2O + N_2^* \rightarrow NO + N + N_2$	8×10^{-11}	[26]	-1.3
$N_2O + N^* \rightarrow N_2 + NO$	$1.5 \times 10^{-11} \exp(-570/T_g)$	[26]	-7.3
$N_2O + O \rightarrow N_2 + O_2$	$1.66 \times 10^{-10} \exp(-14{,}100/T_g)$	[27]	-3.5
$N_2O + O \rightarrow NO + NO$	$1.15 \times 10^{-10} \exp(-13{,}400/T_g)$	[27]	-1.7
$N_2O + O^* \rightarrow N_2 + O_2$	4.93×10^{-11}	[27]	-5.4
$N_2O + O^* \rightarrow N_2 + O_2^*$	$2.43 \times 10^{-12}\ TN_2^{.3} \exp(-9{,}645/T_g)$	[55]	-4.4
$N_2O + O^* \rightarrow NO + NO$	8.22×10^{-11}	[27]	-3.6
$N_2O + NO \rightarrow NO_2 + N_2$	$2.92 \times 10^{-13}\ TN_2^{.23} \exp(-23{,}292/T_g)$	[27]	-1.5
$F_2 + O \rightarrow F + FO$	$1.62 \times 10^{-11} \exp(-5{,}233/T_g)$	[42]	-0.7
$F + O_3 \rightarrow FO + O_2$	$2.82 \times 10^{-11} \exp(-252/T_g)$	[42]	-1.2
$FO + O \rightarrow O_2 + F$	5×10^{-11}	[56]	-2.9
$FO + O^* \rightarrow O_2 + F$	5×10^{-11}	[57]	-4.8

$FO + F \rightarrow F_2 + O$	$6.61 \times 10^{-14} \exp(-9{,}561/T_g)$	[42]	0.7
$NF_3 + N \rightarrow NF + NF_2$	$2.13 \times 10^{-12} T_n^{1.97} \exp(-15{,}120/T_g)$	[58]	-0.5
$NF_2 + N \rightarrow NF + NF$	3.0×10^{-12}	[59]	-0.1
$NF_2 + N \rightarrow N_2 + F + F$	$1.4 \times 10^{-11} \exp(-95/T_g)$	[60]	-3.7
$NF + N \rightarrow N_2 + F$	2.5×10^{-10}	est. [61]	-6.7
$NF_3 + N^* \rightarrow NF + NF_2$	2.13×10^{-12}	est. [58]	-2.9
$NF_2 + N^* \rightarrow NF + NF$	3.0×10^{-12}	est. [59]	-2.5
$NF_2 + N^* \rightarrow N_2 + F + F$	1.4×10^{-11}	est. [60]	-6.1
$NF + N^* \rightarrow N_2 + F$	2.5×10^{-10}	[61]	-9.1
$NF_3 + NF \rightarrow NF_2 + NF_2$	1×10^{-14}	[62]	-0.4
$NF_2 + NF_2 \rightarrow NF + NF_3$	$1.66 \times 10^{-12} \exp(-18{,}600/T_g)$	[63]	0.4
$NF + NF \rightarrow N_2 + F + F$	$6.88 \times 10^{-11} \exp(-1{,}251/T_g)$	[45]	-3.6
$NF + NF \rightarrow N_2 + F_2$	4×10^{-12}	[45]	-5.2
$NF_2 + F_2 \rightarrow F + NF_3$	$3.0 \times 10^{-14} \exp(-4{,}860/T_g)$	[64]	-1.0
$NF_3 + O^* \rightarrow NF_2 + FO$	1.1×10^{-11}	[65]	-1.6
$NF_2 + O \rightarrow NF + FO$	1.79×10^{-12}	[59]	0.7
$NF_2 + O \rightarrow F + FNO$	1.25×10^{-11}	[59]	-2.9
$NF_2 + FO \rightarrow FNO + F + F$	3.8×10^{-12}	[66]	-0.6
$NF_2 + NO_2 \rightarrow FNO + FNO$	$8.6 \times 10^{-14} \exp(-2{,}444/T_g)$	[67]	-2.1
$F_2 + NO \rightarrow F + FNO$	1.2×10^{-14}	[68]	-0.8
$FO + NO \rightarrow F + NO_2$	2.6×10^{-11}	[56]	-0.9
$FO + FO \rightarrow F + F + O_2$	2.09×10^{-12}	[42]	-0.6
$FNO + O \rightarrow F + NO_2$	3.0×10^{-13}	[69]	-0.8
<u>High Temperature Chemistry</u>			
$F_2 + M \rightarrow F + F + M$	$7.6 \times 10^{-12} \exp(-14{,}300/T_g)$	[70]	1.6
$F_2^* + M \rightarrow F + F + M$	7.6×10^{-12}	est. [70]	-11.3
$FO + M \rightarrow F + O + M$	$1.31 \times 10^{-10} \exp(-52{,}740/T_g)$	est. [71]	2.3
$FNO + M \rightarrow F + NO + M$	$1.31 \times 10^{-10} \exp(-53{,}899/T_g)$	est. [71]	2.4
$N_2 + M \rightarrow N + N + M$	$9.86 \times 10^{-5} T_n^{-3.33} \exp(-113{,}220/T_g)$	[72]	9.8
$N_2(v) + M \rightarrow N + N + M$	$9.86 \times 10^{-5} T_n^{-3.33} \exp(-109{,}740/T_g)$	est. [72]	9.5
$N_2^* + M \rightarrow N + N + M$	$9.86 \times 10^{-5} T_n^{-3.33} \exp(-41{,}337/T_g)$	est. [72]	3.6
$N_2^* + M \rightarrow N^* + N + M$	$9.86 \times 10^{-5} T_n^{-3.33} \exp(-69{,}163/T_g)$	est. [72]	6.0
$N_2^{**} + M \rightarrow N + N + M$	$9.86 \times 10^{-5} T_n^{-3.33} \exp(-41{,}337/T_g)$	est. [72]	3.6
$N_2^{**} + M \rightarrow N^* + N + M$	$9.86 \times 10^{-5} T_n^{-3.33} \exp(-69{,}163/T_g)$	est. [72]	6.0
$NF_3 + M \rightarrow NF_2 + F + M$	$3.98 \times 10^{-10} \exp(-18{,}417/T_g)$	[73]	2.6
$NF_2 + M \rightarrow NF + F + M$	$1.26 \times 10^{-9} \exp(-25{,}700/T_g)$	[74]	3.0
$NF + M \rightarrow N + F + M$	$1.31 \times 10^{-10} \exp(-52{,}740/T_g)$	est. [71]	3.1
$NO + M \rightarrow N + O + M$	$2.28 \times 10^{-10} \exp(-74{,}680/T_g)$	[71]	6.6
$NO_2 + M \rightarrow NO + O + M$	$1.88 \times 10^{-4} T_n^{-3.37} \exp(-37{,}640/T_g)$	[75]	3.2
$N_2O + M \rightarrow N_2 + O + M$	$2.36 \times 10^{-10} \exp(-25{,}810/T_g)$	[40]	1.8
$O_2 + M \rightarrow O + O + M$	$1.31 \times 10^{-10} \exp(-52{,}740/T_g)$	[71]	5.2
$O_2(v) + M \rightarrow O + O + M$	$1.31 \times 10^{-10} \exp(-50{,}422/T_g)$	est. [71]	5.0

$O_2^* + M \rightarrow O + O + M$	$1.31 \times 10^{-10} \exp(-41{,}146/T_g)$	est. [71]	4.2
$O_2^{**} + M \rightarrow O + O + M$	$1.31 \times 10^{-10} \exp(-34{,}190/T_g)$	est. [71]	3.6
$O_3 + M \rightarrow O_2 + O + M$	$7.17 \times 10^{-10} \exp(-11{,}170/T_g)$	[71]	1.1
$F + F + M \rightarrow F_2 + M$	2.8×10^{-34} cm^{6}s^{-1}	[70]	-1.6
$F + F + M \rightarrow F_2^* + M$	$2.8 \times 10^{-34} \exp(-131{,}012/T_g)$ cm^{6}s^{-1}	est. [70]	11.3
$F + O + M \rightarrow FO + M$	1.0×10^{-33} cm^{6}s^{-1}	[76]	-2.3
$F + NO + M \rightarrow FNO + M$	$5.9 \times 10^{-32} T_n^{-1.7}$ cm^{6}s^{-1}	[77]	-2.4
$N + N + M \rightarrow N_2 + M$	1.41×10^{-32} cm^{6}s^{-1}	[42]	-9.8
$N + N + M \rightarrow N_2(v) + M$	1.41×10^{-32} cm^{6}s^{-1}	est. [42]	-9.5
$N^* + N + M \rightarrow N_2^* + M$	1.41×10^{-32} cm^{6}s^{-1}	est. [42]	-6.0
$N + N + M \rightarrow N_2^* + M$	1.41×10^{-32} cm^{6}s^{-1}	est. [42]	-3.6
$N^* + N + M \rightarrow N_2^{**} + M$	1.41×10^{-32} cm^{6}s^{-1}	est. [42]	-6.0
$N + N + M \rightarrow N_2^{**} + M$	1.41×10^{-32} cm^{6}s^{-1}	est. [42]	-3.6
$NF_2 + F + M \rightarrow NF_3 + M$	1.03×10^{-30} cm^{6}s^{-1}	[78]	-2.6
$NF + F + M \rightarrow NF_2 + M$	1.03×10^{-30} cm^{6}s^{-1}	est. [78]	-3.0
$N + F + M \rightarrow NF + M$	2.8×10^{-34} cm^{6}s^{-1}	est. [70]	-3.1
$N + O + M \rightarrow NO + M$	9.13×10^{-33} cm^{6}s^{-1}	[42]	-6.6
$NO + O + M \rightarrow NO_2 + M$	$1.0 \times 10^{-31} T_n^{-1.6}$ cm^{6}s^{-1}	[54]	-3.2
$O^* + N_2 + M \rightarrow N_2O + M$	2.8×10^{-36} cm^{6}s^{-1}	[54]	-3.7
$O + O + M \rightarrow O_2 + M$	$5.25 \times 10^{-35} \exp(906/T_g)$ cm^{6}s^{-1}	[42]	-5.2
$O + O + M \rightarrow O_2(v) + M$	5.25×10^{-35} cm^{6}s^{-1}	est. [42]	-5.4
$O + O + M \rightarrow O_2^* + M$	5.25×10^{-35} cm^{6}s^{-1}	est. [42]	-6.2
$O + O + M \rightarrow O_2^{**} + M$	5.25×10^{-35} cm^{6}s^{-1}	est. [42]	-6.8
$O + O_2 + M \rightarrow O_3 + M$	$2.57 \times 10^{-35} \exp(-855/T_g)$ cm^{6}s^{-1}	[45]	-1.1

a) This table is a subset of the mechanism for $Ar/NF_3/O_2$ plasmas. The reactions that would occur in a pure Ar discharge are the same as discussed in Ref. [21]. The electron impact reactions and radiative transitions that would occur in a pure O_2 plasma and a pure N_2 plasma are the same as discussed in Ref. [19] and Ref. [26], respectively.

b) Rate coefficients have units of cm^{3}s^{-1} unless noted. T_e is electron temperature (eV). T_g is gas temperature (K) and T_n is normalized gas temperature (T_g/300 K). ΔH is the change of the enthalpy (eV).

c) Rate coefficients are calculated from the electron energy distributions produced by solutions of Boltzmann's equation using electron impact cross sections. The cross section is for the forward reaction. Reverse cross sections are obtained by detailed balance.

d) The rate of gas heating by elastic collisions is $k_m(3/2)k_B(2m_e/M)(T_e-T_g)$ eV-cm^3/s, for elastic rate coefficient k_m, electron mass m_e, neutral mass M and Boltzmann's constant k_B.

e) The cross section for dissociative attachment of NF_3 from Ref. [1] was modified so as to agree with the electron swarm data.

f) Electron impact excitation of NF_x to the vibrationally excited states, $NF_3(v)$, $NF_2(v)$ and NF(v), and the electronically excited states, $NF(^1\Delta)$ and $NF(^1\sum^+)$, was treated by assuming ground state NF_x as the final product with an energy loss of the activation energy.

g) Reduced gas heating was assumed. Actual product would be the transient excited state with higher potential energy which rapidly decays to states with lower potential energy by emitting a photon.

h) Rate coefficient for dissociative recombination was assumed to be 1×10^{-7} cm^3s^{-1} [3] when measured or calculated data is not available.

i) The total ionization cross section is from Ref. [11], branching ratio from Ref. [12].

j) Ar^* represents any excited atomic state of Ar. The same Penning ionization rate coefficient was used for all pairings of excited states of Ar.

k) Rate coefficient for charge exchange between ions and neutrals was assumed to be 1×10^{-11} cm^3s^{-1} (1×10^{-9} cm^3s^{-1} for resonant charge exchange) [22] when measured or calculated data is not available.

l) The rate of gas heating of the neutral by charge exchange is $k_{ce}(3/2)k_B(T_{ion}-T_g)$ eV-cm^3/s, for charge exchange rate coefficient k_{ce} and ion temperature T_{ion}.

m) Rate coefficient for neutralization between positive and negative ions was assumed to be 2×10^{-7} cm^3s^{-1} [38] when measured or calculated data is not available.

Appendix A References

1. V. Lisovskiy, V. Yegorenkov, P. Ogloblina, J.-P. Booth, S. Martins, K. Landry, D. Douai and V. Cassagne, J. Phys. D: Appl. Phys. **47**, 115203 (2014).
2. J. Tennyson, Phys. Rep. **491**, 29 (2010).
3. G. Bekefi, Principles of Laser Plasmas, John Wiley & Sons, New York (1976).
4. M. Hayashi and T. Nimura, J. Appl. Phys. **54**, 4879 (1983).
5. W. L. Morgan, Kinema Research and Software, https://www.kinema.com.
6. G. Bekefi, Radiation Processes in Plasmas, John Wiley & Sons, New York (1966).
7. L. Josić, T. Wróblewski, Z. L. Petrović, J. Mechlińska-Drewko and G. P. Karwasz, Chem. Phys. Lett. **350**, 318 (2001).
8. D. Rapp and D. D. Briglia, J. Chem. Phys. **43**, 1480 (1965).
9. B. G. Lindsay, M. A. Mangan, H. C. Straub and R. F. Stebbings, J. Chem. Phys. **112**, 9404, (2000).
10. Y. Sakai, T. Okumura and H. Tagashira, Austr. J. Phys. **48**, 419 (1995).
11. M. Hayashi and A. Niwawi, in *Gaseous Dielectrics V*, edited by L. G. Christophorou and D. W. Bouldin (Pergamon, New York, 1987), pp. 27-32.
12. L. E. Kline, W. D. Partlow, R. M. Young, R. R. Mitchell and T. V. Congedo, IEEE Trans. Plasma Sci. **19**, 278 (1991).
13. D. L. Huestis, R. M. Hill, H. H. Nakano and D. C. Lorents, J. Chem. Phys. **69**, 5133 (1978).
14. K. Sasaki, Y. Kawai and K. Kadota, Rev. Sci. Instrum. **70**, 76 (1999).
15. L. G. Piper, J. Chem. Phys. **97**, 270 (1992).
16. B. Gordiets, C. M. Ferreira, M. J. Pinheiro and A. Ricard, Plasma Sources Sci. Technol. **7**, 363 (1998).
17. R. Atkinson, D. L. Baulch, R. A. Cox, R. F. Hampson, J. A. Kerr, M. J. Rossi and J. Troe, J. Phys. Chem. Ref. Data **26**, 521 (1997).
18. J. T. Herron and D. S. Green, Plasma Chem. Plasma Process. **21**, 459 (2001).
19. D. S. Stafford and M. J. Kushner, J. Appl. Phys. **96**, 2451 (2004).
20. N. A. Dyatko, Y. Z. Ionikh, I. V. Kochetov, D. L. Marinov, A. V. Meshchanov, A. P. Napartovich, F. B. Petrov and S. A. Starostin, J. Phys. D **41**, 055204 (2008).
21. P. Tian and M. J. Kushner, Plasma Sources Sci. Technol. **24**, 034017 (2015).

22. Y. Ikezoe, S. Matsuoka, M. Takebe and Viggiano, Gas Phase Ion Molecule Reaction Rate Constants Through 1986, Ion Reaction Research Group of the Mass Spectroscopy Society of Japan, Tokyo, Japan (1987).
23. V. G. Anicich, J. Phys. Chem. Ref. Data **22**, 1469 (1993).
24. P. K. Leichner and R. J. Ericson, Phys. Rev. A **9**, 251 (1974).
25. E. E. Ferguson, Adv. Electron. Electron Phys. **24**, 1 (1968).
26. Y. Sakiyama, D. B. Graves, H.-W. Chang, T. Shimizu and G. E. Morfill, J. Phys. D: Appl. Phys. **45**, 425201 (2012).
27. W. Van Gaens and A. Bogaerts, J. Phys. D: Appl. Phys. **46**, 275201 (2013).
28. R. Johnsen and M. A. Biondi, J. Chem. Phys. **73**, 5045 (1980).
29. B. F. Gordiets, C. M. Ferreira, V. L. Guerra, J. M. A. H. Loureiro, J. Nahorny, D. Pagnon, M. Touzeau and M. Vialle, IEEE Trans. Plasma Sci. **23**, 750 (1995).
30. P. B. Armentrout, D. W. Berman and J. L. Beauchamp, Chem. Phys. Lett. **53**, 255 (1978).
31. M. Touzeau, G. Gousset, J. Jolly, D. Pagnon, M. Vialle, C. M. Ferreira, J. Loureiro, M. Pinheiro, P. A. Sa, Spectroscopy and Kinetics of An Oxygen Glow Discharge. Nonequilibrium in Partially Ionized Gases. Springer, U.S. (1990).
32. J. I. Steinfeld, S. M. Adler-Golden and J. W. Gallagher, J. Phys. Chem. Ref. Data **16**, 911 (1987).
33. R. B. Norton, E. E. Ferguson, F. C. Fehsenfeld and A.L. Schmeltekopf, Planet. Space Sci. **14**, 969 (1966).
34. M. McFarland, D. L. Albritton, F. C. Fehsenfeld, E. E. Ferguson and A. L. Schmeltekopf, J. Chem. Phys. **59**, 6629 (1973).
35. R. M. Snuggs, D. J. Volz, I. R. Gatland, J. H. Schummers, D. W. Martin and E. W. McDaniel, Phys. Rew. A **3**, 487 (1971).
36. F. C. Fehsenfeld, D. L. Albritton, J. A. Burt and H. I. Schiff, Can. J. Chem. **47**, 1793 (1969).
37. C. Lifshitz, R. L. C. Wu, T. O. Tiernan and D. T. Terwilliger, J. Chem. Phys. **68**, 247 (1978).
38. R. E. Olson, J. R. Peterson and J. Moseley, J. Chem. Phys. **53**, 3391 (1970).
39. S. W. Benson and A. E. Axworthy, J. Chem. Phys. **26**, 1718 (1957).
40. E. Meeks, S. R. Vosen, J. W. Shon, R. S. Larson, C. A. Fox, D. Buchenauer, Results from Modeling and Simulation of Chemical Downstream Etch Systems, Sandia Report, SAND96-8241 (1996).

41. R. Atkinson, D. L. Baulch, R. A. Cox, R. F. Hampson, J. A. Kerr, M. J. Rossi and J. Troe, J. Phys. Chem. Ref. Data **26**, 1329 (1997).
42. J. A. Kerr and S. J. Moss, CRC Handbook of Bimolecular and Termolecular Gas Reactions, CRC Press, Boca Raton, FL (1981).
43. G. London, R. Gilpin, H. I. Schiff and K. H. Welge, J. Chem. Phys. **54**, 4512 (1971).
44. A. F. Trotman-Dickenson and G. S. Milne, Tables of Bimolecular Gas Reactions (NSRDS NBS 9), U.S. Government Printing Office, Washington, DC (1967).
45. V. N. Kondratiev, Rate Constants of Gas Phase Reactions: Reference Book. Office of Standard Reference Data, National Bureau of Standards, U.S. Dept. of Commerce; Distributed by National Technical Information Service, Springfield, VA (1972).
46. I. Shkurenkov, D. Burnette, W. R. Lempert, and I. V. Adamovich, Plasma Sources Sci. Technol. **23**, 065003 (2014).
47. R. Atkinson, D. L. Baulch, R. A. Cox, R. F. Hampson, J. A. Kerr and J. Troe, J. Phys. Chem. Ref. Data **18**, 881 (1989).
48. M. Uddi, N. Jiang, I. V. Adamovich and W. R. Lempert, J. Phys. D: Appl. Phys. **42**, 075205 (2009).
49. L. J. Stief, W. A. Payne, J. H. Lee and J. V. Michael, J. Chem. Phys. **70**, 5241 (1979).
50. M. Gonzalez, I. Miquel and R. Sayos, Chem. Phys. Lett. **335**, 339 (2001).
51. J. W. Duff and R. D. Sharma, Geophys. Res. Lett. **23**, 2777 (1996).
52. J. C. Person and D. O. Ham, Radiat. Phys. Chem. **31**, 1 (1988).
53. R. A. Young, G. Black and T. G. Slanger, J. Chem. Phys. **49**, 4758 (1968).
54. R. Atkinson, D. L. Baulch, R. A. Cox, J. N. Crowley, R. F. Hampson, R. G. Hynes, M. E. Jenkin, M. J. Rossi and J. Troe, Atmos. Chem. Phys. **4**, 1461 (2004).
55. M. Gonzalez, R. Sayos and R. Valero, Chem. Phys. Lett. **355**, 123 (2002).
56. R. Atkinson, D. L. Baulch, R. A. Cox, R. F. Hampson, J. A. Kerr and J. Troe, J. Phys. Chem. Ref. Data **21**, 1125 (1992).
57. I. C. Plumb and K. R. Ryan, Plasma Chem. Plasma Process. **6**, 205 (1986).
58. P. R. P. Barreto, A. F. A. Vilela, R. Gargano, S. S. Ramalho and L. R. Salviano, J. Mol. Struct. THEMCHEM **769**, 201 (2006).
59. C. T. Cheah, M. A. A. Clyne and P. D. Whitefield, J. Chem. Soc. Faraday Trans. II **76**, 711 (1980).

60. V. B. Rozenshtein, Y. R. Bedzhanyan and Y. M. Gershenzon, Kinet. Catal. **29**, 22 (1988).
61. J. T. Herron, J. Phys. Chem. Ref. Data **28**, 1453 (1999).
62. B. H. Weiller, R. F. Heidner, J. S. Holloway and J. B. Koffend, J. Phys. Chem. **96**, 9321 (1992).
63. W. Corbin and J. B. Levy, Int. J. Chem. Kinet. **7**, 679 (1975).
64. J. B. Levy and B. K. W. Copeland, J. Phys. Chem. **69**, 3700 (1965).
65. V. I. Sorokin, N. P. Gritsan, A. I. Chichinin, J. Chem. Phys. **108**, 8995 (1998).
66. Y. R. Bedzhanyan, Y. M. Gershenzon and V. B. Rozenshtein, Kinet. Catal. **31**, 1291 (1990).
67. Y. G. Bedzhanyan, Y. M. Gershenson, S. D. Il'in, O. P. Kishkovic, V. B. Rozenshtein, Sov. J. Chem. Phys. **6**, 610 (1990).
68. A. A. Turnipseed and J. W. Birks, J. Phys. Chem. **95**, 6569 (1991).
69. T. J. Wallington, W. F. Schneider, J. J. Szente, M. M. Maricq, O. J. Nielsen and J. Sehested, J. Phys. Chem. **99**, 984 (1995).
70. A. C. Lloyd, Int. J. Chem. Kinet. **3**, 39 (1971).
71. F. Westley, J. H. Herron and R. J. Cvetanovic, Compilation of Chemical Kinetic Data for Combustion Chemistry (NSRDS-NBS 73, Parts 1 and 2), U.S. Government Printing Office, Washington, DC (1987).
72. K. Thielen and P. Roth, AIAA J. **24**, 1102 (1986).
73. V. M. Doroshchenko, N. N. Kudriavtsev, A. M. Sukhov and D. P. Shamshev, Chem. Phys. Lett. **193**, 258 (1992).
74. D. L. Baulch, J. Duxbury, S. J. Grant and D. C. Montague, Evaluated Kinetic Data for High Temperature Reactions (Volume 4) Homogeneous Gas Phase Reactions of Halogen- and Cyanide-containing Species, National Standard Reference Data System (1981).
75. W. Tsang and J. T. Herron, J. Phys. Chem. Ref. Data **20**, 609 (1991).
76. D. R. F. Burgess, M. R. Zachariah, W. Tsang and P. R. Westmoreland, Prog. Energy Combust. Sci. **21**, 453 (1996).
77. M. Matti Maricq, J. J. Szente, T. S. Dibble and J. S. Francisco, J. Phys. Chem. **98**, 12294 (1994).
78. J. B. Koffend, C. E. Gardner and R. F. Heidner III, J. Chem. Phys. **83**, 2904 (1985).

Appendix B Reaction Mechanism of $NF_3/O_2/H_2$ Plasma

This appendix contains the additional reactions required for adding H_2 to NF_3/O_2 mixtures to complete the $NF_3/O_2/H_2$ mechanism. The reaction mechanism for NF_3/O_2 mixtures is listed in Appendix A.

Species in full reaction mechanism[a]:

NF_3	NF_2	NF	NF_3^+	NF_2^+	NF^+	N_2
$N_2(v)$	$N_2(A\ ^3\sum_u^+)$	$N_2(B\ ^3\Pi_g$, higher)		N	$N(^2D)$	N_2^+
N^+	F_2	$F_2(1\ ^1\sum_u^+)$	F	$F(^3S)$	F_2^+	F^+
F^-	O_2	$O_2(v)$	$O_2(a\ ^1\Delta_g)$	$O_2(b\ ^1\sum_g^+)$	O	$O(^1D)$
$O(^1S)$	O_3	O_2^+	O^+	O_2^-	O^-	O_3^-
NO	N_2O	NO_2	NO^+	N_2O^+	FO	FNO
H_2	$H_2(v=1)$	$H_2(v=2)$	$H_2(v\geq3)$	$H_2(B\ ^1\sum_u^+$, higher)		H
H(n=2)	H(n=3)	H_2^+	H^+	H^-	NH_3	$NH_3(v)$
NH_2	NH	NH_3^+	NH_2^+	NH^+	NH_2^-	HF
HF(v=1)	HF(v≥2)	HF^+	OH	H_2O	HO_2	H_2O_2
OH^+	H_2O^+	OH^-	e			

[a] For simplicity in the reaction list, following notation is used for excited states:

$N_2^* \leftrightarrow N_2(A\ ^3\sum_u^+)$	$N^* \leftrightarrow N(^2D)$	$F_2^* \leftrightarrow F_2(1\ ^1\sum_u^+)$	$F^* \leftrightarrow F(^3S)$
$O_2^* \leftrightarrow O_2(a\ ^1\Delta_g)$	$O^* \leftrightarrow O(^1D)$	$H_2^* \leftrightarrow H_2(B\ ^1\sum_u^+$, higher)	$H^* \leftrightarrow H(n=2)$
$H^{**} \leftrightarrow H(n=3)$			

Table B.1 List of reactions in the mechanism of $NF_3/O_2/H_2$ plasma.

Reactions[a]	Rate Coefficient[b]	Reference	ΔH[b] (eV)
<u>Electron Impact H_2/H</u>			
$e + H_2 \rightarrow H_2 + e$	c)	[1]	d)

$e + H_2 \rightarrow H_2(v=1) + e$	c)	[1]	
$e + H_2 \rightarrow H_2(v=2) + e$	c)	[1]	
$e + H_2 \rightarrow H_2(v\geq3) + e$	c)	[1]	
$e + H_2 \rightarrow H + H^-$	c)	[1]	
$e + H_2 \rightarrow H_2^* + e$	c)	[1]	
$e + H_2 \rightarrow H_2^+ + e + e$	c)	[1]	
$e + H_2 \rightarrow H + H + e$	c)	[1]	-7.4
$e + H_2 \rightarrow H + H + e$	c)	[1]	-8.4
$e + H_2 \rightarrow H + H + e$	c)	[1]	-7.2
$e + H_2 \rightarrow H + H^* + e$	c)	[1]	
$e + H_2 \rightarrow H + H^{**} + e$	c)	[1]	
$e + H_2 \rightarrow H + H^+ + e + e$	c)	[1]	
$e + H_2(v=1) \rightarrow H_2(v=1) + e$	c)	[1]	d)
$e + H_2(v=1) \rightarrow H_2(v=2) + e$	c)	[1]	
$e + H_2(v=1) \rightarrow H_2(v\geq3) + e$	c)	[1]	
$e + H_2(v=1) \rightarrow H_2 + e$	c)	[1]	
$e + H_2(v=1) \rightarrow H + H^-$	c)	[1]	
$e + H_2(v=1) \rightarrow H_2^* + e$	c)	[1]	
$e + H_2(v=1) \rightarrow H_2^+ + e + e$	c)	[1]	
$e + H_2(v=1) \rightarrow H + H + e$	c)	[1]	-7.4
$e + H_2(v=1) \rightarrow H + H + e$	c)	[1]	-8.4
$e + H_2(v=1) \rightarrow H + H + e$	c)	[1]	-7.2
$e + H_2(v=1) \rightarrow H + H^* + e$	c)	[1]	
$e + H_2(v=1) \rightarrow H + H^{**} + e$	c)	[1]	
$e + H_2(v=1) \rightarrow H + H^+ + e + e$	c)	[1]	
$e + H_2(v=2) \rightarrow H_2(v=2) + e$	c)	[1]	d)
$e + H_2(v=2) \rightarrow H_2(v\geq3) + e$	c)	[1]	
$e + H_2(v=2) \rightarrow H_2(v=1) + e$	c)	[1]	
$e + H_2(v=2) \rightarrow H_2 + e$	c)	[1]	
$e + H_2(v=2) \rightarrow H + H^-$	c)	[1]	
$e + H_2(v=2) \rightarrow H_2^* + e$	c)	[1]	
$e + H_2(v=2) \rightarrow H_2^+ + e + e$	c)	[1]	
$e + H_2(v=2) \rightarrow H + H + e$	c)	[1]	-7.4
$e + H_2(v=2) \rightarrow H + H + e$	c)	[1]	-8.4
$e + H_2(v=2) \rightarrow H + H + e$	c)	[1]	-7.2
$e + H_2(v=2) \rightarrow H + H^* + e$	c)	[1]	
$e + H_2(v=2) \rightarrow H + H^{**} + e$	c)	[1]	
$e + H_2(v=2) \rightarrow H + H^+ + e + e$	c)	[1]	
$e + H_2(v\geq3) \rightarrow H_2(v\geq3) + e$	c)	[1]	d)
$e + H_2(v\geq3) \rightarrow H_2(v=2) + e$	c)	[1]	
$e + H_2(v\geq3) \rightarrow H_2(v=1) + e$	c)	[1]	
$e + H_2(v\geq3) \rightarrow H_2 + e$	c)	[1]	

$e + H_2(v\geq3) \rightarrow H + H^-$	c)	[1]	
$e + H_2(v\geq3) \rightarrow H_2^* + e$	c)	[1]	
$e + H_2(v\geq3) \rightarrow H_2^+ + e + e$	c)	[1]	
$e + H_2(v\geq3) \rightarrow H + H + e$	c)	[1]	-7.4
$e + H_2(v\geq3) \rightarrow H + H + e$	c)	[1]	-8.4
$e + H_2(v\geq3) \rightarrow H + H + e$	c)	[1]	-7.2
$e + H_2(v\geq3) \rightarrow H + H^* + e$	c)	[1]	
$e + H_2(v\geq3) \rightarrow H + H^{**} + e$	c)	[1]	
$e + H_2(v\geq3) \rightarrow H + H^+ + e + e$	c)	[1]	
$e + H_2^+ \rightarrow H + H^+ + e$	c)	[2]	-6.8
$e + H_2^+ \rightarrow H + H$	c)	[2]	-10.8
$e + H_2^+ \rightarrow H^+ + H^-$	c)	[3]	
$e + H \rightarrow H + e$	c)	[4]	
$e + H \rightarrow H(n=2) + e$	c)	[4]	
$e + H \rightarrow H(n=3) + e$	c)	[4]	
$e + H \rightarrow H^+ + e + e$	c)	[4]	
$e + H^+ \rightarrow H$	$4.5 \times 10^{-13}\ T_e^{-1/2}$	est. [5]	
$e + e + H^+ \rightarrow H^* + e$	$5.12 \times 10^{-27}\ T_e^{-4.5}$	est. [5]	
Electron Impact HF			
$e + HF \rightarrow HF + e$	c), e)	[6]	
$e + HF \rightarrow HF(v=1) + e$	c)	[7]	
$e + HF \rightarrow HF(v\geq2) + e$	c)	[7]	
$e + HF \rightarrow F^- + H$	c)	[8]	
$e + HF \rightarrow H + F + e$	c), e)	[6]	-4.8
$e + HF \rightarrow HF^+ + e + e$	c), e)	[6]	
$e + HF(v=1) \rightarrow HF(v=1) + e$	c), e)	[6]	
$e + HF(v=1) \rightarrow HF(v\geq2) + e$	c)	[7]	
$e + HF(v=1) \rightarrow HF + e$	c), f)		
$e + HF(v=1) \rightarrow F^- + H$	c)	[8]	
$e + HF(v=1) \rightarrow F + H + e$	c), e)	[6]	-4.8
$e + HF(v=1) \rightarrow HF^+ + e + e$	c), e)	[6]	
$e + HF(v\geq2) \rightarrow HF(v\geq2) + e$	c), e)	[6]	
$e + HF(v\geq2) \rightarrow HF(v=1) + e$	c), f)		
$e + HF(v\geq2) \rightarrow HF + e$	c), f)		
$e + HF(v\geq2) \rightarrow F^- + H$	c)	[8]	
$e + HF(v\geq2) \rightarrow F + H + e$	c), e)	[6]	-4.8
$e + HF(v\geq2) \rightarrow HF^+ + e + e$	c), e)	[6]	
$e + HF^+ \rightarrow H + F$	$1 \times 10^{-7}\ T_e^{-1/2}$	est. [9]	-10.1
Electron Impact NH_x			
$e + NH_3 \rightarrow NH_3 + e$	c)	[10]	
$e + NH_3 \rightarrow NH_3(v) + e$	c)	[10]	
$e + NH_3 \rightarrow H^- + NH_2$	c)	[10]	-0.5

$e + NH_3 \rightarrow NH_2 + H + e$	c)	[10]	-0.8
$e + NH_3 \rightarrow NH + H + H + e$	c)	[10]	
$e + NH_3 \rightarrow NH_3^+ + e + e$	c)	[10]	
$e + NH_3 \rightarrow NH_2^+ + H + e + e$	c)	[10]	-0.1
$e + NH_3(v) \rightarrow NH_3(v) + e$	c), g)		
$e + NH_3(v) \rightarrow NH_3 + e$	c), f)		
$e + NH_3(v) \rightarrow H^- + NH_2$	c), g)		-0.5
$e + NH_3(v) \rightarrow NH_2 + H + e$	c), g)		-0.8
$e + NH_3(v) \rightarrow NH + H + H + e$	c), g)		
$e + NH_3(v) \rightarrow NH_3^+ + e + e$	c), g)		
$e + NH_3(v) \rightarrow NH_2^+ + H + e + e$	c), g)		-0.1
$e + NH_2 \rightarrow NH_2 + e$	c), g)		
$e + NH_2 \rightarrow H^- + NH$	c), g)		-1.1
$e + NH_2 \rightarrow NH + H + e$	c), g)		-1.4
$e + NH_2 \rightarrow N + H + H + e$	c), g)		-1.4
$e + NH_2 \rightarrow NH_2^+ + e + e$	c)	[11]	
$e + NH_2 \rightarrow NH^+ + H + e + e$	c)	[11]	
$e + NH \rightarrow NH + e$	c), g)		
$e + NH \rightarrow N + H + e$	c), g)		-2.3
$e + NH \rightarrow NH^+ + e + e$	c)	[11]	
$e + NH \rightarrow N^+ + H + e + e$	c)	[11]	
$e + NH_3^+ \rightarrow NH_2 + H$	$1 \times 10^{-7}\ T_e^{-1/2}$	est. [9]	-2.9
$e + NH_2^+ \rightarrow NH + H$	$1 \times 10^{-7}\ T_e^{-1/2}$	est. [9]	-1.4
$e + NH^+ \rightarrow N + H$	$1 \times 10^{-7}\ T_e^{-1/2}$	est. [9]	-10.2
<u>Electron Impact H_xO_y</u>			
$e + OH \rightarrow OH + e$	c), h)	[12]	
$e + OH \rightarrow OH^+ + e + e$	c)	[13]	
$e + OH^+ \rightarrow O(^1S) + H$	$1 \times 10^{-7}\ T_e^{-1/2}$	est. [9]	-4.8
$e + H_2O \rightarrow H_2O + e$	c)	[14]	
$e + H_2O \rightarrow H^- + OH$	c)	[14]	-1
$e + H_2O \rightarrow O^- + H_2$	c)	[14]	-0.9
$e + H_2O \rightarrow OH^- + H$	c)	[14]	-0.9
$e + H_2O \rightarrow OH + H + e$	c)	[14]	-2.4
$e + H_2O \rightarrow O + H + H + e$	c)	[14]	-3.8
$e + H_2O \rightarrow H_2O^+ + e + e$	c)	[14]	
$e + H_2O \rightarrow OH^+ + H + e + e$	c)	[14]	
$e + H_2O \rightarrow O^+ + H + H + e + e$	c)	[14]	-1.7
$e + H_2O \rightarrow H_2^+ + O + e + e$	c)	[14]	-9.4
$e + H_2O \rightarrow H^+ + OH + e + e$	c)	[14]	-1.1
$e + H_2O^+ \rightarrow OH + H$	$6.6 \times 10^{-6}\ T_e^{-1/2}$	[15]	-8.3
$e + H_2O^+ \rightarrow O + H + H$	$2.88 \times 10^{-6}\ T_e^{-1/2}$	[15]	-3.8
$e + H_2O^+ \rightarrow O + H_2$	$2.52 \times 10^{-6}\ T_e^{-1/2}$	[15]	-8.4

Radiative Transitions			
$H_2^* \rightarrow H_2$	2.5×10^7 s^{-1}	[16]	
HF(v=1) $\rightarrow$ HF	1.89×10^2 s^{-1}	[17]	
HF(v≥2) $\rightarrow$ HF(v=1)	3.88×10^2 s^{-1}	[17]	
HF(v≥2) $\rightarrow$ HF	2.40×10^1 s^{-1}	[17]	
Collisional Quenching			
HF(v=1) + M $\rightarrow$ HF + M	3.8×10^{-15} $T_n^{1/2}$	[18]	-0.5
HF(v≥2) + M $\rightarrow$ HF(v=1) + M	3.8×10^{-15} $T_n^{1/2}$	est. [18]	-0.5
NH_3(v) + M $\rightarrow$ NH_3 + M	3×10^{-13} $T_n^{1/2}$	est. [19]	-0.1
H_2(v=1) + M $\rightarrow$ H_2 + M	7.45×10^{-17} $T_n^{4.3}$	[20]	-0.5
H_2(v=2) + M $\rightarrow$ H_2(v=1) + M	1.49×10^{-16} $T_n^{4.3}$	[20]	-0.5
H_2(v≥3) + M $\rightarrow$ H_2(v=2) + M	2.23×10^{-16} $T_n^{4.3}$	[20]	-0.5
H_2^* + M $\rightarrow$ H_2 + M	2.1×10^{-9}	[21]	-13.7
H^* + M $\rightarrow$ H + M	1×10^{-8}	[22]	-10.2
H^{**} + M $\rightarrow$ H + M	1×10^{-8}	[22]	-12
Positive Ion-Neutral Collisions			
F^+ + HF $\rightarrow$ HF^+ + F	1×10^{-11}	est. [23], i)	-1.4
F^+ + HF(v=1) $\rightarrow$ HF^+ + F	1×10^{-11}	est.	-1.9
F^+ + HF(v≥2) $\rightarrow$ HF^+ + F	1×10^{-11}	est.	-2.4
F^+ + H_2 $\rightarrow$ H_2^+ + F	6.24×10^{-10}	[24]	-2
F^+ + H_2(v=1) $\rightarrow$ H_2^+ + F	6.24×10^{-10}	est. [24]	-2.5
F^+ + H_2(v=2) $\rightarrow$ H_2^+ + F	6.24×10^{-10}	est. [24]	-3
F^+ + H_2(v≥3) $\rightarrow$ H_2^+ + F	6.24×10^{-10}	est. [24]	-3.5
F^+ + H $\rightarrow$ H^+ + F	1×10^{-11}	est.	-3.8
F^+ + H_2O $\rightarrow$ H_2O^+ + F	1×10^{-11}	est.	-3.9
F^+ + OH $\rightarrow$ OH^+ + F	1×10^{-11}	est.	-3.9
F^+ + NH $\rightarrow$ NH^+ + F	1×10^{-11}	est.	-3.9
F^+ + NH_2 $\rightarrow$ NH_2^+ + F	1×10^{-11}	est.	-6.3
F^+ + NH_3 $\rightarrow$ NH_3^+ + F	2.46×10^{-10}	[24]	-7.3
F^+ + NH_3(v) $\rightarrow$ NH_3^+ + F	2.46×10^{-10}	est. [24]	-7.4
F^+ + H_2 $\rightarrow$ H^+ + HF	3.12×10^{-11}	[24]	-5.1
F^+ + H_2(v=1) $\rightarrow$ H^+ + HF	3.12×10^{-11}	[24]	-5.6
F^+ + H_2(v=2) $\rightarrow$ H^+ + HF	3.12×10^{-11}	[24]	-6.1
F^+ + H_2(v≥3) $\rightarrow$ H^+ + HF	3.12×10^{-11}	[24]	-6.6
F^+ + NH_3 $\rightarrow$ NH^+ + HF + H	1.03×10^{-10}	[24]	-0.9
F^+ + NH_3 $\rightarrow$ NH_2^+ + HF	1.62×10^{-9}	[24]	-7.5
F^+ + NH_3(v) $\rightarrow$ NH^+ + HF + H	1.03×10^{-10}	est. [24]	-1
F^+ + NH_3(v) $\rightarrow$ NH_2^+ + HF	1.62×10^{-9}	est. [24]	-7.6
HF^+ + HF $\rightarrow$ HF^+ + HF	1×10^{-9}	est.	
HF^+ + HF(v=1) $\rightarrow$ HF^+ + HF	1×10^{-9}	est.	-0.5
HF^+ + HF(v≥2) $\rightarrow$ HF^+ + HF	1×10^{-9}	est.	-1
HF^+ + F_2 $\rightarrow$ F_2^+ + HF	1×10^{-11}	est.	-0.3

$HF^+ + N_2 \rightarrow N_2^+ + HF$	1×10^{-11}	est.	-0.4
$HF^+ + N_2(v) \rightarrow N_2^+ + HF$	1×10^{-11}	est.	-0.7
$HF^+ + H_2 \rightarrow H_2^+ + HF$	1×10^{-11}	est.	-0.6
$HF^+ + H_2(v=1) \rightarrow H_2^+ + HF$	1×10^{-11}	est.	-1.1
$HF^+ + H_2(v=2) \rightarrow H_2^+ + HF$	1×10^{-11}	est.	-1.6
$HF^+ + H_2(v\geq3) \rightarrow H_2^+ + HF$	1×10^{-11}	est.	-2.1
$HF^+ + N \rightarrow N^+ + HF$	1×10^{-11}	est.	-1.5
$HF^+ + O \rightarrow O^+ + HF$	1×10^{-11}	est.	-2.4
$HF^+ + H \rightarrow H^+ + HF$	1×10^{-11}	est.	-2.4
$HF^+ + NF_3 \rightarrow NF_3^+ + HF$	1×10^{-11}	est.	-2.5
$HF^+ + H_2O \rightarrow H_2O^+ + HF$	1×10^{-11}	est.	-2.5
$HF^+ + OH \rightarrow OH^+ + HF$	1×10^{-11}	est.	-2.5
$HF^+ + NH \rightarrow NH^+ + HF$	1×10^{-11}	est.	-2.5
$HF^+ + N_2O \rightarrow N_2O^+ + HF$	1×10^{-11}	est.	-3.1
$HF^+ + NF \rightarrow NF^+ + HF$	1×10^{-11}	est.	-3.7
$HF^+ + O_2 \rightarrow O_2^+ + HF$	1×10^{-11}	est.	-3.9
$HF^+ + O_2(v) \rightarrow O_2^+ + HF$	1×10^{-11}	est.	-4.1
$HF^+ + NF_2 \rightarrow NF_2^+ + HF$	1×10^{-11}	est.	-4.4
$HF^+ + NH_2 \rightarrow NH_2^+ + HF$	1×10^{-11}	est.	-4.9
$HF^+ + NH_3 \rightarrow NH_3^+ + HF$	1×10^{-11}	est.	-5.9
$HF^+ + NH_3(v) \rightarrow NH_3^+ + HF$	1×10^{-11}	est.	-6
$HF^+ + NO \rightarrow NO^+ + HF$	1×10^{-11}	est.	-6.7
$F_2^+ + HF(v=1) \rightarrow HF^+ + F_2$	1×10^{-11}	est.	-0.2
$F_2^+ + HF(v\geq2) \rightarrow HF^+ + F_2$	1×10^{-11}	est.	-0.7
$F_2^+ + H_2 \rightarrow H_2^+ + F_2$	1×10^{-11}	est.	-0.3
$F_2^+ + H_2(v=1) \rightarrow H_2^+ + F_2$	1×10^{-11}	est.	-0.8
$F_2^+ + H_2(v=2) \rightarrow H_2^+ + F_2$	1×10^{-11}	est.	-1.3
$F_2^+ + H_2(v\geq3) \rightarrow H_2^+ + F_2$	1×10^{-11}	est.	-1.8
$F_2^+ + H \rightarrow H^+ + F_2$	1×10^{-11}	est.	- 2.1
$F_2^+ + H_2O \rightarrow H_2O^+ + F_2$	1×10^{-11}	est.	-2.2
$F_2^+ + OH \rightarrow OH^+ + F_2$	1×10^{-11}	est.	-2.2
$F_2^+ + NH \rightarrow NH^+ + F_2$	1×10^{-11}	est.	-2.2
$F_2^+ + NH_2 \rightarrow NH_2^+ + F_2$	1×10^{-11}	est.	-4.6
$F_2^+ + NH_3 \rightarrow NH_3^+ + F_2$	1×10^{-11}	est.	-5.6
$F_2^+ + NH_3(v) \rightarrow NH_3^+ + F_2$	1×10^{-11}	est.	-5.7
$N_2^+ + HF(v=1) \rightarrow HF^+ + N_2$	1×10^{-11}	est.	-0.1
$N_2^+ + HF(v\geq2) \rightarrow HF^+ + N_2$	1×10^{-11}	est.	-0.6
$N_2^+ + H_2 \rightarrow H_2^+ + N_2$	1.7×10^{-11}	[25]	-0.2
$N_2^+ + H_2(v=1) \rightarrow H_2^+ + N_2$	1.7×10^{-11}	est. [25]	-0.7
$N_2^+ + H_2(v=2) \rightarrow H_2^+ + N_2$	1.7×10^{-11}	est. [25]	-1.2
$N_2^+ + H_2(v\geq3) \rightarrow H_2^+ + N_2$	1.7×10^{-11}	est. [25]	-1.7
$N_2^+ + H \rightarrow H^+ + N_2$	1×10^{-11}	est.	-2

$N_2^+ + H_2O \rightarrow H_2O^+ + N_2$	2.3×10^{-9}	[26]	-2.1
$N_2^+ + OH \rightarrow OH^+ + N_2$	1×10^{-11}	est.	-2.1
$N_2^+ + NH \rightarrow NH^+ + N_2$	1×10^{-11}	est.	-2.1
$N_2^+ + NH_2 \rightarrow NH_2^+ + N_2$	1×10^{-11}	est.	-4.5
$N_2^+ + NH_3 \rightarrow NH_3^+ + N_2$	1.95×10^{-9}	[27]	-5.5
$N_2^+ + NH_3(v) \rightarrow NH_3^+ + N_2$	1.95×10^{-9}	est. [27]	-5.6
$H_2^+ + H_2 \rightarrow H_2^+ + H_2$	1×10^{-9}	est.	
$H_2^+ + H_2(v=1) \rightarrow H_2^+ + H_2$	1×10^{-9}	est.	-0.5
$H_2^+ + H_2(v=2) \rightarrow H_2^+ + H_2$	1×10^{-9}	est.	-1
$H_2^+ + H_2(v\geq3) \rightarrow H_2^+ + H_2$	1×10^{-9}	est.	-1.5
$H_2^+ + N_2(v) \rightarrow N_2^+ + H_2$	1×10^{-11}	est.	-0.1
$H_2^+ + HF(v\geq2) \rightarrow HF^+ + H_2$	1×10^{-11}	est.	-0.4
$H_2^+ + N \rightarrow N^+ + H_2$	1×10^{-11}	est.	-0.9
$H_2^+ + O \rightarrow O^+ + H_2$	1×10^{-11}	est.	-1.8
$H_2^+ + H \rightarrow H^+ + H_2$	6.4×10^{-10}	[28]	-1.8
$H_2^+ + NF_3 \rightarrow NF_3^+ + H_2$	1×10^{-11}	est.	-1.9
$H_2^+ + H_2O \rightarrow H_2O^+ + H_2$	1×10^{-11}	est.	-1.9
$H_2^+ + OH \rightarrow OH^+ + H_2$	1×10^{-11}	est.	-1.9
$H_2^+ + NH \rightarrow NH^+ + H_2$	1×10^{-11}	est.	-1.9
$H_2^+ + N_2O \rightarrow N_2O^+ + H_2$	1×10^{-11}	est.	-2.5
$H_2^+ + NF \rightarrow NF^+ + H_2$	1×10^{-11}	est.	-3.1
$H_2^+ + O_2 \rightarrow O_2^+ + H_2$	1×10^{-11}	est.	-3.3
$H_2^+ + O_2(v) \rightarrow O_2^+ + H_2$	1×10^{-11}	est.	-3.5
$H_2^+ + NF_2 \rightarrow NF_2^+ + H_2$	1×10^{-11}	est.	-3.8
$H_2^+ + NH_2 \rightarrow NH_2^+ + H_2$	1×10^{-11}	est.	-4.3
$H_2^+ + NH_3 \rightarrow NH_3^+ + H_2$	5.7×10^{-9}	[29]	-5.3
$H_2^+ + NH_3(v) \rightarrow NH_3^+ + H_2$	5.7×10^{-9}	est. [29]	-5.4
$H_2^+ + NO \rightarrow NO^+ + H_2$	1×10^{-11}	est.	-6.1
$N^+ + H_2(v=2) \rightarrow H_2^+ + N$	1×10^{-11}	est.	-0.1
$N^+ + H_2(v\geq3) \rightarrow H_2^+ + N$	1×10^{-11}	est.	-0.6
$N^+ + H \rightarrow H^+ + N$	1×10^{-11}	est.	-0.9
$N^+ + H_2O \rightarrow H_2O^+ + N$	1.19×10^{-9}	[26]	-1
$N^+ + OH \rightarrow OH^+ + N$	1×10^{-11}	est.	-1
$N^+ + NH \rightarrow NH^+ + N$	1×10^{-11}	est.	-1
$N^+ + NH_2 \rightarrow NH_2^+ + N$	1×10^{-11}	est.	-3.4
$N^+ + NH_3 \rightarrow NH_3^+ + N$	1.67×10^{-9}	[30]	-4.4
$N^+ + NH_3(v) \rightarrow NH_3^+ + N$	1.67×10^{-9}	est. [30]	-4.5
$N^+ + H_2 \rightarrow NH^+ + H$	5×10^{-10}	[31]	0.2
$N^+ + H_2(v=1) \rightarrow NH^+ + H$	5×10^{-10}	[31]	-0.3
$N^+ + H_2(v=2) \rightarrow NH^+ + H$	5×10^{-10}	[31]	-0.8
$N^+ + H_2(v\geq3) \rightarrow NH^+ + H$	5×10^{-10}	[31]	-1.3
$N^+ + NH_3 \rightarrow NH_2^+ + NH$	4.7×10^{-10}	[30]	-2

$N^+ + NH_3(v) \rightarrow NH_2^+ + NH$	4.7×10^{-10}	est. [30]	-2.1
$N^+ + H_2O \rightarrow NO^+ + H_2$	2.1×10^{-10}	[26]	-6.7
$O^+ + H \rightarrow H^+ + O$	1×10^{-11}	est.	
$O^+ + H_2O \rightarrow H_2O^+ + O$	3.2×10^{-9}	est.	-0.1
$O^+ + OH \rightarrow OH^+ + O$	1×10^{-11}	est.	-0.1
$O^+ + NH \rightarrow NH^+ + O$	1×10^{-11}	est.	-0.1
$O^+ + NH_2 \rightarrow NH_2^+ + O$	1×10^{-11}	est.	-2.5
$O^+ + NH_3 \rightarrow NH_3^+ + O$	1×10^{-11}	est.	-3.5
$O^+ + NH_3(v) \rightarrow NH_3^+ + O$	1×10^{-11}	est.	-3.6
$H^+ + H \rightarrow H^+ + H$	1×10^{-9}	est.	
$H^+ + O \rightarrow O^+ + H$	3.8×10^{-10}	[26]	
$H^+ + NF_3 \rightarrow NF_3^+ + H$	1×10^{-11}	est.	-0.1
$H^+ + H_2O \rightarrow H_2O^+ + H$	8.2×10^{-9}	[26]	-0.1
$H^+ + OH \rightarrow OH^+ + H$	1×10^{-11}	est.	-0.1
$H^+ + NH \rightarrow NH^+ + H$	1×10^{-11}	est.	-0.1
$H^+ + N_2O \rightarrow N_2O^+ + H$	1×10^{-11}	est.	-0.7
$H^+ + NF \rightarrow NF^+ + H$	1×10^{-11}	est.	-1.3
$H^+ + O_2 \rightarrow O_2^+ + H$	1.17×10^{-9}	[26]	-1.5
$H^+ + NF_2 \rightarrow NF_2^+ + H$	1×10^{-11}	est.	-2
$H^+ + NH_2 \rightarrow NH_2^+ + H$	1×10^{-11}	est.	-2.5
$H^+ + NH_3 \rightarrow NH_3^+ + H$	1×10^{-11}	est.	-3.5
$H^+ + NH_3(v) \rightarrow NH_3^+ + H$	1×10^{-11}	est.	-3.6
$H^+ + NO \rightarrow NO^+ + H$	1.9×10^{-9}	[26]	-4.3
$NF_3^+ + H_2O \rightarrow H_2O^+ + NF_3$	1×10^{-11}	est.	
$NF_3^+ + OH \rightarrow OH^+ + NF_3$	1×10^{-11}	est.	
$NF_3^+ + NH \rightarrow NH^+ + NF_3$	1×10^{-11}	est.	
$NF_3^+ + NH_2 \rightarrow NH_2^+ + NF_3$	1×10^{-11}	est.	-2.4
$NF_3^+ + NH_3 \rightarrow NH_3^+ + NF_3$	1×10^{-11}	est.	-3.4
$NF_3^+ + NH_3(v) \rightarrow NH_3^+ + NF_3$	1×10^{-11}	est.	-3.5
$H_2O^+ + H_2O \rightarrow H_2O^+ + H_2O$	1×10^{-9}	est.	
$H_2O^+ + NF_3 \rightarrow NF_3^+ + H_2O$	1×10^{-11}	est.	
$H_2O^+ + OH \rightarrow OH^+ + H_2O$	1×10^{-11}	est.	
$H_2O^+ + NH \rightarrow NH^+ + H_2O$	1×10^{-11}	est.	
$H_2O^+ + N_2O \rightarrow N_2O^+ + H_2O$	1×10^{-11}	est.	-0.6
$H_2O^+ + NF \rightarrow NF^+ + H_2O$	1×10^{-11}	est.	-1.2
$H_2O^+ + O_2 \rightarrow O_2^+ + H_2O$	4.3×10^{-10}	[26]	-1.4
$H_2O^+ + NF_2 \rightarrow NF_2^+ + H_2O$	1×10^{-11}	est.	-1.9
$H_2O^+ + NH_2 \rightarrow NH_2^+ + H_2O$	1×10^{-11}	est.	-2.4
$H_2O^+ + NH_3 \rightarrow NH_3^+ + H_2O$	1×10^{-11}	est.	-3.4
$H_2O^+ + NH_3(v) \rightarrow NH_3^+ + H_2O$	1×10^{-11}	est.	-3.5
$H_2O^+ + NO \rightarrow NO^+ + H_2O$	4.6×10^{-10}	[26]	-4.2
$H_2O^+ + N \rightarrow NO^+ + H_2$	1.9×10^{-10}	[26]	-5.6

$H_2O^+ + O \rightarrow O_2^+ + H_2$	5.5×10^{-11}	[26]	-1.5
$OH^+ + OH \rightarrow OH^+ + OH$	1×10^{-9}	est.	
$OH^+ + NF_3 \rightarrow NF_3^+ + OH$	1×10^{-11}	est.	
$OH^+ + H_2O \rightarrow H_2O^+ + OH$	1×10^{-11}	est.	
$OH^+ + NH \rightarrow NH^+ + OH$	1×10^{-11}	est.	
$OH^+ + N_2O \rightarrow N_2O^+ + OH$	2.13×10^{-10}	[26]	-0.6
$OH^+ + NF \rightarrow NF^+ + OH$	1×10^{-11}	est.	-1.2
$OH^+ + O_2 \rightarrow O_2^+ + OH$	1×10^{-11}	est.	-1.4
$OH^+ + NF_2 \rightarrow NF_2^+ + OH$	1×10^{-11}	est.	-1.9
$OH^+ + NH_2 \rightarrow NH_2^+ + OH$	1×10^{-11}	est.	-2.4
$OH^+ + NH_3 \rightarrow NH_3^+ + OH$	1×10^{-11}	est.	-3.4
$OH^+ + NH_3(v) \rightarrow NH_3^+ + OH$	1×10^{-11}	est.	-3.5
$OH^+ + NO \rightarrow NO^+ + OH$	1×10^{-11}	est.	-4.2
$NH^+ + NH \rightarrow NH^+ + NH$	1×10^{-9}	est.	
$NH^+ + NF_3 \rightarrow NF_3^+ + NH$	1×10^{-11}	est.	
$NH^+ + H_2O \rightarrow H_2O^+ + NH$	1×10^{-11}	est.	
$NH^+ + OH \rightarrow OH^+ + NH$	1×10^{-11}	est.	
$NH^+ + N_2O \rightarrow N_2O^+ + NH$	1×10^{-11}	est.	-0.6
$NH^+ + NF \rightarrow NF^+ + NH$	1×10^{-11}	est.	-1.2
$NH^+ + O_2 \rightarrow O_2^+ + NH$	1×10^{-11}	est.	-1.4
$NH^+ + NF_2 \rightarrow NF_2^+ + NH$	1×10^{-11}	est.	-1.9
$NH^+ + NH_2 \rightarrow NH_2^+ + NH$	1×10^{-11}	est.	-2.4
$NH^+ + NH_3 \rightarrow NH_3^+ + NH$	1.8×10^{-9}	[32]	-3.4
$NH^+ + NH_3(v) \rightarrow NH_3^+ + NH$	1.8×10^{-9}	est. [32]	-3.5
$NH^+ + NO \rightarrow NO^+ + NH$	1×10^{-11}	est.	-4.2
$NH^+ + H_2 \rightarrow NH_2^+ + H$	1.05×10^{-9}	[32]	-2
$N_2O^+ + NH_2 \rightarrow NH_2^+ + N_2O$	1×10^{-11}	est.	-1.8
$N_2O^+ + NH_3 \rightarrow NH_3^+ + N_2O$	1×10^{-11}	est.	-2.8
$N_2O^+ + NH_3(v) \rightarrow NH_3^+ + N_2O$	1×10^{-11}	est.	-2.9
$NF^+ + NH_2 \rightarrow NH_2^+ + NF$	1×10^{-11}	est.	-1.2
$NF^+ + NH_3 \rightarrow NH_3^+ + NF$	1×10^{-11}	est.	-2.2
$NF^+ + NH_3(v) \rightarrow NH_3^+ + NF$	1×10^{-11}	est.	-2.3
$O_2^+ + NH_2 \rightarrow NH_2^+ + O_2$	1×10^{-11}	est.	-1
$O_2^+ + NH_3 \rightarrow NH_3^+ + O_2$	1×10^{-11}	est.	-2
$O_2^+ + NH_3(v) \rightarrow NH_3^+ + O_2$	1×10^{-11}	est.	-2.1
$NF_2^+ + NH_2 \rightarrow NH_2^+ + NF_2$	1×10^{-11}	est.	-0.5
$NF_2^+ + NH_3 \rightarrow NH_3^+ + NF_2$	1×10^{-11}	est.	-1.5
$NF_2^+ + NH_3(v) \rightarrow NH_3^+ + NF_2$	1×10^{-11}	est.	-1.6
$NH_2^+ + NH_2 \rightarrow NH_2^+ + NH_2$	1×10^{-9}	est.	
$NH_2^+ + NH_3 \rightarrow NH_3^+ + NH_2$	1.15×10^{-9}	[32]	-1
$NH_2^+ + NH_3(v) \rightarrow NH_3^+ + NH_2$	1.15×10^{-9}	est. [32]	-1.1
$NH_2^+ + NO \rightarrow NO^+ + NH_2$	1×10^{-11}	est.	-1.8

$NH_2^+ + H_2 \rightarrow NH_3^+ + H$	1.95×10^{-10}	[32]	-1.2
$NH_3^+ + NH_3 \rightarrow NH_3^+ + NH_3$	1×10^{-9}	est.	
$NH_3^+ + NH_3(v) \rightarrow NH_3^+ + NH_3$	1×10^{-9}	est.	-0.1
$NH_3^+ + NO \rightarrow NO^+ + NH_3$	1×10^{-11}	est.	-0.8
Negative Ion-Neutral Collisions			
$O^- + H_2 \rightarrow H_2O + e$	7×10^{-10}	[26]	
$O^- + H_2(v=1) \rightarrow H_2O + e$	7×10^{-10}	est. [26]	
$O^- + H_2(v=2) \rightarrow H_2O + e$	7×10^{-10}	est. [26]	
$O^- + H_2(v\geq3) \rightarrow H_2O + e$	7×10^{-10}	est. [26]	
$O^- + H_2 \rightarrow OH^- + H$	3.3×10^{-11}	[26]	-0.1
$O^- + H_2(v=1) \rightarrow OH^- + H$	3.3×10^{-11}	est. [26]	-0.6
$O^- + H_2(v=2) \rightarrow OH^- + H$	3.3×10^{-11}	est. [26]	-1.1
$O^- + H_2(v\geq3) \rightarrow OH^- + H$	3.3×10^{-11}	est. [26]	-1.6
$O^- + H_2O \rightarrow OH^- + OH$	1.4×10^{-9}	[26]	0.5
$O_2^- + H \rightarrow HO_2 + e$	1.4×10^{-9}	[26]	
$F^- + H \rightarrow HF + e$	1.6×10^{-9}	[33]	
$H^- + H \rightarrow H_2 + e$	1.8×10^{-9}	[33]	
$H^- + NH_3 \rightarrow NH_2^- + H_2$	8.8×10^{-13}	[34]	0.3
$H^- + NH_3(v) \rightarrow NH_2^- + H_2$	8.8×10^{-13}	[34]	0.2
$H^- + N_2O \rightarrow OH^- + N_2$	1.1×10^{-9}	[26]	-3.7
$OH^- + O \rightarrow HO_2 + e$	2×10^{-10}	[26]	
$OH^- + H \rightarrow H_2O + e$	1.8×10^{-9}	[26]	
$NH_2^- + H_2 \rightarrow H^- + NH_3$	2.3×10^{-11}	[35]	-0.3
$NH_2^- + H_2(v=1) \rightarrow H^- + NH_3$	2.3×10^{-11}	[35]	-0.8
$NH_2^- + H_2(v=2) \rightarrow H^- + NH_3$	2.3×10^{-11}	[35]	-1.3
$NH_2^- + H_2(v\geq3) \rightarrow H^- + NH_3$	2.3×10^{-11}	[35]	-1.8
Ion-Ion Neutralization			
$F^- + H_2O^+ \rightarrow F + H_2O$	2×10^{-7}	est. [36], j)	-10.1
$F^- + OH^+ \rightarrow F + OH$	2×10^{-7}	est.	-0.1
$F^- + H_2^+ \rightarrow F + H_2$	2×10^{-7}	est.	
$F^- + H^+ \rightarrow F + H$	2×10^{-7}	est.	
$F^- + NH_3^+ \rightarrow F + NH_2 + H$	2×10^{-7}	est.	-1.9
$F^- + NH_2^+ \rightarrow F + NH + H$	2×10^{-7}	est.	-1
$F^- + NH^+ \rightarrow F + NH$	2×10^{-7}	est.	-0.6
$F^- + HF^+ \rightarrow F + H + F$	2×10^{-7}	est.	-6.7
$O^- + H_2O^+ \rightarrow O + H_2O$	2×10^{-7}	est.	-12
$O^- + OH^+ \rightarrow O + OH$	2×10^{-7}	est.	-0.5
$O^- + H_2^+ \rightarrow O + H_2$	2×10^{-7}	est.	
$O^- + H^+ \rightarrow O + H$	2×10^{-7}	est.	
$O^- + NH_3^+ \rightarrow O + NH_2 + H$	2×10^{-7}	est.	-1.6
$O^- + NH_2^+ \rightarrow O + NH + H$	2×10^{-7}	est.	-1.7
$O^- + NH^+ \rightarrow O + NH$	2×10^{-7}	est.	-2.5

$O^- + HF^+ \rightarrow O + H + F$	2×10^{-7}	est.	-8.6
$O_2^- + H_2O^+ \rightarrow O_2 + H_2O$	2×10^{-7}	est.	-13
$O_2^- + OH^+ \rightarrow O_2 + OH$	2×10^{-7}	est.	
$O_2^- + H_2^+ \rightarrow O_2 + H_2$	2×10^{-7}	est.	
$O_2^- + H^+ \rightarrow O_2 + H$	2×10^{-7}	est.	
$O_2^- + NH_3^+ \rightarrow O_2 + NH_2 + H$	2×10^{-7}	est.	-2.6
$O_2^- + NH_2^+ \rightarrow O_2 + NH + H$	2×10^{-7}	est.	-2.7
$O_2^- + NH^+ \rightarrow O_2 + NH$	2×10^{-7}	est.	-3.5
$O_2^- + HF^+ \rightarrow O_2 + H + F$	2×10^{-7}	est.	-9.6
$O_3^- + H_2O^+ \rightarrow O_3 + H_2O$	2×10^{-7}	est.	-11.4
$O_3^- + OH^+ \rightarrow O_3 + OH$	2×10^{-7}	est.	
$O_3^- + H_2^+ \rightarrow O_3 + H_2$	2×10^{-7}	est.	-0.1
$O_3^- + H^+ \rightarrow O_3 + H$	2×10^{-7}	est.	-1.3
$O_3^- + NH_3^+ \rightarrow O_3 + NH_2 + H$	2×10^{-7}	est.	-1
$O_3^- + NH_2^+ \rightarrow O_3 + NH + H$	2×10^{-7}	est.	-1.1
$O_3^- + NH^+ \rightarrow O_3 + NH$	2×10^{-7}	est.	-0.9
$O_3^- + HF^+ \rightarrow O_3 + H + F$	2×10^{-7}	est.	-8
$H^- + F_2^+ \rightarrow H + F_2^*$	$5 \times 10^{-8} T_n^{-1/2}$	est. [37]	-1.1
$H^- + F^+ \rightarrow H + F^*$	2×10^{-7}	est.	
$H^- + N_2^+ \rightarrow H + N^* + N^*$	2×10^{-7}	est.	-0.2
$H^- + N^+ \rightarrow H + N^*$	2×10^{-7}	est.	
$H^- + O_2^+ \rightarrow H + O_2^*$	2×10^{-7}	est.	
$H^- + O^+ \rightarrow H + O^*$	2×10^{-7}	est.	
$H^- + NF_3^+ \rightarrow H + NF_2 + F$	2×10^{-7}	est.	-10.1
$H^- + NF_2^+ \rightarrow H + NF + F$	2×10^{-7}	est.	-5.2
$H^- + NF^+ \rightarrow H + N^* + F$	2×10^{-7}	est.	-6
$H^- + N_2O^+ \rightarrow H + N_2O$	$2 \times 10^{-7} T_n^{-1/2}$	[26]	-12.1
$H^- + NO^+ \rightarrow H + NO$	2×10^{-7}	est.	-0.2
$H^- + H_2O^+ \rightarrow H + H_2O$	2×10^{-7}	est.	-12.7
$H^- + OH^+ \rightarrow H + OH$	2×10^{-7}	est.	-1.2
$H^- + H_2^+ \rightarrow H + H_2$	2×10^{-7}	est.	
$H^- + H^+ \rightarrow H + H$	2×10^{-7}	est.	-0.1
$H^- + NH_3^+ \rightarrow H + NH_2 + H$	2×10^{-7}	est.	-2.3
$H^- + NH_2^+ \rightarrow H + NH + H$	2×10^{-7}	est.	-2.4
$H^- + NH^+ \rightarrow H + NH$	2×10^{-7}	est.	-3.2
$H^- + HF^+ \rightarrow H + H + F$	2×10^{-7}	est.	-9.3
$H^- + N_2O^+ \rightarrow H + N_2 + O$	1×10^{-7}	[26]	-10.3
$OH^- + F_2^+ \rightarrow OH + F_2^*$	2×10^{-7}	est.	-1
$OH^- + F^+ \rightarrow OH + F^*$	2×10^{-7}	est.	-0.8
$OH^- + N_2^+ \rightarrow OH + N_2^*$	2×10^{-7}	est.	-0.9
$OH^- + N^+ \rightarrow OH + N^*$	2×10^{-7}	est.	-0.3
$OH^- + O_2^+ \rightarrow OH + O_2^*$	$2 \times 10^{-7} T_n^{-1/2}$	[38]	-0.8

$OH^- + O^+ \rightarrow OH + O^*$	$1 \times 10^{-7} T_n^{-1/2}$	[38]	-0.8
$OH^- + NF_3^+ \rightarrow OH + NF_2 + F$	2×10^{-7}	est.	-9.1
$OH^- + NF_2^+ \rightarrow OH + NF + F$	2×10^{-7}	est.	-4.2
$OH^- + NF^+ \rightarrow OH + N^* + F$	2×10^{-7}	est.	-5
$OH^- + N_2O^+ \rightarrow OH + N_2O$	$2 \times 10^{-7} T_n^{-1/2}$	[26]	-11.1
$OH^- + NO^+ \rightarrow OH + NO$	2×10^{-7}	est.	-1
$OH^- + H_2O^+ \rightarrow OH + H_2O$	2×10^{-7}	est.	-11.7
$OH^- + OH^+ \rightarrow OH + OH$	2×10^{-7}	est.	-0.2
$OH^- + H_2^+ \rightarrow OH + H_2$	2×10^{-7}	est.	-0.4
$OH^- + H^+ \rightarrow OH + H$	2×10^{-7}	est.	-1.6
$OH^- + NH_3^+ \rightarrow OH + NH_2 + H$	2×10^{-7}	est.	-1.3
$OH^- + NH_2^+ \rightarrow OH + NH + H$	2×10^{-7}	est.	-1.4
$OH^- + NH^+ \rightarrow OH + NH$	2×10^{-7}	est.	-1.2
$OH^- + HF^+ \rightarrow OH + H + F$	2×10^{-7}	est.	-8.3
$OH^- + N_2O^+ \rightarrow OH + N_2 + O$	1×10^{-7}	[26]	-9.3
$NH_2^- + F_2^+ \rightarrow NH_2 + F_2^*$	2×10^{-7}	est.	-1.1
$NH_2^- + F^+ \rightarrow NH_2 + F^*$	2×10^{-7}	est.	
$NH_2^- + N_2^+ \rightarrow NH_2 + N^* + N^*$	2×10^{-7}	est.	-0.2
$NH_2^- + N^+ \rightarrow NH_2 + N^*$	2×10^{-7}	est.	
$NH_2^- + O_2^+ \rightarrow NH_2 + O_2^*$	2×10^{-7}	est.	
$NH_2^- + O^+ \rightarrow NH_2 + O^*$	2×10^{-7}	est.	
$NH_2^- + NF_3^+ \rightarrow NH_2 + NF_2 + F$	2×10^{-7}	est.	-10.1
$NH_2^- + NF_2^+ \rightarrow NH_2 + NF + F$	2×10^{-7}	est.	-5.2
$NH_2^- + NF^+ \rightarrow NH_2 + N^* + F$	2×10^{-7}	est.	-6
$NH_2^- + N_2O^+ \rightarrow NH_2 + N_2O$	$2 \times 10^{-7} T_n^{-1/2}$	est. [26]	-12.1
$NH_2^- + NO^+ \rightarrow NH_2 + NO$	2×10^{-7}	est.	-0.2
$NH_2^- + H_2O^+ \rightarrow NH_2 + H_2O$	2×10^{-7}	est.	-12.7
$NH_2^- + OH^+ \rightarrow NH_2 + OH$	2×10^{-7}	est.	-1.2
$NH_2^- + H_2^+ \rightarrow NH_2 + H_2$	2×10^{-7}	est.	
$NH_2^- + H^+ \rightarrow NH_2 + H$	2×10^{-7}	est.	-0.1
$NH_2^- + NH_3^+ \rightarrow NH_2 + NH_2 + H$	2×10^{-7}	est.	-2.3
$NH_2^- + NH_2^+ \rightarrow NH_2 + NH + H$	2×10^{-7}	est.	-2.4
$NH_2^- + NH^+ \rightarrow NH_2 + NH$	2×10^{-7}	est.	-3.2
$NH_2^- + HF^+ \rightarrow NH_2 + H + F$	2×10^{-7}	est.	-9.3
$NH_2^- + N_2O^+ \rightarrow NH_2 + N_2 + O$	1×10^{-7}	est. [26]	-10.3
<u>V-V Process</u>			
$HF(v=1) + HF(v=1) \rightarrow HF(v\geq2) + HF$	4.7×10^{-11}	[39]	
$HF(v=1) + H_2 \rightarrow HF + H_2(v=1)$	$7.4 \times 10^{-13} T_n^{1/2}$	[18]	
$HF(v\geq2) + H_2 \rightarrow HF(v=1) + H_2(v=1)$	$7.4 \times 10^{-13} T_n^{1/2}$	est. [18]	
$HF(v=1) + N_2 \rightarrow HF + N_2(v)$	4×10^{-15}	[39]	-0.2
$HF(v\geq2) + N_2 \rightarrow HF(v=1) + N_2(v)$	2.5×10^{-14}	[39]	-0.2
$HF(v=1) + O_2 \rightarrow HF + O_2(v)$	1.4×10^{-15}	[39]	-0.3

$HF(v\geq2) + O_2 \rightarrow HF(v=1) + O_2(v)$	1×10^{-14}	[39]	-0.3
$HF(v=1) + NH_3 \rightarrow HF + NH_3(v)$	1.9×10^{-10}	[39]	-0.4
$HF(v\geq2) + NH_3 \rightarrow HF(v=1) + NH_3(v)$	1.9×10^{-10}	est. [39]	-0.4
$H_2(v=1) + HF \rightarrow H_2 + HF(v=1)$	1.9×10^{-12}	[39]	
$H_2(v=1) + HF(v=1) \rightarrow H_2 + HF(v\geq2)$	7.8×10^{-12}	[39]	
$H_2(v=2) + HF \rightarrow H_2(v=1) + HF(v=1)$	1.9×10^{-12}	est. [39]	
$H_2(v=2) + HF(v=1) \rightarrow H_2(v=1) + HF(v\geq2)$	7.8×10^{-12}	est. [39]	
$H_2(v\geq3) + HF \rightarrow H_2(v=2) + HF(v=1)$	1.9×10^{-12}	est. [39]	
$H_2(v\geq3) + HF(v=1) \rightarrow H_2(v=2) + HF(v\geq2)$	7.8×10^{-12}	est. [39]	
Neutral-Neutral Collisions			
$H_2 + F \rightarrow H + HF(v=1)$	$1.12 \times 10^{-11} T_n^{1/2} \exp(-299/T_g)$	[40]	-0.9
$H_2(v=1) + F \rightarrow H + HF(v=1)$	$1.12 \times 10^{-11} T_n^{1/2}$	est. [40]	-1.4
$H_2(v=2) + F \rightarrow H + HF(v=1)$	$1.12 \times 10^{-11} T_n^{1/2}$	est. [40]	-1.9
$H_2(v\geq3) + F \rightarrow H + HF(v=1)$	$1.12 \times 10^{-11} T_n^{1/2}$	est. [40]	-2.4
$H_2 + F \rightarrow H + HF(v\geq2)$	$6.34 \times 10^{-11} T_n^{1/2} \exp(-299/T_g)$	[40]	-0.4
$H_2(v=1) + F \rightarrow H + HF(v\geq2)$	$6.34 \times 10^{-11} T_n^{1/2}$	est. [40]	-0.9
$H_2(v=2) + F \rightarrow H + HF(v\geq2)$	$6.34 \times 10^{-11} T_n^{1/2}$	est. [40]	-1.4
$H_2(v\geq3) + F \rightarrow H + HF(v\geq2)$	$6.34 \times 10^{-11} T_n^{1/2}$	est. [40]	-1.9
$H_2 + N \rightarrow NH + H$	$2.66 \times 10^{-10} \exp(-12{,}600/T_g)$	[41]	1.3
$H_2(v=1) + N \rightarrow NH + H$	$2.66 \times 10^{-10} \exp(-1{,}056/T_g)$	est. [41]	0.8
$H_2(v=2) + N \rightarrow NH + H$	2.66×10^{-10}	est. [41]	0.3
$H_2(v\geq3) + N \rightarrow NH + H$	2.66×10^{-10}	est. [41]	-0.2
$H_2 + O \rightarrow OH + H$	$1.6 \times 10^{-11} \exp(-4{,}570/T_g)$	[42]	0.1
$H_2(v=1) + O \rightarrow OH + H$	1.6×10^{-11}	est. [42]	-0.4
$H_2(v=2) + O \rightarrow OH + H$	1.6×10^{-11}	est. [42]	-0.9
$H_2(v\geq3) + O \rightarrow OH + H$	1.6×10^{-11}	est. [42]	-1.4
$H_2 + O_2 \rightarrow H + HO_2$	$2.4 \times 10^{-10} \exp(-28{,}500/T_g)$	[43]	2.3
$H_2(v=1) + O_2 \rightarrow H + HO_2$	$2.4 \times 10^{-10} \exp(-22{,}700/T_g)$	est. [43]	1.8
$H_2(v=2) + O_2 \rightarrow H + HO_2$	$2.4 \times 10^{-10} \exp(-16{,}900/T_g)$	est. [43]	1.3
$H_2(v\geq3) + O_2 \rightarrow H + HO_2$	$2.4 \times 10^{-10} \exp(-11{,}100/T_g)$	est. [43]	0.8
$H_2 + O_2(v) \rightarrow H + HO_2$	$2.4 \times 10^{-10} \exp(-26{,}180/T_g)$	est. [43]	2.5
$H_2(v=1) + O_2(v) \rightarrow H + HO_2$	$2.4 \times 10^{-10} \exp(-20{,}380/T_g)$	est. [43]	1.6
$H_2(v=2) + O_2(v) \rightarrow H + HO_2$	$2.4 \times 10^{-10} \exp(-14{,}580/T_g)$	est. [43]	1.1
$H_2(v\geq3) + O_2(v) \rightarrow H + HO_2$	$2.4 \times 10^{-10} \exp(-8{,}780/T_g)$	est. [43]	0.6
$H_2 + N_2O \rightarrow N_2 + H_2O$	$5.73 \times 10^{-12} T_n^{1/2}$	[44]	-3.4
$H_2(v=1) + N_2O \rightarrow N_2 + H_2O$	$5.73 \times 10^{-12} T_n^{1/2}$	est. [44]	-3.9
$H_2(v=2) + N_2O \rightarrow N_2 + H_2O$	$5.73 \times 10^{-12} T_n^{1/2}$	est. [44]	-4.4
$H_2(v\geq3) + N_2O \rightarrow N_2 + H_2O$	$5.73 \times 10^{-12} T_n^{1/2}$	est. [44]	-4.9
$H_2 + OH \rightarrow H_2O + H$	$7.7 \times 10^{-12} \exp(-2{,}100/T_g)$	[43]	-0.6
$H_2(v=1) + OH \rightarrow H_2O + H$	7.7×10^{-12}	est. [43]	-1.1

$H_2(v=2) + OH \rightarrow H_2O + H$	7.7×10^{-12}	est. [43]	-1.6
$H_2(v\geq3) + OH \rightarrow H_2O + H$	7.7×10^{-12}	est. [43]	-2.1
$H_2 + HO_2 \rightarrow H_2O_2 + H$	$5 \times 10^{-11} \exp(-13{,}100/T_g)$	[43]	0.9
$H_2(v=1) + HO_2 \rightarrow H_2O_2 + H$	$5 \times 10^{-11} \exp(-7{,}300/T_g)$	est. [43]	0.4
$H_2(v=2) + HO_2 \rightarrow H_2O_2 + H$	$5 \times 10^{-11} \exp(-1{,}500/T_g)$	est. [43]	-0.1
$H_2(v\geq3) + HO_2 \rightarrow H_2O_2 + H$	5×10^{-11}	est. [43]	-0.6
$H_2 + NH_2 \rightarrow H + NH_3$	$2.09 \times 10^{-12} \exp(-4{,}277/T_g)$	[45]	-0.2
$H_2(v=1) + NH_2 \rightarrow H + NH_3$	2.09×10^{-12}	est. [45]	-0.7
$H_2(v=2) + NH_2 \rightarrow H + NH_3$	2.09×10^{-12}	est. [45]	-1.2
$H_2(v\geq3) + NH_2 \rightarrow H + NH_3$	2.09×10^{-12}	est. [45]	-1.7
$H + F_2 \rightarrow F + HF$	$1.46 \times 10^{-12} \exp(-1{,}207/T_g)$	[46,47]	-4.3
$H + F_2 \rightarrow F + HF(v=1)$	$4.38 \times 10^{-12} \exp(-1{,}207/T_g)$	[46,47]	-3.8
$H + F_2 \rightarrow F + HF(v\geq2)$	$1.4 \times 10^{-10} \exp(-1{,}207/T_g)$	[46,47]	-3.3
$H + N_2 \rightarrow NH + N$	$5.27 \times 10^{-10} T_n^{1/2} \exp(-74{,}280/T_g)$	[48,47]	6.5
$H + N_2(v) \rightarrow NH + N$	$5.27 \times 10^{-10} T_n^{1/2} \exp(-70{,}800/T_g)$	[48]	6.2
$H + O_2 \rightarrow OH + O$	$1.65 \times 10^{-9} T_n^{-0.9} \exp(-8{,}750/T_g)$	[43]	0.7
$H + O_2(v) \rightarrow OH + O$	$1.65 \times 10^{-9} T_n^{-0.9} \exp(-6{,}430/T_g)$	[43]	0.5
$H + O_3 \rightarrow OH + O_2$	$1.4 \times 10^{-10} \exp(-480/T_g)$	[49]	-3.4
$H + FO \rightarrow HF + O$	8.2×10^{-12}	[50]	-3.6
$H + FO \rightarrow OH + F$	1.58×10^{-11}	[50]	-2.2
$H + N_2O \rightarrow NO + NH$	$4.96 \times 10^{-7} T_n^{-2.16} \exp(-18{,}700/T_g)$	[51]	-2.3
$H + N_2O \rightarrow OH + N_2$	$5.13 \times 10^{-14} T_n^{3.15} \exp(-3{,}603/T_g)$	[51]	-2.8
$H + NO_2 \rightarrow OH + NO$	1.28×10^{-10}	[52]	-1.3
$H + NF_3 \rightarrow HF + NF_2$	$1 \times 10^{-9} \exp(-6{,}640/T_g)$	[53]	-3.5
$H + NF_2 \rightarrow HF + NF$	$1.36 \times 10^{-11} \exp(-73/T_g)$	[54,55]	-2.9
$H + NF_2 \rightarrow HF(v=1) + NF$	$0.42 \times 10^{-11} \exp(-73/T_g)$	[54,55]	-2.4
$H + NF_2 \rightarrow HF(v\geq2) + NF$	$0.13 \times 10^{-11} \exp(-73/T_g)$	[54,55]	-1.9
$H + NF \rightarrow HF + N$	2.5×10^{-13}	[52]	-3.1
$H + NH_3 \rightarrow H_2 + NH_2$	$6.54 \times 10^{-13} T_n^{2.76} \exp(-5{,}160/T_g)$	[56]	0.2
$H + NH_3(v) \rightarrow H_2 + NH_2$	$6.54 \times 10^{-13} T_n^{2.76} \exp(-4{,}001/T_g)$	est. [56]	0.1
$H + NH_2 \rightarrow NH + H_2$	$1.05 \times 10^{-10} \exp(-4{,}440/T_g)$	[57]	-0.4
$H + NH \rightarrow H_2 + N$	$5.98 \times 10^{-11} \exp(-166/T_g)$	[58]	-1.3
$H + HF \rightarrow H_2 + F$	$3.32 \times 10^{-12} \exp(-17{,}520/T_g)$	[59]	1.3
$H + HF(v=1) \rightarrow H_2 + F$	$3.32 \times 10^{-12} \exp(-12{,}882/T_g)$	est. [59]	0.8
$H + HF(v\geq2) \rightarrow H_2 + F$	$3.32 \times 10^{-12} \exp(-8{,}245/T_g)$	est. [59]	0.3
$NH_3 + F \rightarrow NH_2 + HF$	0.01×10^{-10}	[52,60]	-1.1
$NH_3 + F \rightarrow NH_2 + HF(v=1)$	0.29×10^{-10}	[52,60]	-0.6
$NH_3 + F \rightarrow NH_2 + HF(v\geq2)$	0.61×10^{-10}	[52,60]	-0.1
$NH_3 + N^* \rightarrow NH + NH_2$	5×10^{-11}	[61]	-0.9
$NH_3 + O \rightarrow OH + NH_2$	$1.6 \times 10^{-11} \exp(-3{,}661/T_g)$	[62]	0.3
$NH_3 + O^* \rightarrow NH_2 + OH$	2.51×10^{-10}	[63]	-1.6
$NH_3 + NH \rightarrow NH_2 + NH_2$	$5.25 \times 10^{-10} \exp(-13{,}440/T_g)$	[64]	0.6

$NH_3(v) + F \rightarrow NH_2 + HF$	0.01×10^{-10}	est. [52,60]	-1.2
$NH_3(v) + F \rightarrow NH_2 + HF(v=1)$	0.29×10^{-10}	est. [52,60]	-0.7
$NH_3(v) + F \rightarrow NH_2 + HF(v\geq 2)$	0.61×10^{-10}	est. [52,60]	-0.2
$NH_3(v) + N^* \rightarrow NH + NH_2$	5×10^{-11}	est. [61]	-1
$NH_3(v) + O \rightarrow OH + NH_2$	$1.6 \times 10^{-11} \exp(-2{,}502/T_g)$	est. [62]	0.2
$NH_3(v) + O^* \rightarrow NH_2 + OH$	2.51×10^{-10}	est. [63]	-1.7
$NH_3(v) + NH \rightarrow NH_2 + NH_2$	$5.25 \times 10^{-10} \exp(-12{,}280/T_g)$	est. [64]	0.5
$NH_2 + N \rightarrow N_2 + H + H$	1.2×10^{-10}	[58]	-2.3
$NH_2 + O \rightarrow H_2 + NO$	8.3×10^{-12}	[65]	-3.7
$NH_2 + O \rightarrow NH + OH$	1.16×10^{-11}	[65]	-0.3
$NH_2 + NO \rightarrow N_2 + H_2O$	$7.92 \times 10^{-13} \exp(-650/T_g)$	[62]	-5.4
$NH_2 + NO \rightarrow N_2 + H + OH$	$1.08 \times 10^{-13} \exp(-650/T_g)$	[62]	-0.2
$NH_2 + NO_2 \rightarrow H_2O + N_2O$	$7.01 \times 10^{-12} T_n^{-1.44} \exp(-1{,}122/T_g)$	[66]	-3.9
$NH_2 + NH_2 \rightarrow NH_3 + NH$	$8.30 \times 10^{-11} \exp(-5{,}018/T_g)$	[58]	-0.6
$NH + N \rightarrow N_2 + H$	4.98×10^{-11}	[58]	-6.5
$NH + O_2 \rightarrow NO + OH$	$0.42 \times 10^{-12} \exp(-770/T_g)$	[62]	-2.6
$NH + O_2 \rightarrow NO_2 + H$	$0.42 \times 10^{-12} \exp(-770/T_g)$	[62]	-1.3
$NH + O_2(v) \rightarrow NO + OH$	0.42×10^{-12}	est. [62]	-2.8
$NH + O_2(v) \rightarrow NO_2 + H$	0.42×10^{-12}	est. [62]	-1.5
$NH + NO \rightarrow H + N_2O$	3.12×10^{-11}	[51]	-1.6
$NH + NO \rightarrow N_2 + OH$	4.5×10^{-11}	[67]	-4.4
$NH + NO_2 \rightarrow OH + N_2O$	$3.5 \times 10^{-13} \exp(1{,}140/T_g)$	[51]	-2.9
$NH + NH \rightarrow NH_2 + N$	$1.4 \times 10^{-14} T_n^{2.89} \exp(1{,}018/T_g)$	[68]	-0.9
$NH + NH \rightarrow N_2 + H + H$	1.16×10^{-9}	[69]	-3.2
$HF + F \rightarrow F_2 + H$	$2.21 \times 10^{-11} \exp(-50{,}640/T_g)$	[46]	4.3
$HF(v=1) + F \rightarrow F_2 + H$	$2.21 \times 10^{-11} \exp(-44{,}843/T_g)$	est. [46]	3.8
$HF(v\geq 2) + F \rightarrow F_2 + H$	$2.21 \times 10^{-11} \exp(-39{,}046/T_g)$	est. [46]	3.3
$HF + O^* \rightarrow OH + F$	1.5×10^{-11}	[70]	-0.5
$HF(v=1) + O^* \rightarrow OH + F$	1.5×10^{-11}	est. [70]	-1
$HF(v\geq 2) + O^* \rightarrow OH + F$	1.5×10^{-11}	est. [70]	-1.5
$HF + OH \rightarrow H_2O + F$	$1 \times 10^{-11} \exp(-12{,}240/T_g)$	[52]	0.7
$HF(v=1) + OH \rightarrow H_2O + F$	$1 \times 10^{-11} \exp(-6{,}443/T_g)$	[52]	0.2
$HF(v\geq 2) + OH \rightarrow H_2O + F$	$1 \times 10^{-11} \exp(-646/T_g)$	[52]	-0.3
$OH + F \rightarrow O + HF$	1.2×10^{-11}	[71,72]	-1.4
$OH + F \rightarrow O + HF(v=1)$	1.53×10^{-11}	[71,72]	-0.9
$OH + F \rightarrow O + HF(v\geq 2)$	0.6×10^{-11}	[71,72]	-0.4
$OH + N \rightarrow NO + H$	4.7×10^{-11}	[52]	-2.1
$OH + N \rightarrow O + NH$	$1.88 \times 10^{-11} T_n^{0.1} \exp(-10{,}675/T_g)$	[65]	1.2
$OH + O \rightarrow H + O_2$	3.5×10^{-11}	[52]	-0.7
$OH + O_2 \rightarrow O + HO_2$	$3.7 \times 10^{-11} \exp(-26{,}500/T_g)$	[43]	2.2
$OH + O_2(v) \rightarrow O + HO_2$	$3.7 \times 10^{-11} \exp(-24{,}180/T_g)$	est. [43]	2
$OH + O_3 \rightarrow HO_2 + O_2$	$1.9 \times 10^{-12} \exp(-1{,}000/T_g)$	[42]	-1.9

$OH + N_2O \rightarrow HO_2 + N_2$	$3.69 \times 10^{-13} \exp(-2{,}740/T_g)$	[51]	-1.3
$OH + NO_2 \rightarrow HO_2 + NO$	$3.03 \times 10^{-11} \exp(-3{,}360/T_g)$	[52]	0.2
$OH + H \rightarrow O + H_2$	$5.21 \times 10^{-11} T_n^{0.67} \exp(-518/T_g)$	[15]	-0.1
$OH + NH_3 \rightarrow NH_2 + H_2O$	$3.5 \times 10^{-12} \exp(-923/T_g)$	[73]	-0.4
$OH + NH_3(v) \rightarrow NH_2 + H_2O$	3.5×10^{-12}	est. [73]	-0.5
$OH + NH_2 \rightarrow O + NH_3$	$3.32 \times 10^{-13} T_n^{0.4} \exp(-250/T_g)$	[62]	-0.3
$OH + NH \rightarrow NO + H_2$	4×10^{-11}	[62]	-3.4
$OH + NH \rightarrow H_2O + N$	4×10^{-11}	[62]	-1.9
$OH + OH \rightarrow O + H_2O$	$1.03 \times 10^{-12} T_n^{1.4} \exp(200/T_g)$	[43]	-0.7
$OH + HO_2 \rightarrow H_2O + O_2$	8×10^{-11}	[42]	-2.9
$OH + H_2O_2 \rightarrow H_2O + HO_2$	$2.9 \times 10^{-12} \exp(-160/T_g)$	[42]	-1.5
$HO_2 + F \rightarrow O_2 + HF$	$8.29 \times 10^{-11} T_n^{0.5}$	[71]	-3.6
$HO_2 + O \rightarrow OH + O_2$	$2.9 \times 10^{-11} \exp(-200/T_g)$	[49]	-2.2
$HO_2 + O_3 \rightarrow OH + O_2 + O_2$	$1.4 \times 10^{-14} \exp(-600/T_g)$	[42]	-1.1
$HO_2 + NO \rightarrow NO_2 + OH$	8.8×10^{-12}	[52]	-0.2
$HO_2 + H \rightarrow OH + OH$	$2.8 \times 10^{-10} \exp(-440/T_g)$	[43]	-1.5
$HO_2 + H \rightarrow H_2 + O_2$	$1.1 \times 10^{-10} \exp(-1{,}070/T_g)$	[42]	-2.3
$HO_2 + H \rightarrow H_2O + O$	9.4×10^{-12}	[42]	-2.2
$HO_2 + NH_2 \rightarrow NH_3 + O_2$	1.3×10^{-11}	[62]	-2.5
$HO_2 + HO_2 \rightarrow H_2O_2 + O_2$	$8.05 \times 10^{-11} T_n^{-1}$	[74]	-1.4
$HO_2 + H_2O \rightarrow H_2O_2 + OH$	$4.65 \times 10^{-11} \exp(-16{,}477/T_g)$	[52]	1.5
$H_2O + F \rightarrow OH + HF$	0.29×10^{-11}	[52,75]	-0.7
$H_2O + F \rightarrow OH + HF(v=1)$	1.05×10^{-11}	[52,75]	-0.2
$H_2O + F \rightarrow OH + HF(v\geq 2)$	0.06×10^{-11}	[52,75]	0.3
$H_2O + N \rightarrow NH + OH$	$6.03 \times 10^{-11} T_n^{1.2} \exp(-19{,}200/T_g)$	[65]	1.9
$H_2O + O \rightarrow OH + OH$	$1.26 \times 10^{-11} T_n^{1.3} \exp(-8{,}605/T_g)$	[43]	0.7
$H_2O + O^* \rightarrow OH + OH$	2×10^{-10}	[61]	-1.2
$H_2O + H \rightarrow H_2 + OH$	$5.24 \times 10^{-12} T_n^{1.9} \exp(-9{,}265/T_g)$	[43]	0.6
$H_2O_2 + F \rightarrow HO_2 + HF$	$4.96 \times 10^{-11} T_n^{0.5}$	[71]	-2.2
$H_2O_2 + O \rightarrow OH + HO_2$	$1.4 \times 10^{-12} \exp(-2{,}000/T_g)$	[43]	-0.8
$H_2O_2 + O^* \rightarrow O_2 + H_2O$	5.2×10^{-10}	[51]	-5.6
$H_2O_2 + O_2 \rightarrow HO_2 + HO_2$	$9 \times 10^{-11} \exp(-19{,}965/T_g)$	[43]	1.4
$H_2O_2 + O_2(v) \rightarrow HO_2 + HO_2$	$9 \times 10^{-11} \exp(-17{,}645/T_g)$	est. [43]	1.2
$H_2O_2 + H \rightarrow H_2O + OH$	$4 \times 10^{-11} \exp(-2{,}000/T_g)$	[43]	-3
$H_2O_2 + H \rightarrow HO_2 + H_2$	$8 \times 10^{-11} \exp(-4{,}000/T_g)$	[43]	-0.9
<u>High Temperature Chemistry</u>			
$H_2 + M \rightarrow H + H + M$	$3.64 \times 10^{-10} \exp(-48{,}226/T_g)$	[58]	4.6
$H_2(v=1) + M \rightarrow H + H + M$	$3.64 \times 10^{-10} \exp(-42{,}426/T_g)$	est. [58]	4.1
$H_2(v=2) + M \rightarrow H + H + M$	$3.64 \times 10^{-10} \exp(-36{,}626/T_g)$	est. [58]	3.6
$H_2(v\geq 3) + M \rightarrow H + H + M$	$3.64 \times 10^{-10} \exp(-30{,}826/T_g)$	est. [58]	3.1
$H_2^* + M \rightarrow H + H + M$	3.64×10^{-10}	est. [58]	-9.1
$NH_3 + M \rightarrow NH_2 + H + M$	$3.65 \times 10^{-8} \exp(-46{,}970/T_g)$	[76]	4.8

$NH_3(v) + M \rightarrow NH_2 + H + M$	$3.65 \times 10^{-8} \exp(-45{,}811/T_g)$	est. [76]	4.7
$NH_3 + M \rightarrow H_2 + NH + M$	$3.65 \times 10^{-8} \exp(-46{,}970/T_g)$	est. [76]	4.4
$NH_3(v) + M \rightarrow H_2 + NH + M$	$3.65 \times 10^{-8} \exp(-45{,}811/T_g)$	est. [76]	4.3
$NH_2 + M \rightarrow NH + H + M$	$5.91 \times 10^{-6} T_n^{-2} \exp(-45{,}930/T_g)$	[76]	4.2
$NH + M \rightarrow N + H + M$	$4.4 \times 10^{-10} \exp(-37{,}940/T_g)$	[76]	3.3
$HF + M \rightarrow H + F + M$	$6.69 \times 10^{-8} T_n^{-1} \exp(-66{,}225/T_g)$	[20]	5.9
$HF(v=1) + M \rightarrow H + F + M$	$3.34 \times 10^{-8} T_n^{-1} \exp(-66{,}225/T_g)$	[20]	5.4
$HF(v\geq2) + M \rightarrow H + F + M$	$2.23 \times 10^{-8} T_n^{-1} \exp(-66{,}225/T_g)$	[20]	4.9
$OH + M \rightarrow O + H + M$	$4 \times 10^{-9} \exp(-50{,}000/T_g)$	[43]	3.9
$HO_2 + M \rightarrow H + O_2 + M$	$2.39 \times 10^{-8} T_n^{-1.18} \exp(-24{,}360/T_g)$	[43]	2.3
$H_2O + M \rightarrow H + OH + M$	$5 \times 10^{-14} \exp(-60{,}289/T_g)$	est. [77]	5.2
$H_2O_2 + M \rightarrow OH + OH + M$	$2 \times 10^{-7} \exp(-22{,}900/T_g)$	[62]	2.2
$H + H + M \rightarrow H_2 + M$	4.8×10^{-33}	[61]	-4.6
$H + H + M \rightarrow H_2(v=1) + M$	4.8×10^{-33}	est. [61]	-4.1
$H + H + M \rightarrow H_2(v=2) + M$	4.8×10^{-33}	est. [61]	-3.6
$H + H + M \rightarrow H_2(v\geq3) + M$	4.8×10^{-33}	est. [61]	-3.1
$H + H + M \rightarrow H_2^* + M$	$4.8 \times 10^{-33} \exp(-115{,}505/T_g)$	est. [61]	9.1
$NH_2 + H + M \rightarrow NH_3 + M$	1.4×10^{-32}	[78]	-4.8
$NH + H_2 + M \rightarrow NH_3 + M$	6.5×10^{-38}	[78]	-4.4
$NH_2 + H + M \rightarrow NH_3(v) + M$	1.4×10^{-32}	est. [78]	-4.7
$NH + H_2 + M \rightarrow NH_3(v) + M$	6.5×10^{-38}	est. [78]	-4.4
$NH + H + M \rightarrow NH_2 + M$	2.6×10^{-35}	[78]	-4.2
$N + H + M \rightarrow NH + M$	2.6×10^{-36}	[78]	-3.3
$H + F + M \rightarrow HF + M$	2.07×10^{-35}	[46]	-5.9
$H + F + M \rightarrow HF(v=1) + M$	2.07×10^{-35}	est. [46]	-5.4
$H + F + M \rightarrow HF(v\geq2) + M$	2.07×10^{-35}	est. [46]	-4.9
$O + H + M \rightarrow OH + M$	1.62×10^{-32}	[79]	-3.9
$H + O_2 + M \rightarrow HO_2 + M$	5.4×10^{-32}	[52]	-2.3
$H + OH + M \rightarrow H_2O + M$	$1.19 \times 10^{-30} T_n^{-2.1}$	est. [80]	-5.2
$OH + OH + M \rightarrow H_2O_2 + M$	$6.9 \times 10^{-31} T_n^{-0.8}$	[49]	-2.2

a) This table is a subset of the mechanism for $NF_3/O_2/H_2$ plasmas. The reactions that would occur in NF_3/O_2 plasmas are the same as discussed in Ref. [81] and listed in Appendix A.

b) Rate coefficients have units of cm^3s^{-1} unless noted. T_e is electron temperature (eV). T_g is gas temperature (K) and T_n is normalized gas temperature (T_g/300 K). ΔH is the change of enthalpy (eV).

c) Rate coefficients are calculated from the electron energy distributions produced by solutions of Boltzmann's equation using electron impact cross sections. The cross section is for the forward reaction. Reverse cross sections are obtained by detailed balance.

d) The rate of gas heating by elastic collisions is $k_m(3/2)k_B(2m_e/M)(T_e-T_g)$ eV-cm^3/s for elastic rate coefficient k_m, electron mass m_e, neutral mass M and Boltzmann's constant k_B.

e) The electron impact cross sections for momentum transfer of HF, HF(v=1) and HF(v≥2) are assumed to be the same as HCl. The electron impact cross sections for dissociation and ionization of HF, HF(v=1) and HF(v≥2) are obtained by shifting the corresponding cross sections of HCl to match the thresholds.

f) The electron impact superelastic cross sections of HF(v=1), HF(v≥2) and NH_3(v) are calculated from detailed balancing.

g) The electron impact cross sections for elastic scattering of NH_3(v), NH_2 and NH are assumed to be the same as the NH_3. The electron impact cross sections for dissociative attachment, dissociation of NH_3(v), NH_2 and NH and ionization of NH_3(v) are obtained by shifting the corresponding cross sections of NH_3 to match the thresholds.

h) The electron impact cross section for elastic scattering of OH is assumed to be the same as CO.

i) Rate coefficient for charge exchange between ions and neutrals was assumed to be 1×10^{-11} cm^{3}s^{-1} (1×10^{-9} cm^{3}s^{-1} for resonant charge exchange) [23] when measured or calculated data is not available.

j) Rate coefficient for neutralization between positive and negative ions was assumed to be 2×10^{-7} cm^{3}s^{-1} [36] when measured or calculated data is not available.

Appendix B References

1. R. Celiberto, R. K. Janev, A. Laricchiuta, M. Capitelli, J. M. Wadehra and D. E. Atems, At. Data Nucl. Data Tables **77**, 161 (2001).
2. C. F. Chan, Reaction Cross Sections and Rate Coefficients Related to the Production of Positive Ions, Lawrence Berkeley Lab. Report No. LBID-632 (1983).
3. H. Tawara, Y. Itikawa, H. Nishimura and M. Yoshino, J. Phys. Chem. Ref. Data **19**, 617 (1990).
4. C. Gorse and M. Capitelli, Atomic and Plasma-Material Interaction Data for Fusion **9**, 75 (2001).
5. G. Bekefi, Radiation Processes in Plasmas, John Wiley & Sons, New York, NY (1966).
6. M. Hayashi, Swarm Studies and Inelastic Electron-Molecule Collisions, 167-187, Springer, New York, NY (1987).
7. K. Rohr and F. Linder, J. Phys. B: At. Mol. Opt. Phys. **9**, 2521 (1976).
8. Y. Xu, G. A. Gallup and I. I. Fabricant, Phys. Rev. A **61**, 052705 (2000).
9. G. Bekefi, Principles of Laser Plasmas, John Wiley & Sons, New York, NY (1976).
10. M. Hayashi, Nonequilibrium Processes in Partially Ionized Gases, 333-340, Springer, Boston, MA (1990).
11. V. Tarnovsky, H. Deutsch and K. Becker, Int. J. Mass Spect. Ion Proc. **167**, 69 (1997).
12. A. Jain and D. W. Norcross, Phys. Rev. A **45**, 1644 (1992).
13. R. Riahi, P. Teulet, Z. B. Lakhdar and A. Gleizes, Eur. Phys. J. D **40**, 223 (2006).
14. Y. Itikawa and N. Mason, J. Phys. Chem. Ref. Data **34**, 1 (2005).
15. B. R. Rowe, F. Vallee, J. L. Queffelec, J. C. Gomet and M. Morlais, J. Phys. Chem. **88**, 845 (1988).
16. J. A. Sanchez and J. Campos, J. Phys. France **49**, 445 (1988).
17. M. A. Kwok and R. L. Wilkins, J. Chem. Phys. **63**, 2453 (1975).
18. J. K. Hancock and W. H. Green, J. Chem. Phys. **57**, 4515 (1972).
19. F. E. Hovis and C. B. Moore, J. Chem. Phys. **69**, 4947 (1978).
20. N. Cohen, A Review of Rate Coefficients in the H_2-F_2 Chemical Laser System Supplement (1977), Report No. SAMSO-TR-78-41 (1978).
21. D. J. Kligler and J. Bokor, Phys. Rev. A **21**, 607 (1980).
22. S. R. Ryan, S. J. Czuchlewski and M. V. McCusker, Phys. Rev. A **16**, 1892 (1977).

23. Y. Ikezoe, S. Matsuoka and M. Takebe, Gas Phase Ion Molecule Reaction Rate Constants Through 1986, Ion Reaction Research Group of the Mass Spectroscopy Society of Japan, Tokyo, Japan (1987).
24. C. A. Mayhew and D. J. Smith, J. Phys. B. **23**, 3139 (1990).
25. K. R. Ryan, J. Chem. Phys. **61**, 1559 (1974).
26. Y. Sakiyama, D. B. Graves, H.-W. Chang, T. Shimizu and G. Morfill, J. Phys. D: Appl. Phys. **45**, 425201 (2012).
27. H. Chatham, D. Hils, R. Robertson and A. C. Gallagher, J. Chem. Phys. **79**, 1301 (1983).
28. Z. Karpas, V. Anicich and W. T. Huntress, J. Chem. Phys. **70**, 2877 (1979).
29. J. K. Kim and W. T. Huntress, J. Chem. Phys. **62**, 2820 (1975).
30. J. B. Marquette, B. R. Rowe, G. Dupeyrat, G. Poissant and C. Rebrion, Chem. Phys. Lett. **122**, 431 (1985).
31. B. R. Rowe, J.-B. Marquette and C. Rebrion, J. Chem. Soc. Farady Trans. II **85**, 1631 (1989).
32. N. G. Adams, D. Smith and J. F. Paulson, J. Chem. Phys. **72**, 288 (1980).
33. F. C. Fehsenfeld, C. J. Howard and E. E. Ferguson, J. Chem. Phys. **58**, 5841 (1973).
34. G. I. Mackay, R. S. Hemsworth and D. K. Bohme, Can. J. Chem. **54**, 1624 (1976).
35. D. K. Bohme, R. S. Hemsworth and H. W. Rundle, J. Chem. Phys. **59**, 77 (1973).
36. R. E. Olson, J. R. Peterson and J. Moseley, J. Chem. Phys. **53**, 3391 (1970).
37. J. Moseley, W. Aberth and J. R. Peterson, Phys. Rev. Lett. **24**,435 (1970).
38. J. I. Steinfeld, S. M. Adler-Golden and J. W. Gallagher, J. Phys. Chem. Ref. Data **16**, 911 (1987).
39. S. R. Leone, J. Phys. Chem. Ref. Data **11**, 953 (1982).
40. N. Cohen and J. F. Bott, Review of Rate Data for Reactions of Interest in HF and DF lasers, Report No. SD-TR-82-86 (1982).
41. D. F. Davidson and R. K. Hanson, Int. J. Chem. Kinet. **22**, 843 (1990).
42. S. Mukkavilli, C. K. Lee, K.Varghese and L. L. Tavlarides, IEEE Trans. Plasma Sci. **16**, 652 (1988).
43. W. Tsang and R. F. Hampson, J. Phys. Chem. Ref. Data **15**, 1087 (1986).
44. T. R. Roose, R. K. Hanson and C. H. Kruger, Decomposition of NO in the Presence of NH_3, Proc. of the 11th International Symposium on Shock Tubes and Waves, University of Washington Press, 245-253 (1978).

45. M. Demissy and R. Leschaux, J. Am. Chem. Sot. **102**, 2897 (1980).
46. D. L. Baulch, J. Duxbury, S. J. Grant and D. C. Montague, Evaluated Kinetic Data for High Temperature Reactions (Volume 4) Homogeneous Gas Phase Reactions of Halogen- and Cyanide-containing Species, National Standard Reference Data System (1981).
47. N. Jonathan, S. Okuda and D. Timlin, Mol. Phys. **24**, 1143 (1972).
48. P. J. S. B. Caridade, S. P. J. Rodrigues, F. Sousa and A. J. C. Varandas, J. Phys. Chem. A **109**, 2356 (2005).
49. R. Atkinson, D. L. Baulch, R. A. Cox, R. F. Hampson, J. A. Kerr and J. Troe, J. Phys. Chem, Ref. Data **18**, 881 (1989).
50. Y. R. Bedzhanyan, E. M. Markin and Y. M. Gershenzon, Kinet. Catal. **33**, 802 (1993).
51. W. Van Gaens and A. Bogaerts, J. Phys. D: Appl. Phys. **46**, 275201 (2013).
52. NIST Chemical Kinetics Database: https://kinetics.nist.gov/kinetics/index.jsp.
53. S. W. Rabideau, J. Magn. Reson. **11**, 163 (1973).
54. C. T. Cheah, M. A. A. Clyne and P. D. Whitefield, J. Chem. Soc. Faraday Trans. II **76**, 711 (1980).
55. R. J. Malins and D. W. Setser, J. Phys. Chem. **85**, 1342 (1981).
56. J. C. Corchado and J. Espinosa-Garcia, J. Chem. Phys. **106**, 4013 (1997).
57. M. Rohrig and H. G. Wagner, Symp. Int. Combust. Proc. **25**, 975 (1994).
58. D. F. Davidson, K. Kohse-Hoinghaus, A. Y. Chang and R. K. Hanson, Int. J. Chem. Kinet. **22**, 513 (1990).
59. J. A. Blauer, J. Phys. Chem. **72**, 79 (1968).
60. A. S. Manocha, D. W. Setser and M. A. Wickramaaratch, Chem. Phys. **76**, 129 (1983).
61. J. C. Person and D. O. Ham, Radiat. Phys. Chem. **31**, 1 (1988).
62. D. L. Baulch, C. J. Cobos, R. A. Cox, C. Esser, P. Frank, T. Just, J. A. Kerr, M. J. Pilling, J. Troe, R. W. Walker and J. Warnatz, J. Phys. Chem. Ref. Data **21**, 411 (1992).
63. J. A. Davidson, H. I. Schiff, G. E. Streit, J. R. McAfee, A. L. Schmeltekopf and C. J. Howard, J. Chem. Phys. **67**, 5021 (1977).
64. M. Rohrig, H.-J. Romming and H. G. Wagner, Ber. Bunsenges. Phys. Chem. **98**, 1332 (1994).
65. N. Cohen and K. R. Westberg, J. Phys. Chem. Ref. Data **20**, 1211 (1991).
66. J. Park and M. C. Lin, J. Phys. Chem. A **101**, 2643 (1997).

67. K. Yamasaki, S. Okada, M. Koshi and H. Matsui, J. Chem. Phys. **95**, 5087 (1991).
68. Z.-F. Zu, D.-C. Fang and X.-Y. Fu, Chem. Phys. Lett. **275**, 386 (1997).
69. G. M. Meaburn and S. Gordon, J. Phys. Chem. **72**, 1592 (1968).
70. A. I. Chichinin, Chem. Phys. Lett. **316**, 425 (2000).
71. D. R. Burgess, M. R. Zachariah, W. Tsang and P. R. Westmoreland, Prog. Energy Combust. Sci. **21**, 453 (1996).
72. S. Gómez-Carrasco, L. González-Sánchez, A. Aguado, M. Paniagua, O. Roncero, M. L. Hernández and J. M. Alvariño, Chem. Phys. Lett. **383**, 25 (2004).
73. R. Atkinson, D. L. Baulch, R. A. Cox, J. N. Crowley, R. F. Hampson, R. G. Hynes, M. E. Jenkin, M. J. Rossi and J. Troe, Atmos. Chem. Phys. **4**, 1461 (2004).
74. D. X. Liu, P. Bruggeman, F. Iza, M. Z. Rong and M. G. Kong, Plasma Sources Sci. Technol. **19**, 025018 (2010).
75. A. M. Zolot and D. J. Nesbitt, J. Chem. Phys. **129**, 184305 (2008).
76. A. A. Konnov and J. D. Ruyck, Combust. Sci. Technol. **152**, 23 (2000).
77. J. T. Herron, J. Phys. Chem. Ref. Data **28**, 1453 (1999).
78. J. Hong, S. Pancheshnyi, E. Tam, J. J. Lowke, S. Prawer and A. B. Murphy, J. Phys. D: Appl. Phys. **50**, 154005 (2017).
79. R. K. Bera and R. J. Hanrahan, J. Appl. Phys. **62**, 2523 (1987).
80. S. Javoy, V. Naudet, S. Abid and C. E. Paillard, Expt. Thermal Fluid Sci. **27**, 371 (2003).
81. S. Huang, V. Volynets, J. R. Hamilton, S. Lee, I.-C. Song, S. Lu, J. Tennyson and M. J. Kushner, J. Vac. Sci. Technol. A **35**, 031302 (2017).

Appendix C Reaction Mechanism of $NF_3/O_2/HBr$ Plasma

This appendix contains the additional reactions required for adding Br_2 to $NF_3/O_2/H_2$ mixtures to complete the $NF_3/O_2/H_2/Br_2$ or $NF_3/O_2/HBr$ mechanism. The reaction mechanism for $NF_3/O_2/H_2$ mixtures is in Appendix B.

Species in full reaction mechanism[a]:

NF_3	NF_2	NF	NF_3^+	NF_2^+	NF^+	N_2
$N_2(v)$	$N_2(A\ ^3\sum_u^+)$	$N_2(B\ ^3\Pi_g$, higher)		N	$N(^2D)$	N_2^+
N^+	F_2	$F_2(1\ ^1\sum_u^+)$	F	$F(^3S)$	F_2^+	F^+
F^-	O_2	$O_2(v)$	$O_2(a\ ^1\Delta_g)$	$O_2(b\ ^1\sum_g^+)$	O	$O(^1D)$
$O(^1S)$	O_3	O_2^+	O^+	O_2^-	O^-	O_3^-
NO	N_2O	NO_2	NO^+	N_2O^+	FO	FNO
H_2	$H_2(v=1)$	$H_2(v=2)$	$H_2(v\geq3)$	$H_2(B\ ^1\sum_u^+$, higher)		H
H(n=2)	H(n=3)	H_2^+	H^+	H^-	NH_3	$NH_3(v)$
NH_2	NH	NH_3^+	NH_2^+	NH^+	NH_2^-	HF
HF(v=1)	HF(v≥2)	HF^+	OH	H_2O	HO_2	H_2O_2
OH^+	H_2O^+	OH^-	Br_2	$Br_2(v)$	Br_2^+	Br
$Br(^2P_{1/2}$, higher)		Br^+	Br^-	HBr	HBr(v=1)	
HBr(v=2)	HBr(v≥3)	HBr^+	BrO	OBrO	e	

[a] For simplicity in the reaction list, following notation is used for excited states:

$N_2^* \leftrightarrow N_2(A\ ^3\sum_u^+)$	$N^* \leftrightarrow N(^2D)$	$F_2^* \leftrightarrow F_2(1\ ^1\sum_u^+)$	$F^* \leftrightarrow F(^3S)$
$O_2^* \leftrightarrow O_2(a\ ^1\Delta_g)$	$O^* \leftrightarrow O(^1D)$	$H_2^* \leftrightarrow H_2(B\ ^1\sum_u^+$, higher)	$H^* \leftrightarrow H(n=2)$
$H^{**} \leftrightarrow H(n=3)$	$Br^* \leftrightarrow Br(^2P_{1/2}$, higher)		

Table C.1 List of reactions in the mechanism of $NF_3/O_2/HBr$ plasma.

Reactions[a)]	Rate Coefficient[b)]	Reference	ΔH[b)] (eV)
Electron Impact Br_2/Br			
$e + Br_2 \rightarrow Br_2 + e$	c), d)	[1]	e)
$e + Br_2 \rightarrow Br + Br^-$	c)	[2]	-1.4
$e + Br_2 \rightarrow Br_2(v) + e$	c), d)	[1]	
$e + Br_2 \rightarrow Br + Br + e$	c), d)	[1]	-1.4
$e + Br_2 \rightarrow Br + Br + e$	c), d)	[1]	-2.3
$e + Br_2 \rightarrow Br + Br + e$	c), d)	[1]	-4.4
$e + Br_2 \rightarrow Br + Br + e$	c), d)	[1]	-5.0
$e + Br_2 \rightarrow Br + Br + e$	c), d)	[1]	-5.0
$e + Br_2 \rightarrow Br_2^+ + e + e$	c)	[2]	
$e + Br_2(v) \rightarrow Br_2(v) + e$	c), d)	[1]	e)
$e + Br_2(v) \rightarrow Br + Br^-$	c)	[2]	-1.4
$e + Br_2(v) \rightarrow Br_2 + e$	c), d)	[1]	
$e + Br_2(v) \rightarrow Br + Br + e$	c), d)	[1]	-1.4
$e + Br_2(v) \rightarrow Br + Br + e$	c), d)	[1]	-2.3
$e + Br_2(v) \rightarrow Br + Br + e$	c), d)	[1]	-4.4
$e + Br_2(v) \rightarrow Br + Br + e$	c), d)	[1]	-5.0
$e + Br_2(v) \rightarrow Br + Br + e$	c), d)	[1]	-5.0
$e + Br_2(v) \rightarrow Br_2^+ + e + e$	c)	[2]	
$e + Br_2^+ \rightarrow Br + Br$	$1 \times 10^{-7}\ T_e^{-1/2}$	est. [3]	
$e + Br \rightarrow Br + e$	c), f)	[4]	e)
$e + Br \rightarrow Br^* + e$	c), f)	[4]	
$e + Br \rightarrow Br^* + e$	c), f)	[4]	
$e + Br \rightarrow Br^* + e$	c), f)	[4]	
$e + Br \rightarrow Br^* + e$	c), f)	[4]	
$e + Br \rightarrow Br^* + e$	c), f)	[4]	
$e + Br \rightarrow Br^* + e$	c), f)	[4]	
$e + Br \rightarrow Br^+ + e + e$	c), f)	[4]	
$e + Br^* \rightarrow Br^+ + e + e$	c), f)	[4]	
$e + Br^+ \rightarrow Br$	$4.5 \times 10^{-13}\ T_e^{-1/2}$	est. [5]	
$e + e + Br^+ \rightarrow Br^*$	$5.12 \times 10^{-27}\ T_e^{-4.5}$	est. [5]	
Electron Impact HBr			
$e + HBr \rightarrow HBr + e$	c)	[6]	e)
$e + HBr \rightarrow Br^- + H$	c)	[6]	-0.2
$e + HBr \rightarrow HBr(v=1) + e$	c)	[6]	
$e + HBr \rightarrow HBr(v=2) + e$	c)	[6]	
$e + HBr \rightarrow HBr(v \geqslant 3) + e$	c)	[6]	
$e + HBr \rightarrow Br + H + e$	c)	[6]	-3.0
$e + HBr \rightarrow Br + H + e$	c)	[6]	-3.9
$e + HBr \rightarrow Br + H + e$	c)	[6]	-9.4
$e + HBr \rightarrow Br + H + e$	c)	[6]	-5.2

$e + HBr \rightarrow HBr^+ + e + e$	c)	[6]	
$e + HBr(v=1) \rightarrow HBr(v=1) + e$	c), g)	[6]	e)
$e + HBr(v=1) \rightarrow Br^- + H$	c), g)	[6]	-0.2
$e + HBr(v=1) \rightarrow HBr(v=2) + e$	c)	[7]	
$e + HBr(v=1) \rightarrow HBr(v \geqslant 3) + e$	c)	[7]	
$e + HBr(v=1) \rightarrow HBr + e$	c), h)	[6]	
$e + HBr(v=1) \rightarrow Br + H + e$	c), g)	[6]	-3.0
$e + HBr(v=1) \rightarrow Br + H + e$	c), g)	[6]	-3.9
$e + HBr(v=1) \rightarrow Br + H + e$	c), g)	[6]	-9.4
$e + HBr(v=1) \rightarrow Br + H + e$	c), g)	[6]	-5.2
$e + HBr(v=1) \rightarrow HBr^+ + e + e$	c), g)	[6]	
$e + HBr(v=2) \rightarrow HBr(v=2) + e$	c), g)	[6]	e)
$e + HBr(v=2) \rightarrow Br^- + H$	c), g)	[6]	-0.4
$e + HBr(v=2) \rightarrow HBr(v \geqslant 3) + e$	c)	[7]	
$e + HBr(v=2) \rightarrow HBr(v=1) + e$	c), h)	[6]	
$e + HBr(v=2) \rightarrow HBr + e$	c), h)	[6]	
$e + HBr(v=2) \rightarrow Br + H + e$	c), g)	[6]	-3.0
$e + HBr(v=2) \rightarrow Br + H + e$	c), g)	[6]	-3.9
$e + HBr(v=2) \rightarrow Br + H + e$	c), g)	[6]	-9.4
$e + HBr(v=2) \rightarrow Br + H + e$	c), g)	[6]	-5.2
$e + HBr(v=2) \rightarrow HBr^+ + e + e$	c), g)	[6]	
$e + HBr(v \geqslant 3) \rightarrow HBr(v \geqslant 3) + e$	c), g)	[6]	e)
$e + HBr(v \geqslant 3) \rightarrow Br^- + H$	c), g)	[6]	-0.7
$e + HBr(v \geqslant 3) \rightarrow HBr(v=2) + e$	c), h)	[6]	
$e + HBr(v \geqslant 3) \rightarrow HBr(v=1) + e$	c), h)	[6]	
$e + HBr(v \geqslant 3) \rightarrow HBr + e$	c), h)	[6]	
$e + HBr(v \geqslant 3) \rightarrow Br + H + e$	c), g)	[6]	-3.0
$e + HBr(v \geqslant 3) \rightarrow Br + H + e$	c), g)	[6]	-3.9
$e + HBr(v \geqslant 3) \rightarrow Br + H + e$	c), g)	[6]	-9.4
$e + HBr(v \geqslant 3) \rightarrow Br + H + e$	c), g)	[6]	-5.2
$e + HBr(v \geqslant 3) \rightarrow HBr^+ + e + e$	c), g)	[6]	
$e + HBr^+ \rightarrow H + Br$	$1 \times 10^{-7}\ T_e^{-1/2}$	est. [3]	-8.1
Radiative Transitions			
$Br^* \rightarrow Br$	$1 \times 10^6\ s^{-1}$	[8]	
$HBr(v=1) \rightarrow HBr$	$7.0\ s^{-1}$	[9]	
$HBr(v=2) \rightarrow HBr(v=1)$	$1.3 \times 10^1\ s^{-1}$	est. [9]	
$HBr(v \geqslant 3) \rightarrow HBr(v=2)$	$1.5 \times 10^1\ s^{-1}$	est. [9]	
Collisional Quenching and			
$Br_2(v) + M \rightarrow Br_2 + M$	1×10^{-10}	est. [10]	-0.04
$HBr(v=1) + M \rightarrow HBr + M$	1.5×10^{-12}	[11]	-0.3
$HBr(v=2) + M \rightarrow HBr(v=1) + M$	1×10^{-13}	est. [11]	-0.3
$HBr(v \geqslant 3) + M \rightarrow HBr(v=2) + M$	1×10^{-13}	est. [11]	-0.3
$Br_2 + M \rightarrow Br_2(v) + M$	$1 \times 10^{-10} \exp(-464/T_g)$	h)	0.04
$HBr + M \rightarrow HBr(v=1) + M$	$1.5 \times 10^{-12} \exp(-3{,}478/T_g)$	h)	0.3

$HBr(v=1) + M \rightarrow HBr(v=2) + M$	$1 \times 10^{-13} \exp(-3{,}478/T_g)$	h)	0.3
$HBr(v=2) + M \rightarrow HBr(v \geqslant 3) + M$	$1 \times 10^{-13} \exp(-3{,}478/T_g)$	h)	0.3
Ion-Neutral Collisions			
$F^+ + Br \rightarrow Br^+ + F$	1×10^{-11}	est. [12], i)	-5.6
$HF^+ + Br \rightarrow Br^+ + HF$	1×10^{-11}	est.	-4.2
$F_2^+ + Br \rightarrow Br^+ + F_2$	1×10^{-11}	est.	-3.9
$N_2^+ + Br \rightarrow Br^+ + N_2$	1×10^{-11}	est.	-3.8
$H_2^+ + Br \rightarrow Br^+ + H_2$	1×10^{-11}	est.	-3.6
$N^+ + Br \rightarrow Br^+ + N$	1×10^{-11}	est.	-2.7
$H^+ + Br \rightarrow Br^+ + H$	1×10^{-11}	est.	-1.8
$O^+ + Br \rightarrow Br^+ + O$	1×10^{-11}	est.	-1.8
$NF_3^+ + Br \rightarrow Br^+ + NF_3$	1×10^{-11}	est.	-1.7
$NH^+ + Br \rightarrow Br^+ + NH$	1×10^{-11}	est.	-1.7
$OH^+ + Br \rightarrow Br^+ + OH$	1×10^{-11}	est.	-1.7
$H_2O^+ + Br \rightarrow Br^+ + H_2O$	1×10^{-11}	est.	-1.7
$N_2O^+ + Br \rightarrow Br^+ + N_2O$	1×10^{-11}	est.	-1.1
$NF^+ + Br \rightarrow Br^+ + NF$	1×10^{-11}	est.	-0.5
$O_2^+ + Br \rightarrow Br^+ + O_2$	1×10^{-11}	est.	-0.3
$Br^+ + Br \rightarrow Br^+ + Br$	1×10^{-9}	est.	
$Br^+ + HBr \rightarrow HBr^+ + Br$	1×10^{-11}	est.	-0.1
$Br^+ + HBr(v=1) \rightarrow HBr^+ + Br$	1×10^{-11}	est.	-0.4
$Br^+ + HBr(v=2) \rightarrow HBr^+ + Br$	1×10^{-11}	est.	-0.7
$Br^+ + HBr(v \geqslant 3) \rightarrow HBr^+ + Br$	1×10^{-11}	est.	-1.0
$Br^+ + NF_2 \rightarrow NF_2^+ + Br$	1×10^{-11}	est.	-0.2
$Br^+ + NH_2 \rightarrow NH_2^+ + Br$	1×10^{-11}	est.	-0.7
$Br^+ + Br_2 \rightarrow Br_2^+ + Br$	1×10^{-11}	est.	-1.3
$Br^+ + Br_2(v) \rightarrow Br_2^+ + Br$	1×10^{-11}	est.	-1.3
$Br^+ + NH_3 \rightarrow NH_3^+ + Br$	1×10^{-11}	est.	-1.7
$Br^+ + NH_3(v) \rightarrow NH_3^+ + Br$	1×10^{-11}	est.	-1.8
$Br^+ + NO \rightarrow NO^+ + Br$	1×10^{-11}	est.	-2.5
$F^+ + HBr \rightarrow HBr^+ + F$	1×10^{-11}	est.	-5.7
$HF^+ + HBr \rightarrow HBr^+ + HF$	1×10^{-11}	est.	-4.3
$F_2^+ + HBr \rightarrow HBr^+ + F_2$	1×10^{-11}	est.	-4.0
$N_2^+ + HBr \rightarrow HBr^+ + N_2$	1×10^{-11}	est.	-3.9
$H_2^+ + HBr \rightarrow HBr^+ + H_2$	1×10^{-11}	est.	-3.7
$N^+ + HBr \rightarrow HBr^+ + N$	1×10^{-11}	est.	-2.8
$H^+ + HBr \rightarrow HBr^+ + H$	1×10^{-11}	est.	-1.9
$O^+ + HBr \rightarrow HBr^+ + O$	1×10^{-11}	est.	-1.9
$NF_3^+ + HBr \rightarrow HBr^+ + NF_3$	1×10^{-11}	est.	-1.8
$NH^+ + HBr \rightarrow HBr^+ + NH$	1×10^{-11}	est.	-1.8
$OH^+ + HBr \rightarrow HBr^+ + OH$	1×10^{-11}	est.	-1.8
$H_2O^+ + HBr \rightarrow HBr^+ + H_2O$	1×10^{-11}	est.	-1.8
$N_2O^+ + HBr \rightarrow HBr^+ + N_2O$	1×10^{-11}	est.	-1.3
$NF^+ + HBr \rightarrow HBr^+ + NF$	1×10^{-11}	est.	-0.6

$O_2^+ + HBr \rightarrow HBr^+ + O_2$	1×10^{-11}	est.	-0.4
$F^+ + HBr(v=1) \rightarrow HBr^+ + F$	1×10^{-11}	est.	-6.0
$HF^+ + HBr(v=1) \rightarrow HBr^+ + HF$	1×10^{-11}	est.	-4.6
$F_2^+ + HBr(v=1) \rightarrow HBr^+ + F_2$	1×10^{-11}	est.	-4.3
$N_2^+ + HBr(v=1) \rightarrow HBr^+ + N_2$	1×10^{-11}	est.	-4.2
$H_2^+ + HBr(v=1) \rightarrow HBr^+ + H_2$	1×10^{-11}	est.	-4.0
$N^+ + HBr(v=1) \rightarrow HBr^+ + N$	1×10^{-11}	est.	-3.1
$H^+ + HBr(v=1) \rightarrow HBr^+ + H$	1×10^{-11}	est.	-2.2
$O^+ + HBr(v=1) \rightarrow HBr^+ + O$	1×10^{-11}	est.	-2.2
$NF_3^+ + HBr(v=1) \rightarrow HBr^+ + NF_3$	1×10^{-11}	est.	-2.1
$NH^+ + HBr(v=1) \rightarrow HBr^+ + NH$	1×10^{-11}	est.	-2.1
$OH^+ + HBr(v=1) \rightarrow HBr^+ + OH$	1×10^{-11}	est.	-2.1
$H_2O^+ + HBr(v=1) \rightarrow HBr^+ + H_2O$	1×10^{-11}	est.	-2.1
$N_2O^+ + HBr(v=1) \rightarrow HBr^+ + N_2O$	1×10^{-11}	est.	-1.6
$NF^+ + HBr(v=1) \rightarrow HBr^+ + NF$	1×10^{-11}	est.	-0.9
$O_2^+ + HBr(v=1) \rightarrow HBr^+ + O_2$	1×10^{-11}	est.	-0.7
$NF_2^+ + HBr(v=1) \rightarrow HBr^+ + NF_2$	1×10^{-11}	est.	-0.2
$F^+ + HBr(v=2) \rightarrow HBr^+ + F$	1×10^{-11}	est.	-6.3
$HF^+ + HBr(v=2) \rightarrow HBr^+ + HF$	1×10^{-11}	est.	-4.9
$F_2^+ + HBr(v=2) \rightarrow HBr^+ + F_2$	1×10^{-11}	est.	-4.6
$N_2^+ + HBr(v=2) \rightarrow HBr^+ + N_2$	1×10^{-11}	est.	-4.5
$H_2^+ + HBr(v=2) \rightarrow HBr^+ + H_2$	1×10^{-11}	est.	-4.3
$N^+ + HBr(v=2) \rightarrow HBr^+ + N$	1×10^{-11}	est.	-3.4
$H^+ + HBr(v=2) \rightarrow HBr^+ + H$	1×10^{-11}	est.	-2.5
$O^+ + HBr(v=2) \rightarrow HBr^+ + O$	1×10^{-11}	est.	-2.5
$NF_3^+ + HBr(v=2) \rightarrow HBr^+ + NF_3$	1×10^{-11}	est.	-2.4
$NH^+ + HBr(v=2) \rightarrow HBr^+ + NH$	1×10^{-11}	est.	-2.4
$OH^+ + HBr(v=2) \rightarrow HBr^+ + OH$	1×10^{-11}	est.	-2.4
$H_2O^+ + HBr(v=2) \rightarrow HBr^+ + H_2O$	1×10^{-11}	est.	-2.4
$N_2O^+ + HBr(v=2) \rightarrow HBr^+ + N_2O$	1×10^{-11}	est.	-1.9
$NF^+ + HBr(v=2) \rightarrow HBr^+ + NF$	1×10^{-11}	est.	-1.2
$O_2^+ + HBr(v=2) \rightarrow HBr^+ + O_2$	1×10^{-11}	est.	-1.0
$NF_2^+ + HBr(v=2) \rightarrow HBr^+ + NF_2$	1×10^{-11}	est.	-0.5
$NH_2^+ + HBr(v=2) \rightarrow HBr^+ + NH_2$	1×10^{-11}	est.	
$F^+ + HBr(v \geqslant 3) \rightarrow HBr^+ + F$	1×10^{-11}	est.	-6.6
$HF^+ + HBr(v \geqslant 3) \rightarrow HBr^+ + HF$	1×10^{-11}	est.	-5.2
$F_2^+ + HBr(v \geqslant 3) \rightarrow HBr^+ + F_2$	1×10^{-11}	est.	-4.9
$N_2^+ + HBr(v \geqslant 3) \rightarrow HBr^+ + N_2$	1×10^{-11}	est.	-4.8
$H_2^+ + HBr(v \geqslant 3) \rightarrow HBr^+ + H_2$	1×10^{-11}	est.	-4.6
$N^+ + HBr(v \geqslant 3) \rightarrow HBr^+ + N$	1×10^{-11}	est.	-3.7
$H^+ + HBr(v \geqslant 3) \rightarrow HBr^+ + H$	1×10^{-11}	est.	-2.8
$O^+ + HBr(v \geqslant 3) \rightarrow HBr^+ + O$	1×10^{-11}	est.	-2.8
$NF_3^+ + HBr(v \geqslant 3) \rightarrow HBr^+ + NF_3$	1×10^{-11}	est.	-2.7
$NH^+ + HBr(v \geqslant 3) \rightarrow HBr^+ + NH$	1×10^{-11}	est.	-2.7

$OH^+ + HBr(v \geqslant 3) \rightarrow HBr^+ + OH$	1×10^{-11}	est.	-2.7
$H_2O^+ + HBr(v \geqslant 3) \rightarrow HBr^+ + H_2O$	1×10^{-11}	est.	-2.7
$N_2O^+ + HBr(v \geqslant 3) \rightarrow HBr^+ + N_2O$	1×10^{-11}	est.	-2.2
$NF^+ + HBr(v \geqslant 3) \rightarrow HBr^+ + NF$	1×10^{-11}	est.	-1.5
$O_2^+ + HBr(v \geqslant 3) \rightarrow HBr^+ + O_2$	1×10^{-11}	est.	-1.3
$NF_2^+ + HBr(v \geqslant 3) \rightarrow HBr^+ + NF_2$	1×10^{-11}	est.	-0.8
$NH_2^+ + HBr(v \geqslant 3) \rightarrow HBr^+ + NH_2$	1×10^{-11}	est.	-0.3
$HBr^+ + HBr \rightarrow HBr^+ + HBr$	1×10^{-9}	est.	
$HBr^+ + HBr(v=1) \rightarrow HBr^+ + HBr$	1×10^{-9}	est.	-0.3
$HBr^+ + HBr(v=2) \rightarrow HBr^+ + HBr$	1×10^{-9}	est.	-0.6
$HBr^+ + HBr(v \geqslant 3) \rightarrow HBr^+ + HBr$	1×10^{-9}	est.	-0.9
$HBr^+ + NF_2 \rightarrow NF_2^+ + HBr$	1×10^{-11}	est.	-0.1
$HBr^+ + NH_2 \rightarrow NH_2^+ + HBr$	1×10^{-11}	est.	-0.6
$HBr^+ + Br_2 \rightarrow Br_2^+ + HBr$	1×10^{-11}	est.	-1.2
$HBr^+ + Br_2(v) \rightarrow Br_2^+ + HBr$	1×10^{-11}	est.	-1.2
$HBr^+ + NH_3 \rightarrow NH_3^+ + HBr$	1×10^{-11}	est.	-1.6
$HBr^+ + NH_3(v) \rightarrow NH_3^+ + HBr$	1×10^{-11}	est.	-1.7
$HBr^+ + NO \rightarrow NO^+ + HBr$	1×10^{-11}	est.	-2.4
$F^+ + Br_2 \rightarrow Br_2^+ + F$	1×10^{-11}	est.	-6.9
$HF^+ + Br_2 \rightarrow Br_2^+ + HF$	1×10^{-11}	est.	-5.5
$F_2^+ + Br_2 \rightarrow Br_2^+ + F_2$	1×10^{-11}	est.	-5.2
$N_2^+ + Br_2 \rightarrow Br_2^+ + N_2$	1×10^{-11}	est.	-5.1
$H_2^+ + Br_2 \rightarrow Br_2^+ + H_2$	1×10^{-11}	est.	-4.9
$N^+ + Br_2 \rightarrow Br_2^+ + N$	1×10^{-11}	est.	-4.0
$H^+ + Br_2 \rightarrow Br_2^+ + H$	1×10^{-11}	est.	-3.1
$O^+ + Br_2 \rightarrow Br_2^+ + O$	1×10^{-11}	est.	-3.1
$NF_3^+ + Br_2 \rightarrow Br_2^+ + NF_3$	1×10^{-11}	est.	-3.0
$NH^+ + Br_2 \rightarrow Br_2^+ + NH$	1×10^{-11}	est.	-3.0
$OH^+ + Br_2 \rightarrow Br_2^+ + OH$	1×10^{-11}	est.	-3.0
$H_2O^+ + Br_2 \rightarrow Br_2^+ + H_2O$	1×10^{-11}	est.	-3.0
$N_2O^+ + Br_2 \rightarrow Br_2^+ + N_2O$	1×10^{-11}	est.	-2.5
$NF^+ + Br_2 \rightarrow Br_2^+ + NF$	1×10^{-11}	est.	-1.8
$O_2^+ + Br_2 \rightarrow Br_2^+ + O_2$	1×10^{-11}	est.	-1.6
$NF_2^+ + Br_2 \rightarrow Br_2^+ + NF_2$	1×10^{-11}	est.	-1.1
$NH_2^+ + Br_2 \rightarrow Br_2^+ + NH_2$	1×10^{-11}	est.	-0.6
$F^+ + Br_2(v) \rightarrow Br_2^+ + F$	1×10^{-11}	est.	-6.9
$HF^+ + Br_2(v) \rightarrow Br_2^+ + HF$	1×10^{-11}	est.	-5.5
$F_2^+ + Br_2(v) \rightarrow Br_2^+ + F_2$	1×10^{-11}	est.	-5.2
$N_2^+ + Br_2(v) \rightarrow Br_2^+ + N_2$	1×10^{-11}	est.	-5.1
$H_2^+ + Br_2(v) \rightarrow Br_2^+ + H_2$	1×10^{-11}	est.	-4.9
$N^+ + Br_2(v) \rightarrow Br_2^+ + N$	1×10^{-11}	est.	-4.0
$H^+ + Br_2(v) \rightarrow Br_2^+ + H$	1×10^{-11}	est.	-3.1
$O^+ + Br_2(v) \rightarrow Br_2^+ + O$	1×10^{-11}	est.	-3.1
$NF_3^+ + Br_2(v) \rightarrow Br_2^+ + NF_3$	1×10^{-11}	est.	-3.0

$NH^+ + Br_2(v) \rightarrow Br_2^+ + NH$	1×10^{-11}	est.	-3.0
$OH^+ + Br_2(v) \rightarrow Br_2^+ + OH$	1×10^{-11}	est.	-3.0
$H_2O^+ + Br_2(v) \rightarrow Br_2^+ + H_2O$	1×10^{-11}	est.	-3.0
$N_2O^+ + Br_2(v) \rightarrow Br_2^+ + N_2O$	1×10^{-11}	est.	-2.5
$NF^+ + Br_2(v) \rightarrow Br_2^+ + NF$	1×10^{-11}	est.	-1.8
$O_2^+ + Br_2(v) \rightarrow Br_2^+ + O_2$	1×10^{-11}	est.	-1.6
$NF_2^+ + Br_2(v) \rightarrow Br_2^+ + NF_2$	1×10^{-11}	est.	-1.1
$NH_2^+ + Br_2(v) \rightarrow Br_2^+ + NH_2$	1×10^{-11}	est.	-0.6
$Br_2^+ + Br_2 \rightarrow Br_2^+ + Br_2$	1×10^{-9}	est.	
$Br_2^+ + Br_2(v) \rightarrow Br_2^+ + Br_2$	1×10^{-9}	est.	-0.04
$Br_2^+ + NH_3 \rightarrow NH_3^+ + Br_2$	1×10^{-11}	est.	-0.4
$Br_2^+ + NH_3(v) \rightarrow NH_3^+ + Br_2$	1×10^{-11}	est.	-0.5
$Br_2^+ + NO \rightarrow NO^+ + Br_2$	1×10^{-11}	est.	-1.2
Positive-Negative Ion Neutralization			
$F^- + Br_2^+ \rightarrow F + Br + Br$	2×10^{-7}	est. [13], j)	-5.1
$F^- + Br^+ \rightarrow F + Br^*$	2×10^{-7}	est.	-0.1
$F^- + HBr^+ \rightarrow F + HBr$	2×10^{-7}	est.	
$H^- + Br_2^+ \rightarrow H + Br + Br$	2×10^{-7}	est.	-7.7
$H^- + Br^+ \rightarrow H + Br^*$	2×10^{-7}	est.	-0.3
$H^- + HBr^+ \rightarrow H + HBr$	2×10^{-7}	est.	-1.5
$NH_2^- + Br_2^+ \rightarrow NH_2 + Br + Br$	2×10^{-7}	est.	-7.7
$NH_2^- + Br^+ \rightarrow NH_2 + Br^*$	2×10^{-7}	est.	-0.3
$NH_2^- + HBr^+ \rightarrow NH_2 + HBr$	2×10^{-7}	est.	-1.5
$O_3^- + Br^+ \rightarrow O_3 + Br^*$	2×10^{-7}	est.	-1.1
$O_3^- + HBr^+ \rightarrow O_3 + HBr$	2×10^{-7}	est.	-0.2
$O_3^- + Br_2^+ \rightarrow O_3 + Br + Br$	2×10^{-7}	est.	-6.4
$OH^- + Br^+ \rightarrow OH + Br^*$	2×10^{-7}	est.	-1.4
$OH^- + HBr^+ \rightarrow OH + HBr$	2×10^{-7}	est.	-0.5
$OH^- + Br_2^+ \rightarrow OH + Br + Br$	2×10^{-7}	est.	-6.7
$O^- + Br^+ \rightarrow O + Br^*$	2×10^{-7}	est.	-1.7
$O^- + HBr^+ \rightarrow O + HBr$	2×10^{-7}	est.	-0.8
$O^- + Br_2^+ \rightarrow O + Br + Br$	2×10^{-7}	est.	-7.0
$O_2^- + Br^+ \rightarrow O_2 + Br^*$	2×10^{-7}	est.	-0.6
$O_2^- + HBr^+ \rightarrow O_2 + HBr$	2×10^{-7}	est.	-1.8
$O_2^- + Br_2^+ \rightarrow O_2 + Br + Br$	2×10^{-7}	est.	-8.0
$Br^- + F^+ \rightarrow Br + F^*$	2×10^{-7}	est.	-1.0
$Br^- + HF^+ \rightarrow Br + H1 + F$	2×10^{-7}	est.	-6.7
$Br^- + F_2^+ \rightarrow Br + F_2^*$	2×10^{-7}	est.	-4.4
$Br^- + N_2^+ \rightarrow Br + N_2^*$	2×10^{-7}	est.	-0.3
$Br^- + H_2^+ \rightarrow Br + H_2$	2×10^{-7}	est.	
$Br^- + N^+ \rightarrow Br + N^*$	2×10^{-7}	est.	-0.2
$Br^- + H^+ \rightarrow Br + H$	2×10^{-7}	est.	
$Br^- + O^+ \rightarrow Br + O^*$	2×10^{-7}	est.	-0.7
$Br^- + NF_3^+ \rightarrow Br + NF_2 + F$	2×10^{-7}	est.	-7.5

$Br^- + NH^+ \rightarrow Br + NH$	2×10^{-7}	est.	-0.6
$Br^- + OH^+ \rightarrow Br + OH$	2×10^{-7}	est.	-0.1
$Br^- + H_2O^+ \rightarrow Br + H_2O$	2×10^{-7}	est.	-10.1
$Br^- + N_2O^+ \rightarrow Br + N_2O$	2×10^{-7}	est.	-9.5
$Br^- + NF^+ \rightarrow Br + N + F$	2×10^{-7}	est.	-5.8
$Br^- + NF^+ \rightarrow Br + N^* + F$	2×10^{-7}	est.	-3.4
$Br^- + O_2^+ \rightarrow Br + O_2^*$	2×10^{-7}	est.	
$Br^- + Br^+ \rightarrow Br + Br^*$	2×10^{-7}	est.	-0.1
$Br^- + HBr^+ \rightarrow Br + HBr$	2×10^{-7}	est.	
$Br^- + NF_2^+ \rightarrow Br + NF + F$	2×10^{-7}	est.	-2.6
$Br^- + NH_2^+ \rightarrow Br + NH + H$	2×10^{-7}	est.	-1.0
$Br^- + Br_2^+ \rightarrow Br + Br + Br$	2×10^{-7}	est.	-5.1
$Br^- + NH_3^+ \rightarrow Br + NH_2 + H$	2×10^{-7}	est.	-1.9
$Br^- + NO^+ \rightarrow Br + NO$	2×10^{-7}	est.	-0.4
$Br^- + H_3O^+ \rightarrow Br + H_2O + H$	2×10^{-7}	est.	-2.8
Neutral-Neutral Collisions			
$Br_2 + H_2 \rightarrow HBr + HBr$	$6.81 \times 10^{-9} \exp(-20{,}400/T_g)$	[14]	-0.6
$Br_2 + H_2(v=1) \rightarrow HBr + HBr$	$6.81 \times 10^{-9} \exp(-14{,}603/T_g)$	est. [14]	-1.1
$Br_2 + H_2(v=2) \rightarrow HBr + HBr$	$6.81 \times 10^{-9} \exp(-8{,}806/T_g)$	est. [14]	-1.6
$Br_2 + H_2(v \geqslant 3) \rightarrow HBr + HBr$	$6.81 \times 10^{-9} \exp(-3{,}009/T_g)$	est. [14]	-2.1
$Br_2(v) + H_2 \rightarrow HBr + HBr$	$6.81 \times 10^{-9} \exp(-19{,}936/T_g)$	est. [14]	-0.6
$Br_2(v) + H_2(v=1) \rightarrow HBr + HBr$	$6.81 \times 10^{-9} \exp(-14{,}139/T_g)$	est. [14]	-1.1
$Br_2(v) + H_2(v=2) \rightarrow HBr + HBr$	$6.81 \times 10^{-9} \exp(-8{,}342/T_g)$	est. [14]	-1.6
$Br_2(v) + H_2(v \geqslant 3) \rightarrow HBr + HBr$	$6.81 \times 10^{-9} \exp(-2{,}545/T_g)$	est. [14]	-2.1
$Br_2 + OH \rightarrow HBr + BrO$	$5.4 \times 10^{-13} \exp(235/T_g)$	[14]	-0.1
$Br_2(v) + OH \rightarrow HBr + BrO$	$5.4 \times 10^{-13} \exp(699/T_g)$	est. [14]	-0.1
$Br_2 + H \rightarrow HBr + Br$	$1.13 \times 10^{-10} T_n \exp(-220/T_g)$	[14]	-1.6
$Br_2(v) + H \rightarrow HBr + Br$	$1.13 \times 10^{-10} T_n$	est. [14]	-1.6
$Br_2 + O \rightarrow Br + BrO$	1.39×10^{-11}	[14]	-0.4
$Br_2(v) + O \rightarrow Br + BrO$	1.39×10^{-11}	est. [14]	-0.4
$Br + H_2 \rightarrow HBr + H$	$2.82 \times 10^{-10} \exp(-9{,}618/T_g)$	[14]	1.0
$Br + H_2(v=1) \rightarrow HBr + H$	$2.82 \times 10^{-10} \exp(-3{,}821/T_g)$	est. [14]	0.5
$Br + H_2(v=2) \rightarrow HBr + H$	2.82×10^{-10}	est. [14]	
$Br + H_2(v \geqslant 3) \rightarrow HBr + H$	2.82×10^{-10}	est. [14]	-0.5
$Br + HO_2 \rightarrow HBr + O_2$	$7.7 \times 10^{-12} \exp(-449/T_g)$	[14]	-1.3
$Br + OH \rightarrow HBr + O$	$4.57 \times 10^{-12} \exp(-8{,}700/T_g)$	[14]	0.3
$Br + H_2O_2 \rightarrow HBr + HO_2$	$1 \times 10^{-11} \exp(-2{,}993/T_g)$	[14]	0.1
$Br + N_2O \rightarrow BrO + N_2$	$3.32 \times 10^{-10} \exp(-18{,}600/T_g)$	[14]	-0.6
$Br + O_3 \rightarrow BrO + O_2$	$1.7 \times 10^{-11} \exp(-798/T_g)$	[14]	-1.3
$Br + HBr \rightarrow Br_2 + H$	$4.52 \times 10^{-10} \exp(-22{,}200/T_g)$	[14]	1.6
$Br + HBr(v=1) \rightarrow Br_2 + H$	$4.52 \times 10^{-10} \exp(-18{,}722/T_g)$	est. [14]	1.3
$Br + HBr(v=2) \rightarrow Br_2 + H$	$4.52 \times 10^{-10} \exp(-15{,}244/T_g)$	est. [14]	1.0
$Br + HBr(v \geqslant 3) \rightarrow Br_2 + H$	$4.52 \times 10^{-10} \exp(-11{,}766/T_g)$	est. [14]	0.7
$Br + FO \rightarrow BrO + F$	$1.24 \times 10^{-10} \exp(-1{,}297/T_g)$	[14]	-0.1

$HBr + O^* \rightarrow BrO + H$	2.96×10^{-11}	[15]	-3.3
$HBr(v=1) + O^* \rightarrow BrO + H$	2.96×10^{-11}	est. [15]	-3.6
$HBr(v=2) + O^* \rightarrow BrO + H$	2.96×10^{-11}	est. [15]	-3.9
$HBr(v \geqslant 3) + O^* \rightarrow BrO + H$	2.96×10^{-11}	est. [15]	-4.2
$HBr + OH \rightarrow Br + H_2O$	1.1×10^{-11}	[14]	-1.6
$HBr(v=1) + OH \rightarrow Br + H_2O$	1.1×10^{-11}	est. [14]	-1.9
$HBr(v=2) + OH \rightarrow Br + H_2O$	1.1×10^{-11}	est. [14]	-2.2
$HBr(v \geqslant 3) + OH \rightarrow Br + H_2O$	1.1×10^{-11}	est. [14]	-2.5
$HBr + H \rightarrow Br + H_2$	$1.73 \times 10^{-11} T_n^{0.5} \exp(-299/T_g)$	[14]	-1.0
$HBr(v=1) + H \rightarrow Br + H_2$	$1.73 \times 10^{-11} T_n^{0.5}$	est. [14]	-1.3
$HBr(v=2) + H \rightarrow Br + H_2$	$1.73 \times 10^{-11} T_n^{0.5}$	est. [14]	-1.6
$HBr(v \geqslant 3) + H \rightarrow Br + H_2$	$1.73 \times 10^{-11} T_n^{0.5}$	est. [14]	-1.9
$HBr + F \rightarrow Br + HF$	0.22×10^{-11}	[14,16]	-2.3
$HBr + F \rightarrow Br + HF(v=1)$	0.74×10^{-11}	[14,16]	-1.8
$HBr + F \rightarrow Br + HF(v \geqslant 2)$	4.52×10^{-11}	[14,16]	-1.3
$HBr(v=1) + F \rightarrow Br + HF$	0.22×10^{-11}	est. [14,16]	-2.6
$HBr(v=1) + F \rightarrow Br + HF(v=1)$	0.74×10^{-11}	est. [14,16]	-2.1
$HBr(v=1) + F \rightarrow Br + HF(v \geqslant 2)$	4.52×10^{-11}	est. [14,16]	-1.6
$HBr(v=2) + F \rightarrow Br + HF$	0.22×10^{-11}	est. [14,16]	-2.9
$HBr(v=2) + F \rightarrow Br + HF(v=1)$	0.74×10^{-11}	est. [14,16]	-2.4
$HBr(v=2) + F \rightarrow Br + HF(v \geqslant 2)$	4.52×10^{-11}	est. [14,16]	-1.9
$HBr(v \geqslant 3) + F \rightarrow Br + HF$	0.22×10^{-11}	est. [14,16]	-3.2
$HBr(v \geqslant 3) + F \rightarrow Br + HF(v=1)$	0.74×10^{-11}	est. [14,16]	-2.7
$HBr(v \geqslant 3) + F \rightarrow Br + HF(v \geqslant 2)$	4.52×10^{-11}	est. [14,16]	-2.2
$HBr + O \rightarrow Br + OH$	$5.8 \times 10^{-12} \exp(-1{,}496/T_g)$	[14]	-0.3
$HBr(v=1) + O \rightarrow Br + OH$	5.8×10^{-12}	est. [14]	-0.6
$HBr(v=2) + O \rightarrow Br + OH$	5.8×10^{-12}	est. [14]	-0.9
$HBr(v \geqslant 3) + O \rightarrow Br + OH$	5.8×10^{-12}	est. [14]	-1.2
$HBr + N \rightarrow Br + NH$	$3.8 \times 10^{-14} \exp(-3{,}478/T_g)$	[14]	0.3
$HBr(v=1) + N \rightarrow Br + NH$	3.8×10^{-14}	est. [14]	
$HBr(v=2) + N \rightarrow Br + NH$	3.8×10^{-14}	est. [14]	-0.3
$HBr(v \geqslant 3) + N \rightarrow Br + NH$	3.8×10^{-14}	est. [14]	-0.6
$BrO + NO \rightarrow Br + NO_2$	$8.7 \times 10^{-12} \exp(259/T_g)$	[14]	-0.8
$BrO + O_3 \rightarrow OBrO + O_2$	$7.01 \times 10^{-14} \exp(-3{,}092/T_g)$	[14]	-1.3
$BrO + BrO \rightarrow Br_2 + O_2$	4.8×10^{-13}	[14]	-2.4
$BrO + BrO \rightarrow Br + Br + O_2$	2.7×10^{-12}	[14]	-0.4
$BrO + BrO \rightarrow Br + OBrO$	$1.28 \times 10^{-12} \exp(-27{,}826/T_g)$	[14]	2.4
$BrO + O \rightarrow Br + O_2$	$1.91 \times 10^{-11} \exp(229/T_g)$	[14]	-2.8
$BrO + OH \rightarrow Br + HO_2$	3.7×10^{-11}	[17]	-0.6
$BrO + OH \rightarrow HBr + O_2$	6.7×10^{-13}	[17]	-2.5
$BrO + HO_2 \rightarrow HBr + O_3$	3.3×10^{-13}	[18]	
$OBrO + O \rightarrow BrO + O_2$	4.25×10^{-12}	[14]	-2.8
$OBrO + NO \rightarrow BrO + NO_2$	1.77×10^{-12}	[14]	-0.8
<u>High Temperature Chemistry</u>			

$Br_2 + M \rightarrow Br + Br + M$	$3.9 \times 10^{-10} \exp(-21{,}630/T_g)$	[19]	2.0
$Br_2(v) + M \rightarrow Br + Br + M$	$3.9 \times 10^{-10} \exp(-21{,}166/T_g)$	est. [19]	1.96
$Br + Br + M \rightarrow Br_2 + M$	$4.08 \times 10^{-34} \exp(856/T_g)$	[19]	-2.0
$Br + Br + M \rightarrow Br_2(v) + M$	$4.08 \times 10^{-34} \exp(392/T_g)$	est. [19]	-1.96
$HBr + M \rightarrow H + Br + M$	$1.56 \times 10^{-7} T_n^{-2} \exp(-$	[19]	3.6
$HBr(v=1) + M \rightarrow H + Br + M$	$1.56 \times 10^{-7} T_n^{-2} \exp(-$	est. [19]	3.3
$HBr(v=2) + M \rightarrow H + Br + M$	$1.56 \times 10^{-7} T_n^{-2} \exp(-$	est. [19]	3.0
$HBr(v \geqslant 3) + M \rightarrow H + Br + M$	$1.56 \times 10^{-7} T_n^{-2} \exp(-$	est. [19]	2.7
$H + Br + M \rightarrow HBr + M$	$5.3 \times 10^{-27} T_n^{-1.87}$	[19]	-3.6
$H + Br + M \rightarrow HBr(v=1) + M$	$5.3 \times 10^{-27} T_n^{-1.87}$	est. [19]	-3.3
$H + Br + M \rightarrow HBr(v=2) + M$	$5.3 \times 10^{-27} T_n^{-1.87}$	est. [19]	-3.0
$H + Br + M \rightarrow HBr(v \geqslant 3) + M$	$5.3 \times 10^{-27} T_n^{-1.87}$	est. [19]	-2.7
$BrO + M \rightarrow Br + O + M$	$1.31 \times 10^{-10} \exp(-27{,}826/T_g)$	est. [20]	2.4
$OBrO + M \rightarrow BrO + O + M$	$1.94 \times 10^{-9} \exp(-27{,}826/T_g)$	est. [19]	2.4
$Br + O + M \rightarrow BrO + M$	1×10^{-33}	est. [21]	-2.4
$BrO + O + M \rightarrow OBrO + M$	$6.17 \times 10^{-31} T_n^{-4.1} \exp(-420/T_g)$	est. [22]	-2.4

a) This table is a subset of the mechanism for $NF_3/O_2/H_2/Br_2$ or $NF_3/O_2/HBr$ plasmas. The reactions that would occur in $NF_3/O_2/H_2$ plasmas are the same as listed in Appendix B.

b) Rate coefficients have units of cm^3s^{-1} unless noted. T_e is electron temperature (eV). T_g is gas temperature (K) and T_n is normalized gas temperature (T_g/300 K). ΔH is the change of enthalpy (eV).

c) Rate coefficients are calculated from the electron energy distributions produced by solutions of Boltzmann's equation using electron impact cross sections. The cross section is for the forward reaction. Reverse cross sections are obtained by detailed balance.

d) The electron impact cross sections for momentum transfer of Br_2 and $Br_2(v)$ are assumed to be the same as Cl_2, while the electron impact cross sections for dissociation of Br_2 and $Br_2(v)$ are obtained by assuming the same profiles as Cl_2 and shifting the corresponding cross sections to match the thresholds.

e) The rate of gas heating by elastic collisions is $k_m(3/2)k_B(2m_e/M)(T_e-T_g)$ eV-cm^3/s for elastic rate coefficient k_m, electron mass m_e, neutral mass M and Boltzmann's constant k_B.

f) The electron impact cross section for momentum transfer of Br is assumed to be the same as Cl, while the electron impact cross sections of excitation and ionization of Br are obtained by assuming the same profiles as Cl and shifting the corresponding cross sections to match the thresholds.

g) The electron impact cross sections for HBr(v=1), HBr(v=2) and HBr(v≥3) are obtained by shifting the corresponding cross sections of HBr to match the thresholds.

h) The electron impact superelastic cross sections of HBr(v=1), HBr(v=2) and HBr(v≥3) are calculated from detailed balancing. The rate coefficients of collisional excitation are obtained from detailed balancing of the reverse reactions (collisional quenching reactions).

i) Rate coefficient for charge exchange between ions and neutrals was assumed to be 1×10^{-11} cm^3s^{-1} (1×10^{-9} cm^3s^{-1} for resonant charge exchange) when measured or calculated data is not available.

j) Rate coefficient for neutralization between positive and negative ions was assumed to be 2×10^{-7} cm^3s^{-1} when measured or calculated data is not available.

Appendix C References

1. J. Gregorio and L. C. Pitchford, Plasma Sources Sci. Technol. **21**, 032002 (2012).
2. M. V. Kurepa, D. S. Babic and D. S. Belic, J. Phys. B: At. Mol. Phys. **14**, 375 (1981).
3. G. Bekefi, Principles of Laser Plasmas, John Wiley & Sons, New York, NY (1976).
4. P. S. Ganas, J. Appl. Phys. **63**, 277 (1988).
5. G. Bekefi, Radiation Processes in Plasmas, John Wiley & Sons, New York, NY (1966).
6. O. Sasic, S. Dujko, T. Makabe and Z. Lj. Petrovic, Chem. Phys. **398**, 154 (2012).
7. J. Horacek and W. Domcke, Phys. Rev. A **53**, 2262 (1996).
8. NIST Atomic Spectra Database: https://physics.nist.gov/PhysRefData/ASD/lines_form.html.
9. R. J. Malins and D. W. Setser, J. Chem. Phys. **73**, 5666 (1980).
10. P. Tian and M. J. Kushner, Plasma Sources Sci. Technol. **26**, 024005 (2017).
11. S. R. Leone, J. Phys. Chem. Ref. Data **11**, 953 (1982).
12. Y. Ikezoe, S. Matsuoka and M. Takebe, Gas Phase Ion Molecule Reaction Rate Constants Through 1986, Ion Reaction Research Group of the Mass Spectroscopy Society of Japan, Tokyo, Japan (1987).
13. R. E. Olson, J. R. Peterson and J. Moseley, J. Chem. Phys. **53**, 3391 (1970).
14. NIST Chemical Kinetics Database: https://kinetics.nist.gov/kinetics/index.jsp.
15. J. M. Cronkhite and P. H. Wine, Int. J. Chem. Kinet. **30**, 555 (1998).
16. K. Tamagake, D. W. Setser and J. P. Sung, J. Chem. Phys. **73**, 2203 (1980).
17. Y. Bedjanian, V. Riffault, G. Le Bras and G. Poulet, J. Phys. Chem. A **105**, 6154 (2001).
18. M. Larichev, F. Maguin, G. Le Bras and G. Poulet, J. Phys. Chem. **99**,15911 (1995).
19. D. L. Baulch, J. Duxbury, S. J. Grant and D. C. Montague, Evaluated Kinetic Data for High Temperature Reactions (Volume 4) Homogeneous Gas Phase Reactions of Halogen- and Cyanide-containing Species, National Standard Reference Data System (1981).
20. F. Westley, J. H. Herron and R. J. Cvetanovic, Compilation of Chemical Kinetic Data for Combustion Chemistry (NSRDS-NBS 73, Parts 1 and 2), U.S. Government Printing Office, Washington, DC (1987).
21. D. R. F. Burgess, M. R. Zachariah, W. Tsang and P. R. Westmoreland, Prog. Energy Combust. Sci. **21**, 453 (1996).
22. R. S. Zhu and M. C. Lin, J. Chem. Phys. **119**, 2075 (2003).

Appendix D Si_3N_4 Etching Mechanism Using Remote $Ar/NF_3/O_2$ Plasma

Gas Phase Species:

F(g)	N_2(g)	N(g)	O_2(g)	O(g)	NO(g)
N_2O(g)	NO_2(g)	SiF_4(g)			

Surface Sites[a]:

SiN(s)	SiNF(s)	$SiNF_2$(s)	$SiNF_3$(s)	N(s)	O(s)

[a] The notation of SiN is used for silicon nitride to simplify the reaction mechanism and primarily achieve balance of surface sites.

Table D.1 List of reactions in Si_3N_4 etching mechanism using remote $Ar/NF_3/O_2$ plasma.

Reactions[a]	Probability[b, c]	Reference	Note
<u>Removal of Si subsites</u>			
$SiN(s) + F(g) \rightarrow SiNF(s)$	0.1		b)
$SiNF(s) + F(g) \rightarrow SiNF_2(s)$	0.1		b)
$SiNF_2(s) + F(g) \rightarrow SiNF_3(s)$	0.1		b)
$SiNF_3(s) + F(g) \rightarrow SiF_4(g) + N(s)$	0.1		b)
<u>Removal of N subsites</u>			
$N(s) + NO(g) \rightarrow N_2O(g) + SiN(s)$	0.1	[1]	b)
$N(s) + N(g) \rightarrow N_2(g) + SiN(s)$	0.1		b)
<u>Surface oxidation to form O sites</u>			
$N(s) + NO(g) \rightarrow N_2(g) + O(s)$	0.1	[1]	b)
<u>Removal of O sites</u>			
$O(s) + NO(g) \rightarrow NO_2(g) + SiN(s)$	0.1	[2]	b)
$O(s) + O(g) \rightarrow O_2(g) + SiN(s)$	0.1		b)
$O(s) + O(s) \rightarrow O_2(g) + SiN(s)$	10^{18}		c)

[a] All gas phase species have units of flux ($cm^{-2}s^{-1}$). All surface species have units of fractional coverage (unitless).

[b] Probability for reactions between gas phase species and surface sites is unitless.

c) Probability for reactions between surface sites and surface sites is $cm^{-2}s^{-1}$. Probability is obtained by $R \times T^2$, where R is the surface reaction rate coefficient and T is the surface site density. In this study, $R = 10^{-12}$ cm^2s^{-1} and $T = 1 \times 10^{15}$ cm^{-2}.

Appendix D References

1. B. E. E. Kastenmeier, P. J. Matsuo, G. S. Oehrlein, R. E. Ellefson and L. C. Frees, J. Vac. Sci. Technol. A **19**, 25 (2001).
2. P. J. Matsuo, B. E. E. Kastenmeier, G. S. Oehrlein and J. G. Langan, J. Vac. Sci. Technol. A **17**, 2431 (1999).

Appendix E SiO_2 Etching Mechanism Using $Ar/C_4F_8/O_2$ Plasma

Table E.1 List of species in SiO_2 etching mechanism using $Ar/C_4F_8/O_2$ plasma.

Gas Phase Species		Notes
Ions, hot neutrals and neutral partners	Ar^+, Ar(h), Ar F^+, F(h), F F_2^+, F_2(h), F_2 O^+, O(h), O O_2^+, O_2(h), O_2 $C_mF_n^+$, C_mF_n(h), C_mF_n	a)
Etch products	CO, CO_2, COF, COH SiF_x, SiF_4	b)
Sputtered Materials	R, SiO_2, Si	c)
Surface Sites		
Photoresist	R(s)	
Silicon oxide	SiO_2(s)	
Passivated oxide surface (complex)	$SiO_2C_mF_n$(s) $SiOCF_3$(s)	d)
Silicon	Si(s)	
Fluorinated silicon surface	SiF_x(s)	e)
Polymer	P(s)	
Activated surface sites	SiO_2^*(s) $SiO_2C_mF_n^*$(s) $SiOCF_3^*$(s) P^*(s)	f)

a) $C_mF_n^+$ denotes CF^+, CF_2^+, CF_3^+, $C_2F_3^+$, $C_2F_4^+$, $C_2F_5^+$, $C_3F_5^+$, $C_3F_6^+$, $C_3F_7^+$, $C_4F_7^+$ and $C_4F_8^+$. C_mF_n(h) and C_mF_n are hot neutrals and thermal neutral partners of $C_mF_n^+$ species.

b) SiF_x denotes SiF, SiF_2 and SiF_3.

c) R is sputtered photoresist in the gas phase.

d) $SiO_2C_mF_n$(s) represents SiO_2CF(s), SiO_2CF_2(s), SiO_2CF_3(s), $SiO_2C_2F_3$(s), $SiO_2C_2F_4$(s), $SiO_2C_3F_5$(s) and $SiO_2C_3F_6$(s).

e) SiF_x(s) denotes SiF(s), SiF_2(s) and SiF_3(s).

f) $SiO_2C_mF_n^*$(s) and P*(s) represent activated surface partners of $SiO_2C_mF_n$(s) and P(s).

Table E.2 List of reactions in SiO_2 etching mechanism using $Ar/C_4F_8/O_2$ plasma.

Reactions[a]	p_0[b]	E_{th}(eV)[b]	E_r(eV)[b]	Notes
Activation of SiO_2				
$SiO_2(s) + I^+ \rightarrow SiO_2^*(s) + I(h)$	0.9			c)
Sputtering of SiO_2				
$SiO_2(s) + I^+ \rightarrow SiO_2 + I(h)$	0.9	70	140	c), d)
$SiO_2^*(s) + I^+ \rightarrow SiO_2 + I(h)$	0.9	70	140	c), d)
Passivation of SiO_2				
$SiO_2(s) + CF \rightarrow SiO_2CF(s)$	0.4			[1]
$SiO_2(s) + CF_2 \rightarrow SiO_2CF_2(s)$	0.3			[1]
$SiO_2(s) + CF_3 \rightarrow SiO_2CF_3(s)$	0.2			[1]
$SiO_2(s) + C_2F_3 \rightarrow SiO_2C_2F_3(s)$	0.2			[1], e)
$SiO_2^*(s) + CF_x \rightarrow SiO_2CF_x(s)$	0.9			e), f)
$SiO_2^*(s) + C_2F_3 \rightarrow SiO_2C_2F_3(s)$	0.9			e)
Further passivation of complex				
$SiO_2CF(s) + CF_2 \rightarrow SiO_2C_2F_3(s)$	10^{-4}			
$SiO_2CF_2(s) + CF \rightarrow SiO_2C_2F_3(s)$	10^{-4}			
$SiO_2CF_2(s) + CF_2 \rightarrow SiO_2C_2F_4(s)$	10^{-4}			
$SiO_2CF_2(s) + C_2F_3 \rightarrow SiO_2C_3F_5(s)$	10^{-4}			
$SiO_2CF_3(s) + CF \rightarrow SiO_2C_2F_4(s)$	10^{-4}			
$SiO_2CF_3(s) + C_2F_3 \rightarrow SiO_2C_3F_6(s)$	10^{-4}			
$SiO_2C_2F_3(s) + CF_2 \rightarrow SiO_2C_3F_5(s)$	10^{-4}			
$SiO_2C_2F_4(s) + CF \rightarrow SiO_2C_3F_5(s)$	10^{-4}			
$SiO_2C_2F_4(s) + CF_2 \rightarrow SiO_2C_3F_6(s)$	10^{-4}			
Fluorination of passivated surface				
$SiO_2CF(s) + F \rightarrow SiO_2CF_2(s)$	0.1			
$SiO_2CF_2(s) + F \rightarrow SiO_2CF_3(s)$	0.1			
$SiO_2C_2F_3(s) + F \rightarrow SiO_2C_2F_4(s)$	0.1			
$SiO_2C_3F_5(s) + F \rightarrow SiO_2C_3F_6(s)$	0.1			
Etching of passivated surface complex				
$SiO_2CF(s) + I^+ \rightarrow SiF + CO_2 + I(h)$	0.75	35	140	c), g)
$SiO_2CF_2(s) + I^+ \rightarrow SiF_2 + CO_2 + I(h)$	0.75	35	140	c), g)
$SiO_2CF_3(s) + I^+ \rightarrow SiF_3 + CO_2 + I(h)$	0.75	35	140	c), g)
$SiO_2C_2F_3(s) + I^+ \rightarrow SiOCF_3(s) + CO + I(h)$	0.75	35	140	c), g)
$SiO_2C_2F_4(s) + I^+ \rightarrow SiOCF_3(s) + COF + I(h)$	0.75	35	140	c), g)
$SiO_2C_3F_5(s) + I^+ \rightarrow SiO_2CF(s) + C_2F_4 + I(h)$	0.75	35	140	c), g)
$SiO_2C_3F_6(s) + I^+ \rightarrow SiO_2CF_3(s) + C_2F_3 + I(h)$	0.75	35	140	c), g)
$SiOCF_3(s) + I^+ \rightarrow SiF_3 + CO + I(h)$	0.75	35	140	c), g)
$SiO_2CF^*(s) + I^+ \rightarrow SiF + CO_2 + I(h)$	0.75	35	140	c), g)
$SiO_2CF_2^*(s) + I^+ \rightarrow SiF_2 + CO_2 + I(h)$	0.75	35	140	c), g)
$SiO_2CF_3^*(s) + I^+ \rightarrow SiF_3 + CO_2 + I(h)$	0.75	35	140	c), g)

$SiO_2C_2F_3^*(s) + I^+ \rightarrow SiOCF_3(s) + CO + I(h)$	0.75	35	140	c), g)
$SiO_2C_2F_4^*(s) + I^+ \rightarrow SiOCF_3(s) + COF + I(h)$	0.75	35	140	c), g)
$SiO_2C_3F_5^*(s) + I^+ \rightarrow SiO_2CF(s) + C_2F_4 + I(h)$	0.75	35	140	c), g)
$SiO_2C_3F_6^*(s) + I^+ \rightarrow SiO_2CF_3(s) + C_2F_3 + I(h)$	0.75	35	140	c), g)
$SiOCF_3^*(s) + I^+ \rightarrow SiF_3 + CO + I(h)$	0.75	35	140	c), g)
Polymer deposition on activated complex				
$SiO_2C_mF_n^*(s) + CF \rightarrow SiO_2C_mF_n^*(s) + P(s)$	0.002			
$SiO_2C_mF_n^*(s) + CF_2 \rightarrow SiO_2C_mF_n^*(s) + P(s)$	0.0015			
$SiO_2C_mF_n^*(s) + CF_3 \rightarrow SiO_2C_mF_n^*(s) + P(s)$	0.001			
$SiO_2C_mF_n^*(s) + C_xF_y \rightarrow SiO_2C_mF_n^*(s) + P(s)$	0.001			e)
$SiOCF_3^*(s) + CF \rightarrow SiOCF_3^*(s) + P(s)$	0.002			
$SiOCF_3^*(s) + CF_2 \rightarrow SiOCF_3^*(s) + P(s)$	0.0015			
$SiOCF_3^*(s) + CF_3 \rightarrow SiOCF_3^*(s) + P(s)$	0.001			
$SiOCF_3^*(s) + C_xF_y \rightarrow SiOCF_3^*(s) + P(s)$	0.001			e)
Polymer deposition on polymer				
$P(s) + CF \rightarrow P(s) + P(s)$	0.002			
$P(s) + CF_2 \rightarrow P(s) + P(s)$	0.0015			
$P(s) + CF_3 \rightarrow P(s) + P(s)$	0.001			
$P(s) + C_xF_y \rightarrow P(s) + P(s)$	0.001			e)
$P^*(s) + CF \rightarrow P^*(s) + P(s)$	0.02			
$P^*(s) + CF_2 \rightarrow P^*(s) + P(s)$	0.015			
$P^*(s) + CF_3 \rightarrow P^*(s) + P(s)$	0.01			
$P^*(s) + C_xF_y \rightarrow P^*(s) + P(s)$	0.01			e)
Polymer chemical sputtering				
$P(s) + I^+ \rightarrow I(h) + CF_2$	0.3	30	140	d), h)
$P^*(s) + I^+ \rightarrow I(h) + CF_2$	0.3	30	140	d), h)
$P(s) + O^+ \rightarrow COF$	0.2	20	100	g)
$P(s) + O_2^+ \rightarrow O(h) + COF$	0.2	20	100	g)
$P^*(s) + O^+ \rightarrow COF$	0.2	20	100	g)
$P^*(s) + O_2^+ \rightarrow O(h) + COF$	0.2	20	100	g)
Polymer chemical erosion				
$P(s) + F \rightarrow CF_2$	0.001			
$P^*(s) + F \rightarrow CF_2$	0.03			
$P(s) + O \rightarrow COF$	0.5			
$P^*(s) + O \rightarrow COF$	0.9			
Fluorination and etching of Si				
$Si(s) + F \rightarrow SiF(s)$	0.01			
$SiF(s) + F \rightarrow SiF_2(s)$	0.02			
$SiF_2(s) + F \rightarrow SiF_3(s)$	0.03			
$SiF_3(s) + F \rightarrow SiF_4$	0.05			
Chemical, Physical Sputtering Si(s), $SiF_x(s)$				

$Si(s) + I^+ \rightarrow Si + I(h)$	0.1	37.5	100	[2], c), d)
$SiF(s) + I^+ \rightarrow SiF + I(h)$	0.3	10	100	c), g)
$SiF_2(s) + I^+ \rightarrow SiF_2 + I(h)$	0.4	10	100	c), g)
$SiF_3(s) + I^+ \rightarrow SiF_3 + I(h)$	0.5	10	100	c), g)
Polymer deposition on Si(s) and $SiF_x(s)$				
$Si(s) + CF \rightarrow Si(s) + P(s)$	0.5			
$Si(s) + CF_2 \rightarrow Si(s) + P(s)$	0.375			
$Si(s) + CF_3 \rightarrow Si(s) + P(s)$	0.25			
$Si(s) + C_xF_y \rightarrow Si(s) + P(s)$	0.25			e)
$SiF_x(s) + CF \rightarrow SiF_x(s) + P(s)$	0.002			
$SiF_x(s) + CF_2 \rightarrow SiF_x(s) + P(s)$	0.0015			
$SiF_x(s) + CF_3 \rightarrow SiF_x(s) + P(s)$	0.001			
$SiF_x(s) + C_xF_y \rightarrow SiF_x(s) + P(s)$	0.001			e)
Redeposition of SiF_x				
$P(s) + SiF_x \rightarrow P(s) + SiF_x(s)$	0.001			
Erosion of photoresist				
$R(s) + I^+ \rightarrow R + I(h)$	0.01	20	100	c), d)
$R(s) + O \rightarrow COH$	10^{-5}			
Redeposition of gas phase photoresist				
$W(s) + R \rightarrow W(s) + R(s)$	0.01			i)
Polymer deposition on photoresist				
$R(s) + CF \rightarrow R(s) + P(s)$	0.02			
$R(s) + CF_2 \rightarrow R(s) + P(s)$	0.015			
$R(s) + CF_3 \rightarrow R(s) + P(s)$	0.01			
$R(s) + C_xF_y \rightarrow R(s) + P(s)$	0.01			e)
	p_0[j)]	E_{th}(eV)[j)]	E_m(eV)[j)]	Notes
Activation by low energy ions				
$SiO_2C_mF_n(s) + I^+ \rightarrow SiO_2C_mF_n^*(s) + I(h)$	0.1	5	70	c), d)
$SiOCF_3(s) + I^+ \rightarrow SiOCF_3^*(s) + I(h)$	0.1	5	70	c), d)
$P(s) + M^+ \rightarrow P^*(s) + M(h)$	0.3	5	30	c), d), k)
Polymer deposition by low energy ions				
$SiO_2C_mF_n(s) + CF_x^+ \rightarrow SiO_2C_mF_n(s) + P(s)$	0.1	5	70	d), e)
$SiO_2C_mF_n(s) + C_xF_y^+ \rightarrow SiO_2C_mF_n(s) + P(s)$	0.1	5	70	d), e)
$SiOCF_3(s) + CF_x^+ \rightarrow SiOCF_3(s) + P(s)$	0.1	5	70	d), e)
$SiOCF_3(s) + C_xF_y^+ \rightarrow SiOCF_3(s) + P(s)$	0.1	5	70	d), e)

[a)] All ions neutralize on surfaces, returning to gas phase as their hot neutral partner. Ions and their hot neutral partners have the same surface reactions with the same probability. Only surface reactions for ions are shown in the table. All such reactions (with the exception of neutralization) should be duplicated for the ion's hot neutral partner.

b) If E_{th} and E_r are blank, the reaction has no energy dependence and the probability of the reaction is a constant, p_0. If E_{th} and E_r have non-zero values, the reaction has an energy dependent probability (Eq. 1). When the probability of reaction is less than unity, the remaining probability is allocated to non-reactive reflection.

c) I^+ denotes all positive ions. I(h) is the hot neutral partner produced by neutralization of I^+ at a surface.

d) Reaction with physical sputtering angular dependence.

e) CF_x denotes CF, CF_2 and CF_3. CF_x^+ and CF_x(h) denote the ion and hot neutral partners of CF_x. Multi-carbon fluorocarbon radicals having two or more dangling bonds are included in the reaction mechanism, collectively referred to as C_xF_y. For the purpose of describing specific reactions, C_2F_3 is used as an example. $C_xF_y^+$ and C_xF_y(h) denote the ion and hot neutral partners of C_xF_y.

f) SiO_2CF_x(s) denotes the group of passivated oxide surface sites by CF_x species, which are SiO_2CF(s), SiO_2CF_2(s) and SiO_2CF_3(s).

g) Reaction with chemical sputtering angular dependence.

h) Polymer sputtered by hot neutrals and ions into the gas phase is represented by CF_2.

i) W(s) represents all surface sites.

j) Probability of surface activation and polymer deposition by low energy ions (Eq. 2).

k) M^+ represents all ions except O^+ and O_2^+. M(h) denotes the hot neutral partner of M^+.

Appendix E References

1. S. S. Kaler, Q. Lou, V. M. Donnelly and D. J. Economou, J. Phys. D: Appl. Phys. **50**, 234001 (2017).
2. N. A. Kubota, D. J. Economou and S. J. Plimpton, J. Appl. Phys. **83**, 4055 (1998).